Reactive transport modeling as a tool for the integrated interpretation of laboratory and field studies in environmental geochemistry

Habilitationsschrift
vorgelegt der
Philosophisch-naturwissenschaftlichen Fakultät
der Universität Bern

von

Christoph Wanner

Januar 2021

TABLE OF CONTENTS

1. INTRODUCTION

1.1 Motivation and outline

Water–rock interaction within the Earth's crust and on its surface is typically controlled by a sequence of coupled processes taking place in porous media at variable space and time scales. For instance, chemical weathering occurring in the shallow subsurface and eventually leading to the formation of soils on the time-scale of 10^2 to 10^3 years is kinetically limited and controlled by the supply of reactive gases such as CO_2 and O_2 (Maher et al., 2009; Li et al., 2017). The complex feedbacks and interrelationships within such coupled systems cannot be understood by traditional geochemical approaches that combine field observations, laboratory analyses and theoretical treatments of the individual uncoupled processes. Conducting processed-based, numerical reactive transport modeling (RTM) offers a unique opportunity for the quantitative, integrated interpretation of such coupled systems. As a consequence, over the past two decades RTM has become an essential tool for the Earth Sciences (Steefel et al., 2005; Li et al., 2017; Druhan and Tournassat, 2019).

Performing RTM is particularly useful for investigating environmental challenges. In their 2030 Agenda for Sustainable Development, the UN General Assembly defined 17 Sustainable Development Goals (SDGs) (United Nations, 2015). Among them, at least four are related to the Earth Sciences:

Goal 6: Ensure availability and sustainable management of water and sanitation for all

Goal 7: Ensure access to affordable, reliable, sustainable and modern energy for all

Goal 13: Take urgent action to combat climate change and its impacts

Goal 15: Protect, restore and promote sustainable use of terrestrial ecosystems, sustainably manage forests, combat desertification, and halt and reverse land degradation and halt biodiversity loss

The link of the listed Goals to the Earth Sciences is given by the fact that they address processes occurring in systems located within or at the surface of the solid Earth. Relevant systems include aquifers used for drinking water supply, geothermal reservoirs, and the Critical Zone, a thin layer at the Earth's surface where chemical weathering takes place (Brantley et al., 2007). All these systems are characterized by a rather strong coupling between physical, geochemical and biogeochemical processes. Therefore, their investigation strongly benefits from the application of RTM.

This *Habilitationsschrift* describes the contributions by the Author to advancing the field of reactive transport modeling. Key accomplishments include (i) the integration of stable isotopes in simulations addressing challenges relevant to environmental geochemistry and (ii) the use of reactive transport models as an exploration tool for geothermal systems. The main aim of this *Habilitationsschrift* is to demonstrate that RTM serves as a powerful tool for obtaining an integrated interpretation of laboratory and/or field studies. Likewise, it aims to emphasize that RTM may contribute towards meeting the UN Sustainable Development Goals 6, 7, 13, and 15.

The following introductory sub-chapters describe the role of coupled processes in environmental geochemistry. These are then followed by an introduction to reactive transport modeling. In Chapter 2, the main contributions by the Author to advancing the field of reactive transport modeling are summarized. Chapters 3–5 present nine of the Author's publications on various RTM applications, which are grouped according to the three major topics addressed (groundwater contamination, geothermal energy, silicate weathering). Finally, common conclusions of the habilitation papers are provided in Chapter 6.

1.2. Coupled processes in environmental geochemistry

The interdisciplinary field of environmental geochemistry studies environmental problems and how these could be solved (Pourret et al., 2020; and references therein). In particular, the discipline investigates how anthropogenic activities and natural processes affect geochemical and biogeochemical cycles of major and trace elements in surface- and subsurface systems and how life is affected by such perturbations. In this *Habilitationsschrift*, the link between environmental geochemistry and the listed sustainability goals is given by the topics of groundwater contamination, geothermal energy and silicate weathering. These topics are introduced in the following sections with an emphasis on the role of coupled processes in the corresponding systems.

1.2.1. Groundwater contamination (UN SDG 6)

Although national statistics are sparse on the global-scale, it is estimated that about one third of the World's population depends on groundwater as its source of drinking water supply (Falkenmark, 2005). Compared to surface waters, the use of groundwater for domestic water provides the key advantage of being less affected by anthropogenic activities, resulting in a much better quality and thus no or only little need for water treatment. As a consequence, in many parts of the world groundwater bodies are the single most important source of drinking-water (Howard et al., 2006). While this is particularly true for rural areas and low-income countries, the same applies for alpine countries where shallow unconsolidated aquifers are frequent and occur on a regional scale. In Switzerland and Austria, for instance, the relative contribution of groundwater to drinking water use accounts for 83 and 98%, respectively (Howard et al., 2006).

Despite being less exposed than surface waters, groundwater may be strongly affected by anthropogenic activities. Typical examples include the improper disposal of industrial or domestic waste (e.g. Wersin et al., 2001; Przydatek and Kanownik, 2019), mining activities (e.g. Nordstrom, 2011), the lack of state-of-the art sanitation systems (e.g. Mukherjee et al., 2019), and the use of fertilizers and pesticides in agriculture (e.g. Buttiglieri et al., 2009). In addition, groundwater quality may be affected by high concentrations of naturally occurring contaminants such as fluoride and arsenic (e.g. Handa, 1975; Wallis et al., 2020).

Groundwater contamination is particularly problematic in arid regions and densely populated areas. In arid regions, groundwater recharge rates are low, causing contaminants to persist over long periods, exceeding several decades or even more (De Vries and Simmers, 2002). In densely populated areas, groundwater contamination is a general issue due to the presence of numerous diffusive and point sources originating from the above-mentioned anthropogenic activities.

The release of contaminants to groundwater bodies and their subsequent retardation is strongly controlled by both inorganic and biogeochemical processes. These include mineral dissolution and precipitation as well as sorption and desorption occurring at solid surfaces. All these processes depend on the bulk water composition such as pH, redox state, and total concentrations of major cations and anions. As a consequence, aqueous complexation reactions are equally important as well. Microbes play a crucial role in the degradation of organic contaminants and may mediate inorganic processes such as mineral dissolution and precipitation, aqueous complexation, as well as sorption and desorption (e.g. Meckenstock et al., 2015; Nazarova et al., 2020).

In addition to geochemical and biogeochemical processes, the contamination hazard for groundwater bodies also depends on hydraulic processes. This is because groundwater flow velocities exert a first order control on the flux and transport rate of mobilized contaminants. Likewise, flow and transport may strongly control the concentrations of major aqueous species, leading to a coupling of hydraulic, geochemical and biogeochemical processes. For instance, microbial iron reduction occurring in biofilms within small pores and the associated release or retardation of contaminants may depend on the combination of advective and diffusive transport of contaminants as well as of nutrients and local biogeochemical reaction networks providing electron donors and acceptors (Steefel et al., 2005). In turn, the local, small-scale processes may provide a feedback to large-

scale flow and transport processes as they affect the physical properties of the subsurface such as porosity and permeability through mineral precipitation and dissolution, as well as biofilm growth (Fig. 1-1).

Overall, environmental geochemistry aiming for a predictive understanding of the coupled processes controlling groundwater quality plays an essential role in maintaining the sustainable use of aquifers. Moreover, because of the great importance of groundwater for global drinking water supply it significantly contributes towards meeting the UN SDG 6. Since groundwater bodies form essential water sources for terrestrial ecosystems, such predictive understanding additionally contributes towards meeting the UN SDG 15.

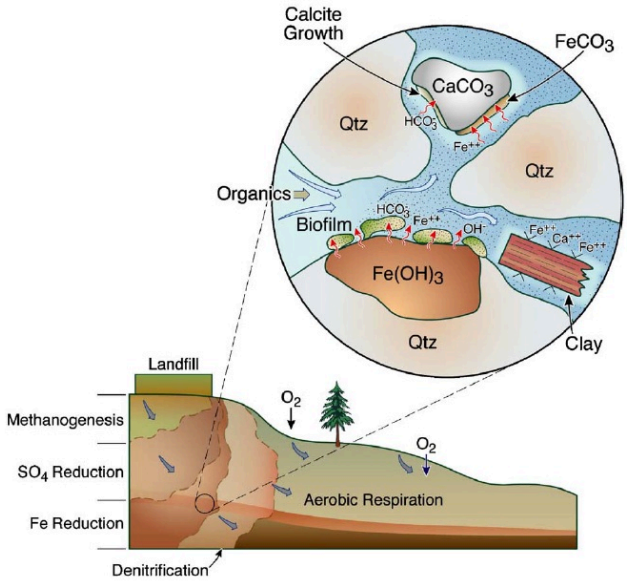

Figure 1-1. Coupling of local biogeochemical reaction networks with large-scale advective flow and transport in an aquifer downstream from an organic-rich landfill. The continuous release of organic carbon leads to the development of oxidation-reduction zones mediated by microbial activity (methanogenesis, SO_4 reduction, Fe reduction, aerobic respiration). Within the Fe reduction zone (inlet), the supply of organic carbon leads to the reductive dissolution of $Fe(OH)_3$ accompanied by the release of Fe^{2+}, HCO_3^- and OH^- to the pore fluid potentially driving calcite ($CaCO_3$) and siderite ($FeCO_3$) precipitation, and thereby reducing the porosity and permeability of the aquifer. From Steefel et al. (2005).

1.2.2. Geothermal energy (UN SDG 7)

Energy from the Earth's interior is called geothermal energy and constitutes a promising renewable energy resource. The great potential is given by the fact that more than 99 vol.% of the Earth has a temperature above 1000 °C, while only 0.1 vol.% is at a temperature below 100 °C (Stober and Bucher, 2014). Thus, the amount of geothermal energy is essentially unlimited. Moreover, compared to other renewables such as wind and solar energy, its availability is not temporally restricted and does not depend on meteorological conditions. Finally, geothermal energy is essentially available everywhere, although the depth at which useful temperatures are attained depends on specific geological settings of a given location. In practice, the successful exploitation of geothermal energy is highly challenging, which is the reason why in 2017 the share of geothermal energy on total global energy consumption accounted for less than 4.2% (REN21, 2019). For the same year, the proportion of geothermal energy on the global electricity production was less than 0.4% (REN21, 2019) and hence almost negligible.

The main challenges for the widespread, successful exploitation of geothermal energy for electricity production are all related to the fact that exploitation of geothermal energy requires the circulation of fluids in the hot subsurface that can be pumped to the surface in order to extract the available heat. Since the permeability of the subsurface is generally low at depths where temperatures exceed the 120 °C threshold for electricity production (Stober and Bucher, 2014), exploitation of geothermal energy often requires the creation

of engineered reservoirs by hydraulic stimulation. Owing to complicated, spatially variable stress states of targeted reservoirs, the engineering of such enhanced geothermal systems (EGS) by hydraulic stimulation is technically challenging and bears the risk of inducing earthquakes of significant magnitudes (Bachmann et al., 2011; Grigoli et al., 2018).

Once a reservoir is successfully stimulated, the circulation of aqueous fluids will cause mineral reactions (i.e. dissolution and precipitation) at the freshly exposed mineral surfaces. If the net mineral volume change associated with mineral dissolution and precipitation is positive, the reservoir porosity and permeability decrease over time, resulting in a decrease of the efficiency of the geothermal system (Alt-Epping et al., 2013). In a worst-case scenario, the entire reservoir will become clogged due to these geochemical processes. While this phenomenon is triggered by the governing mineral reactions, the rate of the porosity change is mainly controlled by the flow rate through the reservoir (Alt-Epping et al., 2013).

Geochemical processes are also highly relevant within operating geothermal power plants, regardless whether they produce from the stimulated reservoirs described above or from more favorable settings such as water-dominated volcanic systems or deep sedimentary aquifers. This is because the interaction with the produced geothermal fluid may lead to corrosion of the pumps, pipes and surface installations, while the drop in pressure and temperature along the geothermal loop may trigger the precipitation of unwanted minerals such as chalcedony and calcite (Mundhenk et al., 2013; Diamond and Alt-Epping, 2014; Wanner et al., 2017). Unwanted mineral precipitation in geothermal power plants is called scaling and is particularly relevant in the heat-exchanger at the surface (Gunnarsson and Arnórsson, 2005; Zarrouk et al., 2014). Owing to the temperature-dependent solubility of scaling minerals, the temperature difference in the heat exchanger defines the maximum amount of scaling that can form per kg of water. The total amount of scaling forming for a given period in time, however, is further controlled by the production rate of the power plant. Thus, the mitigation of scaling in geothermal power plants, which is indispensable for a successful operation, requires a predictive understanding of the governing coupled thermal-hydraulic-chemical (THC) processes.

Besides being relevant for assessing the permeability evolution of stimulated reservoirs and for mitigation of scaling, the field of environmental geochemistry also contributes to the exploration of geothermal systems. The method of solute geothermometry aims to estimate reservoir temperatures of geothermal systems based on chemical analyses of thermal springs sampled at the Earth's surface (Giggenbach, 1988; Spycher et al., 2014). It makes use of the observation that thermal springs are often out of chemical equilibrium under surface conditions. Therefore, solute geothermometry assumes that chemical equilibrium prevails in the reservoir and that this chemical information is preserved when geothermal fluids are ascending to the surface. Accordingly, the temperatures at which the sampled thermal springs are in chemical equilibrium with the host rocks correspond to the estimated reservoir temperature. These temperatures can for instance be determined by performing geochemical speciation calculations (Spycher et al., 2014). Estimating reservoir temperatures is highly relevant because the reservoir temperature limits the maximum amount of energy that can be potentially exploited from a particular geothermal system. The estimation of reservoir temperatures can be strongly improved if the hydraulic processes occurring during upflow of geothermal fluids, such as mixing with shallow groundwater are taken into account as well (Peiffer et al., 2014).

Overall, environmental geochemistry plays an important role in all stages of geothermal power exploitation. Since geothermal energy meets the criteria of a sustainable and modern form of energy, a predictive understanding of the governing THC processes contributes towards meeting the UN SDG 7.

1.2.3. Silicate weathering (UN SDG 13)

Chemical weathering of silicate minerals on the Earth continents plays a crucial role in many global element cycles. Most importantly, such chemical reactions provide nutrients and energy for the sustenance of terrestrial ecosystems (Brantley et al., 2007). Moreover, weathering of Ca-silicates serves as a major natural sink for atmospheric CO_2 (Berner et al., 1983; Godderis et al., 2009; Li and Elderfield, 2013). Silicate weathering consumes CO_2 because carbonic acid (H_2CO_3) resulting from the dissolution of gaseous CO_2

$$CO_2(g) + H_2O \rightarrow H_2CO_3 \rightarrow H^+ + HCO_3^- \quad (1\text{-}1)$$

forms the major proton (H^+) source driving the dissolution of primary minerals as well as the formation of secondary minerals. Therefore, the transformation of for instance anorthite ($CaAl_2Si_2O_8$) to kaolinite ($Al_2Si_2O_5(OH)_4$)

$$CaAl_2Si_2O_8 + 2H^+ + H_2O \rightarrow Ca^{2+} + Al_2Si_2O_5(OH)_4 \quad (1\text{-}2)$$

can be written by combining equations (1-1) and (1-2):

$$CaAl_2Si_2O_8 + 2CO_2(g) + 3H_2O \rightarrow Ca^{2+} + Al_2Si_2O_5(OH)_4 + 2HCO_3^- \quad (1\text{-}3)$$

If carbonates such as calcite ($CaCO_3$) precipitate as pelagic sediments on the seafloor, CO_2 is eventually transformed into a solid phase:

$$CaAl_2Si_2O_8 + CO_2(g) + 2H_2O \rightarrow CaCO_3 + Al_2Si_2O_5(OH)_4 \quad (1\text{-}4)$$

Although the general geochemical concept of silicate weathering is rather simple and can be explained with a small set of equations as outlined above, it is highly challenging to quantify weathering rates on a global scale through time and their effects on global element cycles. The challenges are inherited from the fact that silicate weathering takes place within a thin layer at the Earth's surface called the Critical Zone (Brantley et al., 2007) where a complicated set of coupled processes occur over variable space and time scales (Fig. 1-2). For instance, the dissolution of silicate minerals is a rather slow, kinetically limited process and depends on the available surface area where aqueous fluid can chemically interact with silicate minerals. As a consequence, physical processes such as frost weathering strongly affect chemical weathering rates by controlling the grain size distribution within the Critical Zone. In addition, chemical weathering is coupled to biological activity, producing CO_2 and thereby accelerating the dissolution of primary silicate minerals (eqs. (1-1) to (1-4)). In turn, chemical weathering controls biological activity by providing nutrients and can accelerate physical weathering if the transformation of primary to secondary minerals results in a net mineral volume increase, potentially causing fracturing of rock fragments.

On the global scale, coupled biological-physical-chemical processes occurring in the Critical Zone are affected by climate, tectonic, and anthropogenic forcings varying over different time scales (Fig. 1-2). The Earth climate varies naturally on time scales ranging from tens of thousands to millions of years due to orbital changes and to the variation in the Earth CO_2 degassing of the Earth (e.g. volcanic activity) (Berner et al., 1983). The temperature and CO_2 content of the Earth's atmosphere exerts a strong control on the hydrologic cycle and water flux through the Critical Zone (Beaulieu et al., 2012). In turn, the subsurface water flux and the CO_2 content of the atmosphere strongly affect chemical weathering rates because together they control the supply of dissolved reactive gases such as CO_2 (eqs. (1-1) to (1-4)). Tectonic activity operating on the time-scale of millions of years controls landscape evolution (Anderson et al., 2007) and thus has a major impact on physical weathering rates. Finally, anthropogenic activity may locally affect the water flux through the Critical Zone by, for instance, land use changes, and thereby also affect silicate weathering rates. The same applies for the short-term, anthropogenically induced global warming (Beaulieu, 2012).

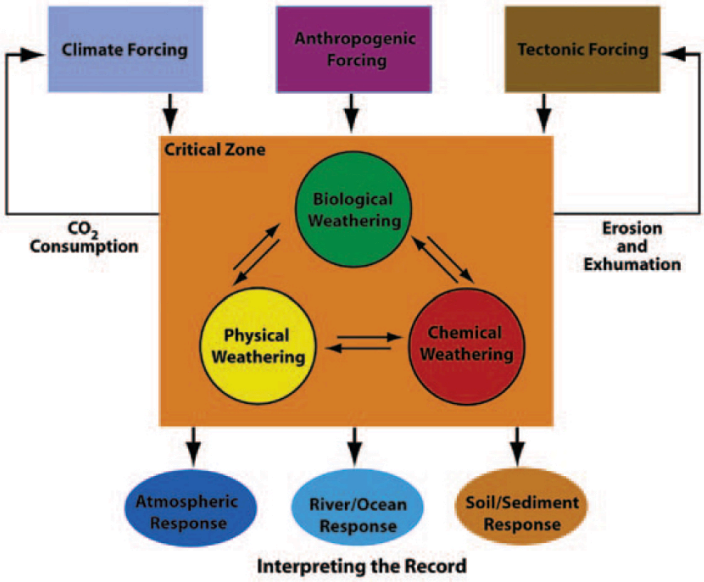

Figure 1-2. Chemical, physical and biological weathering in the Critical Zone are strongly coupled and all of them are controlled by climate, tectonic and anthropogenic forcings. The resulting silicate weathering rates can be estimated by investigating the output from the Critical Zone documented in rivers, soils, and the atmosphere, which may have been preserved in the geological record. From Brantley et al. (2007).

The current global silicate weathering rate can be estimated by quantifying the fluxes of solutes dissolved in major global rivers (Gaillardet et al., 1999). In contrast, owing to the strong coupling between the governing processes and the variation in space and time scales (Fig. 1-2), the estimation of past silicate weathering rates based on the interpretation of sedimentary archives such as paleosols or oceanic sediments is challenging. Therefore, it is still debated how silicate weathering rates have evolved in the past as a function of climate or tectonic activity (Vigier and Goddéris, 2015). For instance, Raymo and Ruddimann (1992) have related the drawdown of atmospheric CO_2 observed over the past 40 Ma to the onset of the Himalayan orogeny by postulating an intensification of global silicate weathering rates. In contrast, Berner et al. (1983) related this CO_2 drawdown to a decrease in total Earth CO_2 degassing of the Earth.

In analogy to the dissolution of silicate minerals, the dissolution of carbonates such as calcite consumes CO_2 ($CaCO_3(s) + CO_2 + H_2O \rightarrow 2HCO_3^- + Ca^{2+}$). On geological timescales, however, the consumed CO_2 is returned back to the atmosphere by the precipitation of carbonates as pelagic sediments on the seafloor ($2HCO_3^- + Ca^{2+} \rightarrow CaCO_3(s) + CO_2 + H_2O$). Therefore, carbonate weathering only operates as an intermediate CO_2 sink. The corresponding timescale is given by the response time of alkalinity (i.e. HCO_3^- concentration) in seawater, which is on the order of 3 ka (Francois and Godderis, 1998).

Overall, environmental geochemistry aiming for a predictive understanding of the coupled processes controlling chemical weathering may improve our understanding of how these phenomena regulate global temperature on timescales ranging from hundreds to millions of years (Beaulieu et al., 2012; Vigier and Goddéris, 2015). Thus, it contributes to assessing the impact of climate change and hence towards meeting the UN SDG 13.

Besides regulating global temperatures on various time scales, the alteration of silicate minerals plays an important role in the engineered, geological storage of CO_2. For instance, the CarbFix project in Iceland re-injects CO_2 produced by the Hellisheiði geothermal power plant into the basaltic subsurface. The concept is highly successful because the chemical interaction between the injected CO_2 and the basaltic mineral phases results in the formation of stable carbonate minerals and thereby minimizes the amount of CO_2 emitted from the geothermal power plant (Clark et al., 2020). In the framework of the UN SDG 13, assessing the efficiency of geological CO_2 storage by silicate weathering plays a crucial role in investigating how climate change can be actively mitigated.

1.3. Introduction to reactive transport modeling (RTM)

1.3.1. RTM as a tool to quantitatively assess coupled processes

Geochemical and biogeochemical processes such as aqueous complexation, mineral dissolution and precipitation, sorption and desorption, as well a microbial growth and decay play a central role in environmental geochemistry. These processes are typically studied through laboratory experiments in combination with a wide range of analytical methods to analyze the corresponding experimental samples. Laboratory experiments are particular useful to study individual reactions and their rates under controlled conditions and thereby obtain a fundamental process-understanding at the sub-millimeter scale. In addition, the quantitative interpretation of field studies requires a simulation tool that is able to capture the coupled behavior of subsurface systems and to upscale experimental findings (Fig. 1-3). This is particularly relevant in many applications of environmental geochemistry as outlined in the previous section. The same, however, also applies to laboratory experiments where geochemical and biogeochemical reactions are transport-limited, such as mineral growth (DePaolo, 2011) or the oxidation of metal surfaces at the presence of passivation layers (Wanner et al., 2011). The main requirements for such tool are to (i) numerically simulate the relevant geochemical and biogeochemical processes in a mechanistic way and (ii) simultaneously capture how they are coupled to flow and transport rates. Over the past 30 years, the field of reactive transport modeling (RTM) has mastered these requirements and thus has become essential for the entire Earth Sciences (Steefel et al., 2005; Li et al., 2017; Druhan and Tournassat, 2019).

The general concept of RTM is introduced in the following section. It should be noted that a detailed description of the numerical background is beyond the scope of this *Habilitationsschrift*. More information on the mathematical concepts of RTM can be found in Steefel et al. (2015) and references therein.

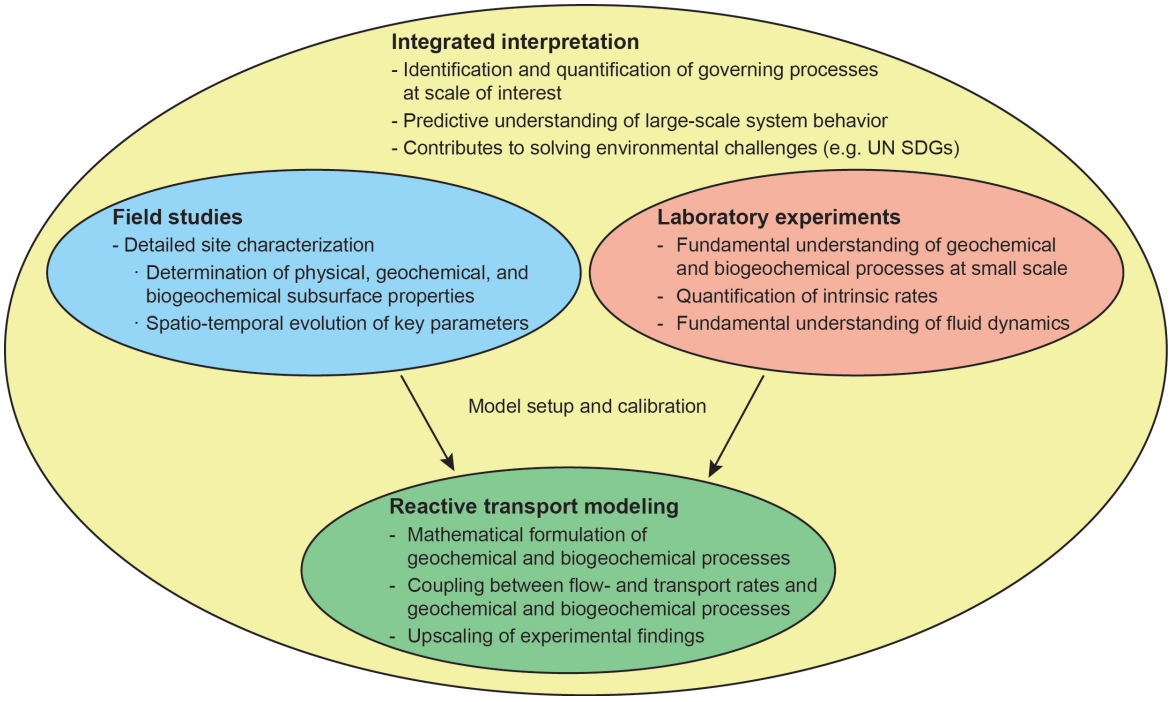

Figure 1-3. Sketch illustrating the role of RTM in obtaining an integrated interpretation of laboratory and/or field studies. The concept applies to the nine *Habilitation* papers presented in Chapters 3–5.

1.3.2. General concept of reactive transport modeling

The overarching principle of reactive transport modeling is that geochemical and biogeochemical reactions occurring along fluid flow paths in porous or fractured media are fully coupled to the governing flow and transport rates. By treating geochemical reactions using a full thermodynamic and kinetic framework, fluid flow rates define the time that is available for a specific reaction to occur between transported fluids and stationary solid phases. For instance, mineral dissolution and precipitation rates r (mol s^{-1} kg_{H2O}^{-1}) are computed based on the transition state theory (Lasaga, 1984),

$$r = A \cdot k \cdot \left[1 - \left(\frac{Q}{K}\right)^m\right]^n \tag{1-5}$$

where A (m^2 kg_{H2O}^{-1}) refers to the mineral's reactive surface area and k is the rate constant (mol m^{-2} s^{-1}). Q and K refer to the ion activity product and equilibrium constant of a mineral dissolution/precipitation reaction, respectively. Exponents m and n are fitting parameters that normally must be experimentally determined although often they are set to unity. The term (1-(Q/K)) ensures that reaction rates are coupled to the thermodynamic state of the system. At chemical equilibrium the ion activity product (Q) is equal to the equilibrium constant (K) and the net reaction rate becomes zero, which has to be the case by definition. The dependence of the rate constant k in eq. (1-5) on temperature and pH is typically formulated as

$$k = k_{25}^{n} exp\left[\frac{-E_a^n}{R}\left(\frac{1}{T} - \frac{1}{298.15}\right)\right] + k_{25}^{ac} exp\left[\frac{-E_a^{ac}}{R}\left(\frac{1}{T} - \frac{1}{298.15}\right)\right] a_{H^+}^{m_{ac}} + k_{25}^{ba} exp\left[\frac{-E_a^{ba}}{R}\left(\frac{1}{T} - \frac{1}{298.15}\right)\right] a_{H+}^{m_{ba}} \tag{1-6}$$

where k_{25} refers to reaction rate constants at 25 °C (mol m^{-2} s^{-1}), E_a is the activation energy (kJ mol^{-1}) and T and R are the temperature (K) and ideal gas constant (8.314 J K^{-1} mol^{-1}), respectively. The superscripts n, ac and ba denote neutral, acidic and basic conditions, respectively, a_{H+} refers to the H^+ activity, and m_{ac} and m_{ba} refer to the reaction order with respect to pH at acidic and basic conditions, respectively. The term (1-(Q/K)) in eq. (1-5) ensures that reaction rates are coupled to the thermodynamic state of the system. At chemically equilibrium the ion activity product (Q) is equal to the equilibrium constant (K) and the net reaction rate becomes zero, which has to be the case by definition.

Similar formulations are used to compute aqueous kinetic and microbially mediated reactions (e.g. Molins et al., 2015). Moreover, reactive transport models typically include equilibrium and kinetic formulations to compute surface complexation and ion exchange reactions, while multi-component aqueous complexation reactions are treated using an entirely thermodynamic (i.e. equilibrium) approach owing to their relatively high rates (Steefel et al., 2015; 2019; and references therein). Thus, reactive transport models are fully process-based and need to be fed by numerous kinetic and thermo-dynamic parameters, which often must be calibrated by a large set of observational data (Fig. 1-3).

Reactive transport codes represent the further development of geochemical speciation and reaction path codes that primarily calculate the equilibrium state of multi-component aqueous systems without considering advective and diffusive transport (Helgeson, 1968; Helgeson et al., 1969; Reed, 1982; Wolery et al., 1990). Nevertheless, it should be noted that geochemical speciation codes are still highly useful for interpreting the chemistry of aqueous solutions (e.g. Wanner et al., 2017; 2018).

The processed-based approach of RTM is also reflected by the characteristic capability of the models to simulate non-isothermal multi-phase flow and transport such as water–brine–gas or water–brine–organic oil mixtures (e.g. Pruess et al., 1999; Pan et al., 2015). The simulation of multi-phase flow is typically enabled by taking into account equations of state to determine the fluid properties (e.g. density, viscosity, volume, enthalpy, mutual solubility) of the simulated phases as a function of pressure, temperature and multi-

component composition of the multi-phase system of interest. For instance, advective mass fluxes of water, u (kg m^{-2} s^{-1}), are calculated according to Darcy's law

$$u = -\frac{k}{\mu}\left(\nabla P - \rho g\right) \tag{1-7}$$

where k is the permeability (m^2), μ is the water viscosity (kg m^{-1} s^{-1}), ∇P (Pa m^{-1}) is the water pressure gradient with respect to distance, ρ is the density of water (kg m^{-3}) and g is the gravitational acceleration (m s^{-2}). Thus, the temperature-dependent definition of fluid viscosity and density couples fluid flow to temperature variations, ensuring the accurate simulation of non-isothermal processes. Likewise, by specifying the permeability as a function of the porosity, fluid flow is coupled to geochemical reactions, which may change the porosity through mineral dissolution or precipitation and hence provide a feedback to flow and transport processes. An example of a porosity-permeability coupling is the Kozeny-Carman relation (Baer, 1972)

$$k = k_i \left(\frac{1-\phi_i}{1-\phi}\right)^2 \left(\frac{\phi}{\phi_i}\right)^3 \tag{1-8}$$

where ϕ_i and ϕ refer to the initial and updated porosity, respectively, and k_i and k are the corresponding permeability values.

One of the most obvious applications of RTM lies in forecasting the future behavior of engineered systems such as groundwater remediation (e.g. Wanner et al., 2012), CO_2 sequestration (e.g. Zheng and Spycher, 2018), or nuclear waster repositories (e.g. Bildstein et al., 2019). In addition, owing to its processes-based approach, reactive transport model simulations are highly useful for unraveling complex interactions between coupled processes and multiple time and space scales (Steefel et al., 2005; Li et al., 2017). Therefore, RTM serves as a synthesizing tool for fundamental Earth Science research and is widely used for the integrated interpretation of laboratory and/or field studies (Fig. 1-3). Examples include elucidating reactive and transport processes in subsurface media ranging from nano-pores such as clay minerals, hydrous silica gels, and cementitious materials (e.g. Tournassat and Steefel, 2019) to the watershed-scale (Li, 2019; Maher and Navarre-Sitchler, 2019), assessing microbial controls on biogeochemical dynamics in the subsurface (e.g. Thullner and Regnier, 2019), and obtaining a predictive understanding of stable isotope fractionation induced by transport and transformation processes (e.g. Druhan et al., 2019).

The applicability of RTM across scales (Fig. 1-4) is enabled by the use of different types of conceptual models. The vast majority of codes and applications use the continuum approach where system properties (e.g. porosity, permeability, mineralogical composition) are averaged over a representative elementary volume, forming the basic model unit for which the governing balance equations are solved (Lichtner, 1996; Steefel et al., 2005; Steefel, 2019). When applied together with the so-called multi-continuum approach, it can be applied to very small scales. The multi-continuum approach is particularly useful to simulate reactive transport within fracture networks characterized by µm-scale fracture apertures (Xu et al., 2001; Xu and Pruess, 2001) or within µm-thick biofilms located on subsurface grains (Xu, 2008). More recently, the discipline of reactive transport modeling has seen the development of pore scale-models, which explicitly treat interfaces between fluid and minerals (Molins et al., 2012; Steefel, 2019). These models are powerful to obtain a predictive understanding of reactive transport problems in single pores and single microbial cells (Li et al., 2008; Scheibe et al., 2009; Fang et al., 2011).

The fact the RTM can be applied to a large range of different time and length scales (Fig. 1-4) is one of its most powerful features. Together with the capability of simulating coupled processes it is the reason why RTM has become such an essential tool and research approach in the Earth Sciences (Steefel et al., 2005; Steefel, 2019). Currently, there exist more than 10 state-of-the-art codes that can simulate fully coupled

geochemical and biogeochemical reactive transport problems in 3D using the continuum approach (Steefel et al., 2015). The maturity of the field of reactive transport modeling is also demonstrated by benchmarking activities showing that the different codes can essentially achieve the same results for a given problem (e.g. Molins et al., 2015; Şengör et al., 2015; Wanner et al., 2015; Poonoosamy et al., 2018; Cheng et al., 2020).

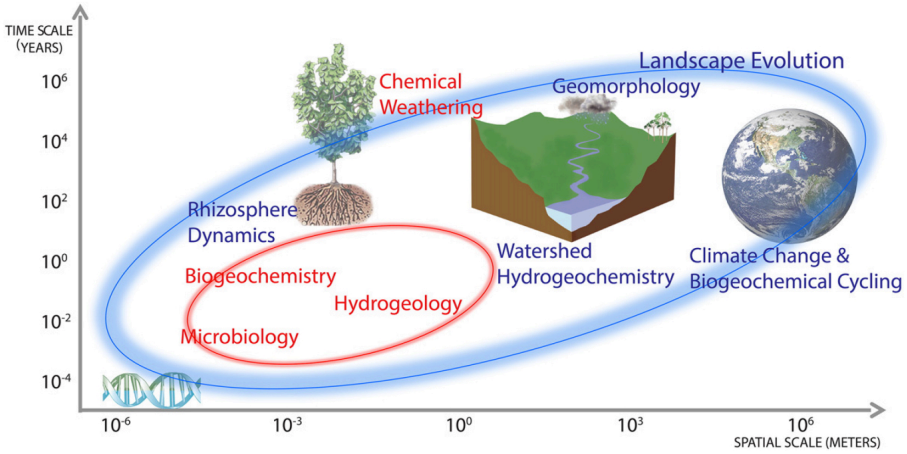

Figure 1-4. Temporal and spatial scales at which RTM is applied. The red ellipsoid marks the most widely used applications whereas the one in blue shows the potential opportunities for the future. From Li et al. (2017).

References

Alt-Epping P., Diamond L. W., Häring M. O., Ladner F. and Meier D. B. (2013) Prediction of water–rock interaction and porosity evolution in a granitoid-hosted enhanced geothermal system, using constraints from the 5 km Basel-1 well. *Appl. Geochem.* **38**, 121-133.

Anderson S. P., von Blanckenburg F. and White A. F. (2007) Physical and Chemical Controls on the Critical Zone. *Elements* **3**, 315-319.

Bachmann C. E., Wiemer S., Woessner J. and Hainzl S. (2011) Statistical analysis of the induced Basel 2006 earthquake sequence: introducing a probability-based monitoring approach for Enhanced Geothermal Systems. *Geophys. J. Int.* **186**, 793-807.

Baer J. (1972) *Dynamics of fluids in porous media*. Dover Publications Inc., New York.

Beaulieu E., Goddéris Y., Donnadieu Y., Labat D. and Roelandt C. (2012) High sensitivity of the continental-weathering carbon dioxide sink to future climate change. *Nat. Clim. Change* **2**, 346-349.

Berner R. A., Lasaga A. C. and Garrels R. M. (1983) The carbonate-silicate geochemical cycle and its effect on atmospheric carbon-dioxide over the past 100 million years. *Am. J. Sci.* **283**, 641-683.

Bildstein O., Claret F. and Frugier P. (2019) RTM for waste repositories. *Rev. Mineral. Geochem.* **85**, 419-457.

Brantley S. L., Goldhaber M. B. and Ragnarsdottir K. V. (2007) Crossing disciplines and scales to understand the critical zone. *Elements* **3**, 307-314.

Buttiglieri G., Peschka M., Frömel T., Müller J., Malpei F., Seel P. and Knepper T. P. (2009) Environmental occurrence and degradation of the herbicide n-chloridazon. *Water Res.* **43**, 2865-2873.

Cheng Y., Arora B., Şengör S. S., Druhan J. L., **Wanner C.**, van Breukelen B. M. and Steefel C. I. (2020) Microbially mediated kinetic sulfur isotope fractionation: reactive transport modeling benchmark. *Comput. Geosci.* in press. https://doi.org/10.1007/s10596-020-09988-9.

Clark D. E., Oelkers E. H., Gunnarsson I., Sigfússon B., Snæbjörnsdóttir S. Ó., Aradóttir E. S. and Gíslason S. R. (2020) CarbFix2: CO_2 and H_2S mineralization during 3.5 years of continuous injection into basaltic rocks at more than 250 °C. *Geochim. Cosmochim. Acta* **279**, 45-66.

De Vries J. J. and Simmers I. (2002) Groundwater recharge: an overview of processes and challenges. *Hydrogeol. J.* **10**, 5-17.

DePaolo D. J. (2011) Surface kinetic model for isotopic and trace element fractionation during precipitation of calcite from aqueous solutions. *Geochim. Cosmochim. Acta* **75**, 1039-1056.

Diamond L. W. and Alt-Epping P. (2014) Predictive modelling of mineral scaling, corrosion and the performance of solute geothermometers in a granitoid-hosted, enhanced geothermal system. *Appl. Geochem.* **51**, 216-228.

Druhan J. L. and Tournassat C. (2019) Preface. *Rev. Mineral. Geochem.* **85**, IV-V.

Druhan J. L., Winnick M. J. and Thullner M. (2019) Stable isotope fractionation by transport and transformation. *Rev. Mineral. Geochem.* **85**, 239-264.

Falkenmark M. (2005) Water usability degradation. *Water Int.* **30**, 136-146.

Fang Y., Scheibe T. D., Mahadevan R., Garg S., Long P. E. and Lovley D. R. (2011) Direct coupling of a genome-scale microbial in silico model and a groundwater reactive transport model. *J. Cotam. Hydrol.* **122**, 96-103.

Francois L. M. and Godderis Y. (1998) Isotopic constraints on the Cenozoic evolution of the carbon cycle. *Chem. Geol.* **145**, 177-212.

Gaillardet J., Dupré B., Louvat P. and Allègre C. J. (1999) Global silicate weathering and CO_2 consumption rates deduced from the chemistry of large rivers. *Chem. Geol.* **159**, 3-30.
Giggenbach W. F. (1988) Geothermal solute equilibria. Derivation of Na-K-Mg-Ca geoindicators. *Geochim. Cosmochim. Acta* **52**, 2749-2765.
Godderis Y., Roelandt C., Schott J., Pierret M. and Francois L. M. (2009) Towards an integrated model of weathering, climate, and biosphere processes. *Rev. Mineral.* **70**, 411-434.
Grigoli F., Cesca S., Rinaldi A. P., Manconi A., López-Comino J. A., Clinton J. F., Westaway R., Cauzzi C., Dahm T. and Wiemer S. (2018) The November 2017 M_w 5.5 Pohang earthquake: A possible case of induced seismicity in South Korea. *Science* **360**, 1003-1006.
Gunnarsson I. and Arnórsson S. (2005) Impact of silica scaling on the efficiency of heat extraction from high-temperature geothermal fluids. *Geothermics* **34**, 320-329.
Handa B. K. (1975) Geochemistry and genesis of fluoride-containing groundwaters in India. *Groundwater* **13**, 275-281.
Helgeson H. C. (1968) Evaluation of irreversible reactions in geochemical processes involving minerals and aqueous solutions—I. Thermodynamic relations. *Geochim. Cosmochim. Acta* **32**, 853-877.
Helgeson H. C., Garrels R. M. and MacKenzie F. T. (1969) Evaluation of irreversible reactions in geochemical processes involving minerals and aqueous solutions—II. Applications. *Geochim. Cosmochim. Acta* **33**, 455-481.
Howard G., Bartram J., Pedley S., Schmoll O., Chorus I. and Berger P. (2006) *Groundwater and public health*, in: Schmoll, O., Howard, G., Chilton, J., Chorus, I. (Eds.), Protecting groundwater for health: managing the quality of drinking-water sources. World Health Organization, London, UK.
Lasaga A. C. (1984) Chemical kinetics of water-rock interactions. *J. Geoph. Res.* **89**, 4009-4025.
Li G. and Elderfield H. (2013) Evolution of carbon cycle over the past 100 million years. *Geochim. Cosmochim. Acta* **103**, 11-25.
Li L., Steefel C. I. and Yang L. (2008) Scale dependence of mineral dissolution rates within single pores and fractures. *Geochim. Cosmochim. Acta* **72**, 360-377.
Li L., Maher K., Navarre-Sitchler A., Druhan J., Meile C., Lawrence C., Moore J., Perdrial J., Sullivan P., Thompson A., Jin L., Bolton E. W., Brantley S. L., Dietrich W. E., Mayer K. U., Steefel C. I., Valocchi A., Zachara J., Kocar B., McIntosh J., Tutolo B. M., Kumar M., Sonnenthal E., Bao C. and Beisman J. (2017) Expanding the role of reactive transport models in critical zone processes. *Earth-Sci. Rev.* **165**, 280-301.
Li L. (2019) Watershed reactive transport. *Rev. Mineral. Geochem.* **85**, 381-418.
Lichtner P. C. (1996) Continuum formulation of multicomponent-multiphase reactive transport. *Rev. Mineral. Geochem.* **34**, 1-82.
Maher K., Steefel C. I., White A. F. and Stonestrom D. A. (2009) The role of reaction affinity and secondary minerals in regulating chemical weathering rates at the Santa Cruz Soil Chronosequence, California. *Geochim. Cosmochim. Acta* **73**, 2804-2831.
Maher K. and Navarre-Sitchler A. (2019) Reactive transport processes that drive chemical weathering: from making space for water to dismantling continents. *Rev. Mineral. Geochem.* **85**, 349-380.
Meckenstock R. U., Elsner M., Griebler C., Lueders T., Stumpp C., Aamand J., Agathos S. N., Albrechtsen H.-J., Bastiaens L., Bjerg P. L., Boon N., Dejonghe W., Huang W. E., Schmidt S. I., Smolders E., Sørensen S. R., Springael D. and van Breukelen B. M. (2015) Biodegradation: updating the concepts of control for microbial cleanup in contaminated aquifers. *Environ. Sci. Technol.* **49**, 7073-7081.
Molins S., Trebotich D., Steefel C. I. and Shen C. (2012) An investigation of the effect of pore scale flow on average geochemical reaction rates using direct numerical simulation. *Water Resour. Res.* **48**.
Molins S., Greskowiak J., **Wanner C.** and Mayer K. U. (2015) A benchmark for microbially mediated chromium reduction under denitrifying conditions in a biostimulation column experiment. *Comput. Geosci.* **19**, 479-496.
Mukherjee A., Duttagupta S., Chattopadhyay S., Bhanja S. N., Bhattacharya A., Chakraborty S., Sarkar S., Ghosh T., Bhattacharya J. and Sahu S. (2019) Impact of sanitation and socio-economy on groundwater fecal pollution and human health towards achieving sustainable development goals across India from ground-observations and satellite-derived nightlight. *Sci. Rep.-UK* **9**, 15193.
Mundhenk N., Huttenloch P., Sanjuan B., Kohl T., Steger H. and Zorn R. (2013) Corrosion and scaling as interrelated phenomena in an operating geothermal power plant. *Corros. Sci.* **70**, 17-28.
Nazarova T., Alessi D. S., Janssen D. J., Bernier-Latmani R. and **Wanner C.** (2020) In situ biostimulation of Cr(VI) reduction in a fast-flowing oxic aquifer. *ACS Earth Space Chem.* **4**, 2018-2030.
Nordstrom D. K. (2011) Mine waters: acidic to circmneutral. *Elements* **7**, 393-398.
Pan L., Spycher N., Doughty C. and Pruess K. (2015) *ECO2N V2.0: a new TOUGH2 fluid property module for mixtures of water, NaCl, and CO_2*. Lawrence Berkeley National Laboratory, Berkeley, Ca. https://tough.lbl.gov/software/
Peiffer L., **Wanner C.**, Spycher N., Sonnenthal E. L., Kennedy B. M. and Iovenitti J. (2014) Multicomponent vs. classical geothermometry: insights from modeling studies at the Dixie Valley geothermal area. *Geothermics* **51**, 154-169.
Poonoosamy J., **Wanner C.**, Alt Epping P., Águila J. F., Samper J., Montenegro L., Xie M., Su D., Mayer K. U., Mäder U., Van Loon L. R. and Kosakowski G. (2018) Benchmarking of reactive transport codes for 2D simulations with mineral dissolution–precipitation reactions and feedback on transport parameters. *Comput. Geosci.* in press. https://doi.org/10.1007/s10596-018-9793-x.
Pourret O., Bollinger J.-C. and van Hullebusch E. D. (2020) On the difficulties of being rigorous in environmental geochemistry studies: some recommendations for designing an impactful paper. *Environ. Sci. Pollut. R.* **27**, 1267-1275.
Pruess K., Oldenburg C. and Moridis G. (1999) *TOUGH2 users's guide, Version 2.0* Lawrence Berkeley National Laboratory, Berkeley, Ca. https://tough.lbl.gov/software/

Przydatek G. and Kanownik W. (2019) Impact of small municipal solid waste landfill on groundwater quality. *Environ. Monit. Assess.* **191**, 169.
Raymo M. E. and Ruddiman W. F. (1992) Tectonic forcing of late Cenozoic climate. *Nature* **359**, 117-122.
Reed M. H. (1982) Calculation of multicomponent chemical-equilibria and reaction processes in systems involving minerals, gases and an aqueous phase. *Geochim. Cosmochim. Acta* **46**, 513-528.
REN21 (2019) *Renewables 2019 Global Status Report*. https://www.ren21.net/gsr-2019/.
Scheibe T. D., Mahadevan R., Fang Y., Garg S., Long P. E. and Lovley D. R. (2009) Coupling a genome-scale metabolic model with a reactive transport model to describe in situ uranium bioremediation. *Microb. Biotechnol.* **2**, 274-286.
Şengör S. S., Mayer K. U., Greskowiak J., **Wanner C.**, Su D. and Prommer H. (2015) A reactive transport benchmark on modeling biogenic uraninite re-oxidation by Fe(III)-(hydr)oxides. *Comput. Geosci.* **19**, 569-583.
Spycher N., Peiffer L., Sonnenthal E. L., Saldi G., Reed M. H. and Kennedy B. M. (2014) Integrated multicomponent solute geothermometry. *Geothermics* **51**, 113-123.
Steefel C. I., DePaolo D. J. and Lichtner P. C. (2005) Reactive transport modeling: An essential tool and a new research approach for the Earth sciences. *Earth Planet. Sci. Lett.* **240**, 539-558.
Steefel C. I., Appelo C. A. J., Arora B., Jacques D., Kalbacher T., Kolditz O., Lagneau V., Lichtner P. C., Mayer K. U., Meussen H., Molins S., Moulton D., Parkhurst D. L., Shao H., Simunek J., Spycher N., Yabusaki S. and Yeh G. T. (2015) Reactive transport codes for subsurface environmental simulation. *Comput. Geosci.* **19**, 445-478.
Steefel C. I. (2019) Reactive transport at the crossroads. *Rev. Mineral. Geochem.* **85**, 1-26.
Stober I. and Bucher K. (2014) *Geothermie*. Springer-Verlag GmbH, Berlin Heidelberg.
Thullner M. and Regnier P. (2019) Microbial controls on the biogeochemical dynamics in the subsurface. *Rev. Mineral. Geochem.* **85**, 265-302.
Tournassat C. and Steefel C. I. (2019) Reactive transport modeling of coupled processes in nanoporous media. *Rev. Mineral. Geochem.* **85**, 75-109.
United Nations (2015) Transformiming our world: the 2030 *Agenda for Sustainable Development*. https://sustainabledevelopment.un.org/post2015/transformingourworld/publication retrieved on December 8, 2020.
Vigier N. and Goddéris Y. (2015) A new approach for modeling Cenozoic oceanic lithium isotope paleo-variations: the key role of climate. *Clim. Past* **11**, 635-645.
Wallis I., Prommer H., Berg M., Siade A. J., Sun J. and Kipfer R. (2020) The river–groundwater interface as a hotspot for arsenic release. *Nat. Geosci.* **13**, 288-295.
Wanner C., Eggenberger U. and Mäder U. (2011) Reactive transport modeling of Cr(VI) treatment under fast flow conditions. *Appl. Geochem.* **26**, 1513-1523.
Wanner C., Eggenberger U. and Mäder U. (2012) A chromate-contaminated site in southern Switzerland, part 2: Reactive transport modeling to optimize remediation options. *Appl. Geochem.* **27**, 655-662.
Wanner C., Druhan J., Amos R., Alt-Epping P. and Steefel C. (2015) Benchmarking the simulation of Cr isotope fractionation. *Comput. Geosci.* **19**, 497-521.
Wanner C., Eichinger F., Jahrfeld T. and Diamond L. W. (2017) Causes of abundant calcite scaling in geothermal wells in the Bavarian Molasse Basin, Southern Germany. *Geothermics* **70**, 324-338.
Wanner C., Pöthig R., Carrero S., Fernandez-Martinez A., Jäger C. and Furrer G. (2018) Natural occurrence of nanocrystalline Al-hydroxysulfates: Insights on formation, Al solubility control and As retention. *Geochim. Cosmochim. Acta* **238**, 252-269.
Wersin P., Abrecht J. and Höhener P. (2001) Large-scale redox plume in glaciofluvial deposits due to sugar-factory wastes and wastewater at Aarberg, Switzerland. *Hydrogeol. J.* **9**, 282-296.
Wolery T. J., Jackson K. J., Bourcier W. L., Bruton C. J., Viani B. E., Knauss K. G. and Delany J. M. (1990) Current status of the EQ3/6 software package for geochemical modeling. *Chemical Modeling of Aqueous Systems II* **416**, 104-116.
Xu T. and Pruess K. (2001) On fluid flow and mineral alteration in fractured caprock of magmatic hydrothermal systems. *J. Geoph. Res.* **106**, 2121-2138.
Xu T., Sonnenthal E., Spycher N., Pruess K., Brimhall G. and Apps J. (2001) Modeling Multiphase Non-Isothermal Fluid Flow and Reactive Geochemical Transport in Variably Saturated Fractured Rocks: 2. Applications to Supergene Copper Enrichment and Hydrothermal Flows. *Am. J. Sci.* **301**, 34-59.
Xu T. (2008) Incorporating aqueous reaction kinetics and biodegradation into TOUGHREACT: Applying a multiregion model to hydrobiogeochemical transport of denitrification and sulfate reduction. *Vadose Zone J.* **7**, 305-315.
Zarrouk S. J., Woodhurst B. C. and Morris C. (2014) Silica scaling in geothermal heat exchangers and its impact on pressure drop and performance: Wairakei binary plant, New Zealand. *Geothermics* **51**, 445-459.
Zheng L. and Spycher N. (2018) Modeling the potential impacts of CO_2 sequestration on shallow groundwater: The fate of trace metals and organic compounds before and after leakage stops. *Greenhouse Gases: Sci. Technol.* **8**, 161-184.

2. CONTRIBUTIONS BY THE AUTHOR TO ADVANCING AND APPLYING RTM

In the past years the Author has contributed to advancing the field of reactive transport modeling. Key accomplishments include the development of approaches for (i) the integration of stable isotopes in reactive transport models and (ii) the use of reactive transport models as an exploration tool for geothermal systems. These contributions are detailed in the following sections and resulted, among others, in the nine peer-reviewed key publications forming the core of this *Habilitationsschrift* (Table 2-1).

2.1. Integration of stable isotopes in reactive transport models

The variation of stable isotope ratios (*R)* in environmental samples, typically expressed as delta values describing the per mil deviation from a standard ($\delta = (R_{sample}/R_{standard} -1) \times 1000$), may serve as a powerful proxy to identify sources and processes that have affected such samples (Wiederhold, 2015). The classical example is the fractionation of the stable isotopes of H and O during the condensation of atmospheric water vapor, causing a variation of δ^2H and $\delta^{18}O$ values in rain as a function of temperature and therefore latitude as well as altitude (Dansgaard, 1964). More recently, analytical developments enabled the determination of stable isotope ratios of environmental contaminants such as Cr, Hg, Cd, Se, and U in aqueous or solid samples, providing important information on the origin and fate of these contaminants in the subsurface (Wiederhold, 2015; and references therein). For instance, the reduction of Cr(VI) to Cr(III), which strongly controls the mobility and toxicity of Cr in the environment, is the only known process that leads to a significant fractionation of the four stable Cr isotopes (Ellis et al., 2004). As a consequence, a variation in Cr isotope ratios of water samples can prove that the reduction of Cr(VI) to Cr(III) is a relevant process and thereby limit the mobility and toxicity of Cr in the subsurface (Berna et al., 2010; Wanner et al., 2012).

While sources and processes can be well identified based on measured stable isotope ratios, the quantification of individual processes is more challenging. This is because stable isotope ratios often reflect the interplay between multiple processes each having a distinctive effect on the resulting isotope ratios. Interpreting isotope ratios is particularly difficult when multiple sources with different isotopic signatures are present and when multiple degradation pathways occur with different isotopic fractionation factors. For reactive systems, an additional difficulty is that effective fractionation factors may be variable and depend on reaction as well as transport rates (DePaolo, 2011). Thus, performing reactive transport modeling is the only viable option if the individual contributions of all potential processes on the resulting isotopic ratios need to be quantitatively assessed. In other words, the integrated interpretation of stable isotope data from laboratory and/or field studies can strongly benefit from the application of RTM.

Despite the apparent benefit, fully coupled reactive transport model applications including the fate of stable isotopes are relatively rare and have only emerged over the past 10–15 years (e.g. Singleton et al., 2005; Van Breukelen et al., 2005; Gibson et al., 2011; Druhan et al., 2012; Jamieson-Hanes et al., 2012; Druhan et al., 2013; Eckert et al., 2013; Druhan et al., 2014; Druhan and Maher, 2017; Druhan et al., 2019). In this *Habilitationsschrift* the integration of stable isotopes in reactive transport model simulations forms a central element. Seven of the nine *Habilitation* papers discuss RTM applications where the stable isotopes of Cr, U, Li, H, and O were explicitly integrated into the simulations (Table 2-1). The main contributions of these studies were (i) the development of approaches to elucidate the effects of small-scale transport processes on larger-scale, effective fractionation factors and (ii) to simulate stable isotope fractionation during the uptake of trace elements (e.g. Li) in precipitating secondary minerals. Both approaches are described below. An additional contribution relates to benchmarking the numerical approaches for simulating isotopic fractionation during mineral precipitation, aqueous speciation, and microbial degradation reactions (Wanner et al., 2015; Cheng et al., 2020, coauthored by the Author).

Table 2-1. Key publications by the Author in the field of reactive transport modeling forming the core of this *Habilitationsschrift* (Chapters 3–5)

Nr .	Authors	Year	Title	Journal	Type of advancement	Type of application
#1	**Wanner, C**., Sonnenthal, E.L	2013	Assessing the control on the effective kinetic Cr isotope fractionation factor: A reactive transport modeling approach	Chemical Geology 337-338, 88-98	Stable isotopes	
#2	Basu, A., **Wanner, C**., Johnson, T.M., Lundstrom, C.C., Sanford, R.A., Sonnenthal, E. L., Boyanov, M.I., Kemner, K.M.	2020	Microbial U isotope fractionation depends on the U(VI) reduction rate	Environmental Science & Technology 54, 2295-2303	Stable isotopes	Groundwater contamination
#3	**Wanner, C**., Druhan, J., Amos, R., Alt-Epping, P., Steefel, C. I.	2015	Benchmarking the simulation of Cr isotope fractionation	Computational Geosciences 19, 497-521	Stable isotopes	
#4	**Wanner, C**., Peiffer, L., Sonnenthal, E.L., Spycher, N., Iovenitti, J., Kennedy, B.M	2014	Reactive transport modeling of the Dixie Valley geothermal area: Insights on flow and geothermometry	Geothermics 51, 130-141	Exploration of geothermal systems	
#5	**Wanner, C**., Diamond, L. W., Alt-Epping, P.	2019	Quantification of 3-D thermal anomalies from surface observations of an orogenic geothermal system (Grimsel Pass, Swiss Alps)	Journal of Geophysical Research: Solid Earth 124, 10839-10854	Exploration of geothermal systems	Geothermal energy
#6	**Wanner, C**., Waber, H.N., Bucher, K.	2020	Geochemical evidence for regional and long-term topography-driven groundwater flow in an orogenic crystalline basement (Aar Massif, Switzerland)	Journal of Hydrology 581, 124374	Exploration of geothermal systems / stable isotopes	
#7	**Wanner, C**., Sonnenthal., E.L., Liu, X-M	2014	Seawater δ^7Li: a direct proxy for global CO_2 consumption by continental silicate weathering?	Chemical Geology 381, 154-167	Stable isotopes	
#8	Liu, X.-M., **Wanner, C**., Rudnick, R., McDonough, W	2015	Processes controlling δ^7Li in rivers illuminated by study of streams and ground waters draining basalts	Earth and Planetary Science Letters 409, 212-224	Stable isotopes	Silicate weathering
#9	**Wanner, C**., Bucher, K., Pogge von Strandmann, P.A.E., Waber, N., Pettke, T.	2017	On the use of Li isotopes as a proxy for water-rock interaction in fractured crystalline rocks: a case study from the Gotthard rail base tunnel	Geochimica et Cosmochimica Acta 198, 396-418.	Stable isotopes	

2.1.1. Multi-region and solid solution approach for integrating Cr and U isotopes

In Wanner and Sonnenthal (2013) a multi-region and solid solution approach was developed to elucidate the effects of small-scale diffusive transport on the effective and hence observable Cr isotope fractionation factor α. For Cr isotopes, α is defined as the ratio of the Cr isotope ratio ($^{53}Cr/^{52}Cr$) in the two stable Cr redox states (Cr(III) and Cr(VI)) and describes the magnitude of Cr isotope fractionation during the reduction of Cr(VI) to Cr(III). The multi-region approach was adopted from Xu et al. (2008) and allowed to physically separate the location of Cr(VI) reduction from the bulk solution (Fig. 2-1). Such an approach was crucial to test the assumption that Cr(VI) reduction occurs as a two-step process with diffusive Cr(VI) transport through a boundary layer ("immobile region") followed by reduction at a reactive site ("mineral region"), and to simulate the corresponding effects on the Cr isotope composition of the bulk solution ("mobile region"). The fate of the two most abundant Cr isotopes was simulated by defining them as individual aqueous species and by assuming that Cr(III) precipitates as an ideal isotopic solid solution forming the final product of Cr reduction. For instance, the reduction of Cr(VI) by Fe^{2+} was simulated as two individual kinetic reactions for ^{52}Cr and ^{53}Cr:

$$^{52}CrO_4^{2-} + 5H^+ + 3Fe^{2+} \rightarrow {}^{52}Cr(OH)_{3(s)} + 3Fe^{3+} + H_2O \quad (2\text{-}1)$$

$$^{53}CrO_4^{2-} + 5H^+ + 3Fe^{2+} \rightarrow {}^{53}Cr(OH)_{3(s)} + 3Fe^{3+} + H_2O \quad (2\text{-}2)$$

$^{52}Cr(OH)_{3(s)}$ and $^{53}Cr(OH)_{3(s)}$ were defined as endmembers of an ideal solid solution with an overall precipitation rate r_{ss} (mol kg_{H2O}^{-1} s^{-1}) corresponding to the sum of the precipitation rate of the two endmembers ($r_{ss} = r_{52Cr} + r_{53Cr}$). The precipitation rates of the individual endmembers were computed using a transition-state theory type (Lasaga, 1984) rate law

$$r_{^{52}Cr} = A \cdot k \left(1 - \frac{Q_{^{52}Cr}}{K_{^{52}Cr}}\right) + A \cdot k \left(x_{^{52}Cr} - 1\right) \quad (2\text{-}3)$$

$$r_{^{53}Cr} = A \cdot k \left(1 - \frac{Q_{^{53}Cr}}{K_{^{53}Cr}}\right) + A \cdot k \left(x_{^{53}Cr} - 1\right) \quad (2\text{-}4)$$

where A ($m^2_{mineral}$ kg_{H2O}^{-1}) and k (mol kg_{H2O}^{-1} m^{-2} s^{-1}) refer to the reactive surface area and the reaction rate constant of the solid solution, respectively. Q_{52Cr} and Q_{53Cr} are the ion activity products of reactions 2-1 and 2-2, and K_{52Cr} and K_{53Cr} refer to the corresponding equilibrium constants. x_{52Cr} and x_{53Cr} are the mole fractions of the precipitating end members and depend on the isotopic composition of the corresponding aqueous phase. With such a formulation, the ratio of the equilibrium constants of the two endmembers refers to the intrinsic isotope fractionation factor considered for a particular simulation ($\alpha_{in}=K_{52Cr}/K_{53Cr}$). Moreover, the formulation ensures that the isotope ratio of the precipitating Cr(III) depends on the Cr isotope ratio of the co-existing Cr(VI) solution.

Performing generic reactive transport simulations using the code TOUGHREACT (Xu et al., 2011) in combination with the developed multi-region and solid solution approach (Fig. 2-1a) suggested that the effective Cr isotope fractionation factor (α_{eff}) is muted by high reduction rates or by slow transport through boundary layers. Subsequently, the approach was applied to simulate a previously published experiment (Dossing et al., 2011) where dissolved Cr(VI) was reduced by the dropwise addition of an Fe(II)-solution and where an unusually low effective Cr isotope fractionation factor was observed (-1.5‰ in terms of the enrichment factor ε, defined as $\varepsilon = (\alpha\text{-}1) \times 1000 \approx \delta^{53}Cr_{Cr(III)} - \delta^{53}Cr_{Cr(VI)}$). Assuming that Cr(VI) reduction only occurs within a small volume near the inlet of the Fe(II)-solution, these simulations well approximated the experimental Cr data when specifying an intrinsic Cr isotope enrichment factor consistent with literature values (ε_{in} = -3.4‰) and calibrating the volume of the "region" where Cr(VI) reduction actually occurs (Fig. 2-1b).

The postulated muting of effective isotope fractionation factors (Wanner and Sonnenthal, 2013) was further confirmed when the same multi-region modeling approach was used to simulate batch experiments investigating the microbial reduction of U(VI) to U(IV) (Basu et al., 2020, coauthored by the Author). The experiments of Basu et al. (2020, coauthored by the Author) were carried out at different U(VI) reduction rates and resulted in highly variable U fractionation factors that inversely correlated with the U(VI) reduction rate. The corresponding simulations reproduced the experimentally determined fractionation factors almost perfectly when varying the reduction rate according to the experimental setup. Together with the results reported in Wanner and Sonnenthal (2013), this emphasized that the spatial decoupling of bulk solutions and reactive sites is highly relevant and should be taken into account for interpreting U and Cr isotope data from the environment. Moreover, it suggested that the same likely applies for similar redox active elements such as Mo and Se.

Obtaining a predictive understanding of effective fractionation factors (α_{eff}) is highly important for assessing the environmental impact caused by Cr and U contaminations. This is because the extent of reduction deduced from corresponding isotope ratios is highly sensitive to the considered fractionation factor (Berna et al., 2010; Wanner et al., 2012). This is illustrated by the classical Rayleigh equation

$$\delta^{53}Cr_x = \left(\left(\delta^{53}Cr_{source} + 1000\right) f^{\alpha_{eff}-1}\right) - 1000 \qquad (2\text{-}5)$$

where $\delta^{53}Cr_x$ and $\delta^{53}Cr_{source}$ refer to the Cr isotope composition measured at a given location x and at the origin of the contamination, respectively, α_{eff} is the effective, system-wide Cr isotope fractionation factor, and *f* refers to the remaining Cr(VI) fraction at location x and thus describes the extent of Cr(VI) reduction occurring between the Cr source and the sampling location.

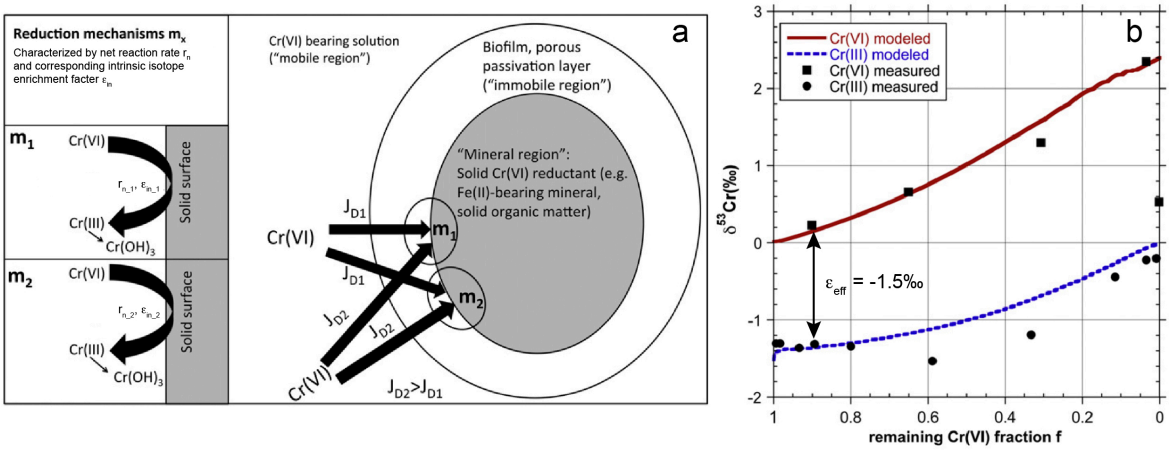

Figure 2-1. a) Conceptual model to simulate Cr(VI) reduction and associated Cr isotope fractionation. The model assumes that Cr(VI) reduction occurs as a two-step process with (i) diffusive Cr(VI) transport (J_D) from the bulk solution ("mobile region") through a boundary layer ("immobile region") to a reactive site such as mineral surfaces or active enzymes where (ii) Cr(VI) reduction is actually occurring ("mineral region"). r_n and ε_{in} refer to the net reduction rate and intrinsic isotope enrichment factor describing the reduction of Cr(VI) to Cr(III) at the reactive site. b) $\delta^{53}Cr$ values observed during the aqueous Cr(VI)-Fe(II) reduction experiment performed by Dossing et al. (2011) (symbols), and corresponding simulation results (lines). For both Cr pools (Cr(VI) and Cr(III)), $\delta^{53}Cr$ values are plotted against the remaining Cr(VI) fraction in the experimental solution. For the simulations ε_{in} was set to -3.4‰, which allowed to reproduce the effective epsilon (-1.5‰) when limiting Cr(VI) reduction to a small region near the inlet of the Fe(II) solution. Modified from Wanner and Sonnenthal (2013).

2.1.2. Update of solid-solution approach for integrating isotopes of trace elements (e.g. Li)

A similar solid-solution approach as developed to integrate Cr and U isotopes in RTM simulations was used to simulate Li isotope fractionation during the uptake of trace amounts of Li by precipitating secondary minerals (Wanner et al., 2014b). The motivation for integrating Li isotopes in reactive transport model simulations was that Li isotope ratios may serve as a powerful tool to track water-rock interaction in crystalline rocks such as during silicate weathering (Pogge von Strandmann et al., 2006; Vigier et al., 2009; Millot et al., 2010). The great potential of Li isotope originates from the fact that the two stable Li isotopes (^{6}Li, ^{7}Li) significantly fractionate during transformation of primary silicate minerals into secondary minerals (Vigier et al., 2008; Wimpenny et al., 2010).

Because Li is incorporated into secondary minerals as a trace element, the integration of Li isotopes in reactive transport model simulations must be treated slightly differently than that of U and Cr isotopes, which constitute major components in the key minerals controlling their fate (e.g., $Cr(OH)_3(s)$ and $UO_2(s)$). Particularly challenging is the fact that, although some suggestions are found in the literature (Pistiner and Henderson, 2003; Vigier et al., 2008), it has not yet been conclusively shown how Li structurally substitutes into relevant secondary minerals such as kaolinite and goethite. Owing to the lack of detailed mineralogical knowledge, the developed approach assumes a solid solution with three different endmembers to simulate Li uptake and associated Li isotope fractionation by secondary minerals: (i) a pure, non-Li bearing endmember, (ii) a pure ^{6}Li bearing mineral endmember and (iii) a pure ^{7}Li bearing endmember. The pure ^{6}Li and ^{7}Li endmembers are hypothetical, but their specification allows fitting experimentally observed aqueous Li concentrations as well as measured amounts of Li that are incorporated in secondary minerals by calibrating the corresponding log(K) values. Besides defining three instead of two endmembers, the initially developed numerical approach is closely related to those used to simulate the fractionation of U and Cr isotopes (eqs. (2-1) to (2-4)) (Wanner et al., 2014b).

The developed approach was eventually used to obtain a predictive understanding of Li concentrations and Li isotope ratios measured in worldwide rivers and thereby relate the Li data to the amount of CO_2 consumed by silicate weathering reactions (Wanner et al., 2014b). One dimensional reactive transport model simulations were run using the code TOUGHREACT (Xu et al., 2011) to assess how Li and its isotopes behave during silicate weathering occurring within (i) granitic aquifers and (ii) rivers draining granitic catchments (Wanner et al., 2014b). Simulation results revealed that riverine δ^7Li is controlled not only by the Li isotope fractionation factor but also by the subsurface residence time, the subsurface weathering intensity and the concentration of a river's suspended load. Applying these findings to Li data collected for worldwide rivers implied that global average riverine and hence seawater δ^7Li values are closely related to the amount of CO_2 globally consumed by continental silicate weathering. As a consequence, the geological seawater δ^7Li record (Misra and Froelich, 2012) may be used to quantify silicate weathering and hence CO_2 consumption rates through geological times. However, the simulations also clearly demonstrated that much more experimental data (e.g. thermodynamic properties of Li-bearing minerals) and hydraulic data (e.g. temporally-variable discharge rates) are needed to quantify CO_2 consumption by silicate weathering based on global riverine and seawater δ^7Li values.

In a second application, the approach for integrating Li isotopes was applied to evaluate Li isotope data collected in streams draining the Columbia River Basalt area in the western USA (Liu et al., 2015, coauthored by the Author). Using a similar 1D model geometry as for simulating granitic systems (Wanner et al., 2014b) allowed to well approximate δ^7Li values and concentration ratios observed in these streams when calibrating the log(K) of secondary Li-bearing kaolinite, the whole rock Li concentration, and the degree of dilution occurring in the streams (Fig. 2-2a). Together with the collected data, these simulations confirmed that Li isotope ratios in streams are strongly controlled by the subsurface residence times of streamwater samples and that Li isotope fractionation is occurring at present within actual rivers due to the interaction between the river water and the suspended load.

In a follow-up study, the numerical approach was updated to include the option of defining a maximum amount of Li that is allowed to precipitate in a given Li-bearing solid solution (Wanner et al., 2017). The motivation for updating the approach was that the incorporation of Li in secondary minerals is typically limited and only occurs at trace concentrations in the ppm range (Tardy et al., 1972). The numerical details describing this option are provided in Chapter 5 and in Wanner et al. (2017). The updated approach was used to simulate the chemical evolution including the fate of Li and its isotopes during the infiltration of meteoric water into a granitic basement of the Central Alps, Switzerland. These simulations were constrained by Li concentrations, Li isotope ratios, as well as major species concentrations measured in groundwater samples discharging into the world's longest and deepest tunnel, the Gotthard railway base tunnel (Wanner et al., 2017). Limiting the Li concentration in secondary kaolinite to 75 mg/kg for the simulations was sufficient to reproduce the observation that groundwater δ^7Li values do not vary in samples discharging from a lithology characterized by high aqueous Li concentrations (1-2 mg/L), and that a strong δ^7Li variation occurs in groundwater samples discharging from another lithology at low Li concentrations (<0.02 mg/L) (Fig. 2-2b). The model-based, integrated interpretation of measured Li data thus suggested that, in addition to the subsurface residence time and the weathering intensity, background aqueous Li concentrations exert a strong control on Li isotope ratios measured in groundwater and rivers. In turn, the strong dependence of δ^7Li on aqueous Li concentrations reveals that quantifying continental silicate weathering rates through time based on, for instance, the Cenozoic seawater δ^7Li record (Misra and Froelich, 2012) will remain challenging.

Overall, integrating Li isotopes in reactive transport model simulations provided detailed insights on the governing processes controlling δ^7Li values in aqueous solutions such as groundwater, rivers and even seawater. This contributed to assessing the strengths and weaknesses of using Li isotopes as a proxy for silicate weathering.

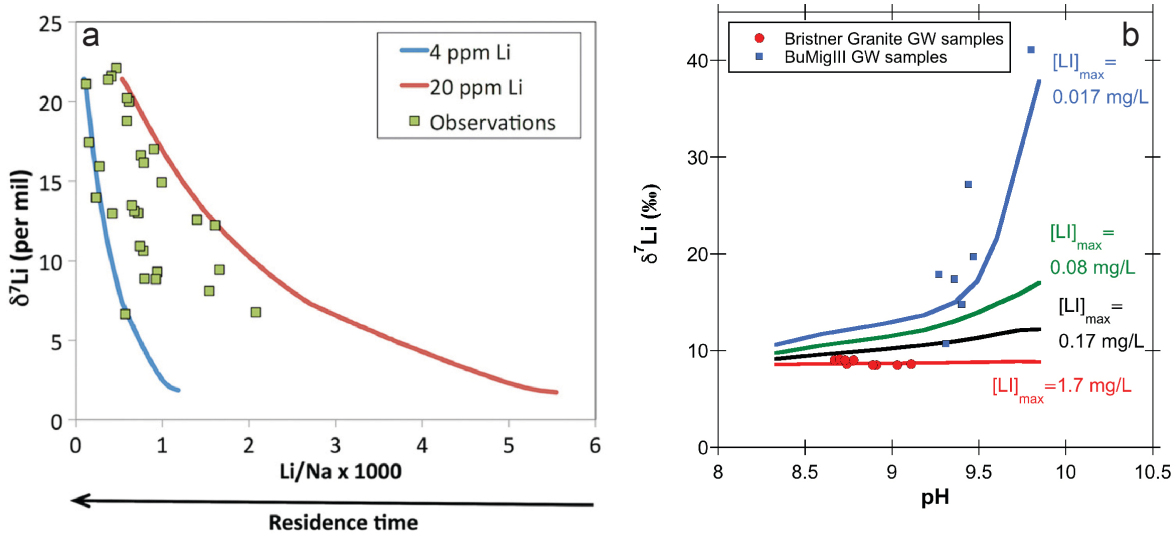

Figure 2-2. Comparisons between measured and simulated Li isotope ratios. a) δ^7Li values vs. Li/Na ratios measured in streams draining the Columbia River Basalt area (symbols) and corresponding simulations results for two different whole rock Li concentrations (lines) (from Liu et al., 2015, coauthored by the Author). In these simulations, the Li/Na ratio and δ^7Li inversely correlated with the subsurface residence time of the streamwater samples. b) δ^7Li vs. pH values measured in groundwater samples discharging from two different lithological units into the Gotthard railway base tunnel (symbols) and corresponding simulation results (lines) for four different aqueous Li concentrations (modified from Wanner et al., 2017). In these simulations, the dependence of δ^7Li on the Li concentration is inherited from limiting the maximum Li concentration in secondary kaolinite to 75 mg/kg.

2.2. The use of reactive transport models as an exploration tool for geothermal systems

In the past 50 years, geochemical tools have been widely used for the exploration of geothermal systems. The most common approach relates to estimating the temperatures of geothermal reservoirs from chemical analyses of thermal springs sampled at the Earth's surface. This approach is called solute geothermometry and is traditionally based on empirical or thermodynamic relationships between species concentrations (e.g. SiO_2) or concentration ratios (e.g. Na/K, K/Mg, Ca/Na) and downhole temperatures in geothermal wells (Fournier and Truesdell, 1973; Fournier, 1979; Fournier and Potter, 1982; Giggenbach, 1988). Alternatively, geochemical modeling is applied to calculate the saturation indices of potential reservoir minerals as a function of temperature (Reed and Spycher, 1984; Spycher et al., 2014). Using geochemical modeling, reservoir temperatures are eventually estimated by the clustering of saturation indices near zero. Since it takes into account the full chemical composition of thermal springs, this method is called multicomponent geothermometry.

All geothermometry methods rely on the assumption that physical (e.g. mixing, boiling, dilution) and chemical processes (e.g. dissolution, precipitation) do not significantly modify the composition of reservoir fluids during their ascent towards the surface. Thus, they assume that the chemical composition of thermal springs reflects chemical equilibrium with respect to the reservoir minerals at reservoir *P*-*T*-conditions. Since this fundamental assumption does not always hold true, it is critical to define under what conditions solute geothermometry methods can be successfully applied. Likewise, it is important to develop approaches to correct for such physical and chemical processes in order to obtain a more reliable estimate of deep reservoir temperatures.

In both cases, RTM plays an important role. Thanks to the coupling of physical and chemical processes, RTM is highly suitable to identify key processes affecting the chemical composition during upflow and to quantify their effects regarding the applicability of various solute geothermometry methods. In turn, once these processes are identified and quantified, the chemical composition of thermal springs can be numerically corrected to obtain an improved estimation of reservoir temperatures. In addition, RTM is highly useful to synthesize results from multiple datasets, including solute geothermometry calculations, and thereby quantify the thermal anomaly of geothermal systems or obtaining more insights into the governing coupled thermal-hydraulic-chemical processes. Thus, RTM may play various roles in the exploration of geothermal systems. Below it is described how the Author contributed to advance these particular RTM applications.

2.2.1. Estimation of reservoir temperatures

The Dixie Valley geothermal area located in the Basin and Range Province in the western USA (Peiffer et al., 2014, coauthored by the Author; and references therein) was used as a model system to assess the applicability of various solute geothermometry methods. With a mean installed capacity of 63 MW and an average reservoir temperatures of 231 °C, Dixie Valley is the hottest and largest geothermal system in the Basin and Range Province (Blackwell et al., 2007). The system has been extensively characterized over the past decades (Goff et al., 2002; Blackwell et al., 2007) and thus constitutes an ideal site for such an assessment.

The evaluation included performing 1D and 2D reactive transport model simulations using the code TOUGHREACT (Xu et al., 2011) and subsequently using the model output for applying various solute geothermometry methods (Peiffer et al., 2014, coauthored by the Author; Wanner et al., 2014a). All simulations were constrained by the geological and hydrogeological setting of the Dixie Valley geothermal area. Running the models for various scenarios of mixing, dilution and rock-water interactions resulted in a large range of chemical compositions for the thermal springs simulated in the numerical models. These compositions were then used to apply different geothermometry methods. Eventually, the resulting temperatures were compared to the "true" reservoir temperatures of the RTM simulations to evaluate the performance of the tested geothermometry methods.

The chosen approach demonstrated that classical geothermometry methods based on element concentrations (e.g. Si) or concentration ratios (e.g. Na/K) yield reasonable temperature estimates in many cases. An important exception, however, is when dilution or mixing with saline waters occurs during ascent of thermal fluids towards the surface. In such cases, multicomponent geothermometry yields much better temperature estimates, especially if poorly constrained concentrations such as Mg and Al are numerically optimized (Peiffer et al., 2014, coauthored by the Author). In contrast, if a fluid ascending to the surface is only affected by cooling, classical geothermometers based on concentration ratios (e.g. Na/K) perform better because these are less affected by mineral dissolution and precipitation during upflow (Wanner et al., 2014a). The combined RTM and solute geothermometry approach, however, also demonstrated that above a critical upflow velocity of 0.1 m d^{-1} and at reactive fracture surface areas below 20 m^2 m^{-3}, the applicability of multicomponent geothermometry is not affected by mineral reactions occurring during upflow (Fig. 2-3).

These findings were eventually applied to thermal springs discharging from the Dixie Valley geothermal area (Peiffer et al., 2014, coauthored by the Author). Constraining multicomponent geothermometry calculations by a large set of chemical analyses of thermal springs, as well as complementary 1D RTM simulations resulted in the identification of two major geothermal reservoirs with significantly different temperatures (240-260 °C vs. 175-190 °C).

A similar approach was applied to determine the deep reservoir temperature of the orogenic geothermal system at Grimsel Pass, Switzerland (Diamond et al., 2018, coauthored by the Author). This system is characterized by the discharge of thermal springs at temperatures up to 28 °C into a shallow tunnel. Fluid flow is driven by the high topography of the area and the presence of a regional fault zone, resulting in fast and nearly vertical fluid ascent towards the discharge locations. Chemical and isotopic analyses of thermal as well as nearby cold springs (Waber et al., 2017, coauthored by the Author) allowed quantification of the shallow admixture of cold water to the ascending thermal fluids. Subsequently, geochemical speciation calculations were performed to numerically correct for the admixture and to obtain an improved estimation of the chemical composition of the thermal fluid at depth. Finally, 1D reactive transport model simulations were run to additionally correct for mineral reactions occurring during upflow. This eventually resulted in an estimated reservoir temperature of at least 230–250°C.

In summary, RTM combined with solute geothermometry methods allowed for a thorough estimation of reservoir temperature in different types of geothermal systems. Since reservoir temperatures limit the maximum energy that can be potentially exploited from a geothermal system, such an approach may contribute to an improved exploration of geothermal systems.

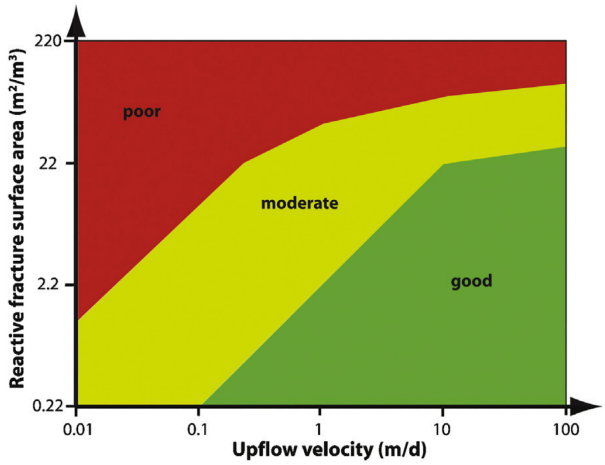

Figure 2-3. Applicability of multicomponent geothermometry as a function of upflow velocities and reactive fracture surface areas. From Wanner et al. (2014a).

2.2.2. Integrated interpretation of multiple datasets

Mountainous orogenic belts such as the Alps are recognized as plays for geothermal power production (Moeck, 2014). To quantitatively assess their geothermal potential and to elucidate the governing thermal-hydraulic-chemical processes, numerical simulations using the code TOUGHREACT (Xu et al., 2011) were performed in 3D for two particular sites in the Central Alps (Wanner et al., 2019; 2020). For both sites, the simulations were constrained and calibrated by multiple datasets and hence served as a synthesizing tool.

For the first site located at Grimsel Pass, Switzerland, the vertical extent of the model was constrained by chemical and isotopic analyses of thermal and cold springs discharging into a shallow tunnel (Wanner et al., 2019). Stable isotope analyses demonstrated that thermal springs originate from meteoric water and suggested that its infiltration occurred at least 500 m above the discharge locations (Fig. 2-4a). Moreover, results from 1D reactive transport model simulations constrained by chemical and radiogenic isotope analyses of the different springs revealed that meteoric water penetrates at least 9–10 km deep into the system where it attains temperatures of at least 230–250°C (Diamond et al., 2018, coauthored by the Author). The permeability of the upflow zone was constrained by hydraulic tests carried out in a borehole intersecting the hydraulically active and steeply-dipping fracture system (Cheng and Renner, 2018). Eventually, large-scale (20 x 20 x 10 km) thermal-hydraulic simulations were performed to quantify the shape, dimensions and magnitude of the 3D subsurface thermal anomaly around the upflow zone. To do so, the geometry of the upflow segment was calibrated by multiple observations of the system (Fig. 2-4a). These included (i) the temperature anomaly observed at the surface, (ii) the total discharge rate of thermal springs, (iii) the corresponding discharge temperature, and (iv) the temperature and depth of the 3.3 Ma old fossil manifestation of the same geothermal system currently outcropping at the surface (Hofmann et al., 2004).

The calibrated model demonstrated that an ellipsoidal thermal plume enclosing 10^2–10^3 PJ of anomalous heat per km depth currently underlies the site at Grimsel Pass (Fig. 2-4b). Moreover, the model suggested that the conditions for geothermal power production were very favorable when the fossil system was active 3.3 Ma ago. For instance, the thermal plume was likely double its present size, corresponding to a theoretical power output on the order of 30–220 MW per km depth. Moreover, at that time the 120 °C threshold for geothermal electricity production was likely situated at less than 2 km depth.

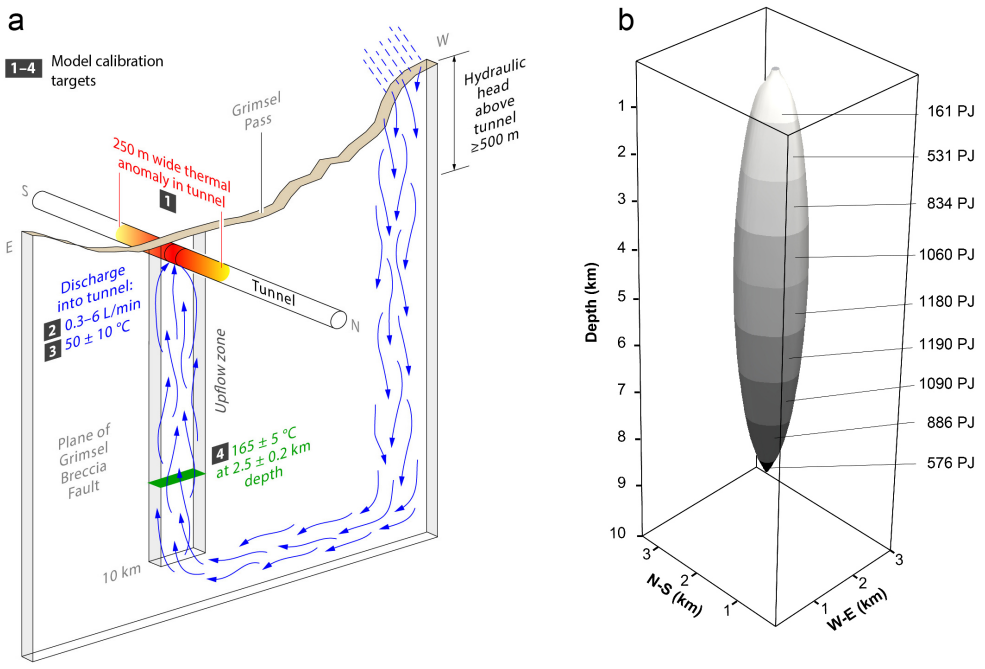

Figure 2-4. a) Conceptual model (not to scale) of the Grimsel Pass geothermal system inferred from multiple observations and used to set up the numerical simulations. Numbers 1–4 show the values of key constraints used as calibration targets for the simulations. b) Anomalous heat per km depth calculated for the model calibrated to the current Grimsel Pass hydrothermal system (Constraints 1–3). Modified from Wanner et al. (2019).

The second application involves thermal-hydraulic-chemical simulations carried out using TOUGHREACT V3 (Xu et al., 2014) for a regional model domain of 20 x 10 x 9 km located in the crystalline basement of the Aar Massif in Switzerland and including the world's largest tunnel, the Gotthard railway base tunnel. For these simulations, the modeling approach used for the Grimsel Pass system was updated to (i) explicitly include the surface topography, which was constrained by a digital elevation model of the model domain, and (ii) simulate the fate of stable water isotopes during the circulation of meteoric water in the orogenic crystalline basement. Interestingly, considering the surface topography for the simulations and calibrating the uptake rate of Cl was sufficient to reproduce all key observations made for the real system. These included the salinity, the temperature, and the stable water isotope composition of a large number (>100) of groundwater samples discharging into the Gotthard railway base tunnel. Moreover, the simulations were able to reproduce the up- and downflow zone identified from the chemical composition of the collected groundwater samples and corresponding multicomponent geothermometry calculations. Subsequently, the model results were used to formulate an integrated interpretation of all information obtained from the groundwater samples discharging into the tunnel. The most important conclusions were (i) the confirmation that fluid flow as well as the occurrence of thermal anomalies in orogenic crystalline basements are controlled by the surface topography and the presence of regional fault zones, and (ii) that down to 9 km depth, penetration of meteoric water is not limited by the decrease in permeability with depth that is typically observed in granitic rocks. This second point suggested that infiltrating meteoric water may reach the brittle–ductile transition zone and thereby attain temperatures well above 150 °C. This further confirmed that orogenic geothermal systems are promising plays for geothermal power production and that exploration should focus on major valley floors because there the hydraulic head gradients and thus upflow rates and heat anomalies reach maximum values. Moreover, the study demonstrated that groundwater residence times in orogenic crystalline basements are likely on the order of several 10 k years, suggesting that groundwater discharging from such systems may act as an archive for palaeohydrologic variations.

A similar modeling approach was applied to the geothermal system at Acoculco in Mexico (Peiffer et al., 2015, coauthored by the Author). This system is manifested by the discrete discharge of large fluxes of cold CO_2 (ca. 25 t/day at T < 30 °C) from a major regional fault zone. Thermal-hydraulic simulations involving two-phases (i.e. immiscible CO_2 gas + CO_2-saturated water) were carried out using the code TOUGH2-ECO2N V2.0 (Pan et al., 2015). These aimed to provide more insights into the processes leading to subsurface CO_2 reservoirs in general, as well as localizing the reservoir beneath Acoculco that feeds the current CO_2 fluxes at the surface. The permeability of the country rock in the model was constrained by the geological characterization of a 2 km deep drillcore. Subsequently, 3D numerical simulations were run for multiple reservoir geometries until the CO_2 fluxes observed at the surface as well as the corresponding discharge temperatures could be reproduced. This modeling exercise eventually led to the conclusion that a hidden reservoir with a significant permeability (>5 x 10^{-15} m^2) is likely located at a depth below 2 km. Based on this conclusion, it was suggested that, future exploration of the system should focus on localizing the postulated reservoir through additional CO_2 flux measurements, geophysical surveys and exploratory drilling to at least 3 km depth.

Overall, constraining and calibrating numerical simulations by multiple datasets has yielded detailed insights into the governing thermal-hydraulic-chemical processes in various types of geothermal systems. Eventually, this has led to the quantification of thermal anomalies as well as the identification of potential geothermal reservoirs. Moreover, it has provided important information for the exploration of similar systems for geothermal power production.

References

Basu A., **Wanner C.**, Johnson T. M., Lundstrom C. C., Sanford R. A., Sonnenthal E. L., Boyanov M. I. and Kemner K. M. (2020) Microbial U isotope fractionation depends on the U(VI) reduction rate. *Environ. Sci. Technol.* **54**, 2295-2303.

Berna E. C., Johnson T. M., Makdisi R. S. and Basu A. (2010) Cr stable isotopes as indicators of Cr(VI) reduction in groundwater: A detailed time-series study of a point-source plume. *Environ. Sci. Technol.* **44**, 1043-1048.

Blackwell D. D., Smith R. P. and Richards M. C. (2007) Exploration and development at Dixie Valley, Nevada: Summary of DOE studies. *Proceedings, thirty-second workshop on geothermal reservoir engineering.* Stanford University, January 22-24, Stanford, Ca. SGP-TR-183

Cheng Y. and Renner J. (2018) Exploratory use of periodic pumping tests for hydraulic characterization of faults. *Geophys. J. Int.* **212**, 543-565.

Cheng Y., Arora B., Şengör S. S., Druhan J. L., **Wanner C.**, van Breukelen B. M. and Steefel C. I. (2020) Microbially mediated kinetic sulfur isotope fractionation: reactive transport modeling benchmark. *Comput. Geosci.* in press. https://doi.org/10.1007/s10596-020-09988-9.

Dansgaard W. (1964) Stable isotopes in precipitation. *Tellus* **16**, 436-468.

DePaolo D. J. (2011) Surface kinetic model for isotopic and trace element fractionation during precipitation of calcite from aqueous solutions. *Geochim. Cosmochim. Acta* **75**, 1039-1056.

Diamond L. W., **Wanner C.** and Waber H. N. (2018) Penetration depth of meteoric water in orogenic geothermal systems. *Geology* **46**, 1063-1066.

Dossing L. N., Dideriksen K., Stipp S. L. S. and Frei R. (2011) Reduction of hexavalent chromium by ferrous iron: A process of chromium isotope fractionation and its relevance to natural environments. *Chem. Geol.* **285**, 157-166.

Druhan J. L., Steefel C. I., Molins S., Williams K. H., Conrad M. E. and DePaolo D. J. (2012) Timing the onset of sulfate reduction over multiple subsurface acetate amendments by measurement and modeling of sulfur isotope fractionation. *Environ. Sci. Technol.* **46**, 8895-8902.

Druhan J. L., Steefel C. I., Williams K. H. and DePaolo D. J. (2013) Calcium isotope fractionation in groundwater: Molecular scale processes influencing field scale behavior. *Geochim. Cosmochim. Acta* **119**, 93-116.

Druhan J. L., Steefel C. I., Conrad M. E. and DePaolo D. J. (2014) A large column analog experiment of stable isotope variations during reactive transport: I. A comprehensive model of sulfur cycling and $\delta^{34}S$ fractionation. *Geochim. Cosmochim. Acta* **124**, 366-393.

Druhan J. L. and Maher K. (2017) The influence of mixing on stable isotope ratios in porous media: A revised Rayleigh model. *Water Resour. Res.* **53**, 1101-1124.

Druhan J. L., Winnick M. J. and Thullner M. (2019) Stable isotope fractionation by transport and transformation. *Rev. Mineral. Geochem.* **85**, 239-264.

Eckert D., Qiu S., Elsner M. and Cirpka O. A. (2013) Model complexity needed for quantitative analysis of high resolution isotope and concentration data from a toluene-pulse experiment. *Environ. Sci. Technol.* **47**, 6900-6907.

Ellis A. S., Johnson T. M. and Bullen T. D. (2004) Using chromium stable isotope ratios to quantify Cr(VI) reduction: Lack of sorption effects. *Environ. Sci. Technol.* **38**, 3604-3607.

Fournier R. O. and Truesdell A. H. (1973) Empirical Na-K-Ca geothermometer for natural waters *Geochim. Cosmochim. Acta* **37**, 1255-1275.

Fournier R. O. (1979) A revised equation for the Na/K geothermometer. *Geoth. Res. Bull.* **11**, 3-12.

Fournier R. O. and Potter R. W. (1982) A revised and expanded silica (quartz) geothermometer. *Geoth. Res. Bull.* **11**, 3-12.

Gibson B. D., Amos R. T. and Blowes D. W. (2011) $^{34}S/^{32}S$ fractionation during sulfate reduction in groundwater treatment systems: reactive transport modeling. *Environ. Sci. Technol.* **45**, 2863-2870.

Giggenbach W. F. (1988) Geothermal solute equilibria. Derivation of Na-K-Mg-Ca geoindicators. *Geochim. Cosmochim. Acta* **52**, 2749-2765.

Goff F., Bergfeld D., Janik J., Counce D. and Murrell M. (2002) *Geochemical data on waters, gases, scales, and rocks from the Dixie Valley Region, Nevada.* Los Alamos National Laboratory Report LA-13972-MS, Los Alamos, NM.

Hofmann B. A., Helfer M., Diamond L. W., Villa I. M., Frei R. and Eikenberg J. (2004) Topography-driven hydrothermal breccia mineralization of Pliocene age at Grimsel Pass, Aar massif, Central Swiss Alps. *Schweiz. Miner. Petrog.* **84**, 271-302.

Jamieson-Hanes J. H., Gibson B. D., Lindsay M. B. J., Kim Y., Ptacek C. J. and Blowes D. W. (2012) Chromium isotope fractionation during reduction of Cr(VI) under saturated flow conditions. *Environ. Sci. Technol.* **46**, 6783-6789.

Lasaga A. C. (1984) Chemical kinetics of water-rock interactions. *J. Geoph. Res.* **89**, 4009-4025.

Liu X.-M., **Wanner C.**, Rudnick R. L. and McDonough W. F. (2015) Processes controlling $\delta^{7}Li$ in rivers illuminated by study of streams and groundwaters draining basalts. *Earth Planet. Sci. Lett.* **409**, 212-224.

Millot R., Vigier N. and Gaillardet J. (2010) Behaviour of lithium and its isotopes during weathering in the Mackenzie Basin, Canada. *Geochim. Cosmochim. Acta* **74**, 3897-3912.

Misra S. and Froelich P. N. (2012) Lithium isotope history of Cenozoic seawater: changes in silicate weathering and reverse weathering. *Science* **335**, 818-823.

Moeck I. S. (2014) Catalog of geothermal play types based on geologic controls. *Renew. Sust. Energ. Rev.* **37**, 867-882.

Pan L., Spycher N., Doughty C. and Pruess K. (2015) *ECO2N V2.0: a new TOUGH2 fluid property module for mixtures of water, NaCl, and CO_2.* Lawrence Berkeley National Laboratory Berkeley, Ca. https://tough.lbl.gov/software/

Peiffer L., **Wanner C.**, Spycher N., Sonnenthal E. L., Kennedy B. M. and Iovenitti J. (2014) Multicomponent vs. classical geothermometry: insights from modeling studies at the Dixie Valley geothermal area. *Geothermics* **51**, 154-169.

Peiffer L., **Wanner C.** and Pan L. (2015) Numerical modeling of cold magmatic CO_2 flux measurements for the exploration of hidden geothermal systems. *J. Geophys. Res.-Sol. Ea.* **120**, 6856-6877.
Pistiner J. S. and Henderson G. M. (2003) Lithium-isotope fractionation during continental weathering processes. *Earth Planet. Sci. Lett.* **214**, 327-339.
Pogge von Strandmann P. A. E., Burton K. W., James R. H., van Calsteren P., Gíslason S. R. and Mokadem F. (2006) Riverine behaviour of uranium and lithium isotopes in an actively glaciated basaltic terrain. *Earth Planet. Sci. Lett.* **251**, 134-147.
Reed M. and Spycher N. (1984) Calculation of ph and mineral equilibria in hydrothermal waters with application to geothermometry and studies of boiling and dilution. *Geochim. Cosmochim. Acta* **48**, 1479-1492.
Singleton M. J., Sonnenthal E. L., Conrad M. E., DePaolo D. J. and Gee G. W. (2005) Multiphase reactive transport modeling of seasonal infiltration events and stable isotope fractionation in unsaturated zone pore water and vapor at the Hanford site. *Vadose Zone J.* **3**, 775-785.
Spycher N., Peiffer L., Sonnenthal E. L., Saldi G., Reed M. H. and Kennedy B. M. (2014) Integrated multicomponent solute geothermometry. *Geothermics* **51**, 113-123.
Tardy Y., Trauth N. and Krempp G. (1972) Lithium in clay-minerals of sediments and soils. *Geochim. Cosmochim. Acta* **36**, 397-&.
Van Breukelen B. M., Hunkeler D. and Volkering F. (2005) Quantification of sequential chlorinated ethene degradation by use of a reactive transport model incorporating isotope fractionation. *Environ. Sci. Technol.* **39**, 4189-4197.
Vigier N., Decarreau A., Millot R., Carignan J., Petit S. and France-Lanord C. (2008) Quantifying Li isotope fractionation during smectite formation and implications for the Li cycle. *Geochim. Cosmochim. Acta* **72**, 780-792.
Vigier N., Gislason S. R., Burton K. W., Millot R. and Mokadem F. (2009) The relationship between riverine lithium isotope composition and silicate weathering rates in Iceland. *Earth Planet. Sci. Lett.* **287**, 434-441.
Waber H. N., Schneeberger R., Mäder U. K. and **Wanner C.** (2017) Constraints on evolution and residence time of geothermal water in granitic rocks at Grimsel (Switzerland). *Proced. Earth Plan. Sc.* **17**, 774-777.
Wanner C., Eggenberger U., Kurz D., Zink S. and Mäder U. (2012) A chromate-contaminated site in southern Switzerland, part 1: Site characterization and the use of Cr isotopes to delineate fate and transport. *Appl. Geochem.* **27**, 644-654.
Wanner C. and Sonnenthal E. L. (2013) Assessing the control on the effective kinetic Cr isotope fractionation factor: A reactive transport modeling approach. *Chem. Geol.* **337**, 88-98.
Wanner C., Peiffer L., Sonnenthal E., Spycher N., Iovenitti J. and Kennedy B. M. (2014a) Reactive transport modeling of the Dixie Valley geothermal area: Insights on flow and geothermometry. *Geothermics* **51**, 130-141.
Wanner C., Sonnenthal E. L. and Liu X.-M. (2014b) Seawater δ^7Li a direct proxy for global CO_2 consumption by continental silicate weathering? *Chem. Geol.* **381**, 154-167.
Wanner C., Druhan J., Amos R., Alt-Epping P. and Steefel C. (2015) Benchmarking the simulation of Cr isotope fractionation. *Comput. Geosci.* **19**, 497-521.
Wanner C., Bucher K., Pogge von Strandmann P. A. E., Waber H. N. and Pettke T. (2017) On the use of Li isotopes as a proxy for water–rock interaction in fractured crystalline rocks: A case study from the Gotthard rail base tunnel. *Geochim. Cosmochim. Acta* **198**, 396-418.
Wanner C., Diamond L. W. and Alt-Epping P. (2019) Quantification of 3-D thermal anomalies from surface observations of an orogenic geothermal system (Grimsel Pass, Swiss Alps). *J. Geophys. Res.-Sol. Ea.* **124**, 10839-10854.
Wanner C., Waber H. N. and Bucher K. (2020) Geochemical evidence for regional and long-term topography-driven groundwater flow in an orogenic crystalline basement (Aar Massif, Switzerland). *J. Hydrol.* **581**, 124374.
Wiederhold J. G. (2015) Metal stable isotope signatures as tracers in environmental geochemistry. *Environ. Sci. Technol.* **49**, 2606-2624.
Wimpenny J., Gislason S. R., James R. H., Gannoun A., Pogge Von Strandmann P. A. E. and Burton K. W. (2010) The behaviour of Li and Mg isotopes during primary phase dissolution and secondary mineral formation in basalt. *Geochim. Cosmochim. Acta* **74**, 5259-5279.
Xu T. (2008) Incorporating aqueous reaction kinetics and biodegradation into TOUGHREACT: Applying a multiregion model to hydrobiogeochemical transport of denitrification and sulfate reduction. *Vadose Zone J.* **7**, 305-315.
Xu T., Spycher N., Sonnenthal E. L., Zhang G., Zheng L. and Pruess K. (2011) TOUGHREACT Version 2.0: A simulator for subsurface reactive transport under non-isothermal multiphase flow conditions. *Comput. Geosci.* **37**, 763-774.
Xu T., Sonnenthal E. L., Spycher N. and Zheng L. (2014) *TOUGHREACT V3.0-OMP reference manual: a parallel simulation program for non-isothermal multiphase geochemical reactive transport*. Lawrence Berkeley National Laboratory, Berekeley, Ca. https://tough.lbl.gov/software/toughreact/.

3. RTM APPLICATIONS RELATED TO GROUNDWATER CONTAMINATION

Scope and significance

The importance of groundwater contamination is emphasized in Chapter 1; the context of the Author's research on this topic is summarized in Chapter 2. This Chapter 3 presents three selected RTM applications related to U and Cr contaminated groundwater bodies. Chromium and U are both carcinogenic and share the common property of being more soluble in their oxidized states (i.e. Cr(VI) and U(VI)) than in their reduced forms (i.e. Cr(III) and U(IV)). Thus, the environmental impact of Cr and U contaminations may be limited if reducing subsurface conditions can be achieved through appropriate remediation techniques. The reduction of Cr(VI) to Cr(III) and the one from U(VI) to U(IV) leads to a rather strong fractionation of Cr and U isotopes. Therefore, a variation in Cr and U isotope ratios of groundwater samples can demonstrate that the reduction of Cr(VI) or U(IV) is actually occurring in the subsurface.

The first two contributions evaluate the causes for the observation that observable isotope enrichment factors ε may be strongly variable. In these applications, the development of a novel multi-region, solid solution approach allowed to separate the location of Cr(VI) or U(VI) reduction from the bulk solution. Generic model results demonstrate that the effective ε is muted by high reduction rates or by slow diffusive transport through boundary layers. This finding is then tested by applying the developed approach to laboratory experiments reporting (i) an unusually low Cr isotope enrichment factor ε (Chapter 3.1) and (ii) a strong inverse correlation between the effective U isotope enrichment factor and the U(VI) reduction rate (Chapter 3.2). In both cases, very little calibration work is required to match the experimental data even when specifying only one single ε value consistent with literature values.

Chapter 3.3 presents a benchmarking exercise aiming to test the numerical approaches for simulating Cr isotope fractionation during Cr(VI) reduction as well as during mineral precipitation reactions. The simulations are carried out for a well characterized Cr(VI) contaminated site in Switzerland and yield literally the same results when using four different state-of-the-art RTM codes.

Overall, the RTM applications presented in Chapters 3.1 and 3.2 provide fundamental insights on the processes controlling effective Cr and U isotope enrichment factors. Together with the benchmarking exercise (Chapter 3.3) demonstrating that multiple RTM codes are capable of accurately simulating stable isotope ratios in aquifers, they may contribute to a more informed assessment and management of groundwater bodies contaminated by Cr and U.

3.1. Assessing the control on the effective kinetic Cr isotope fractionation factor: A reactive transport modeling approach

Source:

Wanner C. and Sonnenthal E. L. (2013) Assessing the control on the effective kinetic Cr isotope fractionation factor: A reactive transport modeling approach. *Chemical Geology*. **337**, 88-98.

Contribution by the Author (CW):

CW and ELS developed the general idea and CW carried out all the simulations. CW had the lead in data interpretation and manuscript writing.

Chemical Geology 337-338 (2013) 88–98

Contents lists available at SciVerse ScienceDirect

Chemical Geology

journal homepage: www.elsevier.com/locate/chemgeo

Assessing the control on the effective kinetic Cr isotope fractionation factor: A reactive transport modeling approach

Christoph Wanner *, Eric L. Sonnenthal

Lawrence Berkeley National Laboratory, 1 Cyclotron Road, Berkeley, CA 94720, United States

ARTICLE INFO

Article history:
Received 4 April 2012
Received in revised form 2 November 2012
Accepted 17 November 2012
Available online 27 November 2012

Editor: B. Sherwood Lollar

Keywords:
Cr(VI) reduction
Cr isotope fractionation
Cr isotope fractionation factor
Reactive transport modeling
Transport limitations
Reaction mechanism

ABSTRACT

The fractionation of stable Cr isotopes is a well-accepted proxy for demonstrating Cr(VI) reduction occurring in geological systems. Published values for experimentally determined effective kinetic Cr isotope enrichment factors (ε_{kin}) vary over the range of 0.4–5.0‰. Most published studies propose a variation in Cr(VI) reduction mechanisms as being responsible for the wide range of ε_{kin}. Alternatively, varying reaction rates and/or transport limitations have been addressed. In this study the different contributions on ε_{kin} were quantitatively addressed by performing a series of reactive transport model simulations. The proposed reaction network is based on a novel multi-continuum approach and expressing isotope fractionation through the formation of a $^{53}Cr(OH)_{3(s)}$–$^{52}Cr(OH)_{3(s)}$ solid solution as the product of Cr(VI) reduction. In doing so, Cr(VI) reduction was considered to occur at solid surfaces and Cr isotope fractionation was modeled by defining an equilibrium enrichment factor.

Simulating Cr(VI) reduction occurring along a 1D flow path suggested that for a given reaction mechanism ε_{kin} can vary over a large range. According to our simulations the upper range of ε_{kin} is defined by a reaction mechanism's theoretical equilibrium enrichment factor. In contrast, high reduction rate and/or transport limitations can shift ε_{kin} to very low values. In a second model simulation our modeling approach was used to propose an alternative kinetic interpretation for the low ε_{kin} observed in Fe(II)–Cr(VI) reduction experiment by others. Our simulations suggest that the individual contributions of reaction rates, transport limitations and reaction mechanisms should be addressed more carefully when interpreting experimentally determined kinetic Cr isotope enrichment factors and Cr isotope data derived from field sites. Reactive transport modeling is a powerful tool, which should be more commonly used to quantitatively assess these individual contributions in experimental systems.

1. Introduction

In nature, Cr mostly occurs in two stable oxidation states. The highly toxic and very soluble oxidized form Cr(VI) is primarily derived from anthropogenic activities such as leather tanning, wood impregnation, galvanization of metal surfaces and cement clinker. Cr(VI) occurs as the chromate oxyanions CrO_4^{2-}, $HCrO_4^-$ and $Cr_2O_7^{2-}$ and can lead to health problems such as lung cancer and dermatitis (Kotas and Stasicka, 2000). Naturally occurring chromium occurs mostly in the reduced form Cr(III), which is an essential nutrient, less soluble, adsorbs strongly on solid surfaces and co-precipitates with Fe(III) hydroxides (Rai et al., 1987; Davis and Olsen, 1995). Exceptions are some rare naturally occurring Cr(VI) minerals such as the lead chromate crocoite ($PbCrO_4$) (Frost, 2004) and Cr(VI) bearing groundwater systems naturally occurring in arid regions (Izbicki et al., 2008).

Significant fractionation of the four stable Cr isotopes (^{50}Cr, ^{52}Cr,^{53}Cr and ^{54}Cr) has been reported for a series of Cr(VI) reduction experiments (Ellis et al., 2002; Sikora et al., 2008; Berna et al., 2010; Zink et al., 2010; Dossing et al., 2011; Basu and Johnson, 2012; Han et al., 2012; Jamieson-Hanes et al., 2012; Kitchen et al., 2012). These experiments showed a general trend of accumulating heavier Cr isotopes in the unreacted Cr(VI) species and an accumulation of the lighter ones in the produced Cr(III) species. In contrast, Cr(III) species did not undergo rapid isotopic exchange during a Cr(III) oxidation experiment (Zink et al., 2010). Variation in Cr isotope composition is, therefore, an accepted proxy for demonstrating that Cr(VI) reduction is occurring in geological systems. Tracking of Cr(VI) reduction is especially powerful when dealing with subsoil Cr(VI) contamination and related remediation actions. A series of case studies demonstrating naturally occurring Cr(VI) reduction has been described recently (Izbicki et al., 2008; Berna et al., 2010; Wanner et al., 2012a,b,c). Tracking Cr(VI) reduction has also been used for unraveling redox conditions throughout Earth's history (e.g., Frei et al., 2009). In this context, observed Cr isotope fractionation was used to unravel the fluctuations in the Precambrian atmospheric oxygenation (Frei et al., 2009) and to evaluate the redox evolution of hydrothermal systems (Schoenberg et al., 2008).

Stable isotope fractionations are caused mainly by differences in the vibrational energies of isotopically light and heavy substances

* Corresponding author. Tel.: +1 5104958147; fax: +1 5104865686.
E-mail address: cwanner@lbl.gov (C. Wanner).

0009-2541/$ – see front matter © 2012 Elsevier B.V. All rights reserved.
http://dx.doi.org/10.1016/j.chemgeo.2012.11.008

(Bigeleisen and Mayer, 1947; Urey, 1947; Schauble et al., 2004). The isotopically lighter forms of any substances have a lower vibrational energy compared to the heavier ones. When substances consisting of multiple isotopic species react and the remaining reactant equilibrates with the reaction product, an unequal distribution of the isotopes is observed. Stable isotope fractionations are usually reported in terms of the isotopic fractionation factor α. For Cr isotopes, α is defined as the ratio of $^{53}Cr/^{52}Cr$ in the two stable Cr redox states (Cr(VI) and Cr(III)). For convenience, fractionation factors are often expressed as isotopic enrichment factors ε (e.g., Schauble et al., 2004; Sikora et al., 2008):

$$\varepsilon = (\alpha - 1)\cdot 1000 \approx \ln(\alpha)\cdot 1000. \quad (1)$$

Schauble et al. (2004) determined a theoretical equilibrium Cr isotope enrichment factor ε_{eq} between aqueous Cr(VI) and aqueous Cr(III) species of 6–7‰ whereas Zink et al. (2010) reported an ε_{eq} of 3.5‰ for a Cr(VI) reduction experiment conducted under highly acidic conditions ($pH \ll 1$) (Table 1). In all other reported Cr(VI) reduction experiments a kinetic type isotopic fractionation behavior was observed (Ellis et al., 2002; Sikora et al., 2008; Berna et al., 2010; Zink et al., 2010; Dossing et al., 2011; Basu and Johnson, 2012; Han et al., 2012; Jamieson-Hanes et al., 2012; Kitchen et al., 2012). Applying a Rayleigh distillation model the cited Cr(VI) reduction studies determined kinetic enrichment factors ε_{kin} within the range of 0.4–5.0‰ (Table 1). Kinetic isotopic fractionation is typically observed for systems undergoing a fast net reaction where the backward reaction is negligible when compared to the overall reaction rate (Young et al., 2002; Zink et al., 2010; DePaolo, 2011).

Variations in observed effective kinetic Cr isotope enrichment factors have been attributed to several causes: (i) The reaction rate of Cr(VI) reduction affects the magnitude of the kinetic Cr isotope enrichment factor such as shown for sulfur isotope fractionation (Rees, 1973; Canfield, 2001). Sikora et al. (2008) showed a kinetic dependence on the kinetic enrichment factor for microbiologically-mediated Cr(VI) reduction experiments using lactate as the electron donor. In these experiments $\varepsilon_{kin} = 1.8$‰ was observed for a high lactate concentration and a high Cr(VI) reduction rate, and $\varepsilon_{kin} = 4.0$‰ was observed for a low lactate concentration and slow Cr(VI) reduction rate (Table 1). (ii) A variation in molecular scale reduction mechanisms has been addressed as a second cause likely inducing a variation of ε_{kin} (Sikora et al., 2008; Zink et al., 2010; Dossing et al., 2011). On the contrary, Zink et al. (2010) did not observe that the resulting Cr isotope fractionation factor is significantly dependent on the pH dependent speciation of Cr(VI) and Cr(III) species (Table 1). This is notable since the actual Cr(VI) reduction mechanism is also dependent on the pH value (e.g., pH = 7–9: $CrO_4^{2-} \Rightarrow Cr(OH)_2^+$; pH < 4: $HCrO_4^- \Rightarrow Cr^{3+}$). (iii) As a third cause, transport limitations, such as a limited diffusive flux towards reactive surfaces, have been reported to shift a system's effective ε_{kin} to lower values (Bender, 1990; Brandes and Devol, 1997; Green et al., 2010). Even though these studies described other isotopic systems (NO_3^-- and O_2-reduction) it is assumed that transport limitations can also affect the kinetic Cr isotopic enrichment factor (Berna et al., 2010).

To the author's knowledge no study has yet quantitatively assessed the individual contributions of the reaction mechanism, the Cr(VI) reduction rate, and transport limitations on the effective kinetic Cr isotope enrichment factor. In this study these contributions were quantitatively addressed by performing a series of reactive transport model simulations of Cr(VI) reduction in a porous medium along a 1D flow path. In the second part, the Fe(II)-added–Cr(VI) reduction experiments performed by Dossing et al. (2011) were simulated and an alternative interpretation proposed.

2. Simulation of Cr(VI) reduction in porous media along a 1D flow path

2.1. Conceptual model

As a model simplification, it is assumed that Cr(VI) reduction occurs at solid surfaces only (Fig. 1). This assumption is based on the observation that Fe(II)-bearing minerals and solid organic matter are the most common naturally occurring Cr(VI) reducing agents (Palmer and Puls, 1994). For both cases, Cr(VI) reduction can be microbiologically-mediated if specific microorganisms are present (Sikora et al., 2008; Han et al., 2010). Most bacteria are fixed on solid surfaces and are

Table 1
Summary of published Cr(VI) reduction experiments.

Reference	e^--Donor	Initial Cr(VI)	Fractionation mode	Effective ε	Comment
Ellis et al. (2002)	Fe^{2+} bearing minerals (magnetite)	0.19 μM/L	Rayleigh-type	3.3 and 3.5‰	
Schauble et al. (2004)	Theoretical calculation		Equilibrium fractionation	6–7‰	
Sikora et al. (2008)	3.3–100 mM lactate	5.1–9.5 μM	Rayleigh-type	4.1–4.5‰	Bioreduction (*Shewanella oneidensis*). Rate = $42 \cdot 10^{-18}$ mol/cell/day[a]
	10,200 mM lactate	9.5 μM	Rayleigh-type	1.8‰	Bioreduction (*Shewanella oneidensis*). Rate = $450 \cdot 10^{-18}$ mol/cell/day[a]
Zink et al. (2010)	0.9 μM H_2O_2	0.9 μM	Rayleigh-type[b]	4.2‰	pH = 0.7
	0.9 μM H_2O_2	0.9 μM	Equilibrium fractionation[b]	7.2‰	pH = 0.7
	13.2 μM H_2O_3	0.9 μM	Rayleigh-type	5.0‰	pH = ca. 7
	13.2 μM H_2O_4	0.9 μM	Equilibrium fractionation	3.5‰	$pH \ll 1$
Berna et al. (2010)	Fe^{2+} bearing minerals (e.g. green rust)	1.92 μM	Rayleigh-type	2.4 and 3.1‰	
Dossing et al. (2011)	0.05 nM Fe^{2+} (batch experiment)	0.42 nM	Rayleigh-type	3.1–4.5‰	
	0.03 mM Fe^{2+}/min (added experiment)	0.78 μM	Rayleigh-type	1.5‰	
Han et al. (2012)	20 mM lactate	50 μM	Rayleigh-type	2‰	Bioreduction (*Pseudomonas stutzeri*); aerobic conditions
	20 mM lactate	50 μM	Rayleigh-type	0.4‰	Bioreduction (Pseudomonas Stutzeri); denitrifying conditions
Basu and Johnson (2012)	Fe(II) doped goethite	17.7 μM	Rayleigh-type	3.91‰	
	FeS (75 μM Fe(II))	19 μM	Rayleigh-type	2.11‰	
	Green rust (100 μM Fe(II))	11 μM	Rayleigh-type	2.65‰	
	$FeCO_3$ (84.2 μM Fe(II))	19 μM	Rayleigh-type	2.67‰	
	4 g of reduced sediment	24 μM	Rayleigh-type	3.18‰	
Kitchen et al. (2012)	60 mM Fe^{2+}	20–22 μM	Rayleigh-type	4.20 ± 0.11‰	pH = 4–5.3
	10 mg humic and 200 μM fulmic acid	21 μM	Rayleigh-type	3.11 ± 0.11‰	pH = 4.5–5
Jamieson-Hanes et al. (2012)	7.5 g organic C (batch experiment)	100 μM	Rayleigh-type	3.50 ± 0.1‰	

[a] Rate observed during first 24 h of experiment.
[b] Fractionation mode not clear since all experiment resulted in the same extent of Cr(VI) reduction. Presented here are the two different possibilities for interpretation (equilibrium vs. kinetic fractionation).

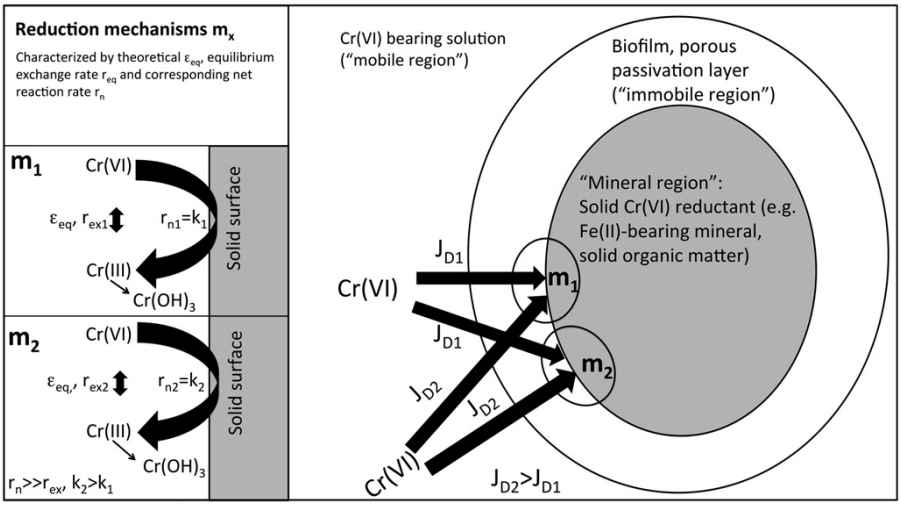

Fig. 1. Conceptual model used to simulate Cr isotope fractionation for porous media along a 1D flow path. The model assumes that Cr(VI) reduction to Cr(III) occurs at solid surfaces and that Cr(III) immediately precipitates as $Cr(OH)_3$ (see inset). Overall Cr(VI) reduction rate is a function of diffusive Cr(VI) transport (J_D) to the solid surface and the net reduction rate r_n. Cr isotope fractionation typically occurs in the surface reaction controlled regime, where r_n is much larger than the gross exchange rate r_{ex} (DePaolo, 2011). The model allows simulating the magnitude of Cr isotope fractionation as a function of different diffusive Cr(VI) fluxes (e.g., J_{D1} and J_{D2}) for one specific reduction mechanisms (characterized by ε_{eq}) occurring at different net molecular reaction rates (e.g., r_{n1} and r_{n2}). For the specified reaction network the reaction rate constant k (Eqs. (6) and (7)) represents a proxy for r_n. The terms "mineral region", "immobile region", and "mobile region" refer to the multi-region approach (Xu, 2008) that was used to setup the model.

immobile (Harvey et al., 1989). Moreover, Cr(VI) reaction products (e.g., $Cr(OH)_3$) passivate the reactive surface sites of solid Cr(VI) reducing agents (Jeen et al., 2007). Accordingly, a passivation layer and/or biofilm is formed around solid surfaces and Cr(VI) has to diffuse through such layers in order to get reduced.

The proposed conceptual model is closely related to the surface kinetic model recently described by DePaolo (2011) to explain Ca isotope fractionation during calcite precipitation experiments. According to DePaolo (2011) surface reactions can occur in four different regimes: (i) a near equilibrium regime, where the net reaction rate (r_n) is much slower than the forward and backward reaction rates (e.g., exchange rate r_{ex}, Fig. 1), respectively, (ii) a surface equilibrium regime with the same requirements than in the near equilibrium regime but with a r_n that is fast enough to induce transport limitations, (iii) a surface reaction limited regime where $r_n \gg r_{ex}$ and (iv) a regime with transport and reaction effects where $r_n \gg r_{ex}$ and with a transport limitation of r_n.

Cr(III), which is the reaction product of Cr(VI) reduction, is almost insoluble over a wide pH-range (Rai et al., 1987) and it is assumed that it almost instantaneously precipitates as $Cr(OH)_3$. Consequently, Cr(VI) reduction either occurs in a surface reaction limited regime, with or without transport limitations induced by the diffusive transport of Cr(VI) through the biofilm, and/or passivation layer (Fig. 1). According to the model of DePaolo (2011), both regimes should tend to enrich the light (e.g., Cr) isotope in the reduced phase (Cr(III)) and a kinetic-type Cr isotope fractionation would be observed.

Our conceptual model (Fig. 1) allows the individual assessment of kinetic Cr isotope fractionation effects induced by surface reaction kinetics and by transport limitation effects, respectively. It assumes that Cr(VI) reduction occurs as one single molecular-scale Cr(VI) reduction mechanism, which is described by a specific equilibrium enrichment factor (Urey, 1947). Accordingly, one single equilibrium enrichment factor ε_{eq} was defined, representing a hypothetical near-equilibrium regime (DePaolo, 2011). Kinetic effects on the effective Cr isotope enrichment factor were assessed by a variation of the specific molecular scale Cr(VI) reduction rate (k) at a constant, non-transport-limited diffusive Cr(VI) flux J_D through the biofilm and/or surface passivation layer (Fig. 1). In contrast, transport limitations were assessed by varying J_D at a constant molecular scale Cr(VI) reduction rate k. Each Cr isotopic species ($^{52}CrO_4^{2-}$ and $^{53}CrO_4^{2-}$) were treated as separate transported species as done for ^{18}O and ^{16}O in Singleton et al. (2004). Fractionation effects due to a variation in diffusion coefficient between ^{52}Cr and ^{53}Cr species were not considered. If the diffusion coefficients differed, our model approach would induce Cr isotope fractionation also due to variation in the diffusive flux within the biofilm and/or passivation layer such as described for Sr isotopes (Watson and Mueller, 2009). This model simplification is justified by the fact that mass differences between the different isotopic Cr(VI) species are rather small (115 vs. 116 g/mol for CrO_4^{2-}).

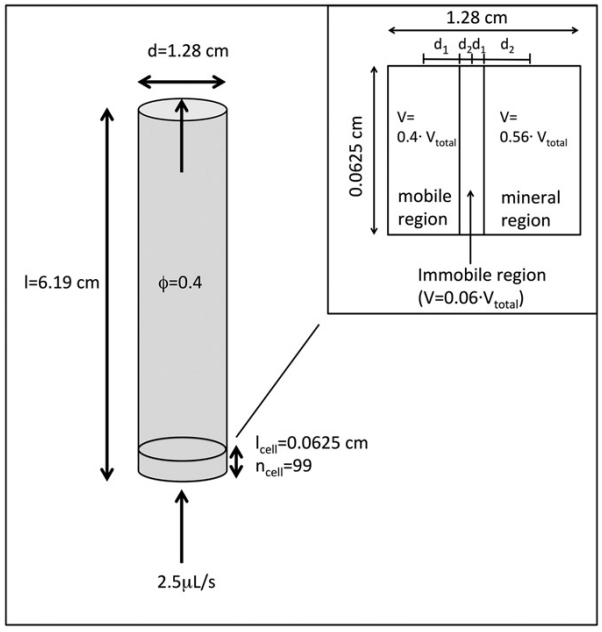

Fig. 2. General setup used to model Cr(VI) reduction along a 1D flow path. The inset gives the front view of one individual grid cell and illustrates how the 99 cells were discretized into the three regions of our multi-region approach.

Table 2
Composition of the injecting fluid.

pH		8.06
$^{53}CrO_4^{2-}$	mol/L	5.09E−07[a]
$^{52}CrO_4^{2-}$	mol/L	4.49E−06[a]
K^+	mol/L	1.46E−03
HCO_3^-	mol/L	1.90E−03
SO_4^{2-}	mol/L	8.06E−05
Ca^{2+}	mol/L	2.28E−04
Fe^{2+}	mol/L	1.00E−04

[a] $\delta^{53}Cr = 0.0‰$.

2.2. Model setup

Cr isotope fractionation effects were simulated for a porous media along an approximately 6.2 cm long 1D flow path (Fig. 2). This model domain was divided into 99 cylindrical cells, each having a thickness of 0.0625 cm. An injection rate of 2.5 μL/s was specified for the first cell and the overall porosity was set to 0.4. These specifications lead to an average linear flow velocity of 7 cm/day simulating Cr(VI) transport that is dominated by advection such as reported for a series of field site Cr(VI) contaminations (Faybishenko et al., 2008; Flury et al., 2009; Wanner et al., 2012a,b,c). The composition of the injecting fluid was specified as listed in Table 2.

The multi-region model approach described by Xu (2008) was used to numerically formulate the conceptual model (Fig. 1). In doing so, a three region model was defined and each of the 99 cells along the column were divided into these three regions (Fig. 2): (i) a mobile region where advective transport occurs, (ii) an immobile region that is affected by diffusive transport only and (iii) a mineral region where mineral dissolution/precipitation reactions take place (Figs. 1 and 2).

Table 3 gives the physical and mineralogical parameters used for the three regions. Porosity and permeability were defined in a similar way as Xu (2008). The distance between the regions and the corresponding interfacial areas were calculated according to the general geometrical setup of the simulated column (Fig. 2).

Transport processes were modeled according to the standard advection diffusion equation in TOUGHREACT (Xu et al., 2011)

$$\frac{\partial(\phi C_i)}{\partial t} = \nabla\cdot(\phi\cdot D_i\cdot\tau\cdot\nabla C_i) - \nabla\cdot(\phi\cdot v\cdot C_i) \quad (2)$$

where C_i (mol/kg_{H2O}) refers to the concentration of aqueous species i, ϕ is the porosity of the porous medium, D_i (m^2/s) refers to the diffusion coefficient of species i, τ refers to the tortuosity, and v (m/s) is the average linear flow velocity. Advective transport takes place essentially only within the mobile region because the permeability of this region is much higher when compared to the other regions (Table 3). Diffusive flux of aqueous species i (J_{Di}) within the immobile region is proportional to

$$J_{Di} \propto \frac{D_{aq}\cdot A}{d_1 + d_2} + \frac{dC_i}{dx} \quad (3)$$

Table 4
Thermodynamic properties of specified mineral reactions.

Reaction	log K (equilibrium constant)[a]
$^{52}CrO_4^{2-} + 5H^+ + 3Fe^{2+} = {}^{52}Cr(OH)_{3(s)} + 3Fe^{3+} + H_2O$	25.69147912
$^{53}CrO_4^{2-} + 5H^+ + 3Fe^{2+} = {}^{53}Cr(OH)_{3(s)} + 3Fe^{3+} + H_2O$	25.69
$CaCO_3 + H^+ = Ca^{2+} + HCO_3^-$	1.8487
$Fe^{3+} + 3H_2O = Fe(OH)_3 + 3H^+$	−3.191

[a] At 25 °C.

where D_{aq} refers to the diffusion coefficient of aqueous species (~10^{-9} m^2/s), A (m^2) is the interfacial area between two adjacent regions, dC_i/dx (mol/kg_{H_2O}/m) is the concentration gradient of species i, and d_1 and d_2 (m) refer to the distances from the centers of two adjacent regions to their mutual interface (Fig. 2).

2.3. Reaction network

Ferrous iron was used as a general Cr(VI) reducing agent. This choice is based on the observation that ferrous iron is one of the most prevalent naturally occurring Cr(VI) reducing agents (Buerge and Hug, 1997). Furthermore, it was assumed that once produced, Cr(III) immediately precipitates as $Cr(OH)_3$. This simplification is justified by the fact that the simulations were performed for systems at near neutral pH-values where the solubility of $Cr(OH)_3$ is low and $Cr(OH)_{3(aq)}$ is the dominant Cr(III) species (Rai et al., 1987; Kotas and Stasicka, 2000). Following this argument, Cr(VI) reduction to Cr(III) was formulated for two Cr isotope species (^{52}Cr and ^{53}Cr) as a kinetic mineral precipitation reaction using Fe(II) as reducing agent:

$$^{52}CrO_4^{2-} + 5H^+ + 3Fe^{2+} = {}^{52}Cr(OH)_{3(s)} + 3Fe^{3+} + H_2O \quad (4)$$

$$^{53}CrO_4^{2-} + 5H^+ + 3Fe^{2+} = {}^{53}Cr(OH)_{3(s)} + 3Fe^{3+} + H_2O \quad (5)$$

It should be pointed out that the coexistence of aqueous Fe(II) and Cr(VI) such as defined for the injecting fluid (Table 2) is not favored from a thermodynamic point of view (Table 4) because the homogenous reaction between Fe^{2+} and CrO_4^{2-} is nearly instantaneous (Buerge and Hug, 1997). Moreover, the simulations were run for circumneutral pH values at which Fe(II) species are only stable if strongly reducing conditions are established (Nordstrom and Munoz, 1985). Although these initial conditions are in disequilibrium, the specified reaction network allows simulation of Cr(VI) reduction at solid surfaces. This was achieved by allowing $Cr(OH)_3$ precipitation and Cr(VI) reduction under kinetic constraints (Eqs. (4) and (5)) within the mineral region only (Fig. 1) while the homogenous reaction between Fe^{2+} and CrO_4^{2-} is suppressed in the other regions. With these specifications, aqueous Fe(II) operates as a representative for any solid or immobile Cr(VI) reducing agents (e.g., bacteria, Fe(II)-bearing minerals), and not as an aqueous reducing agent. Accordingly, the reaction network is in agreement with our

Table 3
Physical and mineralogical parameters of the three regions of the specified multi-region model.

Parameter	Mobile region		Immobile region		Mineral region	
Volume fraction of the medium	0.4		0.06		0.54	
Porosity	1		1		0.05	
Distance to interface (m)	d_1	d_2	d_1	d_2	d_1	d_2
		2.27E−03	3.40E−04	3.40E−04	3.06E−03	
Area between regions (m^2)		1.09E−02		1.09E−02		
Permeability (m^2)	1.00E−11		1.00E−18		1.00E−18	
Mineralogy	No mineral reaction allowed		No mineral reaction allowed		10 vol.% Calcite, $Fe(OH)_3$ and $Cr(OH)_3$ precipitation (Cr(VI) reduction) allowed, remaining solids are non-reactive	

conceptual model assuming that Cr(VI) reduction occurs at solid surfaces only (Fig. 1). The benefit of using aqueous Fe(II) as a representative for Fe(II)-bearing solids is that molecular scale heterogeneous Cr(VI) reduction at reactive Fe(II) surfaces do not have to be formulated explicitly. The same holds true for iron cycling phenomena, such as the partial reductive dissolution of Fe(III)-bearing solids, subsequent homogeneous reactions between aqueous Fe(II) with Cr(VI) and reprecipitation of Fe(III)-bearing solids (Coby et al., 2011). The definition of excess aqueous Fe(II) with respect to Cr(VI) in the injecting fluid (Table 2) ensures that Fe(II) consumption caused by Cr(VI) reduction (Eqs. (4) and (5)) does not affect the overall Cr(VI) reduction rate. In addition, this definition allows specifying constant iron-reducing redox conditions along the entire 1D flow path.

The isotopic endmembers $^{52}Cr(OH)_{3(s)}$ and $^{53}Cr(OH)_{3(s)}$ were treated as one mineral phase assuming an ideal solid solution. In doing so, TOUGHREACT (Xu et al., 2011) calculates the reaction rates of the $^{52}Cr(OH)_3$ (r^{52}_{Cr}) and $^{53}Cr(OH)_3$ (r^{53}_{Cr}) endmembers according to Eqs. (6) and (7),

$$r_{^{52}Cr} = A_{ss}\cdot k_{52}\cdot\left(1-\frac{Q_{^{52}Cr}}{K_{^{52}Cr}X_{^{52}Cr}}\right) = A_{ss}\cdot k\cdot\left(1-\frac{Q_{^{52}Cr}}{K_{^{52}Cr}X_{^{52}Cr}}\right) \quad (6)$$

$$r_{^{53}Cr} = A_{ss}\cdot k_{53}\cdot\left(1-\frac{Q_{^{53}Cr}}{K_{^{53}Cr}X_{^{53}Cr}}\right) = A_{ss}\cdot k\cdot\left(1-\frac{Q_{^{53}Cr}}{K_{^{53}Cr}X_{^{53}Cr}}\right) \quad (7)$$

where A_{ss} refers to the reactive surface area of the solid solution ($m^2_{mineral}/kg_{H_2O}$), k_{52} and k_{53} are the reaction rate constants of the two end members (mol/m^2/s), Q^{52}_{Cr} and Q^{53}_{Cr} refer to the ion activity product of the Cr(VI) reduction reaction (Eqs. 4 and 5), K^{52}_{Cr} and K^{53}_{Cr} are the corresponding equilibrium constants and X_{52} and X_{53} are the mole fractions of the two end members. k_{52} and k_{53} represent the kinetics of the actual molecular scale Cr(VI) reduction reaction. As a model simplification, k_{52} and k_{53} were assumed to be equal and they were treated as one variable k (Eqs. (6) and (7)). This model simplification holds perfectly true for an equilibrium situation where the net Cr(VI) reduction rate is zero but also for an infinitely high net overall Cr(VI) reduction rate, where Cr(VI) is reduced to Cr(III) instantaneously. The total reactive surface area of the $Cr(OH)_3$ solid solution, A_{ss}, was held constant and was fixed to an arbitrary value of 0.014 m^2/kg_{H_2O}. Assuming an initial $Cr(OH)_3$ volume fraction of 10^{-6}, this value corresponds to a specific surface area of 600 m^2/g that is typically used for ferric hydroxides (Dzombak and Morel, 1990). The assumption of constant surface area is based on the fact that the overall Cr(VI) reduction rate is not dependent on the reactive surface area of the $Cr(OH)_3$ solid solution because $Cr(OH)_3$ is not a Cr(VI) reducing agent. However, the rate is dependent on the reactive surface area of solids operating as Cr(VI) reducing agents. To keep things simple, evolving reactive surface areas of solid Cr(VI) reducing agents were not considered by our reaction network. In doing so, our reaction network does not account for the fact that solid Cr(VI) and Fe(II) bearing reductants get passivated by newly-formed reaction products such as $Cr(OH)_{3(s)}$, $Fe(OH)_3$ and carbonates, that may reduce the reactive surface areas with time (Jeen et al., 2007; Wanner et al., 2011). The cited studies also provide two alternative reaction networks that allow simulating the gradual decline of the reactive surface area. These reaction schemes, however, were not included, since reactions with Fe(II) bearing solids were not formulated explicitly and the focus of this work was not on the long term reactivity of solid Cr(VI) reducing agents. The ideal behavior of the $Cr(OH)_3$ solid solution was ensured by Eq. (8) (e.g., Reed, 1982)

$$\frac{Q_{ss}}{K_{ss}} = \left(\frac{Q_{^{52}Cr}}{K_{^{52}Cr}}\right) + \left(\frac{Q_{^{53}Cr}}{K_{^{53}Cr}}\right) \quad (8)$$

while a rate law derived from transition state theory (TST) (Lasaga, 1984) was applied for the solid solution using Eq. (9)

$$r_{ss} = A_{ss}\cdot k\cdot\left(1-\frac{Q_{ss}}{K_{ss}}\right). \quad (9)$$

In these equations, Q_{ss} and K_{ss} refer to the ion activity product and the equilibrium constant of the solid solution, r_{ss} and k are the overall solid solution's reaction rate and reaction rate constant and A_{52} and A_{53} refer to the reactive surface area of the two end members.

Using the solid solution approach described above, Cr isotope fractionation is simulated by means of varying equilibrium constants K^{52}_{Cr} and K^{53}_{Cr} only. According to Urey (1947) K^{52}_{Cr}/K^{53}_{Cr} refers to the theoretical equilibrium fractionation factor α_{eq} for one specific Cr(VI) reduction mechanism. A log(K) of 25.69 was taken for Eq. (5) (Table 4). This value was calculated based on Fe speciation reactions and log(K) values tabulated in the EQ3/6 database (Wolery, 1992) which was derived using SUPCRT92 (Johnson et al., 1992 and references therein) and on thermodynamic Cr data reported by Ball and Nordstrom (1998). The log(K) of Eq. (4) was then set at 25.69147912 (Table 4) to express an equilibrium Cr enrichment factor ε_{eq} of 3.4‰ (i.e., corresponding to $\alpha_{eq} = 10^{25.69147912}/10^{25.69} = 1.0034$). This value approximately represents the average of experimentally determined kinetic Cr isotope enrichment factors (Table 1) and is close to the equilibrium Cr isotope enrichment factor of 3.5‰ that was determined by Zink et al. (2010).

Isotopic data are reported as the $^{53}Cr/^{52}Cr$ ratio in terms of the δ-notation relative to the certified Cr isotope standard NIST SRM 979 and are given in ‰:

$$\delta^{53}Cr = \left(\frac{\left(^{53}Cr/^{52}Cr\right)_{modeled}}{\left(^{53}Cr/^{52}Cr\right)_{SRM979}}\right) - 1 \quad (10)$$

$(^{53}Cr/^{52}Cr)_{modeled}$ is the simulated $^{53}Cr/^{52}Cr$ ratio and $(^{53}Cr/^{52}Cr)_{SRM979}$ the known $^{53}Cr/^{52}Cr$ ratio (=0.11339) of the certified standard.

In addition to $Cr(OH)_3$ precipitation, the reaction network allows the formation of $Fe(OH)_3$ also:

$$Fe^{3+} + 3H_2O = Fe(OH)_3 + 3H^+. \quad (11)$$

Additionally, 10 vol.% of calcite (Table 4) was added to buffer pH changes induced by Cr(VI) reduction (Eqs. (4) and (5)). $Fe(OH)_3$ and calcite precipitation and dissolution reactions were simulated using a thermodynamic approach. Hence, they were allowed to reach thermodynamic equilibrium at each time step. Equilibrium constants for mineral and aqueous species reactions were defined as tabulated in the EQ3/6 database (Wolery, 1992) (Table 4).

2.4. Model results and discussion

The model was run for four different overall Cr(VI) reduction rates by means of a varying Cr(VI) reduction reaction rate constant k (Eqs. (6) and (7)), keeping ε_{eq} constant at 3.4‰. Following the discussion by DePaolo (2011), these runs assessed Cr isotope fractionation in reaction rate controlled regimes as a function of the actual surface reaction rate k (Fig. 1). In a second set of another four model runs, Cr isotope fractionation effects in transport-controlled regimes (DePaolo, 2011) were simulated. For these simulations, the system's overall Cr(VI) reduction rate was varied by means of a varying diffusive flux J_D within the immobile region (Fig. 1) while keeping k constant ($k/k_{max} = 0.1$). The interfacial area A between the three regions was varied by ca. 2.2 orders of magnitude resulting in a variation of the diffusive flux J_D in the same order of magnitude (Eq. (3)). The use of a set of different diffusive fluxes J_D operates as a proxy for a variation in the

extent of the biofilm/passivation layer present around reactive surfaces (Fig. 1). This approach also allows considering the assumption that a biofilm/biological reaction system may have different effective J_D than an equivalently thick chemical passivation layer, which is based on the observation that the permeability of biological reaction systems (e.g., cell membranes) can be relatively low (Hancock and Wong, 1984; Pearson et al., 1999; Nikaido, 2003; Jones and Niederweis, 2010). Small values for J_D correspond to a thick passivation layer or a slow transport path within biological systems. On the contrary, large J_D corresponds to a thin passivation layer or fast transport paths of biological systems. According to DePaolo (2011), transport limitations of chemical systems are a function of the thickness of such layers and occur only when it is larger than a specific minimum extent. Moreover, the thickness highly depends on a specific experimental setup. In a stirred batch experiment for instance, the passivation layer is much smaller when compared to an unstirred experiment. Accordingly, the definition of different values for J_D allows assessing the contribution of transport limitations induced by a specific experimental setup or by specific passivation phenomena on the effective kinetic Cr isotope enrichment factor.

Modeled steady-state Cr(VI) concentration profiles within the mobile region followed a linear trend in a logarithmic C/C_0 plot, where C and C_0 refer to the Cr(VI) concentration at a specific location and at the column inlet (Figs. 3a and 4a). Accordingly, Cr(VI) reduction within the model domain was simulated by means of a first order rate law with respect to the Cr(VI) concentration. We are confident that this is a reasonable simulation of natural systems since a first order behavior has been reported for experiments performed at fixed pH values and in

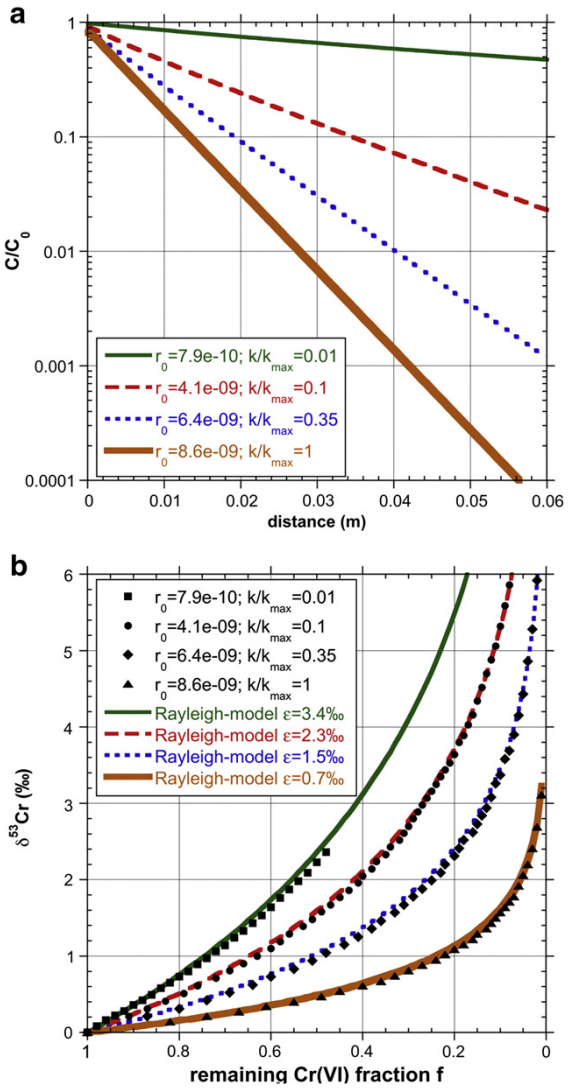

Fig. 3. Model results for varying overall Cr(VI) reduction rates (r_0 = reaction rate in mol/kg_{H_2O}/s at column inlet) defined by means of differing molecular scale Cr(VI) reduction rates k (surface reaction controlled regime) using a constant equilibrium enrichment factor of 3.4‰. a: Steady state Cr(VI) concentration profiles (C/C_0) within the mobile region. b: $\delta^{53}Cr$ vs. reduced Cr(VI) fraction plots for aqueous Cr(VI) of the mobile region. Also shown is the theoretical $\delta^{53}Cr$ evolution of mobile region Cr(VI) following a Rayleigh-type model for ε_{kin} = 3.4‰, 2.3‰, 1.5‰ and 0.7‰.

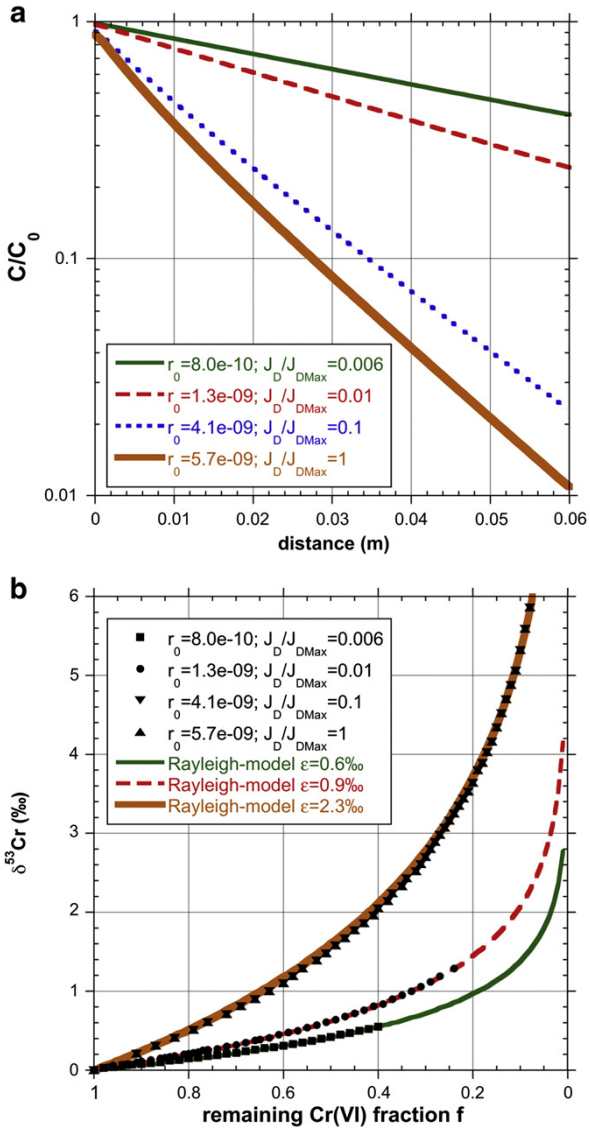

Fig. 4. Model results for varying overall Cr(VI) reduction rates (r_0 = reaction rate in mol/kg_{H_2O}/s at column inlet) defined by means of varying diffusive fluxes J_D within the immobile region (transport-limited regime). a: Steady state Cr(VI) concentration profiles (C/C_0) within mobile region. b: $\delta^{53}Cr$ vs. reduced Cr(VI) fraction plots for aqueous Cr(VI) of the mobile region. Also shown is the theoretical $\delta^{53}Cr$-evolution of mobile region Cr(VI) following a Rayleigh-type model for ε_{kin} = 2.3‰, 0.9‰ and 0.6‰.

the presence of an excess of Cr(VI) reducing agents (Buerge and Hug, 1997). δ^{53}Cr vs. remaining Cr(VI) fraction plots that correspond to the Cr(VI) concentration profiles are illustrated in Figs. 3b and 4b. Modeled δ^{53}Cr-values fit closely with Rayleigh-type fractionation curves expressed as

$$\delta^{53}Cr_x = ((\delta^{53}Cr_0 + 1000)f^{(\alpha kin-1)}) - 1000 \quad (12)$$

where $\delta^{53}Cr_x$ and $\delta^{53}Cr_0$ refer to the Cr isotope composition at location x and at the column inlet (0.0‰, see Table 2), f refers to the remaining Cr(VI) fraction at location x and αkin is the effective kinetic fractionation factor.

Depending on the regime, ε_{kin} showed a different dependence on the overall Cr(VI) reduction rate. For the surface reaction controlled regimes ε_{kin} decreased with increasing overall Cr(VI) reduction rate even though the equilibrium enrichment factor and reduction mechanism, respectively, remained the same (Fig. 3b). These model runs also show that ε_{kin} approaches the defined equilibrium enrichment factor ($\varepsilon_{eq} = 3.4‰$) at slow overall Cr(VI) reduction rates (Fig. 3b). This observation indicates that the maximum effective Cr isotope enrichment factor is defined by the (theoretical) equilibrium enrichment factor for a given Cr(VI) reduction mechanism.

In contrast, ε_{kin} became smaller with decreasing overall Cr(VI) reduction rate for the transport-limited regimes (Fig. 4b). Interestingly, ε_{kin} approaches a maximum value of 2.3‰ for the condition where a high diffusive flux within the immobile region was specified ($J_D/J_{Dmax} = 0.1$ and $J_D/J_{Dmax} = 1$, Fig. 4b). This observation confirms that for non-transport-limited systems, the resulting Cr isotope enrichment factor solely depends on the equilibrium enrichment factor and on the molecular scale Cr(VI) reduction rate.

Regarding the interpretation of experimentally determined kinetic Cr isotope enrichment factors, an important observation is that ε_{kin} does not a priori depend on a system's overall Cr(VI) reduction rate. Such dependence is only true for systems that do not encounter transport limitations. Furthermore it has to be noticed that both high molecular scale Cr(VI) reduction rates and transport limitations can significantly shift the observed ε_{kin} to low values even though the specific Cr(VI) reduction mechanism remains constant.

The observation that simulated δ^{53}Cr-values followed a Rayleigh-type fractionation model lends support that such Rayleigh models are a suitable approach to describe Cr isotope fractionation in dynamic systems and not for well-controlled laboratory experiments only. For example, Fig. 5 illustrates for one particular model run that δ^{53}Cr-values of $Cr(OH)_3$ present within the mineral region can also be approximated with a Rayleigh-type model. It has to be pointed out that the Rayleigh behavior of solid Cr(III) was calculated by means of the same equation as for the Cr(VI) present within the mobile region (Eq. (12)). In contrast, δ^{53}Cr-values of solids obtained from closed system batch experiments follow the Rayleigh curve "Cr(III) Rayleigh-model (accumulation)" (Fig. 5), which accounts for the fact that all solids present within the system accumulate over time (Zink et al., 2010). Accordingly, it is suggested that δ^{53}Cr-values collected during flow-through experiments or at field sites follow the non-accumulative-Rayleigh curve such as proposed by Wanner et al. (2012a). The accuracy of such Rayleigh-models do, however, suffer from uncertainties in the magnitude of the effective field scale kinetic Cr isotope enrichment factor.

3. Model application: simulation of the Dossing et al. (2011) Fe(II)–Cr(VI) reduction experiment

After having shown that variations in kinetic Cr isotope enrichment factors are not necessarily due to changes in Cr(VI) reduction mechanisms, an alternative interpretation is proposed for the Dossing et al. (2011) Fe(II)-added–Cr(VI) reduction experiment. This new interpretation is tested with another reactive transport model.

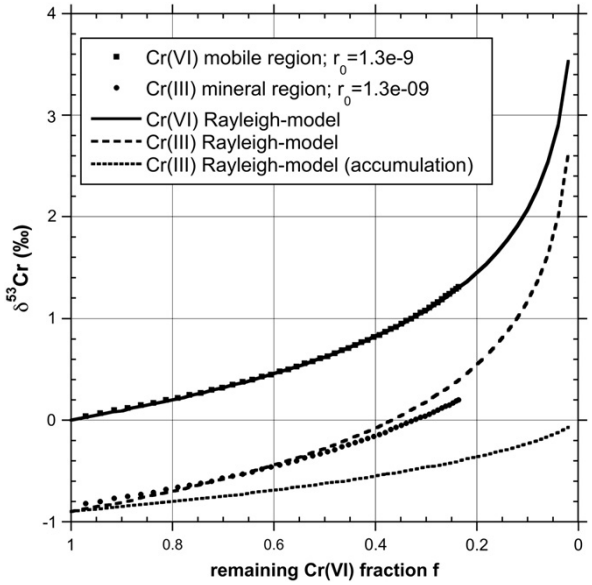

Fig. 5. Rayleigh model for one model run simulating a transport-limited regime ($J_D/J_{Dmax} = 0.01$). δ^{53}Cr-values of Cr(VI) within the mobile region and δ^{53}Cr-values of Cr(III) within the mineral region follow a Rayleigh fractionation model with $\varepsilon_{kin} = 0.9‰$. Also shown is the theoretical δ^{53}Cr evolution of total Cr(III) produced along the 1D flow path (curve 'Cr(III) accumulation').

The experiment was performed by adding a ferrous iron solution at a constant flow rate into a beaker containing a Cr(VI) bearing solution (Dossing et al., 2011). During the course of the experiment the pH-value was fixed to 8.1. The initial Cr(VI) bearing solution was completely reduced within a time period of ca. 70 min. δ^{53}Cr-values of precipitated solid Cr(III) revealed a kinetic Cr isotope enrichment factor of 1.5‰ (Table 1). In contrast, a kinetic enrichment factor of 3.1–4.5‰ was observed for a batch experiment with a fixed initial CrO_4^{2-} and Fe^{2+} concentration (Table 1). Dossing et al. (2011) attributed the low enrichment factor observed in the iron-added experiment to a Cr(VI) reduction mechanism involving the formation of green rust, adsorption of CrO_4^{2-} anions and Cr(VI) reduction within the green rust structure. Alternatively, a kinetic cause for the low observed enrichment factor was ruled out explicitly since it was argued that the Cr(VI) reduction rate was lower in the iron-added experiment when compared to the batch experiment. This statement, however, represented only a qualitative interpretation since actual molecular scale Cr(VI) reduction rates were not quantified explicitly. It is based on the fact that for the Fe(II)-added experiment Fe(II) was added slower than in the batch-experiment where it was injected instantaneously (see Dossing et al., 2011 for more details).

3.1. Conceptual model

In this model we test the assumption of Dossing et al. (2011) that the Cr(VI) reduction rate was low in the iron-added experiment. To test this assumption, a different conceptual model was used to constrain the reactive transport model (Fig. 6). It is known that in the presence of aqueous Fe(II) and at near neutral pH values or at acidic conditions (pH < 3), Cr(VI) is reduced to Cr(III) at a very high reaction rate that is proportional to the Fe(II)/Cr(VI) ratio (Buerge and Hug, 1997). We assume that the Fe(II)/Cr(VI) ratio and the Cr(VI) reduction rate in the vicinity of the Fe(II) inlet location were higher than in the batch experiment. This assumption is based on the observation that the overall $Fe(II)_{added}/Cr(VI)_{initial}$ ratio of the iron-added experiment was the same as the initial Fe(II)/Cr(VI) ratio of the batch experiment after only ca. 3 min (Dossing et al., 2011). Consequently, it is

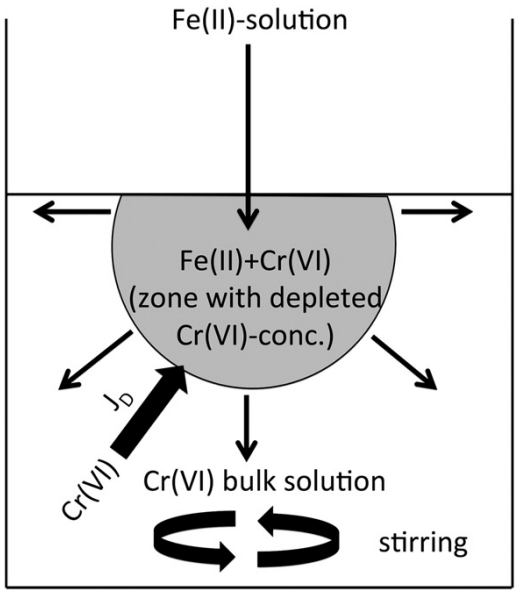

Fig. 6. Conceptual model for simulating the Fe(II)-added–Cr(VI) reduction experiment performed by Dossing et al. (2011): Cr(VI) reduction occurs at a high reaction rate but only within a limited volume with a sufficient amount of Fe(II) (gray domain). Cr(VI) exchange between bulk solution and depletion zone occurs via stirring and diffusive Cr(VI) flux J_D. During the course of the experiment this Cr(VI)-depleted domain increases due to a decrease in the overall Cr(VI) concentration and a wider spread of injected Fe(II).

proposed that a zone with a depleted Cr(VI) concentration and complete Fe(II) consumption was established at the inlet location (Fig. 6). Moreover, it is assumed that the pH-value of the depletion zone is locally different when compared to the bulk solution since Cr(VI) reduction and subsequent $Fe(OH)_3$ precipitation lead to a significant pH change (Eqs. (4), (5) and (11)).

Cr(VI) exchange between the bulk solution and the depletion zone occurred via stirring but also due to a diffusive flux induced by the proposed Cr(VI) concentration gradient (Eq. (3)). The diffusive Cr(VI) flux J_D (Eq. (3)) towards the depletion zone was likely decreasing during the course of the experiment since the bulk Cr(VI) concentration and Cr(VI) concentration gradient, respectively, were decreasing with time (Dossing et al., 2011). The decrease in diffusive Cr(VI) flux most likely led to a gradual increase of the volume of the proposed Cr(VI) depletion (and Fe(II) consumption) zone until it covered the whole experimental volume. This stage corresponds to the time in the experiment when the bulk Cr(VI) concentration was below the detection limit and the Fe(II) concentration started to increase (Dossing et al., 2011).

Because the proposed conceptual model assumes a high molecular scale Cr(VI) reduction rate, which is possibly transport-limited, Cr isotope fractionation is expected to encounter surface reaction as well as transport effects (DePaolo, 2011). These are the requirements where ε_{kin} is most effectively shifted to low values as shown with the simulations presented earlier (Figs. 3 and 4).

3.2. Model setup and simulation results

The same reaction network as described earlier was used to simulate Cr(VI) reaction and Cr isotope fractionation, assuming that Cr(VI) reduction occurs as a single molecular-scale reaction mechanism with a hypothetical equilibrium enrichment factor of 3.4‰. According to the conceptual model (Fig. 6) two grid cells were defined. One grid cell corresponds to the Cr(VI) depletion zone and one to the bulk Cr(VI) solution. The initial size of the Cr(VI) depletion zone is not known. The initial volume of the Cr(VI) depletion zone was, therefore, calculated based on an arbitrary assumption that Fe(II) injected during the first minute is completely consumed by Cr(VI) reduction. This assumption resulted in a volume of 2.48 mL for the depletion zone and a volume of 197.5 mL for the bulk solution (Table 5) taking into account initial bulk Cr(VI) concentration, Fe(II) concentration of the added Fe(II) solution and the stoichiometry of the Cr(VI) reduction reaction considered by the reaction network (Eqs. (4) and (5)). The composition of the initial bulk Cr(VI) solution was specified according to Dossing et al. (2011) (Table 5). Dilute deionized water was assumed for the initial concentration of the Cr(VI) depletion zone. The injection of the Fe(II) solution was simulated by specifying 0.025 mmol of a hypothetical solid $FeCl_2$ phase within the Cr(VI) depletion zone. $FeCl_2$ was defined to kinetically dissolve following a TST rate law similar to Eq. (9) and producing aqueous Fe^{2+} and Cl^-:

$$FeCl_2 = Fe^{2+} + 2Cl^-. \quad (13)$$

An arbitrary high equilibrium constant of log(K) = 50, a reaction rate of 0.18 mmol/s/$kg_{H_2O,}$ and no surface area dependence was defined to ensure the same constant Fe(II) injection rate as in the actual experiment (0.8 mL/min, Fe(II) concentration = 35.81 mmol/L). The specification of chemical equilibrium with a hypothetical "fix_pH" mineral phase

$$fix_pH = H^+ \quad (14)$$

maintained the pH value of the bulk solution at 8.1 (Fig. 7) when using a log(K) of −8.1. In doing so, the model does not have to explicitly

Table 5
Initial conditions of the two domains defined to model the Dossing et al (2011) Fe(II)-added–Cr(VI) reduction experiment.

		Cr(VI) Bulk solution	Cr(VI) depletion zone
Volume[a]	mL	197.5	24.8
Mineralogy[a]		No mineral reaction allowed	50 vol.% NaOH, 50 vol.% $FeCl_2$, $Fe(OH)_3$ and $Cr(OH)_3$ precipitation (Cr(VI) reduction) allowed
Porosity[a]	–	1	0.1
Permeability	m[b]	1.00E−10	1.00E−10
Distance to interface	m	2.25	2.5
Initial area A between cells	m[b]	0.4	0.4
pH		8.1	7
$^{53}CrO_4^{2-}$	mol/L	3.65E−04	1.00E−10
$^{52}CrO_4^{2-}$	mol/L	3.22E−03	1.00E−10
K^+	mol/L	7.18E−03	1.00E−10
Cl^-	mol/L	6.60E−05	1.00E−10
Fe^{2+}	mol/L	1.00E−10	1.00E−10

[a] This definition leads to a initial volume of the Cr(VI) depletion zone of 2.48 mL (1.2‰ of total volume) and initial NaOH and $FeCl_2$ concentrations of 0.025 mmol and 0.08 mmol.
[b] $\delta^{53}Cr = 0.0‰$.

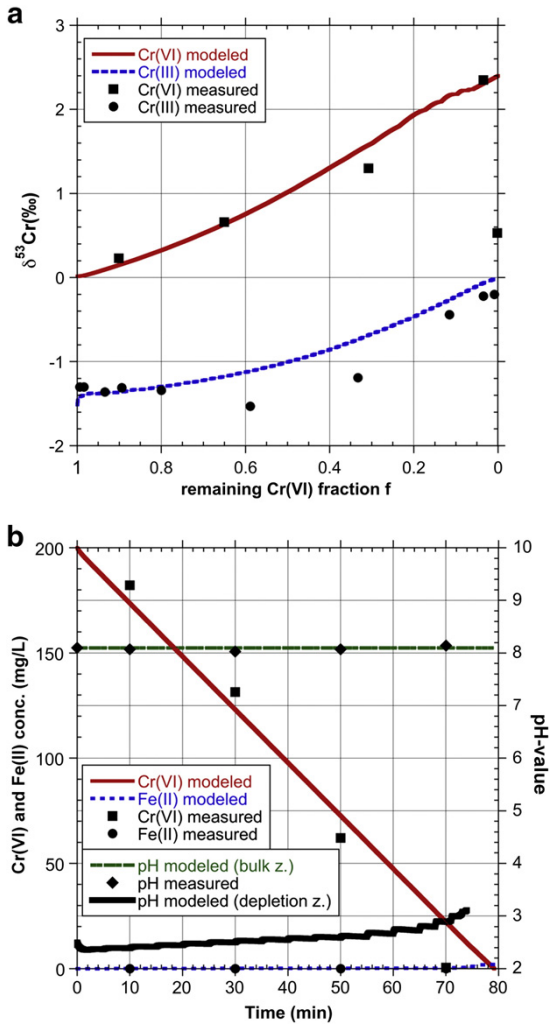

Fig. 7. Comparison between measured and modeled δ^{53}Cr-values (a) and aqueous concentrations (b) of the Dossing et al. (2011) Fe(II)-added–Cr(VI) reduction experiment. Simulated values refer to the bulk solution except for the solid δ^{53}Cr values, which refer to the Cr(VI) depletion zone, and the pH values that are shown for both zones.

consider the injection of a NaOH solution as it was performed during the Dossing et al. (2011) experiment to fix the pH at this value. Diffusive Cr(VI) transport into the depletion zone was simulated based on Eqs. (2) and (3). Small assumed values of 0.25 and 0.225 mm were assigned to d_1 and d_2, respectively (Table 5). The reaction rate constant k for the Cr(VI) reduction (Eqs. (4) and (5)) and the interfacial area between the two grid cells were calibrated in order to get an initial δ^{53}Cr of the Cr(III) formed within the depletion zone of −1.4‰ (Fig. 7). This resulted in $k = 2 \cdot 10^{-5}$ mol/m^2/s and A = 0.4 m^2. It has to be pointed out that resulting δ^{53}Cr values were only sensitive with respect to A unless k was higher than $k = 2 \cdot 10^{-20}$ mol/m^2/s. The specified diffusive flux was most likely higher than in the actual experiment because stirring effects cannot be accurately simulated with TOUGHREACT and had to be compensated by an increased diffusive flux. Furthermore, our simulations did not allow for changing grid cell volumes during a simulation run. The lack of an evolving Cr(VI) depletion zone was compensated by a time-dependent increase in the diffusive Cr(VI) flux J_D. Stopping and restarting the simulation 18 times ensured such an increase in the diffusive Cr(VI) flux because before each restart the interfacial area A (Eq. (3)) between the two zones was increased. The actual values for A (Table 6) were calibrated in order to get a good fit with the measured δ^{53}Cr values for Cr(III) and Cr(VI) respectively (Fig. 7a). Fig. 7b illustrates that the model setup and model calibration also results in a reasonable independent reproduction of measured Fe(II) and Cr(VI) concentrations as well as measured pH-values. Fig. 7b also illustrates that Cr(VI) reduction and subsequent precipitation of $Fe(OH)_3$ lead to initially low pH values within the Cr(VI) depletion zone (pH = 2.3) that only slightly increased during the course of the experiment. The observed minor pH oscillations (Fig. 7b) are a result of the stepwise increase of the interfacial area A (Table 6) leading to unsmooth OH^- diffusion into the Cr(VI) depletion zone.

3.3. Discussion

The successful simulation of the trend of all measured parameters (Fig. 7) lends strong support for our conceptual model (Fig. 6) even though the actual Cr(VI) reduction mechanism and equilibrium enrichment factor, respectively are not known and transport processes (e.g., stirring effects, evolving volumes) could not be fully simulated. The use of an increasing interface area as proxy for the evolving Cr(VI) depletion volume (Table 6) can be justified by the fact that the interfacial area must have increased as the volume of the Cr(VI) depletion zone also increased (Fig. 6). Because the interfacial area A and the reaction rate constant k were the most sensitive parameters in model calibration, it is inferred that the experiment ran in the transport and surface reaction limited regime (DePaolo, 2011), where ε_{kin} is most effectively shifted to low values (Figs. 3 and 4). Accordingly, it is suggested that the low observed enrichment factor is most likely attributed to both, a transport-limited overall Cr(VI) reduction rate and a high molecular-scale Cr(VI) reduction rate r_n. Such a fast reduction rate was possibly induced by the low pH value of the proposed Cr(VI) depletion zone since fast reaction kinetics between Cr(VI) and Fe(II) have been observed for pH values < 3 (Buerge and Hug, 1997). However, the model does not explicitly consider a pH dependence on the molecular scale Cr(VI) reduction rate and it is therefore only inferred that a fast molecular-scale Cr(VI) reduction rate is necessary to obtain the observed Cr isotope fractionation. Our interpretation does not rule out contribution of another Cr(VI) reduction mechanism with a low equilibrium enrichment factor, such as stated by Dossing et al. (2011). However, a specific mechanism solely responsible for the small enrichment factor seems very unlikely since the observed value is smaller than in most other published experiments (Table 1). This observation is notable because

Table 6
Calibrated time dependent interfacial areas between the Cr(VI) depletion zone and the bulk Cr(VI) solution.

Time period (min)	Interfacial area A (m^2)
0–2	0.4
2–5	0.42
5–10	0.45
10–15	0.49
15–20	0.534
20–25	0.581
25–30	0.633
30–35	0.689
35–40	0.75
40–45	0.817
45–50	0.889
50–55	0.966
55–60	1.115
60–65	1.400
65–68	1.700
68–71	2.150
71–73	2.800
73–74	4.000
74–80	[a]

[a] Not simulated, values shown in Fig. 7 were extrapolated.

these other experiments were performed in closed systems that were much closer to equilibrium conditions than the Dossing et al. (2011) Fe(II)-added–Cr(VI) reduction experiment.

4. Conclusions

The simulations presented in this paper illustrate that a system's effective kinetic Cr isotope enrichment factor is dependent on the specific Cr(VI) reduction mechanism (e.g., equilibrium enrichment factor), specific molecular scale Cr(VI) reduction rate and on transport limitations of a system's overall Cr(VI) reduction rate. The simulations also confirmed that for surface reaction-controlled and transport-limited systems the observed effective kinetic Cr isotope enrichment factor could be substantially shifted to very low values even though the molecular scale Cr(VI) reduction mechanism remained constant. Both effects should be addressed when discussing experimental results of Cr(VI) reduction experiments but also when referring to Cr isotope data collected at field sites. In the case of the Dossing et al. experiment, a completely different interpretation could be given by addressing transport limitations and surface kinetic effects.

The fact that the proposed reaction network allowed an independent assessment of the contributions of the individual factors on the resulting enrichment factor confirms that reactive transport modeling is a powerful tool when it comes to data interpretation. Such models do, however, require a lot of quantitative information on the relevant reactive and transport processes, and many details regarding the experimental conditions. Regarding fractionation effects of different Cr(VI) reduction mechanisms, there is currently still a lack of information. An equilibrium enrichment behavior, that is a thermodynamically defined variable for a specific molecular scale Cr(VI) reduction mechanism, was so far only reported for one particular experiment. In order to have a better constraint on the degree of variation of equilibrium Cr isotopic enrichment factors, more experimental data are needed. Moreover, there is a need for more rigorous quantitative assessment of diffusive Cr(VI) transport across passivation layers and biofilms/biological reaction systems. In conjunction with reactive transport modeling such experimental data could help to tightly constrain the Cr isotope fractionation factor for a given reaction mechanism under specific experimental (e.g., transport-limited) conditions. Tightly constrained fractionation factors may then be used in conjunction with large-scale 2D or 3D reactive transport models to obtain a more robust quantification of Cr(VI) reduction efficiencies for environmental systems, and in paleoclimatic interpretations. Such models benefit from the fact that large-scale aquifer heterogeneities can be considered as well. This is important since field-scale Cr(VI) reduction mostly occurs within locally reduced domains (e.g., engineered or naturally occurring) that may be physically separated from the predominant advective contaminant transport domain. Accordingly, transport of Cr(VI) to potential reducing agents or vice versa may introduce another degree of transport limitation in addition to the ones occurring at the experimental/reaction scale.

Acknowledgments

This work was supported by the Subsurface Science Scientific Focus Area funded by the U.S. Department of Energy, Office of Science, Office of Biological and Environmental Research under award number DE-AC02-05CH11231. We thank Nicolas Spycher for constructive discussion. The manuscript was also improved thanks to the comments of two anonymous reviewers.

References

Ball, J.W., Nordstrom, D.K., 1998. Critical evaluation and selection of standard state thermodynamic properties for chromium metal and its aqueous ions, hydrolysis species, oxides, and hydroxides. Journal of Chemical and Engineering Data 43, 895–918.

Basu, A., Johnson, T.M., 2012. Determination of hexavalent chromium reduction using Cr stable isotopes: isotopic fractionation factors for permeable reactive barrier materials. Environmental Science and Technology 46, 5353–5360.

Bender, M.L., 1990. The $\delta^{18}O$ of dissolved O_2 in seawater — a unique tracer of circulation and respiration in the deep sea. Journal of Geophysical Research—Oceans 95, 22243–22252.

Berna, E.C., Johnson, T.M., Makdisi, R.S., Basui, A., 2010. Cr stable isotopes as indicators of Cr(VI) reduction in groundwater: a detailed time-series study of a point-source plume. Environmental Science and Technology 44, 1043–1048.

Bigeleisen, J., Mayer, M.G., 1947. Calculation of equilibrium constants for isotopic exchange reactions. Journal of Chemical Physics 15, 261–267.

Brandes, J.A., Devol, A.H., 1997. Isotopic fractionation of oxygen and nitrogen in coastal marine sediments. Geochimica et Cosmochimica Acta 61, 1793–1801.

Buerge, I.J., Hug, S.J., 1997. Kinetics and pH dependence of chromium(VI) reduction by iron(II). Environmental Science and Technology 31, 1426–1432.

Canfield, D.E., 2001. Biogeochemistry of sulfur isotopes. Stable Isotope Geochemistry: In: Valley, J.W., Cole, D.R. (Eds.), Reviews in Mineralogy and Geochemistry, 43, pp. 607–636.

Coby, A.J., Picardal, F., Shelobolina, E., Xu, H., Roden, E.E., 2011. Repeated anaerobic microbial redox cycling of iron. Applied and Environmental Microbiology 77, 6036–6042.

Davis, A., Olsen, R.L., 1995. The geochemistry of chromium migration and remediation in the subsurface. Ground Water 33, 759–768.

DePaolo, D.J., 2011. Surface kinetic model for isotopic and trace element fractionation during precipitation of calcite from aqueous solutions. Geochimica et Cosmochimica Acta 75, 1039–1056.

Dossing, L.N., Dideriksen, K., Stipp, S.L.S., Frei, R., 2011. Reduction of hexavalent chromium by ferrous iron: a process of chromium isotope fractionation and its relevance to natural environments. Chemical Geology 285, 157–166.

Dzombak, D.A., Morel, F.M.M., 1990. Surface Complexation Modeling: Hydrous Ferric Oxide. John Wiley & Sons, New York.

Ellis, A.S., Johnson, T.M., Bullen, T.D., 2002. Chromium isotopes and the fate of hexavalent chromium in the environment. Science 295, 2060–2062.

Faybishenko, B., Hazen, T.C., Long, P.E., Brodie, E.L., Conrad, M.E., Hubbard, S.S., Christensen, J.N., Joyner, D., Borglin, S.E., Chakraborty, R., Williams, K.H., Peterson, J.E., Chen, J., Brown, S.T., Tokunaga, T.K., Wan, J., Firestone, M., Newcomer, D.R., Resch, C.T., Cantrell, K.J., Willett, A., Koenigsberg, S., 2008. In situ long-term reductive bioimmobilization of Cr(VI) in groundwater using hydrogen release compound. Environmental Science and Technology 42, 8478–8485.

Flury, B., Eggenberger, U., Mäder, U., 2009. First results of operating and monitoring an innovative design of a permeable reactive barrier for the remediation of chromate contaminated groundwater. Applied Geochemistry 24, 687–696.

Frei, R., Gaucher, C., Poulton, S.W., Canfield, D.E., 2009. Fluctuations in Precambrian atmospheric oxygenation recorded by chromium isotopes. Nature 461, 250-U125.

Frost, R.L., 2004. Raman microscopy of selected chromate minerals. Journal of Raman Specroscopy 35, 153–158.

Green, C.T., Bohlke, J.K., Bekins, B.A., Phillips, S.P., 2010. Mixing effects on apparent reaction rates and isotope fractionation during denitrification in a heterogeneous aquifer. Water Resources Research 46.

Han, R., Geller, J.T., Yang, L., Brodie, E.L., Chakraborty, R., Larsen, J.T., Beller, H.R., 2010. Physiological and transcriptional studies of Cr(VI) reduction under aerobic and denitrifying conditions by an aquifer-derived pseudomonad. Environmental Science and Technology 44, 7491–7497.

Han, R., Qin, L., Brown, S.T., Christensen, J.N., Beller, H.R., 2012. Differential isotopic fractionation during Cr(VI) reduction by an aquifer-derived bacterium under aerobic versus denitrifying conditions. Applied and Environmental Microbiology 78, 2462–2464.

Hancock, R.E.W., Wong, P.G.W., 1984. Compounds which increase the permeability of the *Pseudomonas aeruginosa* outer-membrane. Antimicrobial Agents and Chemotherapy 26, 48–52.

Harvey, R.W., George, L.H., Smith, R.L., Leblanc, D.R., 1989. Transport of microspheres and indigenous bacteria through a sandy aquifer: results of natural- and forced-gradient tracer experiments. Environmental Science and Technology 23, 51–56.

Izbicki, J.A., Ball, J.W., Bullen, T.D., Sutley, S.J., 2008. Chromium, chromium isotopes and selected trace elements, western Mojave Desert, USA. Applied Geochemistry 23, 1325–1352.

Jamieson-Hanes, J.H., Gibson, B.D., Lindsay, M.B.J., Kim, Y., Ptacek, C.J., Blowes, D.W., 2012. Chromium isotope fractionation during reduction of Cr(VI) under saturated flow conditions. Environmental Science and Technology 46, 6783–6789.

Jeen, S.W., Jambor, J.L., Blowes, D.W., Gillham, R.W., 2007. Precipitates on granular iron in solutions containing calcium carbonate with trichloroethene and hexavalent chromium. Environmental Science and Technology 41, 1989–1994.

Johnson, J.W., Oelkers, E.H., Helgeson, H.C., 1992. SUPCRT92: a software package for calculating the standard molal thermodynamic properties of minerals, gases, aqueous species, and reactions from 1 to 5000 bar and 0 to 1000 °C. Computer & Geoscience 18, 899–948.

Jones, C.M., Niederweis, M., 2010. Role of porins in iron uptake by *Mycobacterium smegmatis*. Journal of Bacteriology 192, 6411–6417.

Kitchen, J.W., Johnson, T.M., Bullen, T.D., Zhu, J., Raddatz, A., 2012. Chromium isotope fractionation factors for reduction of Cr(VI) by aqueous Fe(II) and organic molecules. Geochimica et Cosmochimica Acta 89, 190–201.

Kotas, J., Stasicka, Z., 2000. Chromium occurrence in the environment and methods of its speciation. Environmental Pollution 107, 263–283.

Lasaga, A.C., 1984. Chemical kinetics of water–rock interactions. Journal of Geophysical Research 89, 4009–4025.

Nikaido, H., 2003. Molecular basis of bacterial outer membrane permeability revisited. Microbiology and Molecular Biology Reviews 67, 593–656.

Nordstrom, D.K., Munoz, J.L., 1985. Geochemical Thermodynamics. Benjamin/Cummings Publishing Company, Redwood City, CA USA.

Palmer, C.D., Puls, R.W., 1994. Natural attenuation of hexavalent chromium in groundwater and soils. EPA Ground Water Issue Paper EPA/540/5-94/505. U.S. Environmental Protection Agency, U.S Government Printing Office, Washington, DC.
Pearson, J.P., Van Delden, C., Iglewski, B.H., 1999. Active efflux and diffusion are involved in transport of *Pseudomonas aeruginosa* cell-to-cell signals. Journal of Bacteriology 181, 1203–1210.
Rai, D., Sass, B.M., Moore, D.A., 1987. Chromium(III) hydrolysis constants and solubility of chromium(III) hydroxide. Inorganic Chemistry 26, 345–349.
Reed, M.H., 1982. Calculation of multicomponent chemical equilibria and reaction processes in systems involving minerals, gases and aqueous phase. Geochimica et Cosmochimica Acta 46, 513–528.
Rees, C.E., 1973. Steady-state model for sulfur isotope fractionation in bacterial reduction processes. Geochimica et Cosmochimica Acta 37, 1141–1162.
Schauble, E., Rossman, G.R., Taylor, H.P., 2004. Theoretical estimates of equilibrium chromium-isotope fractionations. Chemical Geology 205, 99–114.
Schoenberg, R., Zink, S., Staubwasser, M., von Blanckenburg, F., 2008. The stable Cr isotope inventory of solid earth reservoirs determined by double spike MC-ICP-MS. Chemical Geology 249, 294–306.
Sikora, E.R., Johnson, T.M., Bullen, T.D., 2008. Microbial mass-dependent fractionation of chromium isotopes. Geochimica et Cosmochimica Acta 72, 3631–3641.
Singleton, M.J., Sonnenthal, E.L., Conrad, M.E., DePaolo, D.J., Gee, G.W., 2004. Multiphase reactive transport modeling of stable isotope fractionation in unsaturated zone pore water and vapor: application to seasonal infiltration events at the Hanford Site, WA. Vadose Zone Journal 3, 775–785.
Urey, H.C., 1947. The thermodynamic properties of isotopic substances. Journal of the Chemical Society 562–581.
Wanner, C., Eggenberger, Mäder, U., 2011. Reactive transport modeling of Cr(VI) treatment under fast flow conditions. Applied Geochemistry 26, 1513–1523.
Wanner, C., Eggenberger, U., Kurz, D., Zink, S., Mäder, U., 2012a. A chromate-contaminated site in southern Switzerland, part 1: site characterization and the use of Cr isotopes to delineate fate and transport. Applied Geochemistry 27, 644–654.
Wanner, C., Zink, S., Eggenberger, U., Mäder, U., 2012b. Assessing the Cr(VI) reduction efficiency of a permeable reactive barrier using Cr isotope measurements and 2D reactive transport modeling. Journal of Contaminant Hydrology 131, 54–63.
Wanner, C., Eggenberger, Mäder, U., 2012c. A chromate-contaminated site in southern Switzerland, part 2: reactive transport modeling to optimize remediation options. Applied Geochemistry 27, 655–662.
Watson, E.B., Mueller, T., 2009. Non-equilibrium isotopic and elemental fractionation during diffusion-controlled crystal growth under static and dynamic conditions. Chemical Geology 267, 111–124.
Wolery, T.J., 1992. EQ3/6: software package for geochemical modeling of aqueous systems: package overview and installation guide (version 7.0). Lawrence Livermore National Laboratory Report UCRL-MA-110662 PT I. Livermore, California.
Xu, T., 2008. Incorporating aqueous reaction kinetics and biodegradation into TOUGHREACT: applying a multiregion model to hydrobiogeochemical transport of denitrification and sulfate reduction. Vadose Zone Journal 7, 305–315.
Xu, T., Spycher, N.F., Sonnenthal, E., Zhang, G., Zheng, L., Pruess, K., 2011. TOUGHREACT version 2.0: a simulator for subsurface reactive transport under non-isothermal multiphase flow conditions. Computer & Geoscience 37, 763–774.
Young, E.D., Galy, A., Nagahara, H., 2002. Kinetic and equilibrium mass-dependent isotope fractionation laws in nature and their geochemical and cosmochemical significance. Geochimica et Cosmochimica Acta 66, 1095–1104.
Zink, S., Schoenberg, R., Staubwasser, M., 2010. Isotopic fractionation and reaction kinetics between Cr(III) and Cr(VI) in aqueous media. Geochimica et Cosmochimica Acta 74, 5729–5745.

3.2. Microbial U isotope fractionation depends on the U(VI) reduction rate

Source:

Basu A., **Wanner C.**, Johnson T. M., Lundstrom C. C., Sanford R. A., Sonnenthal E. L., Boyanov M. I. and Kemner K. M. (2020) Microbial U isotope fractionation depends on the U(VI) reduction rate. *Environmental Science &. Technology* **54**, 2295-2303.

Contribution by the Author (CW):

CW carried out all the simulations and lead the interpretation of the simulation results. Moreover, CW wrote the RTM sections of the paper and significantly contributed to the remaining parts of the manuscript.

Environmental Science & Technology

pubs.acs.org/est

Article

Microbial U Isotope Fractionation Depends on the U(VI) Reduction Rate

Anirban Basu,* Christoph Wanner, Thomas M. Johnson, Craig C. Lundstrom, Robert A. Sanford, Eric L. Sonnenthal, Maxim I. Boyanov, and Kenneth M. Kemner

Cite This: *Environ. Sci. Technol.* 2020, 54, 2295−2303

Read Online

ACCESS | Metrics & More | Article Recommendations | Supporting Information

ABSTRACT: U isotope fractionation may serve as an accurate proxy for U(VI) reduction in both modern and ancient environments, if the systematic controls on the magnitude of fractionation (ε) are known. We model the effect of U(VI) reduction kinetics on U isotopic fractionation during U(VI) reduction by a novel *Shewanella* isolate, *Shewanella* sp. (NR), in batch incubations. The measured ε values range from 0.96 ± 0.16 to 0.36 ± 0.07‰ and are strongly dependent on the U(VI) reduction rate. The ε decreases with increasing reduction rate constants normalized by cell density and initial U(VI). Reactive transport simulations suggest that the rate dependence of ε is due to a two-step process, where diffusive transport of U(VI) from the bulk solution across a boundary layer is followed by enzymatic reduction. Our results imply that the spatial decoupling of bulk U(VI) solution and enzymatic reduction should be taken into account for interpreting U isotope data from the environment.

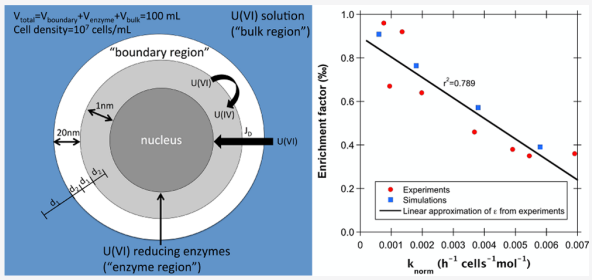

INTRODUCTION

The uranium isotope ratio $^{238}U/^{235}U$ is an effective proxy for understanding microbially mediated uranium (U) reduction, which is an integral part of the global U cycling throughout geologic time. Bacterial reduction of soluble U(VI) to insoluble U(IV) leads to preferential partitioning of ^{238}U in the U(IV) solids with the lowest possible electron density configuration at the nucleus.[1−3] This equilibrium isotopic exchange resulting from the differences in nuclear size and shape is described in the literature as a nuclear volume effect (NVE).[4,5] However, it is not clear how and at which rate the exchange occurs during kinetically controlled and irreversible microbial reduction. With continued bacterial reduction, the residual aqueous U(VI) becomes progressively enriched in ^{235}U. Direct measurement of $^{238}U/^{235}U$ permits the quantification of U cycling in both modern and ancient environments such as contaminated aquifers[6,7] and the rock record,[8] but this is predicated on a robust understanding of the factors that control the magnitude of U isotopic fractionation during microbial U(VI) reduction.

The magnitude of U isotope fractionation caused by bacterial U(VI) reduction is variable. Generally, it is expressed as the enrichment factor ε (ε (‰) = 1000 × (α − 1); α = ($R_{\text{instantaneous U(IV) product}}/R_{\text{U(VI)}}$), where R is $^{238}U/^{235}U$). A field-scale biostimulation of a U(VI)-contaminated aquifer at Rifle, CO, USA, has yielded an apparent fractionation (as ε) of 0.46‰.[9] Laboratory batch incubations with a diverse group of bacteria have revealed a range of ε from 0.7 to 1.0‰.[1] Subsequent experimental work has reported a similar range for batch incubations with single strains.[2,3] The large variability of ε translates to large uncertainties in determining the fraction of reduction of toxic U(VI) in contaminated aquifers[9−11] or the extent of anoxia in ancient oceans,[12] which makes the interpretation of the environmental U isotope data equivocal. To date, the origins and nature of variability of ε for microbial U(VI) reduction have not been fully explored. For similar redox-active elements such as S and N, however, the variation of ε is systematically controlled by the rate of microbial sulfate and nitrate reduction (e.g., refs 13 and 14).

The key role of bacterial physiology in controlling the S isotopic fractionation by sulfate reducers is well understood.[13,15,16] One crucial factor that controls the S isotope fractionation is the balance between the rate of sulfate delivery into the cell and the rate of sulfate reduction in the cell.[13,17] The fractionation is maximized when the transport of sulfate into the cell is unlimited and the electron donor supply is limited, leading to slow reduction.[13] In contrast, when the supply of sulfate is low relative to the supply of the electrons such that the supplied sulfate is rapidly, and nearly quantitatively, reduced, the S isotopic fractionation diminishes

Received: October 2, 2019
Revised: December 30, 2019
Accepted: January 7, 2020
Published: January 7, 2020

to zero. The balance between the reduction rate and supply of sulfate depends on the components of enzymatic reaction machinery and the electron transport chain. Similarly, we expect that microbial U isotopic fractionation may be influenced by the rate of U(VI) reduction relative to the rate of U(VI) supply, despite differences in mechanisms of U(VI) reduction and cellular transport of U(VI).

Bacterial strains from the *Shewanella* genera are particularly well-studied for their U(VI) reduction ability, which has generally been attributed to membrane-associated enzymes—c-type cytochromes associated with the outer membrane or the periplasmic space.[18−22] Consequently, the U(IV) reaction products are observed to form outside the cell, on the cell membrane, and in the periplasmic space in several *Shewanella* species.[21,23] Therefore, the localization of U(VI) reduction in the vicinity of the outer membrane or periplasmic enzymes may influence the balance between the U(VI) delivery and reduction rate.

Here, we demonstrate the effect of variable U(VI) reduction rates on the magnitude of isotopic fractionation in batch incubation experiments with *Shewanella* sp. (NR). We varied the initial U(VI) concentration while keeping other parameters (e.g., electron donor concentration, cell density) the same, and we determined the magnitude of isotopic fractionation. We propose a two-step mechanistic model of U isotopic fractionation with diffusive delivery of aqueous U(VI), followed by enzymatic U(VI) reduction. In this model, we consider a diffusive boundary layer surrounding the cell separating a region of enzymatic reduction from the bulk U(VI) solution. We test this conceptual model by reactive transport simulations of U(VI) reduction by *Shewanella* sp. (NR) to demonstrate the role of reaction kinetics in controlling the overall isotopic fractionation.

METHODS

Media for Bacterial Cultures and U(VI) Incubations. *Shewanella* sp. (NR) cultures were grown anaerobically in 80−100 mL batch cultures at 30 °C using a mineral salt medium described in ref 1. Briefly, the medium contained 200 μM phosphate and 10 mM HCO_3^- buffer with a final pH of 7.2. The cultures were grown on 2.5 mM lactate as the electron donor and 1 mM NO_3^- as the electron acceptor. The medium for U(VI) incubation experiments was identical to the growth medium except that the phosphate concentration was lowered to 20 μM to avoid abiotic U(VI)-phosphate precipitation. All reductants, vitamin solution and resazurin, were omitted from both growth and test medium.

U(VI) Incubation Experiments. A uranyl carbonate solution in 100 mM $NaHCO_3$, prepared from Uranium (normal) metal CRM 112-A, was routinely used as U(VI) stock solution for desired initial U(VI) concentration in our experiments.[1] Each experiment was conducted in duplicate. A ∼10 mL inoculum (10% v/v) of pregrown *Shewanella* sp. (NR) was used for each experiment. The density of the microbial population in each reactor and the inoculum was quantified using a LSR II (BD Biosciences) flow cytometry analyzer. Abiotic control experiments with the test medium, the U(VI) bicarbonate solution, and no bacteria were conducted for selected initial U(VI) concentrations. All reactors were supplemented with 500 μM lactate as the electron donor. During the course of the experiments, all reactors were incubated at 30 °C in the dark, shaken constantly at 125 rpm. Each reactor was sampled for U(VI) concentrations and U isotopes at regular intervals. The samples were filtered using 0.2 μm filters and stored at 4 °C prior to analyses.

U Concentration and Isotope Measurements. For isotopic analysis, we used a ^{233}U + ^{236}U double isotope spike technique to correct for any isotopic fractionation arising from sample purification or mass bias of the instrument during mass spectrometry. An aliquot of double isotope spike solution, composed of ^{236}U and ^{233}U, was added to each sample prior to sample purification by the UTEVA resin.[1,6,7,9,24,25] Reported U(VI) concentrations were determined from isotope dilution calculations using measurements of spike isotopes and natural U isotopes in the samples. The $\delta^{238}U$ values were measured using a Nu Plasma high-resolution multi collector inductively coupled plasma mass spectrometer. The precision of the isotopic measurements was 0.07‰, determined using a modified root-mean-square calculation[26] for nine pairs of full procedural duplicate sample preparations. The relationship between isotopic composition and concentration from each set of U(VI) incubations was determined using a Rayleigh distillation equation

$$\delta_t = (\delta_0 + 1000‰)\left[\frac{c_t}{c_0}\right]^{\alpha-1} - 1000‰ \quad (1)$$

where c_0 and δ_0 are the initial concentration and isotopic composition of U(VI), c_t and δ_t are the concentration and isotopic composition at time t, and α is the isotopic fractionation factor. The α values were calculated from the slope of the best-fit line from linearized plots of $\ln(\delta^{238}U + 1000‰)$ versus $\ln(c_t)$.[27] The uncertainties of ε (2 × standard error) were derived from the uncertainties of the slopes from data scatter about the best-fit lines using a linear estimation method.

For experiments with early rapid U(VI) reduction, the sample taken a few minutes into each experiment is used as the effective starting point for $\delta^{238}U$ and U(VI) concentration (see the Supporting Information for more details). We also exclude some data from time points close to the completion of the reduction (e.g., >88% reduction for the experiment with $U(VI)_{t=0}$ = 18.2 μM) from our isotopic analysis. These data points are aberrantly shifted toward isotopically heavier values, which may be attributed to the contamination of the dissolved U(VI) solution by very fine U(IV) particles that later oxidize to U(VI).

Characterization of U(IV) Precipitates. Solid-phase-associated U in the reactors was separated using a 0.2 μm filter and analyzed using uranium L_{III}-edge X-ray absorption near-edge structure (XANES) at the MRCAT/EnviroCAT beamline, Advanced Photon Source, Argonne National Laboratory. The details of the analysis can be found in ref 28.

Reactive Transport Modeling. A series of reactive transport model simulations using TOUGHREACT V3[29] in combination with the EQ3/6 thermodynamic database[30] as well as uraninite solubility data taken from ref 31 are performed to simulate U(VI) reduction and associated U isotopic fractionation. TOUGHREACT has been widely applied to evaluate isotopic fractionation coupled to the water−rock interaction and biogeochemical processes in a variety of subsurface environments and laboratory experiments.[32,33] Furthermore, the TOUGHREACT approach for simulating isotopic fractionation coupled to redox reactions has been recently benchmarked.[34]

https://dx.doi.org/10.1021/acs.est.9b05935
Environ. Sci. Technol. 2020, 54, 2295−2303

Conceptual Model. Our simplified conceptual model considers that cells are surrounded by boundary layers with U(VI) concentrations lower than those in the bulk solution (Figure 1). Consequently, for our simulations, we assume that

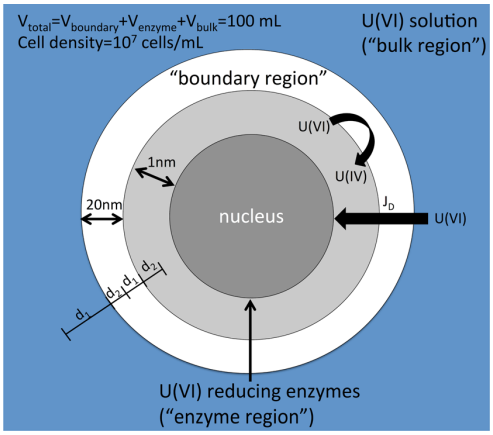

Figure 1. Conceptual model to simulate U(VI) reduction and associated U isotopic fractionation. The model assumes that U(VI) reduction occurs as a two-step process with (i) diffusive U(VI) transport (JD) from the bulk solution (bulk region) to an active site where (ii) enzymatic U(VI) reduction is occurring (enzyme region), which may be at the cell surface or within the periplasmic space. d_1 and d_2 refer to the distances from the centers of two adjacent regions to their mutual interface (Table S2).

U(VI) reduction occurs as a two-step process with (i) diffusive U(VI) transport through boundary layers and (ii) enzymatic U(VI) reduction at the cell surface or within the periplasmic space. A similar conceptual approach was successfully used by ref 32 to demonstrate that Cr isotopic fractionation inherited from Cr(VI) reduction is muted if the reduction rate is high and/or diffusive transport is slow.

Model Setup. U(VI) reduction and associated U isotopic fractionation are simulated for a static batch reactor with no flow. A multiregion approach[35] is used to numerically formulate the conceptual model (Figure 1). To do so, the batch reactor is discretized into three different regions: (i) a bulk region corresponding to the U(VI) solution that is continuously sampled during the experiment, (ii) an enzyme region with enzymatic U(VI) reduction, and (iii) a boundary region separating the previous two.

The physical parameters defined for the three regions are listed in Table S2 (Supporting Information). The simulations are performed for a model volume of 100 mL similar to that of the experiments. The volumes of the individual regions and mutual interfaces are defined assuming a cell density of 10^7 cells/mL, which is the average cell density of our experiments; a cuboid shape of *Shewanella* with a diameter of 0.6 μm and a length of 3.4 μm;[36] and a boundary layer thickness of 20 nm. Although 20 nm approximately corresponds to the thickness of the entire Gram-negative membrane of *Shewanella*,[37] we aim to simulate a general case where the location of U(VI) reduction is physically separated from the bulk U(VI) solution.

The cell density is kept constant during our simulations, indicating that we do not simulate microbial growth occurring in our experiments. The diffusive flux of U(VI) (J_D) through the individual regions of our model (Figure 1) is calculated according to

$$J_D = D_{aq}\cdot\tau\cdot\phi\cdot\frac{A}{d_1+d_2}\cdot\frac{dC}{dx} \quad (2)$$

where D_{aq} refers to the diffusion coefficient of aqueous species, A (m^2) is the interfacial area between two adjacent regions, dC/dx refers to the U(VI) concentration gradient across a region (mol/kg_{H_2O}/m), d_1 and d_2 refer to the distances from the centers of two adjacent regions to their mutual interface (Figure 1), τ is the tortuosity, and ϕ is the porosity, which was set to 0.99. For the simulations, it was assumed that the bulk region is fully mixed because the experiments were continuously stirred. Accordingly, the tortuosity of the bulk region was set to a very high value of 10^8. A value of 10^8 was also defined for the 1 nm thick enzyme region because we assume that U(VI) is not further diffusively transported once it reaches a particular enzyme.

Reaction Network. U(VI) reduction to U(IV) was assumed to occur exclusively within the enzyme region of our model (Figure 1). It was simulated as a kinetic reaction with lactate ($C_3H_5O_3^-$) under the production of HCO_3^- and acetate ($C_2H_3O_2^-$) assuming that U(IV) immediately precipitates as uraninite ($UO_{2(s)}$). To simulate the fate of ^{238}U and ^{235}U, U(VI) reduction was defined for the two dominating U(VI) and U(IV) isotopologues

$$0.5C_3H_5O_3^- + (^{235}UO_2)^{2+} + H_2O = {}^{235}UO_{2(s)} + 0.5HCO_3^- + 0.5C_2H_3O_2^- + 2.5H^+ \quad (3)$$

$$0.5C_3H_5O_3^- + (^{238}UO_2)^{2+} + H_2O = {}^{238}UO_{2(s)} + 0.5HCO_3^- + 0.5C_2H_3O_2^- + 2.5H^+ \quad (4)$$

$^{235}UO_{2(s)}$ and $^{238}UO_{2(s)}$ are defined as end members of an ideal uraninite solid solution with an overall precipitation rate ^{ss}r (mol $kg_{H_2O}^{-1}$ s^{-1}) corresponding to the sum of the precipitation rate of the two end members ($^{^{235}UO_{2(s)}}r$ and $^{^{238}UO_{2(s)}}r$)

$$^{ss}r = {}^{^{235}UO_{2(s)}}r + {}^{^{238}UO_{2(s)}}r \quad (5)$$

The precipitation rate for the $^{235}UO_{2(s)}$ and $^{238}UO_{2(s)}$ end members is calculated according to a transition-state theory-type rate law

$$^{^{235}UO_{2(s)}}r = A\cdot k\left(1-\frac{Q_{^{235}UO_{2(s)}}}{K_{^{235}UO_{2(s)}}}\right) + k_{UO_{2(s)}}\cdot A(x_{^{235}UO_{2(s)}} - 1) \quad (6)$$

$$^{^{238}UO_{2(s)}}r = A\cdot k\left(1-\frac{Q_{^{238}UO_{2(s)}}}{K_{^{238}UO_{2(s)}}}\right) + k_{UO_{2(s)}}\cdot A(x_{^{238}UO_{2(s)}} - 1) \quad (7)$$

where A ($m^2_{mineral}/kg_{H_2O}$) and $k_{UO_{2(s)}}$ (mol $kg_{H_2O}^{-1}$ m^{-2} s^{-1}) refer to the reactive surface area and the reaction rate constant of the solid solution, respectively (Table S3), $Q_{^{235}UO_{2(s)}}$ and $Q_{^{238}UO_{2(s)}}$ are the ion activity products of reactions 3 and 4, $K_{^{235}UO_{2(s)}}$ and $K_{^{238}UO_{2(s)}}$ refer to the corresponding equilibrium constants (Table S3), and $x_{^{235}UO_{2(s)}}$ and $x_{^{238}UO_{2(s)}}$ are the mole fractions of the precipitating end members. To ensure that the

https://dx.doi.org/10.1021/acs.est.9b05935
Environ. Sci. Technol. 2020, 54, 2295−2303

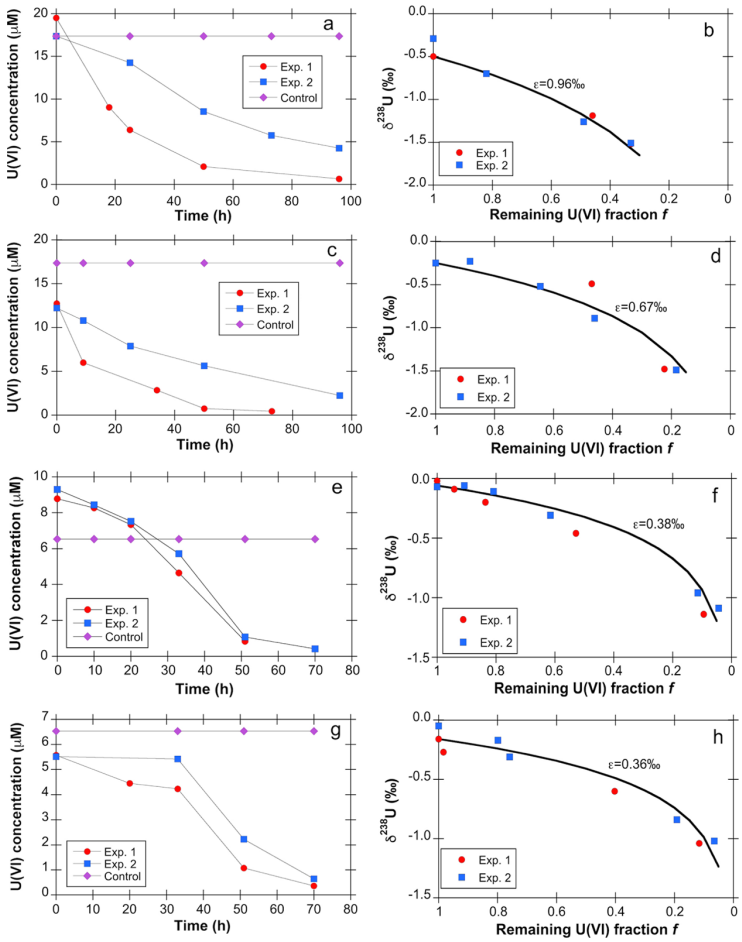

Figure 2. The left panel shows U(VI) concentration decrease during incubation with *Shewanella* sp. (NR) for U(VI) concentrations: (a) ~18.2, (c) ~12.48, (e) ~9.04, and (g) ~5.54 μM. The right panel shows concomitant U isotopic fractionations in (b,d,f,h,j), respectively.

volume ratio of these end members reflects the fluid composition, $x^{235}{}_{UO_{2(s)}}$ and $x^{238}{}_{UO_{2(s)}}$ are calculated according to

$$x^{235}{}_{UO_{2(s)}} = \frac{Q_{^{235}UO_{2(s)}}/K_{^{235}UO_{2(s)}}}{Q_{^{235}UO_{2(s)}}/K_{^{235}UO_{2(s)}} + Q_{^{238}UO_{2(s)}}/K_{^{238}UO_{2(s)}}} \quad (8)$$

$$x^{238}{}_{UO_{2(s)}} = \frac{Q_{^{238}UO_{2(s)}}/K_{^{238}UO_{2(s)}}}{Q_{^{235}UO_{2(s)}}/K_{^{235}UO_{2(s)}} + Q_{^{238}UO_{2(s)}}/K_{^{238}UO_{2(s)}}} \quad (9)$$

By setting $K^{238}{}_{UO_{2(s)}}/K^{235}{}_{UO_{2(s)}} = 1.001$ and by using a constant reactive surface area A and a reaction rate constant $k_{UO_{2(s)}}$ (eqs 6 and 7), we run our simulations with an intrinsic equilibrium ε of 1.0‰ (Table S3).

Initial Conditions. The chemical composition initially specified for the three regions of the model (Figure 1) as well as the variation of the uraninite reaction rate constant with decreasing $U(VI)_{t=0}$ is listed in Tables S4 and S5.

RESULTS AND DISCUSSION

U Concentration and Isotopic Measurements. The U(VI) concentrations and $\delta^{238}U$ measured at regular time intervals in batch incubations are shown in Figure 2. No significant U(VI) removal in control experiments indicates that the test medium does not abiotically reduce U(VI). The XANES analysis of the solid reaction products from the experiments confirms that ~90% of U is reduced to U(IV) (Figure 3). A first-order kinetic model reasonably fits the U(VI) concentration data from each reactor, except for the latest time points. The half-lives of U(VI) ($t_{1/2} = \ln(2)/k$, k = first-order rate constant) range from 15 to 45 h. The normalized first-order rate constants [k_{norm}, defined as $k_{firstorder}/(\text{cell density} \times U(VI)_{t=0})$] vary from 0.0008 to 0.007 h^{-1} $cells^{-1}$ mol^{-1} and decrease linearly with increasing initial U(VI) concentration ($r^2 = 0.762$, Figure S1).

The $\delta^{238}U$ values of the aqueous U(VI) decreased steadily relative to the starting $\delta^{238}U$ composition (~0.0‰) to a minimum of −1.52‰ after 67% reduction (Figure 2 and Table S1). The ε values are determined by fitting the data from each reactor to a Rayleigh distillation model. For each experiment, a single ε fits all data from duplicate experiments. The resulting ε values vary from 0.36 to 0.96‰ (Figure 2 and Table S1) and decrease linearly with increasing k_{norm} ($r^2 = 0.789$, Figure 4), indicating that slower U(VI) reduction yields stronger isotopic fractionation. The uncertainties (2σ) of ε values of the combined duplicate experiments range from ±0.07 to ±0.16‰.

https://dx.doi.org/10.1021/acs.est.9b05935
Environ. Sci. Technol. 2020, 54, 2295−2303

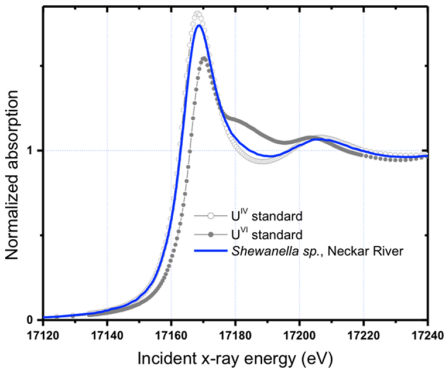

Figure 3. U L_{III}-edge XANES spectrum from the solid phase of incubations with *Shewanella* sp. (NR) (line), compared to U(VI) and U(IV) standards (symbols). The spectrum overlies the U(IV) standard, indicating the predominance of U(IV) species in the sample. The standards are (1) aqueous U(VI)-carbonate species and (2) solid-phase U(IV)-phosphate species produced during U(VI) reduction by *Desulfitobacterium* spp. More information on these standards can be found in ref 28.

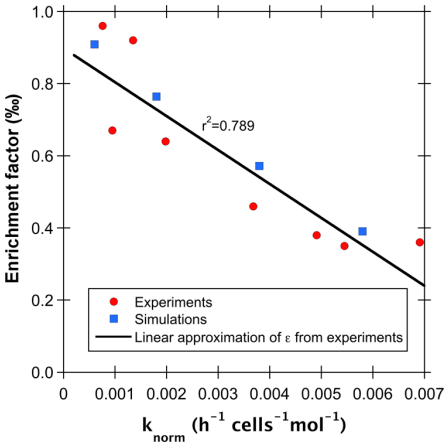

Figure 4. Correlations in the U(VI) reduction experiments with *Shewanella* sp. (NR): Isotopic fractionation ε vs normalized rate constant. Also shown are the isotopic fractionation obtained when running the model with different rate constants for different initial U(VI) concentrations and hence variable rate constants.

Reactive Transport Modeling Results. The first simulation is performed for an initial U(VI) concentration (^{238}U(VI) + ^{235}U(VI)) of 18 μM, while the initial δ^{238}U value is set to 0.0‰ according to the starting δ^{238}U of U(VI). An intrinsic ε of 1.0‰ is defined for enzymatic U(VI) reduction, which roughly corresponds to the maximum ε observed in our experiments. The chemical composition initially specified for the three regions of the model is given in Table S4. The diffusion coefficients for ^{235}U(VI), ^{238}U(VI), and all other aqueous species are set to 10^{-9} m^2 s^{-1}. A good match between experimental data and simulation results is achieved by numerically calibrating the rate constant of the specified U(VI) reduction reaction and the tortuosity of the boundary layer (Figures 5 and 6).

After calibrating the model, simulations are run for initial U(VI) concentrations of 15, 10, and 5 μM. The reaction rate constants for computing U(VI) reduction are adjusted

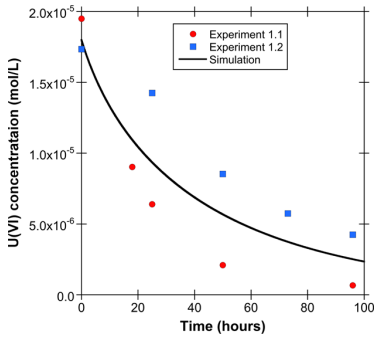

Figure 5. U(VI) concentration as a function of time obtained for an initial U(VI) concentration of ~18 μM and corresponding simulation results (bulk region) illustrating successful calibration of the model.

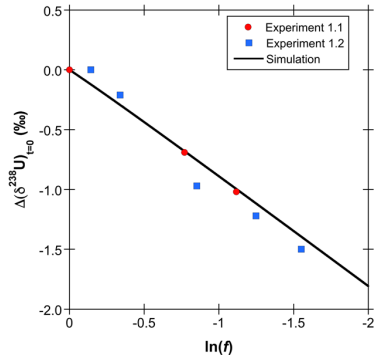

Figure 6. Relative δ^{238}U changes ($\Delta(\delta^{238}U)_{t=0}$) as a function of the natural logarithm of the remaining U(VI) fraction f obtained for an initial U(VI) concentration of ~18 μM and corresponding simulation results (bulk region) illustrating successful model calibration.

according to the correlation observed between k_{norm} and the initial U(VI) concentration (Figure S1). All other parameters are kept the same as in the simulations performed for U(VI)$_{t=0}$ = 18 μM. For all initial U(VI) concentrations, δ^{238}U decreases with progressive U(VI) reduction. When plotted against the fraction of reduction (ln(f)), simulated δ^{238}U values in the bulk region fit perfectly straight lines (r^2 = 1) (Figure 7). This demonstrates that U isotopic fractionation during U(VI) reduction follows a Rayleigh-type distillation with an effective ε that varies between the simulations despite defining a constant input ε of 1.0‰. Therefore, a Rayleigh-type model is applied to calculate the effective ε for all our simulations, which corresponds to the slope of the best-fit lines on δ^{238}U versus ln(f) plots. The ε derived from the simulations also decreases with increasing k_{norm} and matches very well with the ε derived from the experimental data (Figure 4).

Rate Dependence of U Isotopic Fractionation. Similar to microbial S or N isotopic fractionation, the dependence of U isotopic fractionation on the U(VI) reduction rate suggests a diffusive barrier between the reaction site and the bulk U(VI) pool. The diffusive barriers may arise from surface coatings of extracellular polymeric substances enveloping the cell[38−40] or from the cell membrane if a substantial portion of reduction is intracellular (i.e., occurring in the periplasmic space).[21] Therefore, we hypothesize that the site of U(VI) reduction is isolated from the bulk U(VI) solution by a diffusive boundary layer around the cells, impacting the overall

https://dx.doi.org/10.1021/acs.est.9b05935
Environ. Sci. Technol. 2020, 54, 2295−2303

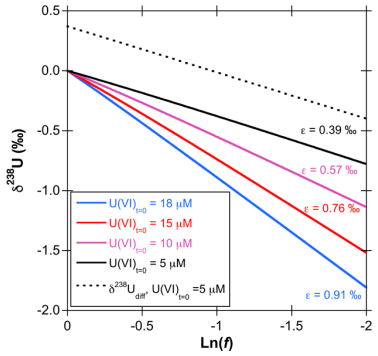

Figure 7. Model results (bulk region) for varying initial U(VI) concentrations. δ^{238}U values obtained for the bulk region are plotted as a function of the natural logarithm of the remaining U(VI) fraction f. All the simulations are plotted on perfectly straight lines ($r^2 = 1$), demonstrating that the simulation results follow a Rayleigh-type fractionation model with a specific effective epsilon, which is expressed by the corresponding slope. For the simulation with a starting U(VI) concentration of 5 μM, $\delta^{238}U_{diff}$ (eq 10) is shown as well to demonstrate that diffusion-induced fractionation causes enrichment of ^{238}U(VI) across the boundary layer ($\delta^{238}U_{diff} > \delta^{238}U_{bulk}$) and that the corresponding epsilon is equal to the one obtained from the evolution of δ^{238}U in the bulk solution.

"effective" U isotopic fractionation. The generally good reproduction of observed fractionation factors (Figure 4) as a function of reaction rate by our reactive transport simulations provides support for this hypothesis, as we discuss below.

In our models, the concentration difference of U(VI) across the diffusive boundary layer causes U(VI) to diffuse across the barrier. Because of reduction, the U(VI) concentration is lower in the enzyme region and diffusion of U(VI) always occurs from the bulk to the enzyme region. Since the diffusive transport step involves no changes in the redox state of U, it does not significantly discriminate between its isotopologues (i.e., ^{238}U(VI) and ^{235}U(VI)) and causes very small isotopic fractionation. It simply controls the availability of the U pool to the reduction step. Therefore, the balance between the kinetics of the diffusion step and the reduction step becomes very important and controls the overall isotopic fractionation. To further discuss this balance, we use two end member scenarios as examples.

First, consider an end member case of a very rapid enzymatic reduction. Here, diffusion of U(VI) through the boundary layer is the rate-limiting step of all the steps involved in the U(VI) reduction process. The concentrations of both ^{238}U(VI) and ^{235}U(VI) in the remaining U(VI) around the enzyme quickly approach zero. As a consequence, a strong U(VI) concentration gradient develops across the boundary layer, and the ratio of the concentration gradients for ^{238}U(VI) and ^{235}U(VI) across the diffusive boundary is close to the ^{238}U-(VI)/^{235}U(VI) ratio in the bulk region. Thus, only minor discrimination between ^{238}U and ^{235}U occurs during further diffusive transport. Outside the boundary layer, ^{238}U-(VI)/^{235}U(VI) in the bulk region remains similar to that of the starting U(VI), and only minor effective isotopic fractionation occurs compared to the intrinsic equilibrium ε of ~1‰ caused by the NVE.[4,5] In the second end member case of extremely slow reduction, diffusion of U(VI) becomes much faster than reduction, causing the boundary layer to disappear. As a consequence, the overall isotopic fractionation approaches intrinsic fractionation.

In between these end member cases where diffusion is not fully rate-limiting, slow enzymatic reduction results in the accumulation of the remaining U(VI) reactant at the inside end of the diffusive boundary layer with an ^{235}U enrichment determined by the intrinsic ε for the reduction. Thus, the overall U(VI) concentration gradient across the boundary layer is less pronounced than in the first end member case, and the ratio of the concentration gradients for ^{238}U(VI) and ^{235}U(VI) deviates from that in the initial bulk U(VI). This, in turn, causes a relatively enhanced diffusion of ^{238}U(VI) across the boundary layer. In these scenarios, the reduction of U(VI) on the inside end of the diffusive boundary layer will generate an effective isotopic fractionation in the bulk U(VI) that is smaller than the intrinsic equilibrium ε of ~1‰ caused by the NVE. Here, the deviation from the intrinsic ε depends on the reduction rate.

Eventually, this coupled kinetic-diffusive effect causes a discrimination of U isotopes during diffusive transport across the boundary layer and hence observable U isotopic fractionation in the bulk region, despite the fact that the diffusivities (i.e., diffusion coefficients) of ^{238}U(VI) and ^{235}U(VI) differ only very slightly. For an additional verification of the consistency of our simulations, the proposed diffusion-induced fractionation ($\delta^{238}U_{diff}$) can be quantified as

$$\delta^{238}U_{diff} = \left(\frac{R_{gradient}}{R_{bulk}} - 1\right) \times 1000‰ \quad (10)$$

where $R_{gradient}$ refers to the simulated ^{238}U(VI)/^{235}U(VI) ratio of the net diffusive flux across the diffusive boundary ($R_{gradient}$ = (d^{238}U(VI)/dx)/(d^{235}U(VI)/dx), with dx = 20 nm, Figure 1) and R_{bulk} refers to the computed ^{238}U(VI)/^{235}U(VI) concentration ratio in the bulk region. Physically, $\delta^{238}U_{diff}$ corresponds to the theoretical U isotopic ratio of the net U(VI) diffusive flux entering the cell, after having been diffusively transported across the boundary layer and right before the U(VI) reduction step takes place at the enzyme. The computed $\delta^{238}U_{diff}$ values are higher than the simulated δ^{238}U values in the bulk region and fit Rayleigh distillation models with effective enrichment factors that are almost identical to the ε values derived from the simulated ^{238}U(VI) and ^{235}U(VI) concentrations in the bulk region (shown by the dotted line, Figure 7). This verifies that the observed and simulated variation in ε (Figures 2 and 7) is mainly due to a preferred diffusion-induced fractionation of ^{238}U(VI) across the boundary layer.

A similar weakening of isotopic fractionation, sometimes described as the reservoir effect, has been reported for the reduction of Se(VI) in sediments of littoral wetland.[10] This phenomenon arising from diffusive limitations within isolated zones of Se(VI) reduction in sediments lowers the effective ε observed in Se(VI) in overlying water as a function of the distance across which Se(VI) diffuses to the reaction sites. Although the conceptual approach is similar with regard to the isolation of reaction sites in the enzyme region, our data can be explained by the diffusion-induced fractionation of U isotopes as described above. Furthermore, in our model, we vary the U(VI) reduction rate while keeping the length of the diffusive boundary the same. Note that there is no back diffusion of ^{235}U-enriched U(VI) from the enzyme to the bulk region, which would have to occur against the U concentration

https://dx.doi.org/10.1021/acs.est.9b05935
Environ. Sci. Technol. 2020, 54, 2295−2303

gradient. Our results identify the U(VI) reaction rate as a crucial factor that controls the effective ε measured in the bulk region.

It is possible to invoke the sequestration of U as U(VI) via adsorption on the cells or as U(VI) solid phases inside the cell prior to reduction as an alternative reaction mechanism that may explain our observations of muted isotopic fractionation from *Shewanella* sp. (NR) experiments. U(VI) removal from the solution via adsorption, however, preferentially removes ^{235}U,[41−43] which is inconsistent with our data (Figure 2). Moreover, the adsorption of U(VI) on microbial cells is unlikely to be the major U removal mechanism because of the presence of U(VI)-complexing anions (1 mM Ca, 10 mM HCO_3^-) and low cell density (~10^7 cells/mL or less) in all of our experiments. Finally, the first-order kinetics of U(VI) removal throughout the course of all experiments suggest a single removal mechanism, which is identified as reduction by the XANES data. Even if some of the U(VI) is adsorbed onto the cell at some point in its journey from bulk solution across the boundary layer, any isotopic fractionation in the opposite direction (i.e., ^{238}U enrichment in bulk U(VI)) during this sorption does not affect our interpretation because of the following reason. Manifestation of U isotopic fractionation in the dissolved U(VI) requires an exchange between U(VI) and U(IV) via reversible weak sorption of U(VI),[24] so eventual desorption reverses any isotopic fractionation caused by the sorption of U(VI). Therefore, we conclude that such a sorption effect is likely negligible.

Based on our results, U isotopic fractionation should be influenced by both the rate and the mechanism of U(VI) reduction. Our conceptual model of a diffusive boundary layer around the bacterial cells and simulation results successfully explain how the rate of U(VI) reduction controls U isotopic fractionation during microbial U(VI) reduction. It should be noted that our model does not consider the role of the reduction mechanism in influencing the U isotopic fractionation. The mechanism of U(VI) reduction is likely to vary with reductants with varying electron-donating capacity, bonding environment, and consequent changes in free energy of the reaction. Previous studies have extended the Marcus theory to show that the kinetic isotopic fractionation during redox reactions is related to both reaction kinetics and the vibrational energy differences between reactants and products and thus reaction mechanism and equilibrium fractionation factors.[43,44] According to the Marcus theory, the logarithm of the rate constant of redox reactions ($\ln(k)$) varies linearly with the free energy change of the reaction (ΔG_r^0).[43−48] This means that thermodynamically more favorable reactions at higher ΔG_r^0 are faster and have lower activation energy differences between two isotopologues, which should yield smaller fractionation. In future studies, the idea of integrating both the kinetics of electron transfer and equilibrium exchange should be considered to explain overall observed U isotope fractionation[48] in addition to the presence of diffusive boundary layers as discussed above. Moreover, it could be assessed whether a coupled kinetic equilibrium effect as derived from the Marcus theory is responsible for observing an equilibrium NVE (preference of ^{238}U in U(IV)) also in kinetically controlled U(VI) reduction experiments such as in the present study.

Environmental Implications. Our rate-dependent model of microbial U isotope fractionation may be used to interpret environmental U isotope data from a range of settings based on variable abundance of organic matter or electron donors. Our model predicts a small and perhaps variable effective fractionation during active bioremediation experiments where the amended organic carbon enhances the U(VI) reduction rate.[9,49] For instance, this is consistent with a rather low effective ε of 0.46‰ reported for an early stage of the Rifle biostimulation experiment.[9] A recent and more detailed study with a richer dataset at the same site has reported effective ε ranging from 0.65 to 0.85‰ with changing acetate concentrations (4−15 mM) and hence variable U(VI) reduction rates.[25] Although the correlation between the reported ε and U(VI) reduction rate is not perfect because the field experiment is far more complex than a well-mixed batch reactor, this study confirms that U isotopic fractionation does indeed vary at the field scale when U(VI) reduction rates are changing. In contrast, in natural situations such as marine and terrestrial sediments with low organic carbon contents, a slow U(VI) reduction rate should produce a larger fractionation approaching a theoretical NVE value of ~1‰.[4,5] For example, at Smith Ranch−Highlands roll-front deposits, with sub-micromolar dissolved U(VI)[5] and generally low organic C content of the host sediments,[50] as well as the lack of a sharp redox gradient evident from a microbial community with diverse and competing metabolism,[51] U(VI) reduction is likely slow. This is consistent with a rather high effective ε value of 0.8‰ inferred from variations in the $\delta^{238}U$ of groundwater at the Smith Ranch−Highlands U mine[7] where a significant fraction of the U(VI) reduction is proposed to be microbially mediated.[51,52] The agreement between the fractionation regime suggested by our model at high and low U(VI) reduction rates and the observed ε from the field sites with high and low U(VI) reduction rate demonstrates a systematic relationship between k_{norm} and ε that may be extended to a wider range of natural settings. If either ε or U(VI) reduction rate is directly measured, the systematic relationship may be used to predict the other one. Therefore, direct measurements of U isotope ratios provide a way to quantify the U(VI) reduction rate, which is particularly difficult to quantify in modern open systems or in the past environments from the rock record.

■ ASSOCIATED CONTENT

Supporting Information

The Supporting Information is available free of charge at https://pubs.acs.org/doi/10.1021/acs.est.9b05935.

U(VI) concentration and U isotope results from bacterial incubations, physical and initial chemical parameters for the multiregion model, thermodynamic and kinetic parameters for U(VI) reduction reactions, reaction rate constants to simulate U(VI) reduction, and correlations between normalized U(VI) reduction rate constants and initial U(VI) concentrations (PDF)

■ AUTHOR INFORMATION

Corresponding Author

Anirban Basu − *Department of Earth Sciences, Royal Holloway, University of London, Egham TW20 0EX, U.K.;* orcid.org/0000-0002-4905-9156; Phone: +44 (0) 1784 443890; Email: Anirban.Basu@rhul.ac.uk; Fax: +44 (0) 1784 471780

https://dx.doi.org/10.1021/acs.est.9b05935
Environ. Sci. Technol. 2020, 54, 2295−2303

Authors

Christoph Wanner − *Institute of Geological Sciences, University of Bern, Bern CH-3012, Switzerland;* orcid.org/0000-0003-3488-8602

Thomas M. Johnson − *Department of Geology, University of Illinois at Urbana−Champaign, Urbana, Illinois 61801, United States*

Craig C. Lundstrom − *Department of Geology, University of Illinois at Urbana−Champaign, Urbana, Illinois 61801, United States*

Robert A. Sanford − *Department of Geology, University of Illinois at Urbana−Champaign, Urbana, Illinois 61801, United States*

Eric L. Sonnenthal − *Lawrence Berkeley National Laboratory, Berkeley, California 94720, United States*

Maxim I. Boyanov − *Biosciences Division, Argonne National Laboratory, Argonne, Illinois 60439, United States; Institute of Chemical Engineering, Bulgarian Academy of Sciences, Sofia 1113, Bulgaria;* orcid.org/0000-0001-8758-5248

Kenneth M. Kemner − *Biosciences Division, Argonne National Laboratory, Argonne, Illinois 60439, United States*

Complete contact information is available at: https://pubs.acs.org/10.1021/acs.est.9b05935

Author Contributions

The manuscript was written through contributions of all authors. All authors have given approval to the final version of the manuscript.

Notes

The authors declare no competing financial interest.

■ ACKNOWLEDGMENTS

This work was supported by the U.S. Department of Energy (USDOE), Office of Science within the Subsurface Biogeochemical Research (SBR) Program under grant DE-SC0001281. We thank the MRCAT/EnviroCAT beamline staff for assistance during XAFS data collection. The XAFS data collection at the Advanced Photon Source and analyses and effort of K.M.K. and M.I.B. were supported by the Argonne Wetlands Hydrobiogeochemistry Scientific Focus Area (SFA) at the Argonne National Laboratory funded by the SBR Program, Office of Biological and Environmental Research, Office of Science, USDOE, under contract DE-AC02-06CH11357. MRCAT/EnviroCAT operations are supported by DOE and the MRCAT/EnviroCAT member institutions. We thank the anonymous reviewers for their insightful comments.

■ REFERENCES

(1) Basu, A.; Sanford, R. A.; Johnson, T. M.; Lundstrom, C. C.; Löffler, F. E. Uranium isotopic fractionation factors during U(VI) reduction by bacterial isolates. *Geochim. Cosmochim. Acta* **2014**, *136*, 100−113.

(2) Stylo, M.; Neubert, N.; Wang, Y.; Monga, N.; Romaniello, S. J.; Weyer, S.; Bernier-Latmani, R. Uranium isotopes fingerprint biotic reduction. *Proc. Natl. Acad. Sci. U.S.A.* **2015**, *112*, 5619−5624.

(3) Stirling, C. H.; Andersen, M. B.; Warthmann, R.; Halliday, A. N. Isotope fractionation of ^{238}U and ^{235}U during biologically-mediated uranium reduction. *Geochim. Cosmochim. Acta* **2015**, *163*, 200−218.

(4) Bigeleisen, J. Nuclear size and shape effects in chemical reactions. Isotope chemistry of the heavy elements. *J. Am. Chem. Soc.* **1996**, *118*, 3676−3680.

(5) Fujii, T.; Moynier, F.; Albarède, F. The nuclear field shift effect in chemical exchange reactions. *Chem. Geol.* **2009**, *267*, 139−156.

(6) Basu, A.; Brown, S. T.; Christensen, J. N.; DePaolo, D. J.; Reimus, P. W.; Heikoop, J. M.; Woldegabriel, G.; Simmons, A. M.; House, B. M.; Hartmann, M.; Maher, K. Isotopic and geochemical tracers for U(VI) reduction and U mobility at an in situ recovery U mine. *Environ. Sci. Technol.* **2015**, *49*, 5939−5947.

(7) Brown, S. T.; Basu, A.; Christensen, J. N.; Reimus, P.; Heikoop, J.; Simmons, A.; Woldegabriel, G.; Maher, K.; Weaver, K.; Clay, J.; DePaolo, D. J. Isotopic evidence for reductive immobilization of uranium across a roll-front mineral deposit. *Environ. Sci. Technol.* **2016**, *50*, 6189−6198.

(8) Lau, K. V.; Maher, K.; Altiner, D.; Kelley, B. M.; Kump, L. R.; Lehrmann, D. J.; Silva-Tamayo, J. C.; Weaver, K. L.; Yu, M.; Payne, J. L. Marine anoxia and delayed Earth system recovery after the end-Permian extinction. *Proc. Natl. Acad. Sci. U.S.A.* **2016**, *113*, 2360−2365.

(9) Bopp, C. J.; Lundstrom, C. C.; Johnson, T. M.; Sanford, R. A.; Long, P. E.; Williams, K. H. Uranium $^{238}U/^{235}U$ isotope ratios as indicators of reduction: Results from an in situ biostimulation experiment at Rifle, Colorado, U.S.A. *Environ. Sci. Technol.* **2010**, *44*, 5927−5933.

(10) Clark, S. K.; Johnson, T. M. Effective isotopic fractionation factors for solute removal by reactive sediments: A laboratory microcosm and slurry study. *Environ. Sci. Technol.* **2008**, *42*, 7850−7855.

(11) Wiederhold, J. G. Metal stable isotope signatures as tracers in environmental geochemistry. *Environ. Sci. Technol.* **2015**, *49*, 2606−2624.

(12) Andersen, M. B.; Romaniello, S.; Vance, D.; Little, S. H.; Herdman, R.; Lyons, T. W. A modern framework for the interpretation of $^{238}U/^{235}U$ in studies of ancient ocean redox. *Earth Planet. Sci. Lett.* **2014**, *400*, 184−194.

(13) Bradley, A. S.; Leavitt, W. D.; Schmidt, M.; Knoll, A. H.; Girguis, P. R.; Johnston, D. T. Patterns of sulfur isotope fractionation during microbial sulfate reduction. *Geobiology* **2015**, *14*, 91−101.

(14) Granger, J.; Sigman, D. M.; Lehmann, M. F.; Tortell, P. D. Nitrogen and oxygen isotope fractionation during dissimilatory nitrate reduction by denitrifying bacteria. *Limnol. Oceanogr.* **2008**, *53*, 2533−2545.

(15) Bradley, A. S.; Leavitt, W. D.; Johnston, D. T. Revisiting the dissimilatory sulfate reduction pathway. *Geobiology* **2011**, *9*, 446−457.

(16) Santos, A. A.; Venceslau, S. S.; Grein, F.; Leavitt, W. D.; Dahl, C.; Johnston, D. T.; Pereira, I. A. C. A protein trisulfide couples dissimilatory sulfate reduction to energy conservation. *Science* **2015**, *350*, 1541−1545.

(17) Leavitt, W. D.; Halevy, I.; Bradley, A. S.; Johnston, D. T. Influence of sulfate reduction rates on the Phanerozoic sulfur isotope record. *Proc. Natl. Acad. Sci. U.S.A.* **2013**, *110*, 11244−11249.

(18) Meyer, T. E.; Tsapin, A. I.; Vandenberghe, I.; De Smet, L.; Frishman, D.; Nealson, K. H.; Cusanovich, M. A.; Van Beeumen, J. J. Identification of 42 possible cytochrome c genes in the Shewanella oneidensis genome and characterization of six soluble cytochromes. *OMICS* **2004**, *8*, 57−77.

(19) DiChristina, T. J.; Fredrickson, J. M. Enzymology of Electron Transport: Energy Generation With Geochemical Consequences. *Rev. Mineral. Geochem.* **2005**, *59*, 27−52.

(20) DiChristina, T. J.; Bates, D. J.; Burns, J. L.; Dale, J. R.; Payne, A. N. Shewanella: novel strategies for anaerobic respiration. In *Past and Present Water Column Anoxia*; Neretin, L. N., Ed.; Springer: Netherlands, 2006; pp 443−469.

(21) Marshall, M. J.; Beliaev, A. S.; Dohnalkova, A. C.; Kennedy, D. W.; Shi, L.; Wang, Z.; Boyanov, M. I.; Lai, B.; Kemner, K. M.; McLean, J. S.; Reed, S. B.; Culley, D. E.; Bailey, V. L.; Simonson, C. J.; Saffarini, D. A.; Romine, M. F.; Zachara, J. M.; Fredrickson, J. K. c-type cytochrome-dependent formation of U(IV) nanoparticles by Shewanella oneidensis. *PLoS Biol.* **2006**, *4*, No. e268.

(22) Wall, J. D.; Krumholz, L. R. Uranium reduction. *Annu. Rev. Microbiol.* **2006**, *60*, 149−166.

(23) Liu, C.; Zachara, J. M.; Fredrickson, J. K.; Kennedy, D. W.; Dohnalkova, A. Modeling the Inhibition of the Bacterial Reduction of U(VI) by β-MnO2(s). *Environ. Sci. Technol.* **2002**, *36*, 1452−1459.
(24) Brown, S. T.; Basu, A.; Ding, X.; Christensen, J. N.; DePaolo, D. J. Uranium isotope fractionation by abiotic reductive precipitation. *Proc. Natl. Acad. Sci. U.S.A.* **2018**, *115*, 8688−8693.
(25) Shiel, A. E.; Johnson, T. M.; Lundstrom, C. C.; Laubach, P. G.; Long, P. E.; Williams, K. H. Reactive transport of uranium in a groundwater bioreduction study: Insights from high-temporal resolution $^{238}U/^{235}U$ data. *Geochim. Cosmochim. Acta* **2016**, *187*, 218−236.
(26) Hyslop, N. P.; White, W. H. Estimating precision using duplicate measurements. *J. Air Waste Manage. Assoc.* **2009**, *59*, 1032−1039.
(27) Scott, K. M.; Lu, X.; Cavanaugh, C. M.; Liu, J. S. Optimal methods for estimating kinetic isotope effects from different forms of the Rayleigh distillation equation. *Geochim. Cosmochim. Acta* **2004**, *68*, 433−442.
(28) Boyanov, M. I.; Fletcher, K. E.; Kwon, M. J.; Rui, X.; O'Loughlin, E. J.; Löffler, F. E.; Kemner, K. M. Solution and microbial controls on the formation of reduced U(IV) species. *Environ. Sci. Technol.* **2011**, *45*, 8336−8344.
(29) Xu, T.; Sonnenthal, E.; Spycher, N. F.; Zheng, L. *TOUGHREACT V3.0-OMP Reference Manual: A Parallel Simulation Program for Non-Isothermal Multiphase Geochemical Reactive Transport*; Earth Sciences Division, Lawrence Berkeley National Laboratory University of California: Berkeley, CA 94720, 2014. http://tough.lbl.gov/assets/docs/TOUGHREACT_V3-OMP_RefManual.pdf.
(30) Wolery, T. J. *EQ3/6: Software Package for Geochemical Modeling of Aqueous Systems: Package Overview and Installation Guide (version 7.0)*, Report UCRL-MA-110662 PT I; Lawrence Livermore National Laboratory: Livermore, California, 1992.
(31) Spycher, N. F.; Issarangkun, M.; Stewart, B. D.; Şengör, S. S.; Belding, E.; Ginn, T. R.; Peyton, B. M.; Sani, R. K. Biogenic uraninite precipitation and its reoxidation by iron(III) (hydr)oxides: A reaction modeling approach. *Geochim. Cosmochim. Acta* **2011**, *75*, 4426−4440.
(32) Wanner, C.; Sonnenthal, E. L. Assessing the control on the effective kinetic Cr isotope fractionation factor: A reactive transport modeling approach. *Chem. Geol.* **2013**, *337*−*338*, 88−98.
(33) Singleton, M. J.; Sonnenthal, E. L.; Conrad, M. E.; DePaolo, D. J.; Gee, G. W. Multiphase reactive transport modeling of seasonal infiltration events and stable isotope fractionation in unsaturated zone pore water and vapor at the Hanford site. *Vadose Zone J.* **2004**, *3*, 775−785.
(34) Wanner, C.; Druhan, J. L.; Amos, R. T.; Alt-Epping, P.; Steefel, C. I. Benchmarking the simulation of Cr isotope fractionation. *Comput. Geosci.* **2014**, *19*, 497−521.
(35) Xu, T. Incorporating aqueous reaction kinetics and biodegradation into TOUGHREACT: Applying a multiregion model to hydrobiogeochemical transport of denitrification and sulfate reduction. *Vadose Zone J.* **2008**, *7*, 305−315.
(36) Abboud, R.; Popa, R.; Souza-Egipsy, V.; Giometti, C. S.; Tollaksen, S.; Mosher, J. J.; Findlay, R. H.; Nealson, K. H. Low-temperature growth of Shewanella oneidensis MR-1. *Appl. Environ. Microbiol.* **2005**, *71*, 811−816.
(37) Phillips, R. Membranes by the numbers. In *Physics of Biological Membranes*; Bassereau, P., Sens, P., Eds.; Springer International Publishing, 2018; pp 73−105.
(38) Xiao, Y.; Zhang, E.; Zhang, J.; Dai, Y.; Yang, Z.; Christensen, H. E. M.; Ulstrup, J.; Zhao, F. Extracellular polymeric substances are transient media for microbial extracellular electron transfer. *Sci. Adv.* **2017**, *3*, No. e1700623.
(39) Li, S.-W.; Sheng, G.-P.; Cheng, Y.-Y.; Yu, H.-Q. Redox properties of extracellular polymeric substances (EPS) from electroactive bacteria. *Sci. Rep.* **2016**, *6*, 39098.
(40) Gao, L.; Lu, X.; Liu, H.; Li, J.; Li, W.; Song, R.; Wang, R.; Zhang, D.; Zhu, J. Mediation of extracellular polymeric substances in microbial reduction of hematite by Shewanella Oneidensis MR-1. *Front. Microb.* **2019**, *10*, 575.
(41) Brennecka, G. A.; Wasylenki, L. E.; Bargar, J. R.; Weyer, S.; Anbar, A. D. Uranium isotope fractionation during adsorption to Mn-Oxyhydroxides. *Environ. Sci. Technol.* **2011**, *45*, 1370−1375.
(42) Jemison, N. E.; Johnson, T. M.; Shiel, A. E.; Lundstrom, C. C. Uranium isotopic fractionation induced by U(VI) adsorption onto common aquifer minerals. *Environ. Sci. Technol.* **2016**, *50*, 12232−12240.
(43) Kavner, A.; John, S. G.; Sass, S.; Boyle, E. A. Redox-driven stable isotope fractionation in transition metals: Application to Zn electroplating. *Geochim. Cosmochim. Acta* **2008**, *72*, 1731−1741.
(44) Kavner, A.; Bonet, F.; Shahar, A.; Simon, J.; Young, E. The isotopic effects of electron transfer: An explanation for Fe isotope fractionation in nature. *Geochim. Cosmochim. Acta* **2005**, *69*, 2971−2979.
(45) Marcus, R. A. Chemical and electrochemical electron-transfer theory. *Annu. Rev. Phys. Chem.* **1964**, *15*, 155−196.
(46) Marcus, R. A. Electron transfer reactions in chemistry. Theory and experiment. *Rev. Mod. Phys.* **1993**, *65*, 599−610.
(47) Marcus, R. A. On the Theory of Electron-Transfer Reactions. VI. Unified Treatment for Homogeneous and Electrode Reactions. *J. Chem. Phys.* **1965**, *43*, 679−701.
(48) Joe-Wong, C.; Weaver, K. L.; Brown, S. T.; Maher, K. Thermodynamic controls on redox-driven kinetic stable isotope fractionation. *Geochem. Persp. Lett.* **2019**, *10*, 20−25.
(49) Anderson, R. T.; Vrionis, H. A.; Ortiz-Bernad, I.; Resch, C. T.; Long, P. E.; Dayvault, R.; Karp, K.; Marutzky, S.; Metzler, D. R.; Peacock, A.; White, D. C.; Lowe, M.; Lovley, D. R. Stimulating the in situ activity of Geobacter species to remove uranium from the groundwater of a uranium-contaminated aquifer. *Appl. Environ. Microbiol.* **2003**, *69*, 5884−5891.
(50) WoldeGabriel, G.; Boukhalfa, H.; Ware, S. D.; Cheshire, M.; Reimus, P.; Heikoop, J.; Conradson, S. D.; Batuk, O.; Havrilla, G.; House, B.; Simmons, A.; Clay, J.; Basu, A.; Christensen, J. N.; Brown, S. T.; DePaolo, D. J. Characterization of cores from an in-situ recovery mined uranium deposit in Wyoming: Implications for post-mining restoration. *Chem. Geol.* **2014**, *390*, 32−45.
(51) Gallegos, T. J.; Campbell, K. M.; Zielinski, R. A.; Reimus, P. W.; Clay, J. T.; Janot, N.; Bargar, J. R.; Benzel, W. M. Persistent U(IV) and U(VI) following in-situ recovery (ISR) mining of a sandstone uranium deposit, Wyoming, USA. *Appl. Geochem.* **2015**, *63*, 222−234.
(52) Bhattacharyya, A.; Campbell, K. M.; Kelly, S. D.; Roebbert, Y.; Weyer, S.; Bernier-Latmani, R.; Borch, T. Biogenic non-crystalline U(IV) revealed as major component in uranium ore deposits. *Nat. Commun.* **2017**, *8*, 15538.

https://dx.doi.org/10.1021/acs.est.9b05935
Environ. Sci. Technol. 2020, 54, 2295−2303

3.3. Benchmarking the simulation of Cr isotope fractionation

Source:

Wanner C., Druhan J., Amos R., Alt-Epping P. and Steefel C. (2015) Benchmarking the simulation of Cr isotope fractionation. *Computational Geosciences* **19**, 497-521.

Contribution by the Author (CW):

CW developed the general idea and formulated the benchmarking excercise. Moreover, CW managed and coordinated the simulation activities of all Co-authors and had the lead in writing the manuscript eventually.

Comput Geosci (2015) 19:497–521
DOI 10.1007/s10596-014-9436-9

ORIGINAL PAPER

Benchmarking the simulation of Cr isotope fractionation

Christoph Wanner · Jennifer L. Druhan · Richard T. Amos · Peter Alt-Epping · Carl I. Steefel

Received: 31 January 2014 / Accepted: 27 June 2014 / Published online: 1 August 2014

Abstract A benchmark problem set consisting of four problem levels was developed for the simulation of Cr isotope fractionation in 1D and 2D domains. The benchmark is based on a recent field study where Cr(VI) reduction and accompanying Cr isotope fractionation occurs abiotically by an aqueous reaction with dissolved Fe^{2+} (Wanner et al., 2012., Appl. Geochem., 27, 644–662). The problem set includes simulation of the major processes affecting the Cr isotopic composition such as the dissolution of various Cr(VI) bearing minerals, fractionation during abiotic aqueous Cr(VI) reduction, and non-fractionating precipitation of Cr(III) as sparingly soluble Cr-hydroxide.

Accuracy of the presented solutions was ensured by running the problems with four well-established reactive transport modeling codes: TOUGHREACT, MIN3P, CRUNCHFLOW, and FLOTRAN. Results were also compared with an analytical Rayleigh-type fractionation model. An additional constraint on the correctness of the results was obtained by comparing output from the problem levels simulating Cr isotope fractionation with the corresponding ones only simulating bulk concentrations. For all problem levels, model to model comparisons showed excellent agreement, suggesting that for the tested geochemical processes any code is capable of accurately simulating the fate of individual Cr isotopes.

Keywords Reactive transport modeling · Benchmark · Cr reduction · Cr isotopes · Remediation

1 Introduction

Chromium(VI) is a serious (e.g., carcinogenic) inorganic contaminant [1] released by anthropogenic activities (e.g., galvanization) as well as from geogenic sources such as oxidative weathering of ultramafic rocks [2]. In contrast, the reduced chromium form, Cr(III), is less toxic [3], sparingly soluble, adsorbs strongly on solid surfaces, and co-precipitates with Fe(III) hydroxides [4, 5]. Reduction of Cr(VI) to Cr(III) is therefore a desirable method for remediation of Cr(VI) contaminated sites. Chromium(VI) reduction either occurs naturally by the presence of organic carbon or Fe^{2+} bearing minerals [6], or by the implementation of in situ remediation measures where organic or inorganic Cr reductants are injected into the aquifer [7–11].

The fractionation of stable Cr isotopes has become a well-accepted proxy for demonstrating Cr(VI) reduction in experimental [12–15] and natural systems [9, 16–19]. These studies generally show that of the prevalent naturally occurring Cr isotopes, the heavier ^{53}Cr accumulates in the unreacted Cr(VI) pool and the lighter ^{52}Cr preferentially

Electronic supplementary material The online version of this article (doi:10.1007/s10596-014-9436-9) contains supplementary material, which is available to authorized users.

C. Wanner (✉) · C. I. Steefel
Earth Sciences Division, Lawrence Berkeley National Laboratory, 1 Cyclotron Road, Berkeley, CA, 94720, USA
e-mail: cwanner@lbl.gov

J. L. Druhan
Department of Geological and Environmental Sciences, Stanford University, Stanford, CA, 94305, USA

R. T. Amos
Department of Earth and Environmental Sciences, University of Waterloo, Waterloo, Ontario, Canada

P. Alt-Epping
Institute of Geological Sciences, University of Bern, Bern, Switzerland

reacts to form Cr(III). In contrast, Cr(III) did not exhibit kinetic isotope discrimination during a Cr(III) oxidation experiment [12]. Cr isotopic fractionation is typically explained with kinetic Rayleigh-type fractionation models because once reduced, Cr precipitates as Cr(III) hydroxides or adsorbs on solid surfaces and thus no longer interacts with the remaining soluble Cr(VI). Ideally such Rayleigh-type models can be applied for natural systems to infer the extent of Cr(VI) reduction assuming that the isotopic fractionation factor is known [20]. This assumption is, however, challenging because various published Cr(VI) reduction experiments have shown that field-scale effective fractionation factors may vary over a broad range (see compilation by Wanner and Sonnenthal [21]). Discrepancies in observed Cr isotopic fractionation factors have been attributed to variable kinetic and transport effects as well as different reaction mechanisms [12, 17, 21–23]. Studies for other isotopic systems confirmed that effective fractionation factors vary for a single reaction mechanism due to varying precipitation rates (e.g., Ca [24, 25]) and/or varying hydrodynamic dispersion (e.g., N, C, [26–28]). The broad range of observed fractionation factors and their dependence on transport and kinetic processes may often require the use of reactive transport modeling for the quantitative interpretation of field scale Cr isotope data.

To date, reactive transport modeling involving Cr isotope fractionation has only been applied in a few selected field and lab studies [21, 29, 30]. Other studies have employed numerical reactive transport codes to simulate isotopic fractionation for other contaminated systems, including sulfur isotopic fractionation during sulfate reduction [31, 32, 34] and carbon and chlorine isotopic fractionation during degradation of organic contaminants [35–40].

The cited isotope modeling studies employ different approaches for simulating aqueous kinetic isotope fractionation. To test the different approaches, this paper aims to provide a benchmark problem set for the simulation of Cr isotope fractionation during aqueous kinetic Cr(VI) reduction. Further, the benchmark tests the simulation of other fundamental geochemical processes that define the fate of individual Cr isotopes. Evaluated processes include non-fractionating Cr(III) precipitation and dissolution of Cr(VI)-bearing minerals in addition to Cr isotope fractionation during aqueous kinetic Cr(VI) reduction. The benchmark problem is largely adapted from an extended field and modeling study of an actual Cr(VI) contaminated site located in Switzerland, where Cr(VI) reduction occurs naturally and where monitored natural attenuation (MNA) is part of the remediation measures [18, 30]. To ensure that results presented here provide accurate simulation results, four different multicomponent reactive transport codes have been used to simulate this problem set. These codes are TOUGHREACT, MIN3P, FLOTRAN, and CRUNCHFLOW. General capabilities and numerical model formulations of these codes are provided in Steefel et al. [41] and references therein.

2 Benchmark problem setup

2.1 Conceptual model

The proposed benchmark problem set is adapted from a series of 2D reactive transport model simulations that were performed to optimize remediation measures for the Cr(VI)-contaminated site located near Rivera (Switzerland) [30]. The focus of these original simulations was on evaluating the extent to which naturally occurring Cr(VI) reduction could be defined as remediation strategy. The simulations were based on an extended field campaign [18] and the subsequently derived conceptual model (Fig. 1, [30]), of which the main points are summarized as follows: The Cr(VI) contamination reaches a depth of up to 10 m and originates from occasional spills of sulfuric (H_2SO_4) and chromic acid (H_2CrO_4), occurring during the on-site production of the latter in the 1950s. The interaction between the spilled chromic acid and the Ca-rich concrete of the former processing plant leads to the formation of highly soluble chromatite ($CaCrO_4$). By contrast, the interaction between the chromic and sulfuric acid with the in situ subsurface lead to the precipitation of sparingly soluble Cr(VI) bearing jarosite ($KFe_3(SO_4)_{1.8}(CrO_4)_{0.2}(OH)_6$). Accordingly, current groundwater Cr(VI) concentrations are controlled by the dissolution of these two Cr(VI)-bearing minerals. It was concluded that Cr(VI)-bearing jarosite forms the dominant Cr(VI)-bearing mineral phase within the saturated zone (e.g., dominating aquifer, Fig. 1), whereas infiltrating rainwater and groundwater table variations lead to an additional dissolution of highly soluble chromatite ($CaCrO_4$) accumulated in the unsaturated and periodically saturated zone.

Due to the presence of Fe^{2+}-bearing minerals such as annite (Fe^{2+} -bearing biotite) and chamosite (Fe^{2+} -bearing chlorite) reducing conditions are established and aqueous Fe^{2+} is available in excess of Cr(VI). Accordingly, dissolved Cr(VI) is reduced to Cr(III) by a homogenous kinetic reaction with Fe^{2+}, introducing Cr isotope fractionation to the system. For the current field site, a minimal Cr(VI) reduction efficiency of 31 % along a 120-m long flow path at a flow velocity of 3.5 m/day was estimated by measuring Cr isotopes and applying a Rayleigh fractionation model [18]. Amorphous $Cr(OH)_3$ is assumed to form the ultimate Cr(VI) reduction product because Cr(III) is only sparingly soluble at near neutral pH values [4] such as observed for the Rivera site (pH-range 5.7–6.6). Many studies have shown that the redox change from Cr(VI) to Cr(III) is the

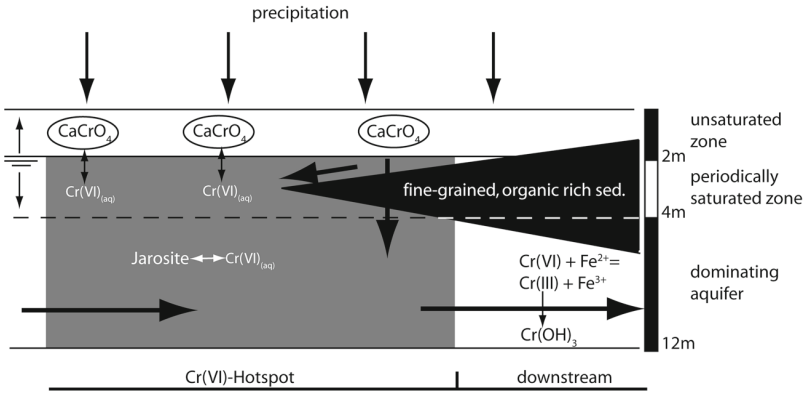

Fig. 1 Conceptual model of the Rivera site illustrating the major processes that are simulated by the benchmark problem set (adapted from Wanner et al. [30])

strongest contributor to observed Cr isotope fractionation e.g., [12, 20, 42]. Accordingly, no Cr isotope fractionation was assumed during $Cr(OH)_3$ precipitation.

In the pH range from 2–6 Cr(VI) concentrations are affected by Cr(VI) sorption to Al- and Fe-hydroxides [43]. In contrast to Cr(VI) reduction, Cr(VI) sorption does not cause significant Cr isotope fractionation [43]. To date, the behavior of Cr(VI) sorption has not been investigated for the Rivera site. Accordingly, the conceptual site model does not include Cr(VI) sorption.

2.2 Benchmark problem set

For the benchmark problem set presented here, the monitored natural attenuation (MNA) remediation scenario such as simulated by Wanner et al. [30] is taken as the comprehensive problem. When compared to this original simulation, the benchmark aims to simulate the fate of individual Cr isotopes for various Cr pools (dissolved Cr(VI) and Cr(III), solid Cr(VI) and Cr(III)) and not for dissolved Cr(VI) only.

The benchmark problem is divided into four levels of increasing complexity. The first problem level addresses the simulation of naturally occurring Cr(VI) reduction for a 1D simulation corresponding to an idealized field-scale 1D flow path, along which a Cr(VI) reduction efficiency of 31 % was inferred [18]. The individual isotopes of Cr, kinetic fractionation due to reduction and non-fractionating precipitation are implemented for the 1D domain in problem level #2. The main purpose of level #2 is to ensure that Cr isotope fractionation (aqueous kinetic fractionation and non-fractionating Cr(III) precipitation) is accurately implemented into the different codes. This can be tested using an analytical Rayleigh distillation model because for a 1D homogenous porous media, Cr isotopic fractionation caused by Cr(VI) reduction typically follows such a behavior [15, 17, 21]. Moreover, the comparison between level #1 and level #2 allows testing whether bulk Cr concentrations remained unchanged when Cr isotope fractionation was added to the simulation.

Level #3 simulates the Cr(VI) plume for a 2D plan view by specifying the site-specific hydrological conditions and the spatial distribution of the Rivera Cr(VI)-contaminated site [18]. It uses the reaction network specified for problem level #1. Level #4 presents the comprehensive problem using the hydrological conditions and spatial distribution of the Cr(VI) contamination specified for problem level #3 with the addition of the Cr isotopic composition of the two Cr(VI) sources and Cr isotope fractionation during aqueous kinetic Cr(VI) reduction. Similar to the two 1D levels, the comparison between level #3 and level #4 allows testing whether the Cr(VI) solubility remains unchanged when the fate of individual Cr isotopes was added to the simulation.

It should be noted that the provided problem set aims to provide a benchmark for simulating fundamental geochemical processes to cause variation in the aqueous Cr isotopic ratio (e.g., kinetic fractionation by aqueous Cr(VI) reduction, non-fractionating Cr(III) precipitation, solubility of various Cr(VI)-bearing minerals). By contrast, we do not provide a benchmark for testing the accurate simulation of transport effects on Cr isotope fractionation (e.g., hydrodynamic dispersion).

3 Mathematical model formulations and numerical implementation

The benchmark problem set presented here requires the simulation of isothermal single-phase fluid flow and advective-diffusive transport of dissolved chemical species. The mathematical formulation of these processes and their numerical implementation differ between the different codes used to solve the benchmark. Different numerical implementations include the variable for which it is solved for when simulating fluid flow (e.g., pressure vs. hydraulic heads), the way boundary conditions are formulated (e.g., ghost cells vs.

indefinitely large grid blocks), and the discretization of the model domain (e.g., full vs. half nodes at the model edge). A detailed comparison of the various numerical implementations of fluid flow and transport processes is provided by Steefel et al. [41].

The geochemical reaction network includes aqueous speciation reactions, kinetic mineral reactions, and kinetic aqueous reactions. The corresponding general mathematical formulation for each code is also provided by Steefel et al. [41] and references therein. To fully understand this benchmark, however, the most important equations are summarized below.

3.1 Aqueous speciation reactions

Reactions among aqueous species except for the reduction of aqueous Cr(VI) to aqueous Cr(III) (5) are assumed to equilibrate instantaneously. Equilibrium reactions are computed by defining the number of independent chemical components as primary or basis species. Any other species are defined as secondary species. The term secondary is inherited from the fact that these species can be expressed as a linear combination (i.e., chemical reaction) of primary species. Using the law of mass action concentrations of secondary species are thus calculated as a function of the concentration of primary species:

$$c_i = K_i^{-1}\gamma_i^{-1}\prod_{j=1}^{N_C} c_j^{\nu_{ij}}\gamma_j^{\nu_{ij}} \tag{1}$$

where c_i is the molal concentration of the ith secondary species, and c_j is the molal concentration of the jth primary species, γ_i and γ_j refer to thermodynamic activity coefficients of the secondary and primary species, respectively, K_i is the equilibrium constant, and ν_{ij} refers to the stoichiometric coefficient of jth basis species in the ith chemical reaction. Primary species considered in the benchmark are provided in Table 1. Secondary species and their corresponding reaction stoichiometry are listed in Table 2 using positive stoichiometric coefficients (υ_j) for primary species that are consumed by the listed reactions, and negative υ_j values to denote primary species that are produced. Table 2 also provides corresponding equilibrium constants obtained using SUPCRT92 [44 and references therein] and tabulated in the EQ3/6 database [45] except for thermodynamic Cr data, which were taken from Ball and Nordstrom [46]. Depending on the code, activity coefficients γ_i and γ_j are calculated using various forms of the Debye-Huckel model (see Steefel et al. [41] and references therein for more information). Ion radii ($r_{e,j}$) of primary and secondary species used in conjunction with these Debye-Huckel models are provided in Table 1 and 2.

Table 1 Primary (component) species and ion radii for Debye-Huckel

Component	Primary species	$r^1_{e,j}$	Charge
c1	H^+	3.08	1
c2	H_2O	0	0
c3	Cl^-	1.81	−1
c4	Na^+	1.91	1
c5	K^+	2.27	1
c6	Mg^{2+}	2.54	2
c7	Fe^{2+}	2.62	2
c8	Fe^{3+}	3.46	3
c9	SO_4^{2-}	3.15	−2
c10	CrO_4^{2-}	3	−2
c11	$^{52}CrO_4^{2-}$	3	−2
c12	$^{53}CrO_4^{2-}$	3	−2
c13	NO_3^-	2.81	−1
c14	HCO_3^-	2.1	−1
c15	Ca^{2+}	2.87	2
c16	$SiO_{2(aq)}$	0	0
c17	Cr^{3+}	3.6	3
c18	$^{52}Cr^{3+}$	3.6	3
c19	$^{53}Cr^{3+}$	3.6	3
c20	Al^{3+}	3.33	3

[1] $r_{e,j}$ refers to the effective ionic radius that is used in conjunction with various forms of the Debye Hueckel activity model to calculate activity coefficients (see Steefel et al. [41] and references therein for more information)

3.2 Mineral dissolution and precipitation reactions

For all of the codes, mineral dissolution and precipitation reaction rates r $\left(\text{molkg}_{\text{H2O}}{}^{-1}\text{s}^{-1}\right)$ are formulated based on transition state theory (TST) [47]

$$r = A \cdot k_{\text{Min}} \exp\left[\frac{-E_a}{R}\left(\frac{1}{T} - \frac{1}{298.15}\right)\right] \cdot \left[1 - \left(\frac{Q}{K}\right)^m\right]^n \tag{2}$$

where A refers to a minerals reactive surface area ($\text{m}^2_{\text{mineral}}/\text{kg}_{\text{H2O}}$), k_{Min} is the reaction rate constant at 25 °C ($\text{mol/m}^2\text{/s}$), E_a refers to the activation energy (kJ/mol), T and R are the temperature (K) and ideal gas constant, Q refers to the ion activity product of a mineral dissolution/precipitation reaction and K is the corresponding equilibrium constant. Exponents m and n are fitting parameters that must be experimentally determined. For this benchmark they were set to one, which is usually the case, but not always. Equation 2 illustrates that precipitation rates r are calculated as negative rates (as $Q/K > 1$), whereas dissolution rates are computed as positive rates ($Q/K < 1$). Reaction stoichiometry of mineral reactions considered by any of the benchmark levels are given in Table 3, whereas kinetic

Table 2 Aqueous complexation reactions and corresponding thermodynamic parameters (log(K),$r_{e,j}$) used for any of the problem levels

Reaction	Secondary species[1]	$r^2_{e,j}$	Charge	Log(K) (25°)	H^+	H_2O	Cl^-	Na^+	K^+	Mg^{2+}	Fe^{2+}	Fe^{3+}	SO_4^{2-}	NO_3^-	HCO_3^-	Ca^{2+}	$SiO_{2(aq)}$	Al^{3+}
a1	$NaOH_{(aq)}$	3	0	14.799	−1	1	0	1	0	0	0	0	0	0	0	0	0	0
a2	AlO_2^-	1.81	−1	22.199	−4	2	0	0	0	0	0	0	0	0	0	0	0	1
a3	AlO^+	2.31	1	10.343	−2	1	0	0	0	0	0	0	0	0	0	0	0	1
a4	$AlOH^{2+}$	2.8	2	5	−1	1	0	0	0	0	0	0	0	0	0	0	0	1
a5	$HAlO_{2(aq)}$	0	0	15.604	−3	2	0	0	0	0	0	0	0	0	0	0	0	1
a6	$CO_{2(aq)}$	0	0	−6.341	1	−1	0	0	0	0	0	0	0	0	1	0	0	0
a7	CO_3^{2-}	2.81	−2	10.325	−1	0	0	0	0	0	0	0	0	0	1	0	0	0
a8	$CaCO_{3(aq)}$	0	0	7.009	−1	0	0	0	0	0	0	0	0	0	1	1	0	0
a9	$CaHCO_3$	2.31	1	−1.043	0	0	0	0	0	0	0	0	0	0	1	1	0	0
a10	$CaOH^+$	2.31	1	12.834	−1	1	0	0	0	0	0	0	0	0	0	1	0	0
a11	$CaSO_{4(aq)}$	0	0	−2.1	0	0	0	0	0	0	0	0	1	0	0	1	0	0
a12	$HFeO_2^-$	1.81	−1	29.202	−3	2	0	0	0	0	1	0	0	0	0	0	0	0
a13	$FeCl^-$	2.31	1	0.165	0	0	1	0	0	0	1	0	0	0	0	0	0	0
a14	FeO^+	2.31	1	5.652	−2	1	0	0	0	0	0	1	0	0	0	0	0	0
a15	$FeCl_{2(aq)}$	0	0	8.181	0	0	2	0	0	0	1	0	0	0	0	0	0	0
a16	$FeO_{(aq)}$	0	0	20.412	−2	1	0	0	0	0	1	0	0	0	0	0	0	0
a17	$FeOH^+$	2.31	1	9.315	−1	1	0	0	0	0	1	0	0	0	0	0	0	0
a18	FeO_2^-	1.81	−1	21.618	−4	2	0	0	0	0	0	1	0	0	0	0	0	0
a19	$FeOH^{2+}$	2.8	2	2.205	−1	1	0	0	0	0	0	1	0	0	0	0	0	0
a20	$FeSO_{4(aq)}$	0	0	−2.2	0	0	0	0	0	0	1	0	1	0	0	0	0	0
a21	$FeSO_4^+$	2.31	1	−1.917	0	0	0	0	0	0	0	1	1	0	0	0	0	0
a22	$HFeO_{2(aq)}$	0	0	12.021	−3	2	0	0	0	0	0	1	0	0	0	0	0	0
a23	$FeCl^{2+}$	2.8	2	−1.475	0	0	1	0	0	0	0	1	0	0	0	0	0	0
a24	$HNO_{3(aq)}$	0	0	1.308	1	0	0	0	0	0	0	0	0	1	0	0	0	0
a25	$H_2SO_{4(aq)}$	0	0	1.021	2	0	0	0	0	0	0	0	1	0	0	0	0	0
a26	HSO_4^-	2.37	−1	−1.975	1	0	0	0	0	0	0	0	1	0	0	0	0	0
a27	$HSiO_3^-$	1.81	−1	9.836	−1	1	0	0	0	0	0	0	0	0	0	0	1	0
a28	$KHSO_{4(aq)}$	0	0	1.502	1	0	0	0	1	0	0	0	1	0	0	0	0	0
a29	KSO_4^-	1.81	−1	−0.875	0	0	0	0	1	0	0	0	1	0	0	0	0	0
a30	$MgCO_{3(aq)}$	0	0	7.356	−1	0	0	0	0	1	0	0	0	0	1	0	0	0
a31	$MgHCO_3^+$	2.31	1	−1.033	0	0	0	0	0	1	0	0	0	0	1	0	0	0
a32	$MgOH^+$	2.31	1	11.682	−1	1	0	0	0	1	0	0	0	0	0	0	0	0
a33	$MgSO_{4(aq)}$	0	0	−2.22	0	0	0	0	0	1	0	0	1	0	0	0	0	0
a34	$NaHCO_{3(aq)}$	0	0	−0.149	0	0	0	1	0	0	0	0	0	0	1	0	0	0
a35	$NaSO_4^-$	1.81	−1	−0.696	0	0	0	1	0	0	0	0	1	0	0	0	0	0
a36	OH^-	1.4	−1	13.991	−1	1	0	0	0	0	0	0	0	0	0	0	0	0

[1]No *Cr* complexes were considered

[2]$r_{e,j}$ refers to the effective ionic radius that is used in conjunction with various forms of the Debye Hueckel activity model to calculate activity coefficients (see Steefel et al. [41] and references therein for more information)

and thermodynamic parameters are provided in Table 4. The model temperature was set to 25 °C. Consequently, the effective rate constant is equal to the one at 25 °C (k_{Min}, Table 4) and activation energies are irrelevant to calculate reaction rates.

3.2.1 Reactive surface area of primary minerals

For initially present (i.e., primary) minerals, reactive surface areas provided in Table 4 refer to bulk reactive surface areas A_m ($m^2_{\mathrm{mineral}}/m^3_{\mathrm{medium}}$). They are converted into units

Table 3 Mineral reactions used for any of the problem levels

Reaction	Minerals	H^+	H_2O	Cl^-	Na^+	K^+	Mg^{2+}	Fe^{2+}	Fe^{3+}	SO_4^{2-}	CrO_4^{2-}	$^{52}CrO_4^{2-}$	$^{53}CrO_4^{2-}$	NO_3^-	HCO_3^-	Ca^{2+}	$SiO_{2(aq)}$	Cr^{3+}	$^{52}Cr^{3+}$	$^{53}Cr^{3+}$	Al^{3+}
m1	$Cr(OH)_{3(am)}$	−3	3	0	0	0	0	0	0	0	0	0	0	0	0	0	0	1	0	0	0
m2	$CO_{2(s)}$	1	−1	0	0	0	0	0	0	0	0	0	0	0	1	0	0	0	0	0	0
m3	Cr-Jarosite[1]	−6	6	0	0	1	0	0	3	1.8	0.2	0	0	0	0	0	0	0	0	0	0
m4	$CaCrO_{4(s)}$[1]	0	0	0	0	0	0	0	0	0	1	0	0	0	0	1	0	0	0	0	0
m5	$CaCrO_{4(s)}$–Iso[1]	0	0	0	0	0	0	0	0	0	0	0.898156	0.101844	0	0	1	0	0	0	0	0
m6	Cr-Jarosite-Iso[1]	−6	6	0	0	1	0	0	3	1.8	0	0.179631	0.020369	0	0	0	0	0	0	0	0
m7	$^{52}Cr(OH)_{3(am)}$[2]	−3	3	0	0	0	0	0	0	0	0	0	0	0	0	0	0	0	1	0	0
m8	$^{53}Cr(OH)_{3(am)}$[2]	−3	3	0	0	0	0	0	0	0	0	0	0	0	0	0	0	0	0	1	0
m9	Chamosite	−10	7	0	0	0	0	2	0	0	0	0	0	0	0	0	1	0	0	0	2
m10	Quartz	0	0	0	0	0	0	0	0	0	0	0	0	0	0	0	1	0	0	0	0
m11	Annite	−10	6	0	0	1	0	3	0	0	0	0	0	0	0	0	3	0	0	0	1

[1]Dissolution only

[2]Specified as solid solution

of $m^2_{mineral}/kg_{H2O}$ to calculate the effective reactive surface area A that goes into the reaction rate (2)

$$A = \frac{A_m}{\rho_w \cdot \varphi} \tag{3}$$

where ρ_w is the water density (997.16 kg_{H2O}/m^3_{water} at 25 °C), φ is the porosity of the porous medium (m^3_{water}/m^3_{medium}) and A_m refer to the reactive surface areas provided in Table 4 ($m^2_{mineral}/m^3_{medium}$).

3.2.2 Reactive surface area of secondary minerals

The calculation of reactive surface areas of newly formed (i.e., secondary) minerals (e.g., $Cr(OH)_3$) differs between the different codes used so solve this benchmark.

TOUGHREACT and CRUNCHLOW are using specific reactive surface areas to calculate reactive surface areas ($A_{2nd,}$ $m^2_{mineral}/kg_{H2O}$) used in conjunction with Eq. 2

$$A_{2nd} = \frac{V_{frac} \cdot A_{specific}}{\rho_w \cdot \varphi} \tag{4}$$

where V_{frac} refers to the mineral volume fraction ($m^3_{mineral}/m^3_{medium}$), and $A_{specific}$ is the corresponding specific surface area ($m^2_{mineral}/m^3_{mineral}$). By doing so, a minimum threshold volume fraction (V_{frac}) has to be defined to calculate the surface area (A_{2nd}) of the very first mineral amount that precipitates (Table 4).

In simulations carried out by MIN3P and FLOTRAN, constant reactive surface areas were used for newly formed secondary minerals (Table 4). In case of MIN3P, minimum initial volume fractions $V^0_{frac} > 0$ have to be specified. It should be noted that these minimum volume fractions refer to true volume fractions, whereas TOUGHREACT and CRUNCHFLOW are only using minimum volume fractions to calculate A_{2nd} (4) and zero mineral volume fractions can be handled.

3.3 Kinetic aqueous reactions

Cr(VI) reduction is modeled as an aqueous kinetic reaction using aqueous Fe(II) as the reductant:

$$CrO_4^{2-} + 3Fe^{2+}_{(aq)} + 8H^+ = Cr^{3+} + 3Fe^{3+} + 4H_2O \tag{5}$$

Generally, kinetic Cr(VI) reduction by aqueous Fe(II) (5) follows a first-order reaction rate with respect to aqueous Fe(II) as well as Cr(VI) [48]. At the Rivera site, however, Fe(II) is available mostly in excess of Cr(VI) [18]. Accordingly, for this benchmark the reaction rate r ($molkg_{H2O}{}^{-1}s^{-1}$) for Eq. 5 is specified as a first-order reaction rate solely with respect to the total Cr(VI) concentration and no dependence on total Fe(II) concentration was considered

$$r = k \cdot (CrO_4^{2-})_{Total} \tag{6}$$

Table 4 Thermodynamic and kinetic parameters of mineral reactions used for any of the problem levels

	Minerals	Formula	Molar volume (cm^3/mol)	Log(K)(25°C)[5]	$Log(k_{Min})$ $\left(molkg_{H20}{}^{-1}m^{-2}s^{-1}\right)^5$	A_m $\left(m^2_{mineral}/m^3_{medium}\right)^2$
m1	$Cr(OH)_{3(am)}$	$Cr(OH)_3$	29.09	9.35	−4	1[3]
m2	$CO_{2(s)}$	CO_2	1.00	−9.5	−4	1
m3	Cr−Jarosite	$KFe_3(SO_4)_{1.8}(CrO_4)_{0.2}(OH)_6$	100.44	−12	−5	1
m4	$CaCrO_{4(s)}$	$CaCrO_4$	98.32	−8.6	−3	1
m5	$CaCrO_{4(s)}$ − Iso	$Ca^{52}Cr_{0.89816}{}^{53}Cr_{0.10184}O_4$	98.32	−8.742933[4]	−3	1
m6	Cr-Jarosite-Iso	$KFe_3(SO_4)_{1.8}(^{52}Cr_{0.89816}{}^{53}Cr_{0.10184}O_4)_{0.2}(OH)_6$	100.44	−12.0285866[4]	−5	1
m7	$^{52}Cr(OH)_{3(am)}$[1]	$^{52}Cr(OH)_3$	29.09	9.350	−8	1[3]
m8	$^{53}Cr(OH)_{3(am)}$[1]	$^{53}Cr(OH)_3$	29.09	9.350	−8	1[3]
m9	Chamosite	$Fe_2Al_2SiO_5(OH)_4$	106.20	32.837	−12	1
m10	Quartz	SiO_2	22.69	−3.752	−13.4	1
m11	Annite	$KFe_3AlSi_3O_{10}(OH)_2$	154.32	29.453	−9.5	1

[1]Specified as solid solution

[2]Specified values refer to bulk surface areas except for m1, m7 and m8 (see note below)

[3]Values refer to constant reactive surface areas used by MIN3P, and FLOTRAN to calculate the precipitation rate of these newly formed phases. Using TOUGHREACT and CRUNCHFLOW, specific surface areas of 1 $m^2_{mineral}/g_{mineral}$ were used in conjunction with Eq. 4 to calculate evolving reactive surface area. For these codes, initial volume fractions of 1e-10, 8.981529e-11 and 1.018437e-11 were specified to calculate the surface area of the very first amount of precipitated $Cr(OH)_3$ (m1), $^{52}Cr(OH)_3$ (m7), and $^{53}Cr(OH)_3$ (m8)

[4]Log(K) values do not have to be adjusted using MIN3P and the values specified for (m3) and (m4) can be used to simulate problem level #4

[5]Specified according to Wanner et al. [30]

where k (s^{-1}) is the reaction rate constant and $(CrO_4^{2-})_{Total}$ refers to the total Cr(VI) concentration. To obtain the observed 31 % Cr(VI) reduction along a 120-m flow path at an average linear flow velocity of 3.5 m/day [18], k was set to 1.268×10^{-7} s^{-1}.

3.4 Simulating the fate of individual Cr isotopes

Cr isotope composition is typically expressed as a δ value given in per mil

$$\delta^{53}Cr_{SRM979} = \frac{R\left(^{53}Cr/^{52}Cr\right)_{modeled}}{R\left(^{53}Cr/^{52}Cr\right)_{SRM979}} - 1 \quad (7)$$

where $R(^{53}Cr/^{52}Cr)_{modeled}$ and $R(^{53}Cr/^{52}Cr)_{SRM979}$ refer to the simulated $^{53}Cr/^{52}Cr$ ratio as well as to the corresponding ratio of the certified standard SRM979 [49], which is 0.11339. Equation 7 and any other expression related to simulated stable Cr isotope ratios is following the guidelines recently presented by Coplen [50].

3.4.1 Cr isotope fractionation during kinetic aqueous Cr(VI) reduction

For the problem levels simulating Cr isotope fractionation (#2, #4), we make the simplification (i.e., assumption) that ^{52}Cr and ^{53}Cr sum up to 100 % bulk Cr ($^{52}Cr+{}^{53}Cr=Cr_{Total}$) even though they only represent about 93 % of total Cr [49]. Accordingly, we do not simulate the fate of the two minor Cr isotopes (^{50}Cr and ^{54}Cr). The fate of ^{52}Cr and ^{53}Cr during Cr(VI) reduction is simulated by replacing Eq. 5 by two separate equations for the two major isotopologues of aqueous Cr(VI) $(^{52}CrO_4)^{2-}$ and $(^{53}CrO_4)^{2-}$:

$$(^{52}CrO_4)^{2-} + 3Fe^{2+}_{(aq)} + 8H^+ = (^{52}Cr)^{3+} + 3Fe^{3+} + 4H_2O \quad (8)$$

$$(^{53}CrO_4)^{2-} + 3Fe^{2+}_{(aq)} + 8H^+ = (^{53}Cr)^{3+} + 3Fe^{3+} + 4H_2O \quad (9)$$

As modeled here, kinetic Cr isotope fractionation is caused by different reduction rates for $(^{52}CrO_4)^{2-}$ (^{52}r) and $(^{53}CrO_4)^{2-}$ (^{53}r). This distinction was implemented in each of the codes utilized for this benchmark. TOUGHREACT

[51], FLOTRAN [52], and CRUNCHFLOW [53 and references therein] employed the method described for C isotope fractionation [36]. In doing so, the concentrations of the specific Cr(VI) isotopologues were used to calculate ^{52}r and ^{53}r

$$^{52}r = k \cdot \left(^{52}\mathrm{CrO_4}\right)^{2-}_{\mathrm{Total}} \tag{10}$$

$$^{53}r = k \cdot \left(^{53}\mathrm{CrO_4}\right)^{2-}_{\mathrm{Total}} \cdot \alpha^{53}\mathrm{Cr}_{\mathrm{Cr(III)/Cr(VI)}} \tag{11}$$

where k (s^{-1}) corresponds to the reaction rate constant used for the reduction of bulk Cr(VI) ((6); 1.268×10^{-7} s^{-1}), and $(^{52}\mathrm{CrO_4})^{2-}_{\mathrm{Total}}$ and $(^{53}\mathrm{CrO_4})^{2-}_{\mathrm{Total}}$ refer to the total concentrations of $(^{52}\mathrm{CrO_4})^{2-}$ and $(^{53}\mathrm{CrO_4})^{2-}$. The term $\alpha^{53}\mathrm{Cr}_{\mathrm{Cr(III)/Cr(VI)}}$ denotes the Cr isotopic fractionation factor, which defines the magnitude of Cr isotope fractionation based on the ratio of the instantaneous ^{53}Cr/^{52}Cr ratio of the product $R(^{53}\mathrm{Cr}/^{52}\mathrm{Cr})_{\mathrm{Cr(III)}}$ to the residual reactant $R(^{53}\mathrm{Cr}/^{52}\mathrm{Cr})_{\mathrm{Cr(VI)}}$:

$$\alpha^{53}\mathrm{Cr}_{\mathrm{Cr(III)/Cr(VI)}} = \frac{R(^{53}\mathrm{Cr}/^{52}\mathrm{Cr})_{\mathrm{Cr(III)}}}{R(^{53}\mathrm{Cr}/^{52}\mathrm{Cr})_{\mathrm{Cr(VI)}}} \tag{12}$$

Cr(VI) reduction experiments with soil samples having a similar mineralogical composition to the Rivera aquifer were performed by Ellis et al. [20] yielding a fractionation factor of 0.9966. Accordingly, $\alpha^{53}\mathrm{Cr}_{\mathrm{Cr(III)/Cr(VI)}}$ was set to 0.9966 for the problem set presented here.

In contrast to the other codes, MIN3P [29, 34, 54] computes ^{52}r and ^{53}r by using the total Cr(VI) concentration and specific reaction rate constants for $(^{52}\mathrm{CrO_4})^{2-}$ (^{52}k) and $(^{53}\mathrm{CrO_4})^{2-}$ (^{53}k) assuming that ^{52}k and ^{53}k sum up to the reaction rate constant of bulk Cr(VI) k (6):

$$\begin{aligned} ^{52}r &= {}^{52}k \cdot \left(\mathrm{CrO_4^{2-}}\right)_{\mathrm{Total}} \\ &= \frac{k}{1 + \alpha^{53}\mathrm{Cr}_{\mathrm{Cr(III)/Cr(VI)}} \cdot R(^{53}\mathrm{Cr}/^{52}\mathrm{Cr})_{\mathrm{Cr(VI)}}} \\ &\quad \times \left(\mathrm{CrO_4^{2-}}\right)_{\mathrm{Total}} \end{aligned} \tag{13}$$

$$\begin{aligned} ^{53}r &= {}^{53}k \cdot \left(\mathrm{CrO_4^{2-}}\right)_{\mathrm{Total}} \\ &= \frac{k \cdot \alpha^{53}\mathrm{Cr}_{\mathrm{Cr(III)/Cr(VI)}} \cdot R(^{53}\mathrm{Cr}/^{52}\mathrm{Cr})_{\mathrm{Cr(VI)}}}{1 + \alpha^{53}\mathrm{Cr}_{\mathrm{Cr(III)/Cr(VI)}} \cdot R(^{53}\mathrm{Cr}/^{52}\mathrm{Cr})_{\mathrm{Cr(VI)}}} \\ &\quad \times \left(\mathrm{CrO_4^{2-}}\right)_{\mathrm{Total}} \end{aligned} \tag{14}$$

For any approach, ^{52}r and ^{53}r sum up to an overall reaction rate that is very close to the one used for problem level #1 (6) ensuring that the overall Cr(VI) reduction rate was essentially the same for levels #1 and #2 as well as for #3 and #4

$$\begin{aligned} &(^{52}r + {}^{53}r)_1 \\ &= k \cdot \left[\left(^{52}\mathrm{CrO_4}\right)^{2-} + \left(^{53}\mathrm{CrO_4}\right)^{2-} \cdot \alpha^{53}\mathrm{Cr}_{\mathrm{Cr(III)/Cr(VI)}}\right] \end{aligned} \tag{15}$$

$$(^{52}r + {}^{53}r)_2 = k \cdot \left[\left(^{52}\mathrm{CrO_4}\right)^{2-} + \left(^{53}\mathrm{CrO_4}\right)^{2-}\right] \tag{16}$$

where $(^{52}r + {}^{53}r)_1$ refers to the sum of ^{52}r and ^{53}r of the TOUGHREACT, CRUNCHFLOW, and FLOTRAN approach, whereas $(^{52}r + {}^{53}r)_2$ refers to the corresponding MIN3P approach. Equation 15 implies that the overall Cr(VI) reduction rate for the TOUGHREACT, CRUNCHFLOW, and FLOTRAN approach is slightly smaller than the one for the bulk problems (levels #1 and #3). However, the rate difference is less than 0.1 % because the normalized bulk earth fraction of ^{53}Cr is on the order of 10 % and $\alpha^{53}\mathrm{Cr}_{\mathrm{Cr(III)/Cr(VI)}}$ was set to 0.9966, which justifies the chosen approach.

3.4.2 Nonfractionating precipitation of Cr(OH)$_3$

In all of the codes, $(^{52}\mathrm{Cr})^{3+}$ and $(^{53}\mathrm{Cr})^{3+}$ precipitate as an ideal $^{52}\mathrm{Cr(OH)_3}$–$^{53}\mathrm{Cr(OH)_3}$ solid solution to remove both Cr(III) isotopologues produced by reactions 8 and 9. To do so, $^{52}\mathrm{Cr(OH)_3}$ and $^{53}\mathrm{Cr(OH)_3}$ are defined as end-members (reactions m7 and m8, Table 3). "Ideal" means that for a given composition, the activities of the two end-members, $a_{x\mathrm{Cr(OH)_3}}$, are equal to the corresponding mole fractions, $x_{x\mathrm{Cr(OH)_3}}$, in the solid solution (i.e., activity coefficient = 1). The overall precipitation rate of the $^{52}\mathrm{Cr(OH)_3}$–$^{52}\mathrm{Cr(OH)_3}$ solid solution, ^{ss}r, is the sum of the precipitation rate of the two end-members

$$^{ss}r = {}^{52\mathrm{Cr(OH)_3}}r + {}^{53\mathrm{Cr(OH)_3}}r \tag{17}$$

where $^{52\mathrm{Cr(OH)3}}r$ and $^{53\mathrm{Cr(OH)3}}r$ refer to the precipitation rate of the two end-members ($\mathrm{molkg_{H2O}^{-1}s^{-1}}$). The calculation of $^{52\mathrm{Cr(OH)3}}r$ and $^{53\mathrm{Cr(OH)3}}r$ differs between the different codes used to solve this benchmark. The corresponding numerical implementation is described as follows illustrating that for any code, the precipitation of Cr(III) does not cause Cr isotope fractionation.

TOUGHREACT and FLOTRAN Using TOUGHREACT [21] and FLOTRAN [52], the precipitation rate for the

$^{52}Cr(OH)_3$ and $^{53}Cr(OH)_3$ end-members is calculated according to

$$^{52}Cr(OH)_3 r = A_{ss} \cdot k_{Min} \cdot \left(1 - \frac{Q_{^{52}Cr(OH)_3}}{K_{^{52}Cr(OH)_3}}\right) + k_{Min} \cdot A_{ss} \cdot \left(x_{^{52}Cr(OH)_3} - 1\right) \quad (18)$$

$$^{53}Cr(OH)_3 r = A_{ss} \cdot k_{Min} \cdot \left(1 - \frac{Q_{^{53}Cr(OH)_3}}{K_{^{53}Cr(OH)_3}}\right) + k_{Min} \cdot A_{ss} \cdot \left(x_{^{53}Cr(OH)_3} - 1\right) \quad (19)$$

where A_{ss} ($m^2_{mineral}/kg_{H2O}$) refers to the reactive surface area of the solid solution (Table 4), k_{min} is the reaction rate constant of the solid solution ($molkg^{-1}_{H2O}m^{-2}s^{-1}$, Table 4), $Q_{52Cr(OH)3}$ and $Q_{53Cr(OH)3}$ refer to the ion activity product of reactions m7 and m8 (Table 3), $K_{52Cr(OH)3}$ and $K_{53Cr(OH)3}$ are the corresponding equilibrium constants, and $x_{52Cr(OH)3}$ and $x_{53Cr(OH)3}$ are the mole fractions of the precipitating end-members. The first term of Eqs. 18 and 19 refers to the precipitation rate of the corresponding end-member as pure minerals (i.e., maximum rate). The second term ensures that end-members precipitation rates linearly decrease with decreasing mole fraction (as $x_{xCr(OH)3} - 1 < 0$). To ensure that the volume ratio of these end-members reflect the fluid composition, $x_{52Cr(OH)3}$ and $x_{53Cr(OH)3}$ are calculated according to

$$x_{^{52}Cr(OH)_3} = \frac{Q_{^{52}Cr(OH)_3}/K_{^{52}Cr(OH)_3}}{Q_{^{52}Cr(OH)_3}/K_{^{52}Cr(OH)_3} + Q_{^{53}Cr(OH)_3}/K_{^{53}Cr(OH)_3}} \quad (20)$$

$$x_{^{53}Cr(OH)_3} = \frac{Q_{^{53}Cr(OH)_3}/K_{^{53}Cr(OH)_3}}{Q_{^{52}Cr(OH)_3}/K_{^{52}Cr(OH)_3} + Q_{^{53}Cr(OH)_3}/K_{^{53}Cr(OH)_3}} \quad (21)$$

where $(Q_{52Cr(OH)3}/K_{52Cr(OH)3})$ and $(Q_{53Cr(OH)3}/K_{53Cr(OH)3})$ refer to the Q/K ratio of reactions m7 and m8, respectively (Table 3).

By setting $K_{52Cr(OH)3} = K_{53Cr(OH)3}$ as well as by using a constant reactive surface area and reaction rate constant (A_{ss} and k_{Min}) (Table 4), the ratio of the two precipitation rates, $(^{53Cr(OH)3}r/^{52Cr(OH)3}r)$ reflects the aqueous $(^{53}Cr)^{3+}/(^{52}Cr)^{3+}$ ratio $(R(^{53}Cr/^{53}Cr)_{Cr(III)})$ and no Cr isotope fractionation is introduced by the precipitation of the $^{52}Cr(OH)_3 - ^{53}Cr(OH)_3$ solid solution.

CRUNCHFLOW Using CRUNCHFLOW [25], $^{52}Cr(OH)_3$ and $^{53}Cr(OH)_3$ precipitation rates are calculated according to

$$^{52}Cr(OH)_3 r = A_{ss} \cdot k_{min} \cdot x_{^{52}Cr(OH)_3} \times \left(1 - \frac{Q_{^{52}Cr(OH)_3}}{K_{ss} \cdot x_{^{52}Cr(OH)_3}}\right) \quad (22)$$

$$^{53}Cr(OH)_3 r = A_{ss} \cdot k_{min} \cdot x_{^{53}Cr(OH)_3} \times \left(1 - \frac{Q_{^{53}Cr(OH)_3}}{K_{ss} \cdot x_{^{53}Cr(OH)_3}}\right) \quad (23)$$

with $x_{52Cr(OH)3}$ and $x_{53Cr(OH)3}$ calculated according to

$$x_{^{52}Cr(OH)_3} = \frac{(^{52}Cr)^{3+}}{Cr^{3+}_{Total}} \quad (24)$$

$$x_{^{53}Cr(OH)_3} = \frac{(^{53}Cr)^{3+}}{Cr^{3+}_{Total}} \quad (25)$$

By analogy of the TOUGHREACT and FLOTRAN approach, the absence of fractionation during Cr(III) precipitation was ensured by setting $K_{52Cr(OH)3} = K_{53Cr(OH)3}$ as well as by using a constant reactive surface area and reaction rate constant (A_{ss} and k_{Min}) (Table 4). It should be noted that for the precipitation of the specified $^{52}Cr(OH)_3$–$^{53}Cr(OH)_3$ solid solution the TOUGHREACT/FLOTRAN calculation (18–21) is fully equivalent to the one used by CRUNCHFLOW (22–25). For solid solutions with more than two end-members, the different implementation may cause different results, which was however not tested by this benchmark.

MIN3P Using MIN3P, $^{52}Cr(OH)_3$ and $^{53}Cr(OH)_3$ precipitation rates are calculated according to

$$^{52}Cr(OH)_3 r = A_{ss} \cdot {}^{52}k \cdot \left(1 - \frac{Q_{Cr(OH)_3}}{K_{Cr(OH)_3}}\right) \quad (26)$$

$$^{53}Cr(OH)_3 r = A_{ss} \cdot {}^{53}k \cdot \left(1 - \frac{Q_{Cr(OH)_3}}{K_{Cr(OH)_3}}\right) \quad (27)$$

with end-member specific reaction rate constants, ^{52}k and ^{53}k, defined as

$$^{52}k = \frac{k_{Bulk}}{1 + R\left(^{53}Cr/^{52}Cr\right)_{Cr(III)}} \quad (28)$$

$$^{53}k = \frac{k_{Bulk} \cdot R\left(^{53}Cr/^{52}Cr\right)_{Cr(III)}}{1 + R\left(^{53}Cr/^{52}Cr\right)_{Cr(III)}} \quad (29)$$

where $R(^{53}Cr/^{52}Cr)_{Cr(III)}$ refers to the ratio between the total dissolved $(^{53}Cr)^{3+}$ and total dissolved $(^{52}Cr)^{3+}$ concentration, and k_{Bulk} is the reaction rate constant of bulk $Cr(OH)_3$ (reaction m1). Combining Eqs. 28 and 29 yields $^{53}k/^{52}k = R(^{53}Cr/^{53}Cr)_{Cr(III)}$, thus illustrating that the ratio of the two precipitation rates, $(^{53Cr(OH)3}r/^{52Cr(OH)3}r)$, reflects $R(^{53}Cr/^{53}Cr)_{Cr(III)}$ as well. Accordingly, by setting $K_{52Cr(OH)3} = K_{53Cr(OH)3}$, no Cr isotope fractionation is introduced by Cr(III) precipitation.

3.4.3 Solubility of Cr bearing minerals

Jarosite and chromatite For the two 2D problem levels (#3, #4), aqueous Cr(VI) is inherited from the dissolution of Cr(VI)-bearing jarosite and chromatite. To add the fate of individual Cr isotopes to the 2D problem (level #4) bulk Cr is replaced by ^{52}Cr and ^{53}Cr (i.e., $Cr_{Total} = {}^{52}Cr + {}^{53}Cr$) in the corresponding reaction stoichiometry (Table 4). As a consequence, the expression for the equilibrium constant of the two minerals slightly differs depending on whether the fate of the individual Cr isotopes is considered or not. For instance, the equilibrium constants for bulk chromatite (K_{CaCrO4}) and ^{52}Cr- and ^{53}Cr-bearing chromatite ($K_{CaCrO4-Iso}$) are expressed as

$$K_{CaCrO_4} = \frac{a_{Ca^{2+}} \cdot a_{CrO_4{}^{2-}}}{a_{CaCrO_4(s)}} \tag{30}$$

$$\begin{aligned} K_{CaCrO_4-Iso} &= \frac{a_{Ca^{2+}} \cdot \left(a_{^{52}CrO_4{}^{2-}}\right)^{\nu^{52}Cr} \cdot \left(a_{^{53}CrO_4{}^{2-}}\right)^{\nu^{53}Cr}}{a_{CaCrO_4-Iso(s)}} \\ &= \frac{a_{Ca^{2+}} \cdot \left(0.9 \cdot a_{(CrO_4{}^{2-})bulk}\right)^{0.9} \cdot \left(0.1 \cdot a_{(CrO_4{}^{2-})bulk}\right)^{0.1}}{a_{CaCrO_4-Iso(s)}} \\ &= K_{CaCrO_4} \cdot 0.72 \end{aligned} \tag{31}$$

where a_x refers to the activity of Ca^{2+}, bulk CrO_4^{2-}, $(^{52}CrO_4)^{2-}$, $(^{53}CrO_4)^{2-}$, bulk $CaCrO_4$ and ^{52}Cr- and ^{53}Cr-bearing chromatite, and ν_{52Cr} and ν_{53Cr} are the stoichiometric coefficients of $(^{52}CrO_4)^{2-}$ and $(^{53}CrO_4)^{2-}$ in reaction m5 (≈0.9 and 0.1). Assuming $CrO_4^{2-}{}_{bulk} = (^{52}CrO_4)^{2-} + (^{53}CrO_4)^{2-}$, K_{CaCrO4}, and $K_{CaCrO4-Iso}$ differ for a given bulk Cr(VI) concentration such as illustrated with Eq. 31. In other words, the solubility of bulk CrO_4^{2-} is not the same if the same value is specified for K_{CaCrO4} and $K_{CaCrO4-Iso}$. Consequently, the equilibrium constants for ^{52}Cr- and ^{53}Cr-bearing jarosite and chromatite (m5 and m6, Table 4) have to be updated to ensure the same bulk Cr(VI) solubility as for level #3:

$$\begin{aligned} K_{CaCrO_4-Iso} &= K_{CaCrO_4} \cdot \left(f_{^{52}Cr}\right)^{\nu^{52}Cr} \\ &\quad \times \left(f_{^{53}Cr}\right)^{\nu^{53}Cr} \end{aligned} \tag{32}$$

$$\begin{aligned} K_{Cr-jarosite-Iso} &= K_{Cr-jarosite} \cdot \left(f_{^{52}Cr}\right)^{\nu^{52}Cr} \\ &\quad \times \left(f_{^{53}Cr}\right)^{\nu^{53}Cr} \end{aligned} \tag{33}$$

K_{CaCrO4} and $K_{Cr-Jarosite}$ correspond to the equilibrium constants of bulk $CaCrO_4$ and bulk jarosite such as used for problem level #3 (m3 and m4, Table 3), f_{52Cr} and f_{53Cr} refer to the normalized fraction of ^{52}Cr and ^{53}Cr (depending on $\delta^{53}Cr_{SRM979}$), and ν_{52Cr} and ν_{53Cr} are the stoichiometric coefficients of $(^{52}CrO_4)^{2-}$ and $(^{53}CrO_4)^{2-}$ in reactions m5 and m6.

It should be noted, that in contrast to the other codes, the jarosite and $CaCrO_4$ log(K) adjustments (32 and 33) are not required using MIN3P. It is not necessary because MIN3P computes mineral solubilities and aqueous kinetic reactions (13 and 14) based on bulk Cr(VI) concentrations.

$Cr(OH)_3$ The solubility of bulk Cr^{3+} ($Cr^{3+} = (^{52}Cr)^{3+} + (^{53}Cr)^{3+}$) remains constant when adding the fate of ^{52}Cr and ^{53}Cr to the simulations because the same log(K) is specified for bulk $Cr(OH)_3$ as well as for the corresponding solid solution end-members (reactions m1, m7 and m8, Table 4).

4 Detailed specification of the four problem levels

4.1 Level #1: Cr(VI) reduction along a 1D flow path

The simulation is carried out for a 1D flow path of 800 m to track Cr(VI) reduction along a large concentration range. The model domain is discretized into 800 cubical grid blocks with a dimension of 1 × 1 × 1 m each. The simulation is run for 1,000 days. The porosity is set to a fixed value of 0.17 for the whole model domain (i.e., no porosity update due to mineral dissolution and precipitation reactions). A constant flux boundary condition is specified for the two model boundaries by assigning an injection rate of 6.887×10^{-3} kg/s into the upstream boundary grid block and an extraction rate of -6.887×10^{-3} kg/s out of the downstream boundary grid block. For a porosity of 0.17 and the specified model domain this injection rate corresponds to a fixed (i.e., constant) average linear flow velocity of 3.5 m/day, which is in agreement with the inferred

groundwater flow velocity along the best constrained flow path at the Riviera site [18].

The diffusion coefficient is set to 10^{-9} m^2/s. The approaches for simulating hydrodynamic dispersion differs between the different codes used to solve this benchmark [41]. Using CRUNCHFLOW, MIN3P, and FLOTRAN hydrodynamic dispersion is simulated by means of a dispersion tensor. By contrast, TOUGHREACT requires the accurate definition of aquifer heterogeneity to simulate hydrodynamic dispersion, which often requires the specification of a multicontinuum [51]. Due to the different treatments, a good match between the codes is challenging for problems involving hydrodynamic dispersion. Accordingly, we did not consider hydrodynamic dispersion for this particular benchmark. In fact, we postulate that matching hydrodynamic dispersion using these four codes would serve as a benchmark of it its own.

With the exception of the upstream boundary grid block, initial total concentrations are defined according to major cation and anion concentrations measured in an uncontaminated groundwater sample (Table 5, [18]). For the upstream boundary grid block, aqueous concentrations are kept constant (fixed boundary condition, see Table 5). They are specified according to a chemical analysis of a typical Cr(VI) contaminated groundwater sample with a Cr(VI) concentration of 0.08 mg/L (Table 5).

Table 5 Initial (levels #1-4) and boundary primary species concentration (levels #1-2) used for the four problem levels

	Unit	Initial concentration (total conc.)	Fixed boundary concentration (total conc.)
pH		6.2	6.2
Na^+	mg/L	4.7	4.7
K^+	mg/L	0.9	0.9
Mg^{2+}	mg/L	2	2
Ca^{2+}	mg/L	13.58	13.58
Cl^-	mg/L	[1]18.77	[1]18.66
SO_4^{2-}	mg/L	8.85	8.85
NO_3^-	mg/L	12.25	12.25
HCO_3^-	mg/L	22.58	22.58
CrO_4^{2-}	mg/L	0	0.08[2]
Fe^{2+}	mg/L	0.01	0.01
Fe^{3+}	mg/L	0	0
$SiO_{2(aq)}$	mg/L	0	0
Cr^{3+}	mg/L	0	0
Al^{3+}	mg/L	0	0

[1]Obtained by employing a charge balance constraint. The measured concentration was 13.2 mg/L

[2]For component problem #2, this concentration was assigned to $^{52}(CrO_4)^{2-}$ 1.39373917E-6 mol/kgH_2O and $^{53}(CrO_4)^{2-}$ (1.58038813E-7 mol/kgH_2O) to specify an initial $\delta^{53}Cr_{SRM979}$ of 0.0 ‰

The reaction network used for problem level #1 is composed of aqueous reactions a1—a36, mineral reactions m1, m2, and m9–m11 (Tables 2 and 3) and the aqueous kinetic reaction reducing Cr(VI) to Cr(III) (5 and 6). The following initial mineral volume fractions are assigned to the whole model domain: 68 % quartz, 10 % annite, 4 % chamosite, 1 % $CO_{2(s)}$, and 0.0 % $Cr(OH)_{3(am)}$ (% of entire porous medium). $CO_{2(s)}$ is a hypothetical phase that was used to fix the $\log(pCO_2)$ to −1.7 by specifying a large reaction rate constant and by setting log(K) to −9.5 (Table 4). A $\log(pCO_2)$ of −1.7 corresponds to the observation that the calculated CO_2 partial pressures of groundwater samples were more or less uniform and close to this value [18].

4.2 Level #2: simulation of Cr isotopic fractionation for the 1D problem

This problem level adds Cr isotope fractionation to level #1 using the same initial specification to simulate flow and transport. The only exception is that the Cr(VI) concentration of the upstream boundary (0.08 mg/L, Table 5) is assigned to $(^{52}CrO_4)^{2-}$ and $(^{53}CrO_4)^{2-}$ instead of the bulk CrO_4^{2-} taking into account the normalized bulk earth fraction of ^{52}Cr and ^{53}Cr, which are 0.89815629 and 0.1018437, respectively [49]. In doing so, inlet $(^{52}CrO_4)^{2-}$ and $(^{53}CrO_4)^{2-}$ concentration are fixed to 1.39373917E-6 and 1.58038813E-7 mol/kg_{H2O} while the total Cr(VI) concentration $(^{52}CrO_4)^{2-} + (^{53}CrO_4)^{2-})$ remains at the same concentration as specified for problem level #1(1.551778e-6 mol/kg = 0.08 mg/L, Table 5). According to Eq. 7, this definition yields an initial $\delta^{53}Cr_{SRM979}$ value of 0.0 ‰.

The reaction network used in this simulation is composed of aqueous reactions a1–a36 (Table 2) and mineral reactions m2 and m7–m11 (Table 3), as well as the aqueous kinetic reactions simulatingthe reduction of $(^{52}CrO_4)^{2-}$ and $(^{53}CrO_4)^{2-}$ to $(^{52}Cr)^{3+}$ and $(^{53}Cr)^{3+}$, respectively (8–14).

4.3 Level #3: simulation of 2D Cr(VI) plume

The 2D flow field is adapted from a previous hydrological flow simulation performed by a consulting company using the software "Groundwater Modeling System" (GMS). A domain of 224 × 236 m is used. It is discretized into 56 × 59 cubical grid blocks having a dimension of 4 × 4 × 1 m each and the simulation is run for 1,000 days.

The model domain is divided into two different flow domains (Fig. 2). The first domain, labeled as aquifer

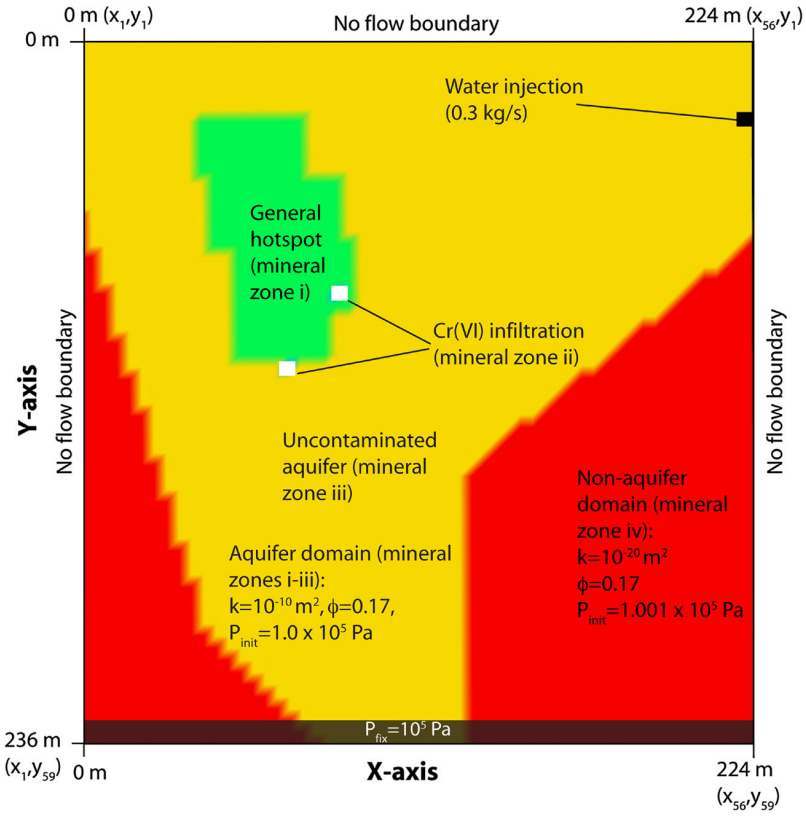

Fig. 2 2D domain for the simulation of problem levels #3 and #4 illustrating the actual aquifer domain and the location of the different mineral zones as well as initial and boundary conditions for setting up the steady state flow field

domain, corresponds to the actual aquifer and consists of mineral zones i–iii such as defined below. The second domain, labeled as non-aquifer domain, corresponds to the part of the rectangular 2D domain where no aquifer is present and consists of mineral zone iv. Permeability and porosity of the aquifer domain are set to fixed values of 10^{-10} m^2 and 0.17, whereas a permeability of 10^{-20} m^2 and the same porosity (0.17) is used for the non-aquifer domain. The aquifer domain comprises grid blocks except the ones with the x, y-coordinates (i.e., x_m, y_n) listed in Table 6 (Fig. 2).

An initial fluid pressure of 1.0×10^5 Pa is specified for the whole model domain. No-flow boundary conditions are defined for the x-begin (x_m, y_1), y-begin (x_1, y_m), and y-end (x_{56}, y_n) boundary. For the x-end boundary (x_m, y_{59}), a flux boundary condition is specified by fixing the fluid pressure to 1×10^5 Pa. The aquifer at the site is mainly fed by meteoric water originating from precipitations along the adjacent mountain ranges. To mimic this observation, a constant water injection rate of 0.3 kg/s is defined for grid block x_{56}, y_7 (Fig. 2).

As for the two 1D levels, the diffusion coefficient is set to 10^{-9} m^2/s and hydrodynamic dispersion was not considered. The same initial total aqueous species concentrations as for problem level #1 is specified for the whole model domain (Table 5). For the water injection grid block (x_{56}, y_7), total aqueous species concentrations are fixed for the entire simulation.

The reaction network used in this simulation is composed of aqueous complexation reactions a1—a36 (Table 2), mineral reactions m1–m4 and m9—m11 (Table 3), and the

Table 6 Grid blocks belonging to the non-aquifer domain (Fig. 2)

(x_1,y_{15-59})	(x_{16},y_{55-59})	(x_{43},y_{29-59})
(x_2,y_{19-59})	(x_{17},y_{56-59})	(x_{44},y_{28-59})
(x_3,y_{22-59})	(x_{18},y_{57-59})	(x_{45},y_{27-59})
(x_4,y_{26-59})	(x_{19},y_{58-59})	(x_{46},y_{26-59})
(x_5,y_{29-59})	(x_{20},y_{59})	(x_{47},y_{25-59})
(x_6,y_{32-59})	(x_{33},y_{37-59})	(x_{48},y_{25-59})
(x_7,y_{36-59})	(x_{34},y_{36-59})	(x_{49},y_{24-59})
(x_8,y_{39-59})	(x_{35},y_{35-59})	(x_{50},y_{23-59})
(x_9,y_{43-59})	(x_{36},y_{34-59})	(x_{51},y_{22-59})
(x_{10},y_{46-59})	(x_{37},y_{34-59})	(x_{52},y_{21-59})
(x_{11},y_{50-59})	(x_{38},y_{33-59})	(x_{53},y_{21-59})
(x_{12},y_{51-59})	(x_{39},y_{32-59})	(x_{54},y_{20-59})
(x_{13},y_{52-59})	(x_{40},y_{31-59})	(x_{55},y_{19-59})
(x_{14},y_{53-59})	(x_{41},y_{30-59})	(x_{56},y_{18-59})
(x_{15},y_{54-59})	(x_{42},y_{30-59})	

aqueous kinetic reaction between aqueous Cr(VI) and Fe(II) (5 and 6). In the case of jarosite, the reaction network includes dissolution only. Jarosite precipitation was suppressed because jarosite is typically formed under highly acidic conditions [55]. Four different initial mineral zones were defined within the model domain (Fig. 2): (i) a general hotspot domain with 67.72 % quartz, 10 % annite, 4 % chamosite, 0.3 % Cr(VI)-bearing jarosite (e.g., Cr-Jarosite), 1 % CO_2(s), and 0.0 % $Cr(OH)_{3(am)}$ (% of entire porous medium). This zone was assigned to the following grid blocks (Fig. 2): (x_{11-19}, y_{8-13}), (x_{12-19}, y_{13-18}), (x_{14-20}, y_{18-23}), (x_{14-21}, y_{23-27}), (x_{20-22}, y_{13-18}), and (x_{21-23}, y_{18-23}) except (x_{22}, y_{22}). (ii) The second, small zone (two grid blocks, "Cr(VI) infiltration") simulates the vertical infiltration of a high Cr(VI) load derived from the dissolution of highly soluble Cr(VI) phases (e.g., chromatite ($CaCrO_4$)) accumulated in the saturated zone [18]. It is assigned to grid blocks (x_{18}, y_{28}) and (x_{22}, y_{22}) (Fig. 2) and contained 65 % quartz, 10 % annite, 4 % chamosite, 3 % chromatite ($CaCrO_4$) 1 % CO_2(s), and 0.0 % $Cr(OH)_{3(am)}$ (% of entire porous medium). (iii) The initial mineral phase distribution of the remaining part of the aquifer domain (mineral zone iii) is the same as for problem level #1 (68 % quartz, 10 % annite, 4 % chamosite and 1 % CO_2(s) and corresponds to the uncontaminated aquifer. (iv) The same initial mineralogical composition as for mineral zone iii was assigned to the non-aquifer domain.

4.4 Level #4: simulation of Cr isotopic fractionation for the 2D problem

This level adds Cr isotope fractionation to level #3 using the same initial specification to simulate flow and transport. The reaction network is composed of aqueous complexation reactions a1—a36 (Table 2), mineral reactions m2 and m5–m11 (Table 3), and aqueous kinetic reactions simulating the reduction of $(^{52}CrO_4)^{2-}$ and $(^{53}CrO_4)^{2-}$ to $(^{52}Cr)^{3+}$ and $(^{53}Cr)^{3+}$, respectively (8–14). The same initial mineral zone distribution as for level #3 is used (Fig. 2). Also, the assigned initial mineral volume fractions are the same except that Cr-Jarosite is replaced by "Cr-Jarosite-Iso" and $CaCrO_{4(s)}$ is replaced by "$CaCrO_{4(s)}$-Iso" (reactions m5 and m6, Table 3). As for level #3, jarosite precipitation is suppressed. With this specification, the two Cr(VI) isotopologues are introduced to the aqueous phase by dissolution of "$CaCrO_4$–Iso" and "Cr–Jarosite–Iso" (Table 3). By using a ratio of the stoichiometric coefficients of $(^{52}CrO_4)^{2-}$ and $(^{53}CrO_4)^{2-}$ that is equal to the ratio of the bulk earth distribution ($^{53}Cr/^{52}Cr = 0.11339$, Table 3) and a sufficiently high reaction rate constant (Table 4) to establish equilibrium for these two minerals the model assumes a source $\delta^{53}Cr_{SRM979}$ value of 0.0 ‰. Assuming $\delta^{53}Cr_{SRM979} = 0.0$ % is based on the observation that anthropogenic Cr(VI) sources (e.g., chromic acid) generally show $\delta^{53}Cr_{SRM979}$ values close to 0.0 ‰ [17, 20]. Partial Cr(VI) reduction prior $CaCrO_4$ and jarosite formation could have shifted the corresponding $\delta^{53}Cr_{SRM979}$ to higher values. However, due to the absence of $\delta^{53}Cr_{SRM979}$ measurements for pure $CaCrO_4$ and jarosite such an effect on $\delta^{53}Cr_{SRM979}$ was not considered. According to Eqs. 32–33 and by assuming $\delta^{53}Cr_{SRM979} = 0.0$ ‰ , log(K) of jarosite and $CaCrO_4$ (m5 and m6, Table 4) are updated to −8.74293 ($CaCrO_{4(s)}$-Iso) and −12.02859 (Cr-Jarosite-Iso) to ensure the same bulk Cr(VI) solubility as for level #3.

5 Results and discussion

5.1 Level #1

5.1.1 General simulation results

Steady state spatial profiles of total aqueous species concentrations involved in Cr(VI) reduction (5) are shown in Fig. 3 together with total Al^{3+} and SiO_2 concentrations, pH value, and precipitated $Cr(OH)_3$ volume fraction profiles. Dissolved Fe^{2+} required for Cr(VI) reduction (5) was inherited by annite and chamosite dissolution inducing a continuous increase of SiO_2 and Al^{3+} along the 1D model domain. The observation that Fe^{2+} also increased linearly along the model domain illustrates that for the given (i.e., large) total ferrous iron concentrations, Fe^{2+} is not significantly affected by Cr(VI) reduction (5) and that chamosite and annite dissolution rates have a strong control on total Fe^{2+} concentration. It should be noted that for annite a reaction rate constant larger than the one reported by Palandri and Kharaka [56] was used (Table 4) to obtain similar Fe^{2+} concentrations as observed in the field (ca. 2 mg/L [18]). Therefore, specified annite dissolution rates do not represent "true" field scale rates, but rather form a (simplified) way of obtaining redox conditions (e.g., Fe^{2+} concentrations), similar to the ones observed in the field. Moreover, the specified annite dissolution rate ensures that Fe^{2+} is available in excess of Cr(VI), thus justifying the definition of a first-order dependence of the Cr(VI) reduction rate on the total Cr(VI) concentration (6).

Due to its low solubility, aqueous Cr^{3+} formed by Eq. 5 precipitated as amorphous $Cr(OH)_3$ yielding low total dissolved Cr^{3+} concentrations on the order of 1e-8 mol/kg_{H2O} or lower (Fig. 3a). With the specified reaction network, about 90 % of the inlet Cr(VI) concentration was reduced along the simulated flow path. The extent of Cr(VI) reduction at $x = 120$ m was ca. 31 % such as inferred for the field site [18]. Chlorine evolution at the downstream model boundary ($x = 800$ m) show that the breakthrough of

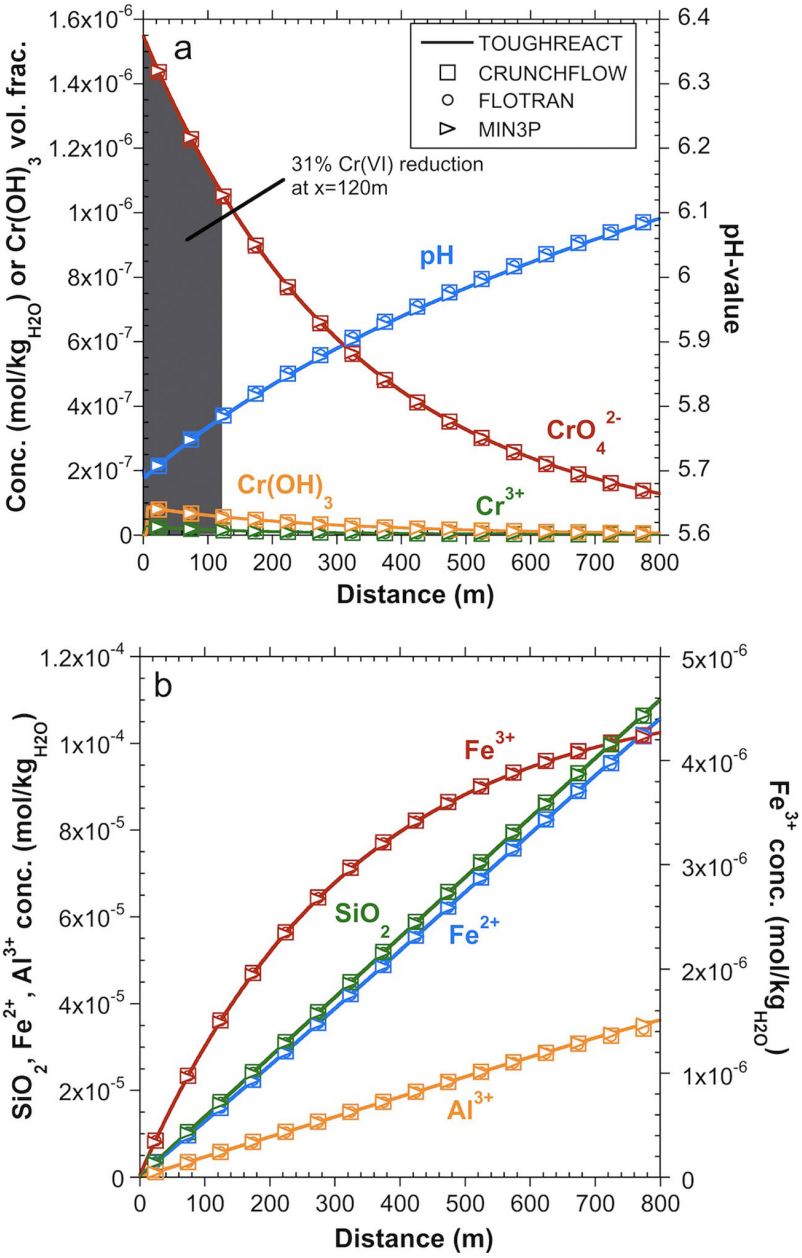

Fig. 3 Steady state profiles of various components obtained for level #1 after a simulated time period of 1,000 days. **a** Total Cr(VI) and Cr(III) concentration, pH value, and $Cr(OH)_3$ volume fraction profiles. The *gray shaded domain* illustrates that 31 % of the initial Cr(VI) is reduced after a flow path of 120 m, such as inferred for the field site [18]. **b** Total Fe(II), Fe(III), $SiO_{2(aq)}$, and Al^{3+} concentration profiles

the influent solution (Table 5) occurred after ca. 230 days (Fig. 4) confirming that the simulation was run at an average linear flow velocity of 3.5 days.

5.1.2 Code comparison

Results obtained from different codes match each other almost perfectly (Fig. 3). The only minor differences were observed for the breakthrough curves (Fig. 4). By neglecting hydrodynamic dispersion, these breakthrough curves are solely inherited from numerical dispersion. Accordingly, the minor breakthrough curve variations illustrate that the different numerical approaches for solving transport introduced a slightly variable degree of numerical dispersion. The numerical dispersion coefficient D_n and corresponding numerical dispersivity (D_n/v) was estimated using an analytical solution [57] for the time dependent Cl^- concentration at the downstream model boundary ($x = 800$ m):

$$c(t)_{x=800\text{ m}} = c_{\text{ini}} + \frac{c_{\text{boun}} - c_{\text{init}}}{2}\text{erfc}\left(\frac{800 - vt}{\sqrt{(4D_n t)}}\right) \quad (34)$$

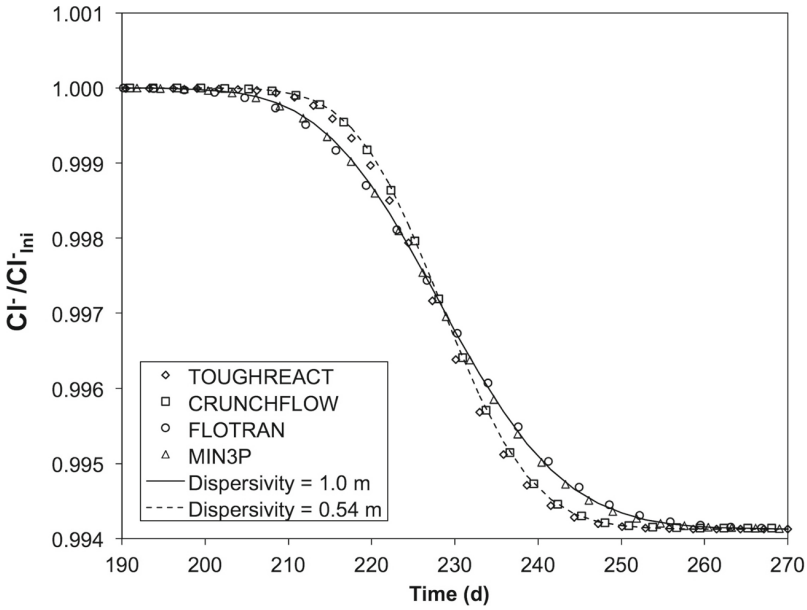

Fig. 4 Temporal evolution of the total Cl^- concentration at the downstream model boundary ($x = 800$ m) for level #1 around the time of breakthrough. Also shown are analytical breakthrough curves for dispersivities of 0.54 and 1.0 m, respectively. By neglecting hydrodynamic dispersion, these disperisivities are solely inherited from numerical dispersion

where c_{ini} and c_{bound} refer to the initial and boundary Cl^- concentrations, v is the average linear flow velocity, D_n refers to the numerical dispersion coefficient. Applying Eq. 34 to the various breakthrough curves yields numerical dispersivities of 0.54 m (TOUGHREACT and CRUNCHFLOW) and 1.0 m (FLOTRAN, MIN3P), respectively.

It should be noted, that this benchmark does not aim to investigate numerical approaches for simulating transport processes. Accordingly, a discussion regarding numerical approaches to cause variable numerical dispersion is beyond the scope of this paper. For an extended discussion, it is referred to Steefel et al. [41] and references therein.

5.2 Level #2

5.2.1 The fate of individual Cr isotopes

$\delta^{53}Cr_{SRM979}$ value profiles (Fig. 5d) for the three Cr pools of the problem (i.e., dissolved Cr(VI), dissolved Cr(III), and solid $Cr(OH)_3$) show that the problem entirely follows a Rayleigh-type fractionation model

$$\delta^{53}Cr_{SRM979\_x} = \left[\left(\delta^{53}Cr_{SRM979\_0} + 1000\right)\cdot f^{(\alpha-1)}\right] - 1000 \quad (35)$$

where $\delta^{53}Cr_{SRM979\_x}$ and $\delta^{53}Cr_{SRM979\_0}$ refer to the $\delta^{53}Cr_{SRM979}$ values at location x and at the column inlet (0.0 ‰ for Cr(VI) and −3.4 ‰ for Cr(III), f refers to the remaining Cr(VI) fraction at location x and $\alpha = \alpha^{53}Cr_{Cr(III)/Cr(VI)} = 0.9966$ is the kinetic fractionation factor that was used to simulate Cr isotope fractionation (8–14). Note that $\delta^{53}Cr_{SRM979}$ values of the precipitated $Cr(OH)_3$ solid solution were calculated in analogue to the ones for dissolved Cr(VI) and Cr(III) (7) using the computed ratio of the volume fractions of the two isotopic end-members ($V_{53Cr(OH)3}/V_{52Cr(OH)3}$) and assuming an equal molar volume for both end-members (29.09 cm^3/mol):

$$\delta^{53}Cr_{SRM979} = \frac{\left(V_{53Cr(OH)_3}/V_{52Cr(OH)_3}\right)}{R\left(^{53}Cr/^{52}Cr\right)_{SRM979}} - 1 \quad (36)$$

The trend of increasing $\delta^{53}Cr_{SRM979}$ values with decreasing Cr(VI) concentrations illustrate that Cr(VI) reduction is accompanied by an accumulation of the heavy Cr isotopes in the remaining aqueous phases whereas formed Cr^{3+} becomes enriched in the lighter Cr isotopes.

5.2.2 Code comparison

Simulated total Cr(III) and Cr(VI) concentration profiles of the two Cr(VI) and Cr(III) isotopologues as well as $^{52}Cr(OH)_3$ and $^{53}Cr(OH)_3$ volume fraction profiles match almost perfectly when comparing results from different codes (Fig. 5a–c). The same applies for the $\delta^{53}Cr$ value profiles of the three Cr pools (Fig. 5d). Moreover, for any code $(^{52}CrO_4)^{2-}$ and $(^{53}CrO_4)^{2-}$ as well as $(^{52}Cr)^{3+}$ and $(^{52}Cr)^{3+}$ sum up almost perfectly to the corresponding bulk species (e.g., CrO_4^{2-}, Cr^{3+}) obtained for level #1 (Fig. 6). The same applies for the steady state $^{52}Cr(OH)_3$ and $^{53}Cr(OH)_3$ volume fractions, which also sum up to the bulk $Cr(OH)_3$ volume fractions obtained for level #1 (Fig. 6).

Our conceptual model assumes that Cr(VI) reduction and accompanying Cr isotopic fractionation is inherited from

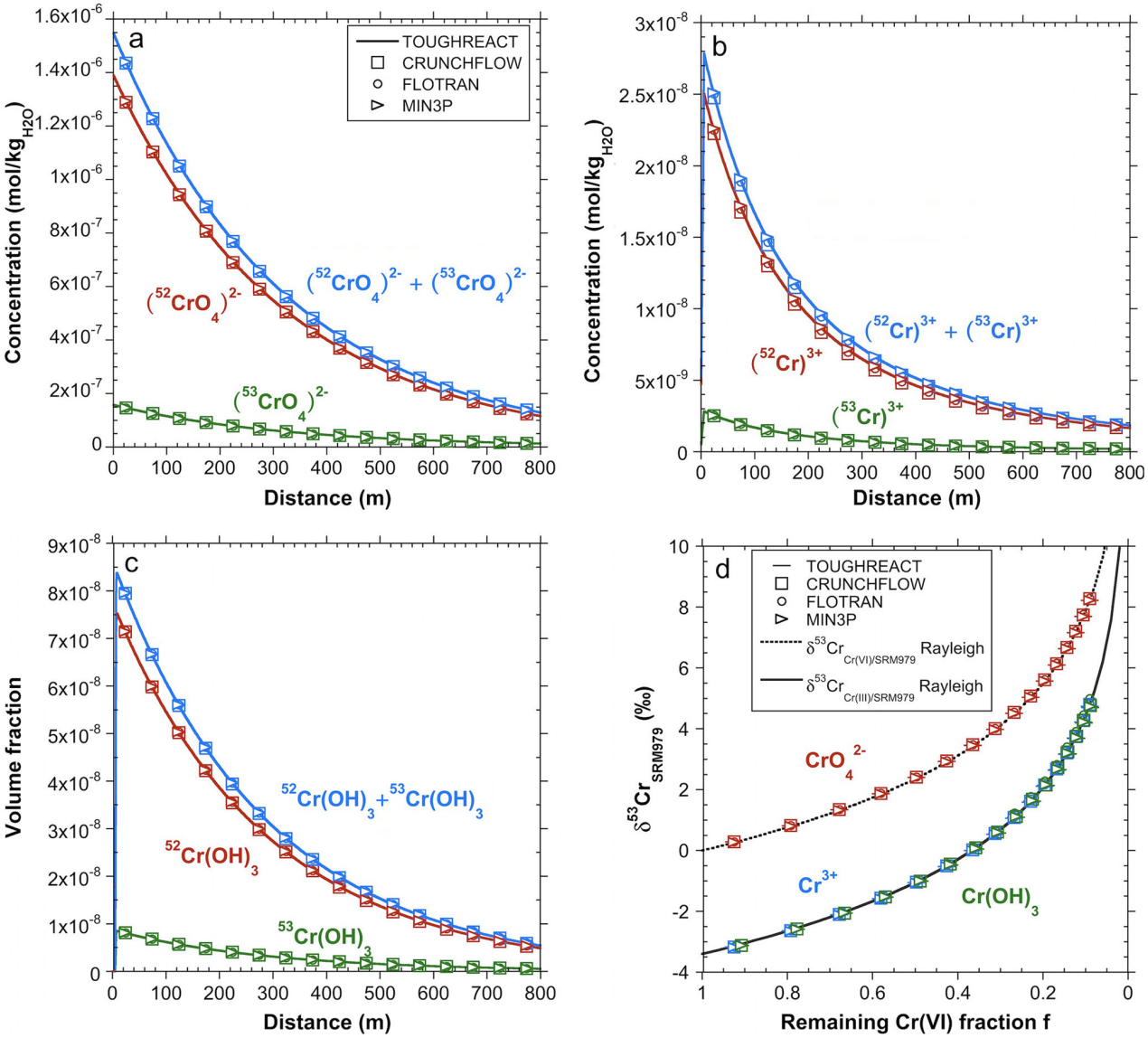

Fig. 5 Steady state profiles obtained for level #2 for different Cr pools after a simulated time period of 1,000 days. **a** Total $(^{52}CrO_4)^{2-}$, $(^{53}CrO_4)^{2-}$, and $(^{52}CrO_4)^{2-} + (^{53}CrO_4)^{2-}$ concentration profiles. **b** Total $(^{52}Cr)^{3+}$, $(^{53}Cr)^{3+}$, and $(^{52}Cr)^{3+} + (^{53}Cr)^{3+}$ concentration profiles. **c** $^{52}Cr(OH)_3$,$^{53}Cr(OH)_3$, and $^{52}Cr(OH)_3 + {}^{53}Cr(OH)_3$ volume fraction profiles **d** Steady state $\delta^{53}Cr_{SRM979}$ values for dissolved CrO_4^{2-} and Cr^{3+} as well as for precipitated $Cr(OH)_3$ as a function of the remaining Cr(VI) fraction f (*open symbols*). Also illustrated are Rayleigh-type fractionation models (Eq. 35) with $\alpha^{53}Cr_{Cr(III)/Cr(VI)} = 0.9966$ for Cr(VI) ($\delta^{53}Cr_{Cr(VI)/SRM979}$) and Cr(III) ($\delta^{53}Cr_{Cr(III)/SRM979}$), which perfectly match the three simulated Cr pools. The observation that Cr^{3+} and $Cr(OH)_3$ both plot on $\delta^{53}Cr_{Cr(III)/SRM979}$ illustrates that no fractionation was induced by $Cr(OH)_3$ precipitation

a first-order irreversible aqueous reaction where the reactionproduct is removed from the solution (Fig. 1). Since these are the main characteristics of a Rayleigh distillation process, the good fit with the analytical Rayleigh equation (Fig. 5d) adds additional confidence to the simulation results. In particular, the good match between the steady state $\delta^{53}Cr_{SRM979}$ profiles of dissolved Cr^{3+} and the ones for precipitated $Cr(OH)_3$ confirms that Cr isotope fractionation was solely accomplished during reduction of Cr(VI) to Cr(III), and no fractionation occurred during precipitation of $Cr(OH)_3$. The good agreement among different codes is especially notable given that the implementation of Cr isotope fractionation is different in different codes (see 10–29).

It should be noted, however, that the good match between the simulation results and the Rayleigh equation is only

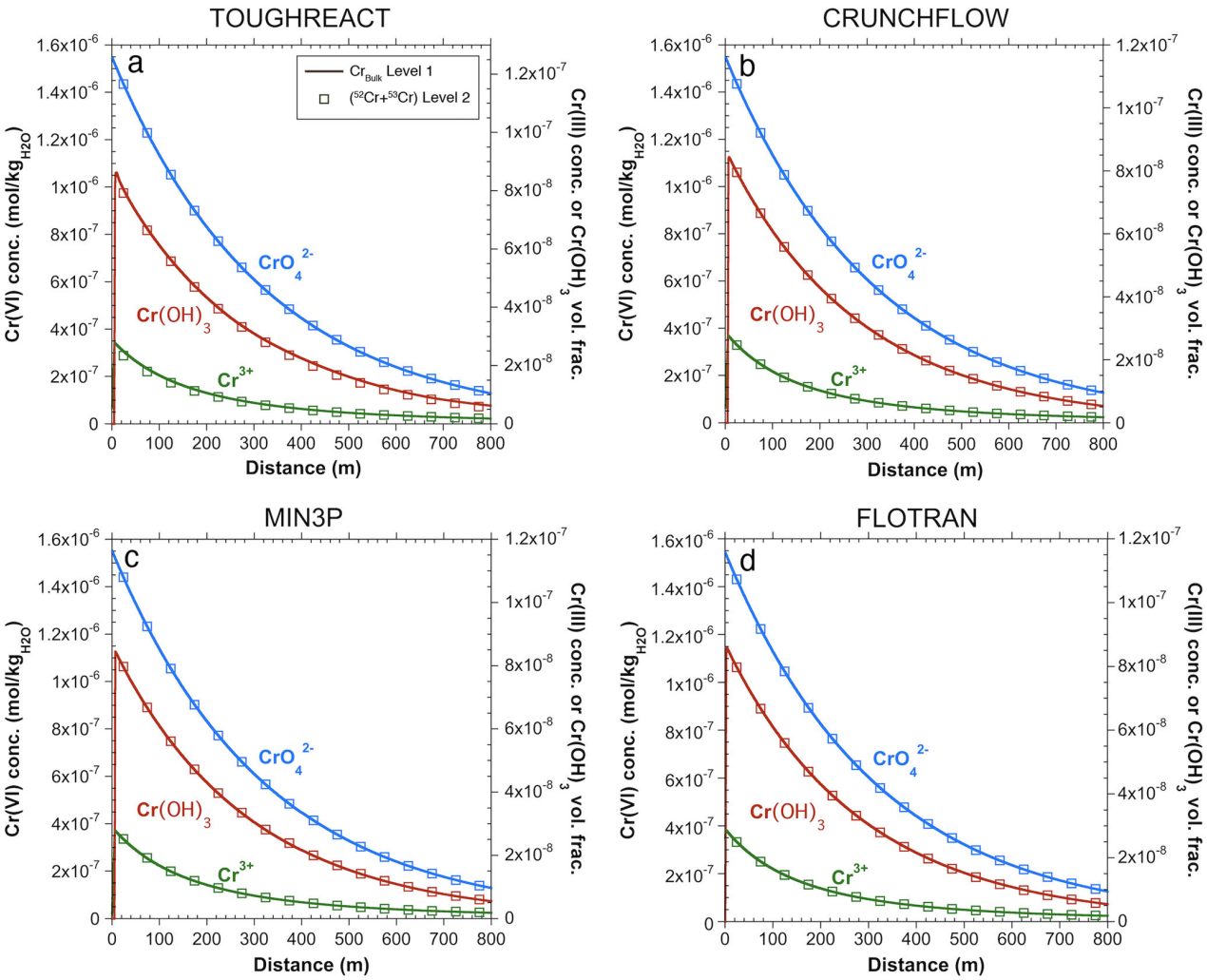

Fig. 6 Comparison between total bulk Cr(VI) and Cr(III) concentration and bulk $Cr(OH)_3$ volume fraction profiles obtained for levels #1 and #2 using different codes. **a** TOUGHREACT, **b** CRUNCHFLOW, **c** MIN3P, and **d** FLOTRAN

obtained because hydrodynamic dispersion was not considered. This limitation occurs because a system's effective fractionation factor is shifted to a value closer to unity (less fractionation) if the Cr(VI) reduction rate is transport-limited [21] or if strong hydrodynamic dispersion is occurring [27, 28]. Accordingly, for substantial longitudinal dispersion, we expect that a well-fitting Rayleigh model would require a fractionation factor closer to unity (less fractionation) than defined as input parameter ($\alpha = 0.9966$).

5.3 Level #3

5.3.1 General simulation results

Steady state total CrO_4^{2-} concentrations (Fig. 7a) demonstrate that the overall Cr(VI) plume in the aquifer is largely dominated by the dissolution of chromatite ($CaCrO_4$) present in the Cr(VI) infiltration zone (Fig. 2). By contrast, steady state total CrO_4^{2-} concentrations were significantly lower in the general hotspot domain (Fig. 7a). These variable Cr(VI) concentrations are inherited by a much higher chromatite solubility when compared to the solubility of jarosite (Table 4). Owing to the specified high reaction rate constant (Table 4), saturation with respect to jarosite is quickly established, thus forming a solubility control on the Cr(VI) plume. The strong Cr(VI) concentration contrast between the two hotspot domains in turn illustrates that the environmental hazards of Cr(VI) contaminations are strongly controlled by the mineralogical composition of Cr(VI) hotspots.

The dissolution of jarosite introduces elevated total Fe^{3+} and SO_4^{2-} concentrations to the aquifer in addition to the Cr(VI) plume (Fig. 7e–f). The steady state total Fe^{3+} concentrations, however, are also affected by Cr(VI) reduction,

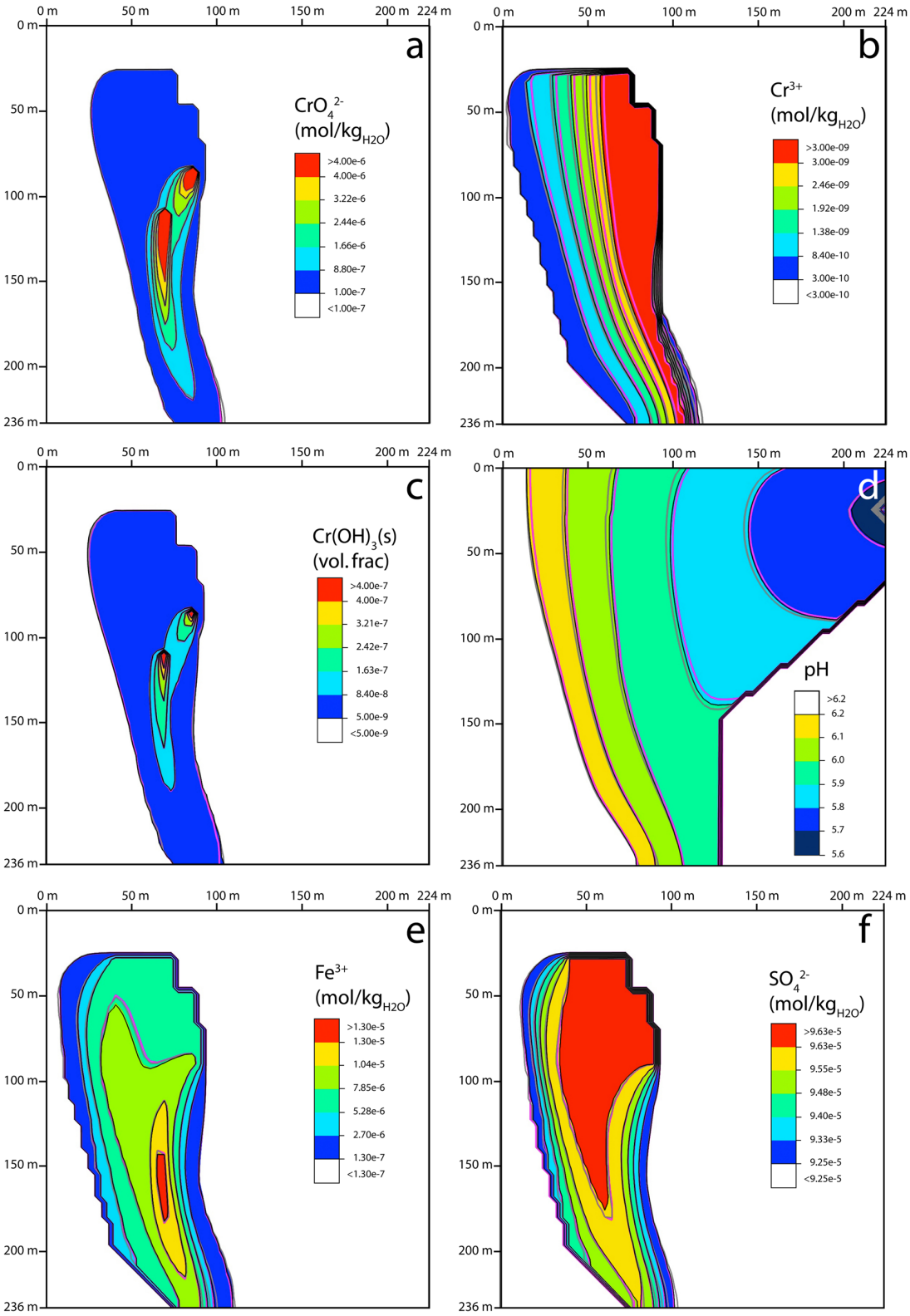

Fig. 7 Steady state spatial distribution of selected total aqueous species concentrations, $Cr(OH)_3$ volume fractions, and fluid pressure obtained for level #3 after a simulated time of 1,000 days. The *colors* and *black contours* indicate results obtained from the TOUGHREACT runs. MIN3P and CRUNCHFLOW results are shown as *gray* and *purple contour lines*, respectively

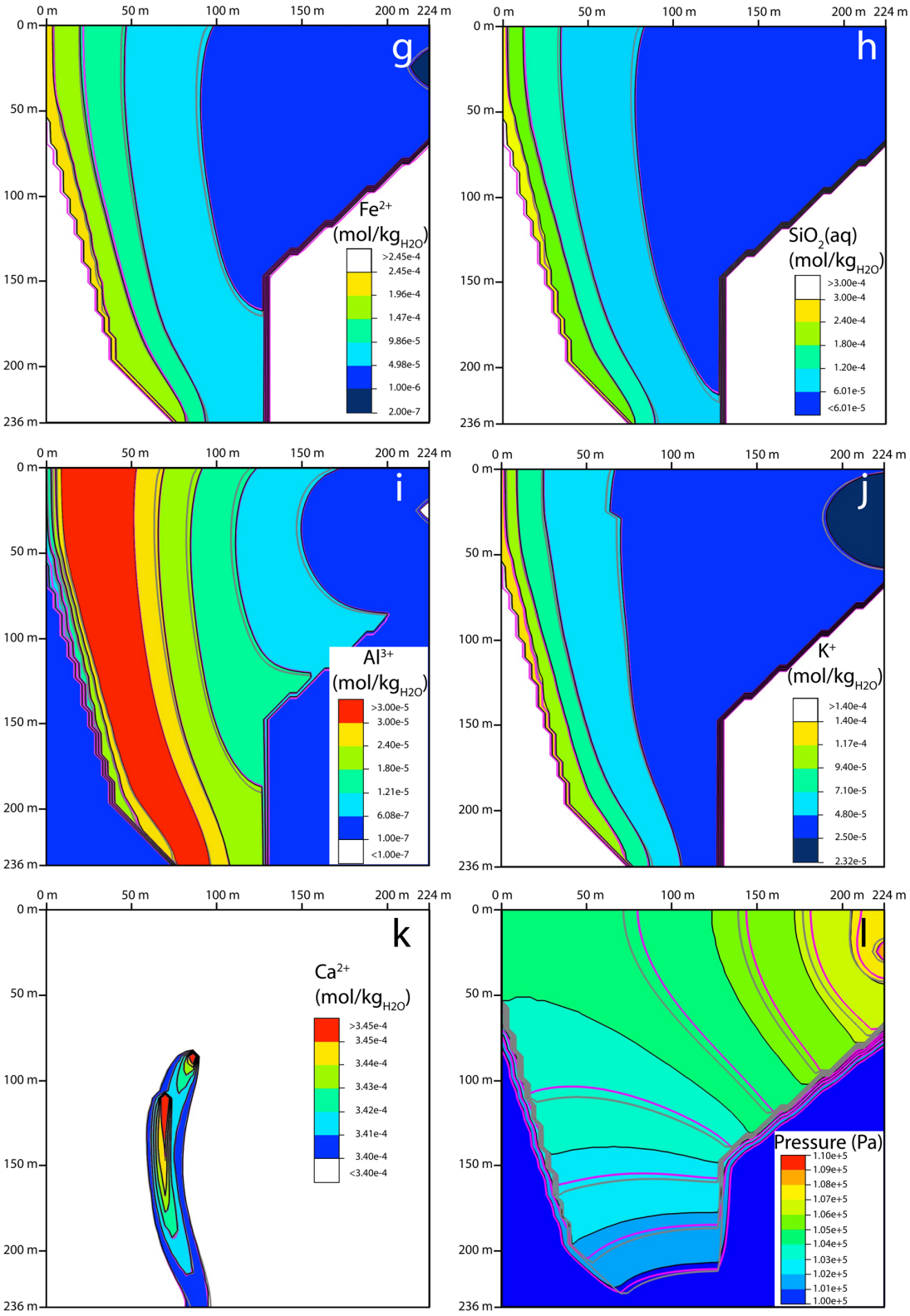

Fig. 7 (continued)

which produces Fe^{3+} in addition to Cr^{3+} (5). Accordingly, the second domain with elevated total Fe^{3+} concentrations is observed near the Cr(VI) infiltration zones in addition to the one generate by jarosite dissolution. The highest total Fe^{3+} concentrations are found slightly downstream of the second (i.e., downstream) Cr(VI) infiltration zone where both Fe^{3+} sources contribute on total Fe^{3+}. The largest $Cr(OH)_3$ volume fractions are observed close to both Cr(VI) infiltration zones (Fig. 7c). By contrast, total Cr^{3+} concentrations (Fig. 7b) are mainly controlled by the pH dependent solubility of $Cr(OH)_3$. Because $Cr(OH)_3$ solubility is higher at lower pH values (Table 3) Cr^{3+} concentrations are decreasing with increasing pH values (Fig. 7d). Total Fe^{2+} concentrations are not substantially affected by Cr(VI) reduction (Fig. 7g) because Fe^{2+} is available in excess of Cr(VI). By analogy to the 1D problem, the Fe^{2+} excess over Cr(VI) is inherited from strong kinetic chamosite and annite dissolution (Table 4). Similar to Fe^{2+}, steady state total SiO_2, Al^{3+}, and K^+ concentrations (Figs. 7h–j) are controlled by the kinetic dissolution of quartz, annite, and chamosite whereas total Ca^{2+} concentrations are controlled by the presence of chromatite in the Cr(VI) infiltration zone (Fig. 7k).

5.3.2 Code comparison

Overall, steady state concentrations obtained from different codes match each other well (Fig. 7). However, minor total concentration differences are observable for a few species (e.g., Cr^{3+}, Fe^{3+}, SO_4^{2-}, pH). We suspect that these differences are inherited from minor flow field differences, illustrated with minor differences in the steady state pressure distributions (Fig. 7l). Minor flow field differences are most likely inherited from a different definition of fluid compressibility and a different approach for model discretization. For instance, MIN3P [54] is the only code using grid blocks that are only half the size at the edge of the grid, resulting in a model domain that is 2 m shorter at each of the four grid boundaries when compared to the CRUNCHFLOW [53 and references therein] and TOUGHREACT [51] grid. Moreover, TOUGHREACT is using a pressure and temperature dependent water compressibility that is slightly larger than 0 to solve for fluid pressures, whereas CRUNCHLOW and MIN3P are using zero water compressibility. CRUNCHFLOW's and MIN3P's use of a zero water compressibility in particular causes a larger pressure for the water injecting grid block when compared to the corresponding TOUGHREACT pressure ($P_{\mathrm{CRUNCHFLOW}} = 1.010 \times P_{\mathrm{TOUGHREACT}}$; $P_{\mathrm{MIN3P}} = 1.019 \times P_{\mathrm{TOUGHREACT}}$), thus inducing a larger pressure gradient across the full model domain in the same order of magnitude. The observation that MIN3P yielded the largest maximum pressure is inherited from defining water injection for one of the small grid blocks at the model edge. Moreover, this definition shifts the location of water injection by about 2 m for the MIN3P model, which also contributed to the observed pressure gradient differences.

A variable pressure distribution and subsequent varying flow velocities cause varying residence times along specific transport paths, thus introducing total concentration differences for species that are controlled by kinetic mineral dissolution (e.g., Fe^{2+}, SiO_2, Al^{3+}, and pH) (Fig. 7d, g–i). Small pH differences (Fig. 7d) in turn are responsible for minor differences observed for species that are controlled by a pH dependent mineral solubility such as SO_4^{2-} and Fe^{3+} (jarosite) and Cr^{3+} ($Cr(OH)_3$) (Fig. 7b, e–f).

Despite of minor flow field differences, breakthrough curves for Cr(VI), HCO_3^-, and K^+ match very well (Fig. 8) confirming that, overall, the flow field was wellmatching.

5.4 Level #4

5.4.1 The fate of individual Cr isotopes

Figure 9a illustrates that the steady state $\delta^{53}Cr_{Cr(VI)/SRM979}$ distribution is not as strongly controlled by the Cr(VI) infiltration zone when compared to the steady state Cr(VI) distribution (Fig. 7a). In particular, maximum $\delta^{53}Cr_{Cr(VI)/SRM979}$ values were obtained for the left hand aquifer boundary (Fig. 2). Large $\delta^{53}Cr_{SRM979}$ values are explained by the minimum pressure gradient and subsequent minimum flow velocities observed for this domain (Fig. 7l). Low velocities in turn increase the aquifer residence time, and thus introduce a larger extent of Cr(VI) reduction along a specific flow path. The different behavior of $\delta^{53}Cr_{Cr(VI)/SRM979}$ and Cr(VI) demonstrates that $\delta^{53}Cr$ values are controlled by the extent of Cr(VI) reduction that a particular Cr(VI) load experienced rather than by the total aqueous Cr(VI) concentration [11, 17]. By contrast, Cr(VI) concentrations are controlled by the solubility of a particular Cr(VI)-bearing mineral.

5.4.2 Code comparison

Comparing results for problem level #4 demonstrates that the tested codes are capable to accurately simulate the fate of Cr isotopes during the tested processes (fractionation during aqueous kinetic Cr(VI) reduction, non-fractionating precipitation of Cr(III), dissolution of Cr(VI) bearing phase). Most importantly, the steady state $\delta^{53}Cr_{SRM979}$ value distribution for the three Cr pools (e.g., Cr(VI), Cr(III), and precipitated $Cr(OH)_3$) derived from different codes match almost as good as for the corresponding 1D problem (Fig. 9a–c vs. Fig. 5d). Moreover, the very similar steady

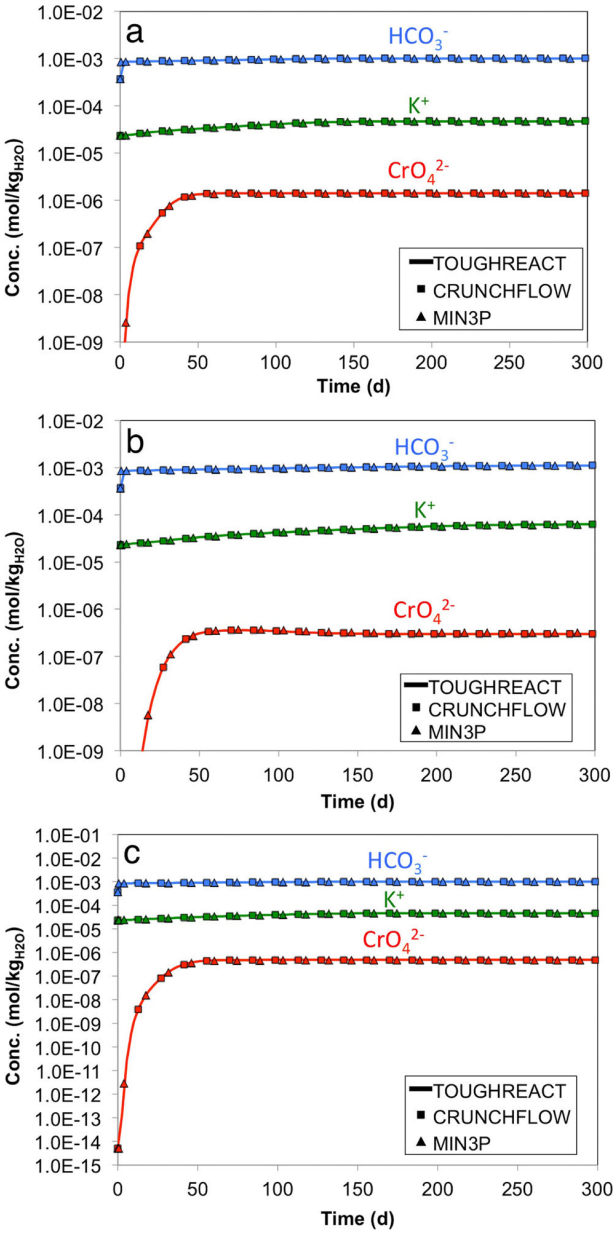

Fig. 8 CrO_4^{2-}, K^+, and HCO_3^- breakthrough curves for level #3 observed at (x_{20}, y_{32}) (**a**), (x_{15}, y_{38}) (**b**), and (x_{21}, y_{36}) (**c**)

state $\delta^{53}Cr_{Cr(OH)3/SRM979}$ and $\delta^{53}Cr_{Cr3+/SRM979}$ distributions (Fig. 9b–c) confirm that Cr isotope fractionation was solely simulated during reduction of Cr(VI) to Cr(III), whereas no fractionation occurred during precipitation of $Cr(OH)_3$.

Minor differences between MIN3P and the two other codes were obtained for $\delta^{53}Cr_{Cr(OH)3/SRM979}$ (Fig. 9c), but only for the left-hand aquifer boundary where the precipitated $Cr(OH)_3$ volume fractions were very small, on the order of 1e–9 or smaller (Fig. 7c). Accordingly, these minor

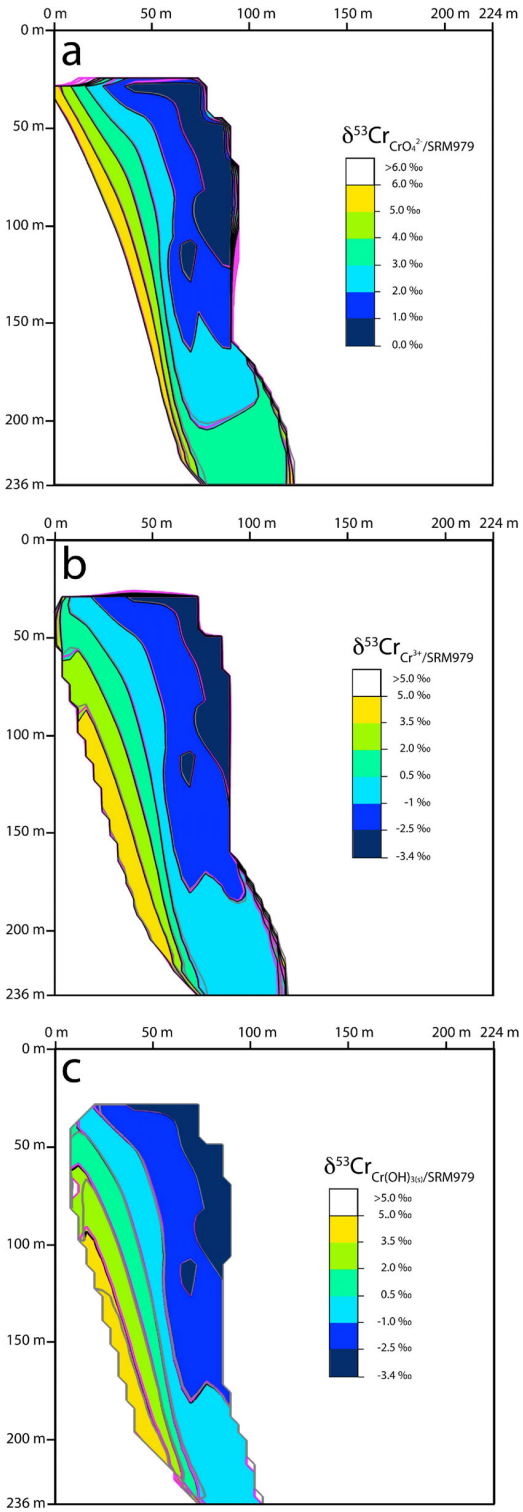

Fig. 9 Steady state spatial $\delta^{53}Cr$ value distribution for the three different Cr pools (Cr(VI), Cr(III), and solid $Cr(OH)_3$) obtained for level #4 after a simulated time of 1,000 days. The *colors* and *black contours* indicate results obtained from the TOUGHREACT runs. MIN3P and CRUNCHFLOW results are shown as *gray* and *purple contour lines*, respectively

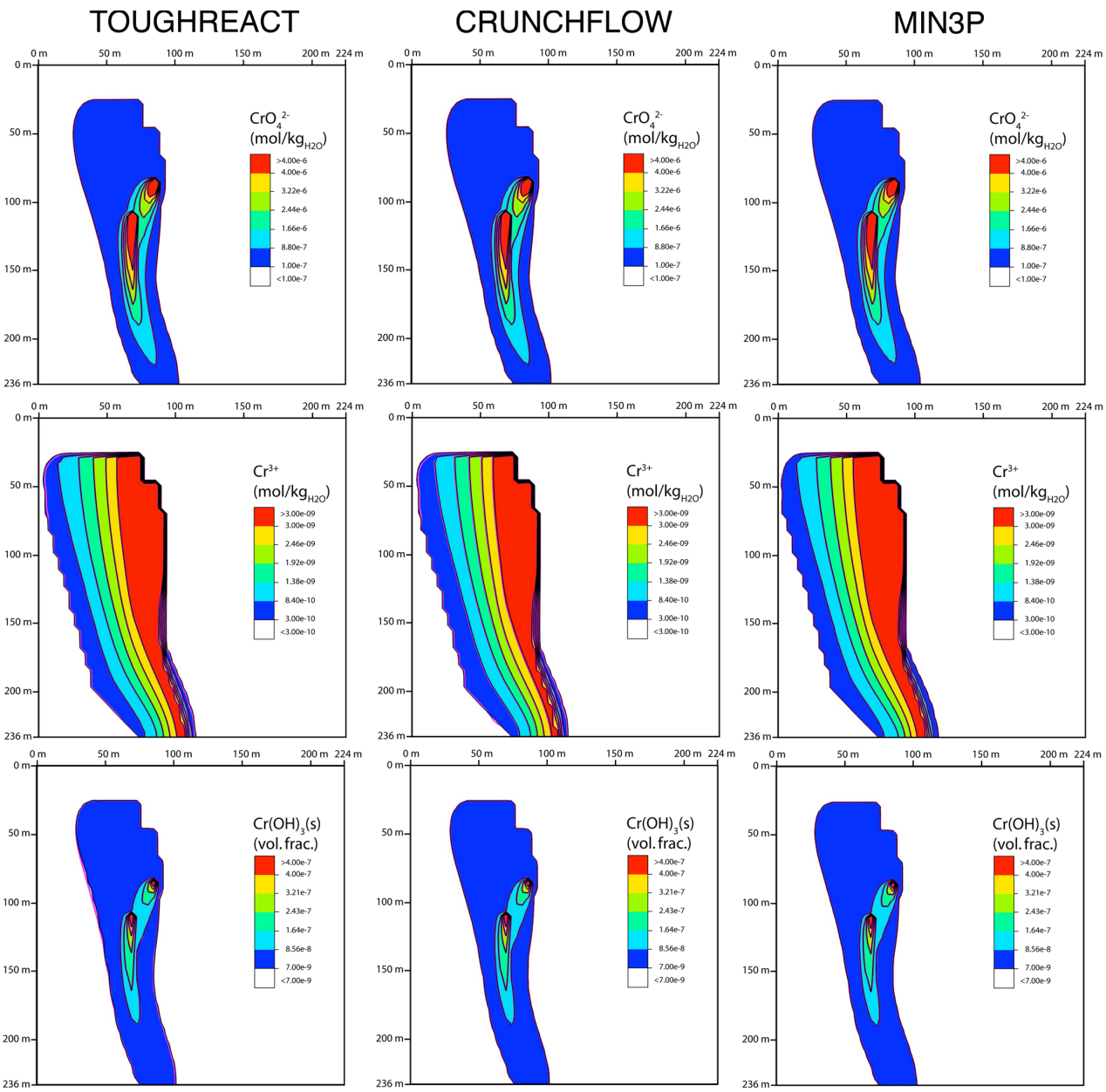

Fig. 10 Steady state spatial distribution of bulk aqueous Cr(VI) and Cr(III) concentrations and bulk $Cr(OH)_3$ volume fractions obtained for problem levels #3 and #4 using TOUGHREACT, CRUNCHLFOW, and MIN3P after a simulated time of 1,000 days. The *colors* and *black contours* denote results for level #3, whereas the *purple contours* refer to the sum of $(^{52}CrO_4)^{2-}$ and $(^{53}CrO_4)^{2-}$, $(^{52}Cr)^{3+}$ and $(^{53}Cr)^{3+}$ as well as $^{52}Cr(OH)_3$ and $^{53}Cr(OH)_3$ obtained for level #4

differences are attributed to the different approaches of calculating precipitation rates of newly formed minerals. The fact that MIN3P is the only code that is using minimum mineral volume fractions larger than zero means that, for small $Cr(OH)_3$ volume fractions (on the order of the defined minimum volume fractions), $\delta^{53}Cr_{Cr(OH)3/SRM979}$ is affected by the specified minimum $^{52}Cr(OH)_3$ and $^{53}Cr(OH)_3$ volume fractions (8.981529e-11 and 1.018437e-11) corresponding to an initial $\delta^{53}Cr_{Cr(OH)3/SRM979}$ of 0.0 ‰. For larger $Cr(OH)_3$ volume fractions, MIN3P derived $\delta^{53}Cr_{Cr(OH)3/SRM979}$ values are no longer affected by the specified minimum volume fractions such that overall, the different approach of handling secondary mineral phases do not cause major differences and a good overall $\delta^{53}Cr_{Cr(OH)3/SRM979}$ match was obtained (Fig. 9c).

The observation that, for any of the codes, steady state total concentration distributions obtained for the sum of the Cr(VI) and Cr(III) isotopologues compare almost perfectly

with corresponding total bulk Cr(VI) and Cr(III) concentrations obtained for level #3 (Fig. 10) adds additional confidence to the simulation results. The same applies for the sum of the $^{52}Cr(OH)_3$ and $^{53}Cr(OH)_3$ end-member volume fractions. The good match between Cr_{total} (problem #3) and $^{52}Cr + {}^{53}Cr$ (problem #4) demonstrates that the overall reaction network remained largely unchanged when adding the simulation of Cr isotope fractionation to the 2D problem. Obtaining such a good match is particularly important because in comparison to the 1D problems, the 2D problems also include solid Cr(VI) sources (reactions m3–m6, Table 4), for which log(K) adjustments had to be performed to obtain the same bulk Cr(VI) solubility when adding the simulation of individual Cr isotopes to the problem (32–33).

6 Summary and conclusion

A benchmark problem set consisting of four problem levels was developed for the simulation of Cr isotope fractionation in 1D and 2D. It was largely adapted from a recent field study where Cr(VI) reduction and accompanying Cr isotope fractionation occurs abiotically by an aqueous reaction with dissolved Fe(II). A first-order reaction rate law with respect to dissolved Fe^{2+} was therefore used to simulate Cr(VI) reduction and Cr isotope fractionation. Owing to its low solubility, Cr(III) produced by this aqueous reaction readily precipitated as a $^{52}Cr(OH)_3$–$^{53}Cr(OH)_3$ solid solution, without additional Cr isotope fractionation. The correct model implementation of Cr isotope fractionation was tested with two 1D problem levels. The first level considered the general flow definition and reaction network only, whereas the second one incorporated the fractionation of Cr isotopes. In addition, two 2D problem levels are provided to ensure the correct model implementation of a solid Cr(VI) source consisting of two different Cr(VI)-bearing mineral phases, which is a typical situation for Cr(VI)-contaminated sites. In analogue to the 1D problem levels, the first 2D level deals with the general flow definition and reaction network, while the Cr isotopic composition of the Cr(VI) source and Cr isotope fractionation was incorporated into the second one.

Correctness of the presented numerical solutions was ensured by running the benchmark problem set with the following four well-established reactive transport modeling codes: TOUGHREACT, MIN3P, CRUNCHFLOW, and FLOTRAN. Results for the 1D Cr isotope fractionation problem were also compared with an analytical Rayleigh-type fractionation model, because it accurately describes Cr isotope fractionation for this first-order irreversible reaction. An additional constraint on the correctness of the results was obtained by comparing results from the problem levels simulating Cr isotope fractionation with the corresponding ones only simulating bulk concentrations. For all problem levels, model to model comparisons showed excellent agreement, suggesting that for the tested geochemical processes (fractionation during aqueous kinetic Cr(VI) reduction, non-fractionating Cr(III) precipitation, dissolution of Cr(VI)-bearing minerals) all of the tested codes are capable to accurately simulate the fate of individual Cr isotopes.

The presented problem set is proposed to serve as a useful benchmark to test the simulation of stable isotope fractionation during aqueous kinetic as well as mineral precipitation reactions. Modelers seeking to incorporate Cr isotope fractionation, or fractionation of any other isotopic species (e.g., C, Li, S), may therefore find the presented benchmark problem set useful to verify their codes for the geochemical processes tested here. It should be noted, however, that for aqueous kinetic reactions the code-specific simulation approaches were solely tested for first-order reaction kinetics. The two 2D problem levels also provide a base case for code verification that could be expanded by specifying a heterogeneous redox and/or permeability distribution in order to assess the effects of hydrodynamic dispersion and localized Cr(VI) reduction on the resulting Cr isotopic composition. The accurate implementation of such transport effects on the fate of stable isotope ratios, however, should be rigorously tested by future benchmark efforts. The same applies for the accurate simulation of stable isotope fractionation in conjunction with reaction orders other than first-order.

Acknowledgments CW was supported by the Subsurface Science Scientific Focus Area funded by the U.S. Department of Energy, Office of Science, Office of Biological and Environmental Research under award number DE-AC02-05CH11231. JD's contribution was funded through a National Science Foundation Division of Earth Sciences Postdoctoral Fellowship under contract number EAR-1144763. RA was funded through an Ontario Research Foundation – Research Excellence Award.

References

1. Kotas, J., Stasicka, Z.: Chromium occurrence in the environment and methods of its speciation. Environ. Pollut. **107**, 263–283 (2000)
2. Oze, C., Bird, D.K., Fendorf, S.: Genesis of hexavalent chromium from natural sources in soil and groundwater. Proc. Natl. Acad. Sci. U. S. A. **104**, 6544–6549 (2007)
3. Szalinska, E., Dominik, J., Vignati, D.A.L., Bobrowski, A., Bas, B.: Seasonal transport pattern of chromium(III and VI) in a stream receiving wastewater from tanneries. Appl. Geochem. **25**, 116–122 (2010)
4. Rai, D., Sass, B.M., Moore, D.A.: Chromium(III) hydrolysis constants and solubility of chromium(III) hydroxide. Inorg. Chem. **26**, 345–349 (1987)

5. Powell, R.M., Puls, R.W., Hightower, S.K., Sabatini, D.A.: Coupled iron corrosion and chromate reduction: mechanisms for subsurface remediation. Environ. Sci. Technol. **29**, 1913–1922 (1995)
6. Palmer, C.D., Puls, R.: W. Iron Metal for Subsurface Remediation; EPA/540/S-94/505; U.S. EPA Ground Water Issue (1994)
7. Naftz, D.L., Morrison, S.J., Davies, J.A., Fuller, C.C.: Handbook of Groundwater remediation using permeable reactive barriers. Elsevier Science, San Diego, USA (2002)
8. Flury, B., Frommer, J., Eggenberger, U., Mäder, U., Nachtegaal, M., Kretzschmar, R.: Assessment of long-term performance and chromate reduction mechanisms in a field scale permeable reactive barrier. Environ. Sci. Technol. **43**, 6786–6792 (2009)
9. Wanner, C., Zink, S., Eggenberger, U., Mäder, U.: Assessing the Cr(VI) reduction efficiency of a permeable reactive barrier using Cr isotope measurements and 2D reactive transport modeling. J. Cotam. Hydrol. **131**, 54–63 (2012)
10. Faybishenko, B., Hazen, T.C., Long, P.E., Brodie, E.L., Conrad, M.E., Hubbard, S.S., Christensen, J.N., Joyner, D., Borglin, S.E., Chakraborty, R., Williams, K.H., Peterson, J.E., Chen, J., Brown, S.T., Tokunaga, T.K., Wan, J., Firestone, M., Newcomer, D.R., Resch, C.T., Cantrell, K.J., Willett, A., Koenigsberg, S.: In Situ long-term reductive bioimmobilization of Cr(VI) in Groundwater using hydrogen release compound. Environ. Sci. Technol. **42**, 8478–8485 (2008)
11. Wanner, C., Zink, S., Eggenberger, U., Mäder, U.: Unraveling the partial failure of a permeable reactive barrier using a multi-tracer experiment and Cr isotope measurements. Appl. Geochem. **37**, 125–133 (2013)
12. Zink, S., Schoenberg, R., Staubwasser, M.: Isotopic fractionation and reaction kinetics between Cr(III) and Cr(VI) in aqueous media. Geochim. Cosmochim. Acta **74**, 5729–5745 (2010)
13. Basu, A., Johnson, T.M.: Determination of Hexavalent chromium reduction using cr stable isotopes: isotopic fractionation factors for permeable reactive barrier materials. Environ. Sci. Technol. **46**, 5353–5360 (2012)
14. Kitchen, J.W., Johnson, T.M., Bullen, T.D., Zhu, J., Raddatz, A.L.: Chromium isotope fractionation factors for reduction of Cr(VI) by aqueous Fe(II) and organic molecules. Geochim. Cosmochim, Acta (2012)
15. Jamieson-Hanes, J.H., Gibson, B.D., Lindsay, M.B.J., Kim, Y., Ptacek, C.J., Blowes, D.W.: Chromium Isotope fractionation during reduction of cr(vi) under saturated flow conditions. Environ. Sci. Technol. **46**, 6783–6789 (2012)
16. Izbicki, J.A., Ball, J.W., Bullen, T.D., Sutley, S.J.: Chromium, chromium isotopes and selected trace elements, western Mojave Desert, USA. Appl. Geochem. **23**, 1325–1352 (2008)
17. Berna, E.C., Johnson, T.M., Makdisi, R.S., Basu, A.: Cr stable isotopes as indicators of Cr(VI) reduction in groundwater: a detailed time-series study of a point-source plume. Environ. Sci. Technol. **44**, 1043–1048 (2010)
18. Wanner, C., Eggenberger, U., Kurz, D., Zink, S., Mäder, U.: A chromate-contaminated site in southern Switzerland, part 1: site characterization and the use of Cr isotopes to delineate fate and transport. Appl. Geochem. **27**, 644–654 (2012)
19. Izbicki, J.A., Bullen, T.D., Martin, P., Schroth, B.: Delta Chromium-53/52 isotopic composition of native and contaminated groundwater, Mojave Desert, USA. Appl. Geochem. **27**, 841–853 (2012)
20. Ellis, A.S., Johnson, T.M., Bullen, T.D.: Chromium isotopes and the fate of hexavalent chromium in the environment. Science **295**, 2060–2062 (2002)
21. Wanner, C., Sonnenthal, E.L.: Assessing the control on the effective kinetic Cr isotope fractionation factor: a reactive transport modeling approach. Chem. Geol. **337**, 88–98 (2013)
22. Dossing, L.N., Dideriksen, K., Stipp, S.L.S., Frei, R.: Reduction of hexavalent chromium by ferrous iron: a process of chromium isotope fractionation and its relevance to natural environments. Chem. Geol. **285**, 157–166 (2011)
23. Sikora, E.R., Johnson, T.M., Bullen, T.D.: Microbial mass-dependent fractionation of chromium isotopes. Geochim. Cosmochim. Acta **72**, 3631–3641 (2008)
24. DePaolo, D.J.: Surface kinetic model for isotopic and trace element fractionation during precipitation of calcite from aqueous solutions. Geochim. Cosmochim. Acta **75**, 1039–1056 (2011)
25. Druhan, J.L., Steefel, C.I., Williams, K.H., DePaolo, D.J.: Calcium isotope fractionation in groundwater: molecular scale processes influencing field scale behavior. Geochim. Cosmochim. Acta **119**, 93–116 (2013)
26. Green, C.T., Bohlke, J.K., Bekins, B.A., Phillips, S.P.: Mixing effects on apparent reaction rates and isotope fractionation during denitrification in a heterogeneous aquifer. Water Resour. Res. **46**, W08525 (2010). doi:10.1029/2009WR008903
27. Abe, Y., Hunkeler, D.: Does the Rayleigh equation apply to evaluate field isotope data in contaminant hydrogeology? Environ. Sci. Technol. **40**, 1588–1596 (2006)
28. Van Breukelen, B.M.V., Prommer, H.: Beyond the Rayleigh Equation: reactive transport modeling of isotope fractionation effects to improve quantification of biodegradation. Environ. Sci. Technol. **42**, 2457–2463 (2008)
29. Jamieson-Hanes, J.H., Amos, R.T., Blowes, D.W.: Reactive Transport modeling of chromium isotope fractionation during Cr(VI) reduction. Environ. Sci. Technol. **46**, 13311–13316 (2012)
30. Wanner, C., Eggenberger, U., Mäder, U.: A chromate-contaminated site in southern Switzerland, part 2: reactive transport modeling to optimize remediation options. Appl. Geochem. **27**, 655–662 (2012)
31. Druhan, J.L., Steefel, C.I., Molins, S., Williams, K.H., Conrad, M.E., DePaolo, D.J.: Timing the onset of sulfate reduction over multiple subsurface acetate amendments by measurement and modeling of sulfur isotope fractionation. Environ. Sci. Technol. **46**, 8895–8902 (2012)
32. Druhan, J.L., Steefel, C.I., Conrad, M.E., DePaolo, D.J.: A large column analog experiment of stable isotope variations during reactive transport: I. A Comprehensive model of sulfur cycling and δ34S fractionation. Geochim. Cosmochim. Acta **124**, 366–393 (2014)
33. Zhang, Y.-C., Prommer, H., Broers, H.P., Slomp, C.P., Greskoviak, J., Van der Grift, B., Van Cappellen, P.: Model-Based integration and analysis of biogeochemical and isotopic dynamics in a nitrate-polluted pyritic aquifer. Environ. Sci. Technol. **47**, 10415–10422 (2013)
34. Gibson, B.D., Amos, R.T., Blowes, D.W.: (29)S/(27)S fractionation during sulfate reduction in groundwater treatment systems: reactive transport modeling. Environ. Sci. Technol. **45**, 2863–2870 (2011)
35. Van Breukelen, B.M., Griffioen, J., Roling, W.F.M., van Verseveld, H.W.: Reactive transport modelling of biogeochemical processes and carbon isotope geochemistry inside a landfill leachate plume. J. Cotam. Hydrol. **70**, 249–269 (2004)
36. Van Breukelen, B.M., Hunkeler, D., Volkering, F.: Quantification of sequential chlorinated ethene degradation by use of a reactive transport model incorporating isotope fractionation. Environ. Sci. Technol. **39**, 4189–4197 (2005)
37. Atteia, O., Franceschi, M., Dupuy, A.: Validation of reactive model assumptions with isotope data: application to the Dover case. Environ. Sci. Technol. **42**, 3289–3295 (2008)

38. Prommer, H., Aziz, L.H., Bolano, N., Taubald, H., Schueth, C.: Modelling of geochemical and isotopic changes in a column experiment for degradation of TCE by zero-valent iron. J. Cotam. Hydrol. **97**, 13–26 (2008)
39. Pooley, K.E., Blessing, M., Schmidt, T.C., Haderlein, S.B., Macquarrie, K.T.B., Prommer, H.: Aerobic biodegradation of chlorinated ethenes in a fractured bedrock aquifer: quantitative assessment by compound-specific isotope analysis (CSIA) and reactive transport modeling. Environ. Sci. Technol. **43**, 7458–7464 (2009)
40. Rolle, M., Chiogna, G., Bauer, R., Griebler, C., Grathwohl, P.: Isotopic Fractionation by transverse dispersion: flow-through microcosms and reactive transport modeling study. Environ. Sci. Technol. **44**, 6167–6173 (2010)
41. Steefel, C.I., Appelo, C.A.J., Arora, B., Jacques, D., Kalbacher, T., Kolditz, O., Lagneau, V., Lichtner, P.C., Mayer, K.U., Meussen, H., Molins, S., Moulton, D., Parkhurst, D.L., Shao, H., Simunek, J., Spycher, N., Yabusaki, S., Yeh, G.T.: Reactive transport codes for subsurface environmental simulation. Computational Geoscience (2014)
42. Schoenberg, R., Zink, S., Staubwasser, M., von Blanckenburg, F.: The stable Cr isotope inventory of solid earth reservoirs determined by double spike MC-ICP-MS. Chem. Geol. **249**, 294–306 (2008)
43. Ellis, A.S., Johnson, T.M., Bullen, T.D.: Using chromium stable isotope ratios to quantify Cr(VI) reduction: lack of sorption effects. Environ. Sci. Technol. **38**, 3604–3607 (2004)
44. Johnson, J.W., Oelkers, E.H., Helgeson, H.C.: SUPCRT92: a software package for calculating the standard molal thermodynamic poroperties of minerals, gases, aqueous species, and reactions from 1 to 5000 bar and 0 to 1000°C. Comput. Geosci. **18**, 899–948 (1992)
45. Wolery, T.J.: EQ3/6: Software package for geochemical modeling of aqueous systems: package overview and installation guide (version 7.0). Livermore, California (1992)
46. Ball, J.W., Nordstrom, D.K.: Critical evaluation and selection of standard state thermodynamic properties for chromium metal and its aqueous ions, hydrolysis species, oxides, and hydroxides. J. Chem. Eng. Data **43**, 895–918 (1998)
47. Lasaga, A.C.: Chemical kinetics of water-rock interactions. J. Geoph. Res. **89**, 4009–4025 (1984)
48. Buerge, I.J., Hug, S.J.: Kinetics and pH dependence of chromium(VI) reduction by iron(II). Environ. Sci. Technol. **31**, 1426–1432 (1997)
49. Shields, W.R., Murphy, T.J., E. J., C., Garner, E.L.: Absolute isotopic abundance ratios and atomic weight of a reference sample of chromium. J. Res. Natl. Bur. Stand. Sect. Phys. Chem. A **70**, 193 (1966)
50. Coplen, T.B.: Guidelines and recommended terms for expression of stable-isotope-ratio and gas-ratio measurement results. Rapid Commun. Mass Spectrom. **25**, 2538–2560 (2011)
51. Xu, T., Spycher, N., Sonnenthal, E.L., Zhang, G., Zheng, L., Pruess, K.: TOUGHREACT Version 2.0: a simulator for subsurface reactive transport under non-isothermal multiphase flow conditions. Comput. Geosci. **37**, 763–774 (2011)
52. Lichtner, P.C.: FLOTRAN users manual: two-phase nonsothermal coupled thermal-hydrologic-chemical (THC) reactive flow and transport code version 2. Los Alamos National Laboratory, New Mexico, USA (2007)
53. Steefel, C., Maher, K.: Fluid-rock interaction: a reactive transport approach. In: Oelkers, E.H., Schott, J. (eds.) Thermodynamics and Kinetics of Water-Rock Interaction. Mineralogical Society of America: 2009, Reviews in Mineralogy, vol. 70, pp. 485–532
54. Mayer, K.U., Frind, E.O., Blowes, D.W.: Multicomponent reactive transport modeling in variably saturated porous media using a generalized formulation for kinetically controlled reactions. Water Resour. Res. **38**, 1174 (2002). doi:10.1029/2001WR000862
55. Baron, D., Palmer, C.D.: Solubility of KFe3(CrO4)2(OH)6 at 4 to 35°C. Geochim. Cosmochim. Acta **60**, 3815–3824 (1996)
56. Palandri, J.L., Kharaka, Y.K.A.: Compilation of rate parameters of water-mineral interaction kinetics for application to geochemical modeling. U.S. Geological Survey Open-File Report 2004-1068; US Geological Survey (2004)
57. Appelo, C.A.J., Postma, D.: Geochemistry, groundwater and pollution, 2nd edn. Balkema, Amsterdam, The Netherlands (2005)

4. RTM APPLICATIONS RELATED TO GEOTHERMAL ENERGY

Scope and significance

Within the context of geothermal energy research provided in Chapters 1 and 2, this Chapter presents three applications where RTM is used as an exploration tool for geothermal systems. Chapter 4.1 describes a series of 2D RTM simulations of the Dixie Valley geothermal system located in the Basin and Range Province in the western USA. The output of these simulations is used for applying various solute geothermometry methods to assess their performance in estimating deep reservoir temperatures. By comparing the inferred reservoir temperature to those obtained from the RTM simulations, the combined approach demonstrates which solute geothermometry method works best for various scenarios of rock-water interactions. Obtaining reliable reservoir temperatures is crucial because the reservoir temperature limits the energy that can be exploited from the deep subsurface.

Chapters 4.2 and 4.3 present results from two RTM applications aiming to identify the governing thermal-hydraulic-chemical processes in two orogenic geothermal systems in the Central Alps, Switzerland, and to quantitatively assess their geothermal potential. All simulations are carried out in 3D and are constrained and calibrated by multiple observations such as chemical and isotopic compositions of thermal and cold springs, temperature measurements along tunnels, and geochemical properties of a hydrothermal breccia. The first RTM application (Chapter 4.2) relates to thermal-hydraulic simulations performed for the geothermal system located at Grimsel Pass. The model results demonstrate that orogenic geothermal systems could result in very favorable conditions for geothermal power production. The second application (Chapter 4.3) simulates the circulation of meteoric water in the crystalline basement of the Aar Massif above and beneath the world's largest tunnel, the Gotthard railway base tunnel. In contrast to the first one, it explicitly takes into account the surface topography and simultaneously simulates the fate of stable water isotopes. The model results confirm the high potential of orogenic belts for geothermal power production, demonstrate that the circulation of meteoric water is controlled by the surface topography and the presence of regional fault zones, and suggest that palaeohydrologic variations have to be taken into account for interpreting the chemical and isotopic composition of groundwater samples discharging from such systems.

Overall, this Chapter illustrates that RTM serves as powerful tool for the integrated interpretation of multiple, field-derived datasets and the exploration of geothermal systems. Key information obtained from the three RTM applications include (i) an assessment of solute geothermometry methods to improve reservoir temperature estimates and (ii) the quantification of thermal anomalies generated by orogenic geothermal systems, which underscores their promise as geothermal resources, and (iii) the identification of favorable settings for such systems, which leads to useful implications for exploration.

4.1. Reactive transport modeling of the Dixie Valley geothermal area: Insights on flow and geothermometry

Source:

Wanner C., Peiffer L., Sonnenthal E., Spycher N., Iovenitti J. and Kennedy B. M. (2014) Reactive transport modeling of the Dixie Valley geothermal area: insights on flow and geothermometry. *Geothermics* **51**, 130-141.

Contribution by the Author (CW):

CW developed the general idea and CW carried out all the simulations. CW had the lead in data interpretation and manuscript writing.

Geothermics 51 (2014) 130–141

Contents lists available at ScienceDirect

Geothermics

journal homepage: www.elsevier.com/locate/geothermics

Reactive transport modeling of the Dixie Valley geothermal area: Insights on flow and geothermometry

Christoph Wanner[a,*], Loïc Peiffer[a,1], Eric Sonnenthal[a], Nicolas Spycher[a], Joe Iovenitti[b], Burton Mack Kennedy[a]

[a] Earth Sciences Division, Lawrence Berkeley National Laboratory, 1 Cyclotron Road, Berkeley, CA 94720, USA
[b] AltaRockEnergy Inc., Sausalito, CA, USA

ARTICLE INFO

Article history:
Received 6 September 2013
Accepted 16 December 2013
Available online 15 January 2014

Keywords:
Reactive transport modeling
Solute geothermometry
Dixie Valley
Fracture flow
Geothermal springs

ABSTRACT

A 2D reactive transport model of the Dixie Valley geothermal area in Nevada, USA was developed to assess fluid flow pathways and fluid rock interaction processes. The model includes two major normal faults and the incorporation of a dual continuum domain to simulate the presence of a small-scale thermal spring being fed by a highly permeable but narrow fracture zone. Simulations were performed incorporating fluid flow, heat conduction and advection, and kinetic mineral-water reactions. Various solute geothermometry methods were applied to simulated spring compositions, to compare estimated reservoir temperatures with "true" modeled reservoir temperatures, for a fluid ascending the simulated fracture and cooling on its way to the surface. Under the modeled conditions (cooling but no mixing or boiling), the classical Na–K(–Ca) geothermometers performed best because these are least affected by mineral precipitation upon cooling. Geothermometry based on computed mineral saturation indices and the quartz geothermometer were more sensitive to re-equilibration upon cooling, but showed good results for fluid velocities above ca. 0.1 m/d and a reactive fracture surface area 1–2 orders of magnitude lower than the corresponding geometric surface area. This suggests that such upflow rates and relatively low reactive fracture surface areas are likely present in many geothermal fields. The simulations also suggest that the presence of small-scale fracture systems having an elevated permeability of 10^{-12} to 10^{-10} m^2 can significantly alter the shallow fluid flow regime of geothermal systems. For the Dixie Valley case, the model implies that such elevated permeabilities lead to a shallow (less than 1 km) convection cell where superficial water infiltrates along the range front normal fault and connects the small-scale geothermal spring through basin filling sediments. Furthermore, we conclude that a fracture permeability on the order of 10^{-12} m^2 may lead to near surface temperature >100 °C whereas a permeability of 10^{-10} m^2 is not realistic because this permeability led to extreme upflow velocities and to a short-circuit of the regional fault zone.

1. Introduction

Although simulations of geothermal systems have in some cases incorporated reactive transport (Xu and Pruess, 2001; Dobson et al., 2003, 2004) most large-scale (2–3D) models for geothermal areas have only taken into account fluid flow and heat transfer (e.g., Clearwater et al., 2012; McKenna and Blackwell, 2004; Moulding and Brikowski, 2012). Fully coupled reactive transport models of field scale geothermal systems are rarely found in the literature. Exceptions are simulations of enhanced geothermal systems (EGS) (Bachler and Kohl, 2005; Sonnenthal et al., 2012; Taron and Elsworth, 2009), formation of scale within geothermal wells (Alt-Epping et al., 2013; Xu et al., 2004) or the simulation of shallow hydrothermal systems (Jones and Xiao, 2006; Xu and Pruess, 2001).

In this study, a 2D reactive transport model of the Dixie Valley geothermal area (Nevada, USA) was developed to assess fluid flow pathways and fluid rock interaction processes. The Dixie Valley geothermal field, located in the Basin and Range province of the western US, was chosen as an example study because it has been used for power production (ca. 63 MW) over the last two decades and has been extensively characterized (Blackwell et al., 2007, and references therein). Our reactive transport model specifically benefits from the availability of an extensive geochemical and isotopic dataset (Goff et al., 2002). Field scale features include geothermal springs with temperatures up to 84 °C (Goff et al., 2002), subsurface temperatures in excess of 280 °C at 3 km depth, the absence of known magmatic heat sources and an elevated basal

* Corresponding author. Tel.: +1 5104958147; fax: +1 5104865686.
E-mail addresses: cwanner@lbl.gov, christoph.wanner@geo.unibe.ch (C. Wanner).
[1] Current address: Instituto de Energías Renovables, Universidad Nacional Autónoma de México, Temixco, Morelos 62580, Mexico.

0375-6505/$ – see front matter © 2013 Elsevier Ltd. All rights reserved.
http://dx.doi.org/10.1016/j.geothermics.2013.12.003

heat flux on the order of 90 mW/m^2 which is typical for the Basin and Range province (McKenna and Blackwell, 2004). Recent investigations also showed that near surface groundwater temperatures can be greater than 100 °C for isolated locations (Iovenitti et al., 2012). The general understanding of Basin and Range geothermal systems is that meteoric water infiltrates via the range top or valley floor, heats up during deep circulation and ascends along the most permeable pathways such as range-bounding normal faults (McKenna and Blackwell, 2004).

To what depth the fluid circulation extends, however, is still under debate. Helium isotopic studies revealed that ca. 7.5% of the He in the Dixie Valley system is derived from mantle sources, requiring fluid input from below the brittle–ductile transition (Kennedy and van Soest, 2006). McKenna and Blackwell (2004) postulated a large scale fluid convection cell where infiltrating meteoric water reaches a depth up to 8 km before it finally ascends to the surface. Moulding and Brikowski (2012), on the contrary, argued that such deep fluid infiltration seems unrealistic considering that the lithostatic stress at this depth reduces the permeability needed to establish significant advective fluid flow (5×10^{-17} m^2, McKenna and Blackwell, 2004). Reduced permeability with increasing depth is especially enhanced below the brittle–ductile transition such as shown by Weis et al. (2012). For a temperature gradient of ca. 115 °C/km, Weis et al. (2012) illustrate that this transitions occurs at a depth of ca. 3–5 km. Blackwell et al. (2007) showed that the average temperature gradient for the Dixie Valley area is 63 °C/km. For isolated locations, however, the temperature gradient reaches values that are much greater than 100 °C/km (Blackwell et al., 2007). These high values suggest that the brittle–ductile transition and accompanying permeability reduction might occur at relatively shallow depth at Dixie Valley. To account for the potentially low rock permeability, Moulding and Brikowski (2012) postulate that the fluid circulation is much shallower when compared to the model of McKenna and Blackwell (2004) by presenting a full 3D model that accounts for horizontal fluid flow within a large-scale fracture plane.

In contrast to the flow simulation studies performed by McKenna and Blackwell (2004) and Moulding and Brikowski (2012), the main objective of our reactive transport modeling study is to evaluate the controlling attributes of hydrothermal convection (e.g. fluid velocity, fracture surface areas, etc.) and their impact on surface fluid chemistry and the use of solute chemical geothermometry.

Geothermometry based on mineral saturation indices has been used as an exploration tool for geothermal systems (Reed and Spycher, 1984; Spycher et al., 2011, 2014). This method, referred to here as multicomponent geothermometry, involves computing multicomponent homogenous equilibria to yield temperature-dependent saturation indices of selected potential reservoir minerals, using full water chemical analyses. The clustering of saturation indices near zero (the equilibrium point) at any temperature, for a group of reservoir minerals, provides an indication of probable reservoir temperature. This method is different than the classical and empirical SiO_2 and Na–K–Ca geothermometers (Fournier and Rowe, 1966; Fournier and Truesdell, 1973) because it relies on more than a few selected chemical components. Both multicomponent and classical geothermometry methods are based on the assumption that the chemical compositions of waters sampled at the surface reflect equilibrium with reservoir minerals at depth. An advantage of multicomponent geothermometry is that it can yield reservoir temperatures in systems that are approaching equilibrium, although not necessarily at equilibrium, and can also be used to deconvolute effects from degassing and mixing (Spycher et al., 2014).

The potential for re-equilibration of geothermal fluids as they ascend from the deep reservoir to the surface is a shortcoming of chemical geothermometry, resulting in the "deep" chemical and temperature signature of the fluid being lost, and thus causing erroneous temperature estimates (Ferguson et al., 2009). To address the re-equilibration issue, we evaluated the necessary upflow velocity along a spring-feeding fracture and the minimum corresponding reactive fracture surface area needed to avoid re-equilibration upon conductive cooling. Varying upflow velocity and fracture reactivity in our model allowed us to define flow and reactive constraint conditions under which geothermometry is expected to be most successful. Moreover, our model simulations provide insight into fluid circulation depths and upflow velocities for typical Basin and Range geothermal systems.

2. Model setup and calibration

2.1. Numerical simulator

All simulations were performed using the newly parallelized version of TOUGHREACT (Sonnenthal et al., http://esd.lbl.gov/research/projects/tough/software/toughreact.html) based on TOUGHREACT V2 (Xu et al., 2011), allowing a computationally efficient simulation of fully coupled reactive transport in variably saturated geologic media. TOUGHREACT is based on the TOUGH2 simulator (Pruess et al., 1999) that simulates fluid flow and heat transfer processes. For this study we used the TOUGH2 equation of state module EOS1 considering fully saturated, non-isothermal water flow occurring as a single phase only. By simulating one single fluid phase, the model does not consider boiling. This constraint forms a model simplification because there are a few fumaroles, and thus boiling occurring at Dixie Valley (McKenna and Blackwell, 2004). Neglecting boiling is, however, justified because our main objective was to assess the effects of conductive cooling during varying upflow velocities as well as fracture reactivity on the use of chemical geothermometry. Moreover, Spycher et al. (2014) and Peiffer et al. (2014) recently discussed in detail how boiling can be taken into account for temperetures estimates using multicomponent geothermometry.

TOUGHREACT simulates water and heat flow using the governing mass balance equations (here shown for single-phase water only):

$$\frac{\partial M_{W,H}}{\partial t} = -\nabla F_{W,H} + q_{W,H} \tag{1}$$

where $M_{W,H}$ is the accumulation term for water M_W (kg/m^3) or heat M_H (J/m^3), $q_{W,H}$ are water or heat sinks (−) or sources (+) and $F_{W,H}$ refers to the water flux F_W (kg m^{-2} s^{-1}) or heat flux F_H (J m^{-2} s^{-1}). For fully saturated, single phase flow problems F_W is equal to the Darcy flux u (m/s)

$$u = -\frac{k}{\mu}(\nabla P - \rho g) \tag{2}$$

where k refers to the permeability (m^2), μ is the water viscosity (kg/m/s), P (Pa) refers to the water pressure and ρ and g are the water density (kg/m^3) and the gravitational acceleration (m/s^2), respectively. Heat flux F_H (J s^{-1} m^{-2}) is defined as:

$$F_H = C_M \cdot T \cdot \rho_M \cdot u - \lambda \cdot \nabla T \tag{3}$$

where λ refers to the wet thermal conductivity of the solid/rock (J s^{-1} m^{-1} K^{-1} = W m^{-1} K^{-1}), T (K) is the temperature of the porous media (rock + water), C_M (J kg^{-1} K^{-1}) and ρ_M (kg/m^3) refer to the specific heat and density of the porous media, and ∇T (K/m) refers to the temperature gradient between solids of adjacent grid blocks.

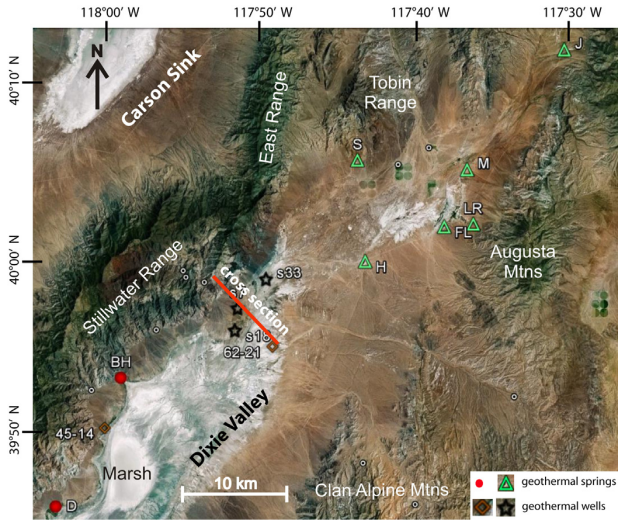

Fig. 1. Overview of the Dixie Valley geothermal area illustrating the location of the cross section used for 2D reactive transport model simulations.

Using TOUGHREACT, transport is simulated in terms of total dissolved concentrations of chemical components using the classical advection diffusion equation

$$\frac{\partial(\phi C_i)}{\partial t} = \nabla \cdot (\phi \cdot D_i \cdot \tau \cdot \nabla C_i) - \phi \cdot u \cdot \nabla(C_i) + R \quad (4)$$

where C_i (mol/kg$_{H_2O}$) refers to the concentration of aqueous component i, ϕ (–) is the porosity of the porous medium, D_i (m^2/s) refers to the diffusion coefficient of species i, τ (–) refers to the tortuosity, and u (m/s) is the Darcy flux (Eq. (2)). R (mol/kg$_{H_2O}^{-1}$ s^{-1}) refers to the total reaction rate of any reaction affecting the component concentration i (e.g., mineral dissolution/precipitation reactions, surface complexation reactions). Flow and transport processes are coupled using a sequential non-iterative approach (see Xu et al., 2011 and references therein for more detail).

2.2. Model geometry, fluid flow and heat transfer simulations

The model was set up for a vertical NW-SE cross-section that is perpendicular to the main axis of Dixie Valley (Fig. 1). The model dimensions are x = 5500 and z (depth) = 4500 m. The cross-section roughly corresponds to the shallow left hand part of the model domain used by McKenna and Blackwell (2004) including half of the Stillwater Range (NW-boundary) and half of the valley floor (SE-boundary). Geological units were defined according to a geological cross-section (Iovenitti et al., 2012) including two major normal faults (Fig. 2a). The model was discretized into 108 × 92 grid blocks having a vertical extent of ca. 48 m each (Fig. 2b). The horizontal grid block size gradually increases with increasing distance from the center of the two major normal faults where a width of 0.707 m was specified. The two normal faults were defined for 8 grid block rows resulting in a total width of ca. 23 m.

A hydrostatic pressure distribution and a conductive geothermal gradient of ca. 70 °C/km were defined as initial conditions, which is close to the average temperature gradient reported for the Dixie Valley area (Blackwell et al., 2007). Fixed boundary conditions of 1 bar and 20 °C were specified at the surface whereas no-flow boundary conditions were used for the bottom and lateral model boundaries. The unsaturated zone was neglected because the emphasis was on the larger scale behavior of the geothermal system. Accordingly, every grid block remained fully saturated throughout all the simulations. No conductive heat flow was

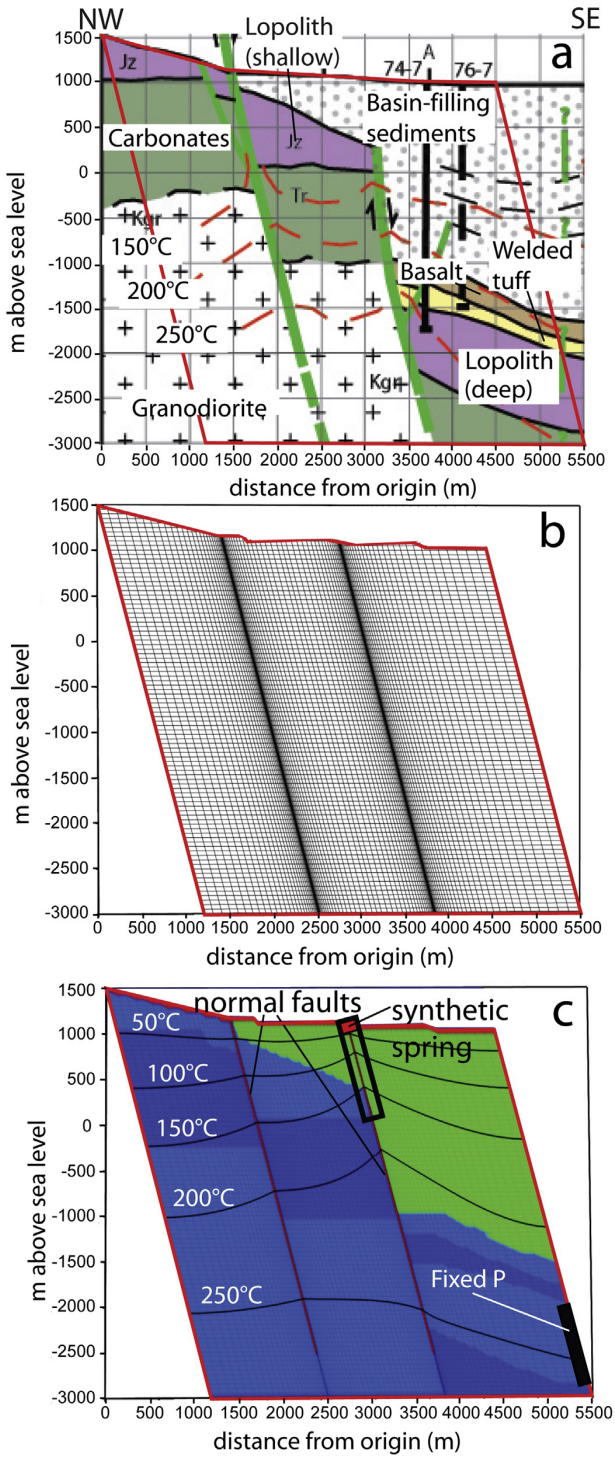

Fig. 2. Model setup and calibrated temperature field. (a) Geological cross section used to constrain the model with field-derived isotherms. (b) Computational mesh used for the simulations illustrating that the resolution was highest for the two normal fault zones. (c) Specified geological units of the model qualitatively illustrated in terms of permeabilities (see Table 1 for exact values), modeled isotherms for the base case model (no dual continuum), locations for which a fixed overpressure of 20% (filled black rectangle) and a dual continuum are defined (open rectangle). Also shown is the location of the "synthetic spring" referred throughout the paper. The red domain defines the actual model domain.

Table 1
Fluid flow parameters and initial fluid and mineralogical composition of the different rock units (Fig. 2).

	Unit	Basin-filling sediments[h]	Carbonates	Lopolith (deep)[a]	Lopolith (shallow)	Granodiorite	Basalt	Welded tuff	Bottom boundary	Surface boundary	Dual continuum	
											Fracture	Matrix
Porosity	–	0.1	0.1	0.1	0.1	0.1	0.1	0.1	0.00001	0.1	0.5	0.1
Permeability	m^2	10^{-15} [h]	10^{-17}	10^{-16}	10^{-16}	10^{-16}	10^{-16}	10^{-19}	10^{-20}	10^{-14}	[b]	10^{-20}
Therm. cond.	$W m^{-1} K^{-1}$	2.5	2.5	2.5	2.5	2.5	2.5	2.5	2.5	2.5	[c]	2.5
pH[d]	–	8.13	8.13	7.55	8.13	8.13	8.13	8.13	8.13	8.13	8.13	8.13
Na^+	mg/kg_{H_2O}	68.28	68.28	579.35	68.28	68.28	68.28	68.28	68.28	68.28	68.28	68.28
Cl^-	mg/kg_{H_2O}	19.71	19.71	318.01	19.71	19.71	19.71	19.71	19.71	19.71	19.71	19.71
HCO_3^-	mg/kg_{H_2O}	142.13	142.13	884.5	142.13	142.13	142.13	142.13	142.13	142.13	142.13	142.13
Ca^{2+}	mg/kg_{H_2O}	0.43	0.43	3.67	0.43	0.43	0.43	0.43	0.43	0.43	0.43	0.43
K^+	mg/kg_{H_2O}	3.15	3.15	49.26	3.15	3.15	3.15	3.15	3.15	3.15	3.15	3.15
SO_4^{2-}	mg/kg_{H_2O}	64.26	64.26	117.13	64.26	64.26	64.26	64.26	64.26	64.26	64.26	64.26
$SiO_2(aq)$	mg/kg_{H_2O}	3.28	3.28	460.86	3.28	3.28	3.28	3.28	3.28	3.28	3.28	3.28
Al^{3+}	mg/kg_{H_2O}	0.04	0.04	0.4	0.04	0.04	0.04	0.04	0.04	0.04	0.04	0.04
Mg^{2+}	mg/kg_{H_2O}	0.74	0.74	0.08	0.74	0.74	0.74	0.74	0.74	0.74	0.74	0.74
Fe^{2+}	mg/kg_{H_2O}	<0.01	<0.01	<0.01	<0.01	<0.01	<0.01	<0.01	<0.01	<0.01	<0.01	<0.01
HS^-	mg/kg_{H_2O}	<0.01	<0.01	10.71	<0.01	<0.01	<0.01	<0.01	<0.01	<0.01	<0.01	<0.01
Fe^{3+}	mg/kg_{H_2O}	<0.01	<0.01	<0.01	<0.01	<0.01	<0.01	<0.01	<0.01	<0.01	<0.01	<0.01
Quartz	vol.%[e,f,g]	15	16	47	47	37	10	24	37	–	15	15
Albite	vol.%	32	0	38	38	23	49	18	23	–	32	32
K-feldspar	vol.%	22	0	0.5	0.5	12	12	11	12	–	22	22
Dolomite	vol.%	–	63	–	–	–	–	–	–	–	–	–
Calcite	vol.%	5	3	11	11	10	–	0	10	–	5	5
Goethite	vol.%	2	–	–	–	0	7	7	0	–	3	3
Pyrite	vol.%	0	1	1	1	5	–	–	5	–	0	0
Clinoptilolite	vol.%	1	–	–	–	–	–	–	–	–	1	1
Illite	vol.%	–	0	–	–	–	–	12	–	–	–	–
Kaolinite	vol.%	–	–	–	–	–	–	–	–	–	–	–
Smectite	vol.%	11	–	–	–		–	–		–	11	11
Magnetite	vol.%	3	–	–	–	–	10	–	–	–	3	3
Chlorite	vol.%	–	3	2	–	7	3	2	7	–	–	–
Laumontite	vol.%	–	–	–	–	–	1	25	–	–	–	–
Tremolite	vol.%	–	1	–	–	–	–	–	–	–	–	–

For the two normal fault domains (Fig. 2) the same mineralogical and initial fluid composition as for the adjacent rock formation was assigned. The permeability and porosity were set to 10^{-14} m^2 and 0.1 according to McKenna and Blackwell (2004).

[a] Aqueous concentrations were fixed at the model boundary of this formation (filled black rectangle, Fig. 2).
[b] The model was run for 3 different permeabilities $k = 10^{-14}$, 10^{-12} and 10^{-10} m^2.
[c] λ was calculated as a function of the permeability according to Eq. (7) resulting in 0.00002, 0.00009 and 0.00043 $W m^{-1} K^{-1}$ for $k = 10^{-14}$, 10^{-12} and 10^{-10} m^2.
[d] For speciation at 1 bar and 25 °C.
[e] An initial volume fraction of 0 means that precipitation was allowed.
[f] –, means that precipitation was not allowed.
[g] The difference to 100% is considered as non-reactive.
[h] The permeability is assumed to be asymmetric. Indicated values denote the horizontal permeability. A value of 10^{-16} m^2 was specified for the vertical permeability.

allowed for the two vertical (side) boundaries and a constant basal heat flux was defined for the bottom boundary. Thermal and fluid flow parameters such as basal heat flux (90 mW/m^2), thermal conductivities (1.25–2.5 $W m^{-1} K^{-1}$), permeabilities (10^{-20} to 10^{-14} m^2) and porosities (0.1) were initially set to the values used by McKenna and Blackwell (2004). These parameters were then calibrated (Table 1) to obtain steady state isotherms similar to the ones illustrated on the geological cross-section (Fig. 2a), which were derived from temperature measurements in geothermal wells (Iovenitti et al., 2012).

Most geothermal wells are producing from a reservoir located in the deep (i.e. south-eastern) section of the Jurassic Humboldt Lopolith (Fig. 2a) (Speed, 1976; Waibel, 1987), referred to here as Lopolith. Accordingly, it is assumed that this section forms the major reservoir formation of the Dixie Valley geothermal field (Lutz et al., 1997). Upflow along both normal faults necessary to explain the shape of the observed isotherms (Fig. 2a) was only obtained when the pressure at the SE model boundary within the deep (i.e. SE) Lopolith section was fixed to a value exceeding the hydrostatic pressure (Fig. 2c). Best results were obtained for an overpressure of 20%. This value is in the same order of magnitude as observed for a wide series of geothermal field sites (Serpen and Niyazi, 2005). However, we do not postulate that such overpressured conditions are actually occurring at Dixie Valley because the fixed overpressure was only defined in terms of a boundary condition to get a reasonable fluid flow for our model. It was necessary because our model domain only consists of half of the Stillwater Range and half of the valley. Without overpressure, no fluid flow from the reservoir toward the surface can be generated. Consequently, the fixed overpressure roughly corresponds to the pressure head within the south-eastern Clan Alpine Mountains that are outside of the actual model domain (Fig. 1). In contrast to our model, the McKenna and Blackwell (2004) model domain includes the full width of the valley and both lateral ridges resulting in a flow field that is largely driven by the surface topography (McKenna and Blackwell, 2004), and no overpressure was required to get a reasonable flow field. However, their model did not consider such refined discretization around faults (Fig. 2b). To obtain the steady state isotherms illustrated in Fig. 2c, the wet thermal conductivity of the basin-filling sediments (Fig. 2a) had to be increased compared to the value adopted by McKenna and Blackwell (2004) (1.25 $W m^{-1} K^{-1}$) and was calibrated to 2.5 $W m^{-1} K^{-1}$. All other thermal and flow parameters were fixed to the values used by McKenna and Blackwell (2004) (Table 1).

2.2.1. Dual continuum domain

The central grid block column of the eastern normal fault above an altitude of ca. 0 m above sea level (Fig. 2c) was defined as a dual continuum. Multiple continuum models are typically used to accurately simulate the observation that predominant advective fluid

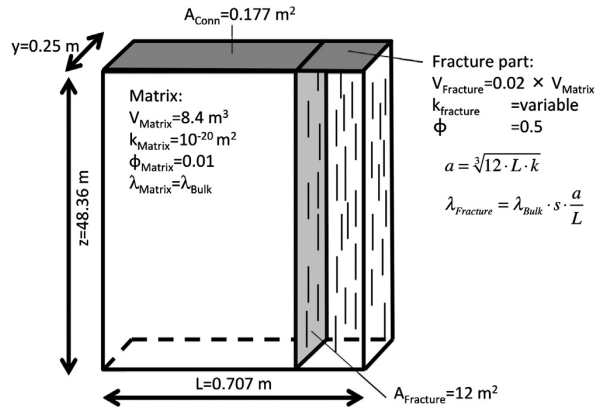

Fig. 3. Conceptual dual continuum model used to simulate fluid flow, heat transfer and reactive transport along the spring-feeding fracture system (dual continuum domain, Fig. 2).

flow occurs along fractures whereas the rock matrix is primarily subject to a diffusive flux (Xu and Pruess, 2001). The use of a dual continuum for our model allowed simulating a small-scale geothermal spring ("synthetic spring") that is located at the top of the dual continuum domain and is fed by a highly permeable but narrow fracture zone (Fig. 2c). Consequently, the first grid block located below the dual continuum domain with a temperature > 150 °C (Fig. 2c) corresponds to the fluid reservoir that feeds the "synthetic spring". The simulated synthetic spring also corresponds well with actual Dixie Valley hot springs because these are also mostly fed by high temperature fluids (i.e. >150 °C) (Peiffer et al., 2014).

Fluid flow along the dual continuum domain was conceptualized as follows (Fig. 3): The domain is characterized by an idealized fractured rock with a set of plane and parallel vertical fractures of equal aperture and spacing. All fractures are lumped into the fracture part of the dual continuum whereas the matrix material (bulk rock) is lumped into the matrix part. In doing so, the fracture spacing L is defined by the width of the dual continuum domain (0.707 m) and the overall fracture porosity $\phi_{Fracture}$ is the ratio between the volume of the fracture part $V_{Fracture}$ and the total volume of the total dual continuum ($V_{DualCont} = V_{Fracture} + V_{Matrix}$) taking into account the assigned porosity for the fracture part of the dual continuum ϕ:

$$\phi_{Fracture} = \frac{V_{Fracture} \cdot \phi}{V_{DualCont}} \tag{5}$$

For the simulation of fluid rock interaction processes in TOUGHREACT, the porosity of the fracture part ϕ should be smaller than 1 by definition (Xu et al., 2011). Accordingly, ϕ was set to an arbitrary value of 0.5. In doing so and by setting $V_{Fracture}/V_{DualCont}$ to 2% the model assumes a $\phi_{Fracture}$ of 1%. To minimize fluid flow within the matrix part of the dual continuum, its permeability was set to 10^{-20} m^2 (Table 1).

To vary the resulting upflow velocity within the fracture part of the dual continuum, we ran simulations for a fracture permeability k of 10^{-10}, 10^{-12} and 10^{-14} m^2. At the same time the overall flow and temperature field remained largely unchanged. For each permeability k the theoretical fracture aperture a was calculated based on the cubic law (Leung and Zimmerman, 2012; Witherspoon et al., 1980)

$$k = \frac{a^3}{12L} \tag{6}$$

where L refers to the fracture spacing (0.707 m). Applying Eq. (6) to our model yields theoretical apertures a of 44 (for $k = 10^{-14}$ m^2), 203 ($k = 10^{-12}$ m^2) and 944 ($k = 10^{-10}$ m^2) μm. Because the conceptual dual continuum model (Fig. 3) assumes that the individual vertical fractures are randomly distributed, the connection area (A_{Conn}, Fig. 3) between two adjacent vertical fracture grid blocks was set to the geometric value of the full dual continuum ($A_{Conn} = 0.25 \times 0.707 = 0.177$ m^2). An estimated value of $A_{Fracture} = 12$ m^2 was specified for the sum of surface areas of these fractures. This value corresponds to the geometric horizontal connection area between fracture and matrix grid blocks. To account for the fact that conductive heat exchange between fracture and matrix only occurs along connected fractures, the heat conductivity $\lambda_{Fracture}$ of the fracture part of the dual continuum was reduced when compared to the corresponding value of the matrix part ($\lambda_{Bulk} = 2.5$ W m^{-1} K^{-1}, Table 1) by taking into account the calculated permeability dependent fracture aperture a (Eq. (6))

$$\lambda_{Fracture} = \lambda_{Bulk} \cdot s \cdot \frac{a}{L} \tag{7}$$

where s refers to a calibration parameter that was used to obtain a temperature at the top of the dual continuum domain of ca. 70 °C at a fracture permeability of 10^{-14} m^2 (s calibrated to 0.13). A temperature of 70 °C corresponds to the upper range of observed spring water temperatures at Dixie Valley (Goff et al., 2002). The physical meaning of using a scaling factor <1 for Eq. (7) is that effective heat conduction is dependent on the true porosity of the fracture part (ϕ, Eq. (5)), which is close to 1 but has to be set to a low value of 0.5 (i.e., larger solid content) to enable fluid rock interaction processes (Eq. (5)) in the fracture continuum. Applying Eq. (7) to the different fractures apertures a yields $\lambda_{Fracture}$ of 0.00002 (for $k = 10^{-14}$ m^2), 0.00009 ($k = 10^{-12}$ m^2) and 0.00043 ($k = 10^{-10}$ m^2) W m^{-1} K^{-1}. Specifying low thermal conductivities for the dual continuum fracture corresponds well with observations from a large-scale underground thermal experiment showing that rock matrix temperatures are generally insensitive to advective heat transport within fractures (Sonnenthal et al., 2005). In fact, our specified fracture thermal conductivities are in the same order of magnitude as those used by Sonnenthal et al. (2005) to match their experimental data for fractured welded tuffs.

2.3. Water–rock interaction processes

Mineral compositions of the geological units (Fig. 2) were determined from X-ray powder diffraction analysis of well-cuttings (bulk rock analysis, Table 1) (Lutz et al., 1997). With the exception of pyrite, dolomite, calcite and goethite, mineral precipitation and dissolution reactions were formulated as kinetic reactions using a rate law derived from transition state theory (Lasaga, 1984)

$$r = A_r \cdot k_{25} \ \exp\left[\frac{-E_a}{R}\left(\frac{1}{T} - \frac{1}{298.15}\right)\right] \cdot \left[1 - \left(\frac{Q}{K}\right)^m\right]^n \tag{8}$$

where r refers to the reaction rate (mol/kg$_{H_2O}$/s), A_r is the reactive surface area (m^2/kg$_{H_2O}$), k_{25} refers to the reaction rate constant at 25 °C (mol m^{-2} s^{-1}), E_a is the activation energy (kJ/mol), T and R are the temperature (K) and ideal gas constant and Q and K refer to the ion activity product and equilibrium constant of a specific mineral reaction (Table 2). Exponents m and n are fitting parameters that must be experimentally determined. For this study they were set to one, which is usually the case, but not always. Reaction rate constants and activation energies were defined according to Palandri and Kharaka (2004) (Table 2). Reactive surface areas (A_r) for the domains except for the fracture domain of the dual continuum were defined according to Dobson et al. (2003) who simulated a hydrothermal experiment using geometric specific reactive surface areas of 6824 cm^2/g (calculated for plates 60 μm × 60 μm × 1.2 μm) for clay minerals and of 394 cm^2/g

Table 2
Reaction stoichiometries, equilibrium constants, reaction rate constants, activation energies and reactive surface areas of considered mineral dissolution/precipitation reactions.

Mineral	Stoichiometry	Log(K)[a]	k (mol m^{-2} s^{-1})[b]	E_a (kJ/mol)[b]	$A_{specific}$ (cm^2/g)	A_{rfrac} (m^2/m$^3_{\text{Porous medium}}$)
Calcite	$CaCO_3 + H^+ = HCO_3^- + Ca^{2+}$	1.809	Equilibrium	–	–	–
Pyrite	$FeS_2 + H_2O = Fe^{2+} + 1.75HS^- + 0.25SO_4^{2-} + 0.25H^+$	−24.669	Equilibrium	–	–	–
Goethite	$FeOOH + 3H^+ = 2H_2O + Fe^{3+}$	0.503	Equilibrium	–	–	–
Dolomite	$CaMg(CO_3)_2 + 2H^+ = Ca^{2+} + Mg^{2+} + 2HCO_3^-$	3.228	Equilibrium	–	–	Not considered
Tremolite	$Ca_2Mg_5((Si_4O_{11})(OH))_2 + 14H^+ = 8SiO_2(aq) + 2Ca^{2+} + 5Mg^{2+} + 8H_2O$	62.611	2.51E−11	94.4	394	Not considered
Quartz	$SiO_2 = SiO_2(aq)$	−4.047	2.46E−13	87.7	394	220; 2.2 or 0.02
Albite	$NaAlSi_3O_8 + 4H^+ = Al^{3+} + Na^+ + 2H_2O + 3SiO_2(aq)$	1.412	2.75E−13	69.8	394	220; 2.2 or 0.02
K-feldspar	$KAlSi_3O_8 + 4H^+ = Al^{3+} + K^+ + 2H_2O + 3SiO_2(aq)$	−1.703	3.89E−13	38.0	394	220; 2.2 or 0.02
Illite	$K_{0.6}Al_{1.8}Mg_{0.25}Al_{0.5}Si_{3.5}O_{10}(OH)_2 + 8H^+ = 5H_2O + 3.5SiO_2(aq) + 0.25Mg^{2+} + 0.6K^+ + 2.3Al^{3+}$	8.055	1.00E−13	22.0	6824	Not considered
Smectite	$K_{0.2}Ca_{0.02}Na_{0.15}AlMg_{0.9}Fe_{0.45}Al_{0.25}Si_{3.75}O_{10}(OH)_2 + 7H^+ = 4.5H_2O + 3.75SiO_2(aq) + 0.9Mg^{2+} + 0.2K^+ + 1.25Al^{3+} + 0.16Fe^{3+} + 0.29Fe^{2+} + 0.15Na^+ + 0.02Ca^{2+}$	10.84	1.65E−13	35.0	394	220; 2.2 or 0.02
Kaolinite	$Al_2Si_2O_5(OH)_4 + 6H^+ = 5H_2O + 2SiO_2(aq) + 2Al^{3+}$	3.199	6.60E−14	22.2	6824	Not considered
Magnetite	$Fe_3O_4 + 8H^+ = Fe^{2+} + 2Fe^{3+} + 4H_2O$	10.475	1.66E−11	18.6	394	220; 2.2 or 0.02
Clinochlore	$AlMg_5AlSi_3O_{10}(OH)_8 + 16H^+ = 12H_2O + 3SiO_2(aq) + 5Mg^{2+} + 2Al^{3+}$	66.315	3.00E−13	88.0	6824	Not considered
Laumontite	$AlMg_5AlSi_3O_{10}(OH)_8 + 8H^+ = 8H_2O + 4SiO_2(aq) + Ca^{2+} + 2Al^{3+}$	11.529	2.50E−13	58.0	394	Not considered
Clinoptilolite	$Ca_{1.73}Fe_{0.02}Al_{3.45}Si_{14.53}O_{35.99}{\cdot}10.93(H_2O) + 13.87H^+ = 17.86H_2O + 14.53SiO_2(aq) + 1.73Ca^{2+} + 3.45Al^{3+} + 0.02Fe^{3+}$	−5.992	2.50E−13	58.0	394	220; 2.2 or 0.02

[a] At 25 °C, according to Soltherm.H06 database (Reed and Palandri, 2006).
[b] According to Palandri and Kharaka (2004).
Equilibrium: aqueous solution was forced to be at equilibrium with respect to the corresponding minerals as long as these are present or supersaturated ($\log(Q/K) > 0$) within a specific grid block.
Not considered: mineral reactions were not considered since these phases were not observed (Table 1).

(calculated for spheres of 60 μm diameter) for all other mineral phases.

Reactive surface areas of the fracture continuum were defined according to

$$A_{rfrac} = \frac{\pi \cdot A_{fm}}{2 \cdot \phi_{Fracture}} \quad (9)$$

where A_{rfrac} is the reactive fracture surface area ($m^2_{\text{reactive surface}}/m^3_{\text{fracture medium}}$), A_{fm} ($m^2_{\text{reactive\_surface}}/m^3_{\text{total\_fracture-matrix\_medium}}$) refers to the fracture-matrix interfacial area per unit volume of the dual continuum ($A_{Fracture}/V_{DualCont}$) and $\phi_{Fracture}$ (Eq. (5)) is the true fracture porosity of the rock (Sonnenthal et al., 2005). TOUGHREACT internally converts A_{rfrac} into A_r to calculate the corresponding reaction rates (Eq. (8)).

For each of the three fracture permeability values considered ($k = 10^{-14}$, 10^{-12} and 10^{-10} m^2), simulations were run for three different reactive fracture surface areas A_{rfrac} (220, 22 and 0.22 m^2/m^3), for a total of 9 simulations. The largest fracture surface area (220 m^2/m^3) corresponds to the value obtained by Eq. (9) assuming a fracture porosity $\phi_{Fracture}$ of 0.01 and using the geometrical fracture-matrix interface area A_{fm} of 1.4 m^2/m^3 ($=A_{Fracture}/V_{DualCont}$) derived from relationships shown in Fig. 3.

Pyrite, dolomite, calcite and goethite were assumed to react under equilibrium constraints, on the basis that the reaction of these minerals is typically fast. In doing so, TOUGHREACT (Xu et al., 2011) forced chemical equilibrium with respect to these mineral phases as long as they were present or formed within specific grid blocks. The code simulates equilibrium mineral reactions, reaction rates (Eq. (8)), and aqueous speciation reactions using equilibrium constants (K) tabulated in the Soltherm.H06 database (Table 2) (Reed and Palandri, 2006).

We specified initial water compositions for the entire model domain except for the deep Lopolith section (i.e. geothermal reservoir, east of the two normal faults) according to a chemical analysis of a groundwater sample collected in the Dixie Valley area (Goff et al., 2002). A moderately saline water composition (Table 1) similar to geothermal brine compositions observed at Dixie Valley (Goff et al., 2002) was specified as the initial composition for the deep Lopolith section. Because we specified a fixed pressure boundary condition within the deep Lopolith section (Fig. 2c), the model assumes constant injection of this moderately saline water into the system along the SE model boundary (Fig. 2c).

The specification of a moderately saline fluid reservoir as a model boundary condition is supported by the infiltration model proposed by Nimz et al. (1999), who postulated that the primary geothermal fluid reservoir was derived from infiltration of a 12–14 ky old glacial lake that partially evaporated, resulting in elevated Na^+ and Cl^- concentrations (Goff et al., 2002).

2.4. Solute chemical geothermometry

Steady state concentrations obtained for the "synthetic spring" (Fig. 2) were processed using the automated multicomponent geothermometer GeoT (Spycher et al., 2014) to compute the temperature at which these synthetic fluids are at chemical equilibrium with reservoir minerals. GeoT temperature estimates are based on the clustering of mineral saturation indices near zero (Reed and Spycher, 1984) over a given temperature range. In the present case we considered albite, K-feldspar, smectite and clinoptilolite, which are minerals initially present in the model grid block directly feeding the simulated fracture (dual continuum domain). This specific grid block yields the deep reservoir fluid feeding the synthetic spring (Fig. 2), and the fluid in this grid block is essentially at chemical equilibrium with respect to these minerals (as established during the TOUGHREACT simulations). Subsequently, estimated reservoir temperatures were compared to the modeled steady state temperature in this specific block (i.e., our "true" reservoir temperature).

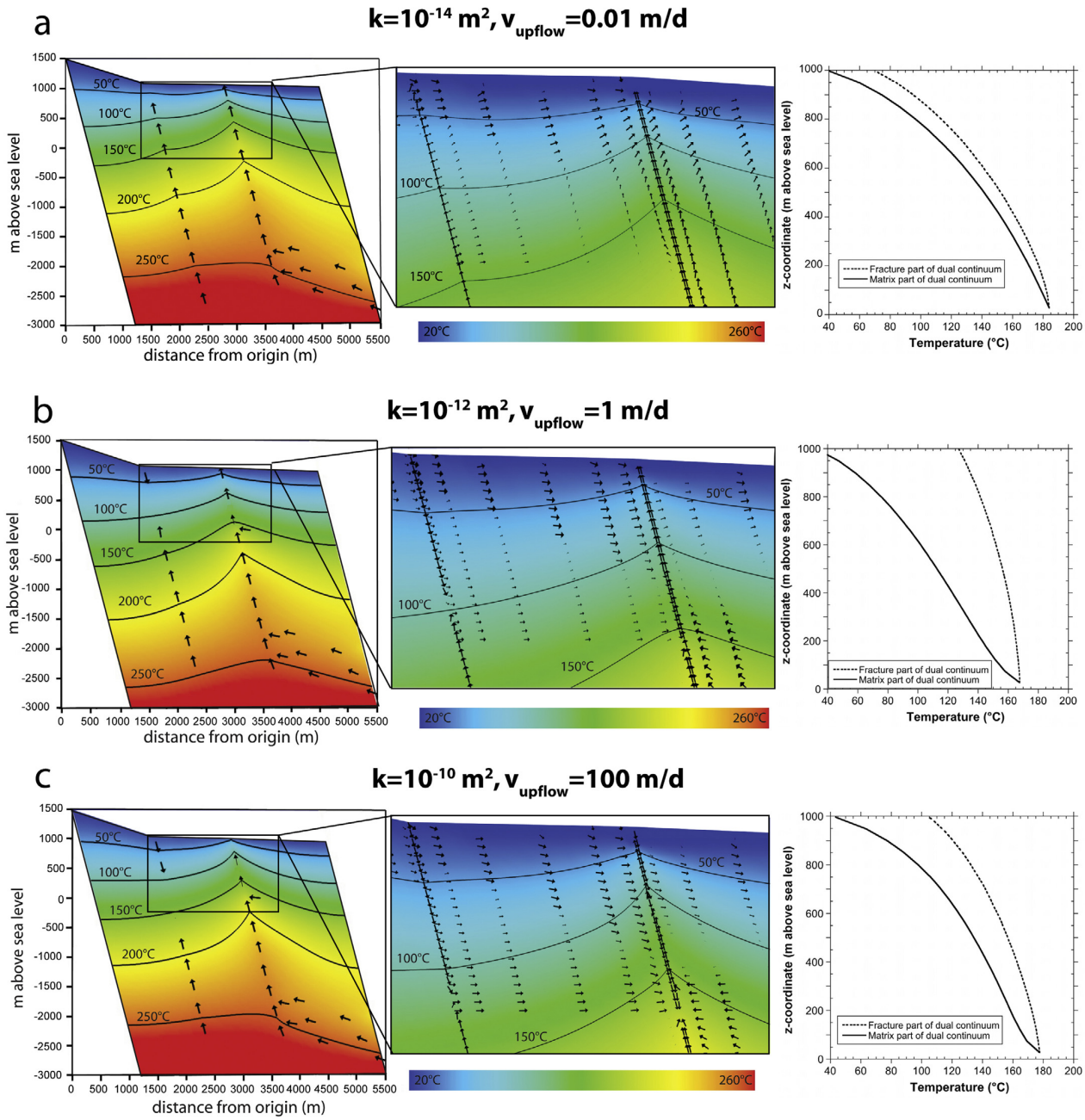

Fig. 4. Steady state temperature distribution and fluid flow field for different permeabilities of the spring-feeding fracture. Temperatures along the dual continuum domain refer to matrix temperatures. Corresponding temperatures of the fracture part are illustrated in graphs on the right. Fluid flow vectors are shown if $v > 1.9 \times 10^{-8}$ m/s (whole model domain, left hand illustrations) or $v > 10^{-10}$ m/s (shallow model domain, blow ups in central illustrations), respectively. The maximum flow vector size corresponds to a velocity of 2×10^{-8} m/s (whole model domain) or 4×10^{-9} m/s (shallow model domain), respectively.

This approach allowed rigorous testing of chemical geothermometry because the reservoir mineralogy is a well defined model input parameter. In contrast, the selection of a reservoir mineral assemblage for applying multicomponent geothermometry at the field scale is always based on interpretation. Poorly chosen assemblages can lead to erroneous temperature estimates because such estimates are highly sensitive to the selected set of minerals (Reed and Spycher, 1984; Peiffer et al., 2014).

We also coupled GeoT computations to the code iTOUGH2 (Finsterle and Zhang, 2011) to estimate unknown or poorly constrained input parameters that may adversely affect temperature estimates (by numerical optimization of the clustering of mineral saturation indices near zero; Spycher et al., 2014). Pang and Reed (1998) reported that small changes in Al concentration can significantly affect temperatures predicted using multicomponent geothermometry. Therefore, in this study, numerical optimization

Table 3
Steady state water compositions obtained at the "synthetic spring" (Fig. 2) for the 9 model runs and chemical compositions observed in wells and springs at Dixie Valley (concentrations refer to mol/kg_{H_2O}).

Model run/sampling location	pH	Na^+	Cl^-	SiO_2	Ca^{2+}	Mg^{2+}	HCO_3^-	K^+	Al^{3+}	SO_4^{2-}	$T_{sampling}$ (°C)
[a] $k = 10^{-14}$ m², $A_{rfrac} = 0.22$ m²/m³	7.32	555.42	266.01	171.99	5.29	0.05	998.17	29.76	4.93E−5	106.65	70.6
$k = 10^{-12}$ m², $A_{rfrac} = 0.22$ m²/m³	6.99	517.16	195.51	140.38	2.52	0.17	1244.03	22.11	2.90E−2	95.45	127.3
$k = 10^{-10}$ m², $A_{rfrac} = 0.22$ m²/m³	6.94	559.08	147.86	163.21	3.97	0.10	1460.55	27.50	4.55E−3	87.07	105.2
$k = 10^{-14}$ m², $A_{rfrac} = 22$ m²/m³	7.40	555.85	266.01	69.87	4.42	0.34	992.95	23.62	9.15E−4	103.87	70.6
$k = 10^{-12}$ m², $A_{rfrac} = 22$ m²/m³	7.01	517.07	195.51	126.01	2.38	0.19	1243.68	22.04	1.71E−2	92.98	127.3
$k = 10^{-10}$ m², $A_{rfrac} = 22$ m²/m³	6.96	558.97	147.86	144.15	3.83	0.11	1460.15	27.41	2.75E−3	85.48	105.2
$k = 10^{-14}$ m², $A_{rfrac} = 220$ m²/m³	7.45	565.69	266.01	43.37	3.95	1.22	996.47	10.92	2.64E−3	103.87	70.6
$k = 10^{-12}$ m², $A_{rfrac} = 220$ m²/m³	7.01	517.36	195.51	94.29	2.36	0.30	1243.73	21.49	3.90E−2	92.94	127.3
$k = 10^{-10}$ m², $A_{rfrac} = 220$ m²/m³	7.18	504.42	157.50	101.14	2.59	0.16	1146.62	24.19	5.79E−3	86.70	105.2
Geothermal wells	8.7–9.6[b]	370–518	320–624	417–642	1–10	<0.03	140–334	40–77	0.4–1.5	149–243	143–174
Low Na/Cl hot springs	8.6	211	162	107	11	0.22	76	5	0.13	121	84
High Na/Cl hot springs	7.4–8.2	141–357	28–228	32–134	23–79	3–30	265–735	9–26	<0.09	66–199	28–77
Low Na/Cl cold springs	7.6–8.2	50–370	135–630	17–44	33–201	29–90	108–392	1–56	<0.01	123–515	8–20
High Na/Cl cold springs	7.4–8.3	16–228	8–141	17–45	5.2	1.4–16	56–172	0.6–8	0.02	8–228	7.4–14.8

[a] Permeability values k and reactive surface areas correspond to the values specified for the spring feeding fracture (Fig. 2).
[b] Measured pH values refer to degassed values. Therefore they are higher than modeled values.

with GeoT was used to estimate the aluminum concentration of the deep fluid from input compositions of the synthetic surface spring. Peiffer et al. (2014) recently showed that such an approach, i.e. optimizing Al concentrations using iTOUGH2 with GeoT, yielded good results at a real field site (Dixie Valley, Nevada). In the present study, Al concentrations were optimized using the iTOUGH2 grid search algorithm and minimizing the absolute values of the median of the saturation indices of considered minerals, as well as the spread of temperatures given by the equilibrium points of each individual minerals.

In addition to multicomponent geothermometry, reservoir temperatures were also calculated by applying classical geothermometers, including SiO_2 (Fournier and Potter, 1982) Na–K–Ca (Fournier and Truesdell, 1973) and Na–K and K–Mg (Giggenbach, 1988). Results were then compared to temperature estimates obtained with multicomponent geothermometry, as well as "true" modeled reservoir temperatures, to evaluate under which flow/reaction conditions each approach worked best.

3. Model results and discussion

3.1. Flow and temperature field

The simulations resulted in average linear flow velocities along the modeled fracture (dual continuum, spring-feeding fracture) of 0.01 m/d, 1 m/d, and 100 m/d (Fig. 4), respectively, for each case of fracture permeability considered. After a simulated time period of 100,000 years, a steady state temperature field was obtained for the whole model domain for all three permeability cases. Note, that in contrast to fluid flow and heat transfer simulations performed by McKenna and Blackwell (2004), we did not observe a transient temperature maximum. The lack of such a maximum is explained by the choice of a constant pressure boundary condition at the south-eastern model boundary within the deep section of the Lopolith (Fig. 2c). Moreover, the initial temperature distribution represented a conductive thermal regime whereas McKenna and Blackwell (2004) specified an initial temperature distribution that represented a convective thermal regime.

Steady state fluid flow and temperature distributions obtained for the whole model domain (Fig. 4) show that hydrothermal convection in the shallow part of the model (Fig. 4, central illustrations/blow ups) is strongly dependent on the permeability of the spring-feeding fracture. Elevated permeabilities of the spring-feeding fracture (10^{-12} and 10^{-10} m²) lead to a shallow convection cell where superficial water infiltrates along the range front normal fault, and connects the south-eastern normal fault and spring-feeding fracture through the basin filling sediments (Fig. 4b and c, blow ups). The observation that superficial water may infiltrate along the range front normal fault illustrates that an overpressure of 20% at the deep Lopolith model boundary and a permeability of 10^{-14} m² of the bulk fault zone (Table 1) are too low to maintain a sufficiently high fluid flow to feed the spring-feeding fracture (Fig. 2) when its permeability, and thus its overall fluid flux is high. For the $k = 10^{-10}$ m² simulation the resulting fluid flow along the spring-feeding fracture ($v = 100$ m/d) even requires a vertical infiltration along the south-eastern normal fault (e.g., flow vectors pointing up and down on right handed fault zone, Fig. 4c blow up). This short-circuit is the primary reason for the relatively small temperature difference between the fracture and matrix parts of the dual continuum observed for this simulation (Fig. 4c).

In contrast, the shallow convection cell with its infiltration of cool water from the surface (20 °C) and the absence of a full short-circuit was most likely the reason why the lowest temperature at the bottom of the dual continuum was observed for the $k = 10^{-12}$ m² simulation (168 °C, Fig. 4b). The faster upflow rate obtained for the $k = 10^{-12}$ m² simulation resulted in a lower temperature gradient within the spring-feeding fracture when compared to the $k = 10^{-14}$ m² run and to temperatures >100 °C for the synthetic spring (Fig. 4b). Also, the temperature difference between the fracture and matrix parts of the dual continuum are higher at $k = 10^{-12}$ m² than at $k = 10^{-14}$ m² (Fig. 4a and b) even though the thermal conductivity was increased to account for the larger theoretical fracture aperture a (Eqs. (6) and (7)).

A meter-scale scale short-circuit (i.e., simultaneous down- and upflow) within a single fault zone such as shown in Fig. 4c (blow up/central illustration) seems not very realistic. Accordingly, this observation may imply that a permeability of 10^{-10} m² and an associated average linear upflow velocity of ca. 100 m/d are too high for spring-feeding fractures. Nevertheless, the observation that a shallow convection cell was established for the $k = 10^{-12}$ m² and $k = 10^{-10}$ m² simulations is in agreement with the modeling study of Moulding and Brikowski (2012) and confirms that shallow convection cells may be a general feature of basin and range geothermal systems in addition to deeper flow paths connecting actual geothermal reservoirs. Interestingly, the synthetic spring temperature of ca. 125 °C obtained for the $k = 10^{-12}$ m² case (Fig. 4b) is in agreement with recent field investigations showing that such elevated temperatures can be found at isolated locations near the surface (AltaRock, personal communication). The reasonable flow field obtained for the $k = 10^{-12}$ m² simulation (Fig. 4b) implies that near surface temperatures >100 °C may be the result of small-scale and shallow fracture systems that are connected to valley-scale normal fault

systems having typical permeabilities on the order of 10^{-14} m^2 (McKenna and Blackwell, 2004).

3.2. Reactive transport simulations

Simulated steady-state water compositions in the uppermost grid block of the modeled fracture (i.e., synthetic spring, Fig. 2) are presented in Table 3 for all simulations (in total, 9 simulations were run corresponding to the combination of 3 different permeability and 3 different surface area cases). Chemical analyses of water samples collected from geothermal wells and springs of the Dixie Valley area are also shown in Table 3 for comparison. The observation that simulated concentrations are in the same range as actual measurements "validates" the initial conceptual model and implies that the model reasonably simulates most of the relevant fluid flow and water–rock interaction processes. It also supports the choice of specified initial fluid and mineral composition (Table 1). Accordingly, the simulation results support the hypothesis that the Dixie Valley geothermal springs are fed by a geothermal reservoir having an elevated dissolved salt concentrations, which may be explained by the infiltration of a 12–14 ky old glacial lake that underwent evaporation to some degree (Nimz et al., 1999; Peiffer et al., 2014).

It should be noted, however, that we did not attempt explicitly to reproduce exact concentrations observed at specific geothermal springs in Dixie Valley. Comparing simulated concentrations with actual spring compositions (Table 3) simply illustrates that the numerical model yields reasonable results that can be further used for assessing the use of chemical geothermometry, as discussed below.

3.3. Solute chemical geothermometry

3.3.1. Reservoir temperature estimates

Reservoir temperatures obtained by processing the TOUGHREACT-simulated spring compositions (Table 3) with GeoT (Spycher et al., 2014) are given in Table 4, together with temperatures derived using classical geothermometers. GeoT estimates refer to the temperature at which the median of absolute saturation indices of the considered minerals (e.g., quartz, albite, K-feldspar, smectite and clinoptilolite) is at its minimum (Spycher et al., 2014). To assess the quality of the temperature estimates, the mean of the temperatures at which each mineral is computed to be at equilibrium (saturation index SI = 0), and the corresponding standard deviations, are also provided in Table 4.

The general observation is that, for any geothermometer, the difference between estimated (94–187 °C) and true model reservoir temperatures (168–184 °C) depends primarily on the reactive fracture surface area and the fluid flow velocity within the spring-feeding fracture (Table 4). High reactive fracture surface areas as well as slow upflow rates (long residence times) tend to favor the establishment of chemical equilibrium between the ascending fluid and the surrounding wall rock and provide longer time for the precipitation of minerals that become supersaturated upon cooling. However, slow upflow rates also promote conductive cooling of the ascending fluid, thus yield a greater temperature drop (along the fracture) when compared to faster upflow rates (Fig. 4), which then tends to slow down overall precipitation rates (Eq. (8)). The effect of these competing mechanisms (more time for reaction but slower reaction rates upon cooling) on temperature estimations is illustrated with the computed evolution of the quartz saturation index SI (SI = log(Q/K)) along the spring-feeding fracture for the 9 model runs (Fig. 5). This figure shows that the temperature (and depth below surface) at which the fluid becomes significantly supersaturated with respect to quartz (e.g., SI > 0.1) drops with increasing reactive fracture surface area and decreasing upflow

Table 4
Model reservoir temperatures and temperatures derived from various solute geothermometers for the different model runs.

Fracture surface area (m^2/m^3)	Upflow velocity (m/d)	Sampling temp. (°C)	Model reservoir temp. (°C)	Al model reservoir (mg/L)	GeoT temp[a] (°C)	Optimized Al^{3+} conc. (mg/L)	Temp. range[b] (°C)	GeoT temp[c] (°C)	Al^{3+} conc. (mg/L)	Temp. range[b] (°C)	Quartz temp. (°C)[d]	Na–K temp. (°C)[e]	Na–K–Ca temp. (°C)[f]	K–Mg temp. (°C)[g]
0.22	0.01	71	184	0.183	155	0.038	166 ± 11	179	0.180	172 ± 19	170	187	180	180
0.22	1	127	168	0.153	155	0.066	161 ± 5	167	0.154	171 ± 15	157	172	173	145
0.22	100	105	178	0.166	161	0.049	168 ± 11	177	0.167	184 ± 33	167	181	178	160
22	0.01	71	184	0.183	119	0.048	117 ± 9	175	2.515	151 ± 26	118	172	169	136
22	1	127	168	0.153	159	0.138	164 ± 4	163	0.159	164 ± 5	151	172	174	143
22	100	105	178	0.166	157	0.065	164 ± 6	169	0.137	174 ± 17	159	181	178	160
220	0.01	71	184	0.183	99	0.052	96 ± 11	111	0.103	124 ± 31	96	128	133	94
220	1	127	168	0.153	135	0.084	143 ± 4	163	0.389	158 ± 11	134	171	172	134
220	100	105	178	0.166	137	0.083	140 ± 8	169	0.478	162 ± 14	138	180	179	149

[a] GeoT temperature estimates obtained by iTOUGH2 AI optimization, minimizing the absolute median of computed saturation index of quartz, albite, K-feldspar and clinoptilolite. Corresponding optimization results are given in the column to the right.
[b] GeoT temperature estimates by computing the mean temperature of equilibrium point (SI = 0) for quartz, albite, K-feldspar and clinoptilolite using the optimized Al concentrations listed in the column to the left. Error estimates refer to the standard deviation.
[c] GeoT temperature estimates (median) obtained by forcing equilibrium with respect to K-feldspar at all temperatures. Corresponding Al concentration are given in the column to the right.
[d] Classical SiO_2 geothermometer (Fournier and Potter, 1982).
[e] Classical/empirical Na–K geothermometer (Giggenbach, 1988).
[f] Classical/empirical Na–K–Ca geothermometer (Fournier and Truesdell, 1973).
[g] Classical/empirical K–Mg geothermometer (Giggenbach, 1988).

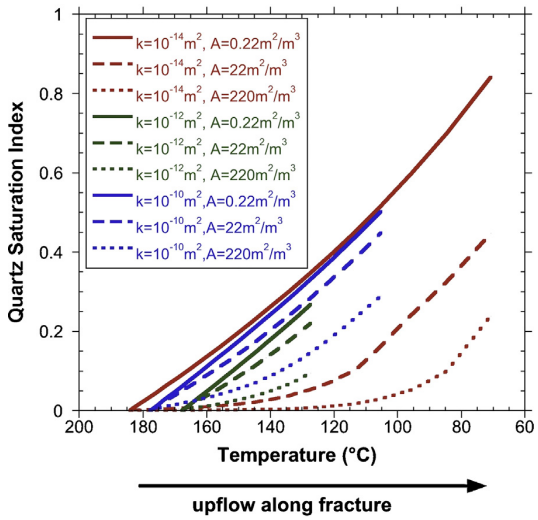

Fig. 5. Computed quartz saturation indices for the 9 model runs as function of the temperature along the fracture part of the dual continuum (Fig. 2).

velocity. The transition from near-equilibrium to supersaturation marks the temperature (and depth) where the quartz precipitation reaction rate becomes too slow to maintain the fluid at equilibrium, because the temperature dependent reaction rate constant (Eq. (8)) becomes too small to maintain equilibrium, even under conditions of large reactive fracture surface areas and long residence times. In other words, fluid reequilibration is not necessarily a linear function of the product of residence time and reactive surface areas.

In the cases considered, reservoir temperature estimates derived from the classical Na–K and Na–K–Ca geothermometers provide the best results (Table 4). Moreover, these geothermometers are much less sensitive to upflow velocity and reactive fracture surface area than the other geothemometers are. Temperature estimation differences between various geothermometers (Table 4), therefore, relate to the variable sensitivity of aqueous species concentrations as a function of mineral precipitation during cooling and upflow such as shown by Peiffer et al. (2014). In particular, multicomponent geothermometry relies on the concentration of all dissolved species, including Al and Mg which are typically present in trace concentrations that are strongly affected by the precipitation of small amounts of Al and Mg silicates upon cooling. In contrast, the Na–K and Na–K–Ca geothermometers depend only on the concentrations of Na, K, and Ca, which are typically large enough to remain essentially unaffected by the precipitation of small amounts of albite and K-feldspar upon cooling (e.g., Peiffer et al., 2014). The concentration of dissolved silica, however, is more significantly affected by the precipitation of quartz (at high temperature, and other silica polymorphs at lower temperatures), thus affecting temperatures derived from the quartz geothermometer (Table 4). Therefore, for cases where cooling is the dominant process affecting fluids as they ascend to ground surface (i.e., no mixing or boiling), the classical Na–K and Na–K–Ca geothermometers are likely to provide best results, whereas multicomponent geothermometry is expected to be more reliable than these geothermometers in cases when boiling and/or mixing occurs (Reed and Spycher, 1984; Spycher et al., 2014).

3.3.2. Al concentrations in the deep reservoir fluid

The high sensitivity of dissolved Al concentrations to small amounts of Al silicate precipitates (Peiffer et al., 2014) requires the use of the Al concentration in the deep reservoir fluid for running multicomponent geothermometry computations (e.g., Pang and Reed, 1998). Here, we tested two approaches to compute dissolved Al at depth: the method proposed by Peiffer et al. (2014), using numerical optimization of the Al concentration with iTOUGH2 coupled with GeoT ("Optimized Al^{3+}" in Table 4), and the "Fix-Al" method proposed by Pang and Reed (1998), in the present case computing the Al concentration by forcing equilibration of the fluid with K-feldspar at all temperatures ("Eq. Al^{3+}" in Table 4). The latter provided temperature estimates closer to the "true" model reservoir temperature (Table 4). However, in some cases, Al concentrations computed in this manner were significantly higher than the "true" Al concentrations at depth in the TOUGHREACT model (Table 4). Al concentrations estimated by numerical optimization were generally 2–4 times lower than the modeled "true" reservoir Al concentrations, yielding somewhat underestimated reservoir temperatures, but smaller standard deviations than the "Fix-Al" method (Table 4). The more accurate temperatures obtained with the "Fix-Al" method, in the cases considered, suggest that this method may perform better than numerical optimization for systems undergoing cooling (without boiling and/or mixing), provided that an appropriate Al-fixing phase (here K-feldspar) is selected. For systems undergoing boiling and/or mixing, numerical optimization of the Al concentration (and other parameters such as gas fraction and dilution factor) provide significant advantages over other solute geothermometry methods (Spycher et al., 2014; Peiffer et al., 2014).

3.3.3. Applicability of multicomponent geothermometry

To define the range of applicability of multicomponent geothermometry in terms of reactive fracture surface area and upflow velocity (for systems without mixing or boiling) we examined the relative difference (ΔT), between temperatures estimated using GeoT and "true" modeled reservoir temperatures, defined as follows

$$\Delta T(\%) = \frac{T_{GeoT} - T_{Model\_reservoir}}{T_{Model\_reservoir} - T_{synthetic\_spring}} \times 100 \quad (10)$$

where T_{GeoT}, $T_{Model\_reservoir}$ and $T_{synthetic\_spring}$ refer to the GeoT-estimated, model reservoir and synthetic spring temperatures, respectively. Such relative temperature difference was defined because the different fracture permeabilities used for each model run yielded significantly different steady state temperature profiles along the spring-feeding fracture (Fig. 4), and thus different synthetic spring temperatures ("sampling temperatures" on Table 4). To simplify the analyses, T_{GeoT} (Eq. (10)) were taken as points falling in the range of temperatures computed using GeoT (irrespective of the Al concentration estimation method), and yielding relative temperature estimate errors (ΔT) roughly proportional to the overall fracture reactivity, which can be expressed as the product of $1/V_{upflow}$ (i.e., residence time) and reactive fracture surface area. This approach yields contour lines of ΔT as function of upflow velocity and reactive surface area, defining domains where the relative error (ΔT) is <15%, 15–30%, and >30%, which we labeled as "good", "moderate", and "poor" for the applicability of multicomponent geothermometry (Fig. 6). Note that in case of Dixie Valley the cutoffs between the good and moderate domain (15%) correspond roughly to a temperature estimate error of 20 °C. Such a temperature estimate error corresponds to an error in effective power production of ca. 10% for a specific pumping rate, considering water enthalpies at 240 °C (1037 kJ/kg) and at 220 °C (943.6 kJ/kg), respectively.

A minimum upflow velocity of about 0.1–1 m/d is needed to avoid re-equilibration during upflow, as shown in Fig. 6. Moreover, depending on the upflow velocity, successful (moderate-good) application of multicomponent geothermometry is obtained with effective reactive fracture surface areas values (A_{rfrac}) of 0.22–22 m^2/m^3. Note that a value of 220 m^2/m^3 corresponds to the

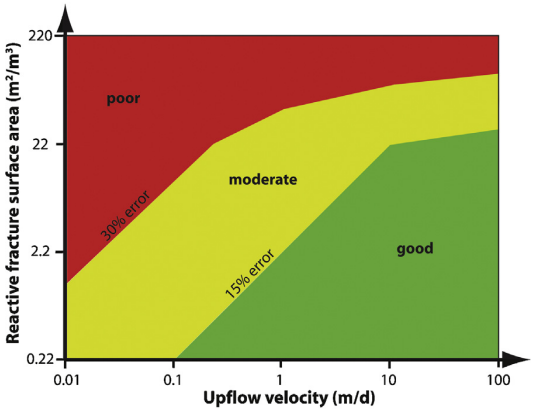

Fig. 6. Geothermometer applicability as a function of upflow velocity and reactive fracture surface area of the spring-feeding fracture (Figs. 2 and 3). "Good" denotes the reactive surface vs. upflow velocity domain where obtained GeoT temperatures and true model reservoir temperatures differ by less than 15%. For the "moderate" domain the difference was 15–30% and for the "poor" domain >30%.

geometric surface area of the modeled fracture, as discussed above, therefore Fig. 6 also implies that the effective reactive fracture surface area has to be 10–100 times smaller than the corresponding geometric surface area for reasonable (moderate-good) temperature predictions. Interestingly, the temperature estimate error is much less sensitive to the upflow velocity if $A_{rfrac} > 22\ m^2/m^3$, which is illustrated by the small slope of the 15% and 30% error contour lines observed for such conditions (Fig. 6). Decreasing slopes with increasing reactive surface areas are explained by the observation that for high reactive surface areas mineral saturation indices remained close to zero over a large temperature range (Fig. 5). Increasing upflow rates associated with a faster cooling, thus have only a minor effect on mineral reaction rates, which in turn is expressed by the flat slope of the temperature error estimate contours (Fig. 6). In contrast, at $A_{rfrac} < 22\ m^2/m^3$ cooling has a strong effect on mineral reaction rates (Fig. 5) and temperature estimate error contours are more sensitive on upflow velocities (i.e. the slope is larger).

4. Summary and conclusions

A 2D reactive transport model of the Dixie Valley geothermal system was developed to improve our general understanding of coupled thermal, hydrodynamic and chemical processes in active geothermal systems. In particular, increasing the permeability of a small-scale fracture system feeding the model's geothermal spring resulted in a shallow (<1 km deep) convection cell. This observation suggests that shallow fluid convection might be a general feature of Basin and Range geothermal systems in addition to deeper flow paths connecting the actual geothermal reservoir. Moreover, simulation results imply that near surface temperatures of >100 °C may be inherited from the presence of small-scale and shallow fractures systems having a permeability on the order of $10^{-12}\ m^2$.

Besides providing insights on hydrologic and thermal processes for a typical Basin and Range geothermal system, the model developed in this study was used to investigate the applicability of various solute geothermometry methods, and the sensitivity of these methods to upflow, cooling and mineral reaction rates, as simulated by varying model-input fracture permeability and reactive surface area. Processing the chemical composition of a simulated geothermal spring using multicomponent and classical geothermometry provided further insights on these methods as exploration tools for geothermal systems. Results suggest that for a fluid in a simple system undergoing cooling without mixing with shallow groundwater, leaching of evaporitic minerals, or boiling, the classical Na–K and Na–K–Ca geothermometers provide the most accurate results, and lowest sensitivity with respect to upflow velocity and reactive fracture surface areas (Table 4). However, previous studies show that when boiling or mixing (Reed and Spycher, 1984; Spycher et al., 2014), or possible leaching of evaporitic minerals (Peiffer et al., 2014) occurs during upflow, classical geothermometers generally provide less accurate temperature estimates than multicomponent geothermometry. The latter method, however, is particularly sensitive to dissolved Al concentrations. The present study suggests that when no mixing or boiling occurs, computing Al concentration by assuming equilibrium of the fluid with a (known) reservoir Al silicate mineral (the "Fix-Al" method of Pang and Reed, 1998) provides more accurate results than numerical optimization of Al concentrations (as done by Peiffer et al., 2014). Numerical optimization, however, is a powerful exploration tool for geothermal systems where surface manifestations of deep hydrothermal convection have been modified and deep temperatures are obscured (Peiffer et al., 2014).

Examining the applicability of multicomponent geothermometry revealed that to predict a system's reservoir temperature, reactive fracture surface areas at least 10–100 times lower than the corresponding geometric fracture surface area, and minimum fluid upflow velocities of ca. 0.1 m/d are needed to avoid reequilibration upon cooling and upflow. In most geothermal systems it is likely that the reactive fracture surface area of primary minerals is small because hydrothermally active fracture systems are commonly coated by secondary minerals such as amorphous silica or calcite that precipitate from the ascending fluids (Alt-Epping et al., 2013; Dobson et al., 2003; Tempel et al., 2011). Moreover, wall rock alteration in these systems is commonly observed (e.g., Reed, 1997). The alteration of primary wall-rock minerals and the subsequent precipitation of secondary minerals reduce the interaction between primary minerals and the ascending fracture fluid. In contrast, matrix fluids being diffusively transported from the fracture into the rock matrix are continuously reacting with the primary wall rock. For the actual fracture surface, however, wall rock alteration works against reaching chemical equilibrium between the primary wall-rock mineralogy and an ascending geothermal fracture fluid, which has exactly the same effect as reducing the reactive fracture surface areas in our simulations. Wall rock alteration is, therefore, a likely process that limits the overall mineral reaction rates within hydrothermally active fractures, and might thus be responsible for the observation that multicomponent geothermometry generally works under different conditions and in a wide range of geothermal areas (Reed and Spycher, 1984; Peiffer et al., 2014).

In contrast to the postulated low reactive fracture surface areas, upflow velocities are less constrained. Our sensitivity analysis (Fig. 6) and the fact that multicomponent geothermometry has been successfully applied in a wide range of geothermal systems (Reed and Spycher, 1984; Peiffer et al., 2014; Spycher et al., 2014) suggest that upflow velocities for many geothermal springs systems are probably on the order of 0.1 m/d or higher.

The different predictive capabilities and sensitivities of the geothermometers considered in this study imply that classical and multicomponent geothermometry should always be applied together, as both have their strengths and weaknesses. Furthermore, taking into account useful insights from field observations as much as possible help to improve reservoir temperature estimates. A good example for such an integrated approach was presented by Peiffer et al. (2014) who used an extensive geochemical data set to estimate actual reservoir temperatures of the Dixie Valley geothermal system in conjunction with classical and multicomponent geothermometry.

The present study also shows that reactive transport modeling is a powerful tool for data interpretation by quantitatively testing hypotheses with respect to fluid flow and water–rock interaction processes. Such models do, however, require numerous site-specific parameters and an understanding of the governing water–rock interaction-, fluid flow- and heat transfer processes. In the case of Dixie Valley, a large dataset of water analyses from geothermal waters as well as XRD analyses of major rock formations helped to constrain the initial and boundary conditions of the model, which led to reasonable simulation of measured spring compositions. This is especially notable considering the fact that we used a fairly simplified system, for which the unsaturated zone was neglected and for which the temperature distribution was calibrated to a temperature field that is not affected by boiling.

Acknowledgments

This work was supported by the U.S. Department of Energy, Geothermal Technologies Program, Energy Efficiency and Renewable Energy Office, Award Nos. DE-EE0002765 and DE-AC02-05CH11231. We thank one anonymous reviewer for a thorough review and constructive comments.

References

Alt-Epping, P., Waber, H.N., Diamond, L., Eichinger, L., 2013. Reactive transport modeling of the geothermal system at Bad Blumau, Austria: implications of the combined extraction of heat and CO_2. Geothermics 45, 18–30.

Bachler, D., Kohl, T., 2005. Coupled thermal–hydraulic–chemical modelling of enhanced geothermal systems. Geophys. J. Int. 161, 533–548.

Blackwell, D.D., Smith, R.P., Richards, M.C., 2007. Exploration and development at Dixie Valley, Nevada: summary of DOE studies. In: Proceedings, Thirty-Second Workshop on Geothermal Reservoir Engineering, Stanford University, Stanford, CA, January 22–24. SGP-TR-183.

Clearwater, E.K., O'Sullivan, M.J., Brockbank, K., Mannington, W.I., 2012. Modeling the OHAAKI geothermal system. In: Proceedings TOUGH Symposium 2012, Lawrence Berkeley National Laboratory, Berkeley, CA, September 17–19, 206–213.

Dobson, P.F., Kneafsey, T.J., Sonnenthal, E.L., Spycher, N., Apps, J.A., 2003. Experimental and numerical simulation of dissolution and precipitation: implications for fracture sealing at Yucca Mountain, Nevada. J. Contam. Hydrol. 62–63, 459–476.

Dobson, P.F., Salah, S., Spycher, N., Sonnenthal, E.L., 2004. Simulation of water–rock interaction in the Yellowstone geothermal system using TOUGHREACT. Geothermics 33, 493–502.

Ferguson, G., Grasby, S.E., Hindle, S.R., 2009. What do aqueous geothermometers really tell us? Geofluids 9, 39–48.

Finsterle, S., Zhang, Y., 2011. Solving iTOUGH2 simulation and optimization problems using the PEST protocol. Environ. Modell. Softw. 26, 959–968.

Fournier, R.O., Potter, R.W., 1982. A revised and expanded silica (quartz) geothermometer. Geotherm. Resour. Council Bull. 11, 3–12.

Fournier, R.O., Rowe, J.J., 1966. Estimation of underground temperatures from silica content of water from hot springs and wet-steam wells. Am. J. Sci. 264, 685.

Fournier, R.O., Truesdell, A.H., 1973. Empirical Na–K–Ca geothermometer for natural waters. Geochim. Cosmochim. Acta 37, 1255–1275.

Giggenbach, W.F., 1988. Geothermal solute equilibria: derivation of Na–K–Mg–Ca geoindicators. Geochim. Cosmochim. Acta 52, 2749–2765.

Goff, F., Bergfeld, D., Janik, J., Counce, D., Murrell, M., 2002. Geochemical data on waters, gases, scales, and rocks from the Dixie Valley Region, Nevada. In: Los Alamos National Laboratory Report LA-13972-MS, Los Alamos, NM.

Iovenitti, J., Blackwell, D.D., Sainsbury, J., Tibuleac, I., Waibel, A., Cladouhos, T., Karlin, R., Isaaks, E., Clyne, M., Ibser, F.H., Callahan, O., Kennedy, B.M., Wannamaker, P., 2012. Proceedings, Thirty-Seventh Workshop on Geothermal Reservoir Engineering , Stanford University, Stanford, CA, January 30–February 1.

Jones, G.D., Xiao, Y., 2006. Geothermal convection in the Tengiz carbonate platform, Kazakhstan: reactive transport models of diagenesis and reservoir quality. AAPG Bull. 90, 1251–1272.

Kennedy, B.M., van Soest, M.C., 2006. A helium isotope perspective on the Dixie Valley, Nevada, hydrothermal system. Geothermics 35, 26–43.

Lasaga, A.C., 1984. Chemical kinetics of water–rock interactions. J. Geophys. Res. 89, 4009–4025.

Leung, C.T.O., Zimmerman, R.W., 2012. Estimating the hydraulic conductivity of two-dimensional fracture networks using network geometric properties. Transp. Porous Media 93, 777–797.

Lutz, S.J., Moore, J.N., Benoit, D., 1997. Geologic framework of Jurassic reservoir rocks in the Dixie Valley geothermal field, Nevada: implications from hydrothermal alteration and stratigraphy. In: Proceedings, Twenty-second Workshop on Geothermal Reservoir Engineering, Stanford University, Stanford, CA, January 27–29.

McKenna, J.R., Blackwell, D.D., 2004. Numerical modeling of transient Basin and Range extensional geothermal systems. Geothermics 33, 457–476.

Moulding, A., Brikowski, T., 2012. Three-dimensional modeling of Basin and Range geothermal systems using TOUGH2-EOS1SC. In: Proceedings, TOUGH Symposium 2012, Lawrence Berkeley National Laboratory, Berkeley, CA, September 17–19, 302–309.

Nimz, G., Janik, C., Goff, F., Dunlap, C., Huebner, M., Counce, D., Johnson, S., 1999. Regional Hydrology of the Dixie Valley Geothermal Field, Nevada: Preliminary Interpretations of Chemical and Isotopic Data. Lawrence Livermore National Laboratory Publication UCRL-JC-135417.

Palandri, J.L., Kharaka, Y.K., 2004. A Compilation of Rate Parameters of Water–Mineral Interaction Kinetics for Application to Geochemical Modeling., pp. 64.

Pang, Z.H., Reed, M., 1998. Theoretical chemical thermometry on geothermal waters: problems and methods. Geochim. Cosmochim. Acta 62, 1083–1091.

Peiffer, L., Wanner, C., Spycher, N., Sonnenthal, E.L., Kennedy, B.M., Iovenitti, J., 2014. Multicomponent vs. classical geothermometry: insights from modeling studies at the Dixie Valley geothermal area. Geothermics, http://dx.doi.org/10.1016/j.geothermics.2013.12.002 (in press).

Pruess, K., Oldenburg, C., Moridis, G., 1999. TOUGH2 Users Guide, Version 2.0. Lawrence Berkeley Laboratory Report LBL-29400, Berkeley, CA.

Reed, M.H., 1997. Hydrothermal Alteration and Its Relationship to Ore Field Composition. John Wiley & Sons, New York.

Reed, M., Palandri, J.L., 2006. SOLTHERM.H06, a Database of Equilibrium Constants for Inerals and Aqueous Species. Available from the authors, University of Oregon, Eugene, Oregon.

Reed, M., Spycher, N., 1984. Calculation of ph and mineral equilibria in hydrothermal waters with application to geothermometry and studies of boiling and dilution. Geochim. Cosmochim. Acta 48, 1479–1492.

Serpen, U., Niyazi, A., 2005. Reinjection problems in overpressured geothermal reservoirs. In: Proceedings, Thirtieth Workshop on Geothermal Reservoir Engineering, Stanford University, Stanford, CA, January 31–February 2.

Sonnenthal, E.L., Ito, A., Spycher, N., Yui, M., Apps, J.A., Sugita, Y., Conrad, M.E., Kawakami, S., 2005. Approaches to modeling coupled thermal, hydrological and chemical processes in the Drift Scale Heater Test at Yucca Mountain. Int. J. Rock Mech. Min. Sci. 42, 698–719.

Sonnenthal, E.L., Spycher, N., Callahan, O., Cladouhos, T., Petty, S., 2012. A thermal–hydrological–chemical model for the enhanced geothermal system demonstration project at Newberry Volcano, Oregon. In: Proceedings, Thirty-Seventh Workshop on Geothermal Reservoir Engineering, Stanford University, Stanford, CA, January 30–February 1. SGP-TR-194.

Speed, R.C., 1976. Geologic map of the Humboldt Lopolith, Geological Society of America Map and Chart Series MC-14, 1:81050 Scale, 4 pp.

Spycher, N., Sonnenthal, E.L., Kennedy, B.M., 2011. Integrating multicomponent chemical geothermometry with parameter estimation computations for geothermal exploration. Geotherm. Resour. Council Trans. 35, 663–666.

Spycher, N., Peiffer, L., Sonnenthal, E.L., Reed, M., 2014. Multicomponent solute geothermometry. Geothermics 51, 113–123.

Taron, J., Elsworth, D., 2009. Thermal–hydrologic–mechanical–chemical processes in the evolution of engineered geothermal reservoirs. Int. J. Rock Mech. Min. Sci. 46, 855–864.

Tempel, R.N., Sturmer, D.M., Schilling, J., 2011. Geochemical modeling of the near-surface hydrothermal system beneath the southern moat of Long Valley Caldera, California. Geothermics 40, 91–101.

Waibel, A.F., 1987. An overview of the geology and secondary mineralogy of the high temperature geothermal systems in Dixie Valley, Nevada. Geotherm. Resour. Council Trans. 11, 479–486.

Weis, P., Driesner, T., Heinrich, C.A., 2012. Porphyry-copper ore shells form at stable pressure–temperature fronts within dynamic fluid plumes. Science 338, 1613–1616.

Witherspoon, P.A., Wang, J.S.Y., Iwai, K., Gale, J.E., 1980. Validity of cubic law for fluid-flow in a deformable rock fracture. Water Resour. Res. 16, 1016–1024.

Xu, T.F., Pruess, K., 2001. On fluid flow and mineral alteration in fractured caprock of magmatic hydrothermal systems. J. Geophys. Res. 106, 2121–2138.

Xu, T.F., Ontoy, Y., Molling, P., Spycher, N., Parini, M., Pruess, K., 2004. Reactive transport modeling of injection well scaling and acidizing at Tiwi field, Philippines. Geothermics 33, 477–491.

Xu, T., Spycher, N., Sonnenthal, E.L., Zhang, G., Zheng, L., Pruess, K., 2011. TOUGHREACT Version 2.0: a simulator for subsurface reactive transport under non-isothermal multiphase flow conditions. Comput. Geosci. 37, 763–774.

4.2. Quantification of 3-D thermal anomalies from surface observations of an orogenic geothermal system (Grimsel Pass, Swiss Alps)

Source:

Wanner C., Diamond L. W. and Alt-Epping P. (2019) Quantification of 3-D thermal anomalies from surface observations of an orogenic geothermal system (Grimsel Pass, Swiss Alps). *Journal of Geophysical Research: Solid Earth* **124**, 10839-10854.

Contribution by the Author (CW):

CW and LWD developed the general idea and CW carried out all the simulations. CW had the lead in data interpretation and manuscript writing.

JGR Solid Earth

RESEARCH ARTICLE
10.1029/2019JB018335

Quantification of 3-D Thermal Anomalies From Surface Observations of an Orogenic Geothermal System (Grimsel Pass, Swiss Alps)

Christoph Wanner[1], Larryn W. Diamond[1], and Peter Alt-Epping[1]

[1]Rock-Water Interaction Group, Institute of Geological Sciences, University of Bern, Bern, Switzerland

Key Points:
- Quantification of the heat anomaly below an orogenic geothermal system, combining geochemical observations with numerical simulations
- Calibrated simulations yield large thermal anomalies of 10^2–10^3 PJ per km depth
- Amagmatic orogens are surprisingly promising plays for geothermal power production

Correspondence to:
C. Wanner,
wanner@geo.unibe.ch

Citation:
Wanner, C., Diamond, L. W., & Alt-Epping, P. (2019). Quantification of 3-D thermal anomalies from surface observations of an orogenic geothermal system (Grimsel Pass, Swiss Alps). *Journal of Geophysical Research: Solid Earth*, *124*, 10,839–10,854. https://doi.org/10.1029/2019JB018335

Received 8 JUL 2019
Accepted 17 SEP 2019
Accepted article online 16 OCT 2019
Published online 6 NOV 2019

Abstract Geothermal systems in amagmatic orogens involve topography-driven infiltration of meteoric water up to 10 km deep into regional-scale faults and exfiltration of the heated water in surface springs. The thermal anomalies along the upflow zones have not been quantified, yet they are key to estimating the geothermal exploitation potential of such systems. Here we quantify the three-dimensional heat anomaly below the orogenic geothermal system at Grimsel Pass, Swiss Alps, where warm springs emanate from an exhumed, fossil hydrothermal zone. We use discharge rates and temperatures of the springs, temperature measurements along a shallow tunnel, and the formation temperature and depth of the fossil system to constrain coupled thermal–hydraulic numerical simulations of the upflow zone. The simulations reveal that upflow rates act as a first-order control on the temperature distribution and that the site is underlain by an ellipsoidal thermal plume enclosing 10^2–10^3 PJ of anomalous heat per km depth. When the fossil system was active (3.3 Ma), the thermal plume was double its present size, corresponding to a theoretical petrothermal power output of 30–220 MW, with the 120 °C threshold for geothermal electricity production situated at less than 2-km depth. We conclude that mountainous orogenic belts without igneous activity and even with only low background geothermal gradients typical of waning orogens are surprisingly promising plays for petrothermal power production. Our study implies exploration should focus on major valley floors because there the hydraulic head gradients and thus upflow rates and heat anomalies reach maximum values.

1. Introduction

Mountainous orogenic belts without recent igneous activity have been hitherto recognized as plays for geothermal power production only because of the deep sedimentary sequences in their foreland basins, which may host high-enthalpy aquifer-hydrothermal resources (Moeck, 2014). However, the mountain ranges themselves also host geothermal activity, evidenced by thermal springs discharging at temperatures ≤80 °C. These apparently low-enthalpy systems are mostly due to deep circulation of meteoric water through major faults, driven by topographically induced hydraulic head gradients. Examples are in the Canadian Rocky Mountains (Grasby et al., 2016; Grasby & Hutcheon, 2001), the Southern Alps of New Zealand (Menzies et al., 2014; Reyes, 2015; Reyes et al., 2010), the central European Alps (Pfeifer et al., 1992; Sonney & Vuataz, 2008, 2009, 2010), Taiwan (Upton et al., 2011), and the Himalayas (Craw et al., 2005; Hochstein & Yang, 1995). As part of the global search for renewable electricity sources, attention is being paid to these "orogenic geothermal systems" not just because of their water-borne heat but also because of the petrothermal heat deposited by conduction in the low-permeability host rocks around their upflow zones.

Meteoric water that circulates through amagmatic orogens can acquire heat only from the crystalline bedrock. The depth of water penetration therefore determines the maximum reservoir temperature attainable at the base of the system. Several approaches have been taken to assess the penetration depth. In exhumed fossil systems, $\delta^{18}O$ and $\delta^{2}H$ analyses of hydrothermal minerals and fluid inclusions combined with petrological calculations and structural arguments suggest infiltration depths in the range of 5–23 km (Barker et al., 2000; Butler et al., 1997; Cartwright & Buick, 1999; Craw, 1997; Jenkin et al., 1994; McCaig et al., 1990; Menzies et al., 2014; Mulch et al., 2004; Nesbitt et al., 1989; Sharp et al., 2005; Upton et al., 1995; Wickham et al., 1993), implying deep reservoir temperatures up to 400–600 °C (Mulch et al., 2004; Upton et al., 1995). In contrast, classical solute geothermometry applied to analyses of hot springs in orogenic

belts usually reveal reservoir temperatures below 150 °C, such as in the Canadian Rocky Mountains (Grasby et al., 2016), the Qilian Mountains in China (Stober et al., 2016), the Pyrenees in Spain (Asta et al., 2010), and the Swiss Alps (Sonney & Vuataz, 2009). Higher reservoir temperatures are found where extreme uplift rates elevate local geothermal gradients (e.g., Alpine Fault, New Zealand, Reyes et al., 2010; Sutherland et al., 2017) or where deep-sourced, nonmeteoric fluids advect heat upon ascent (e.g., Newell et al., 2015). Considering geothermal gradients typical of waning orogens (25–30 °C/km), the reservoir temperatures in meteoric-dominated systems suggest penetration of meteoric water to less than 6-km depth. Recently, Diamond et al. (2018) took an alternative geochemical modeling approach to determine the penetration depth of meteoric water at the Grimsel Pass geothermal site in the Swiss Alps. The compositions of the thermal waters discharging at that site could be matched by performing forward reactive-transport simulations that treat thermodynamic and kinetic processes of mineral dissolution and precipitation along the upflow path. By combining the calculated 250 °C minimum temperature of water–rock equilibration along the deep flow path with the current geothermal gradient of 25 °C/km, this approach confirmed a penetration depth of at least 10 km (Diamond et al., 2018), thereby bridging the results obtained by classic solute geothermometry and petrologic studies.

Water penetration depths of 10 km or more along even a normal orogenic geothermal gradient (e.g., 25 °C/km) can clearly create a thermal plume well above the ~120 °C threshold required to produce electricity. However, except for the estimates of heat recoverable from aqueous fluids in low-enthalpy geothermal systems in New Zealand (Reyes, 2015), little is known regarding the heat anomalies generated by orogenic geothermal systems. This presents a challenge for assessing their exploitation potential as a renewable energy option in regions unendowed with classic aquifer-hydrothermal resources. Important, but unresolved, questions include (i) what are the shapes, dimensions and magnitudes of their deep thermal anomalies in 3-D? (ii) Is there enough heat in the rocks around the fault-hosted upflow zones to permit petrothermal power production? (iii) How sensitive is the resulting thermal anomaly to the penetration depth of meteoric water along the recharge path?

Here, building on the site parameters derived in the case study of Diamond et al. (2018), we present coupled thermal–hydraulic numerical simulations of the Grimsel Pass orogenic geothermal system in the central Swiss Alps. The main aims of these simulations are to (i) quantify the shape, dimensions and magnitude of the 3-D subsurface thermal anomaly around its upflow zone and (ii) to elucidate its governing parameters. Grimsel Pass is favorable for this treatment because it provides both active and exhumed fossil evidence of geothermal activity in the form of warm springs and hydrothermal breccia outcrops. Together, these yield unique insights into the temporal and spatial evolution of the deep heat plume. To constrain our simulations we have combined numerous surface and near-surface observations made on the current geothermal system (e.g., discharge rates and temperature of warm springs, temperature along a shallow tunnel) with those made on the fossil hydrothermal breccia (e.g., inferred depth and temperature of formation). This permits the magnitude and 3-D geometry of the deep subsurface thermal anomaly to be quantified exclusively from direct near-surface observations.

2. Site Description

Grimsel Pass, which lies between the Rhone and Aare Valleys in the Swiss Alps, is the site of several warm springs that emanate at low flow rates (1–4 L/min) and that have temperatures up to 28 °C (Pfeifer et al., 1992; Waber et al., 2017). Fossil geothermal activity at the same site is expressed by hydrothermal alteration of Pliocene (3.3 Ma) age within the Grimsel Breccia Fault (Hofmann et al., 2004). The present-day springs discharge at an altitude of 1,900–1,915 m above sea level into a N–S trending tunnel ~250 m beneath Grimsel Pass, which hosts a trans-European pipeline for natural gas (hereafter referred to as the Transitgas tunnel after the company who built it in 1973; Figure 1). Grimsel Pass is the lowest point along an E–W profile through the local mountainous topography, but, owing to its saddle shape, it is simultaneously the highest point in a N–S profile between the Aare and Rhone valleys. The warm springs are therefore remarkable because they discharge at the high pass, rather than in the adjacent valleys.

Several studies have already characterized the springs and the fossil geothermal activity, as summarized in the following. The thermal waters have relatively reduced redox states ($Eh_{Ag/AgCl} = -250$ to 10 mV), and chemically they are of Ca–Mg-poor, Na–SO_4–HCO_3 type, carrying up to 280 mg/L total dissolved solids (TDS;

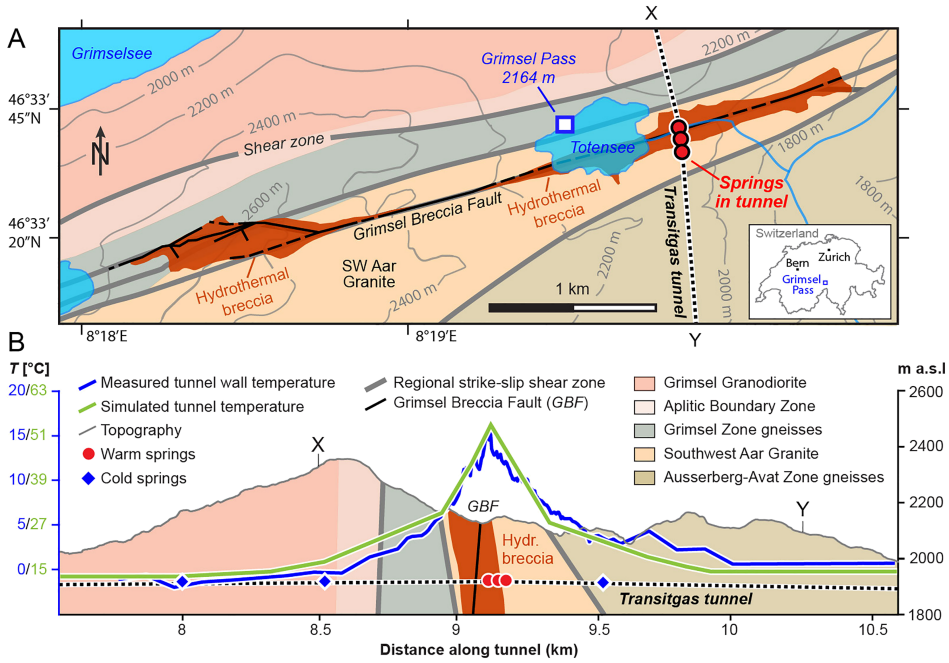

Figure 1. (a) Geological map with Transitgas pipeline tunnel illustrating spatial coincidence between currently active warm springs, regional strike-slip faults, and 3.3-Ma hydrothermally cemented fault-breccias (after Belgrano et al., 2016). (b) Geological cross section along tunnel showing localities of warm springs (>20 °C, circles), cold springs (<20 °C, diamonds), measured tunnel-wall temperature profile (blue; from Egli, Baumann, et al., 2018), and simulated profile (green; this study). The two profiles are plotted at different temperature scales (left *y* axis) to show that our model captures the width of the observed temperature anomaly, whereas the absolute temperatures differ.

Pfeifer et al., 1992; Waber et al., 2017). These properties and their elevated SiO_2, Na, K, Li and F contents, contrast with nearby cold springs, which are poorly mineralized (TDS < 110 mg/L) and of oxidized, Ca–HCO_3 character.

All the thermal springs contain ^{3}H (bomb tritium); thus, they represent mixtures between an old, deeply circulated geothermal end-member that is ^{3}H-free, and a young, cold-water end-member that is ^{3}H-bearing. In the warm spring with the highest solute concentration, the measured ^{3}H activity defines a mixing ratio of about 1:1 (Diamond et al., 2018). Combining this ratio with the ^{14}C concentration shows that the deep geothermal end-member is ^{14}C-free and therefore more than 30 ka old (Waber et al., 2017).

The δ^2H and δ^{18}O values of the thermal springs fall on the local meteoric water line and are well within the range of current rainfall, demonstrating that meteoric water is recharging the geothermal system and that recharge must have occurred at times where the climatic conditions were similar to those of today (Waber et al., 2017). The >30 ka age points to the Middle Würmian interstadial period (which correlates with Marine Oxygen Isotope Stage MIS-3) or to even older warm interglacial periods when significant meteoric recharge was feasible (Dzikowski et al., 2016).

The thermal springs show more negative δ^2H and δ^{18}O values than the nearby cold-water springs, suggesting that the ultimate source of the thermal water is from a distant meteoric infiltration site at a higher altitude than that of Grimsel Pass (Waber et al., 2017). For example, the −15.1‰ δ^{18}O value of the reconstructed end-member thermal water reported by Diamond et al. (2018) is 1.7‰ lower than present surface water (Schotterer et al., 2010). As the local climate during the Middle Würmian MIS-3 or previous interglacial periods was similar to the present (Preusser et al., 2003; Preusser et al., 2011; Spötl & Mangini, 2002), today's δ^{18}H–elevation correlation of −2‰/km in the Grimsel region (Schotterer et al., 2010) can be used to estimate a paleo-infiltration site up to 850 m above Grimsel Pass. Thus, a topographically induced hydraulic head gradient is interpreted to be the main hydraulic force driving ascent of the geothermal water from depth.

Reactive-transport modeling, constrained by the mineralogy of the Pliocene hydrothermally altered breccia, shows that the infiltrating meteoric water reaches a temperature of at least 211 °C and more likely on the order of 230–250 °C along the deepest reaches of its flow path (Diamond et al., 2018).

The Transitgas tunnel crosscuts various steeply dipping crystalline rock units of the Aar Massif (Pfeifer et al., 1992; Figure 1) but the warm springs occur only along a short (<100 m) section of the tunnel where it traverses the Grimsel Breccia Fault. Despite the limited occurrence of warm springs, the tunnel wall shows anomalously high temperatures ($\Delta T = T - T_{\text{background}} \leqslant 16$ °C) along a tunnel section of about 1 km (Egli, Baumann, et al., 2018), suggesting that heat transport is not only occurring by convection along the hydraulically active part of the Grimsel Breccia Fault but also by conduction into the less fractured part of the Aar Massif. The porous, water-conducting Grimsel Breccia Fault, which has been examined in a shallow (115-m depth) research borehole (Egli, Baumann, et al., 2018), dips 85° to the NNW, and therefore, it intersects the tunnel almost perpendicularly. The Breccia Fault is a product of brittle reactivation of an older ductile shear zone that belongs to the Grimsel Pass Fault Zone, a dense set of major ENE trending mylonitic faults that show late strike-slip displacement and that extend along strike over tens of kilometers through the Central Alps (Belgrano et al., 2016; Herwegh et al., 2017). The Grimsel Breccia Fault is named after two ~0.25-km^2 zones containing swarms of narrow, mineralized breccias that outcrop over about 4.5 km along strike of the host fault and that have pipe-like forms in 3-D (Figure 1; Belgrano et al., 2016). These permeable breccia pipes focus ascent of the thermal water to high altitude at Grimsel Pass, while flow toward the deep valleys to the north and south is blocked by intact granite and by ENE trending low-permeability mylonites. Drainage along the Breccia Fault toward the ENE, where the fault outcrops at lower altitude than at Grimsel Pass, is blocked by clay-bearing gouge. Thus, structural controls explain the unexpected occurrence of springs on the high mountain pass, rather than in the adjacent valleys (Figure 1a).

The main host rock of the Grimsel Breccia Fault is the Southwest Aar Granite of Variscan age (Berger et al., 2016; Schaltegger, 1990). Its clasts within the breccias are hydrothermally altered and cemented by a mineral assemblage of quartz and adularia with minor chalcedony, clay minerals, and pyrite (Hofmann et al., 2004). The late-stage adularia in the breccia has been dated at 3.3 ± 0.06 Ma (Hofmann et al., 2004). Fission-track and U–Th/He dates in the distal wall rocks (Egli, Glotzbach, et al., 2018; Vernon et al., 2009) combined with the present rock uplift rate of ~0.9 km/Ma (Hofmann et al., 2004) indicate a recent mean denudation rate of ~0.75 km/Ma, implying the currently exhumed breccia lay ~2.5 km below the paleosurface at 3.3 Ma (Diamond et al., 2018). Fluid inclusion homogenization temperatures corrected for 2.5-km hydrostatic pressure indicate the breccia was mineralized at a temperature of at least 165 ± 5 °C (Diamond et al., 2018). Fluid inclusion analyses show the mineralizing fluid had low salinity (0.5 wt % $NaCl_{eq.}$) and temperature-corrected stable-isotope signatures of the hydrothermal minerals reveal that, like the warm springs, the paleo-fluid was of meteoric origin ($\delta^2H = -110$ to -137‰; $\delta^{18}O = -11$ to -7‰; Hofmann et al., 2004).

In the absence of any Pliocene–Pleistocene igneous activity in the Central Alps, the only source of heat for the water circulating through the Grimsel Pass geothermal system is that dictated by the orogenic geothermal gradient in its wall rocks, which has maintained a value of ~25 °C/km over the past 3.3 Ma (Bodmer, 1982; Vernon et al., 2008).

3. Numerical Model

Our thermal–hydraulic model aims to quantify the current thermal structure of the heat anomaly deep below Grimsel Pass. We therefore simulate only the upflow zone of the geothermal system, using available constraints on the hydraulic head gradients and temperature–depth relations to specify the boundary conditions of the model.

3.1. Constraints on Temperature–Depth Relations

Among the features of the site described in section 2, there are four major thermal–hydraulic, near-surface observations to which our simulations can be compared (Figure 2a). For the remainder of the paper these selected observations will be referred to as calibration targets. The values of these targets are presented in the following.

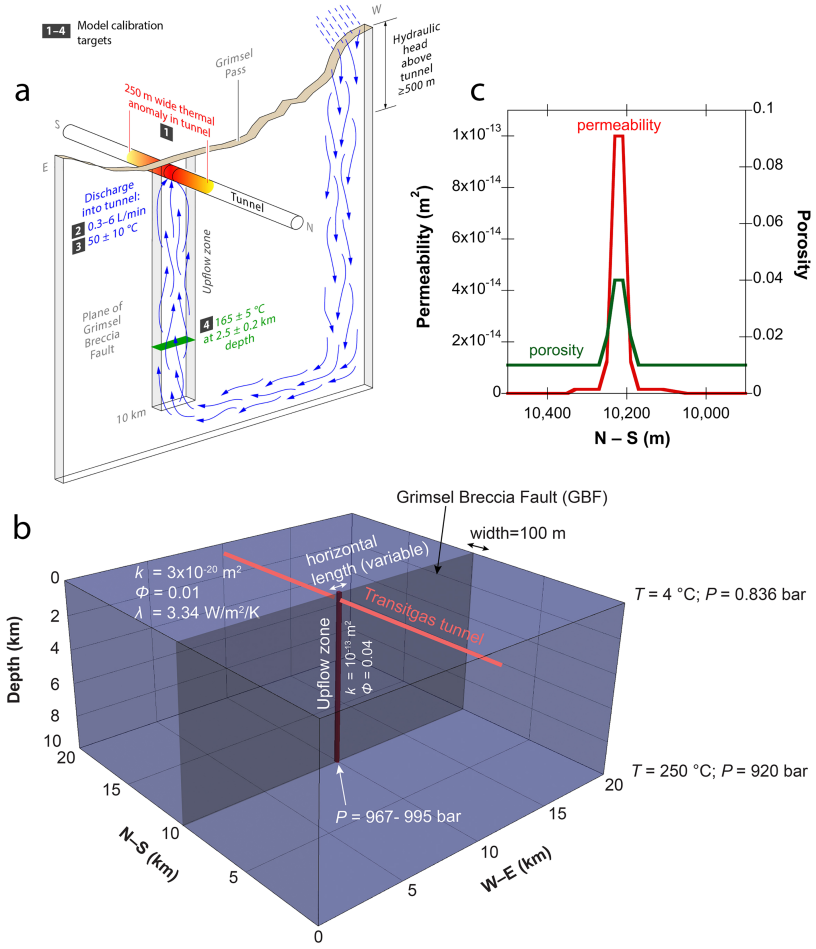

Figure 2. (a) Schematic view (not to scale) of the Grimsel Breccia Fault, the active upflow path of thermal water, and the Transitgas tunnel. Numbers 1–4 show the values of key constraints used as calibration targets for the numerical modeling. Only the upflow segment of the flow path is simulated in this study. (b) Model setup showing the detailed 3-D geometry and the specified initial and boundary conditions for an inferred recharge infiltration depth of 10 km. (c) Specified permeability and porosity profile along the Transitgas tunnel.

3.1.1. Spring Discharge Temperature Within the Transitgas Tunnel

Cooling of the geothermal water upon ascent and mixing with cold surface water results in a discharge temperature of 28 °C. The effect of cold water infiltration on spring temperatures in mountainous terrains depends on several factors: the permeability contrast between hydraulically active fault zones and their surrounding country rocks, the dip angle of the fault zones, and the horizontal distance between the hydraulically active fault zones and the site of surface water infiltration (Ferguson et al., 2009; Forster & Smith, 1989; Lazear, 2006; López & Smith, 1995). Thus, cooling by surface water varies from site to site and for the Grimsel Pass system it is difficult to estimate at which depth and in which geometry this mixing and cooling occurs below the level of the Transitgas tunnel. In the nearby underground Grimsel Test Site, which lies at 450–500-m depth, surface water infiltrates along localized brittle structures but wall-rock temperatures correspond perfectly with those expected from the overburden thickness and the regional geothermal gradient of 25 °C/km (Schneeberger et al., 2017). This suggests that any major cooling by surface water occurs at depths shallower than 500 m. Similarly, in the more distant Gotthard rail base tunnel, which traverses the same crystalline massif as at Grimsel Pass, the effects of cooling by infiltrating meteoric water are observable only along sections of the tunnel with less than 500-m overburden (Rybach & Busslinger, 2013). At Grimsel Pass,

however, surface water could conceivably penetrate deeper into certain zones of the Breccia Fault while thermal water rises up other zones of the same structure. Because we cannot quantify the depth of mixing and because we are primarily interested in the deep thermal structure of the geothermal system, in our model we choose to neglect any cooling due to infiltration of surface water down fractures. This is consistent with previous modeling studies showing that cooling is less significant when upflow is focused within 1D, pipe-like structures (e.g., McKenna & Blackwell, 2004; Taillefer et al., 2017)—which is the case at Grimsel Pass—rather than in planar fault zones that are hydraulically active throughout their 2-D extent (e.g., Dzikowski et al., 2016). Given this assumption, the top ~1 km of our model will represent a hypothetical warm scenario. Therefore, we subtract the effect of near-surface mixing on the spring temperatures by using the mean and standard deviation of the temperature of the unmixed geothermal end-member ($T = 50 \pm 10$ °C) estimated by Diamond et al. (2018). This end-member temperature serves as the first calibration target of our upflow model at 250 m below Grimsel Pass.

3.1.2. Spring Discharge Rates Within the Transitgas Tunnel

The reported total discharge rate of warm springs into the Transitgas tunnel varies between 2 and 8 L/min (Diamond et al., 2018; Pfeifer et al., 1992). Due to the practical difficulties of sampling beneath the gas pipeline, however, the measurement error associated with these rates is conservatively estimated at up to 50%. Moreover, the discharge rates apply to a mixture of deep geothermal fluid and cold surface water. According to Diamond et al. (2018), the cold-water fraction in the warm springs varies from 51 to 70 vol %. Altogether, these considerations yield cold-water corrected discharge rates of the unmixed geothermal fluid of 0.3 to 6 L/min, which serves as the second calibration target in our model at 250 m below Grimsel Pass.

3.1.3. Width of Thermal Anomaly Along Transitgas Tunnel

As evident from the difference between the maximum tunnel wall temperature (16 °C) and the discharge temperatures of the thermal springs (≤28 °C), the tunnel wall temperatures reported by Egli, Baumann, et al. (2018) do not reflect true rock temperatures. The difference is due to several effects. First, most segments of the tunnel wall are covered by a layer of concrete ("shotcrete") with a lower thermal conductivity than the host rocks. Second, cold meteoric water is infiltrating from the surface (at the time of sampling this corresponded to meltwater of final winter snow at ~0 °C; Waber et al., 2017). This inflow is most likely the reason why the variable thickness of rock overburden (0–300 m; Figure 1b) does not seem to influence the tunnel wall temperatures. This interpretation is in agreement with temperature measurements at sites of surface-water influx along the Gotthard rail base tunnel (Rybach & Busslinger, 2013), as explained above. Finally, no attempt was made to correct for the thermal effect of air circulation within the 3-m-diameter, 10.4-km-long tunnel. Because cooling by surface water and air circulation in the tunnel have opposing effects on the width of the temperature anomaly (narrowing versus widening) we believe that, despite the listed artifacts, the temperature profile recorded along the tunnel approximately captures the width of the temperature anomaly induced by the undisturbed geothermal system. Therefore, we take 250 m, corresponding to the length of the tunnel section where the recorded temperature is above half of the observed maximum anomaly ($\Delta T \geq 0.5 \times \Delta T_{max}$, with $\Delta T = T - T_{background}$), as the third calibration target in our model at the tunnel level below Grimsel Pass.

3.1.4. Depth at $T = 165$ °C

A basic premise of our model is that today's thermal springs and the exhumed mineralized breccia at Grimsel Pass belong to the same geothermal system (Hofmann et al., 2004), which has been active, albeit perhaps intermittently, for several million years. All the available information summarized in section 2 is compatible with this premise. Thus, following the approach of Diamond et al. (2018), the paleo-characteristics of the breccia provide us with a window into the subsurface characteristics of the past and possibly into the present-day geothermal activity. Whereas the breccia was mineralized at 2.5 ± 0.2-km depth at 165 ± 5 °C, the background geothermal gradient (25 °C/km) dictates a depth of ~ 6.5 km to heat water to 165 °C. Evidently, advection of heat by the ascending water has raised the 165 °C isotherm by ~ 4 km within the upflow zone, a fact that can be used to constrain our model. Accordingly, we take $T = 165 \pm 5$ °C at 2.5 ± 0.2-km depth as the fourth calibration target within the upflow zone of our model.

3.2. Model Setup

The model was set up as a 3-D cuboid domain (Figure 2b and Table 1) to capture the interplay between three thermal effects: (i) convective heat transport due to fluid flow along the hydraulically active part of

Table 1
Values and Sources of Parameters Used in the Numerical Simulations

Parameter	Value	Source
Dimensions of modeled domain		
N–S and E–W dimensions of total domain	20 × 20 km	Chosen to avoid heat conduction artifacts
Vertical length of total domain	10 km	Depths required to reach a temperature of 250 °C at the background geothermal gradient derived from geochemical modeling (Diamond et al., 2018)
N–S width of upflow zone	100 m	Equal to length of tunnel segment containing warm springs
E–W length of upflow zone	50–150 m	Constrained to less than 4.5-km strike length of breccia
Hydraulic properties		
Hydraulic head driving upflow	500–800 m	Inferred from $\delta^{18}O$ values in Diamond et al. (2018) and from altitude range of present-day topography
Porosity of upflow zone	0.04	Total fracture apertures in borehole
Permeabililty of upflow zone	10^{-13} m^2	Hydraulic tests in upflow zone (Cheng & Renner, 2018)
Porosity of rock outside upflow zone	0.01	He-pycnometry on samples from nearby Grimsel Test Site (Bossart & Mazurek, 1991)
Permeability of rock outside upflow zone	3×10^{-20} m^2	Calculated from hydraulic conductivity determined in nearby Grimsel Test Site (Ota et al., 2003)
Bulk rock density ρ	2660 kg/m^3	Measurements in nearby Grimsel Test Site (Keusen et al., 1989)
Minimum water residence time	30 ka	Waber et al. (2017)
Cold-water corrected discharge rate of thermal water into Transitgas tunnel	0.3–6 L/s	Diamond et al. (2018)
Thermal properties		
Background surface temperature	4 °C	Annual mean
Water discharge temperature in upflow zone	50 ± 10 °C	Mean and standard deviation of geothermal end-member as calculated by Diamond et al. (2018)
Background geothermal gradient	25 °C/km	Vernon et al. (2008)
Steady-state depth at 165 °C in upflow zone	2.5 km	Equal to exhumation depth of 3.3-Ma breccia with formation temperature of 165 ± 5 °C (Diamond et al., 2018)
Thermal conductivity of wet granite	3.34 W m^{-1} K^{-1}	Measurements in nearby Grimsel Test Site (Kuhlmann & Gaus, 2014)
Heat capacity of granite	$C_p = f(T)$	Miao et al. (2014)
Width of temperature anomaly across upflow zone ($\Delta T \geq 0.5 \times \Delta T_{max}$)	250 m	Egli, Baumann, et al. (2018)

the Grimsel Breccia Fault, (ii) conductive heat transport from the underlying deep basement, and (iii) conductive heat loss from the upflow zone into the surrounding rocks of the Aar Massif and to the surface. A large horizontal area of 20 × 20 km was chosen for the model to ensure that heat conduction in the area of interest was not affected by the lateral boundaries of the model. The top of the model domain is flat, without topography and its elevation was set at the altitude of Grimsel Pass (2,164 m above sea level). Thus, the force to drive fluid ascent is given in the model by an appropriate fluid overpressure at the base of the upflow zone (see below). The real topography rises to 500 m above the altitude of the Grimsel Pass some 2.2 km to the west, along the strike of the Grimsel Breccia Fault (and to steadily higher altitudes beyond that, reaching 1,000 m above the pass at 12–14-km distance). We therefore take 500 m as the minimum hydraulic head that drives meteoric water circulation through the system, consistent with the stable isotope constraints (i.e., δ^2H and $\delta^{18}O$ values). The vertical model length was set to 10 km according to the maximum penetration depth of meteoric water estimated by Diamond et al. (2018). To assess the sensitivity of our calibration targets with respect to the penetration depth, however, two additional simulations were run in which the vertical model length was set to 8 and 12 km, respectively.

The hydraulically active upflow zone was placed in the center of the 20 × 20 × 10 km domain and assigned a horizontal N–S width of 100 m, based on the length of the tunnel segment over which the thermal springs occur. Little information is available regarding the horizontal E–W length of the active upflow zone along the Grimsel Breccia Fault (i.e., perpendicular to the tunnel) and indeed there may be other warm springs on the surface outside the tunnel area that are hidden by Quaternary cover. However, the active upflow zone is presumably much shorter than the 4.5-km total length of the breccia bodies. Consequently, multiple simulations were run in which the horizontal E–W length of the active fluid upflow zone was varied between 50 and 150 m.

The Transitgas tunnel was not explicitly defined in the model owing to its small diameter (3 m) and so the simulated tunnel parameters simply correspond to those calculated 250 m below the upper model boundary. Since the tunnel induces a local pressure drop that draws in fluid from the surroundings, we further assume that the current upflow zone is centered on the tunnel (Figure 2b). The entire model domain was discretized into cuboid grid blocks with dimensions of 1 km × 1 km × 200 m in distal regions and decreasing to 1 m × 25 m × 200 m toward the upflow zone, where more detail is required to represent high thermal gradients.

3.3. Initial and Boundary Conditions

The hydraulically active upflow zone was assigned a permeability of 10^{-13} m^2 along the entire vertical extent of the model (Figure 2c and Table 1). This value is based on borehole hydraulic tests performed within the Grimsel Breccia Fault at 90-m depth (Cheng & Renner, 2018). In contrast, the remainder of the model domain was assigned a permeability of 3×10^{-20} m^2 to represent intact granite, in accord with measurements in the nearby underground Grimsel Test Site (Ota et al., 2003). This permeability value ensures that only minor fluid flow occurs outside the upflow zone, consistent with the observed spatial restriction of flow to the breccia body at Grimsel Pass, despite the steep fall of the surface topography to the north, south and southeast of the Pass.

The porosity of the upflow zone was set to 0.04, which corresponds to the total aperture of fractures visible in the televiewer log from the borehole that traverses the Breccia Fault (Egli, Baumann, et al., 2018). The decrease in porosity toward the surrounding rock was set to mimic the observed decrease in spacing and in apertures of fractures mapped across a profile perpendicular to the Breccia Fault (Belgrano et al., 2016). This approach resulted in a linear decrease in porosity to a value of 0.01 outside the upflow zone (Figure 2b), consistent with laboratory measurements of the porosity of the undeformed granite (Bossart & Mazurek, 1991). The corresponding permeability profile was set to follow the cubic law (Witherspoon et al., 1980), assuming that the decrease in porosity is predominantly caused by a decrease in fracture aperture (Figure 2c). The thermal conductivity of the wet rock was set to 3.34 W m^{-1} K^{-1} for the entire model domain based on values reported for the granite within the Grimsel Test Site (Kuhlmann & Gaus, 2014).

Within the model domain we assume an initial hydrostatic pressure distribution and an initial conductive temperature distribution with a geothermal gradient of 25 °C/km. At the four lateral model boundaries, temperature and pressures were fixed to the initially specified values. The upper model boundary was set to 4 °C and 0.836 bar (Figure 2b), whereas at the lower model boundary the initial temperature and pressure depend on the considered penetration depth. For 8 and 10 km, they were set to 200 °C at 745 bar and 250 °C at 920 bar, respectively (Figure 2b), while for a penetration of 12 km the values were set to 300 °C at 1,084 bar. As the altitude of the recharge zone is not known precisely we ran simulations covering a hydraulic head from 500 to 800 m. To do so, the hydrostatic water pressure at the bottom of the upflow zone was varied from 47 to 76 bar to initiate upflow.

3.4. Numerical Simulator

Numerical simulations were performed using TOUGH2 (Pruess et al., 1999), a well-established code for modeling coupled thermo-hydrodynamic processes in geothermal and volcanic systems (e.g., McKenna & Blackwell, 2004; Wanner et al., 2014). All simulations were performed using equation-of-state EOS1, which simulates water flow and coupled heat flow in the single-phase state according to

$$\frac{\partial M_{W,H}}{\partial t} = -\nabla F_{W,H} + q_{W,H} \tag{1}$$

where $M_{W,H}$ is the accumulation term for water M_W (kg/m^3) or heat M_H (J/m^3), $F_{W,H}$ refers to the water flux F_W (kg m^{-2} s^{-1}) or heat flux F_H (J m^{-2} s^{-1}), and $q_{W,H}$ denotes water or heat sinks (−) or sources (+). For fully saturated, single-phase flow problems F_W is equal to the Darcy flux u (m/s)

$$u = -\frac{k}{\mu}(\nabla P - \rho g) \tag{2}$$

where k is the permeability (m^2), μ is the water viscosity (kg m^{-1} s^{-1}), ∇P (Pa m^{-1}) is the water pressure gradient with respect to distance (i.e., hydraulic head gradient), ρ is the density of water (kg/m^3), and g is the gravitational acceleration (m/s^2). Heat flux F_H (J s^{-1} m^{-2}) is defined as

$$F_H = C_M \times T \times \rho_M \times u - \lambda \times \nabla T \quad (3)$$

where C_M (J kg^{-1} K^{-1}) and ρ_M (kg/m^3) are the specific heat capacity and the density of the porous medium (rock + porewater), T (K) is the temperature of the porous medium, λ is the thermal conductivity of the wet rock (J s^{-1} m^{-1} K^{-1} = W m^{-1} K^{-1}), and ∇T (K/m) is the gradient in temperature between adjacent grid blocks. Equation EOS1 calculates the temperature dependence of water properties (e.g., density, specific enthalpy and viscosity) from the Steam Table Equations given by the International-Formulation-Committee (1967).

4. Results and Discussion

4.1. Sensitivity Analysis

Key simulation results are listed in Table 2 for eight different combinations of hydraulic head, horizontal length of the active upflow zone, and meteoric water penetration to illustrate the sensitivity of our calibration targets to the feasible variation in these parameters. Figure 3 illustrates the steady-state temperature distribution for all eight combinations. Increasing the hydraulic head and the horizontal length both increase the temperature within the upflow zone as well as within the adjacent, hydraulically less active part of the Aar Massif. Consequently, this results in increasing tunnel discharge temperatures and widths of the thermal anomaly, while the depth at which the temperature in the upflow zone is 165 °C decreases. This behavior of our calibration targets is observed because both varied parameters affect the amount of hot water infiltrating the system at depth (Figure 2). Whereas increasing the hydraulic head increases upward flux according to Darcy's law (equation (2)), increasing the horizontal length of the upflow zone increases the total fluid injected (in each simulation the area over which the overpressure was defined was increased proportionally to keep the injection rate constant over the entire base of the upflow zone). However, the correlations between the calibration targets and the hydraulic head or the horizontal length of the upflow zone are not fully linear (Table 2). For instance, increasing the hydraulic head from 500 to 650 m at a constant horizontal length of 75 m yields a smaller increase of the simulated discharge temperature in the tunnel (9.4 °C) than when the hydraulic head increases from 650 to 800 m (11.6 °C). Similarly, the temperature increase obtained when increasing the horizontal length from 50 to 100 m (45.3 °C) at a constant head difference of 750 m is smaller than when increasing the length from 100 to 150 m (51.9 °C). This nonlinearity is due to the decrease in fluid density and viscosity with increasing water temperature, and the fact that these fluid properties are important controls on the upflow velocity (equation (2)). This means that the temperature increase initially caused by increasing fluid injection at depth is accelerated by a positive feedback on the flow rate via the temperature dependency of fluid density and viscosity. For instance, the viscosity of pure water decreases from 0.98 to 0.53 g m^{-1} s^{-1} when the temperature increases from 20 to 50 °C, whereas the density decreases from 998.2 to 988.0 kg/m^3. As a consequence, the simulated discharge rate in the tunnel is nearly doubled when increasing the hydraulic head by a factor of only 1.6 (500 to 800 m; Table 2). Likewise, the temperature dependence of fluid viscosity and pressure is the reason why the discharge rate in the tunnel varies for the simulations that were run at a constant hydraulic head of 750 m (Table 2). Since the upflow rate is controlled by the temperature dependence of fluid properties, there is an almost perfect linear correlation between simulated discharge temperatures in the tunnel and total system-wide upflow rates along the hydraulically active part of the host fault (Figure 4). This demonstrates that the total upflow rate is the principal control on the discharge temperature in the tunnel because it is correlated to the amount of heat entering the system at depth.

In contrast to their sensitivity to the hydraulic head and horizontal length of the active upflow zone, our calibration targets are almost insensitive to the variation in penetration depth of meteoric water. This is because conductive heat transport from the upflow zone into the hydraulically inactive part of the surrounding rock mass plays an important role in controlling the temperature distribution of the system in addition to vertical heat advection within the upflow zone. Toward the surface, heat conduction is controlled by the fixed surface temperature of 4 °C. This is the reason why in the model considering 8-km penetration, the 50, 100, and 150 °C isotherms can catch up to those in the models considering deeper penetration (Figure 3a, bottom panel). The importance of heat conduction in controlling the near-surface temperature distribution is also reflected by the weak variation in the simulated width of the thermal anomaly. Thus, the width of the anomaly in the tunnel exhibits the smallest variations among our calibration targets (Table 2). The simulated discharge

Table 2
Observed Versus Simulated Calibration Targets for a Series of Different Combinations of Hydraulic Heads, Horizontal Lengths of the Upflow Zone, and Recharge Penetration Depths

	T_{max}/penetration depth	Hydraulic head (m)	Horizontal length of upflow zone (m)	T_{Tunnel} inflow (°C)[a]	Tunnel discharge rate (kg/min)[b]	Width of T anomaly ($\Delta T \geq 0.5 \times \Delta T_{max}$)	Depth to reach 165 °C (km)	System-wide upflow rate (kg/min)[c]
Observation	≥250 °C/10 km	≥500	?	50 ± 10	0.3–6	250	2.5 ± 0.2	?
Simulations	250 °C/10 km	750	50	28.6	2.5	240	5.6	41.2
		750	100	73.9	4.6	290	3.9	148.7
		750[d]	150	125.8	6.8	350	2.3	321.8
		500	75	29.7	1.9	250	5.5	45.2
		650	75	39.1	2.7	250	5.1	65.8
		800[e]	75	50.7	3.7	260	4.7	90.5
	200 °C/8 km	800[e]	75	53.1	4.0	260	4.9	97.7
	300 °C/12 km	800[e]	75	48.4	3.5	260	4.7	84.7

[a]Steady-state values (Figure 5.) [b]Discharge rate of thermal water integrated over a tunnel section of 100 m and a tunnel diameter of 3 m. [c]Total vertical upflow rate within the entire upflow zone (Figure 2). [d]Model run approximately matching the 165 ± 5 °C formation temperature of the Pliocene breccia at the inferred depth of 2.5 ± 0.2 km. [e]Calibrated models (i.e., best fit with currently observed calibration targets).

temperatures in the tunnel show a minor increase with decreasing penetration depth (Table 2). This is because the hydraulic head gradient driving upflow increases at constant infiltration altitude and decreasing penetration depth.

Similarly to our calibration targets (Table 2), the time required to reach thermal steady state at the simulated tunnel inflow depends on the chosen input parameters and increases with the system-wide upflow rate and hence with increasing discharge temperatures in the tunnel (Figure 5). For the considered parameters it takes up to 10,000 years until full steady-state is reached, although the increase in temperature is negligible after about 2,000 years of continuous, steady-state flow. This is well within the 30-ka minimum time required for each aliquot of meteoric water to flow through the entire recharge–reservoir–discharge path at Grimsel, based on ^{14}C decay (Waber et al., 2017).

4.2. Model Calibration

Our sensitivity analysis has demonstrated that, ignoring cooling effects from surface water infiltration (cf. Forster & Smith, 1989), the temperature distribution of the Grimsel Pass orogenic geothermal system mainly depends on the system-wide fluid upflow rate, which is controlled by the hydraulic head gradient and the extent of the upflow system. Among our various simulations, those that assume a hydraulic head of 800 m and a horizontal length of 75 m successfully reproduce three out of the four calibration targets (Table 2 and Figure 2a). First, the simulated discharge temperatures in the tunnel fall within the temperature range of $T = 50 \pm 10$ °C, as estimated for the unmixed geothermal end-member water (Diamond et al., 2018). Second, the modeled 3.5–4.0-kg/min discharge rates along the 100-m-wide active section of the tunnel fall within the cold-water corrected discharge rates (0.3–6 L/min). Third, the width of the temperature anomaly recorded on the tunnel wall (Egli, Baumann, et al., 2018) is well reconstructed (Table 2), and the simulated tunnel-wall temperature profile reproduces this anomaly almost perfectly (Figure 1b).

In contrast, none of the simulation runs are able to simultaneously reproduce the fourth calibration target derived from the fossil hydrothermal breccia, that is, the 2.5 ± 0.2-km target depth where the temperature in the upflow zone is 165 °C. Instead, the model runs that match the 50 ± 10 °C discharge temperature predict depths between 4.7 and 4.9 km (Table 2). Based on our conclusion that the discharge temperature is directly controlled by the total fluid upflow rate (Figure 4), the discrepancy with respect to the breccia formation depth suggests that upflow rates in the past were higher than today. Our simulations require a system-wide upflow rate of 322 kg/min and hence an increase by a factor of 3.6 to approximately match the 165 °C breccia formation temperature at ~2.5-km depth (Table 2). For such a high upflow rate the predicted, hypothetical paleo-discharge temperature is 126 °C, well above the current value of 50 ± 10 °C. The flow rate and the temperature distribution proposed for the paleo-system are consistent with those of two thermal spas producing from a similar fault-hosted orogenic setting at Brigerbad and Lavey-les-Bains in the nearby Rhone Valley (Sonney & Vuataz, 2008, 2009; Valla et al., 2016). Both sites are currently producing at 700 to 1,200 L/s

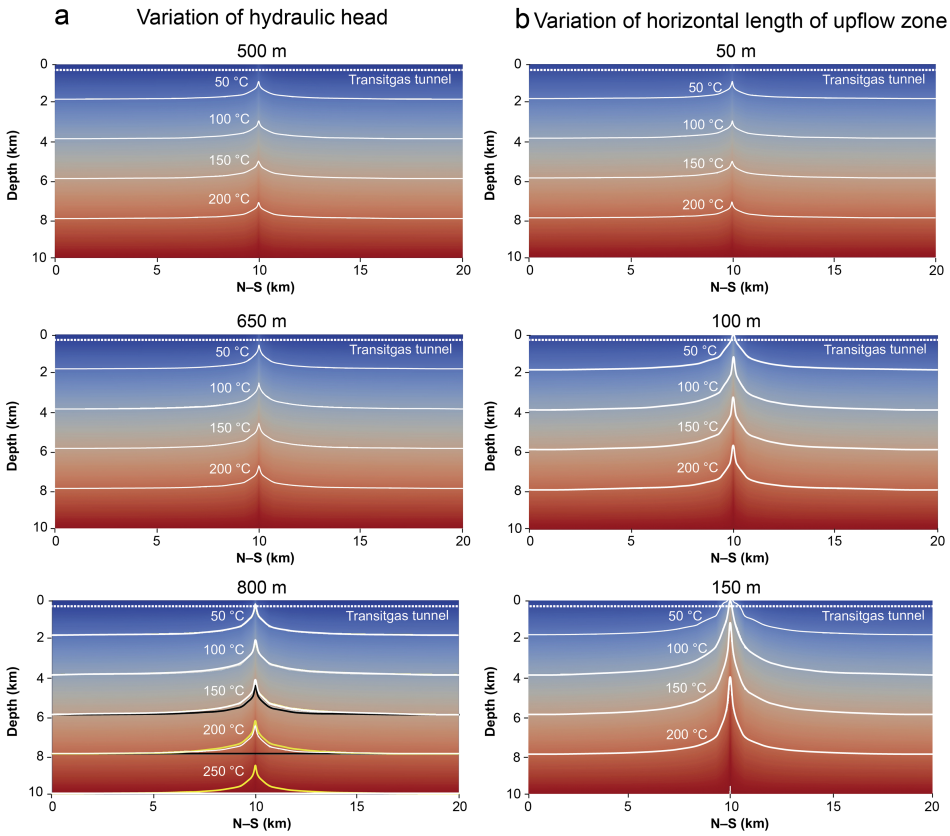

Figure 3. Simulated steady-state temperature distributions for various combinations of hydraulic head and horizontal length of the upflow zone parallel to the Grimsel Breccia Fault for a recharge penetration of 10 km. The panels show the model slice that is perpendicular to the fault and that includes the Transitgas tunnel (Figure 2a). (a) Temperature distribution for constant horizontal length of 75 m and variable hydraulic head. (b) Temperature distribution for constant hydraulic head of 750 m and variable horizontal length of the upflow zone. Note that the bottom panels correspond to the simulations that match observations of (a) the current system and (b) the fossil system. The bottom panel of (a) shows isotherms for penetration depths of 8 km (black), 10 km (white), and 12 km (yellow).

and temperature measurements in shallow boreholes reveal temperatures >100 °C at 1-km depth. Recalling that our model neglects mixing with cold surface water, these values compare well with the 322 kg/min and 126 °C tunnel discharge temperature estimated for the paleo-system at Grimsel Pass (Table 2).

Despite the simultaneous agreement of our model results with three calibration targets, it is impossible to quantify exactly the hydraulic head and the horizontal length of the current upflow system. This is because the model is underconstrained and other combinations of these parameters can equally reproduce the cooling-corrected discharge temperature and discharge rates of the warm springs, as well as the thermal anomaly along the Transitgas tunnel. A similar nonuniqueness applies to permeability variations, which have the same effect on the flow system as variable hydraulic head gradients (equation (2)) and were thus not explicitly explored in our sensitivity analysis. Finally, due to the low sensitivity of the system to the penetration depth of recharging meteoric water (Table 2), our simulations cannot further constrain the maximum penetration depth. Hence, the 10 km postulated by Diamond et al. (2018) remains a minimum value.

4.3. Thermal Anomaly

The simulation results allow us to evaluate the magnitude and 3-D extent of the thermal anomaly induced by the Grimsel Pass geothermal system. To do so, the temperature anomaly ΔT is calculated as the difference between the steady-state temperature distribution of the calibrated models and that corresponding to the natural background (i.e., distal) geothermal gradient. In Figure 6, the anomaly is illustrated for the

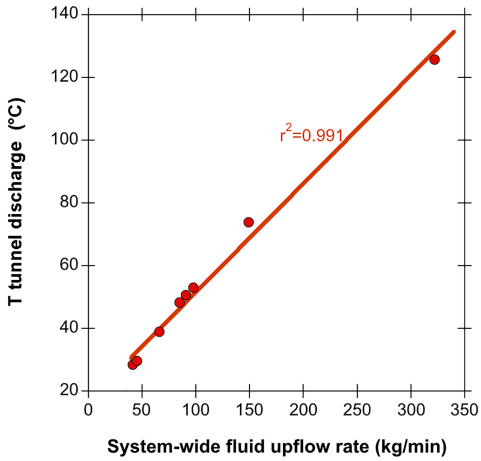

Figure 4. Correlation between simulated tunnel discharge temperatures and system-wide upflow rates, which were varied by running the model with various combinations of hydraulic head and horizontal lengths of the upflow zone (Table 2).

current and fossil systems in terms of a contour surface where $\Delta T = 15$ °C, resulting in vertically elongated ellipsoids. Interestingly, the maximum width of the ellipsoids appears some 4–5 km above the base of the upflow zone in the model. This is because the temperature difference at the lower model boundary is zero (Figure 2) and a certain vertical flow distance is required before ΔT evolves to a steady state. At shallower levels than its maximum width, the thermal anomaly decreases due to conductive cooling toward the 4 °C surface temperature. Similarly to the recorded temperature profile in the tunnel (Figure 1b), the simulated 3-D temperature anomaly is much wider than the actual upflow zone. In reality, however, the magnitude of the anomaly is likely lower in the uppermost kilometer owing to advective cooling by surface water infiltration, which was not considered in our model. In the case of the fossil system, our simulation predicts a maximum horizontal extent of the $\Delta T = 15$ °C anomaly of about 3×3 km (Figure 6b), despite the active upflow zone being limited to 150×100 m.

From the calculated temperature difference ΔT, the anomalous heat H (i.e., the heat in excess of that provided by the background conductive temperature profile) was calculated according to

$$H = \sum_i C_P \times \rho \times V_i \times \Delta T_i \quad (4)$$

where C_p (J kg^{-1} K^{-1}) is the heat capacity of the rock at constant pressure (with a temperature dependency obtained by interpolating heat capacity measurements on a granitic sample similar to the Southwest Aar Granite in Miao et al. (2014), ρ refers to the bulk rock density (2,660 kg/m^3), V_i (m^3) is the volume of grid block i, and ΔT_i (K) denotes the temperature difference between the steady state considering fluid flow and the initial conductive temperature distributions in block i. To calculate the anomalous heat available for an exploitable petrothermal reservoir size, equation (4) was integrated over 1-km depth intervals, resulting in values of 200–3,000 PJ/km (Figure 6).

5. Implications for Exploration for Orogenic Geothermal Systems

The calibrated model indicates that significant thermal anomalies are associated with orogenic spring systems even at low system-wide upflow rates (<100 kg/min), such as in the case of the studied system (Figure 6a). Moreover, the spatial coincidence between fossil and recent hydrothermal manifestations demonstrates that these systems can persist, even if only intermittently, over several million years.

The heat excesses shown in Figure 6 can be converted to theoretical geothermal power outputs by dividing by time and by assuming a thermal recovery factor of 5% (Aravena et al., 2016) during an exploitation period of 20 years. This yields values of 13–94 MW per km depth for the current Grimsel Pass system and 36–222 MW per km depth for the fossil system. Due to the limited extent of the active fluid upflow zone (Figure 2), however, orogenic geothermal systems may need to be stimulated in order to increase the permeability of the hydraulically inactive zones and thereby enable exploitation of their stored heat via doublet-type water circulation. Even though the host faults may be seismically dormant, this step could of course add to the challenge of maintaining induced seismicity at an acceptable level (Bachmann et al., 2011). Moreover, based on the simulated temperature distribution for the current situation at Grimsel Pass (Figure 3a), drilling to a depth of about 3.5 km is required to reach temperatures that allow production of electricity (>120 °C). This inferred depth does not represent a significant benefit versus nominally hot-dry rock systems in central Europe such as at Soultz, France or Basel, Switzerland, where geothermal gradients are somewhat higher at 37–39 °C (Alt-Epping et al., 2013; Genter et al., 2010). Therefore exploration for orogenic hot-spring systems in mountainous terrains should focus on deeply-rooted sites similar to Grimsel Pass, but with higher flow rates. This conclusion follows from our results that high upflow rates increase the 3-D size of the induced thermal anomaly as well as increasing the temperature at a specific depth (Figure 3 and Table 2). Larger and hotter anomalies than the one at Grimsel Pass further ensure a longer exploitation lifetime, which is

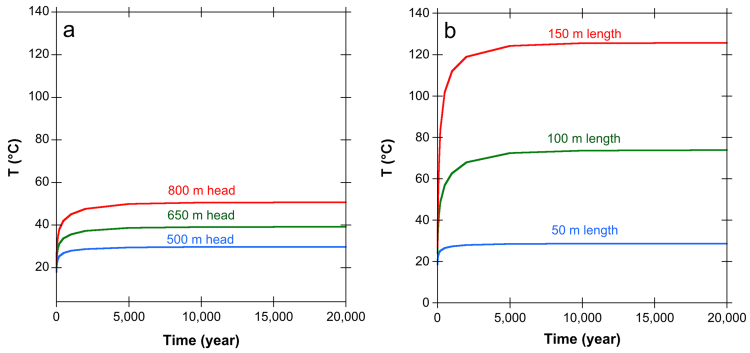

Figure 5. Simulated temporal evolution of discharge temperatures in the tunnel as a function of horizontal length of the upflow zone, hydraulic head, and a fixed recharge penetration depth of 10 km. (a) Horizontal length of 75 m and variable head. (b) Constant hydraulic head of 750 m and variable horizontal length of the upflow zone.

important given that it takes at least several hundred years of undisturbed upflow for such resources to renew (Figure 5).

In the Central Alps, more promising examples of orogenic geothermal systems are present within the same fault-hosted setting at Brigerbad and Lavey-les-Bains in the nearby Rhone Valley (Sonney & Vuataz, 2009; Valla et al., 2016). At both sites, upflow rates and local geothermal gradients are comparable to those revealed by our simulations of the fossil Grimsel Pass system, which implies heat anomalies more than double that of the current Grimsel Pass system (Figure 6 and Table 2). However, according to the systematics inferred from our modeling, the Brigerbad and Lavey-les-Bains sites have higher potential than even the

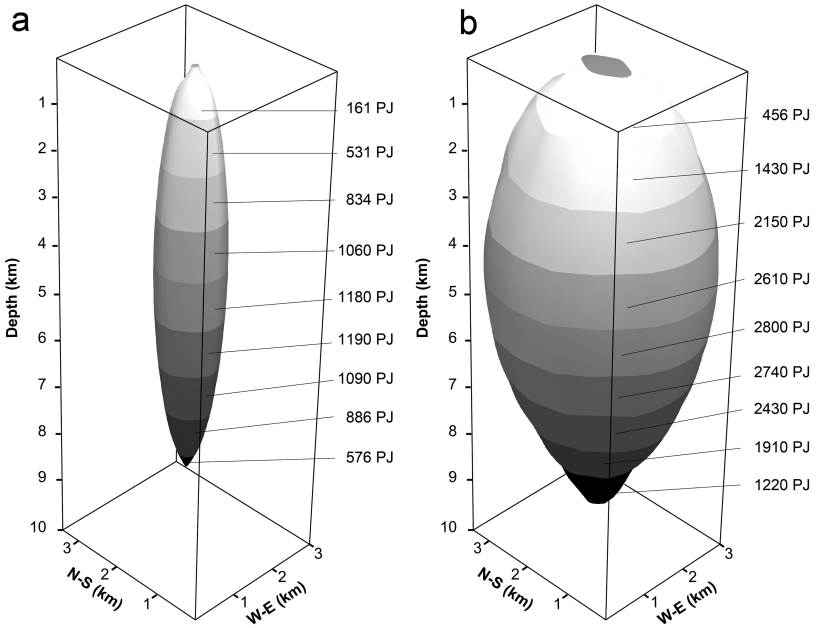

Figure 6. Anomalous heat per km depth calculated for (a) the model calibrated to the current Grimsel Pass hydrothermal system and (b) the model run that reproduces the breccia formation temperature of 165 °C at a depth of ~2.5 km and hence corresponds to the fossil system (Table 2). The shape of the anomalies are illustrated in terms of the $\Delta T = 15$ °C contour surfaces determined from the difference between the steady-state temperature distribution of the calibrated models (Table 2) and the distal background geothermal gradient. Due to their limited extent, the anomalies are shown for a cuboid with a base of 3.5 km × 3 km, located in the center of the total 3-D model domain (Figure 2).

fossil system at Grimsel Pass because they discharge at the valley floor, where hydraulic head gradients and thus upflow rates reach maximum values for a given fault zone permeability and depth of meteoric water penetration. Moreover, the simulations suggest, in accord with the formation temperatures of the mineralized breccias, that the 120 °C isotherm required for electricity production lies at about 2-km depth in such systems (Figure 3b, bottom panel), thereby favoring their accessibility for exploitation.

Finally, based on the observed lack of sensitivity of the shallow temperature anomaly to the penetration depth of recharging meteoric water (Figure 3a, bottom panel), the actual penetration depth does not constitute a key parameter for the exploitation potential of orogenic geothermal systems, as long as the penetration is deep enough to yield temperatures well above the 120 °C threshold for electricity production.

6. Summary and Conclusions

We have developed a new approach to assess the shape, dimensions, and magnitude of the subsurface thermal anomalies in fault-hosted orogenic geothermal systems, which does not rely on deep borehole or geophysical information. This entails combining surface observations of warm springs and fossil hydrothermal mineralization to constrain 3-D thermal–hydraulic numerical modeling. By removing the cooling effect of infiltrating surface water in the top kilometer of the system, our simulations reveal the systematic behavior of the upflow zone: for a fixed length of upflow, hypothetical discharge temperatures as well as the size of the thermal anomaly are controlled by the total, system-wide fluid upflow rate; upflow rates are in turn controlled by the cross section of the hydraulically active fracture zones, their permeability, and the hydraulic head gradient driving the flow. The influence of cold water infiltration into the top of the system will vary from site to site, as has been addressed in previous studies (e.g., Forster & Smith, 1989).

We have calibrated our model against current temperatures and flow rates of thermal springs discharging into a shallow tunnel beneath Grimsel Pass and against the pattern of temperatures along that tunnel wall. This reveals that large ellipsoidal plumes of anomalous heat (10^2–10^3 PJ/km in excess of that dictated by the background geothermal gradient) are generated by orogenic geothermal systems even at low system-wide upflow rates on the order of 100 kg/min. Due to conductive heating of the host rock, these anomalies have much larger footprints than the hydraulically active upflow zones, implying that stimulation measures may be required to exploit them for petrothermal power production. At these low upflow rates, the nominal temperature threshold for electricity production (>120 °C) is not reached at depths shallower than ~3.5 km. However, comparing the calibrated model to the formation temperature of a hydrothermal breccia representing the fossil geothermal system at Grimsel Pass suggests the paleo-system operated at higher flow rates and generated a thermal anomaly about double that of the current system. In this case, the plume corresponds to a theoretical power output of 40–220 MW at 5% recovery and the 120 °C cutoff for electricity production is reached at <2-km depth.

Building on the recent confirmation that meteoric water may penetrate up to 10 km into orogenic faults, our study demonstrates that mountainous orogenic belts without igneous activity and with only low background geothermal gradients (e.g., 25 °C/km) are surprisingly promising plays for petrothermal power production, although renewal rates are on the order of centuries. Our simulations imply that exploration should focus on major valley floors because there the hydraulic head gradients and thus upflow rates and heat anomalies reach maximum values.

Acknowledgments
We thank Transitgas AG for kindly granting access to their pipeline tunnel at Grimsel Pass. Discussions with University of Bern colleagues Thomas Belgrano, Alfons Berger, Daniel Egli, and Marco Herwegh are appreciated. This research was conducted within National Research Programme NRP 70 "Energy Turnaround," funded by Swiss National Science Foundation (SNF) grant 407040_153889 to L.W. Diamond. Geothermal research at the University of Bern is supported by the Swiss Competence Center for Energy Research–Supply for Electricity (SCCER-SoE). Two anonymous reviewers kindly provided constructive comments. All data required to run our simulations and to support our conclusions are provided in the tables and figures of the manuscript, which can also be downloaded at https://doi.org/10.5281/zenodo.3380483.

References

Alt-Epping, P., Diamond, L. W., Häring, M. O., Ladner, F., & Meier, D. B. (2013). Prediction of water–rock interaction and porosity evolution in a granitoid-hosted enhanced geothermal system, using constraints from the 5 km Basel-1 well. *Applied Geochemistry*, *38*, 121–133. https://doi.org/10.1016/j.apgeochem.2013.09.006

Aravena, D., Muñoz, M., Morata, D., Lahsen, A., Parada, M. Á., & Dobson, P. (2016). Assessment of high enthalpy geothermal resources and promising areas of Chile. *Geothermics*, *59*(Part A), 1–13. https://doi.org/10.1016/j.geothermics.2015.09.001

Asta, M. P., Gimeno, M. J., Auqué, L. F., Gómez, J., Acero, P., & Lapuente, P. (2010). Secondary processes determining the pH of alkaline waters in crystalline rock systems. *Chemical Geology*, *276*(1-2), 41–52. https://doi.org/10.1016/j.chemgeo.2010.05.019

Bachmann, C. E., Wiemer, S., Woessner, J., & Hainzl, S. (2011). Statistical analysis of the induced Basel 2006 earthquake sequence: introducing a probability-based monitoring approach for Enhanced Geothermal Systems. *Geophysical Journal International*, *186*(2), 793–807. https://doi.org/10.1111/j.1365-246X.2011.05068.x

Barker, A. J., Bennett, D. G., Boyce, A. J., & Fallick, A. E. (2000). Retrogression by deep infiltration of meteoric fluids into thrust zones during late-orogenic rapid unroofing. *Journal of Metamorphic Geology*, *18*(3), 307–318. https://doi.org/10.1046/j.1525-1314.2000.00257.x

Belgrano, T. M., Herwegh, M., & Berger, A. (2016). Inherited structural controls on fault geometry, architecture and hydrothermal activity: an example from Grimsel Pass, Switzerland. *Swiss Journal of Geosciences*, *109*(3), 345–364. https://doi.org/10.1007/s00015-016-0212-9

Berger, A., Mercolli, I., & Gnos, E. (2016) Geological Map of the Aar Massif, Tavetsch and Gotthard Nappes 1:100000. Landesgeologie der Schweiz.

Bodmer, P. (1982). *Geothermal Map of Switzerland: Schweizerische geophysikalisssche Kommission*. Bern, Switzerland: Kümmerly und Frey.

Bossart, P., & Mazurek, M. (1991). Grimsel Test Site Structural Geology and water flow-paths in the migration shear zone. Nagra Technical Report, NTB 91-12, 1-55.

Butler, R. W. H., Harris, N. B. W., & Whittington, A. G. (1997). Interactions between deformation, magmatism and hydrothermal activity during active crustal thickening; a field example from Nanga Parbat, Pakistan Himalayas. *Mineralogical Magazine*, *61*(404), 37–52. https://doi.org/10.1180/minmag.1997.061.404.05

Cartwright, I., & Buick, I. S. (1999). The flow of surface-derived fluids through Alice Springs age middle-crustal ductile shear zones, Reynolds Range, central Australia. *Journal of Metamorphic Geology*, *17*(4), 397–414. https://doi.org/10.1046/j.1525-1314.1999.00205.x

Cheng, Y., & Renner, J. (2018). Exploratory use of periodic pumping tests for hydraulic characterization of faults. *Geophysical Journal International*, *212*(1), 543–565. https://doi.org/10.1093/gji/ggx390

Craw, D. (1997). Fluid inclusion evidence for geothermal structure beneath the Southern Alps, New Zealand. *New Zealand Journal of Geology and Geophysics*, *40*(1), 43–52. https://doi.org/10.1080/00288306.1997.9514739

Craw, D., Koons, P. O., Zeitler, P. K., & Kidd, W. S. F. (2005). Fluid evolution and thermal structure in the rapidly exhuming gneiss complex of Namche Barwa–Gyala Peri, eastern Himalayan syntaxis. *Journal of Metamorphic Geology*, *23*, 829–845. https://doi.org/10.1111/j.1525-1314.2005.00612.x

Diamond, L. W., Wanner, C., & Waber, H. N. (2018). Penetration depth of meteoric water in orogenic geothermal systems. *Geology*, *46*(12), 1063–1066. https://doi.org/10.1130/G45394.1

Dzikowski, M., Josnin, J. Y., & Roche, N. (2016). Thermal Influence of an Alpine Deep Hydrothermal Fault on the Surrounding Rocks. *Groundwater*, *54*(1), 55–65. https://doi.org/10.1111/gwat.12313

Egli, D., Baumann, R., Küng, S., Berger, A., Baron, L., & Herwegh, M. (2018). Structural characteristics, bulk porosity and evolution of an exhumed long-lived hydrothermal system. *Tectonophysics*, *747-748*, 239–258. https://doi.org/10.1016/j.tecto.2018.10.008

Egli, D., Glotzbach, C., Valla, P. G., Berger, A., & Herwegh, M. (2018). Low temperature thermochronometry (apatite and zircon (U-Th)/He) across an active hydrothermal zone (Grimsel Pass, Swiss Alps). EGU General Assembly 2018, Vienna: Geophysical Research Abstracts, 52, 2749-2765.

Ferguson, G., Grasby, S. E., & Hindle, S. R. (2009). What do aqueous geothermometers really tell us? *Geofluids*, *9*(1), 39–48. https://doi.org/10.1111/j.1468-8123.2008.00237.x

Forster, C., & Smith, L. (1989). The influence of groundwater flow on thermal regimes in mountainous terrain: A model study. *Journal of Geophysical Research*, *94*(B7), 9439–9451. https://doi.org/10.1029/JB094iB07p09439

Genter, A., Goerke, J., Graff, J.-J., Cuenot, N., Krall, G., Schindler, M., & Ravier, G. (2010). Current Status of the EGS Soultz Geothermal Project (France) Paper presented at the World Geothermal Congress, Bali, Indonesia, 25-29 April.

Grasby, S. E., Ferguson, G., Brady, A., Sharp, C., Dunfield, P., & McMechan, M. (2016). Deep groundwater circulation and associated methane leakage in the northern Canadian Rocky Mountains. *Applied Geochemistry*, *68*, 10–18. https://doi.org/10.1016/j.apgeochem.2016.03.004

Grasby, S. E., & Hutcheon, I. (2001). Controls on the distribution of thermal springs in the southern Canadian Cordillera. *Canadian Journal of Earth Sciences*, *38*(3), 427–440. https://doi.org/10.1139/e00-091

Herwegh, M., Berger, A., Baumberger, R., Wehrens, P., & Kissling, E. (2017). Large-scale crustal-block-extrusion during late Alpine collision. *Scientific Reports*, *7*(1), 413. https://doi.org/10.1038/s41598-017-00440-0

Hochstein, M. P., & Yang, Z. (1995). The Himalayan Geothermal Belt (Kashmir, Tibet, West Yunnan). In M. L. Gupta, & M. Yamano (Eds.), *Terrestrial heat flow in geothermal energy in Asia*, (pp. 331–368). New Delhi: Oxford and IBH Publishing.

Hofmann, B. A., Helfer, M., Diamond, L. W., Villa, I. M., Frei, R., & Eikenberg, J. (2004). Topography-driven hydrothermal breccia mineralization of Pliocene age at Grimsel Pass, Aar massif, Central Swiss Alps. *Schweizerische Mineralogische und Petrographische Mitteilungen*, *84*, 271–302. https://doi.org/10.5169/seals-63750

International-Formulation-Committee (1967). *Formulation of the Thermodynamic Properties of Ordinary Water Substance*. Düsseldorf, Germany: IFC Secretariat.

Jenkin, G. R. T., Craw, D., & Fallick, A. E. (1994). Stable isotopic and fluid inclusion evidence for meteoric fluid penetration into an active mountain belt; Alpine Schist, New Zealand. *Journal of Metamorphic Geology*, *12*(4), 429–444. https://doi.org/10.1111/j.1525-1314.1994.tb00033.x

Keusen, H. R., Ganguin, J., Schuler, P., & Buleti, M. (1989). Felslabor Grimsel: Geologie. Nagra. Nagra Technical Report, NTB, 87-14.

Kuhlmann, U., & Gaus, I. (2014). Inverse modelling of the FEBEX in situ test using iTOUGH2. Nagra Arbeitsbericht, NAB 14-20, 1-33.

Lazear, G. D. (2006). Evidence for deep groundwater flow and convective heat transport in mountainous terrain, Delta County, Colorado, USA. *Hydrogeology Journal*, *14*(8), 1582–1598. https://doi.org/10.1007/s10040-006-0058-8

López, D. L., & Smith, L. (1995). Fluid Flow in Fault Zones: Analysis of the Interplay of Convective Circulation and Topographically Driven Groundwater Flow. *Water Resources Research*, *31*(6), 1489–1503. https://doi.org/10.1029/95WR00422

McCaig, A. M., Wickham, S. M., & Taylor, H. P. (1990). Deep fluid circulation in alpine shear zones, Pyrenees, France: field and oxygen isotope studies. *Contributions to Mineralogy and Petrology*, *106*(1), 41–60. https://doi.org/10.1007/bf00306407

McKenna, J. R., & Blackwell, D. D. (2004). Numerical modeling of transient Basin and Range extensional geothermal systems. *Geothermics*, *33*(4), 457–476. https://doi.org/10.1016/j.geothermics.2003.10.001

Menzies, C. D., Teagle, D. A. H., Craw, D., Cox, S. C., Boyce, A. J., Barrie, C. D., & Roberts, S. (2014). Incursion of meteoric waters into the ductile regime in an active orogen. *Earth and Planetary Science Letters*, *399*, 1–13. https://doi.org/10.1016/j.epsl.2014.04.046

Miao, S. Q., Li, H. P., & Chen, G. (2014). Temperature dependence of thermal diffusivity, specific heat capacity, and thermal conductivity for several types of rocks. *Journal of Thermal Analysis and Calorimetry*, *115*(2), 1057–1063. https://doi.org/10.1007/s10973-013-3427-2

Moeck, I. S. (2014). Catalog of geothermal play types based on geologic controls. *Renewable and Sustainable Energy Reviews*, *37*, 867–882. https://doi.org/10.1016/j.rser.2014.05.032

Mulch, A., Teyssier, C., Cosca, M. A., Vanderhaeghe, O., & Vennemann, T. W. (2004). Reconstructing paleoelevation in eroded orogens. *Geology*, *32*, 525–528. https://doi.org/10.1130/g20394.1

Nesbitt, B. E., Muehlenbachs, K., & Murowchick, J. B. (1989). Genetic implications of stable isotope characteristics of mesothermal Au deposits and related Sb and Hg deposits in the Canadian Cordillera. *Economic Geology*, *84*, 1489–1506. https://doi.org/10.2113/gsecongeo.84.6.1489

Newell, D. L., Jessup, M. J., Hilton, D. R., Shaw, C. A., & Hughes, C. A. (2015). Mantle-derived helium in hot springs of the Cordillera Blanca, Peru: Implications for mantle-to-crust fluid transfer in a flat-slab subduction setting. *Chemical Geology*, *417*, 200–209. http://doi.org/10.1016/j.chemgeo.2015.10.003

Ota, K., Möri, A., Alexander, W. R., Frieg, B., & Schild, M. (2003). Influence of the mode of matrix porosity determination on matrix diffusion calculations. *Journal of Contaminant Hydrology*, *61*(1–4), 131–145. https://doi.org/10.1016/S0169-7722(02)00139-0

Pfeifer, H. R., Sanchez, A., & Degueldre, C. (1992). Thermal springs in granitic rocks from the Grimsel Pass (Swiss Alps): The late stage of a hydrothermal system related to Alpine Orogeny. In Y. K. Kharaka, & A. S. Maest (Eds.), *Proceedings of Water-Rock Interaction WRI–7*, (pp. 1327–1330). Park City, Utah: A.A. Balkema, Rotterdam, The Netherlands.

Preusser, F., Geyh, M. A., & Schlüchter, C. (2003). Timing of Late Pleistocene climate change in lowland Switzerland. *Quaternary Science Reviews*, *22*, 1435–1445. https://doi.org/10.1016/S0277-3791(03)00127-6

Preusser, F., Graf, H. R., Keller, O., Krayss, E., & Schlüchter, C. (2011). Quaternary glaciation history of northern Switzerland. *E&G Quaternary Science Journal*, *60*, 282–305. https://doi.org/10.3285/eg.60.2-3.06

Pruess, K., Oldenburg, C., & Moridis, G. (1999). *TOUGH2 users's guide, Version 2.0*, *Rep. LBNL-29400*, (). Berkeley, CA: Lawrence Berkeley National Labortory.

Reyes, A. G. (2015). Low-temperature geothermal reserves in New Zealand. *Geothermics*, *56*, 138–161. https://doi.org/10.1016/j.geothermics.2015.04.004

Reyes, A. G., Christenson, B. W., & Faure, K. (2010). Sources of solutes and heat in low-enthalpy mineral waters and their relation to tectonic setting, New Zealand. *Journal of Volcanology and Geothermal Research*, *192*(3–4), 117–141. https://doi.org/10.1016/j.jvolgeores.2010.02.015

Rybach, L., & Busslinger, A. (2013). Verification of rock temperature prediction along the Gotthard base tunnel - A prospect for coming tunnel projects. Paper presented at the Proceeding World Tunnel Congress 2013 Geneva, Switzerland.

Schaltegger, U. (1990). Post-magmatic resetting of Rb-Sr whole rock ages — a study in the Central Aar Granite (Central Alps, Switzerland). *Geologische Rundschau*, *79*(3), 709–724. https://doi.org/10.1007/BF01879210

Schneeberger, R., Mäder, U. K., & Waber, H. N. (2017). Hydrochemical and Isotopic (δ^2H, δ^{18}O, ^{3}H) Characterization of Fracture Water in Crystalline Rock (Grimsel, Switzerland). *Procedia Earth and Planetary Science*, *17*, 738–741. https://doi.org/10.1016/j.proeps.2016.12.187

Schotterer, U., Schürch, M., Rickli, R., & Stichler, W. (2010). Wasserisotope in der Schweiz - Neue Ergebnisse und Erfahrungen aus dem nationalen Messnetz ISOT. *Gas-Wasser-Abwasser (GWA)*, *12*, 1073–1081.

Sharp, Z. D., Masson, H., & Lucchini, R. (2005). Stable isotope geochemistry and formation mechanisms of quartz veins; Extreme paleoaltitudes of the Central Alps in the Neogene. *American Journal of Science*, *305*, 187–219. https://doi.org/10.2475/ajs.305.3.187

Sonney, R., & Vuataz, F.-D. (2008). Properties of geothermal fluids in Switzerland: A new interactive database. *Geothermics*, *37*(5), 496–509. https://doi.org/10.1016/j.geothermics.2008.07.001

Sonney, R., & Vuataz, F.-D. (2009). Numerical modelling of Alpine deep flow systems: a management and prediction tool for an exploited geothermal reservoir (Lavey-les-Bains, Switzerland). *Hydrogeology Journal*, *17*(3), 601–616. https://doi.org/10.1007/s10040-008-0394-y

Sonney, R., & Vuataz, F.-D. (2010). Remobilisation of deep Na-Cl waters by a regional flow system in the Alps: Case study of Saint-Gervais-les-Bains (France). *Comptes Rendus Geoscience*, *342*(2), 151–161. https://doi.org/10.1016/j.crte.2009.12.011

Spötl, C., & Mangini, A. (2002). Stalagmite from the Austrian Alps reveals Dansgaard-Oeschger events during isotope stage 3: implications for the absolute chronology of Greenland ice cores. *Earth and Planetary Science Letters*, *203*, 507–518. https://doi.org/10.1016/S0012-821X(02)00837-3

Stober, I., Zhong, J., Zhang, L., & Bucher, K. (2016). Deep hydrothermal fluid–rock interaction: the thermal springs of Da Qaidam, China. *Geofluids*, *16*, 711–728. https://doi.org/10.1111/gfl.12190

Sutherland, R., Townend, J., Toy, V., Upton, P., Coussens, J., Allen, M., et al. (2017). Extreme hydrothermal conditions at an active plate-bounding fault. *Nature*, *546*(7656), 137–140. https://doi.org/10.1038/nature22355

Taillefer, A., Soliva, R., Guillou-Frottier, L., Le Goff, E., Martin, G., & Seranne, M. (2017). Fault-Related Controls on Upward Hydrothermal Flow: An Integrated Geological Study of the Têt Fault System, Easter Pyrénées (France). *Geofluids*, *2017*, 1–19. https://doi.org/10.1155/2017/8190109

Upton, P., Craw, D., Yu, B., & Chen, Y.-G. (2011). Controls on fluid flow in transpressive orogens, Taiwan and New Zealand. *Geological Society, London, Special Publications*, *359*(1), 249–265. https://doi.org/10.1144/sp359.14

Upton, P., Koons, P. O., & Chamberlain, C. P. (1995). Penetration of deformation-driven meteoric water into ductile rocks: Isotopic and model observations from the Southern Alps, New Zealand. *New Zealand Journal of Geology and Geophysics*, *38*(4), 535–543. https://doi.org/10.1080/00288306.1995.9514680

Valla, P. G., Rahn, M., Shuster, D. L., & van der Beek, P. A. (2016). Multi-phase late-Neogene exhumation history of the Aar massif, Swiss central Alps. *Terra Nova*, *28*(6), 383–393. https://doi.org/10.1111/ter.12231

Vernon, A. J., van der Beek, P. A., Sinclair, H. D., Persano, C., Foeken, J., & Stuart, F. M. (2009). Variable late Neogene exhumation of the central European Alps: Low-temperature thermochronology from the Aar Massif, Switzerland, and the Lepontine Dome, Italy. *Tectonics*, *28*, TC5004. https://doi.org/10.1029/2008TC002387

Vernon, A. J., van der Beek, P. A., Sinclair, H. D., & Rahn, M. K. (2008). Increase in late Neogene denudation of the European Alps confirmed by analysis of a fission-track thermochronology database. *Earth and Planetary Science Letters*, *270*(3–4), 316–329. https://doi.org/10.1016/j.epsl.2008.03.053

Waber, H. N., Schneeberger, R., Mäder, U. K., & Wanner, C. (2017). Constraints on evolution and residence time of geothermal water in granitic rocks at Grimsel (Switzerland). *Procedia Earth and Planetary Science*, *17*, 774–777. https://doi.org/10.1016/j.proeps.2017.01.026

Wanner, C., Peiffer, L., Sonnenthal, E., Spycher, N., Iovenitti, J., & Kennedy, B. M. (2014). Reactive transport modeling of the Dixie Valley geothermal area: Insights on flow and geothermometry. *Geothermics*, *51*, 130–141. https://doi.org/10.1016/j.geothermics.2013.12.003

Wickham, S. M., Peters, M. T., Fricke, H. C., & O'Neil, J. R. (1993). Identification of magmatic and meteoric fluid sources and upward- and downward-moving infiltration fronts in a metamorphic core complex. *Geology*, *21*(1), 81–84. https://doi.org/10.1130/0091-7613(1993)021<0081:IOMAMF>2.3.CO;2

Witherspoon, P. A., Wang, J. S. Y., Iwai, K., & Gale, J. E. (1980). Validity of cubic law for fluid-flow in a deformable rock fracture. *Water Resources Research*, *16*(6), 1016–1024. https://doi.org/10.1029/WR016i006p01016

4.3. Geochemical evidence for regional and long-term topography-driven groundwater flow in an orogenic crystalline basement (Aar Massif, Switzerland)

Source:

Wanner C., Waber H. N. and Bucher K. (2020) Geochemical evidence for regional and long-term topography-driven groundwater flow in an orogenic crystalline basement (Aar Massif, Switzerland). *Journal of Hydrology* **581**, 124374.

Contribution by the Author (CW):

CW developed the general idea and CW carried out all the simulations. CW had the lead in data interpretation and manuscript writing.

Journal of Hydrology 581 (2020) 124374

Contents lists available at ScienceDirect

Journal of Hydrology

journal homepage: www.elsevier.com/locate/jhydrol

Research papers

Geochemical evidence for regional and long-term topography-driven groundwater flow in an orogenic crystalline basement (Aar Massif, Switzerland)

Christoph Wanner[a,*], H. Niklaus Waber[a], Kurt Bucher[b]

[a] Rock-Water Interaction Group, Institute of Geological Sciences, University of Bern, Baltzerstrasse 3, CH-3012 Bern, Switzerland
[b] Mineralogy and Petrology, University of Freiburg, Albertstr. 23b, D-79104 Freiburg, Germany

ARTICLE INFO

This manuscript was handled by Huaming Guo, Editor-in-Chief, with the assistance of Mingjie Chen, Associate Editor

Keywords:
Fractured rock
Numerical modeling
Swiss Alps
Geothermal energy
Toughreact
Stable water isotopes

ABSTRACT

Detailed knowledge about the circulation of meteoric water in non-magmatic, orogenic belts is fundamental for assessing the potential of such settings for geothermal power production, as well as their use as potential groundwater resources. To get more general insight into these hydrological processes, we have conducted regional (20 × 10 × 9 km) thermal-hydraulic-chemical (THC) simulations of meteoric water circulation in the orogenic, crystalline basement of the Aar Massif in the Central Alps, Switzerland. Model results were compared to numerous geochemical and isotopic analyses of groundwater discharging into the longest and deepest tunnel of the world, the Gotthard railbase tunnel located within the model domain. Explicitly considering the surface topography in our model was sufficient to reproduce all key characteristics of the tunnel inflows (salinity, temperature, $\delta^{18}O$ values, and up- and downward directed flow zones inferred from geochemical constraints). This quantitatively confirms that surface topography operates as the governing control on fluid flow in orogenic crystalline basements with meteoric water infiltration occurring at high altitude and resulting upward directed flow zones along major valleys. Owing to low flow rates below 2 m $year^{-1}$, computed residence times of the longest flow paths were above 100 k years, confirming that groundwater and/or porewater in orogenic crystalline basements may act as an archive for paleohydrologic variations. Moreover, simulation results show that down to the lower model boundary at 9 km depth, penetration of meteoric water is not limited by the decrease in permeability with depth that is typically observed in granitic rocks. This suggests that advective fluid transport in orogenic crystalline basements may reach the brittle-ductile transition zone and that infiltrating meteoric water can attain temperatures well above 150 °C. We conclude that orogenic geothermal systems are promising plays for geothermal power production.

1. Introduction

Fluid flow in crystalline basements is enabled by the occurrence of interconnected fracture networks (Stober and Bucher, 2007; Bucher and Stober, 2010) and the presence of hydrological driving forces (Ingebritsen and Manning, 1999). Although mountain topography has been long ago recognized as key driver for meteoric water circulation in non-magmatic, orogenic belts (e.g. Hubbert, 1940; Forster and Smith, 1988; Ge et al., 2008, Goderniaux et al., 2013), direct observations linking downward and upward directed flow zones are still sparse. On the one hand, numerous studies have described the ascent of meteoric water along deep-reaching faults (i.e. along permeability anomalies) based on the occurrence of thermal springs and their chemical and isotopic composition. Examples include sites in the Canadian Rocky Mountains (Grasby et al., 2016), the Southern Alps of New Zealand (Reyes et al., 2010), the central European Alps (Pfeifer et al., 1992; Sonney and Vuataz, 2008; Diamond et al., 2018), the Black Forest (Stober et al., 1999; Stober and Bucher, 2015), the Pyrenees (Taillefer et al., 2018), the Himalayas (Craw et al., 2005), and locations in China (Bucher et al., 2009; Stober et al., 2016). Other manifestations of ascending fluids include fossil hydrothermal breccias (Hofmann et al., 2004), and positive temperature anomalies (i.e. above those predicted by the local geothermal gradient) recorded along tunnels and boreholes (Pastorelli et al., 2001; Valla et al., 2016). On the other hand, shallow (< 2 km) infiltration of meteoric water into crystalline rocks is evidenced by the occasional occurrence of large inflows (> 100 L s^{-1}) of cold meteoric water into highway or railway tunnels, associated with negative temperature anomalies (Hunziker et al., 1990; Maréchal et al., 1999; Pastorelli et al., 2001). The maximum penetration of meteoric water, however, is still under debate and suggested depths range from 5 to 23 km (Diamond et al., 2018, and references therein). The rheology of the continental crust changes with increasing

* Corresponding author.
E-mail address: wanner@geo.unibe.ch (C. Wanner).

https://doi.org/10.1016/j.jhydrol.2019.124374
Received 9 August 2019; Received in revised form 29 October 2019; Accepted 17 November 2019
Available online 19 November 2019
0022-1694/

depth from brittle to ductile deformation behavior. Below the brittle-ductile transition zone located in a depth of about 12–14 km at a typical crustal geothermal gradient of 25–30 °C km^{-1} (Wintsch et al. 1995; Stober and Bucher, 2007), Darcy-flow is not possible (Stober and Bucher, 2015) and other transport mechanisms are responsible for fluid transfer through the ductile crust (Connolly and Podladchikov, 2015). Thus, the studies reporting the greatest depths invoke penetration of meteoric water below the brittle-ductile transition zone (Wickham et al., 1993; Cartwright and Buick, 1999). The large range in postulated penetration depths, however, may also be inherited from a variation in methodology ranging from stable water isotope analyses of minerals and fluid inclusions in hydrothermal rocks to solute geothermometry and geochemical modeling applied to thermal springs, and does not necessary imply penetration below the brittle-ductile transition zone (see Diamond et al., 2018 and references therein). In any case, it reflects the limited knowledge about structural controls on meteoric water infiltration into crystalline basements and on how infiltration zones are actually connected to deep-reaching fault zones, along which meteoric water can again reach the surface and discharge as thermal springs eventually (Belgrano et al., 2016). This forms a particular challenge for assessing orogenic, crystalline basements as potential groundwater resources (Ge et al., 2008), and for evaluating their potential for geothermal power production (Wanner et al., 2019).

Here we present results from regional 3D (20 × 10 × 9 km) thermal-hydraulic-chemical (THC) simulations of fluid flow in the Aar Massif in the Central Alps, Switzerland. The study area constitutes an ideal site to get more insight into regional hydrogeological processes in orogenic crystalline basements because, (i) numerous chemical and isotopic analyses of water inflows along the World's longest and deepest tunnel, the Gotthard railbase tunnel (Bucher et al., 2012) provide a unique opportunity to study such processes, (ii) the area includes both major valleys as well as mountain peaks, which appear to correlate with distinct upward and downward directed flow zones at the tunnel level, and (iii) major (i.e. regional) structural and thermal anomalies are absent. To overcome the shortage of hydraulic measurements in this regional system, we use the available chemical and isotopic data to constrain our model and to quantitatively evaluate whether mountain topography indeed operates as the first order driving force for regional meteoric water circulation.

2. Geological and hydrogeological setting

The 57 km long Gotthard rail base tunnel crosses the Central Alps at a base level of ca. 500 m a.s.l. The construction was simultaneously carried out in five individual sections, which was enabled by drilling vertical access shafts. Our study exclusively deals with the Amsteg section of the tunnel, corresponding to a 11.5 km long section in the northern part of the tunnel (Fig. 1), because only for this tunnel section groundwater inflows were systemically sampled with a high spatial resolution during construction. The construction took place between 2003 and 2006 using a 400 m long tunnel-boring machine.

The geology and hydrogeology along the Amsteg section of the tunnel have been previously described in detail and are summarized in the following. The section crosscuts the crystalline basement of the Aar Massif, which represents a major NE-SW striking complex of the Variscan basement (120 × 20 km in size). The Aar Massif was overprinted by Alpine greenshist-type metamorphism and associated deformation (Abrecht, 1994; Schaltegger, 1994; Labhart, 1999). The different geological units exposed along the Amsteg section are made of granites, gneisses, and volcanic rocks (e.g. metarhyolites) (Bucher et al., 2012). Mineralogically, these rocks have similar compositions and are dominated by quartz, albite, K-feldspar and chlorite, minor amounts of biotite and muscovite, and accessory pyrite and calcite (Bucher et al., 2012). The thickness of the rock column above the tunnel is between 300 and 2200 m (Fig. 2).

North–South compression during the Alpine orogeny resulted in steeply dipping geological units and E–W trending foliation (Steck and Hunziker, 1994). Brittle deformation caused by exhumation of the Aar Massif and subsequent cooling formed shear fractures and joint systems (Choukroune and Gapais, 1983; Laws et al., 2003). High deformation zones currently strike parallel to the geological units and steeply dip to the S or N (Laws et al., 2003). Thus, the tunnel crosscuts the steeply dipping units and the nearly vertical fracture system at an angle close to 90° (Fig. 2). Based on a hydraulic test performed in a zone with major water inflows in the nearby Sedrun section of the tunnel (Fig. 1), the hydraulic conductivity in such highly deformed zones may be as high as 10^{-6} m s^{-1} (Bucher et al., 2012). In contrast, the geometric mean of the hydraulic conductivity across the entire Sedrun section ranges from 3 to 6 × 10^{-9} m s^{-1} (Masset and Loew, 2013).

During drilling of the Amsteg section, 122 groundwater samples were collected from water conducting fractures before these were permanently sealed with concrete. Owing to the induced pressure drop, the water inflow rate from individual fractures ranged from 0.0004 to 6 L s^{-1}. Full chemical analyses were performed on all 122 groundwater samples with the results being reported in Bucher et al. (2012). Groundwater from the various inflows range from freshwater to strongly mineralized water (TDS = 171–3231 mg L^{-1}). Their chemical composition varies from the general Na-CO_3 and Na-SO_4 chemical types up to about 700 mg L^{-1} total mineralization to the general Na-Cl chemical type at elevated mineralization (> 700 mg L^{-1}). All samples are characterized by an alkaline *pH* ranging from 8.3 to 10.4. In their chemical characteristics, the groundwater samples from the Gotthard railway tunnel thus resemble many other crystalline groundwaters of similar total mineralization (e.g. Nordstrom et al. 1989, Pearson et al. 1991, Waber et al. 2017, Schneeberger et al. 2019). The chemical composition is inherited from water-rock interaction reactions between infiltrating meteoric water and the granitic mineralogy of the crystalline basement. Beside such advective reactive transport along interconnected fracture networks (i.e. the fracture porosity), there are strong indications for a diffusive uptake of mainly Cl, Na, SO_4, Li, and Br from porewater present in the intact, non-fractured, and low permeable rock matrix (i.e. the matrix porosity). This porewater presumably constitutes a remnant of a hydrothermal fluid that evolved during alpine metamorphism (Seelig and Bucher, 2010; Wanner et al., 2017). The important role of matrix porewater on the chemical and isotopic composition of groundwater in crystalline settings originates from strong concentration gradients between fracture groundwater and matrix porewater that are continuously balanced by (mainly) diffusion over time (Waber et al., 2012).

The surface hydrology above the Amsteg section of the tunnel is controlled by the catchment of the Maderaner Valley including the Etzli side Valley (Fig. 1). At the town of Amsteg, the two valleys drain into the Reuss, a major alpine river in Switzerland, at an average annual discharge of 9 m^3 s^{-1} (FOEN, 2015). The average annual precipitation rate in the catchment is altitude dependent and ranges from 1200 mm at 500 m a.s.l. to 1500 mm at 2000 m a.s.l. (MeteoSwiss, 2019).

3. Constraints from geochemical data

Among the numerous physical and chemical parameters reported for groundwater samples collected along the Amsteg section (Bucher et al., 2012), the temperature, *pH*, as well as the concentrations of Cl and Si are particularly useful to constrain our THC simulations as described below. In addition to the published chemical analyses, in this study we carried out analyses of the stable isotopes of the water molecule on 30 out of the 122 groundwater samples collected along the Amsteg section. All these geochemical constraints contribute to establishing a conceptual model of the hydrodynamic functioning of the pre-tunnel stage of the studied crystalline massif and they serve to constrain our THC model as described below.

3.1. Stable water isotopes

Stable isotopes of water, expressed as $\delta^{18}O$ and $\delta^{2}H$ in per mil (‰) relative to Vienna Standard Mean Ocean Water (VSMOW), were analyzed at the Institute of Geological Sciences, University of Bern, by

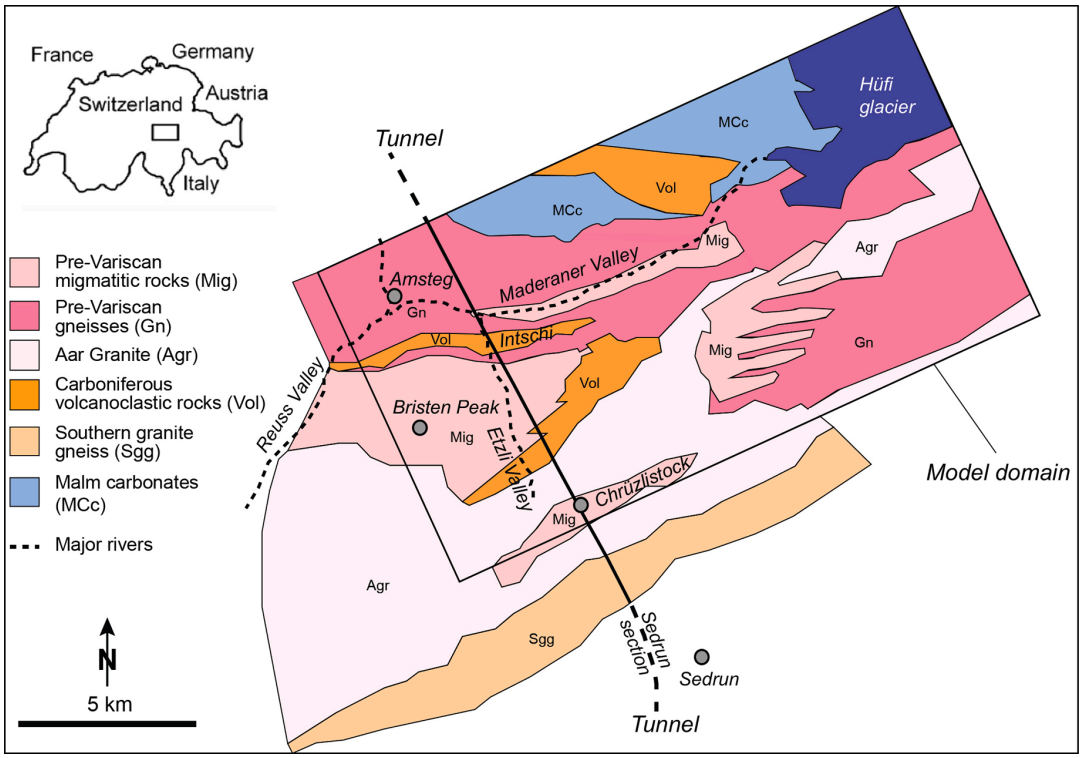

Fig. 1. Geological map of the eastern part of the Aar Massif (modified after Abrecht, 1994). The solid segment of the tunnel refers to the Amsteg section, for which numerous groundwater samples were collected and chemically analyzed (Bucher et al. 2012). The black rectangular illustrates the horizontal extent of the model domain.

isotope ratio infrared spectroscopy (IRIS) using a Picarro L2120-i cavity ring down spectrometer (CRDS) with vaporization module V1102-i, coupled to an HTC PAL auto-sampler (CTC Analytics). Post-run correction of oxygen and hydrogen stable isotope measurements was conducted according to van Geldern and Barth (2012). The analytical error (1σ) was ± 0.1‰ for $\delta^{18}O$ and ± 1.0‰ for $\delta^{2}H$ based on multiple measurements of internal and IAEA standards. Duplicate analyses agreed well within this error. In contrast to the immediately conducted chemical analyses (Bucher et al., 2012), those of the stable water isotopes was performed up to 10 years after the samples were collected during construction of the Amsteg section (2003–2006). To test whether evaporation occurred during sample storage, the concentrations of major cations and anions (Cl^-, Na^+, and SO_4^{2-}) were re-measured at the Institute of Geological Sciences, University of Bern by ion chromatography using a Metrohm ProfIC AnCat MCS IC system. The analytical uncertainty was better than ± 5% based on multiple measurements of high-grade, commercial standard solutions.

Since evaporation was identified, measured $\delta^{18}O$ and $\delta^{2}H$ values were corrected as described in the Supporting Information. Measured and evaporation-corrected values are both listed in Table S1 (Supporting Information) together with the re-measured ion concentrations. Compared to the ion concentrations reported in Bucher et al. (2012), our groundwater samples showed an increase of up to 15% corresponding to the evaporated fraction of the original sample volume. The corrected $\delta^{18}O$ and $\delta^{2}H$ values plot on the global meteoric water line (GMWL) (Fig. 3), demonstrating that all groundwater samples originate from meteoric water that has infiltrated at the surface.

Along the Amsteg section, $\delta^{18}O$ and $\delta^{2}H$ values of our groundwater samples do not show any particular spatial trend (Fig. 2b). This is likely due to the fact that they represent a homogenized (i.e. "averaged") isotope signature of meteoric water infiltrated at different altitudes and different times in the past. The latter is relevant because the residence time of meteoric water circulating in the Aar Massif is substantial and may reach several 10 k years such as demonstrated by the lack of detectable ^{14}C in meteoric water penetrating up to 10 km deep before discharging as thermal springs below Grimsel Pass also located within the Aar Massif (Waber et al., 2017; Diamond et al., 2018). Thus, the main constraint from stable isotope analyses for our model is that all groundwater samples discharging at the tunnel level originate from meteoric water that has infiltrated at the surface at some point in the past. Moreover, given that our groundwater $\delta^{18}O$ and $\delta^{2}H$ values are well within the range of current precipitation in the Aar Massif (e.g. meteorological stations Grimsel and Guttannen, FOEN, 2014) (Fig. 3), infiltration has mainly occurred during times where the average climatic conditions were similar to those in the current Holocene interglacial period (< 11.5 ka). In turn, infiltration was limited or even absent during cold temperature periods and the glacial cycles because this would have likely resulted in $\delta^{18}O$ and $\delta^{2}H$ values at the lower limit or even outside the range of current precipitation (Fig. 3). This is consistent with recent hydrogeological investigations of similar crystalline massifs in France, for which it was suggested that infiltration at high altitude mainly occurred during the Holocene interglacial period, while it was much lower during the preceding glaciation period (Maréchal et al., 1999; Thiebaud et al., 2010; Dzikowski et al., 2016). Hence, the subsurface residence time of meteoric water in our model is constrained to Holocene times (< 11.5 ka) or similar interglacial periods in the past such as the Eemian interglacial dated at 130–115 ka (Preusser et al., 2011).

3.2. Physico-chemical evolution of tunnel inflows along the Amsteg section

3.2.1. Saturation state of chalcedony and quartz

Bucher et al. (2012) have suggested that for "low" *pH* tunnel inflows (*pH* < 9), the dissolved silica concentration is mainly controlled by the solubility of chalcedony, whereas above pH 9.5 it is controlled by quartz. Calculating the saturation state of chalcedony in groundwater

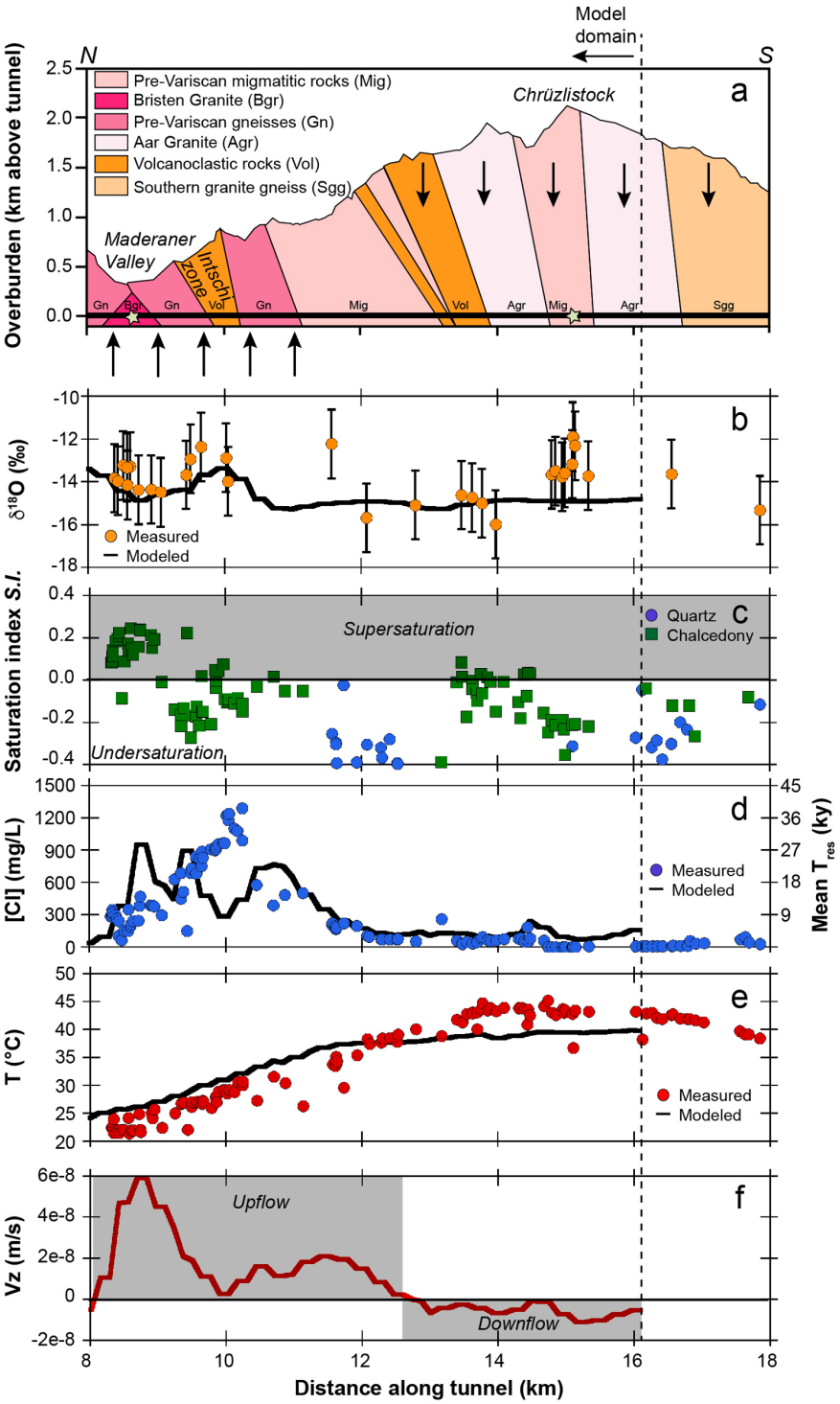

Fig. 2. Profiles through the Amsteg section of the Tunnel. (a) Geological units and downward and upward directed flow zones inferred form geochemical constraints. Star symbols denote locations, for which breakthrough curves are shown in Fig. 10 (modified from Bucher et al., 2012). (b) Measured and computed $\delta^{18}O$ values of groundwater samples. (c) Saturation indices of quartz ($pH > 9.5$) and chalcedony ($pH < 9.5$) in groundwater samples. (d) Measured and computed Cl concentrations of groundwater samples, as well as corresponding average residence times inferred from the computed Cl concentrations. (e) Measured and computed temperatures of groundwater samples. (f) Z-component of the computed flow vectors, suggesting that downflow ($v_Z < 0$ m s^{-1}) occurs at high altitude while a upwards directed flow zone ($v_Z > 0$ m s^{-1}) exists beneath the Maderaner Valley at distances less than 12.5 km along the tunnel.

samples of $pH < 9.5$ and of quartz in those of $pH > 9.5$, using TOUGHREACT V3 (Xu et al., 2014) in combination with the Soltherm.H06 database (Reed and Palandri, 2006), demonstrates that most groundwater samples are near saturation or slightly under-saturated with respect to the silica-controlling phase (saturation index $S.I. = -0.4$ to 0.1) (Fig. 2c). The only exception is observed for tunnel inflows collected beneath the only major valley along the Amsteg section, the Maderaner Valley at ca. 9 km along the tunnel, which show a significant supersaturation ($S.I. > 0.1$) with respect to chalcedony (Fig. 2a, c). Owing to the lower solubility of quartz, this would also be the case if these samples were solubility controlled by quartz instead of chalcedony despite showing pH values below 9.5. Supersaturation with respect to quartz and/or chalcedony is a common feature of thermal waters and it is observed due to (i) the solubility decrease associated

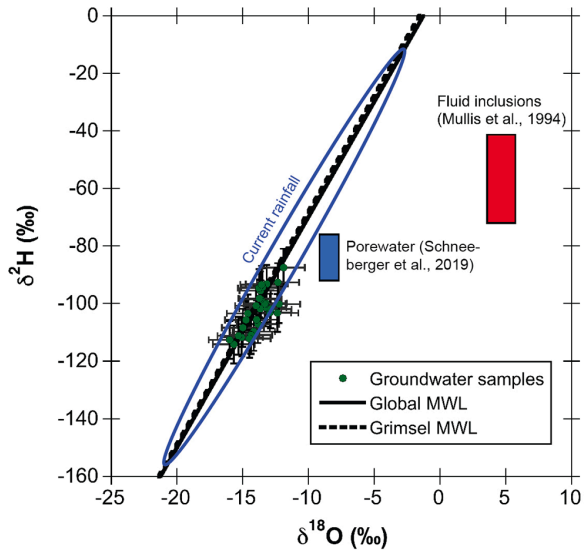

Fig. 3. Stable O–H isotope signatures of 30 groundwater samples collected along the Amsteg section of the tunnel, all showing close association with meteoric water lines (MWL), as well as with current rainfall at the nearby Grimsel and Guttannen meteorological station (FOEN, 2014). Rectangles denote isotope signatures of porewater samples collected in similar geological units of the Aar Massif in the nearby Grimsel Test Site (Schneeberger et al., 2019), as well as in fluid inclusions of fissure quartz collected from different granitic units in the Aar Massif and representing ancient metamorphic fluids (Mullis et al., 1994). Error bars denote combined analytical and numerical errors (see Supporting Information for more details).

with the decrease in temperature upon ascent and cooling of thermal fluids, and (ii) slow precipitation kinetics of quartz and chalcedony in combination with fast upflow (Wanner et al., 2014; Diamond et al., 2018). Thus, based on the observed supersaturation, there is strong geochemical evidence that the groundwater samples collected beneath the Maderaner Valley have experienced temperatures above the discharge temperature and hence have infiltrated into the tunnel from below (Fig. 2a). While we do not attempt to reconstruct the calculated saturation indices, the upflow directed flow zone proposed to occur below the Maderaner Valley serves as important constraint for our model.

3.2.2. Cl concentration profile

The Cl concentration profile along the Amsteg section shows a distinct peak with a maximum concentration of 1300 mg L^{-1} at about 10 km along the tunnel where it intersects a volcanoclastic unit called Intschi zone (Fig. 2a, d). The peak is located roughly 1 km south of the lowest point of the Maderaner Valley where the Cl concentration in the groundwater is around 400 mg L^{-1}. Plotting Cl concentrations against discharge temperatures (Fig. 4a) demonstrates that groundwater samples collected along the Amsteg section fall into two distinct groups. With the exception of two outliers, the first group consists of all samples collected up to a distance of 11.5 km along the tunnel. In these samples, Cl and the discharge temperature are linearly correlated and include all samples forming the Cl peak discussed above. The second group includes the samples at a distance greater than 11.5 km along the tunnel. These samples are characterized by generally low Cl concentrations (< 200 mg L^{-1}) that are not correlated with the discharge temperature.

Since elevated Cl concentrations such as in case of the first group (< 11.5 km) are consistent with longer flow paths and continuous uptake of solutes from the postulated ancient porewater source (Seelig and Bucher, 2010; Bucher et al., 2012; Wanner et al., 2017), we suggest that all groundwater samples of the first group (< 11.5 km) have infiltrated from below, although only the ones collected beneath the lowest point of the Maderaner Valley show evidence for temperatures above the discharge temperature based on the calculated silica phase saturation indices (Fig. 2c). For groundwater samples with low Cl concentrations such as in case of the second group, we suggest that they have infiltrated into the tunnel from above. This is consistent with results from reactive transport modeling (Wanner et al., 2017) showing that the composition of groundwater samples collected at about 15 km beneath the highest peak of the Amsteg section, the Chrüzlistock, and showing very low Cl concentrations (< 3 mg/L) can be explained by a rather simple 1D reactive transport model considering the reaction of infiltrating meteoric water with the granitic mineralogy only (Wanner et al., 2017). Consequently, these particular samples have likely infiltrated into the tunnel from above, consistent with shorter residence times and essentially no uptake of Cl from the postulated ancient porewater source. Owing to their low Cl concentrations and based on the temperature vs. Cl plot (Fig. 4a), the same downward directed flow may apply for all groundwater samples belonging to the second group of samples (> 11.5 km).

The upflow and downflow directed flow zones identified from geochemical constraints (Fig. 2) will serve as calibration target for our model. Moreover, since Cl likely originates from an ancient porewater source (Seelig and Bucher, 2010; Wanner et al., 2017), Cl is used as a residence time tracer in our model and the Cl concentration profile recorded along the Amsteg section (Fig. 2d) will also serve as constraint for our model.

3.2.3. Temperature profile

The temperature of the groundwater samples collected along the Amsteg section closely follows the surface topography (Fig. 2a, e). In fact, the correlation between temperature and overburden is strongly linear and nearly perfect (Fig. 4b). Taking into account the supersaturation with respect to chalcedony and quartz calculated for groundwater samples collected beneath the Maderaner Valley (Fig. 2c), this observation suggests that the upflow rate of the proposed upward directed flow zone is too low to generate any temperature anomaly (i.e. temperatures above those predicted by the local geothermal gradient). Together with the observed tunnel inflow rates, the recorded temperature profile will serve as constraint for our model.

3.3. Correlations in groundwater samples collected along the Bristen Granite

Groundwater samples collected where the tunnel intersects the Bristen Granite beneath the Maderaner Valley (ca. 9 km along the tunnel) show strong linear correlations between major as well as minor solutes and Cl, and between $\delta^{18}O$ and Cl (Fig. 5). Such correlations are typical manifestations of binary fluid mixtures. Elevated Cl, Na, SO_4, Li, and Br concentrations (Wanner et al., 2017) as well as the small tunnel overburden of about 300 m (Fig. 2a) indicating elevated permeability (Fig. 6), suggest that these groundwaters represent a binary mixture between an ascending, highly-mineralized fluid endmember and dilute meteoric water originating from the surface such as demonstrated for other locations within the Aar Massif (Diamond et al., 2018). Significant admixture of dilute meteoric water to the ascending fluid endmember is consistent with the observation that the maximum tunnel inflow rate (6 L s^{-1}) inherited from a major water ingress of shallow water from the surface was recorded at this particular segment of the tunnel. Moreover, it is consistent with the negative linear correlation observed between $\delta^{18}O$ and Cl (Fig. 5c), suggesting that the diluting meteoric water (low Cl, high $\delta^{18}O$) has infiltrated at a low altitude, for instance at the bottom of the Maderaner Valley at about 800 m a.s.l. In turn, this correlation (Fig. 5c) implies that the ascending fluid endmember (high Cl, low $\delta^{18}O$) has originally infiltrated at an altitude that is above the Maderaner Valley before eventually discharging into the tunnel from below. This results in longer residence times and more Cl uptake from the proposed porewater source yielding elevated Cl concentrations, eventually (Fig. 2d). The Cl uptake, however, is not accompanied by a shift of $\delta^{18}O$ values away from

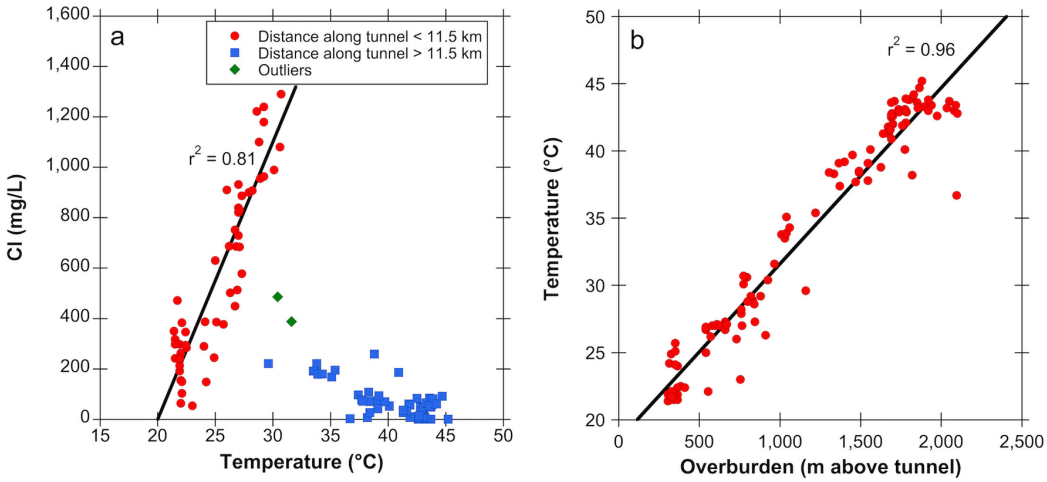

Fig. 4. Correlations observed for groundwater samples collected along the Amsteg section of the tunnel. (a) Linear correlation between Cl concentrations and the discharge temperatures observed for samples collected at a distance of less than 11.5 km along the tunnel. (b) Linear correlation between temperature and overburden, demonstrating that the regional geotherm of 25 °C km^{-1} (Vernon et al., 2008) controls the discharge temperature and that thermal anomalies are absent.

the GMWL towards less negative values, despite that matrix porewater collected within the Aar Massif as well as ancient metamorphic fluids trapped in fluid inclusions show elevated $\delta^{18}O$ and $\delta^{2}H$ values (Mullis et al., 1994, Schneeberger et al., 2019; Fig. 3). Compared to Cl, the shift in $\delta^{18}O$ (and likewise $\delta^{2}H$) is limited because (i) infiltrating meteoric water has a very high H_2O concentration of 55.6 mol L^{-1} (i.e. [H_2O] = 1 kg L^{-1} at T = 4 °C), (ii) the isotopic signature of infiltrating meteoric water covers a large range that does not substantially differ from the range of expected porewater (Fig. 3), and (iii) the concentration gradient controlling diffusive uptake of heavy $\delta^{18}O$ is given by the gradient of the $^{1}H_2{}^{18}O$ and $^{1}H_2{}^{16}O$ isotopologues (i.e. same molecule but different mass), which are in the per mil range per distant unit only. In case of Cl, the low concentrations of infiltrating meteoric water (μM range) as well as the strong concentration gradient (M range per distant unit) result in a significantly higher uptake from the ancient porewater source. While fully assessing the causes for the missing $\delta^{18}O$ shift is beyond the scope of the present work, its absence is consistent with analyses of mineralized thermal springs collected within the Aar Massif (Diamond et al., 2018) and groundwater samples collected from the nearby Gotthard highway tunnel (Pastorelli et al., 2001). In any case, the absence of observable $\delta^{18}O$ shifts during meteoric water circulation forms an important constraint for our model.

The identified admixture of cold meteoric water implies that the Cl and Si concentrations and hence the silica supersaturation of the deep fluid endmember ascending where the tunnel intersects the Bristner Granite beneath the Maderaner Valley at about 9 km along the tunnel is actually higher than the obtained values (Fig. 2c, d). Thus, without dilution with meteoric water possibly caused by the tunnel construction work, the peak in the Cl profile (Fig. 2d) might have actually occurred there and not as currently observed at about 10 km where the tunnel intersects the volcanoclastic Intschi zone (Fig. 2a). The correlations identified for the Bristen Granite groundwaters samples, however, fail to match the corresponding parameters of the Intschi zone (Fig. 5). This demonstrates that the two units are not directly linked hydrologically, although they both lie within the upward directed flow zone postulated to occur at a distance < 11.5 km along the tunnel (Fig. 2a). The absence of a direct flow connection between the two units serves as additional constraint for our model.

4. Model setup

Our forward thermal-hydraulic-chemical simulations aim to assess the role of surface topography on controlling regional meteoric water circulation in orogenic crystalline basements. Therefore, simulations were performed for a large 3D domain (20 × 10 × 9 km) including the entire Amsteg section of the Gotthard railbase tunnel, and by explicitly considering the surface topography combined with stable water isotopes.

4.1. Numerical model

All simulations were performed using TOUGHREACT V3 (Xu et al., 2014), a well-established integral finite difference code for modeling coupled thermo-hydrodynamic-chemical processes in geothermal and volcanic systems (e.g., Wanner et al., 2014). All simulations were performed using equation-of-state EOS1, which simulates water and coupled heat flow in the single-phase state according to the mass balance equation

$$\frac{\partial M_{W,H}}{\partial t} = -\nabla F_{W,H} + q_{W,H} \quad (1)$$

where $M_{W,H}$ is the accumulation term for water M_W (kg m^{-3}) or heat M_H (J m^{-3}), $q_{W,H}$ are water or heat sinks (−) or sources (+) and $F_{W,H}$ refers to the water flux F_W (kg m^{-2} s^{-1}) or heat flux F_H (J m^{-2} s^{-1}). For fully saturated, single-phase flow problems F_W is equal to the Darcy flux u (m s^{-1})

$$u = -\frac{k}{\mu}(\nabla P - \rho g) \quad (2)$$

where k is the intrinsic permeability (m^2), μ is the water viscosity (Pa s), ∇P (Pa m^{-1}) is the water pressure gradient with respect to distance (i.e., hydraulic head gradient), ρ is the density of water (kg m^{-3}) and g is the acceleration due to gravity (m s^{-2}). Heat flux F_H (J m^{-2} s^{-1}) is defined as

$$F_H = C_M \times T \times \rho_M \times u - \lambda \times \nabla T \quad (3)$$

where C_M (J kg^{-1} K^{-1}) and ρ_M (kg m^{-3}) are the specific heat capacity and the density of the porous medium (rock + porewater), T (K) is the temperature of the porous medium, λ is the thermal conductivity of the wet rock (J s^{-1} m^{-1} K^{-1} = W m^{-1} K^{-1}), and ∇T (K m^{-1}) is the gradient in temperature between adjacent grid blocks. The porous medium parameters ρ_M and C_M are calculated as

$$\rho_M = (1 - \phi) \times \rho_R + \phi \times \rho_W \quad (4)$$

$$C_M = (1 - \phi) \times C_R + \phi \times C_W \quad (5)$$

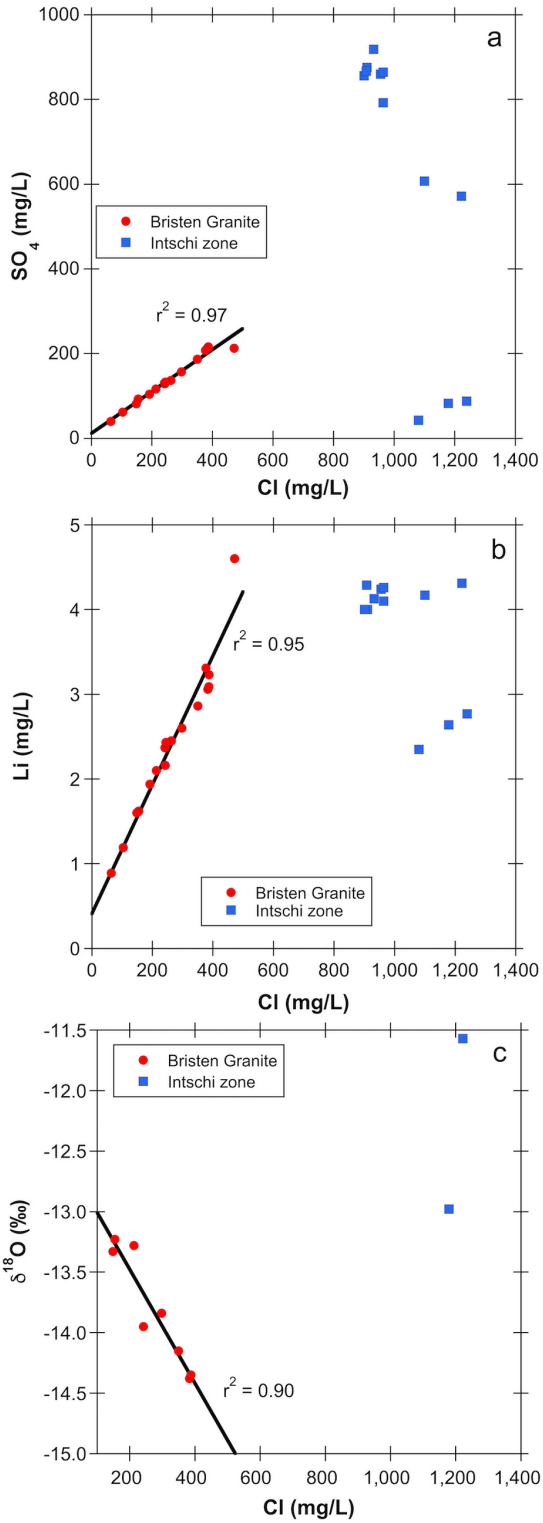

Fig. 5. Linear correlations observed for groundwater samples collected along the Bristen Granite unit below the Maderaner Valley at ca. 9 km along the tunnel (Fig. 2). (a) SO_4 vs. Cl. (b) Li vs. Cl. (c) $\delta^{18}O$ vs. Cl. None of the correlations match the compositions of the samples with the highest Cl concentrations, which were collected within the Intschi zone at ca. 10 km along the tunnel (Fig. 2d).

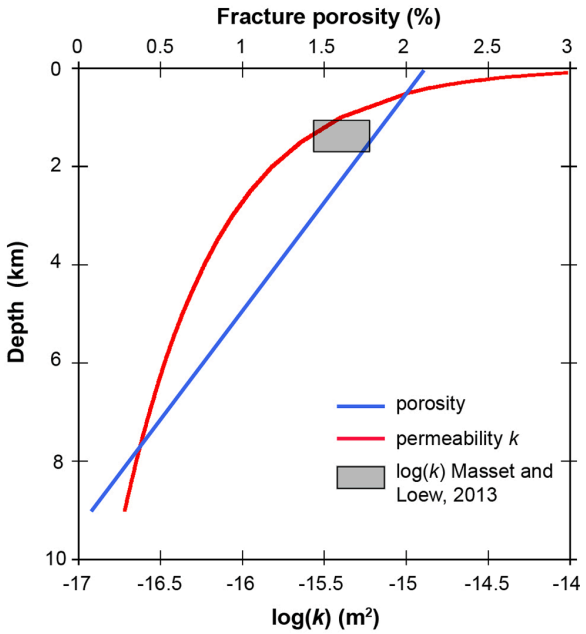

Fig. 6. Depth-dependent porosity and vertical permeability (z-direction) distribution used to run the numerical simulations. The gray rectangular denotes the range in permeability reported for the nearby Sedrun section (Masset and Loew, 2013). Compared to the vertical permeability, the one in x- and y-direction was reduced by a factor of 10 to account for the steeply dipping units and nearly vertical fracture systems (Fig. 2a), suggesting that flow is directed vertically.

where the subscripts $_R$ and $_W$ denote the corresponding rock and water values, respectively, and ϕ is the porosity. Equation EOS1 calculates the temperature dependence of water properties (e.g., density, specific enthalpy and viscosity) from the steam table equations given by the International Formulation Committee (1967).

4.2. Model geometry

Along the Amsteg section, the surface topography is mainly shaped by the Maderaner Valley and the surrounding mountain peaks. Therefore, the horizontal extent of the model was constrained by the catchment of the Valley covering an area of about 20 × 10 km (Figs. 1 and 7). This means that the southernmost part of the Amsteg section was not simulated. The upper model boundary was defined by numerically shaping an initially regular mesh with a digital elevation model (DEM) of the area using the "fit surface" PyTOUGH method (Croucher, 2015). Such approach eventually created an irregular mesh with a horizontal resolution of 250 × 250 m. The altitude of the lower model boundary was somewhat arbitrarily set to −5400 m a.s.l. to allow fluid circulation below the tunnel. The vertical extent of the grid blocks gradually increased from 150 m near the surface to a maximum extent of 600 m at altitudes below 0 m a.s.l., yielding a total of about 82,000 grid blocks.

In the absence of transmissivity, as well as fracture connectivity, spacing, and aperture data, and under consideration of the large model domain (20 × 10 × 9 km) the complex interconnected, hydraulically active fracture network was conceptionalized as a single (i.e. homogenously fractured) rock continuum, where the assigned porosity refers to the fracture porosity of the entire rock volume. This means that our simulations do not explicitly distinguish between advective flow along the hydraulically active fracture network of the Aar Massif and the diffusive and conductive interaction with the adjacent intact rock matrix. Similarly, since our model aims at unraveling the regional flow system, the model does not explicitly include the tunnel. As such, the

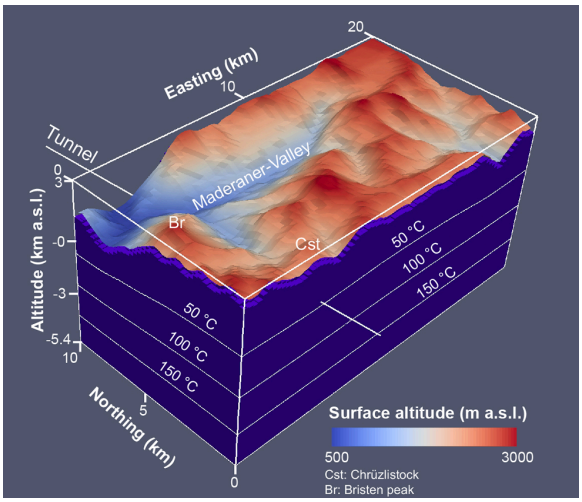

Fig. 7. Model geometry and initially specified conductive temperature distribution corresponding to a geothermal gradient of 25 °C km^{-1} (Vernon et al., 2008).

model neglects the pressure drop induced by the tunnel and simulation results refer to the pre-tunnel stage of the system.

4.3. Simulating stable water isotopes and the continuous uptake of Cl

The main benefits of using a fully coupled THC simulator such as TOUGHREACT are (i) to include the transport of stable water isotopes in terms of a water source tracer in our simulations and (ii) to adopt the continuous uptake of Cl from the proposed porewater source (Seelig and Bucher, 2010; Wanner et al., 2017). The fate of the three most abundant stable water isotopologues ($^1H_2{}^{16}O$, $^1H_2{}^{18}O$, $^1H^2H^{16}O$), corresponding to a cumulative abundance of > 99.9%, was simulated following the approach described by Singleton et al. (2005). To do so, $^1H_2{}^{18}O$ and $^1H^2H^{16}O$ were defined as primary species with distinct total concentrations in addition to the $^1H_2{}^{16}O$ species used by default. This allows calculating δ^2H and $\delta^{18}O$ values from the modeled $[^1H^2H^{16}O]/[^1H_2{}^{16}O]$ and $[^1H_2{}^{18}O]/[^1H_2{}^{16}O]$ total concentration ratios ($R_{modeled}$)

$$\delta = \left(\frac{R_{modeled}}{R_{VSMOW}} - 1\right) \times 1000 \quad (6)$$

where R_{VSMOV} refers to the corresponding ratios in VSMOW. For our simulations, δ^2H and $\delta^{18}O$ values were fixed at the upper model boundary to define altitude dependent values for the infiltrating meteoric water and to use them as water source tracer. In the absence of historical rainwater data, the actual $\delta^{18}O$ values were constrained by the long-term $\delta^{18}O$ monitoring of current rainwater collected along the nearby Grimsel transect yielding an average value of −13.25‰ at 1980 m a.s.l. (i.e. at the Grimsel station) and an altitude effect on $\delta^{18}O$ of −0.2‰ per 100 m elevation gain (Schotterer et al., 2010). The corresponding δ^2H values were defined by assuming that they lie on the GMWL (i.e., $\delta^2H = 8 \times \delta^{18}O + 10$; Schotterer et al., 2010), which is consistent with our stable water isotope analyses (Fig. 3). Except for the upper model boundary, $\delta^{18}O$ and δ^2H values were initially set to arbitrary values of −10 and −70‰, respectively (Table 1).

Since the model was defined as a single, fractured rock continuum, the uptake of Cl from the proposed ancient porewater source (Seelig and Bucher, 2010; Wanner et al., 2017) to the initially Cl free meteoric water was abstracted by specifying the kinetic release of Na and Cl from a generic solid NaCl source ($NaCl_{(s)} = Na^+ + Cl^-$) with a fixed dissolution rate of 3×10^{-14} mol $kg_{H2O}{}^{-1}$ s^{-1} (0.03 mg $kg_{H2O}{}^{-1}$ a^{-1}).

Table 1
Values and sources of parameters used in the numerical simulations.

Parameter	Value	Meaning/source
Dimension of model		
N-S and E-W	10 × 20 km	Extent of Maderaner-Valley catchment
Base of model	−5400 m a.s.l.	6 km below tunnel, allows simulating fluid flow below tunnel
Upper boundary	Surface topography	Digital elevation model
Hydraulic properties		
Vertical permeabililty (except lower boundary)	$\log k\ (m^2) = -1.38 \times \log(z) - 15.4$	Stober and Bucher (2007, 2015)
Permeability at lower boundary	10^{-34} m^2	Infinitely low to define a no flux boundary for fluid flow
Porosity	Linear decrease from 2.1 to 0.1	Maximum and minimum values measured in nearby Grimsel Test Site (Bossart and Mazurek, 1991). Linear behavior specified because no porosity–permeability relation available for the studied site.
Fixed pressure at surface	1 bar	Atmospheric pressure
Fixed pressure at lower boundary	685–718 bar	Hydrostatic pressure distribution assuming fully saturated conditions
Thermal properties		
Background surface temperature	4 °C	Annual mean at average altitude (1850 m a.s.l.)
Geothermal gradient	25 °C km^{-1}	Vernon et al. (2008)
Thermal conductivity of wet granite	3.34 W m^{-1} K^{-1}	Measurements in nearby Grimsel Test Site (Kuhlman and Gaus,2014)
Fixed T at lower boundary	186 °C	Allows considering heat flux across lower boundary corresponding to a geotherm of 25 °C km^{-1}. T = 186 °C results from altitude difference between the lower (−5400 m a.s.l.) and the mean of the upper boundary (1850 m a.s.l.)
Specific heat	920 J kg^{-1} K^{-1}	Result of inverse modeling of in-situ experiment in nearby Grimsel test site (Kuhlman and Gaus, 2014)
Rock density	2690 kg m^{-3}	Measurements in nearby Grimsel Test Site (Keusen et al., 1989)
Chemical parameters		
Fixed $\delta^{18}O$ at upper boundary	Altitude dependent (−10.9‰ at 800 m a.s.l;. −15.9‰ at 3300 m a.s.l.)	Schotterer et al. (2010)
Fixed δ^2H at upper boundary	Altitude dependent (−77.2‰ at 800 m a.s.l;. −117.2‰ at 3300 m a.s.l.)	Schotterer et al. (2010)
Initial $\delta^{18}O$ and δ^2H	−10 and −70‰	Arbitrary, outside of measured range
Initial Cl conc.	1e-10 mol $kg_{H2O}{}^{-1}$	Meteoric water assumed to be Cl free
$NaCl_{(s)}$ dissolution rate	3×10^{-14} mol $kg_{H2O}{}^{-1}$ s^{-1}	Calibrated to match shape of Cl proile along Amsteg section (Fig. 2d)

This rate was numerically estimated by approximating the Cl concentration profile observed along the Amsteg section (Fig. 2d). The calibrated rate agrees well with fracture area normalized Cl uptake rates of 0.07–0.12 mg m^{-2} a^{-1} estimated for groundwater circulating in the granitic basement in the region of Laxemar, Sweden (Waber et al., 2012). In Waber et al. (2012), the uptake of Cl from such porewater source was associated with a shift of $\delta^{18}O$ and $\delta^{2}H$ values away from the GMWL towards higher values, which was not observed for our samples (Fig. 3). Therefore, the uptake of water with significantly less negative $\delta^{18}O$ and $\delta^{2}H$ values than meteoric water from the proposed porewater source was neglected in our model.

4.4. Initial and boundary conditions

At the upper model boundary the temperature and pressure were prescribed to 1 bar and 4 °C, respectively. In doing so, we neglect the unsaturated zone and assume that the entire basement is fully saturated, which means that the water table is constrained by the topographic surface and that infiltration and exfiltration is allowed through the entire upper model boundary. Multiple studies have shown that this approximation is valid for the simulation of regional flow problems in orogenic crystalline settings (Tiedeman et al., 1998; Bossong et al., 2003; Caine et al., 2006; Taillefer et al., 2018). For our study, it is particularly justified by the lack of detailed information on the local water table and the rather large vertical model extent (≤9 km), for which the regional flow field is only weakly affected by the extent of the unsaturated zone. By allowing the flux of meteoric water through the upper model boundary during the entire course of our simulations, we assume (i) that the Hüfi-Glacier located < 3200 m a.s.l. in the N–E part of the model domain (Fig. 1) represents a hydrological-active, warm-based glacier and (ii) that the meteoric water infiltration rate during past glaciation periods remained constant. While assumption (i) is justified given that in the Alps, evidence for hydraulically active, warm-based glaciers up to an altitude of 2600 m a.s.l. has been reported even during the last glacial maximum (18 ka ago) when the mean annual temperature was 12 ± 3 °C lower than today (Peyron et al., 1998; Wirsig et al., 2016), (ii) represent an important model simplification of which the implications will be discussed together with the model results.

Initially, a hydrostatic pressure distribution and a typical regional conductive geothermal gradient of 25 °C km^{-1} (Vernon et al., 2008) were defined throughout the model domain (Fig. 7). The lateral and lower model boundaries were defined as no flux boundaries with respect to fluid flow whereas the lateral boundaries were defined as no flux boundaries for heat transport as well. The definition of the later model boundaries as no flux boundaries is justified by the absence of heat sources other than the one responsible for the regional geothermal gradient and because cross-catchment flow (i.e. across the horizontal boundaries) is likely negligible. Across the lower model boundary, conductive heat transport was allowed by fixing the temperature to 186 °C, which is consistent with the mean surface altitude of 1850 m a.s.l. within the model domain and a geothermal gradient of 25 °C km^{-1}.

The permeability of the fractured rock continuum (k) was defined as a function of depth according to the relation derived from hydraulic tests performed in similar settings worldwide (Stober and Bucher, 2007; Stober and Bucher, 2015),

$$\log(k) = -1.38 \times \log(z) - 15.4 \quad (7)$$

where z refers to the depth (km) below the surface and k is the intrinsic vertical permeability (m^2). Fig. 6 shows that this relation is able to match the permeability recorded along the nearby Sedrun section of the tunnel (Masset and Loew, 2013). To account for the steeply dipping units (Fig. 2a) and nearly vertical fracture systems suggesting that flow is directed vertically, a permeability anisotropy factor of 10 was considered between horizontal and vertical direction with higher values associated with the orientation of factures. Consequently, the specified permeability in x- and y- direction was 10 times lower than the one defined by equation (7). In analogy to the permeability, the porosity was also specified as a function of depth. In the absence of any information on the porosity–permeability relationship, our simulations consider a linear fracture porosity decrease with depth (Fig. 6). The maximum and minimum values (2.1 and 0.1%) were taken from Hg porosity measurements performed on gneisses and granites of a water conducting shear zone exposed in the nearby Grimsel Test Site (Bossart and Mazurek, 1991).

Other physical and thermal properties (e.g. density, thermal conductivity) were defined according to measurements performed in the nearby Grimsel Test Site (Keusen et al., 1989; Kuhlman and Gaus, 2014). All model parameter are listed in Table 1. Initial and boundary conditions for simulating the fate of Cl and stable water isotopes were defined as described above in detail, and the corresponding values are listed in Table 1.

5. Model results and discussion

5.1. General flow system

Selected results for the full model domain are shown in Figs. 8 and 9. Computed average linear vertical flow velocities (Fig. 8a) demonstrate that meteoric water infiltration occurs at high altitude ($v_z \leq 0$, lower limit of color scale), whereas upward directed flow zones are found beneath major valleys such as the Maderaner Valley ($v_z \geq 0$). The temporal evolution of $\delta^{18}O$ values displays "plumes" of water with low $\delta^{18}O$ values originating from the infiltration at high altitude (Fig. 9). These plumes reach the lower model boundary (−5.4 km a.s.l.) after a few 10 k years, and then migrate laterally before ascending towards the surface of major valleys where they yield isotopically light values as well. Because our model considers continuous uptake of Cl along flow paths, these regional circulation systems are also expressed by the simulated Cl concentration distribution at chemical steady state (Fig. 8b), which is achieved after about 150 ka during the course of the simulation (Fig. 10). Downward directed flow is indicated by the increase of Cl along the flow path towards greater depth (Fig. 8b). In turn, upward directed flow below major valleys is manifested by elevated Cl concentrations indicating maximum residence times.

Despite the infiltration of cold water at the surface (T = 4 °C) and the upflow of heated water from the lower model boundary (T = 186 °C), these flow zones only yield minor temperature anomalies compared to the initially specified conductive temperature distribution (Fig. 8 vs. Fig. 7). This is because flow velocities and hence water fluxes are rather small and heat transport is dominated by conduction rather than by advection. Below the Maderaner Valley for instance, the computed upflow velocity is about 2 m $year^{-1}$, whereas the model predicts a downflow velocity below the Chrüzlistock of less than 0.5 m $year^{-1}$ (Fig. 2f).

5.2. Model results vs. geochemical constraints

The comparison between parameter profiles observed along the Amsteg section of the tunnel and the corresponding simulation results is given in Fig. 2. Despite that the tunnel was not explicitly considered in our model, the agreement is quite good. First, our model predicts positive z-velocities and thus ascending water up to a distance of about 12.5 km along the tunnel and negative z-velocities indicating downflow for the remainder of the Amsteg section (Fig. 2f). These flow zones are consistent with the interpretation of the spatial distribution of the silica phase saturation state (Fig. 2c), the Cl concentrations (Fig. 2d), and the Cl vs. temperature correlation observed in groundwater exfiltrating into the tunnel (Fig. 4a), although the computed upflow zone extends up to 12.5 along the tunnel while Fig. 4a suggests that the first (i.e. ascending) group of groundwater samples extends up to 11.5 km only. The maximum upflow velocity was computed for the segment where the tunnel crosscuts the Bristen Granite beneath the Maderaner Valley (at ca. 9 km) (Fig. 2f). This is the only segment along the tunnel where

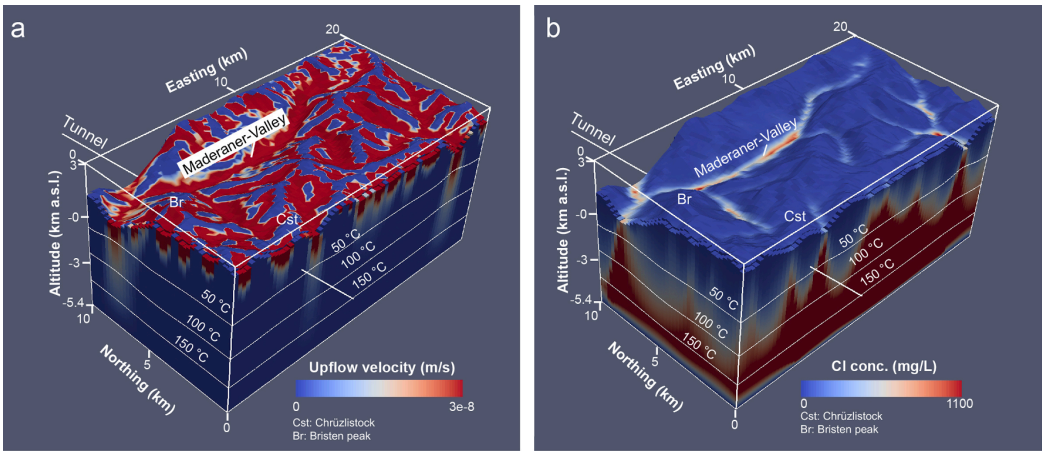

Fig. 8. Selected model output for the full model domain at steady state. (a) Upflow velocity distribution (i.e. positive z-component of the computed average linear flow vectors), suggesting that downflow ($v_z < 0$ m s^{-1}, lower limit of color scale) occurs at high altitude, whereas upwards directed flow zones ($v_z > 0$ m s^{-1}) are found beneath major valleys. (b) Cl-concentration distribution, demonstrating that water discharging into major valleys show the highest Cl-concentrations and hence experienced the longest residence times. Steady state isotherms are shown on (a) and (b) and their similarity to the initially specified temperature distribution (Fig. 7) demonstrates that the computed flow system does not cause significant thermal anomalies.

the collected groundwater was supersaturated with respect to quartz and chalcedony (Fig. 2c), which is indicative of an ascending fluid (Wanner et al., 2014). The simulated coupled thermal-hydraulic processes further yield a temperature profile that matches the observed profile within reasonable uncertainty (Fig. 2e). The total flux of ascending water computed for the entire Bristen Granite segment was 0.008 L s^{-1}, which is ca. 850 times lower than the total discharge recorded along this particular segment (6.97 L s^{-1}). Because the tunnel was not explicitly considered in our model, however, it is challenging to directly compare computed flow rates to those measured in the tunnel. The strong discrepancy is likely related to the facts that the construction of the tunnel induced a strong pressure drop of likely more than 100 bar (Masset and Loew, 2013) and that with the chosen model setup (e.g. discretization/resolution, not considering the tunnel), shallow mixing with dilute meteoric water from the surface is not fully captured by the model.

Second, the model is capable of reconstructing the shape of the observed Cl concentration profile (Fig. 2d), although it over- and underestimates the Cl concentration along the Bristen Granite and the Intschi zone, respectively. In analogy to the flow rate discrepancy, the overestimation of the Cl concentration along the Bristen Granite (at ca. 9 km) is due to the fact that shallow mixing with dilute meteoric water from the surface as identified from the corresponding correlations (Fig. 5) is not fully captured with the chosen model setup. In contrast, the underestimation along the Intschi zone (at ca. 10 km along the tunnel) is likely due to a different chemical composition of the porewater in the differently composed lithologies, which was not considered by the model. Differences in the composition of the porewater serving as an important Cl source is suggested by the lack of correlations between groundwater samples from the Bristen Granite and the Intschi zone (Fig. 5). The model is consistent with such explanation in the sense that the computed origin of meteoric water discharging along the Bristner Granite and the Intschi zone strongly differs. Computed streamlines (Fig. 11) suggest that groundwater discharging along the Bristen Granite originates to the South-West near the Bristen peak, whereas groundwater samples ascending beneath the Intschi zone originate to the South-East in the vicinity of the Chrüzlistock.

Third, the simulated $\delta^{18}O$ values along the Amsteg section fall within the range observed for groundwater samples (Fig. 2b), although simulations yield smaller $\delta^{18}O$ variations along the tunnel and a slightly lower mean $\delta^{18}O$ value (−14.6‰ vs. −13.9‰). This is because (i) with the chosen model setup shallow mixing with dilute meteoric water from the surface is not fully captured by the model, and (ii) the $\delta^{18}O$ and $\delta^{2}H$ values assigned to infiltrating meteoric water were kept constant at the modern altitude dependent rainwater values (Schotterer et al., 2010). The fact that our model is able to approximate the $\delta^{18}O$ profile observed at the tunnel level confirms that infiltration of meteoric water must have mainly occurred at a period of time with climatic conditions similar to those of the current Holocene interglacial period (< 11.5 ka).

5.3. Timing of meteoric water infiltration

Along the tunnel, the mean residence times inferred from the simulated steady state Cl concentration profile and the specified constant Cl uptake rate of 3×10^{-14} mol kg_{H2O}^{-1} s^{-1} ($t_{average}$ = [Cl]/Cl_{Uptake_rate}) range from 3000 years below the Chrüzlistock to about 28,000 years beneath the Maderaner Valley (Fig. 2d). Since groundwater at the tunnel level represent mixtures of different flow paths, the actual travel time of a single water molecule or dissolved species can be much higher such as inferred from the Cl breakthrough curves computed for these two locations (Fig. 10). For the upward directed flow zone below the Maderaner Valley, the Cl breakthrough curve (Fig. 10b) demonstrates that it takes more than 100 k years of simulation time until meteoric water that has infiltrated near the Bristen peak reaches the tunnel level after having penetrated down to several kilometers below the tunnel (Fig. 11). In contrast, beneath the Chrüzlistock, computed Cl breakthrough curves (Fig. 10a) are consistent with the average residence times inferred from the Cl concentration profile (Fig. 2d), suggesting that meteoric water reaches the tunnel level after about 3000 years. It should be noted, however, that these travel times represent rough estimations only. This is because they are proportional to the poorly constrained porosity and permeability distribution (Fig. 6) and because the infiltration rate of meteoric water was likely reduced during the last glaciation period and was certainly not constant over the past 150 ka such as assumed for our simulations. Nevertheless, since our model predicts travel times much less than 10 ka for groundwater samples collected along the postulated downward directed flow zone beneath the Chrüzlistock (Fig. 10a), it is evident that they must have infiltrated into the Aar Massif during the current Holocene interglacial period (< 11.5 ka). In contrast, travel times much longer than 10 ka obtained for groundwater samples collected along the postulated upward directed flow zone below the Maderaner Valley (Fig. 10b) implies that these samples must have mostly infiltrated during similar but past climatic periods. Possible candidates are the Eemian (115–130 ka) or

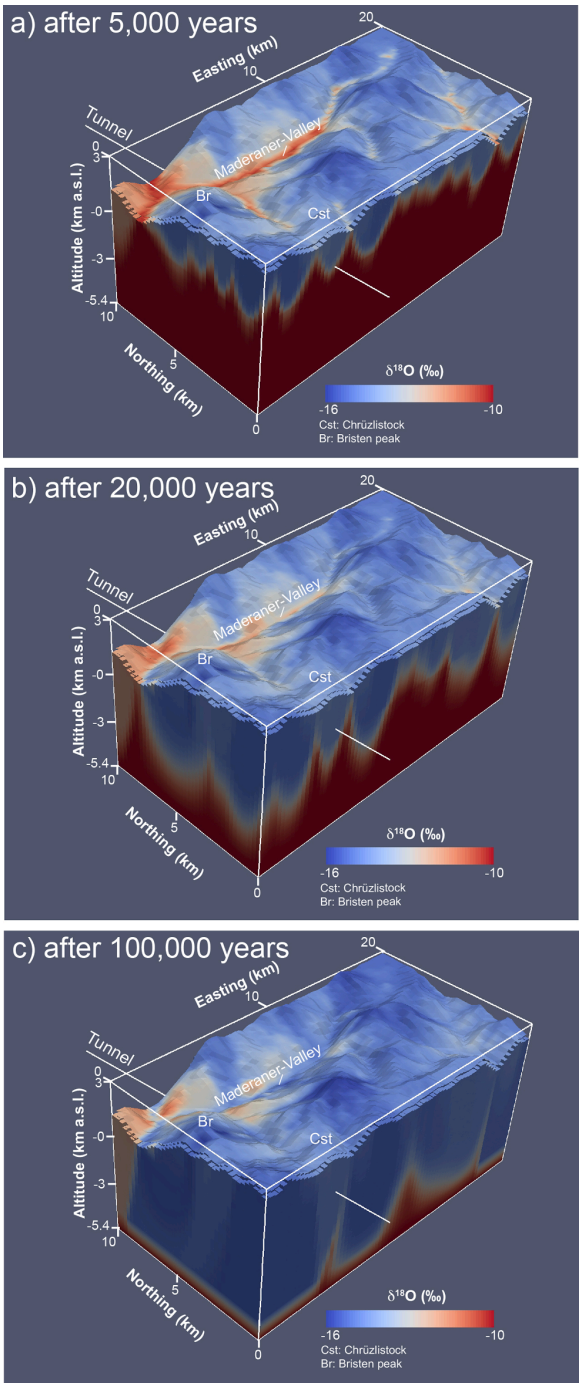

Fig. 9. Simulated $\delta^{18}O$ value distribution after (a) 5000 years, (b) 20,000 years, and (c) 100,000 years of simulation time.

the Meikirch interglacial (200–185 ka), of which the former is surprisingly consistent with the computed breakthrough curve.

6. Implication for the circulation of meteoric water in orogenic crystalline basements

Despite the comparatively simple nature of our model and the absence of any calibration work in addition to estimating the Cl uptake rate, the model is able to reasonably match all constraints identified from the chemical and isotopic composition of groundwater samples collected along the Amsteg section (Fig. 2). We consider this result as a strong quantitative confirmation that mountain topography operates as the most important driving force for meteoric water circulation in orogenic crystalline basements. Our simulations also confirm that in such settings, meteoric water can easily penetrate down to several kilometer depth into the brittle continental crust. For the simulated domain, the topographic driving force is large enough for meteoric water to penetrate down to a depth of 9 km below the surface where the background permeability estimated for granitic basement rocks is less than 3×10^{-17} m^2 (Fig. 6). Accordingly, penetration down to several kilometer depth does not seem to be restricted by the presence of major fault zones with elevated permeability. Similarly, the topographic driving force was sufficient to push the infiltrated meteoric water horizontally before it ascends beneath major valleys, despite that the specified horizontal permeability was one order of magnitude lower than the vertical one ($< 3 \times 10^{-18}$ m^2 at 9 km depth). This means that topography-driven flow can be sustained at a low horizontal permeability and does not necessary rely on regional fault zones.

In terms of practical applications, our simulations are in agreement with recent studies showing that in orogenic crystalline basements, thermal anomalies predominantly occur where major fault zones with permeabilities significantly above the background values considered in our model are exposed at valley floors (Taillefer et al., 2018; Wanner et al., 2019). This is because for such settings, the combination of hydraulic and structural driving forces is optimal. Thus, such settings represent ideal targets for the exploitation of orogenic geothermal systems such as proposed recently (Wanner et al., 2019). In the Central Alps, promising examples are found within fault-hosted settings of the western part of the Aar Massif at Brigerbad and of the Aiguilles Rouges Massif at Lavey-les-Bains (Sonney and Vuataz, 2009; Valla et al., 2016). Both sites are (i) located at the valley floor of the Rhone Valley, (ii) characterized by the occurrence of thermal springs discharging at temperatures up to 65 °C, and (iii) currently used as thermal spas. Moreover, Pastorelli et al. (2001) have shown that thermal anomalies also occur in the Gotthard region such as in the nearby highway tunnel and in an adjacent 500 m deep exploration borehole (28 °C in 450 m depth). Interestingly, these anomalies are also found beneath a major valley, about 3 km south of the town of Andermatt. Hence, they are fully consistent with our model results and further demonstrate that orogenic geothermal systems are promising plays for geothermal power production.

Finally, our simulations confirm that circulation of meteoric water in orogenic crystalline basements is slow and that significant infiltration of meteoric water may have occurred during past interglacial periods dating back more than 100 ka. This reinforces that groundwater and/or porewater in crystalline basements may act as an archive for palaeohydrologic variations (Waber et al., 2012). In terms of groundwater resources, the low tunnel inflow rate computed for the most prominent upward directed flow zone beneath the Maderaner Valley (0.008 L s^{-1}) suggest that deep circulation of meteoric water does not play a major role on the regional water cycle, at least under the prevailing Alpine Climatic conditions with atmospheric precipitation well above 1000 mm year^{-1} (MeteoSwiss, 2019). However, for drier climatic conditions such as on the Tibet plateau with annual precipitation rates below 200 mm year^{-1}, such rates might be significant for sustaining river baseflow and spring discharge (Ge et al., 2008).

7. Summary and conclusions

Detailed knowledge about the circulation of meteoric water in non-magmatic, orogenic belts is fundamental for assessing the potential of such settings for geothermal power production (Wanner et al., 2019), as well as their use as potential groundwater resources (Ge et al., 2008). To get more general insight into such regional hydrogeological

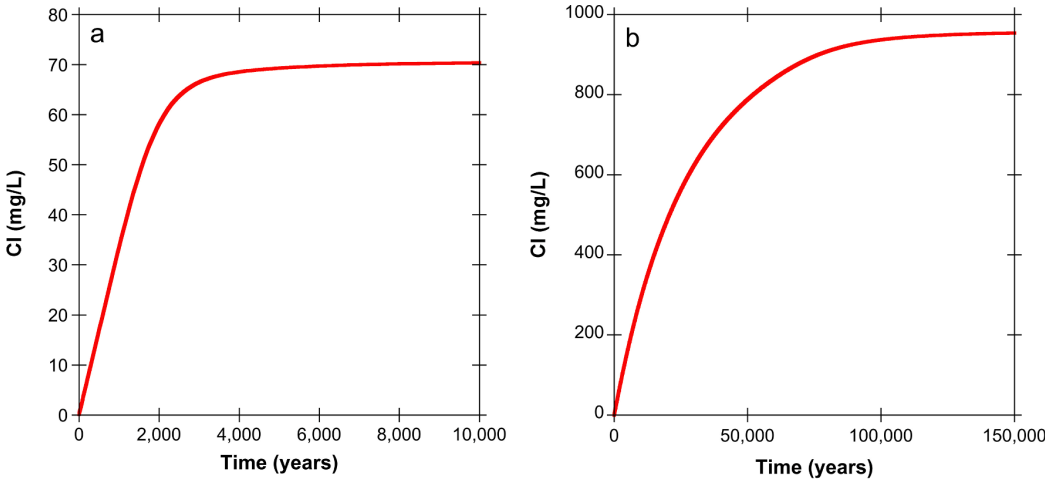

Fig. 10. Simulated Cl breakthrough curves for two different locations along the Amsteg section of the tunnel (Fig. 2a). (a) Cl breakthrough relating to a distance of 15 km along the tunnel where it intersects a migmatitic rock unit (Mig) below the Chrüzlistock. (b) Cl breaktrhough relating to a distance of 9 km along the tunnel where it crosses the center of the Bristen Granite unit below the Maderaner Valley.

processes, and to particularly test the hypothesis that mountain topography operates as a first order driving force for meteoric water circulation, we have conducted regional (20 × 10 × 9 km) thermal-hydraulic-chemical simulations of meteoric water circulation in the orogenic, crystalline basement of the Aar Massif in the Central Alps, Switzerland. In the absence of detailed hydraulic and structural data, the simulations were constrained by 122 chemical analyses of groundwater samples collected during drilling of the World's longest and deepest tunnel, the Gotthard railbase tunnel. Explicitly considering the surface topography in combination with a previously published depth-dependent permeability distribution for fractured crystalline rocks in our model was sufficient to reproduce key features of the chemical analyses (e.g. salinity and temperature distribution), and up- and downward directed flow zones inferred from geochemical constraints. To do so, the only parameter that had to be calibrated in the model was the Cl uptake rate along the flow path. Performing additional stable water isotope measurements and including their fate in the numerical simulations allowed gaining further insights into the timing of meteoric water infiltration and subsequent circulation. The main conclusions of this study are:

- Despite the lack of detailed structural and hydraulic data, 3D thermal-hydraulic-chemical simulations constrained by geochemical data allows assessing regional and long-term topography-driven flow in orogenic crystalline basements.
- Simulation results quantitatively confirm that the surface topography indeed operates as a very strong driving force for meteoric water circulation in orogenic crystalline basements. Owing to the induced hydraulic head gradient, meteoric water infiltration occurs at high altitude whereas upward directed flow zones (i.e. exfiltration) are found along major valleys.
- Down to 9 km depth, penetration of meteoric water is not limited by the decrease in permeability typical of granitic basement rocks, suggesting that advective fluid transport down to the brittle-ductile transition zone is likely occurring in such systems. Without the occurrence of permeability anomalies (i.e. major fault zones), however, the permeability and hence the flow rates are too low for the formation of major thermal anomalies despite that in case of the

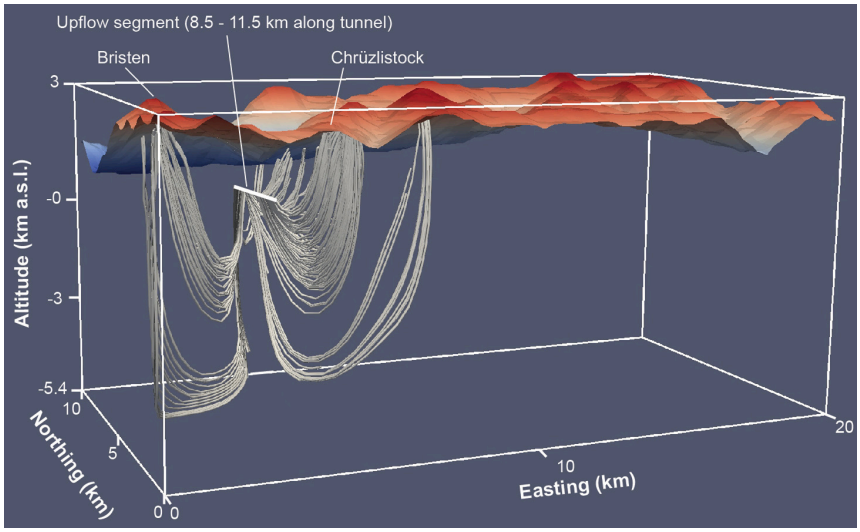

Fig. 11. Computed streamlines of meteoric water infiltrating at the upper model boundary and discharging from below into the identified upflow segment between 8.5 and 11.5 km along the tunnel (Fig. 2a).

studied system meteoric water may attain temperatures well above 150 °C during such deep infiltration.

- Based on the upward directed flow zones predicted along major valleys, our simulations suggest that positive temperature anomalies do occur if fluid upflow is promoted by the presence of major faults zones with elevated permeability. Within the Aar and other crystalline alpine massifs, such conditions are found frequently as manifested by the occurrence of multiple hot springs currently used as thermal spas. Thus, we consider orogenic geothermal systems as promising plays for geothermal power production.
- Due to the low permeability, circulation of meteoric water is slow (< 2 m year^{-1}) and average groundwater residence times may strongly exceed the time period of the current interglacial stage (> 11.5 ka). This further underlines that groundwater and/or porewater in orogenic crystalline basements may act as an archive for palaeohydrologic variations during past interglacial periods.

Declaration of Competing Interest

The authors declare that they have no known competing financial interests or personal relationships that could have appeared to influence the work reported in this paper.

Acknowledgments

Research in geothermal energy at the University of Bern is supported by the Swiss Competence Center for Energy Research–Supply of Electricity (SCCER-SoE). Daniel Egli is acknowledged for numerically rotating the grid of the digital elevation model into the model domain. Constructive comments of three anonymous reviewers are greatly appreciated.

Appendix A. Supplementary data

Supplementary data to this article can be found online at https://doi.org/10.1016/j.jhydrol.2019.124374.

References

Abrecht, J., 1994. Geologic units of the Aarmassif and their pre-Alpine rock associations: a critical review. Schweiz. Miner. Petrog. 74, 5–27.
Belgrano, T.M., Herwegh, M., Berger, A., 2016. Inherited structural controls on fault geometry, architecture and hydrothermal activity: an example from Grimsel Pass, Switzerland. Swiss J. Geosci. 109, 345–364.
Bossart, P., Mazurek, M., 1991. Grimsel Test Site Structural Geology and water flow-paths in the migration shear zone. Nagra Technical Report NTB 91-12, 1-55.
Bossong, C.R., Caine, J.S., Stannard, D.I., Flynn, J.L., Stevens, M.R., Heiny-Dash, J.S., 2003. Hydrologic conditions and assessment of water resources in the Turkey Creek Watershed, Jefferson County, Colorado, 1998–2001. USGS Water-Resources Investigations Report 03-4034.
Bucher, K., Zhang, L., Stober, I., 2009. A hot spring in granite of the Western Tianshan, China. Appl. Geochem. 24, 402–410.
Bucher, K., Stober, I., 2010. Fluids in the upper continental crust. Gefluids 10, 241–253.
Bucher, K., Stober, I., Seelig, U., 2012. Water deep inside the mountains: Unique water samples from the Gotthard rail base tunnel, Switzerland. Chem. Geol. 334, 240–253.
Caine, J.S., Manning, A.H., Verplanck, P.L., Bove, D.J., Kahn, K.G., Ge, S., 2006. Well construction information, lithologic logs, water level data, and overview of research in Handcart Gulch, Colorado: An alpine watershed affected by metalliferous hydrothermal alteration. U.S. Geol. Surv. Open File 06–1189.
Cartwright, I., Buick, I.S., 1999. The flow of surface-derived fluids through Alice Springs age middle-crustal ductile shear zones, Reynolds Range, central Australia. J. Metamorph. Geol. 17, 397–414.
Choukroune, P., Gapais, D., 1983. Strain pattern in the Aar Granite (Central Alps): Orthogneiss developed by bulk inhomogeneous flattening. J. Struct. Geol. 5, 411–418.
Connolly, J.A.D., Podladchikov, Y.Y., 2015. An analytical solution for solitary porosity waves: dynamic permeability and fluidization of nonlinear viscous and viscoplastic rock. Geofluids 15, 269–292.
Craw, D., Koons, P.O., Zeitler, P.K., Kidd, W.S.F., 2005. Fluid evolution and thermal structure in the rapidly exhuming gneiss complex of Namche Barwa-Gyala Peri, eastern Himalayan syntaxis. J. Metamorph. Geol. 23, 829–845.
Croucher, A.E., 2015. Recent developments in the PyTOUGH scripting library for TOUGH2 simulations. Proceedings 37th New Zealand Geothermal Workshop. Taupo, New Zealand: The University of Auckland.
Diamond, L.W., Wanner, C., Waber, H.N., 2018. Penetration depth of meteoric water in orogenic geothermal systems. Geology 46, 1063–1066.
Dzikowski, M., Josnin, J.Y., Roche, N., 2016. Thermal Influence of an Alpine Deep Hydrothermal Fault on the Surrounding Rocks. Groundwater 54, 55–65.
FOEN (2014) ISOT module of the NAQUA - National Groundwater monitoring program. Swiss Federal Office For the Environment (FOEN) http://www.bafu.admin.ch/bafu/en/home/topics/water/info-specialists/state-of-waterbodies/state-of-groundwater/naqua-national-groundwater-monitoring/isot-module.html. (Accessed 27 may 2019).
FOEN, 2015. Einzugsgebietsgliederung Schweiz, EZGG: Topoggraphische Einzugsgebiete der Schweizer Gewässer. Swiss Federal Office For the Environment (FOEN). http://www.bafu.admin.ch/ezgg-ch. (Accessed 8 October 2019).
Forster, C., Smith, L., 1988. Groundwater flow systems in mountainous terrain: 2. Controlling factors. Water Resour. Res. 24, 1011–1023.
Ge, S., Wu, Q.B., Lu, N., Jiang, G.L., Ball, L., 2008. Groundwater in the Tibet Plateau, western China. Geophys. Res. Lett. 35.
Goderniaux, P., Davy, P., Bresciani, E., de Dreuzy, J.-R., Le Borgne, T., 2013. Partitioning a regional groundwater flow system into shallow local and deep regional flow compartments. Water Res. Res. 49, 2274–2286.
Grasby, S.E., Ferguson, G., Brady, A., Sharp, C., Dunfield, P., McMechan, M., 2016. Deep groundwater circulation and associated methane leakage in the northern Canadian Rocky Mountains. Appl. Geochem. 68, 10–18.
Hofmann, B.A., Helfer, M., Diamond, L.W., Villa, I.M., Frei, R., Eikenberg, J., 2004. Topography-driven hydrothermal breccia mineralization of Pliocene age at Grimsel Pass, Aar massif, Central Swiss Alps. Schweiz. Miner. Petrog. 84, 271–302.
Hubbert, M.K., 1940. The theory of groundwater motion. J. Geol. 48, 785–944.
Hunziker, J.C., Martinotti, G., Marini, L., 1990. The waters of the Simplon tunnel (Swiss-Italian Alps) and of the adjacent Ossola district (Italy): geothermal considerations. Geoth. Res. T. 14-II, 1477–1482.
Ingebritsen, S.E., Manning, C.E., 1999. Geological implications of a permeability-depth curve for the continental crust. Geology 27, 1107–1110.
International-Formulation-Committee, 1967. Formulation of the Thermodynamic Properties of Ordinary Water Substance. IFC Secretariat, Düsseldorf, Germany.
Keusen, H.R., Ganguin, J., Schuler, P., Buleti, M., 1989. Felslabor Grimsel: Geologie. *Nagra Technischer Bericht* **NTB** 87–114.
Kuhlman, U., Gaus, I., 2014. Inverse modelling of the FEBEX in situ test using iTOUGH2. Nagra Arbeitsbericht NAB 14–20, 1–33.
Labhart, T.P., 1999. Aarmassiv, Gotthardmassiv und Tavetscher Zwischenmassiv: Aufbau und Entstehungsgeschichte. In: Loew, S., Wyss, R. (Eds.), Symposium Geologie Alptransit, Zürich. Balkema, Rotterdam, pp. 31–43.
Laws, S., Eberhardt, E., Loew, S., Descoeudres, F., 2003. Geomechanical Properties of Shear Zones in the Eastern Aar Massif, Switzerland and their Implication on Tunnelling. Rock Mech. Rock Eng. 36, 271–303.
Maréchal, J.C., Perrochet, P., Tacher, L., 1999. Long-term simulations of thermal and hydraulic characteristics in a mountain massif: The Mont Blanc case study, French and Italian Alps. Hydrogeol. J. 7, 341–354.
Masset, O., Loew, S., 2013. Quantitative hydraulic analysis of pre-drillings and inflows to the Gotthard Base Tunnel (Sedrun Lot, Switzerland). Eng. Geol. 164, 50–66.
MeteoSwiss (2019) Climate diagrams and normals per station. Swiss Federal Office of Meteorology and Climatology (MeteoSwiss) http://www.meteoswiss.admin.ch/home/climate/swiss-climate-in-detail/climate-normals/climate-diagrams-and-normals–per-station.html. (Accessed 27 May 2019).
Mullis, J., Dubessy, J., Poty, B., O'Neil, J., 1994. Fluid regimes during late stages of a continental collision: Physical, chemical, and stable isotope measurements of fluid inclusions in fissure quartz from a geotraverse through the Central Alps, Switzerland. Geochim. Cosmochim. Acta 58, 2239–2267.
Nordstrom, D.K., Ball, J.W., Donahoe, R.J., Whittemore, D., 1989. Groundwater chemistry and water–rock interactions at Stripa. Geochim. Cosmochim. Acta 53, 1727–1740.
Pastorelli, S., Marini, L., Hunziker, J., 2001. Chemistry, isotope values (δD, $\delta^{18}O$, $\delta^{34}S_{SO4}$) and temperatures of the water inflows in two Gotthard tunnels, Swiss Alps. Appl. Geochem. 16, 633–649.
Pearson, F.J., Balderer, W., Loosli, H.H., Lehmann, B.E., Matter, A., Peters, T., Schmassmann, H., Gautschi, A., 1991. Applied Isotope Hydrogeology – A case study in Northern Switzerland. Studies in Environmental Science 43. Elsevier, Amsterdam, pp. 481.
Peyron, O., Guiot, J., Cheddadi, R., Tarasov, P., Reille, M., de Beaulieu, J.-L., Bottema, S., Andrieu, V., 1998. Climatic Reconstruction in Europe for 18,000 YR B.P. from Pollen Data. Quaternary Res. 49, 183–196.
Pfeifer, H.R., Sanchez, A., Degueldre, C., 1992. Thermal springs in granitic rocks from the Grimsel Pass (Swiss Alps): The late stage of a hydrothermal system related to Alpine Orogeny. In: Kharaka, Y.K., Maest, A.S. (Eds.), Proceedings of Water-Rock Interaction WRI-7. A.A. Balkema, Rotterdam, The Netherlands, Park City, Utah, pp. 1327–1330.
Preusser, F., Graf, H.R., Keller, O., Krayss, E., Schlüchter, C., 2011. Quaternary glaciation history of northern Switzerland. E&G Quaternary Sci. J. 60, 282–305.
Reed, M., Palandri, J.L., 2006. SOLTHERM.H06, a database of equilibrium constants for minerals and aqueous species. Available from the authors. University of, Oregon, Eugene, USA.
Reyes, A.G., Christenson, B.W., Faure, K., 2010. Sources of solutes and heat in low-enthalpy mineral waters and their relation to tectonic setting, New Zealand. J. Volcanol. Geoth. Res. 192, 117–141.
Schaltegger, U., 1994. Unravelling the pre-Mesozoic history of the Aar and Gotthard massifs (Central Alps) by isotopic dating — a review. Schweiz. Miner. Petrog. 74, 41–51.
Schneeberger, R., Kober, F., Lanyon, B.G.W., Mäder, U., Spillmann, T., Blechschmidt, I., 2019. Grimsel Test Site: Revisiting the site-specific geoscientific knowledge. Nagra Technischer Bericht NTB 19-01.

Schotterer, U., Schürch, M., Rickli, R., Stichler, W., 2010. Wasserisotope in der Schweiz - Neue Ergebnisse und Erfahrungen aus dem nationalen Messnetz ISOT. Gas-Wasser-Abwasser (GWA) 12, 1073–1081.
Seelig, U., Bucher, K., 2010. Halogens in water from the crystalline basement of the Gotthard rail base tunnel (central Alps). Geochim. Cosmochim. Acta 74, 2581–2595.
Singleton, M.J., Sonnenthal, E.L., Conrad, M.E., DePaolo, D.J., Gee, G.W., 2005. Multiphase reactive transport modeling of seasonal infiltration events and stable isotope fractionation in unsaturated zone pore water and vapor at the Hanford site. Vadose Zone J. 3, 775–785.
Sonney, R., Vuataz, F.-D., 2008. Properties of geothermal fluids in Switzerland: A new interactive database. Geothermics 37, 496–509.
Sonney, R., Vuataz, F.-D., 2009. Numerical modelling of Alpine deep flow systems: a management and prediction tool for an exploited geothermal reservoir (Lavey-les-Bains, Switzerland). Hydrogeol. J. 17, 601–616.
Steck, A., Hunziker, J., 1994. The Tertiary structural and thermal evolution of the Central Alps—compressional and extensional structures in an orogenic belt. Tectonophysics 238, 229–254.
Stober, I., Richter, A., Brost, E., Bucher, K., 1999. The Ohlsbach Plume – Discharge of deep saline water from the crystalline basement of the Black Forest. Germany. *Hydrogeol. J.* 7, 273–283.
Stober, I., Bucher, K., 2007. Hydraulic properties of the crystalline basement. Hydrogeol. J. 15, 213–224.
Stober, I., Bucher, K., 2015. Hydraulic conductivity of fractured upper crust: insights from hydraulic tests in boreholes and fluid-rock interaction in crystalline basement rocks. Geofluids 15, 161–178.
Stober, I., Zhong, J., Zhang, L., Bucher, K., 2016. Deep hydrothermal fluid–rock interaction: the thermal springs of Da Qaidam, China. Geofluids 16, 711–728.
Taillefer, A., Guillou-Frottier, L., Soliva, R., Magri, F., Lopez, S., Courrioux, G., Millot, R., Ladouche, B., Le Goff, E., 2018. Topographic and Faults Control of Hydrothermal Circulation Along Dormant Faults in an Orogen. Geochem. Geophy. Geosy. 19, 4972–4995.
Thiebaud, E., Gallino, S.p., Dzikowski, M., Gasquet, D., 2010. The influence of glaciations on the dynamics of mountain hydrothermal systems: numerical modeling of the La Léchère system (Savoie, France). B. Soc. Géol. Fr. 181, 295–304.
Tiedeman, C.R., Goode, D.J., Hsieh, P.A., 1998. Characterizing a Ground Water Basin in a New England Mountain and Valley Terrain. Groundwater 36, 611–620.
Valla, P.G., Rahn, M., Shuster, D.L., van der Beek, P.A., 2016. Multi-phase late-Neogene exhumation history of the Aar massif, Swiss central Alps. Terra Nova 28, 383–393.
van Geldern, R., Barth, J.A.C., 2012. Optimization of instrument setup and post-run corrections for oxygen and hydrogen stable isotope measurements of water by isotope ratio infrared spectroscopy (IRIS). Limnol. Oceanogr-Meth. 10, 1024–1036.
Vernon, A.J., van der Beek, P.A., Sinclair, H.D., Rahn, M.K., 2008. Increase in late Neogene denudation of the European Alps confirmed by analysis of a fission-track thermochronology database. Earth Planet. Sci. Lett. 270, 316–329.
Waber, H.N., Gimmi, T., Smellie, J.A.T., 2012. Reconstruction of palaeoinfiltration during the Holocene using porewater data (Laxemar, Sweden). Geochim. Cosmochim. Acta 94, 109–127.
Waber, H.N., Schneeberger, R., Mäder, U.K., Wanner, C., 2017. Constraints on evolution and residence time of geothermal water in granitic rocks at Grimsel (Switzerland). Proced. Earth Plan. Sc. 17, 774–777.
Wanner, C., Peiffer, L., Sonnenthal, E., Spycher, N., Iovenitti, J., Kennedy, B.M., 2014. Reactive transport modeling of the Dixie Valley geothermal area: Insights on flow and geothermometry. Geothermics 51, 130–141.
Wanner, C., Bucher, K., Pogge von Strandmann, P.A.E., Waber, H.N., Pettke, T., 2017. On the use of Li isotopes as a proxy for water–rock interaction in fractured crystalline rocks: A case study from the Gotthard rail base tunnel. Geochim. Cosmochim. Acta 198, 396–418.
Wanner, C., Diamond, L.W., Alt-Epping, P., 2019. Quantification of 3-D thermal anomalies from surface observations of an orogenic geothermal system (Grimsel Pass, Swiss Alps). J. Gephys. Res.-Sol. Ea. 124. https://doi.org/10.1029/2019JB018335.
Wickham, S.M., Peters, M.T., Fricke, H.C., O'Neil, J.R., 1993. Identification of magmatic and meteoric fluid sources and upward- and downward-moving infiltration fronts in a metamorphic core complex. Geology 21, 81–84.
Wintsch, R.P., Christoffersen, R., Kronenberg, A.K., 1995. Fluid-rock reaction weakening of fault zones. J. Geophys. Res. 100, 13021–13032.
Wirsig, C., Zasadni, J., Ivy-Ochs, S., Christl, M., Kober, F., Schlüchter, C., 2016. A de-glaciation model of the Oberhasli, Switzerland. J. Quaternary Sci. 31, 46–59.
Xu, T., Sonnenthal, E.L., Spycher, N., Zheng, L., 2014. TOUGHREACT V3.0-OMP Reference Manual: A Parallel Simulation Program for Non-Isothermal Multiphase Geochemical Reactive Transport. LBNL Manual http://eesatough.lbl.gov/licensing/toughreact.html.

5. RTM APPLICATIONS RELATED TO SILICATE WEATHERING

Scope and significance

Chapters 1 and 2 above highlight the importance of silicate weathering as a major natural sink for atmospheric CO_2 and demonstrate how Li isotope ratios serve as proxies to track and quantify modern and past silicate weathering rates. This Chapter 5 presents three RTM applications where Li isotopes are integrated in reactive transport model simulations. Chapter 5.1 describes an update of the solid solution approach used to simulate the fate of Cr and U isotopes (see Chapter 3), which eventually enabled the integration of Li isotopes as well. It further presents results from 1D reactive transport model simulations assessing the processes controlling the fate of Li and its isotopes in granitic catchments. Subsequently, these model results are compared to Li data collected from worldwide rivers to assess whether Li isotope ratios measured in seawater samples can be correlated to the amount of CO_2 globally consumed by continental silicate weathering.

In Chapter 5.2 the same RTM approach is used to evaluate Li isotope ratios measured in groundwater and streamwater samples collected from the Columbia River Basalt area in the western USA. Using a 1D model geometry similar to that used for simulating the granitic systems allows the observed δ^7Li values and the concentration ratios between Li and major elements (e.g. Li/Na) to be satisfactorily reproduced. This permits the identification of the main parameters and processes controlling Li isotope ratios in today's rivers.

Chapter 5.3 presents a follow-up study in which the numerical approach is modified to allow definition of a maximum amount of Li that may precipitate in Li-bearing secondary minerals. The updated approach is used to simulate the fate of Li and its isotopes during the infiltration of meteoric water into the crystalline Aar massif in central Switzerland. Limiting the Li concentration in secondary kaolinite leads to a simple explanation for a complex set of Li concentrations and δ^7Li variations observed in groundwater samples discharging into the Gotthard railway base tunnel.

Overall, the integration of Li isotopes in the RTM applications presented in Chapter 5 provides important information regarding the key processes controlling Li isotope ratios in groundwater, rivers and seawater. Thus, these applications contribute to assessing the use of Li isotopes as a proxy for silicate weathering and may contribute to better quantify this important natural sink for CO_2.

5.1. Seawater δ^7Li: a direct proxy for global CO_2 consumption by continental silicate weathering?

Source:

Wanner C., Sonnenthal E. L. and Liu X.-M. (2014) Seawater δ^7Li a direct proxy for global CO_2 consumption by continental silicate weathering? *Chemical Geology* **381**, 154-167.

Contribution by the Author (CW):

CW developed the general idea and carried out all the simulations. Moreover, CW had the lead in data interpretation and manuscript writing.

Chemical Geology 381 (2014) 154–167

Contents lists available at ScienceDirect

Chemical Geology

journal homepage: www.elsevier.com/locate/chemgeo

Seawater δ^7Li: A direct proxy for global CO_2 consumption by continental silicate weathering?

Christoph Wanner [a,*], Eric L. Sonnenthal [a], Xiao-Ming Liu [b,c]

[a] Earth Sciences Division, Lawrence Berkeley National Laboratory, 1 Cyclotron Road, Berkeley, CA 94720, USA
[b] Geophysical Lab, Carnegie Institute of Washington, DC 20015, USA
[c] Department of Geology, University of Maryland — College Park, College Park, MD 20742, USA

ARTICLE INFO

Article history:
Received 11 February 2014
Received in revised form 6 May 2014
Accepted 8 May 2014
Available online 16 May 2014

Editor: Michael E. Böttcher

Keywords:
Li isotopic fractionation
Seawater δ^7Li
Silicate weathering
Reactive transport modeling
CO_2 consumption

ABSTRACT

The fractionation of stable Li isotopes (^{6}Li, ^{7}Li) has become a promising proxy for assessing changes related to continental silicate weathering patterns. Recently, the first complete record of Cenozoic seawater Li isotopic composition (δ^7Li) was reported (Misra and Froelich, 2012, Science 335, 818–821) showing a stepwise increase of +9‰ over the last 56 Ma. This increase was attributed to a general change in continental silicate weathering behavior caused by tectonic uplift. In particular, the low global average riverine δ^7Li inferred for the Paleocene–Eocene boundary was explained by congruent silicate weathering of primary silicate minerals, which is inconsistent with the stoichiometry of secondary minerals and the resultant water chemistry.

In this study, we present a novel reactive transport modeling approach that explicitly includes Li isotopic fractionation to assess alternative geochemically-constrained interpretations that do not rely on congruent weathering. Simulations show that riverine δ^7Li is mainly controlled by the subsurface residence time, the corresponding weathering intensity, and the concentration of a river's suspended load. Based on these factors, we suspect that the low δ^7Li observed at the Paleocene–Eocene boundary was inherited from a high weathering intensity with predominant weathering of previously formed secondary mineral phases (e.g., clays, oxides) having low δ^7Li values. Moreover, we conclude that the Cenozoic δ^7Li increase was caused by an increasing amount of primary silicate mineral dissolution inherited from an increasing suspended river load concentration and a decreasing weathering intensity both likely induced by tectonic uplift. In contrast, Cenozoic cooling and corresponding pCO_2 and precipitation variations do not seem to have a distinct control on the Cenozoic δ^7Li record. Finally, our simulations revealed a close relation between δ^7Li and CO_2 consumption by silicate weathering implying that the Cenozoic seawater δ^7Li record could be potentially used to quantify such CO_2 consumption through time. However, more experimental and modeling work is required to quantify the correlation between seawater δ^7Li and global CO_2 consumption by silicate weathering. Key parameters are the temperature-dependent thermodynamic properties of specific Li-bearing primary and secondary minerals (e.g., crystallographic Li substitution reaction, maximum Li substitution, Li solubility, Li isotopic fractionation factor) as well as the determination of global average subsurface and river discharges through time.

1. Introduction

Continental chemical weathering forms a major CO_2 sink and is therefore an important input parameter for climate models (e.g., Berner et al., 1983; Francois and Godderis, 1998; Berner and Kothavala, 2001; Godderis et al., 2009; Li and Elderfield, 2013). However, the present and past global CO_2 consumption by continental silicate weathering has not been precisely quantified (Li and Elderfield, 2013). Climate models simulating the carbon cycle over Earth's history typically calibrate CO_2 consumption by chemical weathering against the observed seawater $^{87}Sr/^{86}Sr$ ratio. Using $^{87}Sr/^{86}Sr$ is challenging because it reflects chemical weathering of carbonates, as well as weathering of silicate minerals (Oliver et al., 2003; Godderis et al., 2009). Tracking the individual contribution of continental silicate weathering is, however, crucial because it may demonstrate whether an observed global CO_2 drawdown is caused by increased tectonic activity, such as the onset of the Himalayan orogeny ca. 30 Ma ago (Raymo and Ruddiman, 1992), or by a decrease in total Earth CO_2 degassing (Berner et al., 1983). In contrast to Sr, lithium is a trace element that is almost exclusively found in silicate minerals, which makes it a useful tracer for silicate weathering (e.g., Huh et al., 1998, 2001; Kisakürek et al., 2004; Rudnick et al., 2004; Kisakürek et al., 2005; Pogge von Strandmann et al., 2006; Vigier et al., 2009; Millot et al., 2010; Pogge von Strandmann et al., 2010; Liu et al., 2013). In particular, tracking Li isotopic fractionation is promising because the two stable Li isotopes (^{6}Li, ^{7}Li) fractionate

* Corresponding author. Tel.: +1 5104958147.
E-mail addresses: cwanner@lbl.gov, christoph.wanner@geo.unibe.ch (C. Wanner).

http://dx.doi.org/10.1016/j.chemgeo.2014.05.005
0009-2541/

when Li-bearing primary silicate minerals (e.g., micas) are weathered and secondary mineral phases (e.g., clays) are formed (Zhang et al., 1998; Pistiner and Henderson, 2003; Vigier et al., 2008; Wimpenny et al., 2010a).

Hathorne and James (2006) presented the first record of seawater Li isotopic composition (δ^7Li) over the past 18 Ma using foraminifera as a proxy. Misra and Froelich (2012) extended the record to 68 Ma showing a +9‰ increase over the last ca. 56 Ma. Unlike the steady $^{87}Sr/^{86}Sr$ increase, δ^7Li increased stepwise, which was attributed to specific tectonic events (e.g., Himalayan orogeny) (Misra and Froelich, 2012). Specifically, the latter authors argued that tectonic uplift shifted the global silicate weathering pattern from a congruent, transport-limited regime to an incongruent, weathering-limited regime. However, the latter interpretation cannot be fully justified from a geochemical perspective, because secondary minerals typically observed under a transport-limited weathering regime (e.g., Fe- and Al-oxides) are inconsistent with congruent silicate weathering.

Among the earth sciences, reactive transport modeling has become a powerful tool for a predictive understanding of many subsurface systems (Steefel et al., 2005). To the best of our knowledge, it has not yet been used for a quantitative understanding of Li isotopic fractionation processes. Instead, field-derived Li isotopic data were usually explained by using closed system Rayleigh distillation models (Kisakürek et al., 2004; Rudnick et al., 2004; Yoon, 2010; Tipper et al., 2012). Such models greatly simplify Li isotope fractionation processes because they only consider fractionation effects associated with the precipitation of Li-bearing minerals from an aqueous solution having a specific initial Li concentration. In contrast, they neglect that aqueous Li concentrations, and thus corresponding Li isotope fractionation effects, are also controlled by the simultaneous dissolution of Li-bearing primary minerals. Recently, Bouchez et al. (2013) presented a box-type mass balance and flux model that considers both dissolution of Li-bearing primary minerals and the precipitation of Li-bearing secondary minerals. Similar to Rayleigh-type models, the Bouchez et al. (2013) model does not take into account mineralogical, kinetic and thermodynamic properties of mineral phases involved in Li isotope fractionation processes (e.g., mineral stoichiometry, dissolution and precipitation rates, mineral solubilities).

In this paper we present a reactive transport modeling approach explicitly including the fractionation of Li isotopes to quantitatively test alternative interpretations for the Cenozoic seawater δ^7Li record that do not rely on congruent silicate weathering. By doing so, we show that global average riverine and seawater δ^7Li values are mainly controlled by the cumulative extent of water–rock interaction taking place along a flow path and are thus closely related to the corresponding CO_2 consumption.

2. Global Li isotopic fractionation model

2.1. The Misra and Froelich (2012) model

Using a mass balance approach Misra and Froelich (2012) argued that the change in seawater δ^7Li was solely attributed to a change in riverine δ^7Li. The conclusion that changing seawater δ^7Li values are mainly caused by a changing fate of continental Li seems reasonable as there is evidence that the seawater hydrothermal fluid input and oceanic Li isotopic fractionation processes remained roughly constant during the Cenozoic (Rowley, 2002; Müller et al., 2008). However, the rate of past oceanic crust production is still under debate. For example, various GEOCARB models (e.g., Berner, 1994; Berner and Kothavala, 2001) consider a variable hydrothermal fluid input. Moreover, the low seawater δ^7Li values observed at the Paleocene–Eocene boundary (Misra and Froelich, 2012) could be inherited from a lower global average riverine δ^7Li value (at constant riverine Li flux), from a lower dissolved riverine Li flux (at a constant δ^7Li value), or from a combination of both. In fact, it is rather unlikely that processes causing a shift of the global average riverine Li isotopic composition do not vary the global average riverine Li flux and [Li].

It is well accepted that Li isotopic fractionation is mainly associated with secondary mineral precipitation (Kisakürek et al., 2005; Pogge von Strandmann et al., 2006; Vigier et al., 2009; Millot et al., 2010; Pogge von Strandmann et al., 2010). By contrast, Li isotopes stoichiometrically dissolve from primary silicate minerals (Pistiner and Henderson, 2003; Huh et al., 2004). Riverine δ^7Li is thus controlled by the ratio of Li released by primary silicate mineral dissolution to Li removed by secondary mineral precipitation and by Li isotopic fractionation associated with precipitation. Consequently, host rock mineralogy does not show a distinct control on riverine δ^7Li (Kisakürek et al., 2005; Millot et al., 2010). Changing global average riverine δ^7Li values thus reflect a changing silicate weathering pattern only.

For the Paleocene–Eocene boundary (~56 Ma ago) a global average riverine δ^7Li value of +3‰ was inferred (Misra and Froelich, 2012), being ca. 20‰ lower than the average δ^7Li value of modern rivers. Misra and Froelich (2012) concluded that this light value was inherited from congruent weathering of primary silicate minerals having a δ^7Li value in the same order of magnitude, whereas the current value is inherited from incongruent silicate weathering including secondary mineral precipitation (e.g., clays, oxides, and hydroxides) and accompanying Li isotopic fractionation. Whereas average continental bulk rock δ^7Li values close to +3‰ are justified by the studies of Teng et al. (2004, 2008, 2009) reporting δ^7Li values for the average ($\delta^7Li = +2.0 \pm 2.3$‰), upper ($\delta^7Li = 0 \pm 2$‰) and lower continental crust ($\delta^7Li = +1.6 \pm 8.9$‰), congruent silicate weathering seems rather questionable. Specifically, Misra and Froelich (2012) argued that the global weathering regime at the Paleocene–Eocene boundary was similar to the current low-relief, peneplained type and transport-limited weathering pattern inferred for the Guayana Shield (Edmond et al., 1995). The Guayana Shield is located at the border of Venezuela, Colombia and Brazil and one of the so far lowest riverine δ^7Li values was measured for a sample collected from this area (+6.6‰, Huh et al., 1998). Edmond et al. (1995) indeed characterized the weathering regime of the Guayana Shield as being weathering-intense and transport-limited but they explicitly stated that primary silicate minerals are incongruently dissolved. In fact, only incongruent silicate mineral dissolution can explain the formation of thick saprolites with an accumulation of quartz, clays, Fe- and Al-oxides typically observed at locations experiencing a high weathering intensity (White et al., 2001; Kisakürek et al., 2004; Rudnick et al., 2004; Liu et al., 2013). Incongruent silicate weathering is also consistent with the low Al solubility at near neutral pH values, typical of these systems.

Furthermore, it is questionable if the average riverine δ^7Li value at the Paleocene–Eocene boundary was as low as +3‰. If this is true, similar riverine δ^7Li values should be found somewhere on Earth today reflecting weathering conditions for an isolated location that are similar to the global weathering pattern observed in the past (Hathorne and James, 2006). In fact, the compilation of available current riverine δ^7Li values showed that the minimum values were larger, on the order of 6‰ (Misra and Froelich, 2012). Values close to +6‰, however, have so far only been published for two specific samples and only one of them originated from a weathering intense location (Guyana Shield, Huh et al., 1998). The other sample was collected from a Siberian river (Yana) where the weathering intensity is lower (Huh et al., 1998). Nevertheless, it is notable that +6‰ is in the same order of magnitude as the asymptotic riverine δ^7Li value Misra and Froelich (2012) obtained for the Paleocene–Eocene ocean by performing a sensitivity analysis on their mass balance calculations. Based on this analysis, the lack of present river δ^7Li values less than +6‰, and a recent refinement of the Li cycle at the Paleocene–Eocene boundary ($\delta^7Li_{riverine} = +12$‰, Li and West, 2014), we propose that the Paleocene–Eocene riverine δ^7Li was likely around +6‰ or larger. Inferring a global average riverine δ^7Li that is higher than the value of the upper continental crust ($\delta^7Li = 0.0 \pm 2$‰, Teng et al., 2004) implies that Li isotopic fractionation between bulk

crustal rocks and global rivers was taking place. Moreover, it rules out congruent weathering as being responsible for the minimum seawater δ^7Li observed at the Paleocene–Eocene boundary.

2.2. Alternative hypotheses explaining the Cenozoic seawater δ^7Li value record

Following the arguments of Misra and Froelich (2012), we assume that increasing Cenozoic seawater δ^7Li values are mainly attributed to a change in riverine δ^7Li. We do, however, not *a priori* assume that the riverine Li flux and the hydrothermal seawater Li input remained constant. Nevertheless, we focus on changing riverine δ^7Li values rather than on the possible effects of changing Li isotopic fractionation processes in the ocean (i.e., reverse weathering) and of a variable seawater hydrothermal Li input. Also, we assume that the composition of the continental crust exposed to chemical weathering remained roughly constant since the Paleocene–Eocene boundary, thus neglecting the potential effects of time-varying lithology on global average riverine and seawater δ^7Li values. Similar to Misra and Froelich (2012), we speculate that the Cenozoic seawater δ^7Li value increase is most likely inherited from a changing continental silicate weathering pattern induced by an increasing global relief owing to major global orogenies (e.g., Himalayan, Andean orogeny) and by the cooling trend observed since the humid Paleocene–Eocene thermal maximum (PETM) (Miller et al., 1987; Clementz and Sewall, 2011). An increasing relief (Fig. 1) and cooler temperatures have the following first order effects on chemical silicate weathering, which have potentially caused the observed δ^7Li shift:

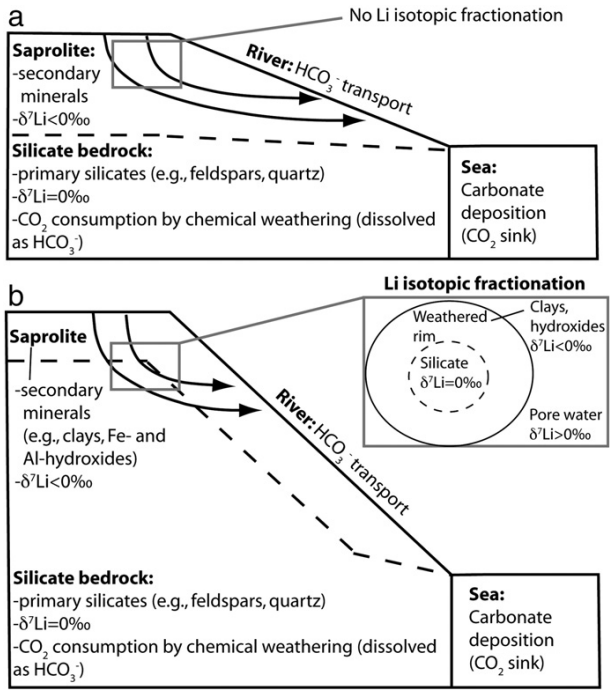

Fig. 1. Proposed weathering and Li isotopic fractionation model for the Paleocene–Eocene boundary (a) and for today (b) in terms of idealized crustal cross sections along a major river system. Black arrows show typical flow paths for meteoric water infiltrating into the subsurface and being transported in groundwater systems before exfiltrating into a major river system. Increasing Cenozoic seawater δ^7Li values (Misra and Froelich, 2012) are explained by an increasing availability of bedrock (primary) silicates for chemical weathering (i.e., decreasing weathering intensity) as the global relief increases and the average saprolite thickness becomes smaller. For the current weathering pattern, chemical weathering of primary silicates and subsequent precipitation of secondary minerals (clays, Fe- and Al-hydroxides) fractionate Li isotopes by accumulating ^{7}Li in the groundwater and ^{6}Li in the precipitating mineral phases. If only secondary silicate minerals are exposed to chemical weathering such as inferred for the Paleocene–Eocene boundary (a) no significant Li isotopic fractionation occurs. An increasing relief also yields decreasing subsurface residence times as well as increasing suspended river load concentrations, both potentially affecting riverine δ^7Li in addition to the decreasing weathering intensity.

1) An increasing relief shifts the hydraulic gradient to higher values, increasing flow velocities and shortening residence times along a specific subsurface flow path (Fig. 1). Cooler temperatures decrease the dissolution rates of primary silicate minerals (Lasaga, 1984). Hence, increasing relief and cooler temperatures limit water–rock interaction along specific flow paths.
2) For a low relief, such as inferred for the Paleocene–Eocene boundary (Misra and Froelich, 2012), the hydraulic gradient is low and the average subsurface residence time is high. Long residence times under hot and humid climatic conditions (Miller et al., 1987; Clementz and Sewall, 2011) cause a high degree of water rock-interaction with plenty of newly formed secondary mineral phases, which is usually described as a weathering-intensive or transport-limited weathering pattern (Misra and Froelich, 2012). We thus assume that at the Paleocene–Eocene boundary, the global average saprolite thickness (composed of mostly quartz, clays, Fe- and Al-oxides) was higher than it is today (Fig. 1). Following this argument, and taking into account an increasing global relief as well as decreasing temperatures, the degree of exposure of the silicate bedrock to chemical weathering must have increased over the last 56 Ma, which is equivalent to proposing a decreasing weathering intensity. It should be noted that our use of "weathering intensity" throughout this paper strictly refers to the chemical index of alteration (CIA), which is the commonly used proxy for expressing the chemical weathering intensity of a particular rock or soil sample (Nesbitt and Young, 1982). This definition is particularly useful because it takes into account the ratio between immobile (e.g., Al) and mobile (e.g., Na, Ca, K) elements, on which the amount of newly formed clays, oxides and hydroxides has a first order control. Alternatively, riverine aqueous species concentrations (e.g., [Si], normalized [Si]) have been proposed to operate as weathering intensity proxies (Kisakürek et al., 2005; Pogge von Strandmann et al., 2006). The drawback of using riverine aqueous species concentrations is that, once chemical equilibrium is reached, their concentrations become discharge independent (Maher, 2011), whereas chemical silicate weathering fluxes and corresponding weathering rates are linearly increasing with increasing discharge (Gaillardet et al., 1999; Maher, 2011). The strong dependence on discharge also implies that chemical silicate weathering rates do not necessarily correspond to weathering intensity. For instance, a relatively low chemical weathering rate was calculated for the weathering intense Guyana Shield (Gaillardet et al., 1999).
3) Owing to the higher hydraulic gradient, an increasing global relief shifts the physical erosion rate (i.e., denudation rate) to higher values (Bouchez et al., 2013). A higher denudation rate leads to an increase of the suspended river load concentration, as long as the suspended load is not deposited in lowland areas (Milliman and Meade, 1983; Gaillardet et al., 1999). Consequently, we speculate that the global average suspended river load concentration increased over the last 56 Ma such as already argued by Misra and Froelich (2012).

3. Methods

A series of thermodynamically- and kinetically-controlled reactive transport model simulations using TOUGHREACT V2 (Xu et al., 2011) was performed to assess the effect of the identified changing weathering parameters on Cenozoic global average riverine and seawater δ^7Li (i.e., decreasing subsurface residence time, cooling trend, decreasing weathering intensity, increasing suspended river load concentration). TOUGHREACT has been used to evaluate isotopic fractionation coupled to water–rock interaction and hydrological processes in a variety of

subsurface environments and laboratory experiments (e.g., Sonnenthal et al., 1998; Singleton et al., 2005; Wanner and Sonnenthal, 2013).

3.1. Model setup

Two different types of simulations were carried out to model silicate weathering and associated Li isotopic fractionation (i) in the subsurface and (ii) within rivers (Fig. 2).

3.1.1. Subsurface simulations

Reactive transport of infiltrating meteoric water along a typical subsurface flow path (e.g., arrows in Fig. 1) was simulated for a fully water-saturated, 200 m long porous media with an assumed porosity of 10%. The unsaturated zone was neglected because our focus was on assessing the sensitivity (i.e., trends) of dissolved δ^7Li values as a function of residence time, climate, and weathering intensity rather than on simulating detailed flow features of infiltration through the unsaturated zone and recharge to aquifers and rivers. Subsurface simulations were run for an average linear flow velocity of 1 m/d to simulate a system dominated by advection. The 200 m long model domain (Fig. 2) was divided into 200 cubic grid blocks of $1 \times 1 \times 1$ m each to numerically solve the governing differential equations using TOUGHREACT's integral finite differences approach (Xu et al., 2011).

Pure water in equilibrium with atmospheric CO_2 was specified as initial and boundary fluid compositions. In doing so, atmospheric CO_2 is partially dissolved and provides H^+ necessary for silicate weathering reactions such as illustrated for the weathering of albite to kaolinite:

$$CO_{2(g)} + H_2O = HCO_3^- + H^+ \quad (1)$$

$$2NaAlSi_3O_8 + 2H^+ + H_2O = Al_2Si_2O_5(OH)_4 + 2Na^+ + 4SiO_2 \quad (2)$$

The CO_2 partial pressure pCO_2 was fixed during the course of the simulations to approximate the buffering caused by an almost unlimited CO_2 source from the atmosphere. This specification allows tracking the amount of CO_2 consumed by silicate weathering reactions assuming that the reaction product HCO_3^- exiting the model domain is further transported to the sea, where it precipitates as carbonates (Godderis et al., 2009) (Fig. 1).

A granitic mineral assemblage (quartz, potassium-feldspar, plagioclase, biotite) was assigned to the solid part of the porous media to simulate typical continental silicate weathering processes. Subsequently, the model was divided into a "fresh granite" domain and a domain that experienced previous weathering (e.g., "altered granite") (Fig. 2), thus corresponding to the saprolite zone of our conceptual model (Fig. 1). By varying the volume ratio between the "fresh granite" and "altered granite" domain the effect of the proposed increasing exposure of the silicate bedrock to chemical weathering on δ^7Li was assessed. By running the model for a variable "fresh granite" contribution (i.e., varying volume ratios) we simulated the effect of a varying chemical weathering intensity (i.e., varying saprolite thicknesses) on δ^7Li because a large "fresh granite" or large "altered granite" contribution corresponds to a low or high weathering intensity, respectively. Accordingly, we also assess earlier findings reporting that the chemical silicate weathering intensity forms a first order control on aqueous δ^7Li (Huh et al., 2001; Kisakürek et al., 2005; Pogge von Strandmann et al., 2006).

A mineralogical composition typical for the Sierra Nevada Batholith (Economos et al., 2010) was defined for the "fresh granite" domain (Table 1). The initial mineralogical definition included a bulk Li concentration of 24 ppm (Economos et al., 2010), which is similar to the average upper-crustal Li concentration of 35 ± 11 ppm (Teng et al., 2004). Owing to their similar ionic radii, Li^+ substitutes easily for Mg^{2+} into the structural octahedral sites of silicate minerals (Vigier et al., 2008). Furthermore, Li tends to accumulate in biotite (Kretz et al., 1989). Accordingly, Li was introduced into the model by specifying Li-bearing biotite using a $Mg^{2+}{}_{-1}Li^{+}{}_{1}K^{+}{}_{1}$ exchange (Table 2). Because in granitic environments, silicate mineral phases are predominantly weathered to kaolinite (White, 2002; Rudnick et al., 2004; Maher et al., 2009), and because goethite is the most widespread form of secondary iron oxides (Tardy and Nahon, 1985) Li-bearing kaolinite, and Li-bearing goethite were allowed to precipitate. By neglecting secondary Ca- and Mg-bearing minerals we do not fully investigate the fate of these two elements during silicate weathering. Our conceptual model (Fig. 1), however, assumes that riverine [Ca] and [Mg] are affected by carbonate weathering to ensure that carbonate precipitation and subsequent CO_2 consumption are occurring in the ocean, eventually.

TOUGHREACT V2 (Xu et al., 2011) computes mineral dissolution and precipitation reactions as kinetic reactions based on transition state theory (TST) (Lasaga, 1984)

$$r = A \cdot k \cdot \left(1 - \left(\frac{Q}{K}\right)^m\right)^n \quad (3)$$

where A refers to the mineral reactive surface area ($m^2_{mineral}/kg_{H2O}$), k is the reaction rate constant ($mol/m^2/s$), Q refers to the ion activity product of a mineral dissolution/precipitation reaction (Table 2) and K is the corresponding equilibrium constant. Exponents m and n are

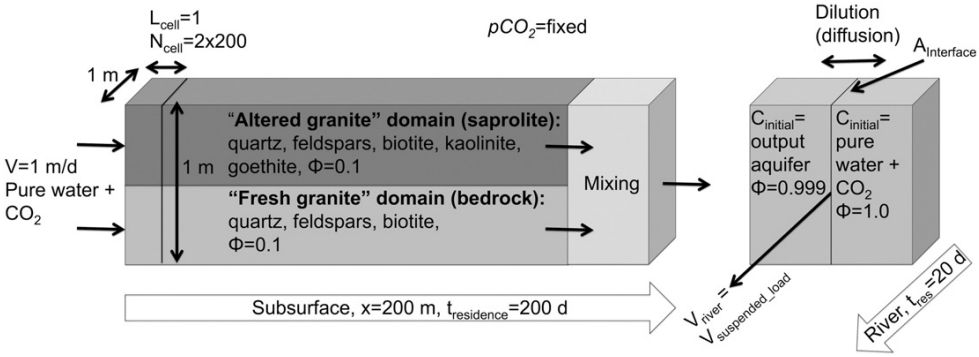

Fig. 2. Model setup for simulating reactive transport in the subsurface and within rivers. Subsurface simulations were run for meteoric water infiltrated and transported along a 200 m long flow path eventually exfiltrating into a river system (e.g., arrows in Fig. 1). They were run for various fresh-to-altered granite volume fractions to simulate the effects of a varying silicate weathering intensity on δ^7Li. Fluids flowing along the two model domains were fully mixed in the downstream model boundary ("mixing") to track the integrated Li isotopic signal. River simulations were run as batch simulations (no flow) assuming that the suspended load is transported at the same velocity as river water. Moreover, river simulations consider a diffusive dilution of the exfiltrated groundwater with water that experienced no previous water–rock interaction (i.e., pure water + CO_2). For both systems (subsurface and river), Li isotopic fractionation is simulated to occur during kaolinite and goethite precipitation.

Table 1
Initial and boundary conditions.

		Simulation of current weathering pattern		Simulation of Paleocene–Eocene boundary weathering pattern	
		Subsurface	River	"Fresh granite"	"Altered granite"
pH	–	5.63	[a]8.79	5.37	5.37
HCO_3^-	mol/kg_{H2O}	[b]1.51E−5	[a]4.18E−3	[c]4.52E−05	[c]4.52E−05
Na^+	mol/kg_{H2O}	1.0E−10	[a]3.45E−6	1.0E−10	1.0E−10
K^+	mol/kg_{H2O}	1.0E−10	[a]1.67E−4	1.0E−10	1.0E−10
Mg^{2+}	mol/kg_{H2O}	1.0E−10	[a]2.00E−5	1.0E−10	1.0E−10
Ca^{2+}	mol/kg_{H2O}	1.0E−10	[a]2.22E−3	1.0E−10	1.0E−10
Al^{3+}	mol/kg_{H2O}	1.0E−10	[a]8.31E−7	1.0E−10	1.0E−10
$^6Li^+$	mol/kg_{H2O}	[d]7.68095e−11	[a]4.5097E−8	[d]7.68095E−11	[d]7.68095E−11
$^7Li^+$	mol/kg_{H2O}	[d]9.23191E−10	[a]5.4726E−7	[d]9.23191E−10	[d]9.23191E−10
$SiO_{2(aq)}$	mol/kg_{H2O}	1.0E−10	[a]3.36E−4	1.0E−10	1.0E−10
$O_{2(aq)}$	mol/kg_{H2O}	2.5E−4	2.5E−4	2.5E−4	2.5E−4
Fe^{2+}	mol/kg_{H2O}	1.0E−10	[a]6.59E−19	1.0E−10	1.0E−10
$CO_{2(s)}$	Vol frac (of solids)	0.01	0.01	0.01	0.01
Albite	Vol frac (of solids)	0.304	0.304	0.304	0.304
Anorthite	Vol frac (of solids)	0.076	0.076	0.076	0.076
Orthoclase	Vol frac (of solids)	0.29	0.29	0.29	0.29
Quartz	Vol frac (of solids)	0.31	0.31	0.31	0.31
Annite	Vol frac (of solids)	0.04	0.04	0.04	0.04
Li-phlogopite	Vol frac (of solids)	0.01	0.01	0.01	0.01
Kaolinite	Vol frac (of solids)	0.0	0.0	0.0	0.004[e]
^6Li (kaolinite)	Vol frac (of solids)	0.0	0.0	0.0	0.00031020[e]
^7Li (kaolinite)	Vol frac (of solids)	0.0	0.0	0.0	0.00368979[e]
Goethite	Vol frac (of solids)	0.0	0.0	0.0	0.0003[e]
^6Li (kaolinite)	Vol frac (of solids)	0.0	0.0	0.0	0.00002326[e]
^7Li (kaolinite)	Vol frac (of solids)	0.0	0.0	0.0	0.00027673[e]
Porosity	–	0.1	0.99	0.1	0.1

[a] Read out from downstream boundary of subsurface model run.
[b] Calculated by assuming equilibrium with pCO_2 of 370 ppmV ($\log(pCO_2) = -3.43$).
[c] Calculated by assuming equilibrium with pCO_2 of 1200 ppmV ($\log(pCO_2) = -2.92$).
[d] Specification corresponds to an initial δ^7Li of 0.0‰.
[e] Read out from model run with "fresh granite" domain only.

fitting parameters that must be experimentally determined. For this study they were taken as equal to one, which is usually, but not always the case. In order to calculate effective precipitation and dissolution rates (Eq. (3)) reaction rate constants were defined according to Palandri and Kharaka (2004) whereas equilibrium constants were taken from the Soltherm.H06 database (Reed and Palandri, 2006), which was derived using SUPCRT92 (Johnson et al., 1992). Mineral stoichiometries, thermodynamic and kinetic parameters, and initial mineral and fluid compositions are summarized in Tables 1 and 2.

3.1.2. River simulations

River simulations were conducted essentially as batch simulations, where the flow velocity was set to zero (Fig. 2). In doing so, it was assumed that the reactive suspended load (i.e., solid phase) is transported at the same velocity as river water, which is in agreement with current knowledge about transport of suspended river loads (Fryirs and Brierley, 2013). Simulating reactive transport in rivers by means of a batch simulation is justified because only the relative transport velocity between aqueous and solid phases (i.e., suspended load) matters, whereas the actual velocity of the two phases has no effect as long as aqueous and solid phases are transported at the same velocity.

Two grid blocks of 1 × 1 × 1 m each were defined to simulate that subsurface waters exfiltrating into river systems are diluted by river water, which previously experienced no or only minor water–rock interaction. Consequently, steady-state concentrations obtained at the downstream model boundary of the subsurface simulations were taken as input concentrations for one of the two grid blocks, while pure water in equilibrium with CO_2 was defined as the initial concentration for the second grid block (Fig. 2). It should be noted, that this particular grid block has no geochemical meaning other than ensuring that exfiltrated subsurface water is diluted during its transport in the river. Due to the initial concentration gradient, a diffusive flux J_{Di} occurred between the two grid blocks, expressed as

$$J_{D_i} = \frac{\Phi \cdot \tau \cdot D_{aq} \cdot A_{Interface}}{d_1 + d_2} \cdot \frac{dC_i}{dx} \quad (4)$$

where D_{aq} refers to the molecular diffusion coefficient of aqueous species (~10^{-9} m^2/s), $A_{Interface}$ (m^2) is the interfacial area between the two grid blocks, dC_i/dx (mol/kg_{H2O}/m) is the concentration gradient of species i, d_1 and d_2 (m) refer to the distances from the center of the two grid blocks to their mutual interface, and Φ and τ are the porosity and tortuosity, respectively. Reactions between the suspended river load and river waters were only considered for the grid block initially containing exfiltrating subsurface water. By setting the corresponding porosity to a very large value of 99.9% (Fig. 2), it was ensured that the suspended load only forms a minor fraction of the total river volume. The tortuosity was set to 1.0 for both grid blocks.

The same initial granitic mineralogical composition as for the subsurface "fresh granite" domain was assigned to the suspended river load (Table 1). In doing this, we assume that the suspended load contains a significant amount of primary silicate minerals in addition to the dominant clays and oxides (Gaillardet et al., 1999). This model assumption is consistent with Bouchez et al. (2011) who observed that the mineralogical composition of the suspended load is dependent on the particle size and that primary silicate minerals (e.g., quartz, albite) are enriched in the coarser fraction. Consequently, new goethite and kaolinite are allowed to precipitate and Li isotopic fractionation in the simulated river thus occurs in the same fashion as in the subsurface simulations. As long as primary silicate minerals are exposed to chemical weathering, our river simulations are not sensitive to the ratio between primary and secondary minerals. Accordingly, we did not change the initial mineral volume fraction when compared to the subsurface simulations (Table 1).

Table 2
Simulated silicate weathering reactions.

Mineral phase	[a]log(K)	[b]k (mol/m^2/s)	[c]A-"fresh granite" (cm^2/g)	A-"altered granite" (cm^2/g)	A-"river simulation" (cm^2/g)	Hydrolysis reaction
$CO_{2(s)}$[d]	−11.25	1.00e−04	100	100	100	$CO_{2(s)} + H_2O = H^+ + HCO_3^-$
Albite[e1]	1.41	2.75E−13	1	0	6000 or 375[f]	$NaAlSi_3O_8 + 4H^+ = Na^+ + 3SiO_{2(aq)} + Al^{3+} + 2H_2O$
Anorthite[e1]	24.52	7.59E−10	1	0	6000 or 375	$CaAl_2Si_2O_8 + 8H^+ = Ca^{2+} + 2SiO_{2(aq)} + 3Al^{3+} + 4H_2O$
Orthoclase	−0.20	3.89E−13	1	0	6000 or 375	$KAlSi_3O_8 + 4H^+ = K^+ + 3SiO_{2(aq)} + Al^{3+} + 2H_2O$
Quartz	−4.05	2.46E−13	1	0	6000 or 375	$SiO_{2(s)} = SiO_{2(aq)}$
Annite[e2]	29.37	3.16E−11	2.4	0	6000 or 375	$KFe_3AlSi_3O_{10}(OH)_2 + 10H^+ = Al^{3+} + K^+ + 3Fe^{2+} + 6H_2O + 3SiO_2$
Li-phlogopite [e2,g]	37.43	3.98E−13	2.4	0	6000 or 375	$K_{1.144}Mg_{2.856}Li_{0.144}(AlSi_3O_{10})(OH)_2 + 10H^+ = 1.144\ K^+ + 2.856\ Mg^{2+} + 0.01104322\ ^6Li^+ + 0.13295678\ ^7Li^+ + Al^{3+} + 3SiO_{2(aq)}$
Kaolinite[e3]	7.55	6.6E−14	6824	6824	6000 or 375	$Al_2Si_2O_5(OH)_4 + 6H^+ = 2Al^{3+} + 2SiO_{2(aq)} + 5H_2O$
^{6}Li (kaolinite)[e3,h]	−2.60877392	6.6E−14	6824	6824	6000 or 375	$^6Li = {}^6Li^+$
^{7}Li(kaolinite)[e3,h]	−2.6	6.6E−14	6824	6824	6000 or 375	$^7Li = {}^7Li^+$
Goethite[e4]	−8.3710	1.15E−8	6824	6824	6000 or 375	$Fe(OH)_3 + 2H^+ = 0.25O_{2(aq)} + 1.5H_2O + Fe^{2+}$
^{6}Li (goethite)[e4,h]	−2.60877392	1.15E−8	6824	6824	6000 or 375	$^6Li = {}^6Li^+$
^{7}Li (goethite)[e4,h]	−2.6	1.15E−8	6824	6824	6000 or 375	$^7Li = {}^7Li^+$

[a] With the exception of kaolinite, which was defined according to Yang and Steefel (2008), equilibrium constants log(K) were defined according to Reed and Palandri (2006).
[b] Reaction rate constants k were defined according to Palandri and Kharaka (2004).
[c] Reactive surface areas of primary silicate minerals (feldspars, quartz, biotite) were calibrated to get a Li concentration larger than the global average riverine Li conc. (0.265 μmol/L) at the downstream aquifer model boundary ("mixing", Fig. 2). Reactive surface areas of secondary minerals (e.g., kaolinite, goethite) were set to 6824 cm^2/g according to Dobson et al. (2003).
[d] Hypothetical solid $CO_{(s)}$ phase to fix pCO_2 (=model CO_2 source). Different values were defined to fix pCO_2 to 1200 ppmV (log(K) = −10.739) and 370 ppmV (log(K) = −11.252).
[ex] Endmember of solid solution x.
[f] River simulations were run for two different reactive surface areas to simulate the effects of a varying suspended river load on riverine δ^7Li values. 6000 cm^2/g allowed matching the current global average riverine δ^7Li value after a simulated river residence time of 20 days.
[g] Corresponds to a phlogopite Li concentration of 2400 ppm to get an initial bulk granite Li conc. of 24 ppm according to Economos (2010) (at a phlogopite vol fraction of 0.01), and a δ^7Li value of 0.0‰.
[h] Li isotopic endmember of defined solid solution (Fig. 3). $K_{6Li}/K_{7Li} = 0.98 = \Delta^7Li_{solution\text{-}kaolinite} = -20‰$. log(K) was calibrated to get maximum Li concentration in goethite and kaolinite of about 200 ppm.

3.2. Simulation of Li isotopic fractionation

To simulate Li isotopic fractionation, ^{6}Li and ^{7}Li were incorporated into the mineral stoichiometries of biotite, kaolinite and goethite (Table 2). An initial δ^7Li value of 0.0‰ was assumed for Li-bearing biotite corresponding to the average δ^7Li value of the upper continental crust (Teng et al., 2004). Assuming stoichiometric biotite dissolution, our simulations agree with previous studies showing that no or only minor Li isotopic fractionation occurs during mineral dissolution (Pistiner and Henderson, 2003; Huh et al., 2004). In contrast, our model considers Li isotopic fractionation during Li incorporation into precipitating kaolinite and goethite, using a solid solution approach similar to the one described for simulating Sr and Cr isotopic fractionation (Sonnenthal et al., 1998; Wanner and Sonnenthal, 2013). It should be noted, however, that Li must be treated slightly differently because it is incorporated into secondary minerals as a trace element, whereas Cr and Sr can be major constituents of minerals controlling the fate of Cr and Sr isotopes (e.g., $Cr(OH)_3$ and $SrCO_3$). Particularly challenging is the fact that, although some suggestions are found in the literature (Pistiner and Henderson, 2003; Vigier et al., 2008), it has not yet been shown how Li structurally substitutes into kaolinite and goethite. Because of this lack of detailed mineralogical knowledge, our model assumes a solid solution with three different endmembers (Fig. 3) to simulate Li uptake and associated Li isotopic fractionation during kaolinite and goethite precipitation: (i) a pure, non-Li bearing kaolinite and goethite endmember, (ii) a pure ^{6}Li bearing mineral endmember and (iii) a pure ^{7}Li bearing endmember. The pure ^{6}Li and ^{7}Li endmembers are hypothetical, but their specification allows fitting experimentally observed aqueous Li concentrations as well as measured amounts of Li that are incorporated in secondary minerals by calibrating the corresponding log(K) values.

The precipitation rate r_{prec} of the Li bearing kaolinite and goethite solid solution is defined as the sum of the individual endmember (Fig. 3) precipitation rates $r_{pure2nd}$, r_{6Li} and r_{7Li}:

$$r_{prec} = r_{pure2nd} + r_{^6Li} + r_{^7Li} \quad (5)$$

The rate of a specific endmember, r_{endm}, is calculated according to a TST-like expression

$$r_{endm} = A \cdot k \cdot \left(1 - \frac{Q_{endm}}{K_{endm}}\right) + k \cdot A \cdot (x_{endm} - 1) \quad (6)$$

where x_{endm} refers to the mole fraction of a specific secondary mineral endmember. For the hypothetical, pure ^{6}Li and ^{7}Li endmembers x_{6Li} and x_{7Li} are calculated according to:

$$x_{^6Li} = \frac{Q_{^6Li}/K_{^6Li}}{Q_{^6Li}/K_{^6Li} + Q_{^7Li}/K_{^7Li}} \quad (7)$$

$$x_{^7Li} = \frac{Q_{^7Li}/K_{^7Li}}{Q_{^6Li}/K_{^6Li} + Q_{^7Li}/K_{^7Li}} \quad (8)$$

Eqs. (7) and (8) ensure that the amount of Li that is incorporated into goethite and kaolinite reflects the Li concentration of the aqueous solution. Accordingly, the amount of Li removed by precipitation

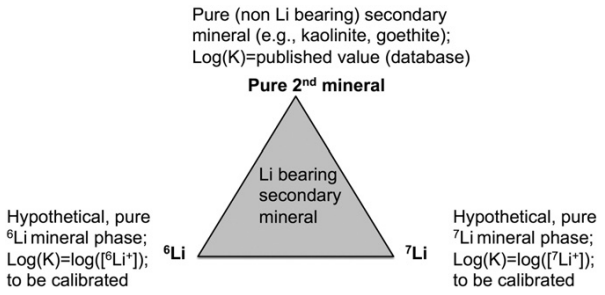

Fig. 3. Schematic illustration of the composition of modeled Li bearing secondary minerals, which were simulated as ideal solid solutions. The three endmembers were defined as pure goethite or kaolinite with known thermodynamic properties, and hypothetical, but pure ^{6}Li and pure ^{7}Li, for which log(K) values have to be calibrated by matching observed secondary mineral and aqueous Li concentrations.

increases with increasing aqueous Li concentration. By doing so, our model is in good agreement with an experimental study showing that [Li] of synthesized smectites is linearly correlated with the corresponding aqueous [Li] (Decarreau et al., 2012).

Using the solid solution approach described above allows conveniently specifying a particular Li isotopic fractionation factor α and corresponding enrichment factor ε for our simulations:

$$\alpha = \frac{K_{^6Li}}{K_{^7Li}} \tag{9}$$

$$\varepsilon = (\alpha - 1) \cdot 1000 \approx \Delta^7Li = \delta^7Li_{2ndMin} - \delta^7Li_{solution} \tag{10}$$

Experimentally-determined Li isotopic enrichment factors for Li incorporation into precipitating minerals have so far only been reported for smectite, yielding values between −1.6 (at T = 250 °C) and −16.5‰ (at T = 25 °C), depending on the experimental temperature (Vigier et al., 2008; personal communication). Other studies determined Δ^7Li values between dissolved and suspended Li loads in rivers yielding $\Delta^7Li_{suspended\text{-}dissolved}$ from −6 to −36‰ (Huh et al., 2001; Kisakürek et al., 2005; Pogge von Strandmann et al., 2006, 2010). Because of this relatively sparse dataset, we assigned a Li isotopic enrichment factor of −20‰ for kaolinite as well as for goethite precipitation, which is within the range of Li isotopic enrichment factors reported or inferred for secondary mineral precipitation.

Li adsorption on solid surfaces has been proposed as an additional process causing Li isotopic fractionation (Zhang et al., 1998; Pistiner and Henderson, 2003). Significant fractionation (ε = −13‰) was reported for an experiment involving Li adsorption via surface complexation reactions at gibbsite surfaces (Pistiner and Henderson, 2003). Moreover, enrichment factors of −21‰ and −29‰ were experimentally determined for Li adsorption on kaolinite and vermiculite, respectively (Zhang et al., 1998). These enrichment factors, however, were determined by solely studying the dissolved Li and no information regarding the surface complexation or substitution reaction is available. In contrast, very little Li isotopic fractionation was observed during Li exchange (i.e., ion exchange reaction) with smectite interlayers (Pistiner and Henderson, 2003; Vigier et al., 2008). Overall, experimental data suggest that Li isotopic fractionation is caused by surface complexation reactions associated with a changing Li coordination chemistry or by Li substitution into crystal lattices. In contrast, physical Li adsorption by ion exchange reactions does not seem to cause significant fractionation. Similar to Bouchez et al. (2013) our model does not distinguish between Li exchange-, Li surface complexation-, or Li substitution reactions and Li uptake by secondary minerals and associated Li isotopic fractionation is solely simulated as a crystallographic substitution reaction during the formation of kaolinite and goethite such as discussed earlier.

Li isotope fractionation inherited from differences in the aqueous ^{6}Li and ^{7}Li diffusive flux was neglected because kaolinite and goethite precipitation was not assumed to be transport-limited by Li diffusion.

4. Model results and discussion

4.1. Simulation of the current weathering pattern (Fig. 1b)

To simulate the inferred current weathering pattern with predominant weathering of primary silicate minerals (Fig. 1) a "fresh granite" mineralogical composition was assigned to the entire subsurface model domain (i.e., 100% "fresh granite") and the pCO_2 was fixed to the approximate current atmospheric pCO_2 of ca. 370 ppm volume (ppmV) (Keeling, 1960). The solubility of the pure, but hypothetical Li-bearing kaolinite and goethite endmember (log(K)) was calibrated to −2.6 (Table 2) to get a maximum kaolinite and goethite Li concentration within the subsurface domain of 200 ppm. A maximum value of 200 ppm is in agreement with Li concentration measurements in continental clays (Tardy et al., 1972). For the subsurface simulations, reactive surface areas for primary mineral phases were set to 1–2 cm^2/g (Table 2) to obtain a Li concentration at the end of the subsurface domain (4.08 μg/L, Fig. 4a, d) that is larger than the global average riverine value of 1.83 μg/L (Misra and Froelich, 2012). A reactive surface area of 1–2 cm^2/g also ensured that chemical equilibrium was not fully established within the subsurface domain and that primary mineral dissolution was occurring along the full domain (Fig. 4b, e). Reactive surface areas of precipitating kaolinite and goethite were set to the high value of 6824 cm^2/g based on Dobson et al. (2003).

With the specified parameters, our model yielded a continuous δ^7Li increase along the subsurface model domain reaching a dissolved δ^7Li value of roughly +10‰ at the downstream model boundary (Fig. 4a, d). It should be noted that the slope of the δ^7Li increase with residence time is dependent on the specified enrichment factor. For lower factors (i.e., less fractionation), longer residence time is needed to reach the same δ^7Li as for ε = −20‰, or vice versa. However, the correlation between δ^7Li and residence time is not sensitive to the specified enrichment factor. A δ^7Li value of +10‰ is significantly lower than the current global average riverine δ^7Li value of +23‰ (Misra and Froelich, 2012) implying that Li isotopic fractionation occurring in rivers forms a major contribution on riverine δ^7Li. This simulation finding is supported by δ^7Li values derived from groundwaters and rivers draining the Columbia River basalt as well as small granitic catchments yielding significantly larger δ^7Li values for river samples (Lemarchand et al., 2010; Liu et al., in revision). Consequently, the reactive surface area of the suspended river load $A_{suspended\_load}$ was calibrated to 6000 cm^2/g (Table 2) for the corresponding river simulation to match the global average riverine δ^7Li value (+23‰) after a simulated river residence time of 20 days, for which all river simulations were run (Fig. 4a). Similarly, the interfacial area between the two grid blocks of the river simulation $A_{interface}$ (Eq. (4), Fig. 2) was set to 2560 m^2 to result in dilution of the exfiltrated groundwater by a factor of roughly 2. In doing so, the obtained Li concentration at the end of the river simulation (0.79, μg/L, Fig. 4a) was somewhat lower but still in the same order of magnitude as the global average riverine Li concentration of 1.83 μg/L (Misra and Froelich, 2012).

To explore the sensitivity of riverine δ^7Li on the reactivity of the suspended river load and thus on the actual suspended load concentration, the river simulation was also performed for an $A_{suspended\_load}$ of 375 cm^2/g (Table 2). This value is 16 times lower than the initial surface area (6000 cm^2/g), and thus corresponds to the Misra and Froelich (2012) interpretation proposing that "the riverine Li flux has changed the ratio of dissolved to suspended partitioning from 4:1 in Paleocene to 1:4 today". Simulation results show that only minor Li isotopic fractionation takes place if the reactivity of the suspended load is this low (Fig. 4d). The high sensitivity of riverine δ^7Li on $A_{suspended\_load}$ implies that an increasing suspended river load concentration may have formed an important contribution on the seawater and global average riverine δ^7Li increase observed during the Cenozoic (Misra and Froelich, 2012).

Our simulation results also imply that riverine δ^7Li values increase with increasing subsurface residence time (Fig. 4a, d). This particular finding is in good agreement with seasonal riverine δ^7Li variations observed in streams draining the Columbia river basalt west of the Cascade Range, where seasonal precipitation and thus subsurface residence time variations are large (Liu et al., in revision). It is, however, unlikely that a Cenozoic global average subsurface residence time increase caused the Cenozoic seawater δ^7Li increase because for an increasing relief (e.g., over the Cenozoic), residence times tend to decrease and not to increase.

4.2. Simulation of the Paleocene–Eocene boundary weathering pattern (Fig. 1a)

A series of simulations with a varying "fresh granite" volume fraction corresponding to a varying contribution of "fresh granite" weathering

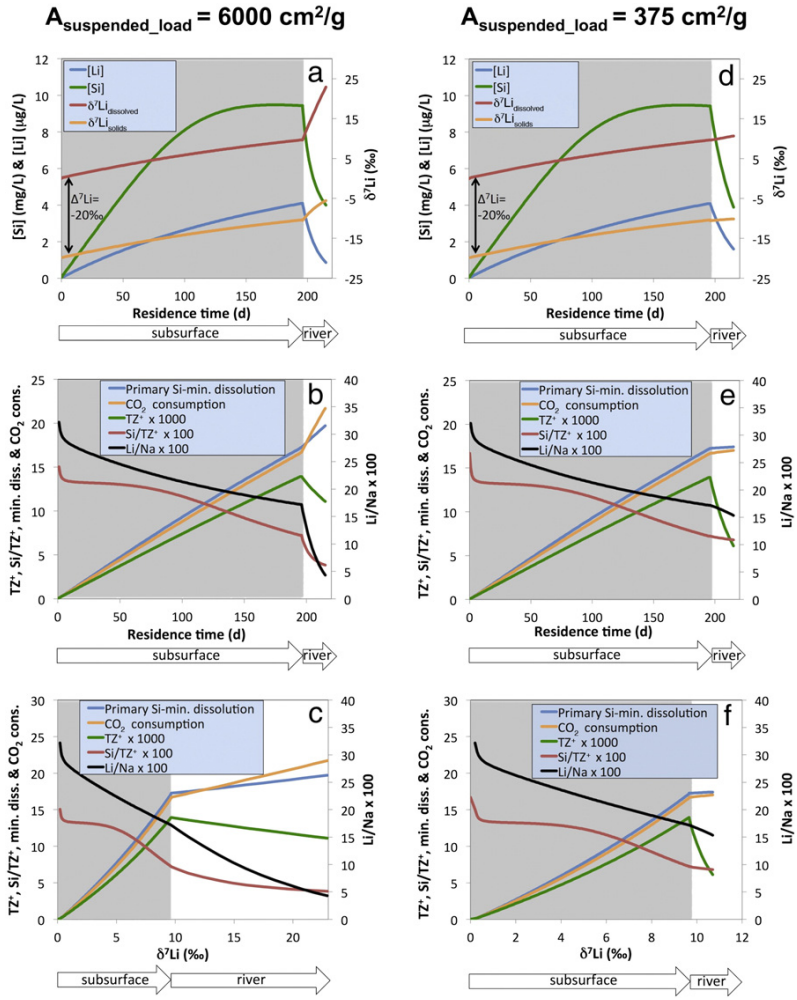

Fig. 4. Model results for the simulated current weathering pattern with 100% "fresh granite" contribution (Fig. 1b). (a) and (d) illustrate steady state [Li] and [Si] along the full model domain (subsurface + river), as well as corresponding δ^7Li profiles ($\delta^7Li_{dissolved}$ and $\delta^7Li_{kaolinite} = \delta^7Li_{goethite} = \delta^7Li_{solids}$) for a reactive suspended river load surface area of 6000 cm^2/g and 375 cm^2/g, respectively, illustrating that the simulated $\Delta^7Li_{solids\text{-}dissolved}$ was equal to the initially specified Li isotope enrichment factor of $\varepsilon = -20‰$. (b) and (e) present corresponding steady state profiles of typical silicate weathering tracers such as TZ^+ (in meqv/kg), Si/TZ^+, Li/TZ^+ and Li/Na (molar ratio). Also shown are the cumulative primary mineral dissolution (quartz + feldspars + biotite) and corresponding CO_2 consumption profiles (in kmol) during a simulated time period of 100 years. (c) and (f) illustrate the relationship between the parameters shown in (b) and (e) as a function of $\delta^7Li_{dissolved}$. Note that profiles except the ones shown in (c) and (f) are plotted against fluid residence time to simultaneously illustrate subsurface and river simulations. Along the subsurface domain (gray shaded area) fluid residence time (x-axis) also corresponds to the distance along the subsurface domain because the flow velocity was 1 m/d.

(i.e., varying weathering intensity) was run to match riverine δ^7Li values inferred for the Paleocene–Eocene boundary. These simulations were run for a fixed pCO_2 of 1200 ppmV to account for the atmospheric pCO_2 inferred for the Paleocene–Eocene boundary (Li and Elderfield, 2013). For the "altered granite" domain the reactive surface area of primary silicates was set to zero, thus simulating an extreme weathering intensity where primary minerals are either fully replaced or fully coated by secondary minerals. Moreover, the initial presence of Li-bearing kaolinite and goethite was specified for this model domain, whereas their Li isotopic composition and initial volume fractions (e.g., $\delta^7Li = -10‰$, Table 1) were input from the results of a pure "fresh granite" run (i.e., 100% "fresh granite") after a simulated time period of 100 years. In contrast to the runs simulating the current weathering pattern, the varying weathering intensity runs were only performed for the subsurface domain (Fig. 2) because our simulation results imply that only minor Li isotopic fractionation occurs within rivers where the suspended river load concentration is low (Fig. 4d), which has been inferred for the Paleocene–Eocene boundary (Misra and Froelich, 2012).

Model results show that downstream δ^7Li values become more positive with an increasing contribution of "fresh granite" weathering (i.e., decreasing weathering intensity) (Fig. 5a). A strong correlation between δ^7Li and fresh granite is, however, only observed for fresh granite contributions <10%, which is inherited from the strong Li solubility contrast between the "fresh granite" (i.e., Li-bearing biotite) and the "altered granite" domain (i.e., Li bearing kaolinite and goethite) (Fig. 6). Nevertheless, our simulations imply that a decreasing weathering intensity over the Cenozoic may have formed an important contribution to the Cenozoic seawater and global average riverine δ^7Li increase (Misra and Froelich, 2012) in addition to the increasing suspended river load concentration (Fig. 4a, d). Moreover, our simulations show that low global average riverine δ^7Li values inferred for the Paleocene–Eocene boundary (Misra and Froelich, 2012) may have been inherited from predominant dissolution of previously formed secondary

mineral phases having a low δ^7Li value (e.g., −10‰, Fig. 6a) and a minor contribution of primary silicate rock dissolution and corresponding precipitation of newly formed secondary mineral phases associated with Li isotopic fractionation. For our simplified system (Fig. 2), a fresh granite contribution of about 5% is required to obtain a δ^7Li value similar to the minimum value inferred for the Paleocene–Eocene boundary at the downstream subsurface model boundary (e.g., +6‰, Fig. 5a). It should be noted that this particular interpretation is entirely different from the one of Misra and Froelich (2012) because it does not rely on congruent weathering of primary silicate minerals.

4.2.1. Model uncertainty and mass balance considerations

If a significant proportion of Li was adsorbed to goethite and kaolinite surfaces rather than fully substituted into the crystal structure, Li solubility of weathering-intense, secondary mineral dominated systems could be much higher than shown in Fig. 6a. Especially for estuaries where the ionic strength is higher than it is in aquifers or rivers, Li complexed to kaolinite and goethite surfaces could be readily desorbed by surface complexation reactions involving other, highly concentrated cations (e.g., Na, K, Ca, Mg). Such estuarine desorption has been shown for various other trace metals (Du Laing et al., 2009).

Distinguishing between Li surface complexation and Li substitution reactions in our model would simply change the slope and curvature of the δ^7Li vs. weathering intensity relation (Fig. 5a). Consequently, it would also change the amount of fresh granite weathering that is required to obtain an inferred δ^7Li value of +6‰. The same applies if we were using a Li isotopic enrichment factor other than −20‰, or if exchanged/complexed Li did not show the same δ^7Li value than structural Li, which was observed for Mg (Wimpenny et al., 2014). However, our main model observations, the overall inverse correlation between weathering intensity and riverine δ^7Li would remain unchanged (Fig. 5a).

The above discussion illustrates that riverine [Li] derived from our model should be considered as an end-member, minimum [Li] scenario for the Paleocene–Eocene boundary ([Li] = 0.25 μg/L, Fig. 5a). Updating the Misra and Froelich (2012) mass balance calculation with this [Li] as well as the inferred minimum riverine δ^7Li (+6‰) yields seawater δ^7Li and [Li] of +24‰ and 112 μg/L, respectively. Whereas the calculated seawater δ^7Li is close to the observed value (+22‰, Misra and Froelich, 2012), 112 μg/L is significantly lower than the inferred Paleocene–Eocene seawater [Li] (179 μg/L), which is based on the assumption that seawater [Li] remained constant throughout the Cenozoic (Misra and Froelich, 2012). If seawater [Li] was indeed constant, the contradiction with the updated mass balance calculation could be resolved by increasing the hydrothermal Li flux by a factor of about 1.6 or by increasing continental discharge by a factor of ca. 7.3, both having only a minor effect on seawater δ^7Li (<1‰). However, only the hydrothermal [Li] flux increase seems to be in a reasonable order of magnitude (Otto-Bliesner, 1995; Berner and Kothavala, 2001).

When discussing mass balance calculations for the global Li cycle it should by noted that the calculations performed by Misra and Froelich (2012) are highly sensitive to Li isotopic fractionation occurring in the ocean during Li uptake by pelagic sediments and alteration of the basaltic oceanic crust (i.e., reverse weathering). For oceanic Li isotopic fractionation to cause a seawater δ^7Li shift less than +16‰, the Paleocene–Eocene boundary mass balance also works (i.e., seawater

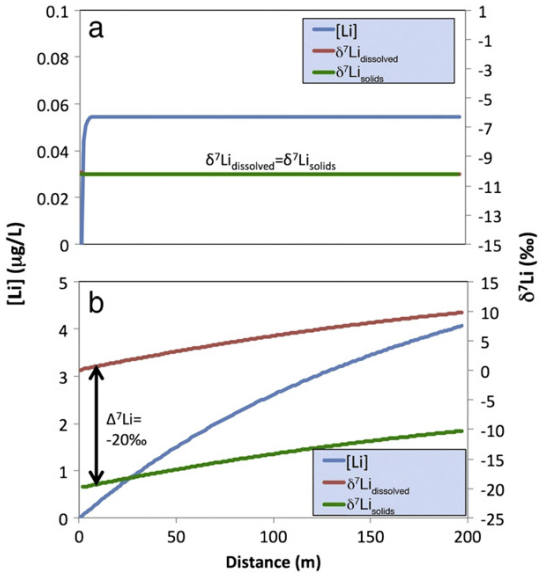

Fig. 6. Simulated steady-state [Li] and δ^7Li profiles along the altered (a) and fresh granite domain (b) of the Paleocene–Eocene boundary weathering pattern (Fig. 1a).

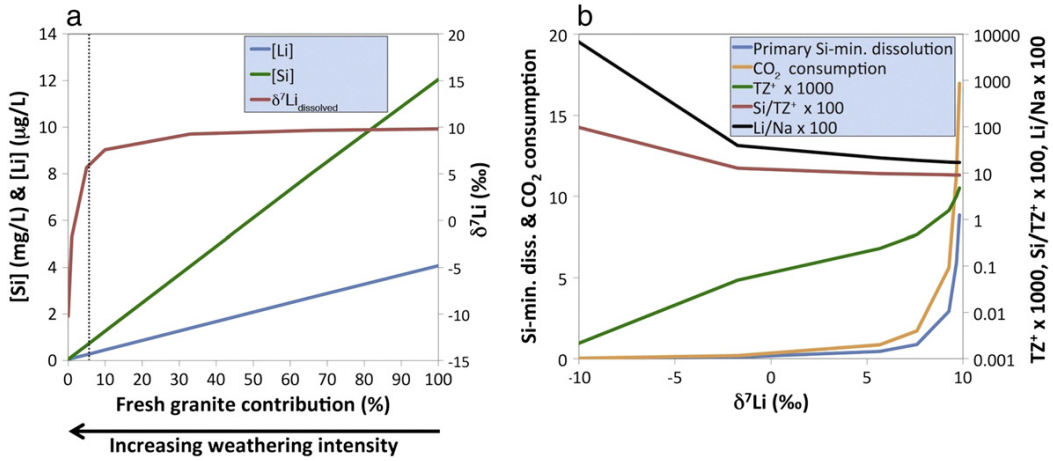

Fig. 5. Model results for the simulated Paleocene–Eocene boundary weathering pattern (Fig. 1a). (a) Steady state [Si], [Li] and δ^7Li at the downstream subsurface model boundary ("mixing", Fig. 2) plotted as a function of the simulated "fresh granite" contribution or inverse weathering intensity, respectively. The dashed line illustrates that 5% fresh granite contribution is required to get an assumed Paleocene–Eocene boundary riverine δ^7Li value of +6‰, which in turn yields a corresponding [Li] of 0.25 μg/L. (b) Cumulative amounts of primary mineral dissolution (feldspars, biotite, quartz) and CO_2 consumption (in kmol) within the entire subsurface model domain during a simulated time period of 100 years as a function of steady state δ^7Li values at the downstream subsurface model boundary. Also shown are steady state TZ^+ (in meqv/kg), Si/TZ^+ and Li/Na (molar ratio) at the downstream subsurface model boundary as a function of corresponding δ^7Li values.

$\delta^7Li = +22‰$) for riverine δ^7Li and/or [Li] (i.e., Li flux) larger than the ones derived from our end-member considerations ([Li] = 0.25 μg/L, $\delta^7Li = +6‰$, Fig. 5a).

In summary, a reasonable mass balance can be formulated with riverine [Li] and δ^7Li derived from our model ([Li] = 0.25 μg/L, $\delta^7Li = +6‰$, Fig. 5a). This suggests that for the Paleocene–Eocene boundary, riverine [Li] could have been significantly lower than it is today (Fig. 5a). However, it has to be appreciated that any mass balance calculation for past global Li cycles is affected by a relatively large uncertainty and it is beyond the scope of this study to provide accurate numbers for the one at the Paleocene–Eocene boundary. Without knowing the true global average riverine δ^7Li and [Li] for the Paleocene–Eocene boundary, our study can thus not rule out a (minor) contribution from a changing seawater hydrothermal Li flux and a changing magnitude of oceanic Li isotopic fractionation on the Cenozoic seawater δ^7Li increase.

5. Implications for using δ^7Li as a silicate weathering proxy

Previous studies did not show a distinct correlation between riverine δ^7Li and traditional silicate weathering proxies such as [Si], total cation charge TZ^+ ($TZ^+ = Na^+ + K^+ + 2\,Mg^{2+} + 2Ca^{2+}$), normalized [Si] ($Si/TZ^+$), [Li], $^{87}Sr/^{86}Sr$, and Li/Na (Huh et al., 1998, 2001; Pogge von Strandmann et al., 2006; Millot et al., 2010; Pogge von Strandmann et al., 2010). For instance, Huh et al. (1998) did not observe a clear correlation between riverine δ^7Li and $^{87}Sr/^{86}Sr$, δ^7Li and [Li], as well as between δ^7Li and TZ^+, whereas δ^7Li tended to be slightly negatively correlated with Si/TZ^+ when compiling available global river data. Completing the Huh et al. (1998) compilation with the numerous studies that have emerged since the original publication displays an even more random distribution between δ^7Li and TZ^+ (Fig. 7a). The same was observed for δ^7Li vs. [Li] (Misra and Froelich, 2012). In contrast, the weak negative correlation between δ^7Li and Si/TZ^+ is still identified when updating the global river compilation (Fig. 7b). For specific river systems, additional correlations were observed. Examples include the strong inverse correlation between δ^7Li and $^{87}Sr/^{86}Sr$ as well as between δ^7Li and Si/TZ^+ observed for the Orinoco drainage basin (Huh et al., 2001) and the inverse correlation between δ^7Li and [Si] as well as between δ^7Li and [Li] observed in rivers draining mostly basalt (Pogge von Strandmann et al., 2010; 2006). More recently, Millot et al. (2010) and Liu et al. (in revision) have shown that δ^7Li can display a negative correlation with Li/Na that also might have global significance. In fact, a negative correlation between δ^7Li and Li/Na is also identified in our updated global river compilation (Fig. 7c).

Plotting [Li], [Si] and TZ^+ along our model domain as well as against δ^7Li reveals that δ^7Li only forms a distinct correlation with such concentration proxies for a particular system (subsurface vs. river) (Figs. 4a-c and 5a–b). The transition from a positive correlation in the subsurface to a negative one within rivers occurs because once exfiltrated into a river, aqueous species concentrations decrease due to mixing with more diluted river water, while Li isotopic fractionation is ongoing. We thus propose that the identified great importance of Li isotopic fractionation occurring in rivers forms the main reason why concentration proxies do not show a distinct correlation with global riverine δ^7Li values (e.g., δ^7Li vs. TZ^+, Fig. 7a; δ^7Li vs. [Li], Misra and Froelich, 2012). If Li isotopic fractionation was only occurring in the subsurface we would expect a positive correlation between δ^7Li and concentrations proxies such as TZ^+ (i.e., subsurface trend, Fig. 7a) because δ^7Li and TZ^+ (and any other concentration proxies) mainly reflect the subsurface residence time (Fig. 4a–b) as well as the corresponding weathering intensity (Fig. 5a–b). Instead, our simulations suggest that riverine δ^7Li values reflect a particular combination of Li isotopic fractionation occurring within the subsurface as well as in rivers such as illustrated with the corresponding trends (Fig. 7a).

Subsurface and riverine trends shown in Fig. 7a are derived from simulating a monolithological subsurface that does not fully reach chemical equilibrium. Accordingly, the simulation results should be considered as simplified trends only. The observation that in natural aquifers δ^7Li and [Li] are not always positively correlated (Tomascak et al., 2003; Négrel et al., 2010; Meredith et al., 2013) implies that additional parameters such as host rock mineralogy, hydrodynamic mixing of various groundwater types and aquifer residence time distribution in relation to chemical equilibrium (Maher, 2011) must be all taken into account to fully understand the relation between δ^7Li and concentration proxies of a particular system (subsurface + river). Moreover,

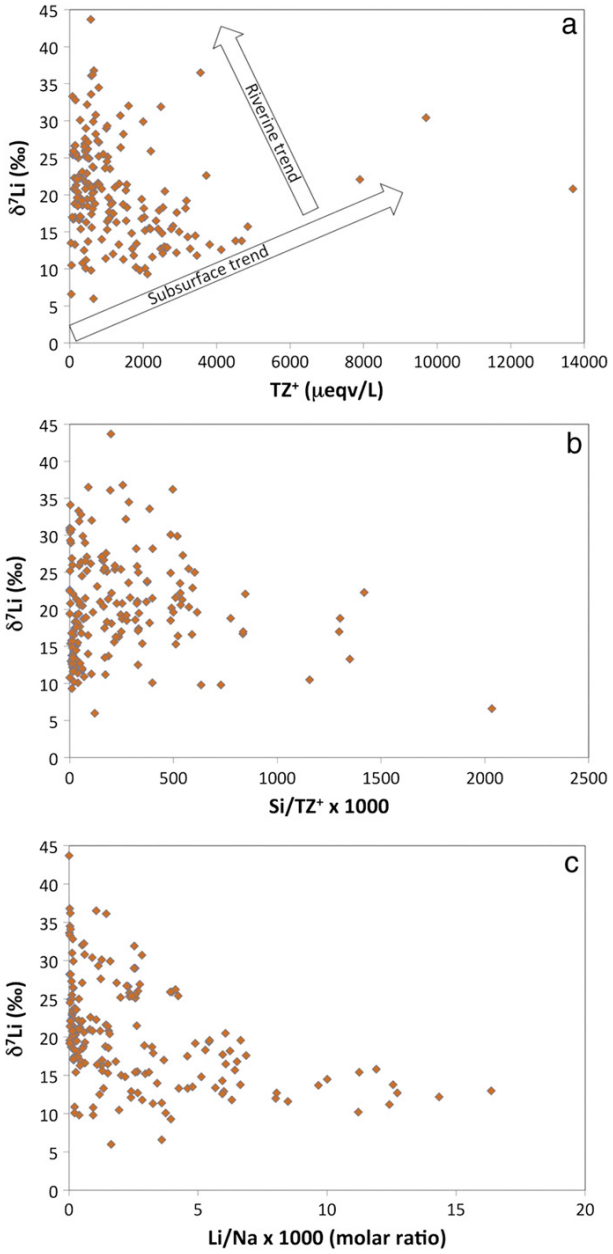

Fig. 7. Compilation of previously published riverine δ^7Li (Huh et al., 1998, 2001; Pogge von Strandmann et al., 2006; Vigier et al., 2009; Millot et al., 2010; Pogge von Strandmann et al., 2010; Wimpenny et al., 2010b) plotted against various weathering tracers. (a) δ^7Li vs. TZ^+ ($TZ^+ = [Na^+] + [K^+] + 2[Ca^{2+}] + 2[Mg^{2+}]$) and corresponding subsurface and riverine trend identified from simulation results (Fig. 4). (b) δ^7Li vs. Si/TZ^+. (c) δ^7Li vs. Li/Na. Samples affected by hydrothermal springs are not shown.

we emphasize that the riverine trend in Fig. 7a does not imply that δ^7Li is increasing with distance along a river, which would be in contradiction to field observations (Kisakürek et al., 2005; Pogge von Strandmann et al., 2006). For our river simulations a correlation between δ^7Li and residence time (i.e., distance) is observed (Fig. 4a) because the ratio between Li isotopic fractionation occurring in rivers vs. the one occurring in aquifers is increasing with increasing river residence time. In other words, for natural rivers we only expect increasing riverine δ^7Li with distance if the ratio of riverine Li isotopic fractionation vs. subsurface fractionation is increasing with flow distance. This ratio, however, is only changing if the subsurface residence time distribution is changing along a river.

Our simulation results agree well with the globally observed negative correlations between δ^7Li and Li/TZ$^+$ and between δ^7Li and Li/Na (Fig. 7b–c) because the parameters that increase δ^7Li (residence time increase, suspended river load concentration increase, weathering intensity decrease) cause a decrease in the simulated Si/TZ$^+$ and Li/Na ratio (Figs. 4c and 5b). For a silicate setting also affected by newly formed secondary Ca- and Mg-bearing phases, we would expect a similar behavior for Ca/TZ$^+$ and Mg/TZ$^+$ as well as for Ca/Na and Mg/Na. The simulated negative correlation between δ^7Li and Si/TZ$^+$ as well as between δ^7Li and Li/Na (Figs. 4c and 5b) is mainly observed because the δ^7Li increase is inherited from an increasing amount of Li being incorporated in kaolinite and goethite with increasing aqueous [Li], whereas Na remains in solution. Precipitation of Li-bearing kaolinite also removes Si from the aqueous solution, which explains why Si/TZ$^+$ is decreasing with increasing Si concentration (Figs. 4a–b and 5a). The Si/TZ$^+$ decrease is most prominent if [Si] approaches a solubility controlled maximum such as observed towards the end of our subsurface domain (i.e., t > 100d, Fig. 4a–b). In fact, the low sensitivity of δ^7Li on Si/TZ$^+$ for short subsurface residence times (Fig. 4b) is likely the reason why the negative correlation between δ^7Li and Si/TZ$^+$ is less pronounced than the one between δ^7Li and Li/Na in global rivers (Fig. 7b–c).

5.1. Seawater δ^7Li: a proxy for Cenozoic continental silicate weathering rates?

We propose that Si/TZ$^+$ as well as Li/Na are only particular and thus somewhat arbitrary proxies that correlate with δ^7Li (Figs. 7b–c). Most importantly, it has not been shown yet how these ratios could serve as quantitative proxies for silicate weathering rates. We therefore postulate that the extent of water–rock interaction occurring along a particular flow path (subsurface + river) forms a more fundamental parameter that defines a system's δ^7Li. In fact, our simulation results (Figs. 4c and 5b) clearly show that the amount of primary silicate mineral dissolution (quartz, feldspars, biotite) is positively correlated with δ^7Li. The correlation occurs because the amount of mineral dissolution reflects an aquifer's residence time, the suspended river load concentration, and the weathering intensity, which have been identified to form the major controls on riverine δ^7Li. Our simulations thus imply that aqueous δ^7Li is highly correlated with the cumulative extent of water–rock interaction occurring along a particular flow path (in moles) suggesting that δ^7Li is almost a perfect silicate weathering tracer. The positive correlation between δ^7Li and silicate mineral dissolution (Figs. 4c and 5b), however, does not necessarily imply a correlation between δ^7Li and silicate weathering rates (in mol/year). To obtain such weathering rates for a particular flow path, amounts of primary silicate mineral dissolution have to be multiplied by subsurface and riverine discharges. Subsurface and riverine discharges are closely related to the corresponding residence times. Accordingly, the previously identified lack of sensitivity of Cenozoic residence time variations on the Cenozoic seawater δ^7Li record implies that this particular δ^7Li record is not sensitive to discharge variations either. This finding is supported by Otto-Bliesner (1995) reporting that continental runoff remained roughly constant over the Cenozoic (±10%).

Assuming minor effects from discharge variations, the simulated positive correlation between primary silicate mineral dissolution and riverine δ^7Li (Figs. 4c and 5b) suggests that the Cenozoic seawater δ^7Li increase (Misra and Froelich, 2012) was most likely caused by globally increasing continental silicate weathering rates. This finding strongly supports the Misra and Froelich (2012) hypothesis arguing that the Cenozoic seawater δ^7Li increase is inherited from increasing riverine δ^7Li values as a result of major Cenozoic tectonic uplift (e.g., Himalayan orogeny). The main argument for this statement is that uplift has a first order control on both parameters identified to increase silicate weathering rates as well as riverine δ^7Li values (decreasing weathering intensity and increasing suspended river load concentration, Figs. 4c and 5a). This agreement is notable because our understanding of Li isotope fractionation processes does not rely on congruent weathering and is thus entirely different from the one of Misra and Froelich (2012).

In contrast to tectonic uplift, Cenozoic cooling occurring since the humid PETM (Miller et al., 1987; Clementz and Sewall, 2011) does not seem to have a distinct effect on δ^7Li. Whereas Cenozoic cooling may have contributed to the Cenozoic weathering intensity decrease and corresponding δ^7Li increase, cooling reduces the amount of primary silicate mineral dissolution along a specific flow path and drives δ^7Li to lower values (Fig. 4c). δ^7Li measurements from streams draining the Columbia River basalt under significantly different climatic conditions (dry vs. wet) confirm that climate does not necessarily have a first order control on riverine δ^7Li (Liu et al., in revision).

6. Implications for CO_2 consumption by silicate weathering

The identified positive correlation between δ^7Li and the amount of primary silicate mineral dissolution (Figs. 4c and 5b) suggests that, over the last 56 Ma, riverine δ^7Li was closely correlated to the amount of CO_2 consumed by silicate weathering reactions (Table 2) assuming that carbonic acid ($H_2O + CO_2$, Eq. (1)) forms the major proton source for these reactions and that continental discharge remained roughly constant (Otto-Bliesner, 1995). Accordingly, the Cenozoic seawater δ^7Li record and the derived global average riverine δ^7Li record provide a potential opportunity to quantify the amount of CO_2 that was consumed by silicate weathering reactions throughout the Cenozoic.

In particular, reactive transport modeling such as performed here allows explicitly quantifying the amount of CO_2 that was consumed along a specific flow path by integrating the amount of each mineral $N_{Mineral}$ (mol) that was dissolved along the full model domain during a specific simulation period:

$$N_{CO_2} = 4 \cdot \sum N_{albite} + 8 \cdot \sum N_{anorthite} + 4 \cdot \sum N_{Kspar} + 10 \cdot \sum N_{biotite} + 0 \cdot \sum N_{quartz} - 6 \cdot \sum N_{kaolinite} - 2 \cdot \sum N_{goethite} \quad (11)$$

The dissolved mineral amounts ($N_{Mineral}$) are scaled by the amount of H^+ that is required to dissolve 1 mol of a specific mineral phases (e.g., 4 for albite, Table 2) because 1 mol of H^+ is added to the solution (i.e., CO_2 is consumed by mineral dissolution) if 1 mol of atmospheric CO_2 is dissolved (Eq. (1)). The amount of kaolinite precipitation times 6 and the amount of goethite precipitation times 2, respectively (i.e., stoichiometric coefficient of H^+, Table 2) were subtracted because kaolinite and goethite precipitation adds H^+ to the system and liberates the same mole amount of CO_2 to keep the pCO_2 at the specified fixed value. It should be noted that Eq. (11) assumes that dissolved HCO_3^- precipitates as carbonates in the ocean (Fig. 1).

Applying Eq. (11) to our simulation runs indeed yields a positive correlation between δ^7Li and CO_2 consumption (Figs. 4c and 5b) implying that CO_2 consumption by continental silicate weathering increased over the Cenozoic. This finding agrees well with the carbon cycle model of Li and Elderfield (2013) also suggesting an increase in continental silicate weathering and corresponding CO_2 consumption rates over the Cenozoic. However, our modeling approach relies on

thermodynamic parameters for Li-bearing minerals that are only roughly constrained so far (e.g., fractionation factor, crystallographic substitution reaction, Li concentration of secondary minerals, Li solubility). Accordingly, our modeling approach should only be applied to qualitatively identify geochemical trends related to Li isotopic fractionation such as performed here. Once these thermodynamic parameters have been determined, a reliable quantification of the amount of CO_2 consumed by silicate weathering over the Cenozoic would require incorporating basalt weathering in addition to granite weathering, because basalt weathering accounts for more than 30% of global CO_2 consumption by silicate weathering even though basalts only form about 8% of exposed silicate rocks today (Gaillardet et al., 1999).

Our CO_2 consumption calculations also show that the amount of CO_2 consumed by pure "fresh granite" weathering (e.g., 100% contribution) was the same for the current and the Paleocene–Eocene weathering pattern simulations (17 kmol, Figs. 4b and 5b). The same applies for the simulated δ^7Li values at the downstream subsurface model boundary (+10‰). This observation emphasizes that CO_2 consumption by continental silicate weathering reactions is more sensitive to specific primary silicate mineral phases that are exposed to chemical weathering rather than to atmospheric pCO_2. Moreover, it suggests that pCO_2 variations during the Cenozoic (Li and Elderfield, 2013) do not seem to have a distinct control on the Cenozoic seawater δ^7Li record.

To extend the use of seawater δ^7Li values to reconstruct CO_2 consumption by continental silicate weathering for geological times other than the past 56 Ma, potential significant changes in continental river discharge have to be taken into account as well. Whereas discharge variations seem less important for the Cenozoic, a dramatic acceleration of the hydrological cycle caused by a short term atmospheric pCO_2 increase shifted seawater δ^7Li values by about −10‰ within a short period of time (100 ky) during Cretaceous Oceanic Anoxic Event 2 (OAE2) (Pogge von Strandmann et al., 2013). Because an accelerated hydrological cycle likely shifted discharge to higher values and residence times to lower values, the low OAE2 δ^7Li values correspond well with our simulated positive correlation between residence time and δ^7Li (Fig. 4a). Interestingly, the negative δ^7Li excursion observed for OAE2 was attributed to enhanced continental silicate weathering forming a negative feedback on the inferred pCO_2 increase (Pogge von Strandmann et al., 2013). This finding is opposite to the one made for the Cenozoic because for the past 56 Ma, inferred increasing silicate weathering rates are manifested by a δ^7Li increase (Misra and Froelich, 2012; this study) while for OAE2 they are accompanied by a δ^7Li decrease (Pogge von Strandmann et al., 2013). This apparent contradiction is, however, well explained by our modeling results revealing that seawater and inferred riverine δ^7Li values are simply a function of the amount of silicate weathering and corresponding CO_2 consumption along a specific flow path (in moles) (Figs. 4c and 5b). However, they are not necessarily correlated with silicate weathering and CO_2 consumption rates (in mol/year) on which discharge has a first order control (Gaillardet et al., 1999). The opposing behavior of δ^7Li with increasing silicate weathering rates thus highlights the importance of reconstructing past discharge rates, which, owing to the strong correlation between silicate weathering rates and discharge (Gaillardet et al., 1999), is indispensable for quantifying past CO_2 consumption rates based on seawater δ^7Li measurements.

7. Summary and conclusions

A novel reactive transport modeling approach was developed to simulate Li isotopic fractionation during Li uptake by secondary mineral phases. Simulation results show that riverine δ^7Li is controlled not only by the Li isotopic fractionation factor but also by the subsurface residence time of infiltrating meteoric water, the corresponding weathering intensity and the concentration of a river's suspended load.

Based on these identified factors, we presented a new interpretation of the previously reported Cenozoic seawater δ^7Li record (Misra and Froelich, 2012) that does not rely on geochemically unlikely congruent weathering. In particular, modeling results imply that the low seawater δ^7Li observed at the Paleocene–Eocene boundary could be inherited from a high weathering intensity with predominant weathering of previously-formed secondary mineral phases (e.g., clays, oxides, hydroxides) having a low δ^7Li and a low contribution of incongruent silicate mineral dissolution with associated secondary mineral formation and Li isotopic fractionation. Moreover, simulation results imply that the Cenozoic seawater δ^7Li increase was likely caused by an increasing amount of primary silicate mineral dissolution (i.e., decreasing weathering intensity, increasing suspended river load concentration) inherited from tectonic uplift and a corresponding global relief increase. In contrast, Cenozoic cooling and corresponding pCO_2 and precipitation variations do not seem to have a distinct control on the Cenozoic seawater δ^7Li record. It is thus emphasized that our modeling results strongly favor the original Raymo and Ruddiman (1992) model stating that a tectonically-driven increase in silicate weathering rates may have caused the inferred Cenozoic atmospheric pCO_2 decrease. However, another Li isotope study has shown that for dramatic, short term events increasing atmospheric pCO_2 and triggering warmer temperatures (e.g., Cretaceous OAE2), silicate weathering and corresponding CO_2 consumption rates can be dramatically increased without major tectonic uplift (Pogge von Strandmann et al., 2013).

The identified strong correlation between Cenozoic silicate weathering rates and δ^7Li implies that seawater and global average riverine δ^7Li values are closely related to global CO_2 consumption by continental silicate weathering. For an actual quantitative correlation, however, more experimental and modeling work is required. Key parameters are the temperature-dependent thermodynamic properties of specific Li bearing primary and secondary minerals (e.g., crystallographic Li substitution and surface complexation reactions, maximum Li substitution, Li solubility, Li isotopic fractionation factor) as well as the determination of global average continental discharge through time.

Incorporating Li isotopic fractionation into reactive transport model simulations of subsurface and river systems also improved the understanding of the δ^7Li distribution observed in global rivers today. Simulation results revealed that Li isotopic fractionation occurs in the subsurface as well as in river systems. Fractionation occurring in both systems seems to be the main reason why no or only weak correlations between global riverine δ^7Li values and traditional silicate weathering proxies such as [Si], [Li], Si/TZ^+ are observed. The lack of correlation is observed because once exfiltrated into rivers, elemental concentrations are diluted by a larger flux of superficial river waters while Li isotopic fractionation is still ongoing.

Finally, this study illustrates that reactive transport modeling is a powerful tool for a (semi)-quantitative interpretation of stable isotope ratios. In comparison to closed system Rayleigh-type or steady state flux models, it bears the advantage of considering the full thermodynamic properties of involved mineral phases (e.g., mineral stoichiometry, mineral solubility, kinetic dissolution/precipitation) as well as assessing the effect of transport on isotopic fractionation. The presented solid solution approach can be easily applied to other isotopic systems (e.g., Si, Mg, Ca, Mo), which have also been shown to serve as potentially powerful weathering proxies (Ziegler et al., 2005; Tipper et al., 2012; Voegelin et al., 2012; Moore et al., 2013).

Acknowledgments

This work was supported by the U.S. Department of Energy, Geothermal Technologies Program, Energy Efficiency and Renewable Energy Office, award no. GT-480010-12. Postdoctoral fellowship support was provided to X-ML by the Carnegie Institution of Washington. The manuscript significantly benefited from a helpful editorial handling by Michael Böttcher, and very constructive comments by Philip Pogge von Strandmann and an additional, anonymous reviewer.

References

Berner, R.A., 1994. 3GEOCARB II: a revised model of atmospheric CO_2 over Phanerozoic time. Am. J. Sci. 294, 56–91.

Berner, R.A., Kothavala, Z., 2001. GEOCARB III: a revised model of atmospheric CO_2 over Phanerozoic time. Am. J. Sci. 301, 182–204.

Berner, R.A., Lasaga, A.C., Garrels, R.M., 1983. The carbonate-silicate geochemical cycle and its effect on atmospheric carbon-dioxide over the past 100 million years. Am. J. Sci. 283, 641–683.

Bouchez, J., Gaillardet, J., France-Lanord, C., Maurice, L., Dutra-Maia, P., 2011. Grain size control of river suspended sediment geochemistry: clues from Amazon River depth profiles. Geochem. Geophys. Geosyst. 12, Q03008.

Bouchez, J., Von Blanckenburg, F., Schuessler, J.A., 2013. Modeling novel stable isotope ratios in the weathering zone. Am. J. Sci. 313, 267–308.

Clementz, M.T., Sewall, J.O., 2011. Latitudinal gradients in greenhouse seawater $\delta^{18}O$: evidence from Eocene Sirenian Tooth Enamel. Science 332, 455–458.

Decarreau, A., Vigier, N., Pálková, H., Petit, S., Vieillard, P., Fontaine, C., 2012. Partitioning of lithium between smectite and solution: an experimental approach. Geochim. Cosmochim. Acta 85, 314–325.

Dobson, P.F., Kneafsey, T.J., Sonnenthal, E.L., Spycher, N., Apps, J.A., 2003. Experimental and numerical simulation of dissolution and precipitation: implications for fracture sealing at Yucca Mountain, Nevada. J. Cotam. Hydrol. 62–63, 459–476.

Du Laing, G., Rinklebe, J., Vandecasteele, B., Meers, E., Tack, F.M.G., 2009. Trace metal behaviour in estuarine and riverine floodplain soils and sediments: a review. Sci. Total Environ. 407, 3972–3985.

Economos, R.C., Memeti, V., Paterson, S.R., Miller, J.S., Erdmann, S., Zak, J., 2010. Causes of compositional diversity in a lobe of the Half Dome granodiorite, Tuolumne Batholith, Central Sierra Nevada, California. Earth Environ. Sci. Trans. R. Soc. 100, 173–183.

Edmond, J.M., Palmer, M.R., Measures, C.I., Grant, B., Stallard, R.F., 1995. The fluvial geochemistry and denudation rate of the Guayana Shield in Venezuela, Colombia, and Brazil. Geochim. Cosmochim. Acta 59, 3301–3325.

Francois, L.M., Godderis, Y., 1998. Isotopic constraints on the Cenozoic evolution of the carbon cycle. Chem. Geol. 145, 177–212.

Fryirs, K.A., Brierley, G.J., 2013. Geomorphic Analysis of River Systems: An Approach to Reading the Landscape. John Wiley & Sons.

Gaillardet, J., Dupré, B., Louvat, P., Allègre, C.J., 1999. Global silicate weathering and CO_2 consumption rates deduced from the chemistry of large rivers. Chem. Geol. 159, 3–30.

Godderis, Y., Roelandt, C., Schott, J., Pierret, M., Francois, L.M., 2009. Towards an integrated model of weathering, climate, and biosphere processes. In: Oelkers, E.H., Schott, J. (Eds.), Towards an integrated model of weathering, climate, and biosphere processes. Mineralogical Society of America. Rev. Mineral, 70, pp. 411–434.

Hathorne, E.C., James, R.H., 2006. Temporal record of lithium in seawater: a tracer for silicate weathering. Earth Planet. Sci. Lett. 246, 393–406.

Huh, Y., Chan, L.H., Zhang, L., Edmond, J.M., 1998. Lithium and its isotopes in major world rivers: implications for weathering and the oceanic budget. Geochim. Cosmochim. Acta 62, 2039–2051.

Huh, Y., Chan, L.H., Edmond, J.M., 2001. Lithium isotopes as a probe of weathering processes: Orinoco River. Earth Planet. Sci. Lett. 194, 189–199.

Huh, Y., Chan, L.H., Chadwick, O.A., 2004. Behavior of lithium and its isotopes during weathering of Hawaiian basalt. Geochem. Geophys. Geosyst. 5, Q09002.

Johnson, J.W., Oelkers, E.H., Helgeson, H.C., 1992. SUPCRT92: a software package for calculating the standard molal thermodynamic properties of minerals, gases, aqueous species, and reactions from 1 to 5000 bar and 0 to 1000 °C. Comput. Geosci. 18, 899–948.

Keeling, C.D., 1960. The concentration and isotopic abundances of carbon dioxide in the atmosphere. Tellus 12, 200–203.

Kisakürek, B., Widdowson, M., James, R.H., 2004. Behaviour of Li isotopes during continental weathering: the Bidar laterite profile, India. Chem. Geol. 212, 27–44.

Kisakürek, B., James, R.H., Harris, N.B.W., 2005. Li and δ7Li in Himalayan rivers: proxies for silicate weathering? Earth Planet. Sci. Lett. 237, 387–401.

Kretz, R., Loop, J., Hartree, R., 1989. Petrology and Li–Be–B geochemistry of muscovite–biotite granite and associated pegmatite near Yellowknife, Canada. Contrib. Mineral. Petrol. 102, 174–190.

Lasaga, A.C., 1984. Chemical kinetics of water–rock interactions. J. Geophys. Res. 89, 4009–4025.

Lemarchand, E., Chabaux, F., Vigier, N., Millot, R., Pierret, M.-C., 2010. Lithium isotope systematics in a forested granitic catchment (Strengbach, Vosges Mountains, France). Geochim. Cosmochim. Acta 74, 4612–4628.

Li, G., Elderfield, H., 2013. Evolution of carbon cycle over the past 100 million years. Geochim. Cosmochim. Acta 103, 11–25.

Li, G., West, A.J., 2014. Increased continental weathering flux through the Cenozoic inferred from the lithium isotope evolution of seawater. Earth Planet. Sci. Lett. (accepted for publication).

Liu, X.-M., Rudnick, R.L., McDonough, W.F., Cummings, M.L., 2013. Influence of chemical weathering on the composition of the continental crust: insights from Li and Nd isotopes in bauxite profiles developed on Columbia River Basalts. Geochim. Cosmochim. Acta 115, 73–91.

Liu, X.-M., Wanner, C., Rudnick, R.L., McDonough, W.F., 2014. Novel interpretation of large Li isotopic variations produced by streams and ground waters draining basalts. Earth Planet. Sci. Lett. (in revision).

Maher, K., 2011. The role of fluid residence time and topographic scales in determining chemical fluxes from landscapes. Earth Planet. Sci. Lett. 312, 48–58.

Maher, K., Steefel, C.I., White, A.F., Stonestrom, D.A., 2009. The role of reaction affinity and secondary minerals in regulating chemical weathering rates at the Santa Cruz Soil Chronosequence, California. Geochim. Cosmochim. Acta 73, 2804–2831.

Meredith, K., Moriguti, T., Tomascak, P., Hollins, S., Nakamura, E., 2013. The lithium, boron and strontium isotopic systematics of groundwaters from an arid aquifer system: implications for recharge and weathering processes. Geochim. Cosmochim. Acta 112, 20–31.

Miller, K.G., Fairbanks, R.G., Mountain, G.S., 1987. Tertiary oxygen isotope synthesis, sea level history, and continental margin erosion. Paleoceanography 2, 1–19.

Milliman, J.D., Meade, R.H., 1983. World-wide delivery of river sediment to the oceans. J. Geol. 91, 1–21.

Millot, R., Vigier, N., Gaillardet, J., 2010. Behaviour of lithium and its isotopes during weathering in the Mackenzie Basin, Canada. Geochim. Cosmochim. Acta 74, 3897–3912.

Misra, S., Froelich, P.N., 2012. Lithium isotope history of Cenozoic seawater: changes in silicate weathering and reverse weathering. Science 335, 818–823.

Moore, J., Jacobson, A.D., Holmden, C., Craw, D., 2013. Tracking the relationship between mountain uplift, silicate weathering, and long-term CO_2 consumption with Ca isotopes: Southern Alps, New Zealand. Chem. Geol. 341, 110–127.

Müller, R.D., Sdrolias, M., Gaina, C., Steinberger, B., Heine, C., 2008. Long-term sea-level fluctuations driven by ocean basin dynamics. Science 319, 1357–1362.

Négrel, P., Millot, R., Brenot, A., Bertin, C., 2010. Lithium isotopes as tracers of groundwater circulation in a peat land. Chem. Geol. 276, 119–127.

Nesbitt, H.W., Young, G.M., 1982. Early Proterozoic climates and plate motions inferred from major element chemistry of lutites. Nature 299, 715–717.

Oliver, L., Harris, N., Bickle, M., Chapman, H., Dise, N., Horstwood, M., 2003. Silicate weathering rates decoupled from the $^{87}Sr/^{86}Sr$ ratio of the dissolved load during Himalayan erosion. Chem. Geol. 201, 119–139.

Otto-Bliesner, B.L., 1995. Continental drift, runoff, and weathering feedbacks: implications from climate model experiments. J. Geophys. Res.-Atmos. 100, 11537–11548.

Palandri, J.L., Kharaka, Y.K., 2004. A compilation of rate parameters of water–mineral interaction kinetics for application to geochemical modeling. US Geological Survey. Report 2004-1068.

Pistiner, J.S., Henderson, G.M., 2003. Lithium-isotope fractionation during continental weathering processes. Earth Planet. Sci. Lett. 214, 327–339.

Pogge von Strandmann, P.A.E., Burton, K.W., James, R.H., van Calsteren, P., Gíslason, S.R., Mokadem, F., 2006. Riverine behaviour of uranium and lithium isotopes in an actively glaciated basaltic terrain. Earth Planet. Sci. Lett. 251, 134–147.

Pogge von Strandmann, P.A.E., Burton, K.W., James, R.H., van Calsteren, P., Gislason, S.R., 2010. Assessing the role of climate on uranium and lithium isotope behaviour in rivers draining a basaltic terrain. Chem. Geol. 270, 227–239.

Pogge von Strandmann, P.A.E., Jenkyns, H.C., Woodfine, R.G., 2013. Lithium isotope evidence for enhanced weathering during Oceanic Anoxic Event 2. Nat. Geosci. 6, 668–672.

Raymo, M.E., Ruddiman, W.F., 1992. Tectonic forcing of late Cenozoic climate. Nature 359, 117–122.

Reed, M., Palandri, J.L., 2006. SOLTHERM.H06, A Database of Equilibrium Constants for Minerals and Aqueous Species. Available from the Authors. University of Oregon, Eugene.

Rowley, D.B., 2002. Rate of plate creation and destruction: 180 Ma to present. Geol. Soc. Am. Bull. 114, 927–933.

Rudnick, R.L., Tomascak, P.B., Njo, H.B., Gardner, L.R., 2004. Extreme lithium isotopic fractionation during continental weathering revealed in saprolites from South Carolina. Chem. Geol. 212, 45–57.

Singleton, M.J., Sonnenthal, E.L., Conrad, M.E., DePaolo, D.J., Gee, G.W., 2005. Multiphase reactive transport modeling of seasonal infiltration events and stable isotope fractionation in unsaturated zone pore water and vapor at the Hanford site. Vadose Zone J. 3, 775–785.

Sonnenthal, E.L., Spycher, N., Apps, J.A., Simmons, A., 1998. Thermo-hydro-chemical Predictive Analysis for the Drift-scale Heater Test. Lawrence Berkeley National Laboratory (Level 4 Milestone SPY289M4).

Steefel, C.I., DePaolo, D.J., Lichtner, P.C., 2005. Reactive transport modeling: an essential tool and a new research approach for the Earth sciences. Earth Planet. Sci. Lett. 240, 539–558.

Tardy, Y., Nahon, D., 1985. Geochemistry of laterites, stability of Al-goethite, Al-hematite, and Fe^{3+}-kaolinite in bauxites and ferricretes — an approach to the mechanism of concretion formation. Am. J. Sci. 285, 865–903.

Tardy, Y., Trauth, N., Krempp, G., 1972. Lithium in clay-minerals of sediments and soils. Geochim. Cosmochim. Acta 36, 397.

Teng, F.Z., McDonough, W.F., Rudnick, R.L., Dalpé, C., Tomascak, P.B., Chappell, B.W., Gao, S., 2004. Lithium isotopic composition and concentration of the upper continental crust. Geochim. Cosmochim. Acta 68, 4167–4178.

Teng, F.-Z., Rudnick, R.L., McDonough, W.F., Gao, S., Tomascak, P.B., Liu, Y., 2008. Lithium isotopic composition and concentration of the deep continental crust. Chem. Geol. 255, 47–59.

Teng, F.-Z., Rudnick, R.L., McDonough, W.F., Wu, F.-Y., 2009. Lithium isotopic systematics of A-type granites and their mafic enclaves: further constraints on the Li isotopic composition of the continental crust. Chem. Geol. 262, 370–379.

Tipper, E.T., Calmels, D., Gaillardet, J., Louvat, P., Capmas, F., Dubacq, B., 2012. Positive correlation between Li and Mg isotope ratios in the river waters of the Mackenzie Basin challenges the interpretation of apparent isotopic fractionation during weathering. Earth Planet. Sci. Lett. 333–334, 35–45.

Tomascak, P.B., Hemming, N.G., Hemming, S.R., 2003. The lithium isotopic composition of waters of the Mono Basin, California. Geochim. Cosmochim. Acta 67, 601–611.

Vigier, N., Decarreau, A., Millot, R., Carignan, J., Petit, S., France-Lanord, C., 2008. Quantifying Li isotope fractionation during smectite formation and implications for the Li cycle. Geochim. Cosmochim. Acta 72, 780–792.

Vigier, N., Gislason, S.R., Burton, K.W., Millot, R., Mokadem, F., 2009. The relationship between riverine lithium isotope composition and silicate weathering rates in Iceland. Earth Planet. Sci. Lett. 287, 434–441.

Voegelin, A.R., Nägler, T.F., Pettke, T., Neubert, N., Steinmann, M., Pourret, O., Villa, I.M., 2012. The impact of igneous bedrock weathering on the Mo isotopic composition of stream waters: natural samples and laboratory experiments. Geochim. Cosmochim. Acta 86, 150–165.

Wanner, C., Sonnenthal, E.L., 2013. Assessing the control on the effective kinetic Cr isotope fractionation factor: a reactive transport modeling approach. Chem. Geol. 337, 88–98.

White, A.F., 2002. Determining mineral weathering rates based on solid and solute weathering gradients and velocities: application to biotite weathering in saprolites. Chem. Geol. 190, 69–89.

White, A.F., Bullen, T.D., Schulz, M.S., Blum, A.E., Huntington, T.G., Peters, N.E., 2001. Differential rates of feldspar weathering in granitic regoliths. Geochim. Cosmochim. Acta 65, 847–869.

Wimpenny, J., Gislason, S.R., James, R.H., Gannoun, A., Pogge Von Strandmann, P.A.E., Burton, K.W., 2010a. The behaviour of Li and Mg isotopes during primary phase dissolution and secondary mineral formation in basalt. Geochim. Cosmochim. Acta 74, 5259–5279.

Wimpenny, J., James, R.H., Burton, K.W., Gannoun, A., Mokadem, F., Gíslason, S.R., 2010b. Glacial effects on weathering processes: new insights from the elemental and lithium isotopic composition of West Greenland rivers. Earth Planet. Sci. Lett. 290, 427–437.

Wimpenny, J., Colla, C.A., Yin, Q.-Z., Rustad, J.R., Casey, W.H., 2014. Investigating the behaviour of Mg isotopes during the formation of clay minerals. Geochim. Cosmochim. Acta 128, 178–194.

Xu, T., Spycher, N., Sonnenthal, E.L., Zhang, G., Zheng, L., Pruess, K., 2011. TOUGHREACT Version 2.0: a simulator for subsurface reactive transport under non-isothermal multiphase flow conditions. Comput. Geosci. 37, 763–774.

Yang, L., Steefel, C.I., 2008. Kaolinite dissolution and precipitation kinetics at 22 °C and pH 4. Geochim. Cosmochim. Acta 72, 99–116.

Yoon, J., 2010. Lithium as a silicate weathering proxy: problems and perspectives. Aquat. Geochem. 16, 189–206.

Zhang, L., Chan, L.-H., Gieskes, J.M., 1998. Lithium isotope geochemistry of pore waters from ocean drilling program Sites 918 and 919, Irminger Basin. Geochim. Cosmochim. Acta 62, 2437–2450.

Ziegler, K., Chadwick, O.A., Brzezinski, M.A., Kelly, E.F., 2005. Natural variations of $\delta^{30}Si$ ratios during progressive basalt weathering, Hawaiian Islands. Geochim. Cosmochim. Acta 69, 4597–4610.

5.2. Processes controlling δ^7Li in rivers illuminated by study of streams and groundwaters draining basalts

Source:

Liu X.-M., **Wanner C.**, Rudnick R. L. and McDonough W. F. (2015) Processes controlling δ^7Li in rivers illuminated by study of streams and groundwaters draining basalts. *Earth and Planetary Science Letters* **409**, 212-224.

Contribution by the Author (CW):

CW carried out all the simulations and lead the interpretation of the simulation results. Moreover, he wrote the RTM sections of the paper and heavily contributed to the remaining parts of the manuscript.

Earth and Planetary Science Letters 409 (2015) 212–224

Contents lists available at ScienceDirect

Earth and Planetary Science Letters

www.elsevier.com/locate/epsl

Processes controlling δ^7Li in rivers illuminated by study of streams and groundwaters draining basalts

Xiao-Ming Liu [a,b,*], Christoph Wanner [c], Roberta L. Rudnick [a], William F. McDonough [a]

[a] Department of Geology, University of Maryland, College Park, College Park, MD, USA
[b] Geophysical Lab, Carnegie Institute of Washington, Washington, DC, USA
[c] Earth Sciences Division, Lawrence Berkeley National Laboratory, Berkeley, CA, USA

ARTICLE INFO

Article history:
Received 28 February 2014
Received in revised form 23 September 2014
Accepted 18 October 2014
Available online 19 November 2014
Editor: J. Lynch-Stieglitz

Keywords:
lithium isotopes
chemical weathering
rivers and groundwaters
reactive transport modeling

ABSTRACT

We evaluate the factors influencing the abundance, [Li], and isotopic composition of riverine Li delivered to the oceans through analyses and modeling of [Li] and δ^7Li in streams and groundwaters draining a single continental lithology, the Columbia River Basalts (CRBs). The streams were sampled in different climate zones that lie east (dry), and west (wet) of the Cascades Mountains, and during two different seasons (summer and late winter) in order to evaluate climatic and seasonal influences on Li isotopes in rivers. Dissolved Li ($\delta^7Li_{dis} = +9.3$ to $+30.4$) is systematically heavier than that of fresh or weathered CRBs (-4.7 to $+6.0$, Liu et al., 2013), suspended loads (-5.9 to -0.3), and shallow groundwaters ($+6.7$ to $+9.4$), consistent with previous studies showing that Li isotope fractionation is affected by equilibration between stream water and secondary minerals. However, the lack of correlation between δ^7Li_{dis} and climate zone, the uniform secondary minerals and bedrock, coupled with the highly variable (>20‰) δ^7Li_{dis} indicate that other factors exert a strong control on δ^7Li_{dis}. In particular, the heavier Li in streams compared to the shallow groundwaters that feed them indicates that continued isotopic fractionation between stream water and suspended and/or bed loads has a major influence on riverine δ^7Li. Seasonal δ^7Li variation is observed only for streams west of the Cascades, where the difference in precipitation rate between the dry and wet seasons is greatest. Reactive transport model simulations reveal that riverine δ^7Li is strongly controlled by subsurface residence times and the Li isotope fractionation occurring within rivers. The latter explains why there is no positive correlation between δ^7Li and traditional weathering proxies such as Si or normalized Si in rivers, as riverine Li isotope fractionation drives δ^7Li to higher values during transport, whereas the concentrations of major cations and anions are diluted. The varying residence time for groundwaters feeding the western streams in summer (long residence times, higher δ^7Li, greater weathering) and winter (short residence times, lower δ^7Li, less weathering) explains the observed seasonal variations. A global, negative correlation between δ^7Li and Li/Na for streams and rivers draining basaltic catchments reflects the overall transport time, hence the amount of silicate weathering. Based on our results, the increase of δ^7Li in seawater during the Cenozoic is unlikely related to changing climate, but may reflect mountain building giving rise to increased silicate weathering.

1. Introduction

Chemical weathering of silicate rocks on Earth's surface plays a critical role in regulating the global carbon cycle over geological time-scales (e.g., Berner et al., 1983). Basalt weathering, in particular, may significantly contribute to the global silicate weathering flux. For example, Gaillardet et al. (1999), suggested a minimum of 25% of the silicate weathering flux to the oceans derives from weathering of basalt. Attempts to illuminate chemical weathering processes using natural samples generally take two approaches: studies of river waters (e.g., Dessert et al., 2001; Gaillardet et al., 1999), and studies of weathering profiles or weathered regoliths (e.g., Brimhall et al., 1991; Nesbitt and Wilson, 1992). River chemistry is able to provide rate-related constraints, such as chemical weathering fluxes and CO_2 consumption rates (Gaillardet et al., 1999), although only for the present.

Li isotopes can potentially provide insights into the weathering flux from the continents over time (Liu and Rudnick, 2011), and changing climate, if the changes in δ^7Li in the seawater record (Misra and Froelich, 2012) can be deciphered. The Li isotopic

* Corresponding author at: Geophysical Lab, Carnegie Institute of Washington, 5251 Broad Branch Rd. NW, Washington, DC 20015-1305, USA. Tel.: +1 (301) 825 6841, fax: +1 (202) 478 8901.
E-mail address: xliu@gl.ciw.edu (X.-M. Liu).

http://dx.doi.org/10.1016/j.epsl.2014.10.032
0012-821X/

composition in seawater is a function of the input of rivers and hydrothermal fluid, and the output into secondary minerals formed via low temperature basalt alteration and sediment clay authigenesis (referred to as "reverse weathering") (Chan et al., 1992). The dramatic (8‰) increase in δ^7Li in seawater through the Cenozoic has been interpreted to reflect the changing composition of riverine inputs that, in turn, reflect climatic and tectonic influences on continental weathering (Misra and Froelich, 2012). Assuming a constant hydrothermal input, the significant increase in δ^7Li through the Cenozoic may indicate increases in the riverine input (a greater flux and/or higher δ^7Li), an increased output flux of low δ^7Li, or both. Therefore, understanding the controls on riverine Li isotopes is a first-order requirement for understanding the secular evolution of seawater.

Li is contained mainly in silicates and is released, with attendant isotopic fractionation, during weathering (e.g., Huh et al., 2001, 1998; Kisakürek et al., 2005, 2004; Rudnick et al., 2004). Lithium's two stable isotopes, ^{7}Li and ^{6}Li, have great fractionation potential due to their 17% mass difference. Differences in Li isotopic composition are expressed as $\delta^7\text{Li}\ (‰) = ([^7\text{Li}/^6\text{Li}]_{\text{sample}}/[^7\text{Li}/^6\text{Li}]_{\text{standard}} - 1) \times 1000$, where the standard used is a lithium carbonate, L-SVEC (Flesch et al., 1973). Lithium is a water-soluble trace element, but neither primary basalt dissolution nor metamorphic dehydration appear to cause significant Li isotopic fractionation (Marschall et al., 2007; Pistiner and Henderson, 2003; Qiu et al., 2011a, 2011b, 2009; Teng et al., 2007; Wimpenny et al., 2010a). By contrast, Li isotopes fractionate significantly during incongruent continental weathering, due to the formation of secondary minerals, such as clays (e.g., Huh et al., 1998; Kisakürek et al., 2004; Pistiner and Henderson, 2003; Pogge von Strandmann et al., 2006; Rudnick et al., 2004; Teng et al., 2004). Lithium has a few more advantages as a potential geochemical tracer of weathering. Li has only one redox state (+1 charge), and is thus insensitive to changes in oxygen fugacity compared to Fe, Cr, Cu, Mo, etc. In addition, Li is not a nutrient, so its elemental and isotopic behavior is not directly influenced by biological processes (e.g., Lemarchand et al., 2010). Finally, Li is enriched in silicates and depleted in carbonates, so its abundance and isotopic composition in rivers mainly reflect continental silicate weathering (one caveat is that riverine Li can be significantly influenced by the presence of evaporites, e.g., Huh et al., 1998).

Studies investigating the use of δ^7Li as a weathering proxy (Huh et al., 2001, 1998; Millot et al., 2010; Pogge von Strandmann et al., 2006; Vigier et al., 2009) have not fully discerned why the Li isotope composition of rivers does not show consistent correlation with certain silicate weathering proxies. For instance, Huh et al. (1998) did not observe a clear correlation between $\delta^7\text{Li}_{\text{dis}}$ and $^{87}\text{Sr}/^{86}\text{Sr}$, $\delta^7\text{Li}_{\text{dis}}$ and [Li] (using square brackets around elements to indicate concentration) as well as between $\delta^7\text{Li}_{\text{dis}}$ and Si/TZ^+ (Total cation charge, $\text{TZ}^+ = \text{Na}^+ + 2\text{Mg}^{2+} + \text{K}^+ + 2\text{Ca}^{2+}$ in 10^{-3} equivalents per liter, mEq/L) when compiling global river data. By contrast, for the Orinoco drainage basin a strong inverse correlation was observed between $\delta^7\text{Li}_{\text{dis}}$ and $^{87}\text{Sr}/^{86}\text{Sr}$ as well as between $\delta^7\text{Li}_{\text{dis}}$ and Si/TZ^+ (Huh et al., 2001). In addition, in some studies a correlation between δ^7Li and chemical weathering rates (in mass/area/time) was observed (Vigier et al., 2009), whereas in others no clear relationship could be identified (Millot et al., 2010). The lack of consistent correlation may reflect variations in climate (e.g., tropical vs. temperate climates), lithologies, hydrology, and sampling seasons encompassed in previous river studies. Here we seek to illuminate the causes of Li isotopic fractionation produced during weathering by studying surface waters draining a single lithology (basalt) as a function of climate, season, and groundwater residence time. The Columbia River Basalts (CRBs) afford this opportunity due to their large areal extent, which encompasses different climate zones and allows sampling within a single lithology having limited isotopic variability. Understanding the processes that control $\delta^7\text{Li}_{\text{dis}}$ will, in turn, afford greater insight into the changing δ^7Li observed in seawater with time.

2. Geological setting, climate and samples

The geological setting of the sampling area is described in Liu et al. (2013) and a brief account is provided here. The CRBs are continental flood basalts that erupted during the Miocene (between 17 Ma and 6 Ma) in the US Pacific Northwest, covering large parts of southern Washington, northeastern Oregon and parts of western Idaho (Fig. 1).

The CRBs crop out both east and west of the Cascade Mountain Range. The Cascades developed progressively from subduction zone magmatism since the Late Eocene, with topography increasing more or less steadily since the Late Oligocene (Kohn et al., 2002 and references therein). The mountains created two different climate zones that affected the CRBs via the rain shadow effect; regions west of the Cascades have high mean annual precipitation (MAP) (1500–2000 mm), whereas annual precipitation east of the Cascades is less than 300 mm (Kohn et al., 2002; Takeuchi et al., 2010). In addition, the monthly precipitation rates vary more in the west, where the mean monthly precipitation rate during the wet season (October–May) is up to 10 times greater than that during the dry season (June–September) (Fig. A1). By contrast, differences in monthly precipitation rates east of the Cascades are usually less than a factor of 2.

The advantages of studying streams and groundwaters in this area include: 1) The streams only drain a single lithology, the CRBs. 2) Sampling streams from different climate zones allows investigation of how annual precipitation rates, and thus climate, may have influenced riverine Li isotopic composition. 3) Due to the variable seasonal precipitation (Fig. A1), sampling in two seasons allow us to assess the effect of seasonally variable precipitation rates and corresponding variable surface runoff (Fig. A2) on Li isotopic compositions. 4) Sampling of groundwaters that are the potential sources of the streams allows distinction between Li isotope fractionation occurring in subsurfaces and fractionation occurring in rivers.

3. Samples and analytical methods

3.1. Sampling

Dissolved and suspended load samples from 10 CRB streams were collected in July 2010, and again in March 2012 to study possible seasonal variations; samples from the mouths of the much larger Deschutes and John Day rivers, which have lithologically diverse catchments, were also taken for comparison. In addition, five groundwater samples were collected in March 2012, as well as an additional stream (Mosquito Creek, R11) (Fig. 1).

At each site, pH, temperature, electrical conductivity, and total dissolved solids (TDS) were measured using a multi-meter (Hanna® Instruments) with analytical accuracy of ±0.05, ±0.5 °C, ±2% µS/cm, and ±2% ppm, respectively. All stream water samples were obtained using a peristaltic pump and filtered using a 142 mm filter holder system with 0.2 µm cellulose acetate filters. Filtered waters were collected in pre-cleaned Nalgene® bottles. Filters were placed in air-tight Ziploc plastic bags for transport back to the lab. The suspended loads of the stream waters were recovered from the filters in the clean lab. The sample tubing was pumped dry after each sample collection and one liter of deionized water was pumped through the system to clean it between each sampling event. At the start of sampling at a new site, a liter of sample water was first collected into the pre-cleaned bottles

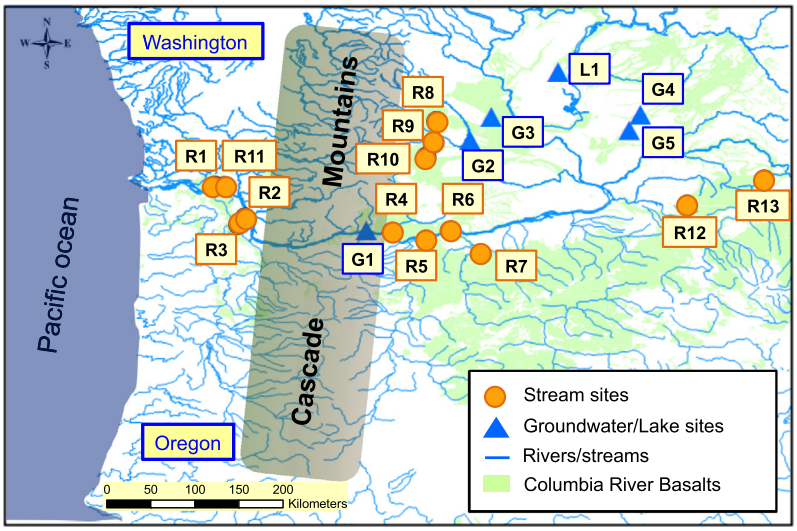

Fig. 1. Map of sample locations. Geological data are from USGS. Stream sample locations are shown in orange circles and numbered with Rx. R11 was only sampled during late winter of 2012 and the rest rivers were sampled both in summer of 2010 and late winter of 2012. Groundwater sample locations and one lake sample location are shown in blue triangles, all of which were sampled during late winter. (For interpretation of the references to color in this figure legend, the reader is referred to the web version of this article.)

and then discarded. Finally, about two liters of water were collected, acidified using five drops (~0.25 ml) of concentrated HCl and stored in Nalgene® bottles for transport to the lab. Following this procedure, two 125 ml pre-cleaned Nalgene® bottles were filled with water for anion (without acidification) and major and trace cation analyses (acidified using two drops of ~0.1 ml concentrated HCl).

Groundwaters were sampled either from existing pumping systems that tap into deep-seated subsurfaces or faucets fed by shallow wells. The sampling method outlined above for streams was also used for the groundwaters (Table 2). One groundwater sample (G4, Lind) was taken from a new municipal well in the town of Lind, WA, which taps into a subsurface buried 220 m below ground and is estimated to be >50 ka old based on radiocarbon age dating (T. Tolan, personal communication). A second groundwater sample (G1, Spring Creek) was collected at the Spring Creek National Fish Hatchery from a subsurface ~200 m deep, containing little or no modern water and having an overall age of thousands of years (Hinkle, 1996). Thus, these two groundwaters are unlikely to be the sources of waters in the streams.

3.2. Major and trace elements in dissolved loads

Major and trace cations in dissolved loads were analyzed using an Element 2 single collector Inductively Coupled Plasma-Mass Spectrometer (ICP-MS) at the University of Maryland. Calibration curves were created using pure element solutions (Alfa Aesar®) and standard and water samples were doped with the same amount of indium to correct for instrumental drift ([In] = 2 ppb). The accuracy and precision of the analyses were determined by repeat analyses of the international river standard SLRS-5, with accuracy of cations assessed at better than 4% ($n = 11$ for SLRS-5), except for K (<10%), based on its certified value (Table A.1).

Major anion concentrations were measured by ion chromatography in the Biogeochemical Lab at the University of Maryland. Anion concentrations were measured using a Dionex ICS-1500 ion chromatograph, equipped with an AS14 4-mm analytical column and a guard column. An eluent of 3.5 mM of Na_2CO_3 with 1.0 mM $NaHCO_3$ was used at a flow rate of 0.3 mL/min. The detection limits of the ion chromatograph are 0.01 mg/L, 0.01 mg NO_3/L and 0.02 mg SO_4/L for Cl^-, NO_3^- and SO_4^{2-}, respectively. The accuracy of the analyses are better than ~5% based on repeat analyses of standards (see Table A.2). HCO_3^- concentrations were estimated based on charge balance.

3.3. Lithium isotope analyses

All sample preparation and analyses were performed in the Geochemical Laboratory at the University of Maryland. A description of sample dissolution, column chemistry, analytical blanks and instrumental analysis is provided in the electronic appendix (Text A1). Long-term precision is better than ±1‰ (2σ); several USGS rock standards were run repeatedly during the course of this study (Table A.3). BHVO-1 yielded δ^7Li of $+4.6 \pm 1.0$ ($n = 5$) cf. 4.0 to 5.6 in the literature (GeoReM database: http://georem.mpch-mainz.gwdg.de/); BCR-2 yielded δ^7Li of $+2.9 \pm 1.5$ ($n = 3$) cf. 2.6 to 4.6 in the literature (GeoReM database); and AGV-1 yielded δ^7Li of $+5.2 \pm 0.6$ ($n = 3$) cf. 4.6 and 6.7 for AGV-1 in Liu et al. (2010) and Magna et al. (2004), respectively.

3.3.1. Handling of dissolved loads

Approximately 30 ml to 2 L of filtered stream and groundwaters (depending on the volume collected) were first weighed and then evaporated in large Savillex® Teflon beakers (160 ml) or Teflon evaporation dishes (400 ml) on a hot plate ($T < 100\,°C$). A 3:1 mixture of HF–HNO_3 was added to the samples, which were then transferred into screw-top Savillex® Teflon beakers (15 ml) placed onto a hot plate ($T < 120\,°C$) for an overnight dissolution followed by an evaporation step. The sample was then treated with concentrated HNO_3 and HCl until all solids were dissolved and the final solutions were clear. The final dried sample was picked up in 4 N HCl for column separation.

3.3.2. Dissolution of suspended loads

Suspended load samples were washed off the filters into large Savillex® Teflon beakers (160 ml) using Milli-Q water and then transferred into screw-top Teflon beakers and dried on a hot plate ($T < 70\,°C$). The dried samples were then scraped off the beaker and weighed into clean Teflon beakers; sample sizes ranged from several milligrams to tens of milligrams. The samples were then dissolved using a 3:1 mixture of HF and HNO_3 in a screw-top

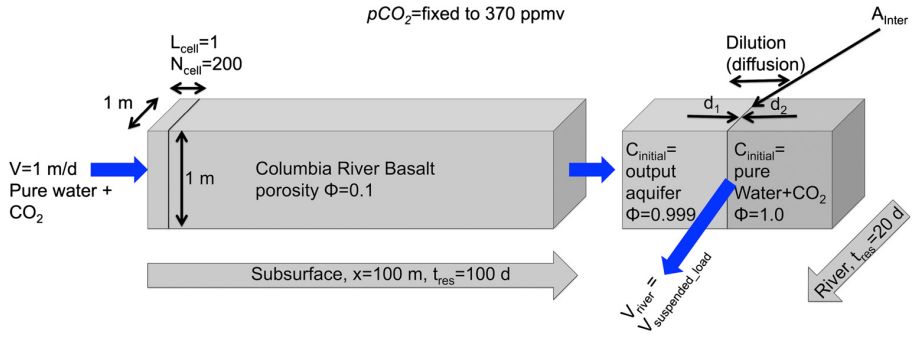

Fig. 2. Model setup illustrating that simulations were run for a 100 m long subsurface that eventually exfiltrates into a river. River simulations were run as batch simulations (no flow) assuming that the suspended load is transported at the same velocity as river water. Moreover, river simulations consider a diffusive dilution of the exfiltrated groundwater with water that experienced no previous water–rock interaction (i.e., pure water+CO_2). For both systems (subsurface and river), Li isotope fractionation is simulated to occur during hematite and kaolinite precipitation.

Teflon beaker on a hot plate ($T \approx 90\,^{\circ}C$), dried, then pickup up by HNO_3 and HCl addition until all solids were dissolved and the final solutions were clear. The final dried sample was dissolved in 4 N HCl for column separation.

3.4. Reactive transport modeling

In order to investigate the influence of silicate weathering on δ^7Li_{dis}, a series of thermodynamically- and kinetically-controlled reactive transport model simulations were carried out using the code TOUGHREACT V2 (Xu et al., 2011). TOUGHREACT has been used to evaluate isotopic fractionation coupled to water–rock interaction and hydrological processes in a variety of subsurface environments and laboratory experiments (e.g., Singleton et al., 2005; Sonnenthal et al., 1998; Wanner and Sonnenthal, 2013). Each modeled scenario is composed of two individual simulations to model silicate weathering and associated Li isotope fractionation (i) during subsurface flow and (ii) within rivers (Fig. 2). The model setup is closely related to the simulations performed by Wanner et al. (2014) modeling Li isotope fractionation associated with granite weathering. Accordingly, only a short model description is provided below. Input parameters and specific code capabilities used to simulate Li isotope fractionations are described in detail in the electronic appendix (Text A2).

3.4.1. Subsurface simulations

Reactive transport along a basaltic subsurface was simulated for a fully saturated, 100 m long porous media having a porosity of 10%, the porosity previously used to simulate Columbia River Basalt weathering (Taylor and Lasaga, 1999). Fracture flow, the presence of highly porous flow tops, as well as the unsaturated zone, were not incorporated into the model because our focus is on assessing the sensitivity (i.e., trends) of dissolved δ^7Li values as a function of residence time (i.e., amount of weathering), rather than on simulating detailed flow features of actual unsaturated zones feeding subsurfaces and streams. Subsurface simulations were run for an average linear groundwater flow velocity of 1 m/d to simulate a system dominated by advection.

Pure water in equilibrium with atmospheric CO_2 was specified as the initial and boundary fluid compositions. A starting mineralogical composition similar to the normative mineralogy reported for different Columbia River Basalt members (BVSP, 1981) (e.g., plagioclase, pyroxene, olivine, glass) was assigned to the solid part of the porous medium (see Tables A.4 and A.5 for mineral stoichiometries, corresponding thermodynamic and kinetic parameters and specified initial and boundary conditions). Simulations were run for two different initial bulk Li concentrations of 4 and 20 ppm, encompassing most of the range of [Li] observed in fresh CRB (Liu et al., 2013), and to assess whether the initial Li concentration influences riverine δ^7Li values.

Because Li is moderately incompatible during igneous differentiation (Brenan et al., 1998), Li is assumed to be mostly contained within a glassy basalt matrix and is introduced into the model from a Li-bearing volcanic glass phase tabulated in the THERMODEM database (Blanc et al., 2012). Li-bearing hematite and kaolinite were allowed to precipitate. It should be noted that kaolinite and hematite are likely not the only secondary minerals forming, but they serve as representatives for any other potentially precipitating Fe- and Al-bearing minerals.

To simulate the fate of individual Li isotopes, ^6Li and ^7Li were incorporated into the mineral stoichiometries of primary Li-bearing volcanic glass, and secondary kaolinite and hematite. An initial δ^7Li value of +1 was assumed for Li-bearing glass, which corresponds to the average δ^7Li value measured for two different CRBs members (Liu et al., 2013). Similar to the model of Bouchez et al. (2013), we do not distinguish between Li exchange-, Li surface complexation-, or Li substitution reactions and Li uptake by secondary minerals and associated Li isotopic fractionation is solely simulated during Li incorporation into precipitating kaolinite and hematite. Li bearing secondary mineral precipitation is simulated by means of a solid solution approach, such as described in detail by Wanner et al. (2014), as well as in Text A2. A fractionation factor ($\Delta^7Li_{2ndMin\text{-}solution} = \delta^7Li_{2ndMin} - \delta^7Li_{solution}$) of $-10‰$ was assigned for hematite and kaolinite precipitation, which is within the range of Li isotope fractionation factors reported or inferred for secondary mineral precipitation (Huh et al., 2001; Kisakürek et al., 2005; Pistiner and Henderson, 2003; Pogge von Strandmann et al., 2006, 2010; Vigier et al., 2009; Zhang et al., 1998). An extended discussion of fractionation factors can be found in Text A2.

3.4.2. River simulations

River simulations were conducted essentially as batch simulations, where the flow velocity was set to zero. In doing so, it was assumed that the reactive suspended load (i.e., solid phase) is transported at the same velocity as the river water, which is in agreement with current knowledge about the transport of suspended river loads (Fryirs and Brierley, 2013).

Two grid blocks were defined to simulate groundwater exfiltrating into river systems, which is diluted by river water that previously experienced less water–rock interaction processes. By setting the interfacial area (A_{inter}, Fig. 2) between the two grid blocks to 7000 m^2, the Li concentration of the exfiltrating groundwater was diluted by a factor of ~10 during a simulated river residence time of 20 days, roughly corresponding to the Li concentration difference observed between streams and groundwaters (Tables 1, 2).

Table 1
Sample locations, field measurements, major and trace element concentrations and Li isotopic compositions in dissolved and suspended loads of rivers.

2010 summer	Units	Cameron	Milton	N. Scapoose	Silva	Deschutes	John Day	Hay	Wenas	Cowiche	Ahtanum	Mill	Asotin
Sample #		R1	R2	R3	R4	R5	R6	R7	R8	R9	R10	R12	R13
Longitude	°	−123.16707	−122.84415	−122.91550	−121.26745	−120.90903	−120.65085	−120.31797	−120.79715	−120.82127	−120.90663	−118.11638	−117.29242
Latitude	°	46.20735	45.86973	45.79293	45.71217	45.63033	45.72850	45.47992	46.89620	46.66437	46.51642	46.00358	46.27363
Location[a]		west	west	west	east	east	east	east	east	east	east	east	east
T	°C	15.6	18.6	15.2	18.1	19.2	21.9	19.6	12.6	18.8	14.6	14.1	18.1
pH		7.2	7.7	7.9	8.0	8.7	8.5	7.8	7.9	8.0	7.8	7.8	8.1
Conductivity	μS/cm	21	64	65	130	120	160	310	95	88	65	74	82
TDS	mg/L	10	32	32	64	58	82	150	47	44	32	35	41
Na	mg/L	2.7	4.9	5.3	6.5	9.6	7.0	17	3.9	4.0	3.2	3.8	3.5
Mg	mg/L	0.8	2.1	1.9	5.4	4.7	5.9	11	4.5	3.8	2.7	2.5	3.1
Al	μg/L	30	12	22	6.5	6.1	4.7	1.8	9.1	15	10	6.5	20
Si	mg/L	6.5	17	22	31	20	14	41	29	32	27	29	30
K	mg/L	0.4	1.1	1.3	1.5	1.7	1.4	3.7	1.6	2.1	1.8	2.3	2.3
Ca	mg/L	1.7	4.9	5.2	11	6.8	16	28	8.9	7.9	6.3	6.6	8.0
Fe	μg/L	130	320	170	28	21	32	54	130	180	79	50	35
F^-	mg/L	0.06	0.08	0.04	0.56	–	0.13	0.13	0.04	0.06	0.03	0.07	0.08
Cl^-	mg/L	2.6	4.0	18	54	13	8.5	8.6	16	13	16	3.2	2.8
NO_3^-	mg/L	–	–	–	–	–	–	0.01	–	–	0.01	–	–
SO_4^{2-}	mg/L	2.1	4.7	5.5	39	1.3	4.3	18	2.7	1.4	5.1	3.4	1.9
HCO_3^-	mg/L	0.9	0.9	1.3	1.0	1.5	2.7	−0.4	0.6	1.1	0.9	0.9	1.5
Li_{dis}	μg/L	0.1	0.7	1.6	0.4	4.7	1.6	3.2	0.7	1.1	0.7	0.9	1.0
δ^7Li_{dis}		21.1	22.1	14.9	30.4	12.2	16.6	20.0	20.2	17.0	13.0	10.6	9.3
Li_{sus}	μg/g	–	–	14	–	7.5	15	–	24	–	–	–	7.2
δ^7Li_{sus}		–	–	−5.6	–	4.2	−1.6	–	-3.1	–	–	–	−4.2

2012 winter	Units	Cameron	Milton	N. Scapoose	Silva	Deschutes	John Day	Hay	Wenas	Cowiche	Ahtanum	Mill	Asotin	Mosquito
Sample #		R1	R2	R3	R4	R5	R6	R7	R8	R9	R10	R12	R13	R11
Longitude	°	−123.16707	−122.84415	−122.91550	−121.26745	−120.90903	−120.65085	−120.31797	−120.79715	−120.82127	−120.90663	−118.11638	−117.29242	−123.06510
Latitude	°	46.20735	45.86973	45.79293	45.71217	45.63033	45.72850	45.47992	46.89620	46.66437	46.51642	46.00358	46.27363	46.20202
Location[a]		west	west	west	east	east	east	east	east	east	east	east	east	west
T	°C	5.8	6.0	5.2	5.6	8.0	6.9	9.0	1.4	2.2	2.9	4.3	5.2	5.6
pH		6.7	6.9	8.3	7.6	8.0	7.7	7.8	7.6	7.6	7.6	7.4	7.6	6.7
Conductivity	μS/cm	14	31	37	65	110	130	320	97	100	91	51	74	20
TDS	mg/L	7	16	18	33	52	62	160	48	51	44	25	37	10
Na	mg/L	2.2	3.1	3.2	4.2	8.2	5.6	16	4.0	4.6	3.9	3.1	2.9	2.4
Mg	mg/L	0.6	1.0	1.0	2.7	4.0	4.4	10	4.3	4.4	3.6	1.7	2.7	0.8
Al	μg/L	16	4.9	8.9	86	43	40	2.1	57	23	22	180	240	12
Si	mg/L	4.1	9.2	12	21	22	19	34	27	30	30	24	27	4.8
K	mg/L	0.3	0.6	0.8	0.9	1.5	1.3	3.8	1.5	1.9	2.0	1.5	1.7	0.3
Ca	mg/L	1.6	2.8	3.1	6.3	6.4	12	27	8.6	8.8	7.9	4.8	6.9	1.9
Fe	μg/L	20	14	16	55	34	51	57	93	76	55	220	250	37
F^-	mg/L	0.01	0.02	0.03	0.04	0.10	0.08	0.42	0.09	0.10	0.07	0.15	0.08	0.01
Cl^-	mg/L	3.3	2.6	2.9	1.6	1.8	1.2	11	0.4	0.9	0.4	0.5	0.7	2.7
NO_3^-	mg/L	2.0	3.3	2.8	0.0	0.4	0.3	1.5	0.0	0.0	0.0	0.2	0.3	4.8
SO_4^{2-}	mg/L	0.5	1.2	1.6	0.7	1.8	3.9	15	2.0	3.2	1.6	0.6	1.3	0.5
HCO_3^-	mg/L	0.6	0.4	0.7	2.5	2.6	2.6	3.9	1.7	1.8	3.1	7.2	9.6	0.6
Li_{dis}	μg/L	0.1	0.4	0.9	0.3	3.5	1.1	2.9	0.5	1.1	0.8	0.7	0.7	0.2
δ^7Li_{dis}		17.4	13.0	8.8	14.0	12.5	13.5	18.8	21.6	16.1	13.1	10.9	8.9	15.9
Li_{sus}	μg/g	16	20	66	18	13	20	21	24	16	16	19	36	17
δ^7Li_{sus}		−1.4	−2.5	−4.5	−0.9	−0.3	−1.5	−0.2	−3.1	−5.7	−5.9	−2.8	−5.2	−1.0

[a] Location relative to the Cascades (west or east).
Note: "–" Under detection limit.

Table 2
Sample locations, field measurements, major and trace element concentrations and Li isotopic compositions of groundwaters and one alkaline lake.

Groundwater	Units	Spring Creek	Selah	Ryegrass	Lind	Hatton	Soap Lake
Sample #		G1	G2	G3	G4	G5	L1
Longitude	°	−121.54613	−120.44327	−120.20900	−118.62250	−118.74282	−119.49877
Latitude	°	45.72737	46.69758	46.94738	46.96828	46.79410	47.42263
Sampling[a]		well	faucet	faucet	well	faucet	
T	°C	17.6	18.1	14.7	28.6	10.9	10.2
pH		8.8	8.0	7.7	9.1	7.9	9.6
Conductivity	μS/cm	180	320	340	350	510	>3999
TDS	mg/L	90	160	170	180	250	> 2000
Na	mg/L	33	21	13	78	19	280
Mg	mg/L	0.4	12	15	0.3	19	4.4
Al	μg/L	6.9	27	0.5	4.9	0.1	–
Si	mg/L	45	33	40	64	35	4.9
K	mg/L	4.5	3.9	2.9	3.9	4.0	590
Ca	mg/L	1.9	17	19	3.1	40	6.9
Fe	μg/L	47	6.9	5.7	17	54	1.3
F^-	mg/L	0.76	0.48	0.39	3.3	0.28	0.31
Cl^-	mg/L	3.6	8.6	7.0	7.9	46	130
NO_3^-	mg/L	0.01	–	11	0.1	18	–
SO_4^{2-}	mg/L	1.5	3.7	12	4.7	50	210
HCO_3^-	mg/L	3.5	1.8	2.4	2.4	3.4	−0.87
Li_{dis}	μg/L	21	9.8	6.5	8.9	3.3	1.5
δ^7Li_{dis}		6.8	8.1	9.4	21.4	6.7	20.5

[a] Sampling methods (well or faucet).
Note: "–" Below detection limit.

Reactions between the suspended river load and river waters were only considered for the grid block initially containing exfiltrating groundwater.

The suspended river load was assigned the same initial mineralogical composition as the subsurface (Table A.5), assuming that this load contains a significant amount of primary silicate minerals in addition to the dominant clays and oxides (Gaillardet et al., 1999). This model assumption is consistent with Bouchez et al. (2011) who observed that the mineralogical composition of the suspended load is dependent on the particle size and that primary silicate minerals (e.g., feldspar) are enriched in the coarser fraction. Consequently, Li isotope fractionation in the simulated river is assumed to occur in the same fashion as in the subsurface simulations.

4. Results

Data for field measurements (pH, temperature, electrical conductivity, and TDS), major and trace elements, in addition to Li isotopic data are given in Tables 1 and 2, for streams and groundwaters, respectively. A comparison between summer and late winter data is shown in Figs. A3 and A4 for field parameters and selected dissolved species, respectively.

4.1. Field measurements

Streams sampled in July 2010 display a temperature range from 13 to 22 °C with pH ranging from 7.2 to 8.7, while the streams sampled in March 2012 are cooler (1 to 9 °C), but have a similar range in pH (6.7 to 8.3). Groundwaters are warmer (10 to 29 °C), and have higher pH (7.7 to 9.6), compared to the streams sampled at the same time of the year (March). TDS in streams east of the Cascades do not show significant seasonal variations (32 to 154 mg/L in July, and 25 to 158 mg/L in March, Table 1) with the exception of Silva creek, where TDS varies by a factor of two between seasons (64 in summer vs. 33 ppm in winter). By contrast, TDS in the three streams west of the Cascades differ by up to a factor two between seasons (7–18 mg/L in July, 10–32 mg/L in March). Groundwaters range to higher TDS values (90 to 253 mg/L, Table 2). The maximum TDS value was measured in a meromictic lake (i.e., a stratified lake that does not mix between layers), the TDS of which exceeded the range of the multi-meter.

4.2. Major elements

Major cations and anions in stream water and groundwater samples are plotted using a classic Piper Diagram (Piper, 1953), a trilinear diagram consisting of two equilateral triangles for cations and anions, respectively, which are projected onto a central diamond (Fig. 3). In the lower triangles, the points are expressed as a percentage of the total amount of cations or anions in milliequivalents per liter. River and groundwaters are plotted in Figs. 3a and 3b for summer and winter, respectively. River waters have clustered cation patterns in both summer and winter illustrating that the water chemistry is inherited from a single lithology. Three shallow groundwaters plot within the same domain as the streams, while two deep groundwaters (G1: Spring Creek, and G4: Lind) show very different cation and anion patterns. Major elements such as Na, Si and Ca, correlate with Mg, and hence with each other (Fig. A5). Similarly, the total cation charge, TZ^+ ($TZ^+ = Na^+ + 2Mg^{2+} + K^+ + 2Ca^{2+}$ in 10^{-3} equivalents per liter, mEq/L), also correlates ($R^2 = 0.98$) with [Mg] in stream waters. Groundwaters, except for the two deep groundwaters (G1: Spring Creek, and G4: Lind), follow the same major element correlation, but with higher concentrations. The sample from Silva Creek taken in July, 2010, has much higher [Cl^-] (54 mg/L) and [SO_4^{2-}] (39 mg/L), compared to the other streams studied here and natural streams elsewhere (where [Cl^-] and [SO_4^{2-}] are typically less than 10 mg/L), indicating that this creek may have been subjected to anthropogenic contamination in the summer months (e.g., fertilizers).

Major cations in streams show very little variation between summer and winter; however, anions show large variations (Fig. 3). Although little variation is observed for cation ratios, actual concentrations (e.g., Si, Mg, and Na) tend to be slightly higher during the summer sampling campaign (Table 1, Fig. A4). This observation corresponds well with pH values and TDS concentrations, which were also slightly larger during the summer sampling campaign (Table 1, Fig. A3). In the case of [Si] and TDS, the seasonal concentration increase is most prominent in the western streams, with an increase of up to a factor two. By contrast, in the eastern streams both concentration variations ([Si] and TDS) were significantly smaller, by a factor less than ∼1.3 (Table 1). In addition, although there is some seasonal variation of anion concentrations

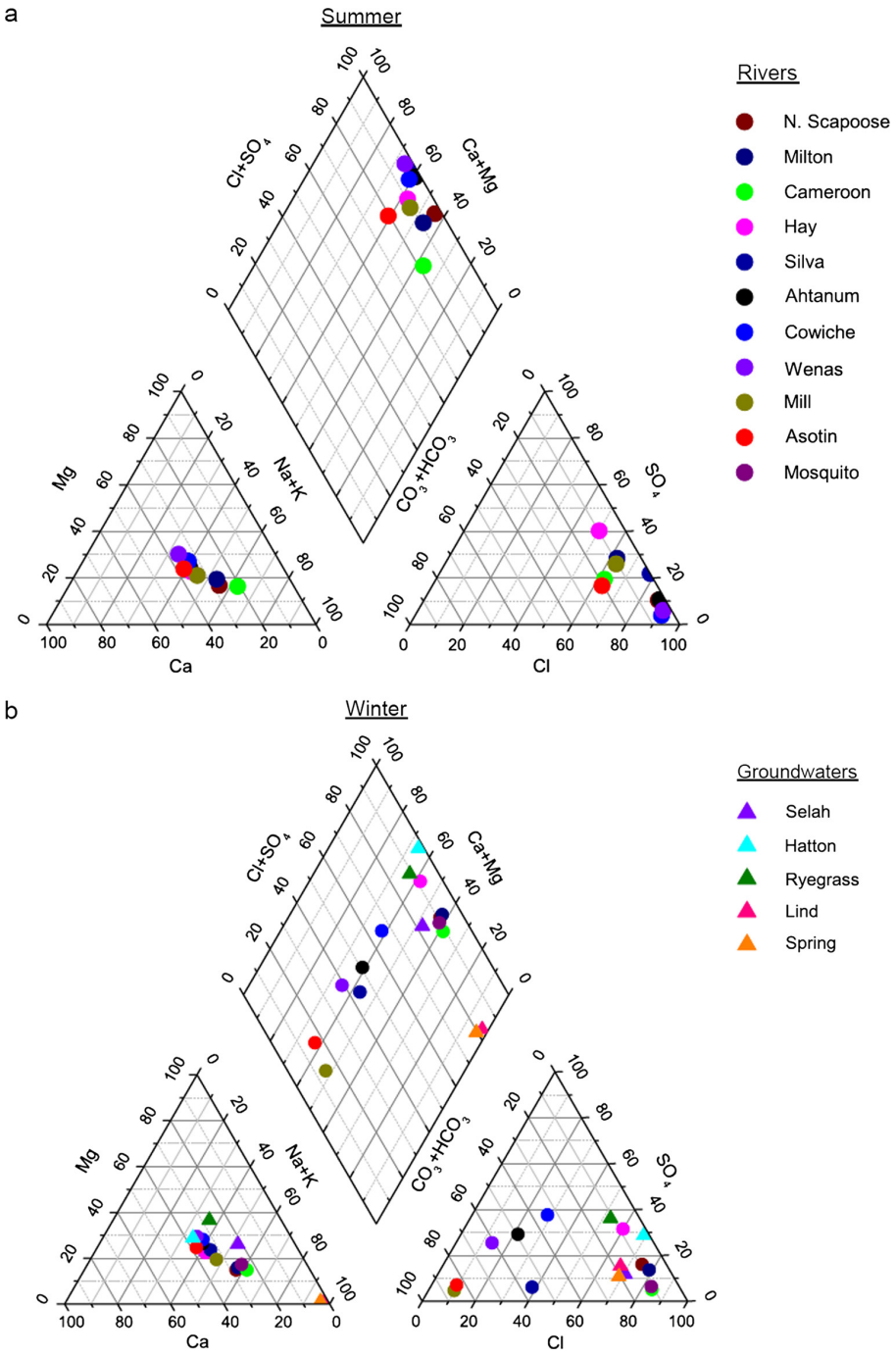

Fig. 3. Piper diagram (Piper, 1953) of streams and groundwaters in summer (a) and late winter (b). Stream waters and groundwaters are shown in circles and triangles, respectively. (For interpretation of the colors in this figure, the reader is referred to the web version of this article.)

among streams, the overall pattern likely reflects a mixture of water sources, since all streams and shallow groundwaters plot along a straight line; the two deep groundwaters fall off the trend in the upper diamond plot (Fig. 3).

4.3. Li elemental and isotopic data

The Li concentrations of dissolved loads vary from 0.2 to 4.7 μg/L for both sampling seasons. For individual streams, there is little difference in [Li] between the two sampling campaigns (Table 1, Fig. 4), where [Li] shows a weak positive correlation with [Mg] ($R^2 = 0.7$) and [Si] ($R^2 = 0.4$). δ^7Li_{dis} ranges from +10 to +30 in the streams sampled during the summer, and shows a similar range in the streams sampled in the late winter (+9 to +22). In streams east of the Cascades, δ^7Li_{dis} does not change with season, except for Silva Creek (+30 vs. +14‰), which may reflect anthropogenic contamination, based on the high contents of [Cl^-] and [SO_4^{2-}]. A previous study has shown that anthropogeni-

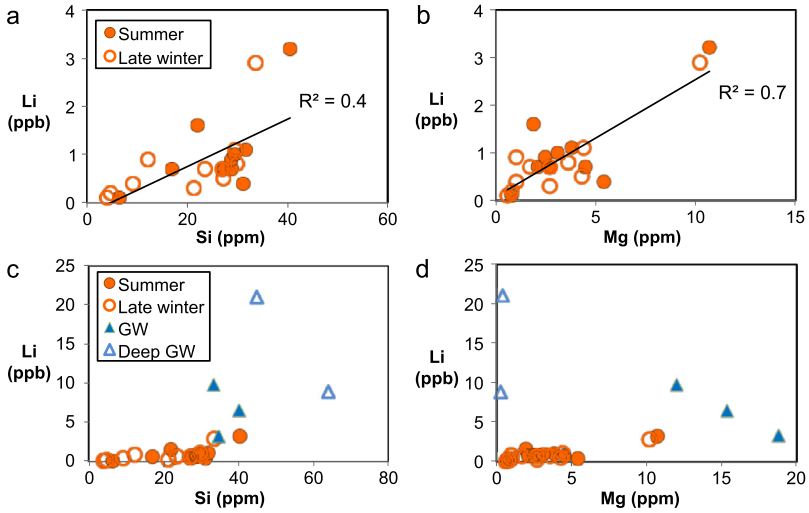

Fig. 4. Plots of [Li] versus [Si] and [Mg] in streams and groundwaters. Summer and late winter stream waters are shown in open and closed orange circles, respectively. Groundwaters feeding the streams are in solid blue triangles, deep seated and ancient groundwaters are shown in open blue symbols. (For interpretation of the references to color in this figure legend, the reader is referred to the web version of this article.)

cally contaminated groundwaters may show very heavy δ^7Li values (up to ~+1000‰), due to the use of heavy Li-enriched fertilizer (Négrel et al., 2010). By contrast, the streams to the west of the Cascades show consistently higher δ^7Li values in the summer compared to the winter (Fig. 5).

Varying from 2 to 21 μg/L (Table 1), groundwater [Li] is significantly higher than in the streams. Moreover, with the exception of the two groundwaters from deep wells (shown as open triangles in the figures), [Li] in groundwaters show similar correlations with [Si], but not with [Mg], as seen in stream waters (Fig. 4). Except for the deep-seated Lind well water (G4, +21.4‰), groundwater δ^7Li (δ^7Li_{GW}) are between +6.7 and +9.4‰, which is on the very low end of observed δ^7Li_{dis} (Tables 1, 2).

[Li] in the suspended loads varies from 7 to 24 μg/g in the streams sampled during the summer, and shows a greater range in the streams sampled during the late winter (from 13 to 66 μg/g). The δ^7Li of the suspended load (δ^7Li_{sus}) is generally the same from season to season, except for the Dechutes River, which shows a large change in δ^7Li_{sus} according to season (from +4.2 in summer to −0.3 in late winter). With the exception of the summer Deschutes River sample, δ^7Li_{sus} are lower compared to the average δ^7Li measured in fresh CRBs ($\delta^7Li = 1.1$, Liu et al., 2013). The low δ^7Li_{sus} are comparable to the lower than average δ^7Li observed in weathered CRB ($\delta^7Li = -5$ to 0) and the upper continental crust ($\delta^7Li = 0$ on average, Teng et al., 2004).

4.4. Simulation results

4.4.1. [Li] and δ^7Li

Simulated steady-state [Li] and [Si] profiles along our model domain (subsurface + river), as well as corresponding δ^7Li profiles (i.e., δ^7Li_{dis}, δ^7Li_{2ndMin} and $\delta^7Li_{bulk\text{-}rock}$) are shown in Figs. 6a and 6b for two different parental basalt Li concentrations of 4 and 20 ppm. Increasing [Li] in basalt yields larger dissolved Li concentrations for a specific subsurface residence time (Fig. 6a), but does not change δ^7Li values, as illustrated by superimposing δ^7Li_{dis} vs. residence time behavior (Fig. 6b). These results thus imply that subsurface and riverine δ^7Li values are not sensitive to the Li concentrations of the parent rock, nor to the subsequent variable riverine [Li]. This simulation result is supported by a lack of correlation observed between δ^7Li_{dis} and [Li] (Table 1).

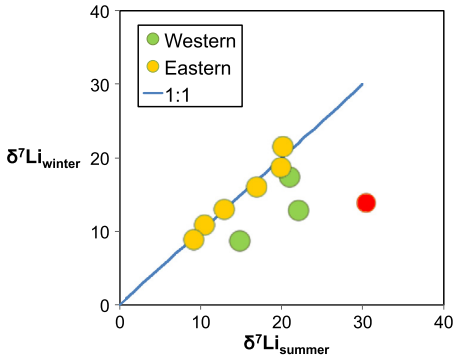

Fig. 5. Figure δ^7Li_{dis} in summer vs. winter for western and eastern streams. The sample showing suspected anthropogenic contamination (Silva, eastern) is plotted as a red circle (see main text for details). (For interpretation of the references to color in this figure legend, the reader is referred to the web version of this article.)

The δ^7Li_{dis} and δ^7Li_{2ndMin} values steadily increase with increasing subsurface and/or riverine residence time in the model (Fig. 6b). The slope of the δ^7Li increase with time is dependent on the specified fractionation factor. For a lower fractionation factor (i.e., less fractionation), longer residence time is needed to reach the same δ^7Li as for $\Delta^7Li = -10$‰, or vice versa. However, the pattern of increasing δ^7Li with increasing residence time is not sensitive to the specified fractionation factor. The δ^7Li_{dis} increases seen along the model domain are produced by our solid solution approach (Wanner et al., 2014), ensuring that [Li] in precipitating hematite and kaolinite increases with increasing [Li]. This assumption is consistent with an experimental study showing that [Li] in synthesized smectite increases linearly with aqueous [Li] (Decarreau et al., 2012). Because the dissolution rate of the parent rock remains constant (Table A.4), the ratio between Li that is incorporated into hematite and kaolinite, and the Li being released from the parent rock increases with increasing residence time, thus, continuously driving δ^7Li_{dis} and δ^7Li_{2ndMin} to higher values. The Li isotopic composition of the bulk rock is not changed (Fig. 6b) because the amount of secondary minerals formed during the 100 years for which the simulation were run were to low to drive the bulk rock δ^7Li to lower values. In contrast to δ^7Li_{dis} and

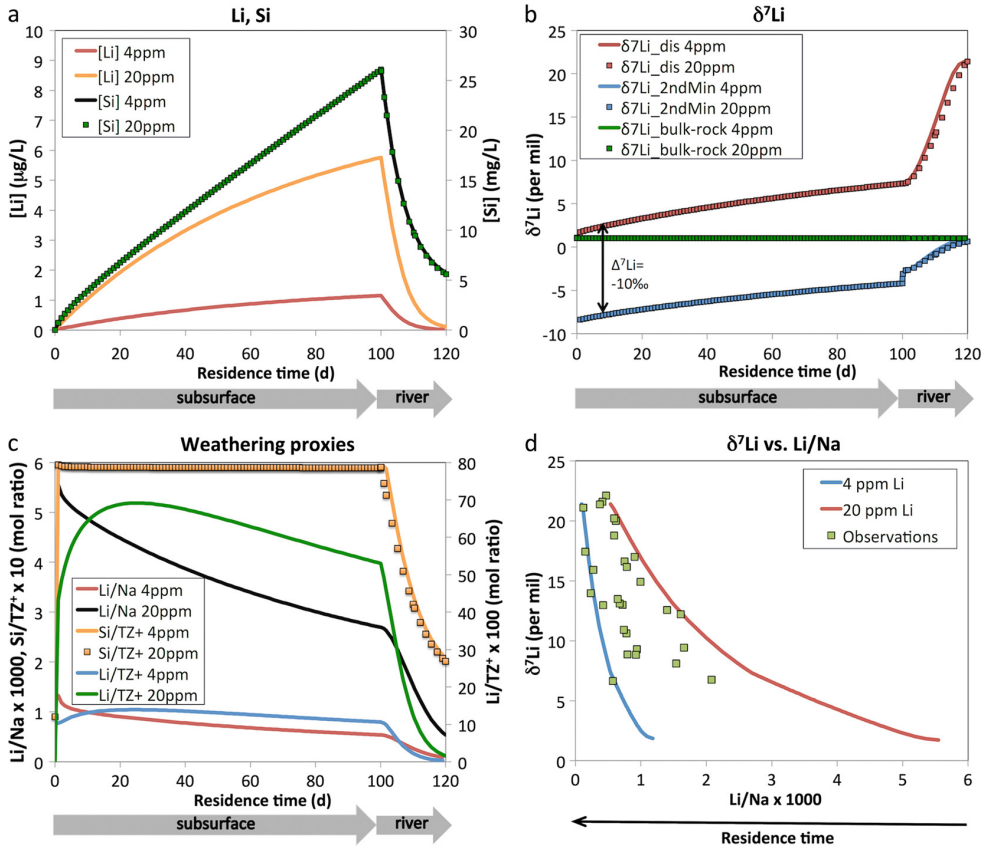

Fig. 6. Model results for initial CRB Li concentrations of 4 ppm and 20 ppm. (a) Illustrates steady state Li and Si concentration profiles along the full model domain (subsurface + river). (b) Presents corresponding steady-state δ^7Li profiles for aqueous Li (δ^7Li_{dis}), Li in precipitating secondary clays ($\delta^7Li_{kaolinite} = \delta^7Li_{hematite}$ summarized as δ^7Li_{2ndMin}) and Li of the bulk solid. (c) illustrates steady state profiles of typical silicate weathering tracers such as Si/TZ$^+$, Li/TZ$^+$ and Li/Na. (d) Comparison between the simulated δ^7Li vs. Li/Na relation (curves) and the one observed in groundwaters and streams draining the Columbia River Basalt (Tables 1 and 2). Decreasing Li/Na ratio reflects increasing subsurface and/or river residence time. All profiles are plotted against fluid residence time to simultaneously illustrate subsurface and river simulations. In the subsurface domain, fluid residence time (x-axis) also corresponds to the distance along the subsurface domain because the flow velocity was 1 m/d.

δ^7Li_{2ndMin}, aqueous [Li] and [Si] decrease (Fig. 6a) due to dilution when water flowing along the subsurface exfiltrates into the river.

4.4.2. Weathering proxies

Simulated profiles for silicate weathering proxies such as [Si], normalized Si (Si/TZ$^+$), [Li], normalized Li (Li/TZ$^+$), and Li/Na that have been previously used to constrain silicate weathering intensity (e.g., Huh et al., 2001, 1998; Millot et al., 2010; Pogge von Strandmann et al., 2010, 2006) are shown in Fig. 6c. These profiles reflect a proxy's ideal behavior, because processes potentially affecting the use of a specific weathering proxy (e.g., biological activity, anthropogenic contamination, salt leaching) were not considered in our simulations.

A negative correlation between δ^7Li_{dis} and Li/Na (Fig. 6c) reflects Li incorporation into hematite and kaolinite, whereas Na remains in solution. Accordingly, although [Li] also increases with residence time in the subsurface, the Li/Na ratio's decrease with increasing residence time is due to Li incorporation into these secondary minerals. Other weathering proxies show a distinct correlation with δ^7Li_{dis} only within a specific model domain (subsurface vs. river). In particular, concentration proxies such as [Si] and [Li] are positively correlated with δ^7Li_{dis} along the subsurface domain, but once exfiltrated, the correlations change sign because Li isotope fractionation is ongoing, whereas aqueous species concentrations decrease due to mixing with more superficial (i.e., meteoric) water.

5. Discussion

The observation that riverine δ^7Li_{dis} (+9 to +30) is systematically higher than δ^7Li values of the corresponding suspended loads ($\delta^7Li_{sus} = -6$ to 0), as well as fresh and weathered CRBs (δ^7Li = −5 to +5, Liu et al., 2013), confirms that high δ^7Li_{dis} is mainly generated by Li isotope fractionation occurring during basalt weathering (e.g., Huh et al., 2001, 1998; Pogge von Strandmann et al., 2010, 2006).

The most striking observation from our measurements, however, is the large variation in δ^7Li_{dis} (about 20‰ in summer, and >10‰ in late winter) covering almost the entire range of δ^7Li (+6 to +32) reported in major world rivers (Huh et al., 1998). This observation is especially remarkable because we sampled only small streams and groundwaters within the CRBs, for which catchment lithological differences are small. Some previous studies attribute large δ^7Li_{dis} variations to formation of different secondary minerals that have different fractionation factors with water (Millot et al., 2010; Wimpenny et al., 2010b). However, we see no evidence that the large δ^7Li_{dis} variations in our study are due to the presence of different Li-bearing secondary minerals, as saturation index (SI) calculations (Fig. A7) and studies of weathering profiles (Liu et al., 2013) suggest that all of the streams and groundwaters are saturated with the same secondary mineral assemblage (hematite, kaolinite and gibbsite). We therefore postulate that factors other than mineralogical differences (i.e., primary and

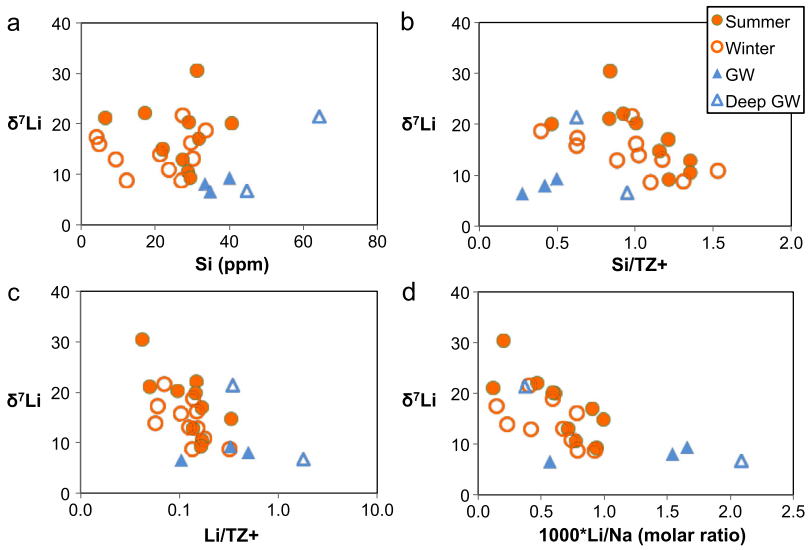

Fig. 7. δ^7Li_{dis} versus [Si], Si/TZ^+, Li/TZ^+, and $1000\times Li/Na$ (molar ratio) in stream waters and groundwaters. Summer and late winter stream waters are shown in open and closed orange circles, respectively. Groundwaters feeding streams are in solid blue triangles, deep-seated groundwaters are in open blue triangles. The total cation charge (TZ^+) is defined as $TZ^+ = Na^+ + 2Mg^{2+} + K^+ + 2Ca^{2+}$ in 10^{-3} equivalents per liter, mEq/L. (For interpretation of the references to color in this figure legend, the reader is referred to the web version of this article.)

secondary Li bearing phases) have a major control on the Li isotopic composition of the streams.

5.1. Residence time

The rise of δ^7Li with increasing residence time seen in the simulation (Fig. 6b) implies that subsurface residence time in particular, and the hydrological cycle in general have major controls on δ^7Li_{dis}. In fact, in a plot of δ^7Li_{dis} vs. Li/Na, our sample observations fall between the two curves defined by the minimum and maximum simulated bulk rock [Li] (Fig. 6d). We infer that the Li/Na ratio is an excellent proxy for residence time, because [Na] is at least three orders of magnitude higher than [Li] (Tables 1 and 2) and thus is not as strongly affected by small amounts of secondary mineral precipitation. However, Li/Na is also affected by the bulk rock concentration and the slope of the δ^7Li_{dis} vs. Li/Na correlation seems to be a function of the bulk rock [Li], whereas the location along a particular correlation (i.e., the measured δ^7Li_{dis} value) defines the residence time (Fig. 6d).

Significant seasonal precipitation variations are only observed for areas west of the Cascades (Fig. A1). Since precipitation rates have a primary control on the hydrological cycle, this observation suggests that western streams are characterized by a more seasonally variable subsurface residence time distribution, whereas eastern streams show a less variable residence time distribution. Accordingly, the strong control of δ^7Li_{dis} by residence time accounts for the seasonal δ^7Li_{dis} variations observed in streams west of the Cascades and the lack of variations seen in eastern streams (Tables 1, 2).

The increase in δ^7Li_{dis} seen with an increasing river to subsurface residence time ratio (Fig. 6b) also explains why riverine δ^7Li_{dis} is generally greater than groundwater δ^7Li_{dis} (Fig. 7 and Tables 1 and 2). Accordingly, our observations and simulation results support the hypothesis that suspended river loads are reactive due to the presence of fine-grained primary silicate mineral particles, and therefore continued Li isotope fractionation is occurring within streams. This is also supported by a recent study of Lemarchand et al. (2010), who found δ^7Li_{dis} in streams draining a granitic catchment to be significantly greater than that of springs feeding these streams.

5.2. Climate control

There is no clear distinction in δ^7Li_{dis} values between western and eastern streams, suggesting that the amount of annual precipitation, and thus climatic conditions, do not have a direct influence on δ^7Li. This lack of climatic influence is consistent with the results of Millot et al. (2010), who suggested that neither mean annual precipitation nor distance to the coast have an influence on δ^7Li_{dis} in waters from the Mackenzie River basin. In addition, despite the large temperature difference between summer and late winter (~10 °C), there is no change in riverine δ^7Li_{dis} in eastern streams.

Interestingly, as discussed in the previous section, a clear seasonal control on δ^7Li_{dis} was observed for streams west of the Cascades (Fig. 5), which is probably related to the large seasonal difference in monthly precipitation observed there (Fig. A1). The proposal that average subsurface residence time is longer during drier periods is in good agreement with significantly larger TDS and [Si] observed for western streams during the summer compared to the winter (Table 1). A correlation between subsurface residence times and aqueous concentrations, and thus TDS, is expected because longer residence times allow for increased mineral dissolution and exchange (Fig. 6). Overall, climate indirectly affects δ^7Li as precipitation rates control the hydrological cycle and thus residence time distributions. However, δ^7Li is a poor proxy for climate because many other parameters affect the hydrological cycle as well (e.g., mountain building, pCO_2, temperature, vegetation).

5.3. δ^7Li as a tracer of chemical weathering

This study has illuminated the factors that control Li isotopic fractionation in the dissolved loads of rivers (δ^7Li_{dis}). Li isotopic fractionation in rivers is caused by fractionation between solution and secondary minerals (e.g., Huh et al., 2001, 1998; Pogge von Strandmann et al., 2010, 2006), and it has been suggested that the large variability in δ^7Li_{dis} may be partially caused by different fractionation factors associated with Fe–Mn oxyhydroxides in places without soils or clays (Millot et al., 2010; Wimpenny et al., 2010b). Our study shows that δ^7Li_{dis} is not simply controlled by mineral-specific fractionation, as there is no correlation

between δ^7Li_{dis} and SI of the oversaturated secondary minerals, such as hematite and kaolinite (Fig. A7). We have shown that parameters such as reservoir residence time and reaction between suspended and dissolved loads in rivers can significantly influence δ^7Li_{dis}, given a constant fractionation factor between solution and secondary minerals (Fig. 6), and there is no need (or evidence) to call upon variable fractionation factors related to the dominance of different secondary to explain variable δ^7Li_{dis} in rivers.

Our simulations (Fig. 6) agree very well with observations (Fig. 7), as we see a clear negative correlation between δ^7Li_{dis} and the Li/Na ratio, whereas, δ^7Li_{dis} does not correlate with [Si] or Si/TZ^+, and shows only a weak negative correlation with Li/TZ^+ (Fig. 6c). Based on our simulations and data, we infer that, with the exception of Li/Na, δ^7Li_{dis} and various silicate weathering proxies based on elemental concentrations (e.g., [Li], [Si], TZ^+) are only correlated when a natural system is dominated by either Li isotope fractionation occurring in the subsurface (in which case there is a positive correlation between δ^7Li_{dis} and the weathering proxies), or occurring in rivers (in which case there is a negative correlation between δ^7Li_{dis} and the proxies). If Li isotope fractionation occurs in both settings, there will be no correlation, as seen in our results. This finding may explain why correlations between δ^7Li_{dis} and concentration proxies are observed in some studies (e.g., Huh et al., 2001; Pogge von Strandmann et al., 2010), but not in others (this study; Millot et al., 2010).

Overall, this study also has implications for using Li isotopes as tracers of chemical weathering in rivers, and consequently, in seawater through time. In previous studies, multiple weathering proxies, such as [Si] and Si/TZ^+, [Li], combined with Li isotopes (e.g., Huh et al., 2001, 1998; Pogge von Strandmann et al., 2006), have been used to try to constrain silicate weathering intensity. However, correlations between δ^7Li_{dis} and these proxies may be produced or destroyed due to the effects we simulated, such as the residence time in the subsurface (as suggested in Millot et al., 2010), Li isotope fractionation and mineral dissolution in rivers. Our study suggests that δ^7Li_{dis} is more robust than other tracers of silicate weathering, because it is linked to the degree of water–rock interactions along a specific flow path (e.g., in the subsurface and in rivers). In general, the larger the δ^7Li_{dis} in a specific river, the more water–rock interactions (primary mineral dissolution + secondary mineral precipitations) have occurred such as shown by Wanner et al. (2014). We demonstrate that, in rivers draining single lithology catchments, δ^7Li_{dis} is negatively correlated with Li/Na, suggesting that the combined δ^7Li_{dis} vs. Li/Na plot (Fig. 7d) may be a sensitive indicator of the extent of chemical weathering occurring in streams and groundwater reservoirs. Moreover, this finding is observed globally by clear negative correlations between δ^7Li_{dis} vs. Li/Na for river waters worldwide that drain only or mainly basalts (Fig. 8). The global correlations observed in Fig. 8 is well related to our simulations (Fig. 6d), where we show that a perfect correlation is only observed for constant basalt [Li], which is clearly not the case when comparing basalts from the world over (e.g., [Li] = 3 to 23 ppm in fresh CRBs).

Finally, δ^7Li_{dis} is influenced by many hydrological parameters, so it is not straightforward to use δ^7Li_{dis} as a silicate weathering tracer in terms of interpreting secular evolution of riverine inputs to seawater. For example, for very fast flow at a high discharge, the overall silicate weathering rate (in moles/year) is very high. However, the δ^7Li value should remain low because of the short residence time. Assuming the rise in δ^7Li in seawater in the past 60 Ma (Misra and Froelich, 2012) is due primarily to changing riverine input with minor effects of discharge variations (Wanner et al., 2014), our work suggests that this signature reflects increased silicate weathering rates on the continents, which may or may not be directly related to changing climate (as we see no direct correlation between δ^7Li_{dis} and climate), but could well be due to tectonic uplift that causes an increase in water–rock reaction.

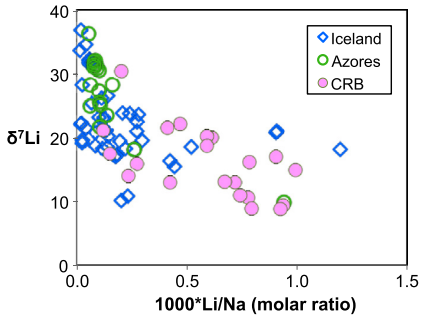

Fig. 8. δ^7Li versus 1000×Li/Na (molar ratio) in dissolved loads of streams and rivers draining basalts. Data are from this study, Pogge von Strandmann et al. (2006, 2010), and Vigier et al. (2006, 2009).

6. Conclusions

The main conclusions from this study are:

1. Large δ^7Li_{dis} variations (up to 20‰) are observed in streams that only drain basalts, suggesting that Li isotopic compositions in streams are controlled by factors other than the lithology of their catchments.
2. δ^7Li_{dis} is significantly higher than δ^7Li of groundwaters, suggesting that Li isotope fractionation occurring in rivers themselves play a major role on riverine δ^7Li_{dis}.
3. A lack of direct correlation between climatic conditions (i.e., mean annual precipitation, temperature) and riverine δ^7Li_{dis}, and correlations between seasonal precipitation variations and δ^7Li_{dis} suggest that subsurface residence times strongly influence riverine δ^7Li_{dis}.
4. Model simulations of reactive transport with variable residence times show that Li isotope fractionation occurs in both the subsurface and in rivers, causing many traditional silicate weathering proxies (e.g., [Si], Si/TZ^+) to show no, or only a weak correlation with δ^7Li_{dis}.
5. δ^7Li_{dis} and Li/Na in dissolved loads of rivers are only sensitive to the amount of water–rock interaction over time and are, thus, useful tracers of the degree of silicate chemical weathering occurring in single lithology catchments.
6. If the increase is δ^7Li in seawater through the Cenozoic is due primarily to changing riverine input, our results suggest that the increase may be uniquely related to tectonic uplift, which causes increased weathering due to the increase in denudation and the decreasing weathering intensity. Climatic controls on chemical weathering are apparently not as important.

Acknowledgements

We thank Richard Ash for assistance with the ICP-MS/MC-ICP-MS analyses, Igor Puchtel for help in the clean lab, Shuiwang Duan and Tammy Newcomer for major anion analyses, Terry Tolan for sampling guidance and discussion, Marshall Gannett, Steve Hinkle, Steve Cox, and Mike Free for help with fieldwork logistics, and Christie Galen for accompanying up in the field and showing us great birds. Sujay Kaushal kindly provided access to his Biogeochemistry laboratory and provided guidance on water sampling. We are grateful for discussions and comments from Jerome Gaillardet and Cin-Ty Lee. The manuscript benefited greatly from the review comments of three anonymous reviewers. Jean Lynch-Stieglitz is also thanked for her editorial handling and constructive

comments. This work was supported by a grant from the National Science Foundation (EAR 0948549 to RLR and WFM) and an Ann G. Wylie Dissertation Fellowship awarded to X-ML from the University of Maryland. X-ML acknowledges postdoctoral fellowship support from the Carnegie Institution of Washington. CW was supported by the U.S. Department of Energy, Geothermal Technologies Program, Energy Efficiency and Renewable Energy Office, Award No GT-480010-12.

Appendix A. Supplementary material

Supplementary material related to this article can be found online at http://dx.doi.org/10.1016/j.epsl.2014.10.032.

References

Basaltic Volcanism Study Project, 1981. Basaltic Volcanism on the Terrestrial Planets. Pergamon Press, Inc., New York. 1286 pp.

Berner, R.A., Lasaga, A.C., Garrels, R.M., 1983. The carbonate–silicate geochemical cycle and its effect on atmospheric carbon–dioxide over the past 100 million years. Am. J. Sci. 283, 641–683.

Blanc, P., Lassin, A., Piantone, P., Azaroual, M., Jacquemet, N., Fabbri, A., Gaucher, E.C., 2012. Thermoddem: a geochemical database focused on low temperature water/rock interactions and waste materials. Appl. Geochem. 27, 2107–2116.

Bouchez, J., Gaillardet, J., France-Lanord, C., Maurice, L., Dutra-Maia, P., 2011. Grain size control of river suspended sediment geochemistry: clues from Amazon River depth profiles. Geochem. Geophys. Geosyst. 12, Q03008. http://dx.doi.org/10.1029/2010GC003380.

Bouchez, J., von Blanckenburg, F., Schuessler, J.A., 2013. Modeling novel stable isotope ratios in the weathering zone. Am. J. Sci. 313, 267–308.

Brenan, J.M., Neroda, E., Lundstrom, C.C., Shaw, H.F., Ryerson, F.J., Phinney, D.L., 1998. Behaviour of boron, beryllium, and lithium during melting and crystallization: constraints from mineral-melt partitioning experiments. Geochim. Cosmochim. Acta 62, 2129–2141.

Brimhall, G.H., Lewis, C.J., Ford, C., Bratt, J., Taylor, G., Warin, O., 1991. Quantitative geochemical approach to pedogenesis – importance of parent material reduction, volumetric expansion, and eolian influx in lateralization. Geoderma 51, 51–91.

Chan, L.H., Edmond, J.M., Thompson, G., Gillis, K., 1992. Lithium isotopic composition of submarine basalts – implication for the lithium cycle in the oceans. Earth Planet. Sci. Lett. 108, 151–160.

Decarreau, A., Vigier, N., Pálková, H., Petit, S., Vieillard, P., Fontaine, C., 2012. Partitioning of lithium between smectite and solution: an experimental approach. Geochim. Cosmochim. Acta 85, 314–325.

Dessert, C., Dupré, B., Francois, L.M., Schott, J., Gaillardet, J., Chakrapani, G., Bajpai, S., 2001. Erosion of Deccan Traps determined by river geochemistry: impact on the global climate and the $^{87}Sr/^{86}Sr$ ratio of seawater. Earth Planet. Sci. Lett. 188, 459–474.

Flesch, G., Anderson, A., Svec, H., 1973. A secondary isotopic standard for $^{6}Li/^{7}Li$ determinations. Int. J. Mass Spectrom. Ion Phys. 12, 265–272.

Fryirs, K.A., Brierley, G.J., 2013. Geomorphic Analysis of River Systems: An Approach to Reading the Landscape. John Wiley & Sons.

Gaillardet, J., Dupré, B., Louvat, P., Allègre, C.J., 1999. Global silicate weathering and CO_2 consumption rates deduced from the chemistry of large rivers. Chem. Geol. 159, 3–30.

Hinkle, S.R., 1996. Age of ground water in basalt aquifers near Spring Creek National Fish Hatchery, Skamania County, Washington. U.S. Geological Survey Water-Resources Investigations Report. U.S. Fish and Wildlife Service, U.S. Dept. of the Interior.

Huh, Y., Chan, L.H., Zhang, L., Edmond, J.M., 1998. Lithium and its isotopes in major world rivers: implications for weathering and the oceanic budget. Geochim. Cosmochim. Acta 62, 2039–2051.

Huh, Y., Chan, L.H., Edmond, J.M., 2001. Lithium isotopes as a probe of weathering processes: Orinoco River. Earth Planet. Sci. Lett. 194, 189–199.

Kisakürek, B., Widdowson, M., James, R.H., 2004. Behaviour of Li isotopes during continental weathering: the Bidar laterite profile, India. Chem. Geol. 212, 27–44.

Kisakürek, B., James, R.H., Harris, N.B.W., 2005. Li and $\delta^{7}Li$ in Himalayan rivers: proxies for silicate weathering? Earth Planet. Sci. Lett. 237, 387–401.

Kohn, M.J., Miselis, J.L., Fremd, T.J., 2002. Oxygen isotope evidence for progressive uplift of the Cascade Range, Oregon. Earth Planet. Sci. Lett. 204, 151–165.

Lemarchand, E., Chabaux, F., Vigier, N., Millot, R., Pierret, M.C., 2010. Lithium isotope systematics in a forested granitic catchment (Strengbach, Vosges Mountains, France). Geochim. Cosmochim. Acta 74, 4612–4628.

Liu, X.-M., Rudnick, R.L., 2011. Constraints on continental crustal mass loss via chemical weathering using lithium and its isotopes. Proc. Natl. Acad. Sci. USA 108, 20873–20880.

Liu, X.-M., Rudnick, R.L., Hier-Majumder, S., Sirbescu, M.-L.C., 2010. Processes controlling lithium isotopic distribution in contact aureoles: a case study of the Florence County pegmatites, Wisconsin. Geochem. Geophys. Geosyst. 11, Q08014. http://dx.doi.org/10.1029/2010GC003063.

Liu, X.-M., Rudnick, R.L., McDonough, W.F., Cummings, M.L., 2013. Influence of chemical weathering on the composition of the continental crust: insights from Li and Nd isotopes in bauxite profiles developed on Columbia River Basalts. Geochim. Cosmochim. Acta 115, 73–91.

Magna, T., Wiechert, U.H., Halliday, A.N., 2004. Low-blank isotope ratio measurement of small samples of lithium using multiple-collector ICPMS. Int. J. Mass Spectrom. 239, 67–76.

Marschall, H.R., Pogge von Strandmann, P.A.E., Seitz, H.-M., Elliott, T., Niu, Y., 2007. The lithium isotopic composition of orogenic eclogites and deep subducted slabs. Earth Planet. Sci. Lett. 262, 563–580.

Millot, R., Vigier, N., Gaillardet, J., 2010. Behaviour of lithium and its isotopes during weathering in the Mackenzie Basin, Canada. Geochim. Cosmochim. Acta 74, 3897–3912.

Misra, S., Froelich, P.N., 2012. Lithium isotope history of cenozoic seawater: changes in silicate weathering and reverse weathering. Science 335, 818–823.

Négrel, P., Millot, R., Brenot, A., Bertin, C., 2010. Lithium isotopes as tracers of groundwater circulation in a peat land. Chem. Geol. 276, 119–127.

Nesbitt, H.W., Wilson, R.E., 1992. Recent chemical weathering of basalts. Am. J. Sci. 292, 740–777.

Piper, A.M., 1953. A Graphic Procedure in the Geochemical Interpretation of Water Analysis. U.S. Dept. of the Interior, Geological Survey, Water Resources Division, Ground Water Branch, Washington.

Pistiner, J.S., Henderson, G.M., 2003. Lithium-isotope fractionation during continental weathering processes. Earth Planet. Sci. Lett. 214, 327–339.

Pogge von Strandmann, P.A.E., Burton, K.W., James, R.H., van Calsteren, P., Gislason, S.R., Mokadem, F., 2006. Riverine behaviour of uranium and lithium isotopes in an actively glaciated basaltic terrain. Earth Planet. Sci. Lett. 251, 134–147.

Pogge von Strandmann, P.A.E., Burton, K.W., James, R.H., van Calsteren, P., Gislason, S.R., 2010. Assessing the role of climate on uranium and lithium isotope behaviour in rivers draining a basaltic terrain. Chem. Geol. 270, 227–239.

Qiu, L., Rudnick, R.L., McDonough, W.F., Merriman, R.J., 2009. Li and $\delta^{7}Li$ in mudrocks from the British Caledonides: metamorphism and source influences. Geochim. Cosmochim. Acta 73, 7325–7340.

Qiu, L., Rudnick, R.L., Ague, J.J., McDonough, W.F., 2011a. A lithium isotopic study of sub-greenschist to greenschist facies metamorphism in an accretionary prism, New Zealand. Earth Planet. Sci. Lett. 301, 213–221.

Qiu, L., Rudnick, R.L., McDonough, W.F., Bea, F., 2011b. The behavior of lithium in amphibolite- to granulite-facies rocks of the Ivrea–Verbano Zone, NW Italy. Chem. Geol. 289, 76–85.

Rudnick, R.L., Tomascak, P.B., Njo, H.B., Gardner, L.R., 2004. Extreme lithium isotopic fractionation during continental weathering revealed in saprolites from South Carolina. Chem. Geol. 212, 45–57.

Singleton, M.J., Sonnenthal, E.L., Conrad, M.E., DePaolo, D.J., Gee, G.W., 2005. Multiphase reactive transport modeling of seasonal infiltration events and stable isotope fractionation in unsaturated zone pore water and vapor at the Hanford site. Vadose Zone J. 3, 775–785.

Sonnenthal, E., Spycher, N., Apps, J., Simmons, A., 1998. Thermo-hydro-chemical predictive analysis for the Drift-Scale Heater Test. Yucca Mountain Project, Level 4.

Takeuchi, A., Hren, M.T., Smith, S.V., Chamberlain, C.P., Larson, P.B., 2010. Pedogenic carbonate carbon isotopic constraints on paleoprecipitation: evolution of desert in the Pacific Northwest, USA, in response to topographic development of the Cascade Range. Chem. Geol. 277, 323–335.

Taylor, A.S., Lasaga, A.C., 1999. The role of basalt weathering in the Sr isotope budget of the oceans. Chem. Geol. 161, 199–214.

Teng, F.Z., McDonough, W.F., Rudnick, R.L., Dalpe, C., Tomascak, P.B., Chappell, B.W., Gao, S., 2004. Lithium isotopic composition and concentration of the upper continental crust. Geochim. Cosmochim. Acta 68, 4167–4178.

Teng, F.Z., McDonough, W.F., Rudnick, R.L., Wing, B.A., 2007. Limited lithium isotopic fractionation during progressive metamorphic dehydration in metapelites: a case study from the Onawa contact aureole, Maine. Chem. Geol. 239, 1–12.

Vigier, N., Burton, K.W., Gislason, S.R., Rogers, N.W., Duchene, S., Thomas, L., Hodge, E., Schaefer, B., 2006. The relationship between riverine u-series disequilibria and erosion rates in a basaltic terrain. Earth Planet. Sci. Lett. 249, 258–273.

Vigier, N., Gislason, S.R., Burton, K.W., Millot, R., Mokadem, F., 2009. The relationship between riverine lithium isotope composition and silicate weathering rates in Iceland. Earth Planet. Sci. Lett. 287, 434–441.

Wanner, C., Sonnenthal, E.L., 2013. Assessing the control on the effective kinetic Cr isotope fractionation factor: a reactive transport modeling approach. Chem. Geol. 337, 88–98.

Wanner, C., Sonnenthal, E.L., Liu, X.-M., 2014. Seawater $\delta^{7}Li$: a direct proxy for global CO_2 consumption by continental silicate weathering? Chem. Geol. 381, 154–167.

Wimpenny, J., Gislason, S.R., James, R.H., Gannoun, A., Pogge Von Strandmann, P.A.E., Burton, K.W., 2010a. The behaviour of Li and Mg isotopes during primary phase

dissolution and secondary mineral formation in basalt. Geochim. Cosmochim. Acta 74, 5259–5279.
Wimpenny, J., James, R.H., Burton, K.W., Gannoun, A., Mokadem, F., Gislason, S.R., 2010b. Glacial effects on weathering processes: new insights from the elemental and lithium isotopic composition of West Greenland rivers. Earth Planet. Sci. Lett. 290, 427–437.
Xu, T., Spycher, N., Sonnenthal, E.L., Zhang, G., Zheng, L., Pruess, K., 2011. TOUGHREACT Version 2.0: a simulator for subsurface reactive transport under non-isothermal multiphase flow conditions. Comput. Geosci. 37, 763–774.
Zhang, L.B., Chan, L.H., Gieskes, J.M., 1998. Lithium isotope geochemistry of pore waters from Ocean Drilling Program Sites 918 and 919, Irminger Basin. Geochim. Cosmochim. Acta 62, 2437–2450.

5.3. On the use of Li isotopes as a proxy for water-rock interaction in fractured crystalline rocks: a case study from the Gotthard rail base tunnel

Source:

Wanner C., Bucher K., Pogge von Strandmann P. A. E., Waber H. N. and Pettke T. (2017) On the use of Li isotopes as a proxy for water–rock interaction in fractured crystalline rocks: A case study from the Gotthard rail base tunnel. *Geochimica et Cosmochimica Acta* **198**, 396-418.

Contribution by the Author (CW):

CW developed the general idea, organized all analyses, and carried out all the simulations. Moreover, CW had the lead in data interpretation and manuscript writing.

Available online at www.sciencedirect.com

ScienceDirect

Geochimica et Cosmochimica Acta 198 (2017) 396–418

Geochimica et Cosmochimica Acta

www.elsevier.com/locate/gca

On the use of Li isotopes as a proxy for water–rock interaction in fractured crystalline rocks: A case study from the Gotthard rail base tunnel

Christoph Wanner [a,*], Kurt Bucher [b], Philip A.E. Pogge von Strandmann [c], H. Niklaus Waber [a], Thomas Pettke [a]

[a] Rock-Water Interaction Group, Institute of Geological Sciences, University of Bern, Baltzerstrasse 3, CH-3012 Bern, Switzerland
[b] Mineralogy and Petrology, University of Freiburg, Albertstr. 23b, 79104 Freiburg, Germany
[c] Institute of Earth and Planetary Sciences, University College London and Birkbeck, University of London, UK

Received 16 June 2016; revised 2 November 2016; accepted in revised form 5 November 2016; Available online 18 November 2016

Abstract

We present Li isotope measurements of groundwater samples collected during drilling of the 57 km long Gotthard rail base tunnel in Switzerland, to explore the use of Li isotope measurements for tracking water–rock interactions in fractured crystalline rocks at temperatures of up to 43 °C. The 17 groundwater samples originate from water-conducting fractures within two specific crystalline rock units, which are characterized by a similar rock mineralogy, but significantly different fluid composition. In particular, the aqueous Li concentrations observed in samples from the two units vary from 1–4 mg/L to 0.01–0.02 mg/L. Whereas δ^7Li values from the unit with high Li concentrations are basically constant (δ^7Li = 8.5–9.1‰), prominent variations are recorded for the samples from the unit with low Li concentrations (δ^7Li = 10–41‰). This observation demonstrates that Li isotope fractionation can be highly sensitive to aqueous Li concentrations. Moreover, δ^7Li values from the unit with low Li concentrations correlate well with reaction progress parameters such as pH and [Li]/[Na] ratios, suggesting that δ^7Li values are mainly controlled by the residence time of the fracture groundwater. Consequently, 1D reactive transport modeling was performed to simulate mineral reactions and associated Li isotope fractionation along a water-conducting fracture system using the code TOUGHREACT. Modeling results confirm the residence time hypothesis and demonstrate that the absence of δ^7Li variation at high Li concentrations can be well explained by limitation of the amount of Li that is incorporated into secondary minerals. Modeling results also suggest that Li uptake by kaolinite forms the key process to cause Li isotope fractionation in the investigated alkaline system (pH >9), and that under slow flow conditions (<10 m/year), this process is associated with a very large Li isotope fractionation factor ($\varepsilon \approx -50$‰). Moreover, our simulations demonstrate that for simple and well-defined systems with known residence times and low Li concentrations, δ^7Li values may help to quantify mineral reaction rates if more thermodynamic data about the temperature-dependent incorporation of Li in secondary minerals as well as corresponding fractionation factors become available in the future. In conclusion, δ^7Li values may be a powerful tool to track water–rock interaction in fractured crystalline rocks at temperature higher than those at the Earth's surface, although their use is restricted to low Li concentrations and well defined flow systems.

Keywords: Reactive transport; Li isotope fractionation; Kaolinite; Tunnel inflow; Hydrothermal fluid

* Corresponding author. Fax: +41 316314843.
E-mail address: wanner@geo.unibe.ch (C. Wanner).

http://dx.doi.org/10.1016/j.gca.2016.11.003
0016-7037/

1. INTRODUCTION

The intensity of water–rock interaction in fractured crystalline rocks forms a key parameter in various applications within the field of environmental geochemistry. Examples include enhanced geothermal systems (EGS) where heat extraction mainly depends on accessible fracture surface areas and where water–rock interaction may cause permeability and porosity to decrease over time (Alt-Epping et al., 2013; Stober and Bucher, 2015), nuclear waste repositories to be constructed in crystalline rock environment (e.g., Nordstrom et al., 1989; Molinero et al., 2008; Gimeno et al., 2014) and groundwater contamination affecting fractured crystalline aquifers. The intensity of water–rock interaction in (fractured) crystalline rocks was also proposed to be essential for the global carbon cycle because the interaction of meteoric water with silicate minerals (i.e., chemical weathering) forms an important CO_2 sink (e.g., Berner et al., 1983; Gislason et al., 1996; Francois and Goddéris, 1998).

Lithium is a trace element that is almost exclusively found in silicate minerals, which makes it a useful tracer for tracking the interaction between water and silicate minerals such as during chemical silicate weathering (Kisakürek et al., 2005; Pogge von Strandmann et al., 2006; Vigier et al., 2009; Millot et al., 2010b; Liu et al., 2015). In particular, tracking Li isotope fractionation is a powerful tool because the two stable Li isotopes (^{6}Li, ^{7}Li) significantly fractionate during transformation of primary silicate minerals into secondary minerals (Zhang et al., 1998; Pistiner and Henderson, 2003; Vigier et al., 2008; Wimpenny et al., 2010). It is generally agreed that Li isotope fractionation is mainly associated with secondary mineral precipitation whereas Li isotopes dissolve stoichiometrically during (primary) silicate mineral dissolution (Pistiner and Henderson, 2003; Huh et al., 2004). Li isotope fractionation is also promising to track water–rock interaction at temperatures higher than those at the Earth's surface. Vigier et al. (2008) experimentally showed that at a temperature of 250 °C the Li isotope enrichment factor for structural Li incorporation into smectite is −1.6‰ and thus greater than the measurement uncertainty for Li isotope measurements. Moreover, Marschall et al. (2007) used a temperature dependent enrichment factor based on a compilation of other studies (Chan et al., 1993; Wunder et al., 2006) to simulate the fate of Li isotopes in subducting slabs suggesting that the Li isotope enrichment factor at 250 °C is on the order of −6‰.

The numerous studies focusing on chemical silicate weathering at the Earth's surface demonstrate a large range in δ^7Li (2–43‰) of dissolved Li, mostly from river waters (e.g., Huh et al., 1998; Kisakürek et al., 2005; Pogge von Strandmann et al., 2006; Millot et al., 2010b; Dellinger et al., 2015; Liu et al., 2015). Whereas the literature agrees that increasing the ratio of Li uptake by secondary minerals to Li release from primary mineral dissolution drives δ^7Li to higher values, it is still under debate if and how temporal and spatial δ^7Li distributions can be used as a proxy for geomorphic and/or climatic variations. In particular, the increasing seawater δ^7Li values observed over the last ca. 56 Ma (Misra and Froelich, 2012) have been attributed either to increasing tectonic activities (Misra and Froelich, 2012; Li and West, 2014; Wanner et al., 2014) or to a decreasing soil production rate and thus to cooler climatic conditions (Vigier and Goddéris, 2015). In contrast to surface water samples, δ^7Li in water from hydro-geothermal sites with temperatures of up to 335 °C varies only in a narrow range of 0–11‰ (Chan et al., 1993, 1994; Millot and Négrel, 2007; Millot et al., 2010a; Henchiri et al., 2014; Sanjuan et al., 2014; Pogge von Strandmann et al., 2016). Despite this relatively narrow range, it was proposed that for such systems δ^7Li may operate as a geothermometer to estimate the corresponding reservoir temperature. Also it was proposed to use δ^7Li from hydro-geothermal sites as proxy for the origin of the hydrothermal fluid, and/or as proxy for the intensity of water–rock interaction (Millot and Négrel, 2007; Millot et al., 2010a).

In this study, we present Li isotope measurements of groundwater collected during the construction of the 57 km long Gotthard rail base tunnel in Switzerland. Major anion and cation concentrations have been reported by Seelig and Bucher (2010) and Bucher et al. (2012). Our groundwater samples originate from water-conducting fractures within two specific crystalline rock units and show on-site temperatures of up to 43 °C. The hydrogeochemical conditions are thus similar to those at future EGS sites although the temperature is significantly lower than the target EGS temperature of 180 °C or greater. The main objective was to explore the use of Li isotope measurements to track water–rock interaction in an EGS-like system with temperatures higher than those at the Earth's surface. Furthermore, an essential part of our study was to simulate Li isotope fractionation occurring in a fractured crystalline aquifer using the reactive transport modeling code TOUGHREACT V3 (Xu et al., 2014). In this context, TOUGHREACT was updated to allow defining a maximum amount of Li that can be incorporated into secondary minerals.

2. SITE DESCRIPTION AND SAMPLING

The new 57 km long Gotthard rail base tunnel in Switzerland is the longest and deepest tunnel in the world. The tunnel crosses the Alps at a base level of ca. 500 m a.s.l. and its construction was divided into five sections, which were excavated separately by drilling vertical access shafts. Our study relates to the Amsteg section in the northern part of the tunnel (Fig. 1). This 11.5 km long section was constructed between 2003 and 2006 using a 400 m long tunnel-boring machine (TBM). The section exclusively penetrates crystalline basement rocks of the Aar massif, which is a NE-SW trending complex of Variscan basement overprinted by Alpine metamorphism and deformation (Abrecht, 1994; Schaltegger, 1994; Labhart, 1999). The units intersected along the Amsteg section show a similar mineralogical composition with dominating quartz, albite, K-feldspar and chlorite and minor amounts of biotite and muscovite as well as secondary calcite and accessory pyrite (Bucher et al., 2012). The thickness of the rock column above the tunnel is up to 2200 m (Fig. 1). According to Bucher et al. (2012), the chemical composition of groundwater samples at tunnel level is dominated by the

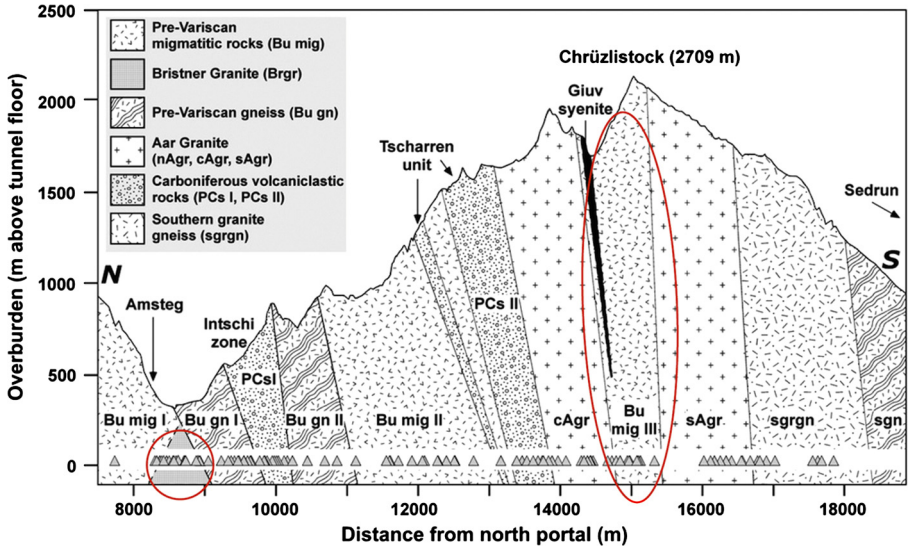

Fig. 1. Geological cross section through the Amsteg section of the Gotthard rail base tunnel (modified from Bucher et al., 2012). The two sections from which water and rock samples were taken for Li concentration and Li isotope measurements are highlighted.

infiltration of meteoric water at the surface and subsequent reaction with the fractured crystalline rocks during transport to the tunnel level. This infiltration model agrees with steeply dipping rock units (Fig. 1) and the presence of a predominant, nearly vertical fracture system. Preliminary δ^2H and $\delta^{18}O$ measurements indicate a dominating meteoric origin of groundwater collected. More information regarding the geology and hydrology of the Amsteg section is provided by Bucher et al. (2012) and references therein.

A total of 122 groundwater samples were collected from water conducting fractures. Groundwater samples were collected from natural inflows along fractures after these were cut by the TBM and before they were sealed with concrete. Due to the induced pressure drop, the water was flowing from the fractures with discharge rates between 0.0003 L/s and 6 L/s. Based on differences in dissolved Li concentrations, 17 groundwater samples from two distinct geological units within the Amsteg section, the Bristner Granite and the migmatitic unit called BuMigIII (Fig. 1) were selected for the analyses of Li and Li isotopes. In addition, Li concentrations were determined on rock samples of the two units that were retrieved from cored test drillings performed in front of the TBM. At similar average water influx into the tunnel (Bucher et al., 2012), groundwater draining the Bristner Granite shows Li concentration between 1 and 4 mg/L and much lower concentrations of 0.01–0.02 mg/L in the BuMigIII.

3. METHODS

3.1. Li concentration measurements

3.1.1. Solid Li

Bulk rock Li concentrations were measured by atomic adsorption spectroscopy using a Vario 6 spectrometer from Analytic Jena at the University of Freiburg, Germany. To do so, cores retrieved from test drillings into the Bristner Granite and into BuMigIII were milled to a fine powder. For each sample, 0.1 g was digested in 5 mL 65% HNO_3 and 1 mL 33% H_2O_2. To ensure that the entire sample was digested, samples were exposed to 160 °C for 6 min and to 215 °C for 25 min using a MLS microwave. The analytical uncertainty was ±5%.

Selected trace element concentrations including Li of individual mineral phases and phase mixtures within the Bristner Granite and BuMigIII were measured by Laser ablation ICP-MS at the University of Bern, Switzerland, on polished thin sections (50 μm). The system at the University of Bern consists of a Geolas Pro 193 nm ArF Excimer laser (Lambda Physik, Germany) coupled with an ELAN DRCe quadrupole mass spectrometer (QMS; Perkin Elmer, USA). Details on the setup and optimization strategies are given in Pettke et al. (2012). Daily optimization of the analytical conditions were performed to satisfy a ThO production rate of <0.2% (i.e., Th/ThO intensity ratio <0.002) and to achieve robust plasma conditions monitored by a Th/U sensitivity ratio of 1 as determined on the SRM610 glass standard. External standardization was performed employing SRM610 from NIST with preferred values reported in Spandler et al. (2011), and bracketing standardization provided a linear drift correction. Internal standardization was done by summing the major element oxides to 100 wt% or 98–97 wt% for biotite and hydrous mineral mixtures (containing muscovite, biotite, minor chlorite and Fe_2O_3). Data were reduced using SILLS (Guillong et al., 2008), with limits of detection calculated for each element in every analysis following the formulation detailed in Pettke et al. (2012).

3.1.2. Dissolved Li

Li concentrations available from the previous study (Bucher et al., 2012) were determined using a DX-120 ion chromatograph (IC), with a detection limit of 0.01 mg/L and an analytical uncertainty of 0.005 mg/L for concentrations below 0.1 mg/L. Because groundwater samples originating from BuMigIII displayed Li concentrations on the

order of the detection limit (0.01–0.02 mg/L), Li concentration measurements were repeated for these samples using an Analytic Jena ContrAA 700 BU atomic adsorption spectrometer in the graphite furnace mode (GFAAS) at the University of Bern. Standardization was performed using the Merck 4 Certipur standard and tested with the Sigma 6 and Merck 4 Li single element standards. Within the standardization range of 1.25–5 µg/L, the Li recovery was >90% yielding an analytical uncertainty of ±10%. Reported Li concentrations are average values of triplicate analyses.

3.2. Li isotope measurements

Lithium isotope measurements of groundwater samples were performed as detailed in Pogge von Strandmann and Henderson (2015) and Pogge von Strandmann et al. (2011). Briefly, this entailed running approximately 20 ng of Li through a two-step cation exchange column method, containing AG50W X-12 resin, and using dilute HCl as an eluent.

Samples were then analyzed on a Nu Instruments HR MC-ICP-MS at Oxford University, by sample-standard bracketing with the standard L-SVEC. Individual analyses consisted of three separate repeats of 10 ratios (10 s integration time per ratio), giving a total integration time of 300 s/sample during each analytical session. At an uptake rate of 75 µl/min, the sensitivity for a 20 ng/ml solution is ~18 pA of ^{7}Li using 10^{11} Ω resistors. Background instrumental Li intensity, typically ~0.01pA, was subtracted from each measurement. Li isotope measurements are reported as ^{7}Li/^{6}Li ratio in terms of the δ-notation relative to the Li isotope standard L-SVEC ($\delta^{7}Li = 0.0‰$) and are given in ‰:

$$\delta^{7}Li = \left[\left(\frac{^{7}Li/^{6}Li_{sample}}{^{7}Li/^{6}Li_{L-SVEC}}\right) - 1\right] \cdot 1000 \quad (1)$$

To assess accuracy and precision, both seawater and the international USGS standard BCR-2 were analyzed. Both standards analyzed with these samples (seawater: $\delta^{7}Li = 31.5 \pm 0.4‰$; BCR-2: $2.7 \pm 0.3‰$) agree well with their long-term averages (seawater: $31.2 \pm 0.6‰$, $n = 46$; BCR-2: $2.6 \pm 0.3‰$, $n = 17$; Pogge von Strandmann et al., 2011; Pogge von Strandmann and Henderson, 2015). The total procedural blank for Li isotopes is effectively undetectable (<0.005 ng Li).

3.3. Reactive transport modeling

A series of 1D reactive transport simulations using TOUGHREACT V3 (Xu et al., 2014) was performed to simulate the interaction of infiltrating meteoric water with granitic rock and its specific effects on aqueous δ^{7}Li. TOUGHREACT has been previously applied to evaluate isotopic fractionation coupled to water–rock interaction and hydrological processes in a variety of subsurface environments and laboratory experiments (Sonnenthal et al., 1998; Singleton et al., 2005; Wanner and Sonnenthal, 2013). Specifically, it has been used to simulate Li isotope fractionation in granitic as well as basaltic systems (Wanner et al., 2014; Liu et al., 2015). Furthermore, the TOUGHREACT approach for simulating isotopic fractionation coupled to mineral precipitation has been recently benchmarked (Wanner et al., 2015).

3.3.1. Model formulation

3.3.1.1. Mineral dissolution and precipitation. TOUGHREACT V3 (Xu et al., 2014) computes mineral dissolution and precipitation reactions (mol/s/kg$_{H_2O}$) as kinetic reactions based on transition state theory (TST) (Lasaga, 1984):

$$r = A_r \cdot k \cdot \left[1 - \left(\frac{Q}{K}\right)^{m}\right]^{n} = A_{rfrac} \cdot k \cdot \left[1 - \left(\frac{Q}{K}\right)^{m}\right]^{n} \quad (2)$$

where A_r refers to the mineral reactive surface area (m^2/kg$_{H_2O}$). In case of fracture flow, A_r is assumed to be the same for each mineral (Xu et al., 2014) and corresponds to the reactive surface area of the simulated vertical fracture system A_{rfrac}. Q and K refer to the ion activity product and equilibrium constant of a mineral dissolution/precipitation reaction, respectively. Exponents m and n are fitting parameters that must be experimentally determined. However, for or this study, they were taken to be unity. The temperature and pH dependent rate constant k is formulated as:

$$k = k_{25}^{n}\exp\left[\frac{-E_a^{n}}{R}\left(\frac{1}{T} - \frac{1}{298.15}\right)\right] + k_{25}^{ac}\exp\left[\frac{-E_a^{ac}}{R}\left(\frac{1}{T} - \frac{1}{298.15}\right)\right]a_{H^+}^{m_{ac}} + k_{25}^{ba}\exp\left[\frac{-E_a^{ba}}{R}\left(\frac{1}{T} - \frac{1}{298.15}\right)\right]a_{H+}^{m_{ba}} \quad (3)$$

where k_{25} refers to reaction rate constants at 25 °C (mol/m^2/s), E_a is the activation energy (kJ/mol) and T and R are the temperature (K) and ideal gas constant, respectively. The superscripts n, ac and ba denote neutral, acidic and basic conditions, respectively, a_{H+} refers to the H^+ activity, and m_{ac} and m_{ba} refer to the reaction order with respect to H^+ (i.e., pH) at acidic and basic conditions, respectively. In order to calculate effective precipitation and dissolution rates (Eqs. (2) and (3)), reaction rate constants were defined according to the compilation of Palandri and Kharaka (2004) whereas equilibrium constants were taken from the Soltherm.H06 database (Reed and Palandri, 2006). Mineral stoichiometries, thermodynamic and kinetic parameters of minerals considered for our simulations are summarized in Table 1.

3.3.1.2. Simulation of Li isotope fractionation. The fate of individual Li isotopes was simulated according to the approach recently presented by Wanner et al. (2014). To do so, ^{6}Li and ^{7}Li were defined as primary aqueous species and were incorporated into the mineral stoichiometry of Li-bearing minerals. Similar to the model of Bouchez et al. (2013), our approach does not distinguish between Li exchange-, Li surface complexation or Li incorporation into a crystal. Accordingly, Li isotope fractionation is solely simulated during Li incorporation of dissolved Li into precipitating minerals. Besides the lack of fractionation factors distinguishing between Li incorporation, Li exchange and sorption, the low exchange capacity of crystalline rocks (Mazurek et al., 2003) is supportive to such assumption. Incorporation of Li in secondary clay minerals is limited and occurs only at trace concentrations in the ppm range (e.g., Tardy et al., 1972). The concentration differences by orders of magnitudes between major and trace elements

Table 1
Simulated mineral dissolution and precipitation reactions.

Mineral phase	[a]log(*K*) $T = 25$ °C	[a]log(*K*) $T = 60$ °C	[b]k_{25}^{n} (mol/m^2/s)	[b]E_a^n (kJ/mol)	[b]k_{25}^{ac} (mol/m^2/s)	[b]E_a^{ac} (kJ/mol)	[b]m_{ac}	[b]k_{25}^{ba} (mol/m^2/s)	[b]E_a^{ba} (kJ/mol)	[b]m_{ba}	Hydrolysis reaction (written with primary species)
Albite	1.4	0.3	2.75e−13	69.8	6.92e−11	65.0	0.457	2.51e−16	71.0	−0.57	$NaAlSi_3O_8 + 4H^+ = Na^+ + 3SiO_{2(aq)} + Al^{3+} + 2H_2O$
Orthoclase	−0.5	−1.3	3.89e−13	38.0	8.71e−11	51.7	0.50	6.31e−22	94.1	−0.82	$KAlSi_3O_8 + 4H^+ = K^+ + 3SiO_{2(aq)} + Al^{3+} + 2H_2O$
Quartz	−4.0	−3.5	4.57e−14	90.1	6.92e−30	65.0	0.457	[d]1.00e−14	[d]0.0	−0.5	$SiO_{2(s)} = SiO_{2(aq)}$
Annite[c1]	29.4	24.2	2.82e−13	22.0	–	–	–	–	–	–	$KFe_3AlSi_3O_{10}(OH)_2 + 10H^+ = Al^{3+} + K^+ + 3Fe^{2+} + 6H_2O + 3SiO_2$
Phlogopite[c1,e]	37.4	31.5	2.82e−13	22.0	–	–	–	–	–	–	$K_{1.026}\,Mg_{2.974}Li_{0.026}AlSi_3O_{10}(OH)_2 + 10H^+ = Al^{3+} + K^+ + 3Mg^{2+} + 6H_2O + 3SiO_2 + 0.00199\ ^6Li^+ + 0.02401\ ^7Li^+$
Muscovite	8.7	4.62	1.00e−13	22.0	–	–	–	–	–	–	$KAl_2AlSi_3O_{10}(OH)_2 + 10H^+ = 3Al^{3+} + K^+ + 6H_2O + 3SiO_2$
Chamosite[c2]	41.1	32.9	3.02e−13	88.0	–	–	–	–	–	–	$(Fe)_5Al(AlSi_3O_{10})(OH)_8 + 16H^+ = 5Fe^{2+} + 2Al^{3+} + 3SiO_2 + 12\ H_2O$
Clinochlore[c2]	55.9	46.0	3.02e−13	88.0	–	–	–	–	–	–	$(Mg)_5Al(AlSi_3O_{10})(OH)_8 + 16H^+ = 5Mg^{2+} + 2Al^{3+} + 3SiO_2 + 12\ H_2O$
Kaolinite[c3]	3.2	0.7	1.98e−13	22.2	–	–	–	–	–	–	$Al_2Si_2O_5(OH)_4 + 6H^+ = 2Al^{3+} + 2SiO_{2(aq)} + 5H_2O$
$^6Li_{kaolinite}$[c3]	−4.9409764	−4.9409764	1.98e−13	22.2	–	–	–	–	–	–	$^6Li = {}^6Li^+$
$^7Li_{kaolinite}$[c3]	−4.9187	−4.9187	1.98e−13	22.2	–	–	–	–	–	–	$^7Li = {}^7Li^+$
Pyrite	217.4	191.1	2.80e−5	56.9	–	–	–	–	–	–	$FeS_2 + H_2O + 3.5\ O_{2(aq)} = Fe^{2+} + 2SO_4^{2-} + 2H^+$
Calcite	1.8	1.3	1.55e−6	23.5	–	–	–	–	–	–	$CaCO_3 + H^+ = HCO_3^- + Ca^{2+}$
Li-source[f]	[f]	[f]	[f]	[f]	–	–	–	–	–	–	$Li_{0.04}Na_{0.96}Cl = 0.00305\ ^6Li^+ + 0.03695\ ^7Li^+ + 0.96Na^+ + Cl^-$
Secondary species	$AlOH^{2+}$, $Al(OH)_2^+$, $HAlO_2$, AlO_2^-, $KAlO_2$, $NaAlO_2$, $AlSO_4^+$, $Al(SO_4)_2^-$, $CO_{2(aq)}$, CO_3^{2-}, $CaCO_{3(aq)}$, $CaHCO_3^+$, $CaCl^+$, $CaCl_2$, $CaOH^+$, $CaSO_4$, HCl, $FeCl^+$, $FeCl_2$, FeO, $FeOH^+$, $HFeO_2$, $FeSO_4$, KCl, $KHSO_4$, KOH, KSO_4^-, $MgCO_3$, $MgHCO_3^+$, $MgCl^+$, $MgOH^+$, $MgSO_4$, NaCl, NaOH, $NaCO_3^-$, $NaHCO_3$, $NaSO_4^-$, OH^-, HSO_4^-, HS^-, S^{2-}, $H_2S_{(aq)}$, $HSiO_3^-$, $H_2SiO_4^{2-}$, $CaHSiO_3^+$, $MgHSiO_3^+$, $NaHSiO_3$										

[–] No pH dependence of the rate constant considered at acidic and/or basic conditions.

[a] Equilibrium constants log(*K*) were defined according to the Soltherm.H06 database (Reed and Palandri, 2006). The temperature dependence is calculated according to $\log(K)_{T[K]} = a * \ln(T_K) + b + c * T_K + d/T_K + e/T_K^2$. *a*, *b*, *c*, *d* and *e* are constants defined in the database. For the listed mineral phases, however, the interpolation between 25 and 60 °C is almost linear.

[b] Reaction rate constants k, activation energies E_a and rate dependence on pH (m_{ac} and m_{ba}) were defined according to Palandri and Kharaka (2004).

[cx] Endmember of solid solution *x*.

[d] A constant value for k_{25}^{ba} of 1e−14 refers to a temperature of ca. 65 °C according to Eq. (3) and taking into account an activation energy of 108,366 (Palandri & Kharaka, 2004). A rate constant slightly higher than proposed in the Palandri and Kharaka (2004) compilation was required to get quartz solubility controlled SiO_2 concentrations such as observed for our water samples (Bucher et al., 2012).

[e] Corresponds to a phlogopite Li concentration of 217 ppm to get an initial bulk rock Li conc. of 8.8 μg/g (Table 2) (at a phlogopite vol. fraction of 0.02), and a δ^7Li value of 1.7‰.

[f] Hypothetical solid phase defined to simulated a porewater or unknown mineral Li source with a δ^7Li value of 8.7‰. Corresponding parameters are given in the text for each scenario.

in such secondary minerals may pose convergence problems due to the large differences in exponents in the ion-activity product included in the rate law (Eq. (2)). To circumvent this problem, precipitation of Li-bearing secondary minerals was simulated defining a solid solution with three different endmembers (see Wanner et al., 2014): (i) a pure, non Li-bearing secondary mineral endmember, (ii) a pure ^{6}Li endmember and (iii) a pure ^{7}Li endmember. The pure ^{6}Li and ^{7}Li endmembers are hypothetical, but their specification solves the above mentioned numerical problems, and their log(K) values are obtained by fitting to the observed aqueous Li concentration and the amounts of Li analyzed in secondary minerals. The precipitation rate r_{prec} of the solid solution of Li-bearing secondary minerals is then calculated as the sum of the individual endmember precipitation rates r_{2nd_min} (pure secondary mineral), r_{6Li} and r_{7Li}:

$$r_{prec} = r_{2nd\_min} + r_{^6\mathrm{Li}} + r_{^7\mathrm{Li}} \quad (4)$$

The rate of a specific endmember, r_{endm}, is calculated according to a TST-like expression:

$$r_{endm} = A \cdot k \cdot \left(1 - \frac{Q_{endm}}{K_{endm}}\right) + k \cdot A \cdot (x_{endm} - 1) \quad (5)$$

where x_{endm} refers to the mole fraction of a specific secondary mineral endmember. For the hypothetical, pure ^{6}Li and ^{7}Li endmembers $x_{6\mathrm{Li}}$ and $x_{7\mathrm{Li}}$ are calculated according to:

$$x_{^6\mathrm{Li}} = \frac{(Q_{^6\mathrm{Li}}/K_{^6\mathrm{Li}})}{(Q_{^6\mathrm{Li}}/K_{^6\mathrm{Li}}) + (Q_{^7\mathrm{Li}}/K_{^7\mathrm{Li}}) + (Q_{2nd\_min}/K_{2nd\_min})} \quad (6)$$

$$x_{^7\mathrm{Li}} = \frac{(Q_{^7\mathrm{Li}}/K_{^7\mathrm{Li}})}{(Q_{^6\mathrm{Li}}/K_{^6\mathrm{Li}}) + (Q_{^7\mathrm{Li}}/K_{^7\mathrm{Li}}) + (Q_{2nd\_min}/K_{2nd\_min})} \quad (7)$$

Eqs. (6) and (7) ensure that the amount of Li that is incorporated into a secondary mineral reflects the Li concentration of the aqueous solution. Accordingly, the amount of Li removed by precipitation increases with increasing aqueous Li concentration. By doing so, our model is in agreement with an experimental study showing that Li concentrations of synthesized smectites are correlated with corresponding aqueous Li concentrations (Decarreau et al., 2012). Decarreau et al. (2012), however, also showed that the total amount of Li that can be incorporated is limited due to structural reasons. We therefore updated TOUGHREACT so that the user now has the option to specify the maximum amount of Li that is allowed to precipitate in a given solid solution. To do so, the user needs to define the maximum Li mol fraction $x_{maxLi} = x_{6\mathrm{Li}} + x_{7\mathrm{Li}}$ that corresponds to a particular maximum Li content (e.g., in μg/g) in a specific mineral solid solution phase. For the pure (hypothetical) ^{6}Li and ^{7}Li endmembers, the maximum mol fraction then become:

$$x_{^6\mathrm{Li}\_max} = x_{max\mathrm{Li}} \frac{(Q_{^6\mathrm{Li}}/K_{^6\mathrm{Li}})}{(Q_{^6\mathrm{Li}}/K_{^6\mathrm{Li}}) + (Q_{^7\mathrm{Li}}/K_{^7\mathrm{Li}})} \quad (8)$$

$$x_{^7\mathrm{Li}\_max} = x_{max\mathrm{Li}} \frac{(Q_{^7\mathrm{Li}}/K_{^7\mathrm{Li}})}{(Q_{^6\mathrm{Li}}/K_{^6\mathrm{Li}}) + (Q_{^7\mathrm{Li}}/K_{^7\mathrm{Li}})} \quad (9)$$

Subsequently, $x_{6\mathrm{Li}\_max}$ and $x_{7\mathrm{Li}\_max}$ are compared with $x_{6\mathrm{Li}}$ and $x_{7\mathrm{Li}}$ as calculated by Eqs. (6) or (7). If $x_{6\mathrm{Li}} > x_{6\mathrm{Li}\_max}$ and $x_{7\mathrm{Li}} > x_{7\mathrm{Li}\_max}$ the precipitation rate of the pure ^{6}Li and ^{7}Li endmembers are no longer calculated according to Eq. (5) and become:

$$r_{^6\mathrm{Li}} = r_{pure2nd} \cdot x_{^6\mathrm{Li}\_max} \quad (10)$$

$$r_{^7\mathrm{Li}} = r_{pure2nd} \cdot x_{^7\mathrm{Li}\_max} \quad (11)$$

Using the solid solution approach described above allows defining an experimentally determined or otherwise inferred isotope fractionation factor α and corresponding enrichment factor ε associated with mineral precipitation for a particular simulation run:

$$\alpha = \frac{K_{^6\mathrm{Li}}}{K_{^7\mathrm{Li}}} \quad (12)$$

$$\varepsilon = (\alpha - 1) \cdot 1000 \approx \Delta^7\mathrm{Li} = \delta^7\mathrm{Li}_{2nd\_min} - \delta^7\mathrm{Li}_{solution} \quad (13)$$

It should be noted that our approach for simulating Li isotope fractionation is different from other approaches (Lemarchand et al., 2010; Bouchez et al., 2013; Pogge von Strandmann et al., 2014). Instead of exclusively focusing on the Li system, we use a fully-coupled reactive transport modeling code (see Steefel et al., 2015 for a summary of available codes). In doing so, our approach may simulate the chemical evolution of an entire porous media and parameters other than aqueous Li concentrations and δ^7Li values can be used to constrain the model as well.

4. RESULTS

4.1. Solid [Li] measurements

Li concentration data of primary minerals and mineral mixtures from the Bristner Granite and the migmatitic unit BuMigIII are summarized in Table 2. The full chemical analysis of each laser ablation ICP-MS measurement is listed in the electronic appendix. Bulk rock Li concentrations average at 6 for the Bristner Granite and 9 μg/g for BuMigIII. In both units, elevated average Li concentrations of 463 (Bristner Granite) and 217 μg/g (BuMigIII) were observed in sheet silicates such as chloritized biotite and muscovite. Further differences between the two units include higher Li concentrations in K-feldspar (45 μg/g) of the BuMigIII compared to those in K-feldspar (2.4 μg/g) of the Bristner Granite (Table 2).

4.2. Aqueous Li concentrations and δ^7Li values

Concentrations and δ^7Li values of aqueous Li of 17 groundwater samples originating from the Bristner Granite and BuMigIII are presented in Table 3 in conjunction with field parameters and major cations and anions concentrations reported in Bucher et al. (2012). Computed saturation indices of selected primary and secondary minerals are listed in Table 4. Groundwater temperature correlates with the thickness of the rock column above the tunnel. In the Bristner Granite, groundwater discharges at temperatures from 21.5 to 25.1 °C at a corresponding rock overburden of <500 m. In the BuMigIII groundwater, temperature is remarkably constant (42.6–43.7 °C) at a corresponding overburden of ca. 2000 m, except for sample A103 (36.7 °C), which also displays differences in the chemical composition (e.g., Ca, Mg, pH). Groundwater sample A126 displays strongly elevated SO_4 and Ca concentrations compared to the majority of BuMigIII groundwater (Table 3). In

Table 2
Solid Li concentration measurements performed using AAS for bulk rock concentrations and laser ablation ICP-MS for individual mineral phases.

		Mineral stoichiometry[a]	Li (μg/g)[b]	Stdv. (1ε)	N[c]	Mg/Li
Bristner Granite	Plagioclase	$NaAlSi_3O_8$	2.1	±1.1	7	1–3
	K-Feldspar	$KAlSi_3O_8$	2.4	±1.6	2	<1
	Quartz	SiO_2	4.4	±0.9	3	<1
	Chloritized biotite	$K_{0.5}Fe_{3\text{-}3.5}Al_{<1}(AlSi_3O_{10})(OH)_{5\text{-}8}$	464	±90	2	4
	[e]Muscovite	$KAl_2(AlSi_3O_{10})(OH)_8$	462	±53	4	2
	Bulk rock		6.1	±0.2	2	3
BuMigIII	[d]Plagioclase	$NaAlSi_3O_8$	7.7	±5.1	10	25–35
	K-Feldspar	$K_{0.6}Na_{0.4}AlSi_3O_8$	45	–	1	35
	Quartz	SiO_2	<0.1	–	3	–
	Chloritized biotite	$K_{0.03\text{-}0.3}(Mg,Fe)_{2\text{-}3}Al_{<1}(AlSi_3O_{10})(OH)_{2\text{-}8}$	217	±32	5	65–85
	[d]Muscovite			–	10	–
	Bulk rock		8.8	–	1	138

[a] Inferred stoichiometry based on the full chemical composition of the specific mineral phases listed in the electronic appendix.
[b] Concentrations refer to average concentrations obtained from N measurements and are derived from ^{7}Li conc. measurements (see electronic appendix) taking into account the bulk earth Li isotope abundance.
[c] Number of measurements performed on specific mineral phases.
[d] In case of BuMigIII, plagioclase is heavily altered to sericitic muscovite. Also, muscovite is too small to perform individual measurements. Accordingly, plagioclase measurements including the reported Mg/Li value also contain a muscovite component.
[e] Muscovite measurements for the Bristner Granite refer to a mixture between chloritized biotite and muscovite.

accordance with the anhydrite saturation index close to zero (Table 4), this was attributed to anhydrite dissolution during flow along anhydrite-bearing fractures (Bucher et al., 2012). Aqueous Li concentrations vary between 1.6 and 3.2 mg/L in groundwater from the Bristner Granite compared to 0.010 and 0.017 mg/L in groundwater from the BuMigIII. The orders of magnitude difference in Li concentration is striking given the similarity of the bulk rock Li concentrations, which differ only by a factor of about 1.5 (Table 2).

Similar to aqueous Li concentrations, δ^7Li values of groundwater from the two units show a distinct behavior. The high-Li groundwaters of the Bristner Granite show very little variation in their δ^7Li values (8.5–9.1‰). In contrast, the low-Li groundwaters from BuMigIII show a very strong variation (10–41‰). These latter groundwaters display a positive correlation between δ^7Li values and pH but a negative correlation between δ^7Li and aqueous Li concentrations and the molar Li/Na ratio, except for the exceptional groundwater samples A103 and A126, as discussed above (Fig. 2a–c). Moreover, δ^7Li and Li seem to follow a Rayleigh-type fractionation model with $\alpha = 0.95$ ($\varepsilon = -50$‰) (Fig. 2d), suggesting a single process being responsible for the observed variation in δ^7Li values.

5. DISCUSSION

5.1. Source of aqueous Li

Seelig and Bucher (2010) demonstrated that Cl is a passive tracer in groundwater of the Amsteg section of the Gotthard rail base tunnel and suggested that Cl is derived from porewaters trapped in the matrix of the crystalline rocks. Further, they proposed that the trapped porewater represents the remnants of a hydrothermal fluid that evolved during alpine metamorphism. Interestingly, in the Bristner Granite groundwater, Li concentrations correlate well with Cl concentrations ($r^2 = 0.95$, Fig. 3) inferring that Li is derived from the same porewater source as Cl. This observation is important because it demonstrates that meteoric water infiltrating into a crystalline basement may pick up Li from sources other than from interaction with rock forming minerals.

In contrast to the Bristner Granite groundwater, Cl and Li concentrations in BuMigIII groundwater are orders of magnitude lower and no clear correlation is observed (Table 3). The molar Cl/Li ratio, however, is of the same order of magnitude as recorded for the Bristner Granite water samples (10–30). This observation suggests that a porewater of a similar composition may form a major Li source for BuMigIII groundwater as well. Alternative Li sources are the dissolution of Li-bearing minerals or mixing of the infiltrating meteoric water with an external groundwater (i.e., originating from another lithology) characterized by an elevated Li concentration and a similar Li/Cl ratio as observed in the Bristner Granite groundwater.

5.2. Secondary minerals

Lithium uptake by precipitation of Fe- and Al-bearing secondary mineral or adsorption of Li to these minerals have been proposed to form the major processes for Li isotope fractionation observed in the shallow subsurface (Zhang et al., 1998; Pistiner and Henderson, 2003; Vigier et al., 2008; Wimpenny et al., 2010). Based on computed saturation indices (Table 4), kaolinite is the only secondary Al-bearing secondary phase that is potentially precipitating from the BuMigIII groundwater under the given condition ($SI > 0$), whereas the Bristner Granite groundwater is supersaturated with respect to gibbsite and illite as well. To assess the precipitation of kaolinite from BuMigIII groundwater, it has to be acknowledged that the

Table 3
Aqueous δ^7Li and Li concentration measurements (this study) and major species concentrations reported by Bucher et al. (2012).

	Sample	Tunnel meter	Over-burden (m.a.t.)	Temp (°C)	pH	Flow rate (L/s)	Li^+ (mg/L)	δ^7Li (‰)	Ca^{2+} (mg/L)	Mg^{2+} (mg/L)	Na^+ (mg/L)	K^+ (mg/L)	Fe (mg/L)	Al (mg/L)	[a]C(4) as HCO_3^- (mg/L)	SO_4^{2-} (mg/L)	Cl^- (mg/L)	F^- (mg/L)	SiO_2 (mg/L)	Mg/Li (mol ratio)	Cl/Li (mol ratio)
	A005	8509	320	22.0	9.11	0.10	1.62	8.6 ± 0.2[b]	1.8	0.1	251	10.0	0.27	0.747	264	93	155	19.0	18.9	0.01	18.6
	A038	8566	315	24.2	9.03	0.002	1.60	8.5 ± 0.0	5.2	0.1	266	11.6	<0.02	0.101	318	82	149	23.8	24.2	0.01	18.1
	A042	8903	350	25.1	8.67	0.04	3.09	9.0 ± 0.2	3.7	0.2	511	17.2	<0.02	0.016	395	216	386	27.2	24.0	0.02	24.3
	A035	8381	345	21.5	8.74	0.00	2.60	8.6 ± 0.2	3.0	0.2	405	9.9	0.35	<0.01	371	157	297	27.6	19.1	0.03	22.3
	A039	8575	305	21.4	8.78	0.15	2.86	9.0 ± 0.5	3.0	0.1	461	13.9	<0.02	0.024	314	187	350	26.8	17.8	0.01	23.8
Bristner	A043	8920	350	24.1	8.70	0.03	3.23	9.1 ± 0.2	3.0	0.2	499	17.3	0.07	0.012	365	214	387	26.6	20.1	0.02	23.3
Granite	A037	8432	325	21.5	8.91	0.01	2.16	8.5 ± 0.4	1.9	0.1	348	12.5	<0.02	0.008	310	129	242	26.9	22.8	0.01	21.8
	A007	8611	325	21.9	8.89	0.01	2.10	8.5 ± 0.7	1.6	0.1	311	10.3	0.18	0.392	316	116	213	24.4	18.9	0.01	19.7
	A041	8737	330	22.1	8.73	0.10	3.06	9.0 ± 0.2	3.3	0.2	512	15.6	<0.02	0.054	354	213	383	27.1	22.9	0.02	24.4
	A099	14,850	1975	42.6	9.40	0.02	0.013	14.8 ± 0.3	5.6	<0.1	26.1	0.9	<0.02	0.093	11.0	40	1.2	1.6	28.2	<2.1	17.4
	A100	14,951	2050	43.7	9.31	0.07	0.014	10.7 ± 0.5	5.2	<0.1	26.6	0.7	<0.02	0.135	13.9	40	0.8	1.6	28.2	<2.0	10.5
	A102	14,986	2090	43.4	9.47	0.20	0.013	19.7 ± 0.1	5.5	<0.1	25.0	0.5	<0.02	0.098	13.5	36	0.7	1.7	23.3	<2.2	11.1
BuMigIII	A029	15,095	2100	42.8	9.80	2.50	0.010	41.1 ± 0.6	9.0	0.5	30.2	1.2	1.03	0.033	13.9	38	1.2	3.1	30.7	13.7	24.3
	A103	15,106	2095	36.7	8.29	0.01	0.016	22.3 ± 0.1	13.5	0.2	26.8	1.5	0.29	0.641	68.0	31	2.6	1.8	30.2	4.0	32.5
	A104	15,136	2090	43.4	9.36	0.15	0.017	17.4 ± 0.3	11.0	<0.1	27.5	0.8	<0.02	0.077	13.1	54	1.2	3.9	28.3	<1.7	13.9
	A027	14,794	1920	43.0	9.44	0.02	0.012	27.2 ± 0.4	5.0	<0.1	26.6	0.9	<0.02	0.094	9.1	39	0.8	1.6	32.2	<2.4	13.1
	A126	15,334	2035	43.2	9.27	0.02	0.054	17.9 ± 0.1	412.0	<0.1	86.1	1.4	0.31	0.042	17.7	1189	7.8	2.6	26.6	<0.5	25.2

[a] In case of BuMigIII HCO_3^- concentrations were calculated to maintain charge balance.
[b] 2σ uncertainty.

Table 4
Saturation indices of selected primary and secondary minerals calculated using TOUGHREACT in conjunction with the Soltherm.H06 database (Reed and Palandri, 2006).

	Sample	pH	Quartz	Chalcedony	Orthoclase	Albite	Calcite	Anhydrite	Kaolinite (Soltherm. H06)[a]	Kaolinite (EQ3/6)[a]	Gibbsite	$Al(OH)_3$ (am)	Illite	Log f_{CO2}
Bristner Granite	A005	9.11	0.41	0.09	3.64	3.35	0.15	−3.59	6.83	4.13	1.69	−1.96	4.33	−3.74
	A038	9.03	0.54	0.22	3.22	2.89	0.61	−3.19	5.51	2.80	0.90	−2.75	2.90	−3.57
	A042	8.67	0.60	0.28	2.73	2.51	0.16	−3.02	4.71	2.00	0.45	−3.21	1.81	−3.12
	A035	8.74	0.50	0.17	0.42	0.34	0.14	−3.19	0.83	−1.87	−1.39	−5.05	0.81	−3.21
	A039	8.78	0.45	0.13	2.37	2.20	0.09	−3.15	4.55	1.85	0.52	−3.14	1.49	−3.33
	A043	8.70	0.52	0.20	2.36	2.13	0.07	−3.11	4.24	1.53	0.29	−3.36	1.21	−3.18
	A037	8.91	0.54	0.22	2.13	1.88	0.04	−3.45	3.53	0.82	−0.08	−3.74	0.50	−3.46
	A007	8.89	0.47	0.15	3.53	3.32	−0.05	−3.57	6.81	4.11	1.63	−2.03	4.14	−3.43
	A041	8.73	0.56	0.24	3.12	2.94	0.13	−3.07	5.58	2.87	0.91	−2.74	2.81	−3.23
BuMigIII	A099	9.40	0.08	−0.22	0.25	0.11	−0.01	−2.97	1.95	−0.55	−0.46	−3.83	−1.77	−5.34
	A100	9.31	0.13	−0.17	0.40	0.42	−0.02	−3.00	2.54	0.05	−0.21	−3.58	−1.22	−5.14
	A102	9.47	−0.04	−0.34	−0.41	−0.25	0.12	−3.03	1.61	−0.89	−0.51	−3.88	−2.42	−5.34
	A029	9.80	−0.15	−0.45	−0.78	−0.98	0.54	−2.83	−0.22	−2.71	−1.31	−4.69	−3.86	−5.77
	A103	8.29	0.51	0.20	2.72	2.35	0.04	−2.78	7.21	4.65	1.75	−1.70	3.66	−3.41
	A104	9.36	0.10	−0.20	0.13	0.11	0.30	−2.58	1.90	−0.60	−0.51	−3.88	−1.91	−5.23
	A027	9.44	0.12	−0.19	0.33	0.23	−0.10	−3.02	1.95	−0.55	−0.50	−3.87	−1.70	−5.47
	A126	9.27	0.09	−0.22	−0.03	−0.33	1.29	−0.26	1.42	−1.08	−0.73	−4.10	−2.56	−5.34

[a] To discuss the possible precipitation of kaolinite, the saturation index was calculated using log(K) values tabulated in the EQ3/6 database (Wolery, 1992) in addition to the ones tabulated in the Soltherm database (Table 1, Reed and Palandri, 2006).

equilibrium constant of kaolinite is associated with a large uncertainty (Trotignon et al., 1999), which is reflected by its changing saturation state in BuMigIII groundwater when using different thermodynamic databases (Table 4). The range of log(K) values for kaolinite tabulated in different thermodynamic databases is at least partly related to differences in solubility experiments (e.g. acid vs alkaline conditions, temperature), but also to analytical difficulties (e.g. Al and Si colloids). Fig. 4 shows the relation of the kaolinite equilibrium constant tabulated in the Soltherm.H06 (Reed and Palandri, 2006) and EQ3/6 database (Wolery, 1992). Temperature dependent log(K) tabulated in the Soltherm. H06 database reproduces well log(K) values derived from kaolinite solubility experiments performed at temperatures of 60, 90 and 110 °C and at similar pH values, as observed in our system (up to pH 9) (Devidal et al., 1996). In contrast, temperature dependent log(K) values derived from the EQ3/6 database (Wolery, 1992) overestimate the Devidal et al. (1996) values. However, they are within the range of kaolinite solubilities determined for temperatures between 22 and 25 °C (Polzer and Hem, 1965; Kittrick, 1966; Reesman and Keller, 1968; May et al., 1986; Yang and Steefel, 2008) and the solubility experiment performed by Nagy et al. (1991) at 80 °C and pH 3. Overall, computed saturation indices (Table 4) and thermodynamic considerations (Fig. 4) support the use of the Soltherm.H06 database and suggest that kaolinite is the dominating secondary Al phase precipitating from the BuMigIII groundwater. The restricted access to water-conducting fractures, however, did not allow confirmation of the presence of kaolinite although it has been observed as low-T alteration product in various crystalline rock environments (e.g., Grimaud et al., 1990; Michard et al., 1996; Gimeno et al., 2014).

Our groundwater samples display dissolved oxygen concentrations below detection limit demonstrating that reducing conditions are established. Under reducing conditions, the formation of Fe(III)-oxides such as goethite, ferrihydrite, lepidocrocite, and hematite is absent (Schwertmann, 1988). Accordingly, their formation and corresponding sorption reactions are restricted to the domain very close to the surface where the dissolved oxygen concentration in infiltrating meteoric water is in equilibrium with atmospheric oxygen. The limited formation of Fe-bearing secondary minerals infers that Li isotope fractionation is primarily caused by Li uptake by kaolinite (BuMigIII) or other Al-bearing secondary minerals (Bristner Granite).

5.3. Diffusive Li isotope fractionation and anthropogenic Li contamination

If Li influx into the fracture groundwater were occurring entirely by diffusion from a porewater Li source, diffusive fractionation is a likely process to cause a δ^7Li variation in addition to Li uptake by secondary minerals (Richter et al., 2006; Bourg and Sposito, 2007). Owing to the difference in mass, the diffusion coefficient of ^{6}Li is larger than that for ^{7}Li leading to enrichment in ^{6}Li (low δ^7Li) in the groundwater. Accordingly, diffusive Li isotope fractionation would partially mask the δ^7Li increase inherited from Li isotope fractionation associated with secondary mineral precipitation. Indeed, it would yield an even higher intrinsic fractionation factor than the −50‰ obtained from the Rayleigh-type model (Fig. 2d).

In contrast to diffusive Li isotope fractionation, anthropogenic contamination of Li can be excluded based on the infiltration area in remote high-alpine area and the high

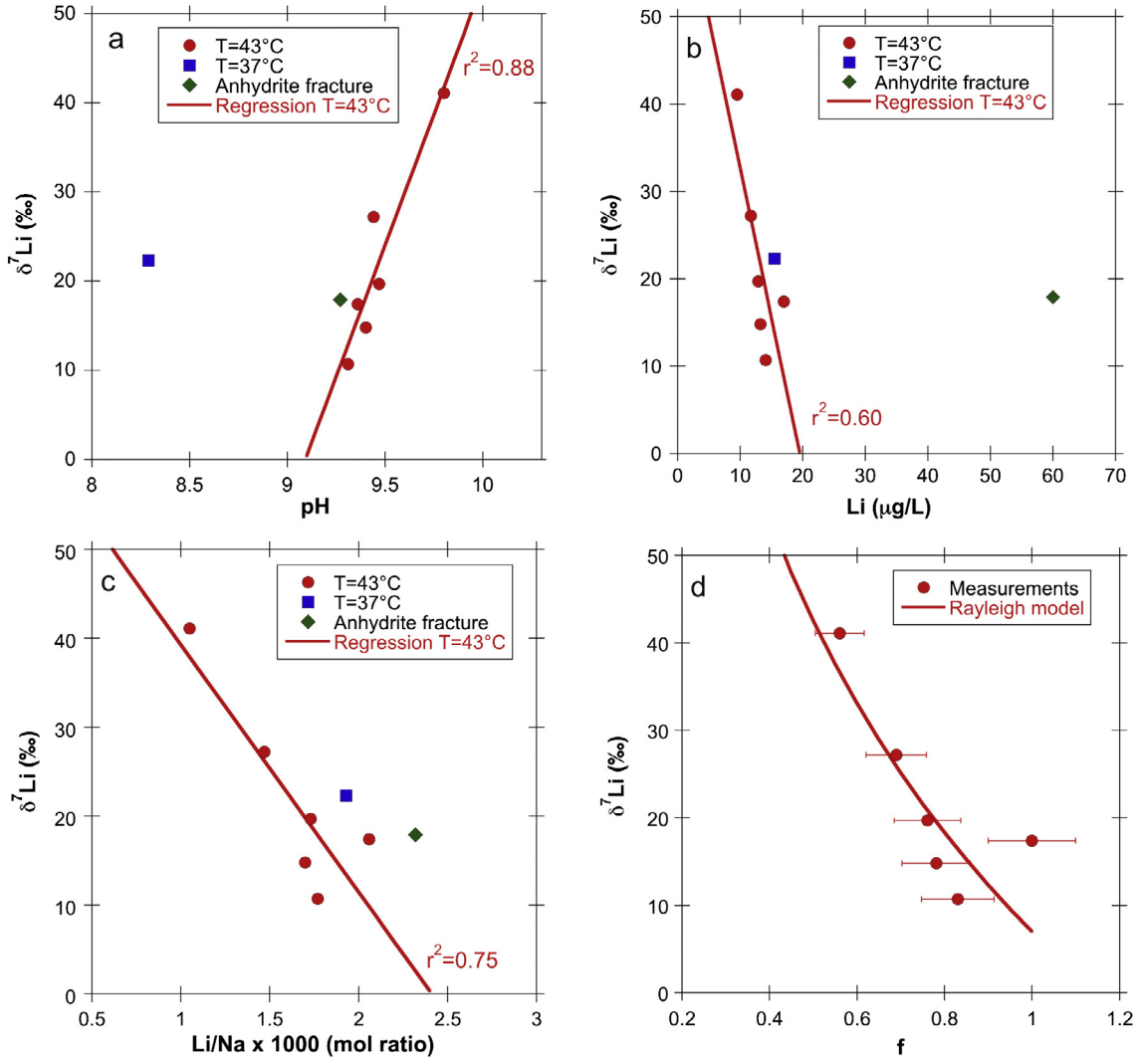

Fig. 2. δ^7Li values of BuMigIII water samples plotted against the pH (a), the [Li] (b), and the molar Li/Na ratio (c). The shown correlations were obtained by not considering the two samples with special features (e.g., anhydrite dissolution and low temperature). (d) Rayleigh model ($\delta^7Li = \delta^7Li_{Ini} + 1000)f^{\alpha-1}) - 1000$) using an enrichment factor ε of −50‰ ($\varepsilon = (\alpha - 1) * 1000$), an initial δ^7Li of 7‰ and a [Li] of 17 µg/L at $f = 1$.

hydraulic pressure of about 100 bar at the discharge locations (Masset and Loew, 2013). Also, if any artifacts occurred during sampling, major species concentrations were affected as well and their concentrations could not be approximated by solely simulating water–rock interaction between meteoric water and pristine granite such as shown below.

5.4. Hypothesis for observed δ^7Li variation

The most striking observation from our measurements is that significant δ^7Li variation only occurs at low Li concentrations, suggesting that the variation is highly sensitive to the aqueous Li concentration. The second key observation is the negative correlation between δ^7Li and the Li concentration as well as the positive correlation between δ^7Li and pH seen in the BuMigIII groundwater (Fig. 2a and b). Our approach is to first explore the process(es) controlling the Li system in a single hydrogeochemical system such as the BuMigIII groundwater, before comparing the different settings (BuMigIII vs. Bristner Granite).

The BuMigIII groundwaters likely have different residence times within the rock column above the tunnel due to a variation in fracture permeability and connectivity. Variable residence times are consistent with the 2 orders of magnitude variation in flow rates (Table 3) and the observed trends in chemical and Li-isotope composition (Fig. 2a and c). In granitic systems, the pH increases with reaction progress (Nordstrom et al., 1989; Grimaud et al., 1990; Bucher et al., 2012; Gimeno et al., 2014) and the Li/Na ratio may form an excellent proxy for the degree of water–rock interaction (e.g., residence time, reaction progress) that inversely correlates with δ^7Li (Liu et al., 2015). The Li/Na ratio is indicative because Na concentrations are several orders of magnitude greater than Li concentrations, and thus not as strongly affected by minor

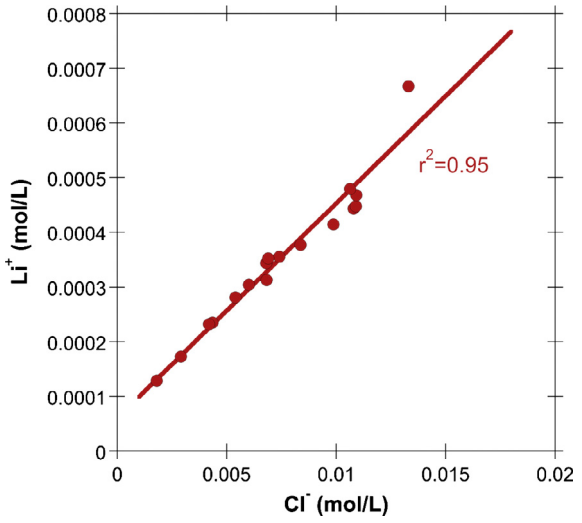

Fig. 3. Excellent linear correlation between Li^+ and Cl^- observed for groundwater samples collected from the Bristner Granite.

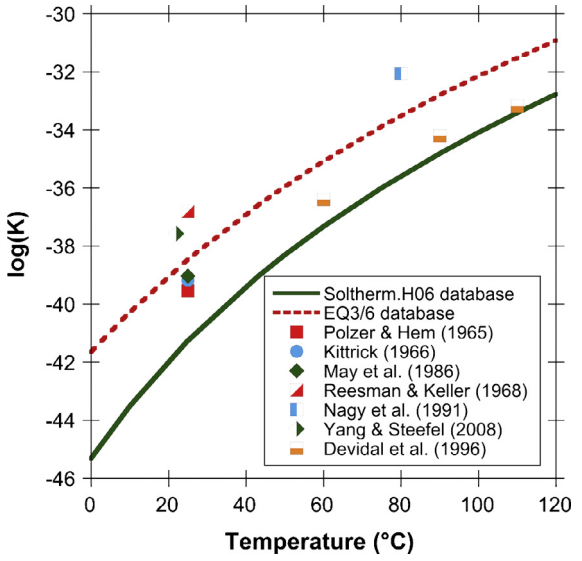

Fig. 4. Comparison between experimentally determined and tabulated log(*K*) values for the following kaolinite hydrolysis reaction: $Al_2Si_2O_5(OH)_4 + 3H_2O = 2Al(OH)_4^- + 2SiO_2 + 2H^+$.

uptake by secondary mineral precipitation (e.g., kaolinite). In case of a discrete Li influx such as from an external groundwater source (Fig. 5b), Na release from primary minerals is ongoing, which also yields a decrease of the Li/Na ratio with flow distance and reaction progress.

Higher residence time of groundwater results in increased water–rock interaction and thus increased precipitation of Li-bearing kaolinite, which drives δ^7Li to higher values (Wanner et al., 2014). Observing a negative correlation between δ^7Li and the Li concentration must thus be inherited form the spatial release rate of the actual Li source along the infiltration path in relation to the corresponding Li uptake rate by secondary minerals. The

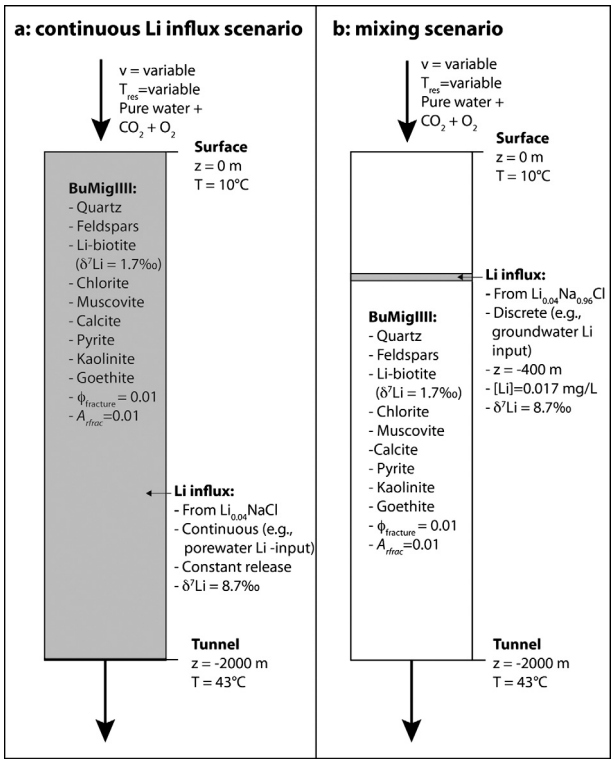

Fig. 5. Li influx scenarios and corresponding model setups for simulating the infiltration of meteoric water into the BuMigIII rock column above the tunnel.

amount of data to quantitatively assess the role of the potential Li sources (Li-bearing minerals, porewater, external groundwater), however, are limited. Therefore and in terms of a sensitivity analysis, a series of reactive transport model simulations were performed by varying the Li source as well as the parameters controlling the Li system in order to unravel how these parameters affect aqueous δ^7Li values and Li concentrations in the BuMigIII groundwater.

6. REACTIVE TRANSPORT MODELING

6.1. Model setup

Reactive transport model simulations were performed for a simplified vertical, fully-saturated 2000 m long 1D flow path consisting of 1000 grid blocks of 2 m length (Fig. 5). A fixed linear temperature gradient of 10–43 °C was specified from the upstream to the downstream model boundary. With these specifications, the model represents the geometry where the tunnel intersects with BuMigIII. In contrast to other studies (DePaolo, 2006; Waber et al., 2012; Brown et al., 2013), our model does not explicitly consider diffusion between water flowing along fractures and porewater residing in the intact rock matrix. In doing so, we exclusively simulate reactive transport along one particular fracture system. The porosity and permeability relevant for fluid flow in fractured crystalline rocks depend on the fracture spacing and aperture (Caine and Tomusiak, 2003; MacQuarrie and Mayer, 2005; Sonnenthal et al.,

2005). None of these parameters are explicitly known for the present system so that individual simulations were run at a constant flow rate using a fixed fracture porosity of 1% (Fig. 5). To account for the unknown residence time within the rock column above the tunnel, simulations were run for flow velocities ranging from 0.2 to 20 m/year, which approximately reflect the variation of flow rates observed for the BuMigIII samples (0.01–2.5 L/s). The specified velocity range also covers the range in hydraulic conductivity ($3–7 \times 10^{-8}$ m/s) reported for fracture zones along the nearby Sedrun section of the tunnel (Masset and Loew, 2013).

6.2. Initial and boundary conditions

Water in equilibrium with atmospheric CO_2 and O_2 was specified as initial and upper boundary condition to simulate the infiltration of meteoric water into the BuMigIII rock column above the tunnel (Table 5). The solid part of the model domain is given by the granitic composition of the BuMigIII rock (Table 5). Plagioclase has only a minor anorthite component and pure albite was used in the calculations. In contrast, biotite and chlorite were defined as solid solutions between the corresponding Fe (annite and chamosite) and Mg endmembers (phlogopite and clinochlore) according to the analyzed Mg/Fe ratios (el. Appendix).

6.2.1. Li source and secondary minerals

Li was introduced by defining two different Li sources: (i) Li-bearing biotite with a Li concentration of 217 μg/g as measured in chloritized biotite of the BuMigIII rock (Table 2) and (ii) a hypothetical $Li_{0.04}Na_{0.96}Cl$ solid phase that acts either as a proxy for matrix porewater or an external, ad-mixed groundwater Li source. The Cl/Li ratio of 25 defined for this hypothetical phase corresponds to the ratio obtained from the linear correlation between Cl and Li observed for Bristner Granite groundwater (Fig. 3), while charge balance was maintained by including Na. An initial δ^7Li value of 1.7‰ was assigned to Li-bearing biotite, corresponding to the average δ^7Li value determined for a large series of different granites (Teng et al., 2009). In contrast, the average Bristner Granite groundwater δ^7Li value of 8.7‰ (Table 3) was assigned to the hypothetical $Li_{0.04}Na_{0.96}Cl$ solid phase based on our concept that Li in the BuMigIII is derived from a similar source as in the Bristner Granite.

While all simulations considered the Li-bearing biotite source, two scenarios were run for the $Li_{0.04}Na_{0.96}Cl$ source. The first scenario considered a constant zero order dissolution rate of 2×10^{-15} mol/kg_{H_2O}/s occurring along the entire model domain and corresponding to a Li influx from a porewater source (continuous Li influx scenario, Fig. 5a). This yields a Li concentration of 0.017 mg/L at the tunnel level what corresponds to the maximum concen-

Table 5
Initial and boundary conditions defined for performing reactive transport model simulations.

		Initial condition	Boundary condition (infiltrating fluid)
Temperature	°C	Variable	10
pH	–	5.67	5.67
C(4) as HCO_3^-	mol/kg_{H_2O}	1.5e−5	1.5e−5
Na^+	mol/kg_{H_2O}	1.0e−10	1.0e−10
K^+	mol/kg_{H_2O}	1.0e−10	1.0e−10
Mg^{2+}	mol/kg_{H_2O}	1.0e−10	1.0e−10
Ca^{2+}	mol/kg_{H_2O}	1.0e−10	1.0e−10
Al^{3+}	mol/kg_{H_2O}	1.0e−10	1.0e−10
Li^+	mol/kg_{H_2O}	1.0e−10	1.0e−10
$SiO_{2(aq)}$	mol/kg_{H_2O}	1.0e−10	1.0e−10
$O_{2(aq)}$	mol/kg_{H_2O}	3.9e−4	3.9e−4
Fe^{2+}	mol/kg_{H_2O}	1.0e−10	1.0e−10
[b]Albite	vol. frac. (of solids)	0.31	0.0
Orthoclase	vol. frac. (of solids)	0.03	0.0
Quartz	vol. frac. (of solids)	0.48	0.0
[a1]Annite	vol. frac. (of solids)	0.02	0.0
[a1]Phlogopite	vol. frac. (of solids)	0.02	0.0
Muscovite	vol. frac. (of solids)	0.1	0.0
[a2]Chamosite	vol. frac. (of solids)	0.0075	0.0
[a2]Clinochlore	vol. frac. (of solids)	0.0075	0.0
Pyrite	vol. frac. (of solids)	0.01	0.0
Calcite	vol. frac. (of solids)	0.01	0.0
Kaolinite[a3]	vol. frac. (of solids)	0.0	0.0
$^6Li_{kaolinite}$[a3]	vol. frac. (of solids)	0.0	0.0
$^7Li_{kaolinite}$[a3]	vol. frac. (of solids)	0.0	0.0
Porosity	–	0.01	1.0

[ax] End-member of solid solution *x*.
[b] Specified mineralogical composition is based on XRF analyses performed on BuMigIII (Seelig and Bucher, 2010) as well as on laser ablation ICP-MS measurements (electronic appendix).

tration observed in BuMigIII groundwater samples (Fig. 2). The second set considered a single point Li influx after an arbitrary flow distance of 400 m and simulates a situation where Li in the BuMigIII groundwater is ad-mixed by an external fracture groundwater to the infiltrating meteoric water (mixing scenario, Fig. 5b). To do so, the Li concentration of the simulated groundwater mixture was set to 0.017 mg/L at $z = -400$ m.

Kaolinite is the only secondary Al-phase precipitating in our model and Li uptake by kaolinite is the only process to cause Li isotope fractionation. Based on the observation that the SiO_2 concentrations of the 122 tunnel waters are solubility-controlled by quartz above a pH of ca. 9 (Bucher et al., 2012), secondary quartz was allowed to precipitate as well. The same applies for goethite.

6.2.2. Sensitivity analysis

Our approach for simulating Li isotope fractionation allows defining a Li isotope fractionation factor as well as a maximum amount of Li that can be incorporated in secondary minerals. Since both parameters are unknown, simulations were run for Li isotope enrichment factors of −25, −37.5 and −50‰ associated with Li uptake by kaolinite and for maximum Li concentrations in kaolinite of 25, 50 and 75 μg/g to test their impact on the model results. Whereas these maximum Li concentrations cover the Li concentration range observed in natural kaolinite (Tardy et al., 1972; Vigier and Goddéris, 2015), Li isotope enrichment factors of −37.5 and −50‰ are outside the range inferred so far for secondary mineral precipitation (≈−10 to −30‰) (Zhang et al., 1998; Huh et al., 2001; Pistiner and Henderson, 2003; Kisakürek et al., 2005; Pogge von Strandmann et al., 2006, 2010; Vigier et al., 2008). The range in ε was expanded to higher values because the Li concentration and isotope data from BuMigIII groundwater revealed an ε-value of −50‰ when applying a Rayleigh-type model (Fig. 2d). A temperature effect on epsilon such as observed for hydro-geothermal system (Marschall et al., 2007; Vigier et al., 2008; Verney-Carron et al., 2015; Pogge von Strandmann et al., 2016) was not considered because within the temperature range of our model (10–43 °C), it is likely smaller than the uncertainty of ε-values reported for Li uptake by secondary minerals as well as the ε-range considered in the sensitivity analyses. Additional sensitivity simulations included a reduction of the kaolinite precipitation rate constant by 67% and 33% of the initially chosen value (base case, Table 1), a variation of the δ^7Li value specified for the $Li_{0.04}Na_{0.96}Cl$ phase and a variation of the location of the input of the external groundwater Li source. An overview of the simulated parameter combinations is given in Table 6.

6.3. Model results and discussion

6.3.1. General system behavior

The general water–rock interaction progress along the 2000 m model domain is shown for a general situation where the system is reactive enough to approach chemical equilibrium within the model domain (Fig. 6). The profiles shown in Fig. 6 are referred to such a general reaction progress because it depends on the product of two unknown parameters such as reactive fracture surface area (A_{rfrac}) and residence time (Eq. (2)). If the system was more or less reactive, the profiles except the temperature profile would be horizontally shifted towards lower or greater distances, respectively, whereas the general profile shape would remain similar.

The relative change in mineral volume fraction (Fig. 6c) demonstrates that albite dissolution and kaolinite precipitation are driving the general chemical system in addition to quartz and calcite precipitation, as previously described for low-T crystalline groundwater environments (Nordstrom et al., 1989; Grimaud et al., 1990; Trotignon et al., 1999; Gimeno et al., 2014), and as reflected by the calculated mineral states (Table 4). In contrast, other primary minerals (K-feldspar, chlorite, biotite, muscovite) show only minor volume changes whereas goethite formation is restricted to the first grid block where pyrite is oxidized by oxygen dissolved in the infiltrating meteoric water (Fig. 5). A prominent feature typical for the evolution of crystalline groundwaters is the strong increase in pH from about 8.5 to 9.7, which at the considered reaction progress occurs between 1000 and 1500 m along the model domain (Fig. 6a). The increase in pH is correlated to the maximum

Table 6
Parameter values chosen for the various model runs.

Scenario	Scenario #	Max $[Li]_{kaolinite}$ (ppm)	*$k_{kaolinite}$	$\varepsilon_{kaolinite}$	$\delta^7Li_{Li0.04Na0.96Cl}$ (‰)	Li influx location (m)
Continuous Li influx	C1	75	Base case	−50	8.7	–
Mixing scenario (single point Li influx)	M1	25	Base case	−50	8.7	−400
	M2	50	Base case	−50	8.7	−400
	M3	75	Base case	−50	8.7	−400
	M4	75	Base case	−37.5	8.7	−400
	M5	75	Base case	−25	8.7	−400
	M6	75	Base case × 2/3	−50	8.7	−400
	M7	75	Base case × 1/3	−50	8.7	−400
	M8	75	Base case	−50	8.7	−200
	M9	75	Base case	−50	8.7	−1200
	M10	50	Base case	−50	1.7	−400

* Base case: $k_{25} = 1.98e{-}13$ (Table 1).

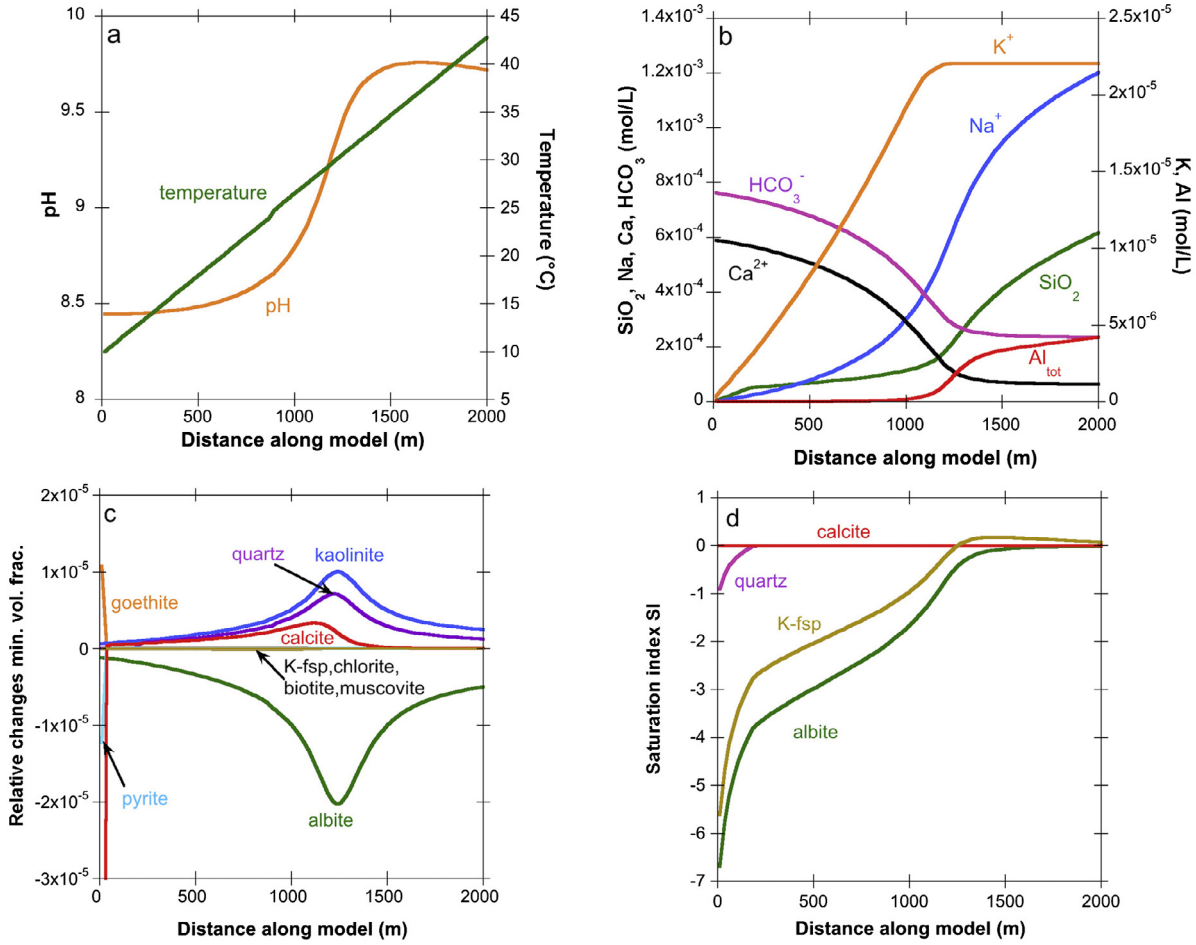

Fig. 6. General behavior of the simulated interaction between infiltrating meteoric water and the granitic BuMigIII. Steady state profiles along the model are shown for temperature and pH (a), total major species concentrations (b), changes in mineral volume fractions relative to $t = 0$ after a simulated time of 10,000 years (c), and saturation indices of selected mineral phases (d). All profiles refer to a general situation where chemical equilibrium is approached along the flow path (e.g., $v = 1$ m/year and $A_{rfrac} = 0.01$ $m^2/m^3_{fractured\_medium}$).

albite dissolution and kaolinite formation (Fig. 6c). Across this interval, coupled albite dissolution and kaolinite precipitation is thus the main reaction governing the pH increase:

$$NaAlSi_3O_8 + H^+ + 0.5H_2O = 0.5Al_2Si_2O_5(OH)_4 + Na^+ + 2SiO_2 \quad (14)$$

The actual driving force for reaction (14) is the supply of protons by the dissolution and dissociation of atmospheric CO_2:

$$CO_{2(g)} + H_2O = H_2CO_3 = H^+ + HCO_3^- \quad (15)$$

Prior to the strong pH increase, the system is controlled by calcite, i.e., by the initial dissolution and subsequent precipitation caused by the calcite solubility decrease with increasing temperature ($Ca^{2+}_{(aq)} + HCO^-_{3(aq)} = CaCO_{3(s)} + H^+$) (Fig. 6c). As the Ca^{2+} and HCO_3^- concentrations decrease due to continuous calcite precipitation along the flow path, calcite precipitation is diminished (Fig. 6b and c) and the pH is no longer controlled by calcite precipitation. At this point, coupled albite dissolution and kaolinite precipitation is accelerated by the pH dependence of the corresponding rates (*cf.* Eq. (3), Table 1) as well as by the linear temperature increase along the flow path (Fig. 6a). As the system approaches equilibrium with respect to albite (Fig. 6d), further albite dissolution and subsequent kaolinite precipitation are slowed down and the pH becomes controlled by the speciation of dissolved Si ($H_4SiO_4 = H_3SiO_4^- + H^+$), which becomes important above pH 9–9.5.

The maximum in coupled albite dissolution and kaolinite precipitation is reflected by the Na concentration profile showing a maximum increase along the same interval as the strong pH increase (Fig. 6b). In contrast, dissolved Si is controlled by the solubility of quartz, which strongly increases above pH 9 when $H_3SiO_4^-$ becomes the dominant Si species. Owing to the linear temperature increase (Fig. 6a), Na^+, Al^{3+} and Si concentrations are still increasing at the downstream model boundary (Fig. 6b) because the solubility of albite and quartz are increasing with temperature (Table 1). In turn, the pH slightly drops towards the model boundary because of the temperature-dependence of the equilibrium pH of the simulated granitic system.

6.3.2. Behavior of Li

The modeled Li concentration of ~0.6 µg/L inherited from biotite dissolution at the tunnel level is very low (not shown) and demonstrates that only minor amounts of aqueous Li can be derived from interaction between the infiltrating meteoric water and the BuMigIII rocks. Such a minor Li contribution is consistent with a molar Mg/Li ratio in the BuMigIII water samples (<14, Table 3) that is much lower than that in chloritized biotite forming the primary Li host of the BuMigIII rock (ca. 65–85, Table 2). An additional Li input such as from the matrix porewater, an external groundwater or an unknown mineral source is thus required to explain the observed Li concentrations (Table 3).

For both Li influx scenarios modeled with the hypothetical $Li_{0.04}Na_{0.96}Cl$ phase (Fig. 5), the model yields a strong δ^7Li increase between 1000 and 1500 m (Fig. 7a and b). At the considered reaction progress, this interval corresponds to the maximum in kaolinite precipitation (Fig. 6c). This suggests that Li isotope fractionation is coupled to kaolinite precipitation and that δ^7Li values are highly sensitive to the amount of kaolinite precipitation. Consequently, when kaolinite precipitation slows down towards the downstream model boundary, the δ^7Li increase slows down as well (Fig. 7b) or even starts to decrease (Fig. 7a) depending on the simulated scenario.

For the continuous Li influx scenario (Fig. 5a), the Li concentration increases over most part of the domain because the Li influx outpaces the Li uptake by secondary kaolinite precipitation, except for a short interval where kaolinite precipitation is maximal (Fig. 7a). Consequently, for this scenario, δ^7Li is positively correlated to the Li concentration with the exception of the downstream model boundary where δ^7Li is decreasing (Fig. 7a and c) because the Li load in the fracture fluid becomes dominated by the ongoing Li influx with a δ^7Li of 8.7‰. For the mixing scenario (Fig. 5b), the Li concentration decreases after the single point Li input yielding throughout a negative correlation with δ^7Li (Fig. 7b and c).

6.3.3. Application to BuMigIII groundwater

The observation that only the mixing scenario yields a negative correlation between δ^7Li and the Li concentration, as observed in BuMigIII groundwater (Fig. 2), suggests that Li is inherited from a discrete rather than from a continuous Li influx. Whereas mixing with an external groundwater is a likely candidate for single point Li influx, it is also possible that it occurred from a not yet identified rock type enriched in Li-bearing mineral(s), with a composition that is significantly different from that of the BuMigIII rock exposed at the tunnel level.

To further apply the mixing scenario (Fig. 5b) to the BuMigIII system, the model was run for a variable reaction progress along the 2000 m long flow path by varying the flow velocity while keeping the reactive fracture surface area constant. Consequently, steady state major species concentrations computed for the tunnel level ($z = -2000$ m) are plotted against the pH to illustrate their dependence on the overall reaction progress and to compare them with measured BuMigIII groundwater data

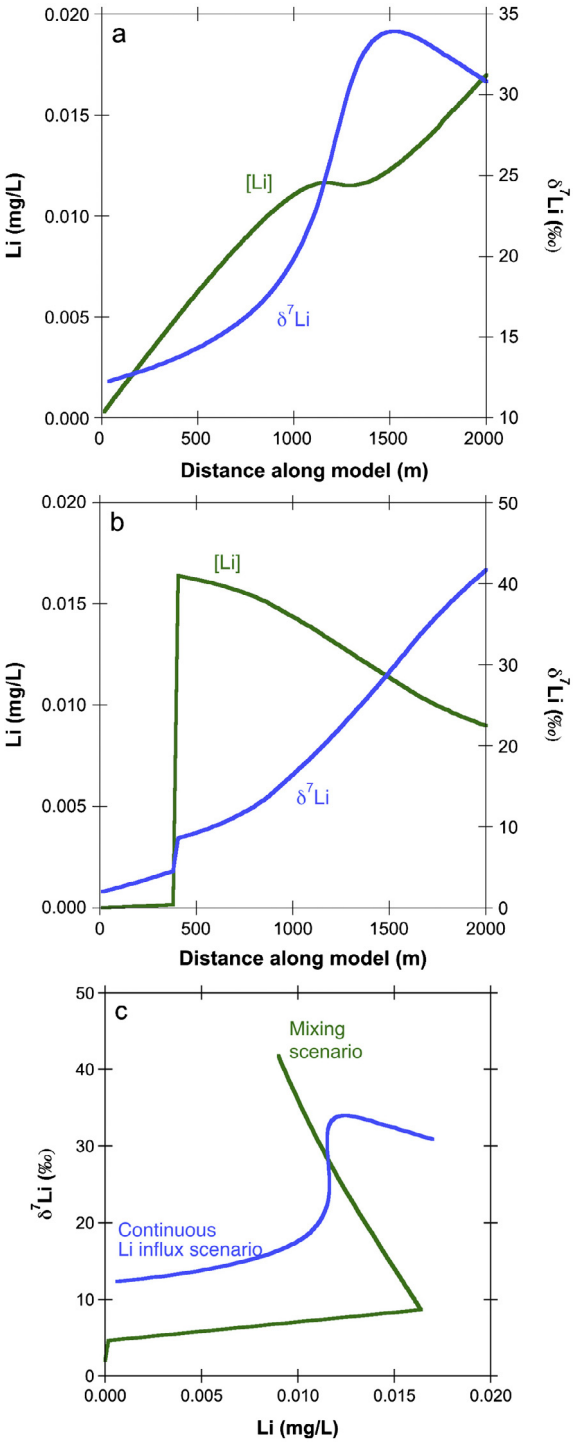

Fig. 7. General behavior of Li in the two Li influx scenarios (Fig. 5) at the same reaction progress as shown in Fig. 6. (a) continuous Li influx sceneario. (b) mixing scenario. (c) correlation between δ^7Li and Li. Results correspond to a Li isotope enrichment factor and maximum amount of Li in kaolinite of −50‰ and 75 µg/g, respectively (simulations C1 and M3, Table 6).

(Fig. 8). Although the fits are not perfect, the fact that the order of magnitude is reproducible suggests that the model captures the governing mineral reactions. Differences

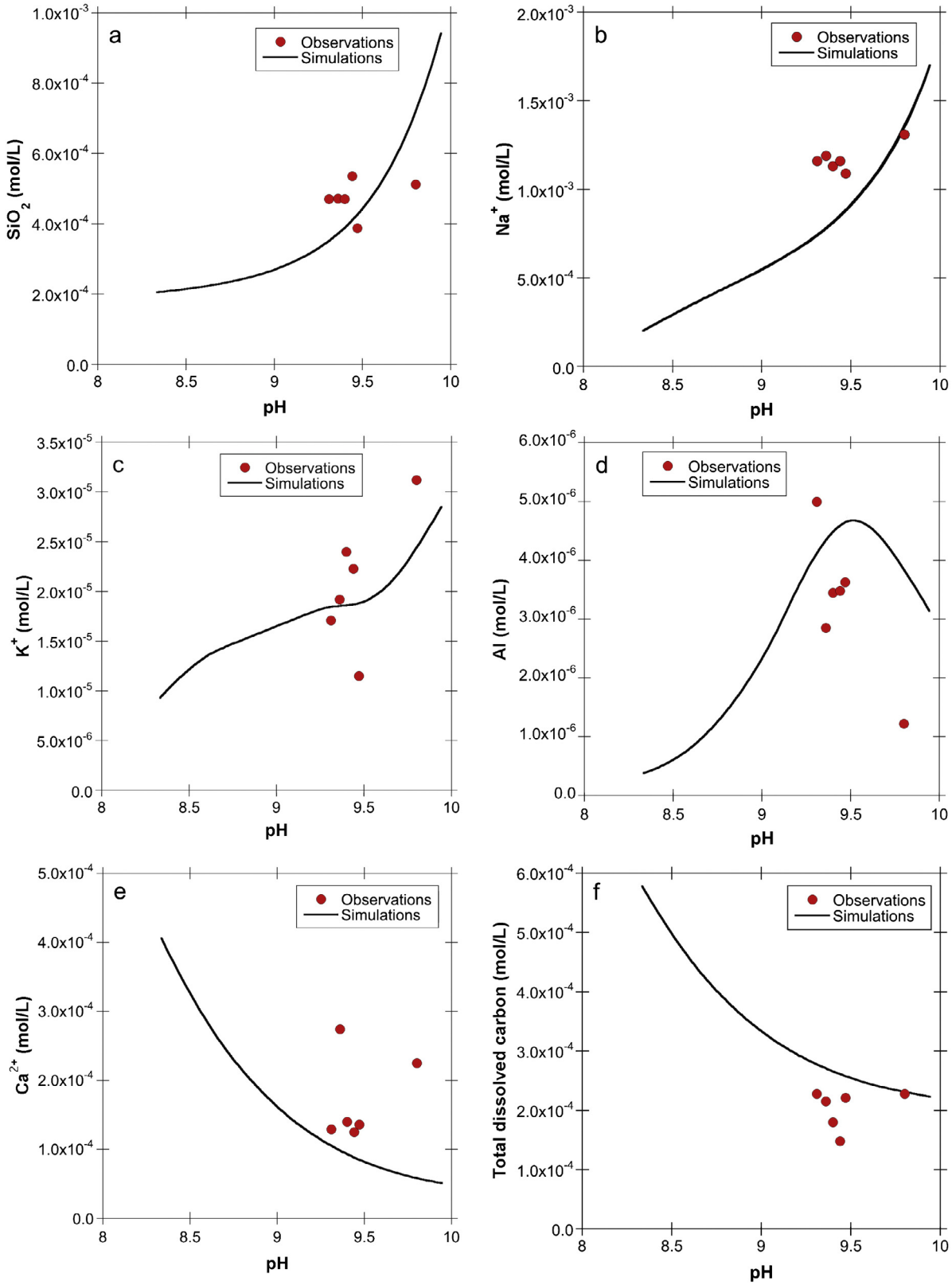

Fig. 8. Major species concentrations computed for the tunnel level and plotted against the pH to illustrate their behavior with respect to a variable reaction progress along the model domain (e.g., variable residence time). Also shown are corresponding measurements of BuMigIII groundwater samples.

between modeled and observed concentrations are likely inherited from the assumptions of constant flow velocity and homogeneous mineralogy along the flow path.

6.3.3.1. Li system

The sensitivity of our model parameters on the Li system was tested by comparing measured δ^7Li and Li concentrations with computed steady state values obtained at the tunnel level for a variable reaction progress along the flow path and for 7 combinations of Li isotope enrichment factors, maximum Li concentrations in kaolinite, and kaolinite precipitation rate constants. Fig. 9 illustrates that all varied parameters have an effect on the Li concentration and/or on δ^7Li. Higher amounts of Li incorporation into kaolinite as well as higher amounts of kaolinite precipitation increase the δ^7Li value and decrease the Li concentration for a given reaction progress (i.e., pH) because both parameters increase the ratio between the Li uptake by kaolinite and the external Li input. Increasing the Li isotope enrichment factor also yields an increase in the δ^7Li value for a given reaction progress (i.e., pH), but does obviously not change the Li concentration. The sensitivity analyses carried out for the location of the single point Li influx yielded only minor dependence as long as it occurred before the system evolved to the maximum kaolinite formation rate (not shown).

In general, simulations performed for the mixing scenario approximate the observed pH dependence of measured δ^7Li values (Fig. 9), although in a non-linear manner, and the observed Li concentrations can be repro-

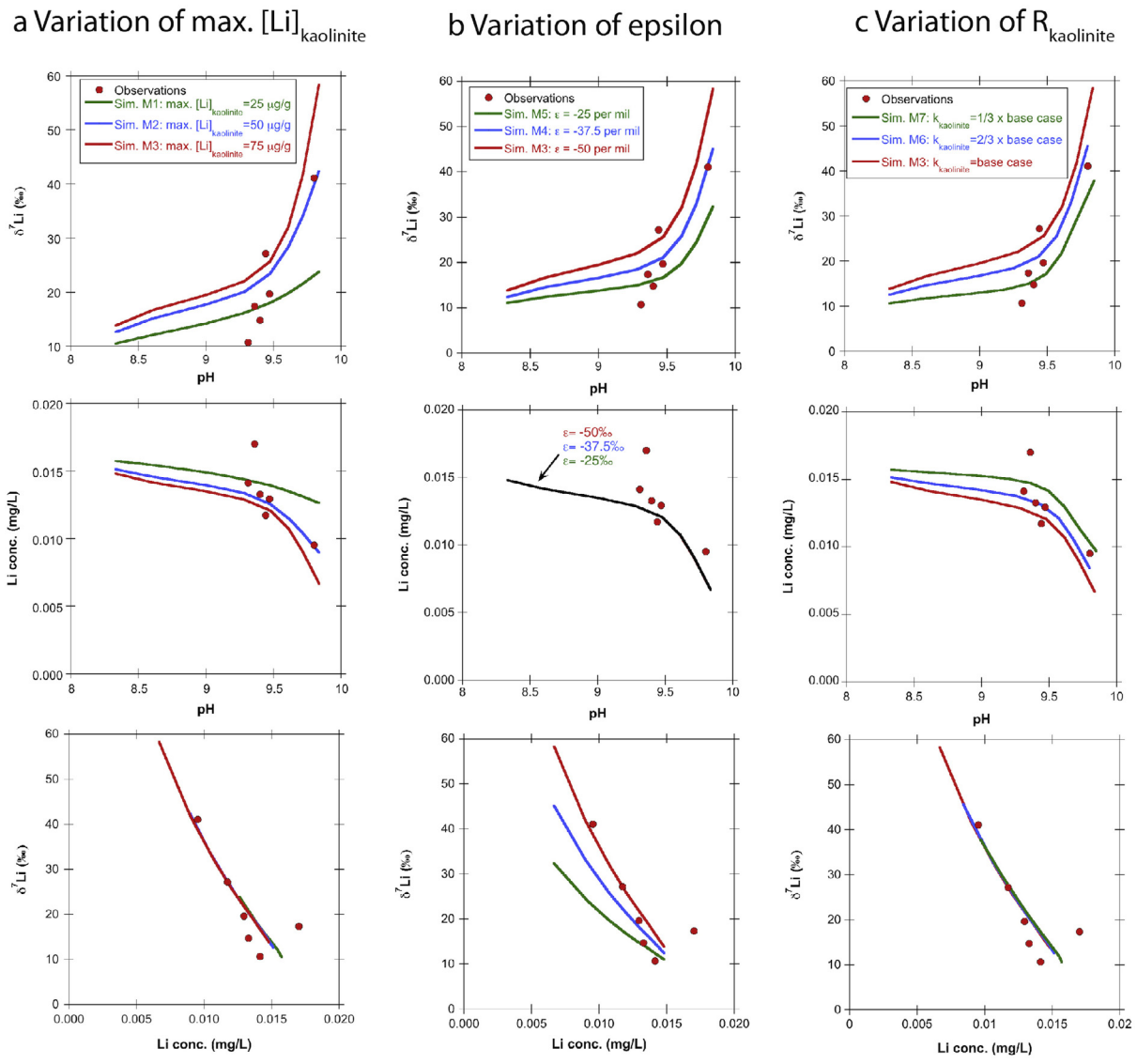

Fig. 9. Sensitivity analyses performed for the mixing scenario (Fig. 5b). (a) compares measured δ^7Li and [Li] with values computed as a function of the reaction progress along the model domain (i.e., as a function of pH/residence time) and for a variable maximum Li concentration in kaolinite. (b) Shows the same parameters as in (a), but for a varying Li isotope enrichment factor. In (c) the comparison between model and observations is shown for a varying kaolinite precipitation rate.

duced. The best match between modeled and measured data is obtained for a Li isotope enrichment factor of −50‰, a maximum Li concentration in kaolinite of 75 μg/g and a slightly reduced kaolinite precipitation rate constant (i.e., simulation M7; Fig. 9). A similar fit, however, is obtained when setting the δ^7Li value of the single point Li source to 1.7‰ while limiting the amount of Li in kaolinite to 50 μg/g (Fig. 10). The observation that different parameter combinations result in similar good fits demonstrates that the system is under-determined and that not all parameters affecting the Li system can be calibrated in a quantitative way. The observed negative correlation between δ^7Li and Li concentration, however, can only be approximated if the Li isotope enrichment factor is as high as −50‰ (Fig. 9). An enrichment factor of −50‰ also corresponds to that obtained from the Rayleigh-type model (Fig. 2d). This is an interesting observation because $\varepsilon = -50$‰ is clearly outside the range of Li isotope enrichment factor reported or inferred for secondary mineral precipitation (≈−10 to −30‰) (Zhang et al., 1998; Huh et al., 2001; Pistiner and Henderson, 2003; Kisakürek et al., 2005; Pogge von Strandmann et al., 2006, 2010; Vigier et al., 2008), although vigorous determination of the temperature-dependence of Li isotope fractionation involving mineral precipitation have so far only been reported for Li incorporation during smectite precipitation (Vigier et al., 2008). Since a contribution from diffusive Li isotope fractionation would yield an even higher intrinsic enrichment factor and an anthropogenic Li contamination is unlikely, the reason for the high apparent Li isotope enrichment factor is unclear and further research is required to unravel whether this is related to the slow flow rates and/or alkaline conditions of our system.

Overall, our model results reveal that the large δ^7Li variation observed in BuMigIII groundwater samples (10–41‰) are related to their pH range of 9.3–9.8. Over this pH window, the amount of coupled albite dissolution and kaolinite precipitation is at its maximum (Fig. 6). Consequently, a variation in reaction progress along the infiltration path (e.g., variable residence time) strongly affects the amount of Li-bearing kaolinite precipitation and thus the δ^7Li value. Simulation results also reveal that the observed Li isotope fractionation is independent of the origin of Li (ad-mixing of external groundwater, in-diffusion from porewater, dissolution of unidentified minerals) as long as this addition occurred before the infiltrating meteoric water evolved to its maximum kaolinite formation. This latter point further argues against a continuous addition of Li by diffusion from the porewater as there is no reason why such addition should stop at a certain point along the flowpath in the same rock unit.

6.3.4. Application to Bristner Granite groundwater

Based on the finding that the mixing scenario (Fig. 5b) can explain the δ^7Li variation observed in BuMigIII samples (Fig. 10), the same modeling approach was used to explore the sensitivity of δ^7Li on the Li concentration and to particularly test whether the absence of δ^7Li variation

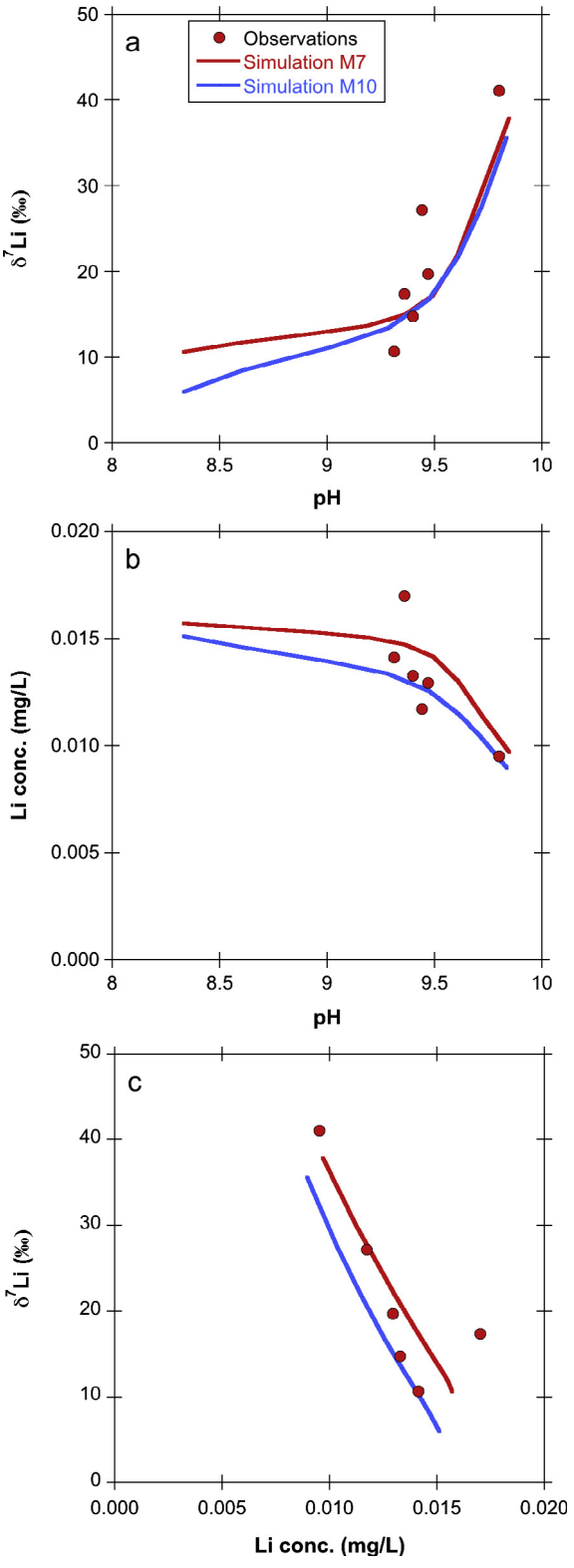

Fig. 10. Two parameter combinations that can well approximate the correlations between δ^7Li, Li and pH observed in the BuMigIII groundwater when running the model for a variable reaction progress (e.g., by varying the residence time).

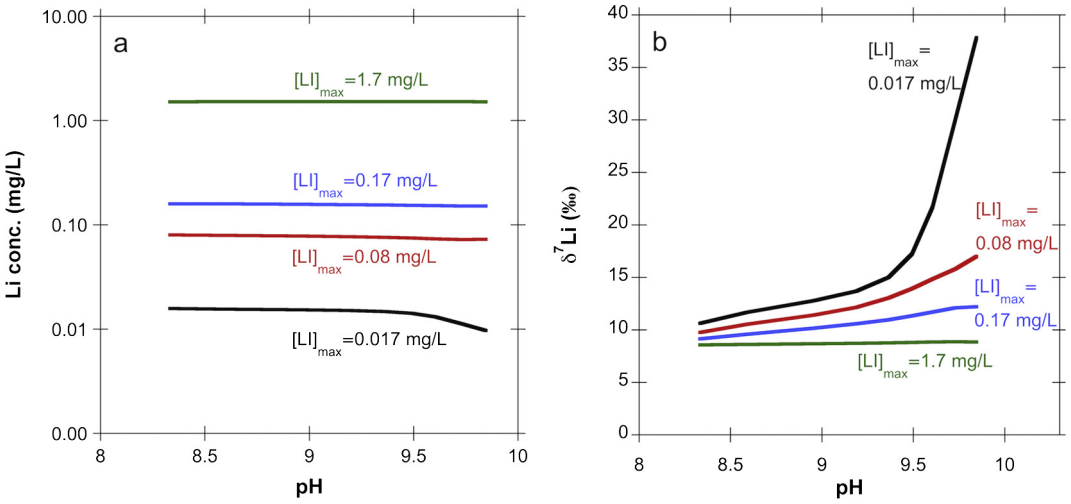

Fig. 11. Sensitivity of δ^7Li values on the aqueous Li concentration. Computed Li concentration (a) and δ^7Li (b) at the tunnel level are shown for a varying Li concentration of the simulated groundwater mixture (Fig. 5b) as a function of the reaction progress (i.e., pH).

in Bristner Granite groundwater is simply caused by its high Li concentration (Table 3). To do so, the mixing scenario (Fig. 5b) was run by setting the Li concentration of the simulated groundwater mixture to 0.017, 0.08, 0.17, and 1.7 mg/L, whereas the other parameters were kept constant at the values used in simulation M7 (Table 6). As can be seen from Fig. 11, the simulated δ^7Li values strongly depend on the Li concentration in the groundwater. At a Li concentration representing the range of Bristner Granite groundwater (1.7 mg/L), the predicted δ^7Li value does not differ from the value specified for the single point Li influx (δ^7Li = 8.7‰). A change in the δ^7Li values is only obtained if the Li concentration in the groundwater is lowered by a factor of 10 or more. The reason for these effects lies in the amount of Li that was allowed to be incorporated into precipitating kaolinite (75 μg/g). Accordingly, the ratio between Li that is incorporated into kaolinite and Li obtained from the single point influx decreases with increasing Li concentration in such influx. Because this ratio is also reflected in the δ^7Li value, the computed δ^7Li values become lower as the concentration of Li from the influx increases. The ability of the model to predict the absence of δ^7Li at high Li concentration supports the existence of a maximum amount of Li that can be structurally incorporated into precipitating kaolinite, which is in agreement with mineralogical and experimental findings (Tardy et al., 1972; Decarreau et al., 2012; Vigier and Goddéris, 2015). Such limitation further constitutes the likely reason for the low δ^7Li values and absence of δ^7Li variation observed for the Bristner Granite groundwater where the Li concentration is up to 500 times higher than in BuMigIII groundwater (Table 3).

7. IMPLICATIONS FOR USING δ^7LI AS A WATER–ROCK INTERACTION PROXY

The comparison between analytical and simulation results confirms that for a relatively simple hydrological system, aqueous δ^7Li is controlled by the cumulative amount of Li-bearing secondary mineral formation in relation to the Li release from primary mineral or other Li sources (Wanner et al., 2014; Pogge von Strandmann et al., 2016). Because secondary mineral formation is coupled to the dissolution of primary minerals, δ^7Li may be used in conjunction with major species concentrations to estimate mineral reaction rates using modeling approaches such as the one presented here. However, even for monolithological systems, an accurate quantification of these rates based on δ^7Li remains challenging. The first issue is that δ^7Li values are strongly affected by the reactivity of system (Fig. 9), which is controlled by the flow velocity (or the residence time, respectively), and the reactive surface areas. Secondly, dissolution and precipitation rates of silicate minerals are highly pH and temperature dependent (Fig. 6), demonstrating that the spatial temperature and pH distribution must be known to constrain reaction rates for a given flow system. Finally, our sensitivity analysis suggest that aqueous δ^7Li values are controlled by the amount of Li that can be taken up by secondary minerals, as well as the corresponding fractionation factor (Fig. 9). None of these parameters are fully characterized for the entire suite of Li bearing secondary minerals. For well-constrained hydrogeological systems, however, the listed challenges are likely resolved in the future once more experimental data will become available. Our model results based on actual data from a crystalline groundwater environment at elevated temperatures and including kaolinite precipitation indicate that δ^7Li values might be especially useful to better constrain the formation rate of secondary minerals for which kinetic data are still scarce (Yang and Steefel, 2008 and Refs. therein). Moreover, the strong δ^7Li variation observed at temperatures above those at the Earth's surface (Table 3) demonstrates the potential for using δ^7Li as water–rock interaction proxy at elevated temperatures. If the sensitivity of δ^7Li on the Li concentration, however, is as high as inferred from Fig. 11, the use of

δ^7Li to constrain mineral reaction rates is restricted to systems with low Li concentrations, which does usually not apply for hydro-geothermal systems (Chan et al., 1994; Millot and Négrel, 2007; Millot et al., 2010a; Sanjuan et al., 2014, 2016).

In contrast to well-defined systems, we suspect that quantifying continental silicate weathering rates through time based on the Cenozoic seawater δ^7Li record and the reconstructed riverine δ^7Li evolution (Misra and Froelich, 2012; Li and West, 2014; Vigier and Goddéris, 2015) will remain challenging. Because rivers are characterized by specific subsurface residence time distributions, the identified sensitivity of δ^7Li on the subsurface residence time implies that an accurate estimation requires capturing of subsurface residence time variations through time (e.g., discharge variations) under a changing climate and at an increasing tectonic activity (Misra and Froelich, 2012; Vigier and Goddéris, 2015). Another major challenge is that δ^7Li variations are likely controlled by the corresponding Li concentration such as inferred by our simulation results (Fig. 11) and likely manifested by the absence of δ^7Li variation in the Bristner Granite groundwater. This apparent sensitivity of δ^7Li on the Li concentration implies reconstructing the evolution of the continental Li flux distribution through time in addition to subsurface residence variations. In this context, first Cenozoic continental Li flux reconstructions have been presented recently (Li and West, 2014; Vigier and Goddéris, 2015).

8. SUMMARY AND CONCLUSIONS

The use of Li isotope measurements for tracking water–rock interaction in fractured crystalline aquifers at temperatures of up to 43 °C was assessed by performing Li isotope measurements on 17 groundwater samples collected during drilling of the new Gotthard rail base tunnel in Switzerland. A particular effort was made to match δ^7Li values as well as major species concentrations by reactive transport model simulations using the code TOUGHREACT V3. In doing so, the possibility of defining a maximum amount of a trace element that is incorporated into the structure of a precipitating mineral was added as a new capability to TOUGHREACT V3. The main conclusions from this study are:

1. The alteration of fracture surfaces by a circulating fluid may lead to a strong variation of δ^7Li values at temperatures of up to 43 °C. A strong δ^7Li variation, however, was only observed if the Li concentration was low (0.01–0.02 mg/L). For high Li concentrations on the order of 1–4 mg/L, no variation was observed suggesting that the amount of Li that can be incorporated into secondary minerals is limited and that the use of δ^7Li values as a proxy for water–rock interaction is restricted to low Li concentrations.
2. Li uptake by kaolinite precipitation or by the precipitation of other Al-bearing phases forms the key process to cause Li isotope fractionation in fractured crystalline aquifers characterized by a granitic mineralogical composition. Our data suggests that under slow flow conditions (<10 m/year), at temperatures <50 °C, and alkaline conditions (pH >9), this Li uptake is associated with a very large Li isotope fractionation factor ($\varepsilon \approx -50‰$).
3. For the samples with low Li concentrations, δ^7Li values are mainly controlled by the cumulative amount of kaolinite precipitation occurring along the flow path. Consequently, aqueous δ^7Li values are sensitive to fluid residence times, reactive fracture surface areas, and pH values, all controlling overall silicate mineral reaction rates.
4. Incorporating the fate of Li isotopes into fully coupled reactive transport model simulations allows a predictive understanding of measured Li isotope ratios. For simple and well-defined systems with known residence times and low Li concentrations, δ^7Li values may help to quantify mineral reaction rates and associated parameters (e.g., reactive surface area). An accurate quantification, however, currently suffers from the lack of thermodynamic data such as the temperature dependent amount of Li that can be incorporated into secondary minerals as well as corresponding fractionation factors.
5. In crystalline aquifers with high Li concentrations such as in the Bristner Granite, groundwater Li is likely inherited from an ancient hydrothermal fluid still residing in the pore space of the intact rock matrix.

ACKNOWLEDGMENTS

This work is dedicated to H.-J. (Jöggu) Ziegler, head geologist of the Gotthard rail base tunnel who brought CW first into contact with the intriguing water samples from the Gotthard rail base tunnel and who passed away on the same day CW started to look for available samples. Research in geothermal energy at the University of Bern is supported by the Swiss Competence Center for Energy Research–Supply of Electricity (SCCER-SoE). PPvS and Li isotope analyses were funded by NERC Advanced Research Fellowship NE/I020571/2. Finally, we thank the associated editor, Horst Marschall, and 4 anonymous reviewers for their constructive comments that greatly improved the manuscript.

APPENDIX A. SUPPLEMENTARY DATA

Supplementary data associated with this article can be found, in the online version, at http://dx.doi.org/10.1016/j.gca.2016.11.003.

REFERENCES

Abrecht J. (1994) Geologic units of the Aarmassif and their pre-Alpine rock associations: a critical review. *Schweiz. Mineral. Petrogr. Mitt.* **74**, 5–27.

Alt-Epping P., Diamond L. W., Häring M. O., Ladner F. and Meier D. B. (2013) Prediction of water–rock interaction and porosity evolution in a granitoid-hosted enhanced geothermal system, using constraints from the 5 km Basel-1 well. *Appl. Geochem.* **38**, 121–133.

Berner R. A., Lasaga A. C. and Garrels R. M. (1983) The carbonate-silicate geochemical cycle and its effect on atmospheric carbon-dioxide over the past 100 million years. *Am. J. Sci.* **283**, 641–683.

Bouchez J., Von Blanckenburg F. and Schuessler J. A. (2013) Modeling novel stable isotope ratios in the weathering zone. *Am. J. Sci.* **313**, 267–308.

Bourg I. C. and Sposito G. (2007) Molecular dynamics simulations of kinetic isotope fractionation during the diffusion of ionic species in liquid water. *Geochim. Cosmochim. Acta* **71**, 5583–5589.

Brown S. T., Kennedy B. M., DePaolo D. J., Hurwitz S. and Evans W. C. (2013) Ca, Sr, O and D isotope approach to defining the chemical evolution of hydrothermal fluids: example from Long Valley, CA, USA. *Geochim. Cosmochim. Acta* **122**, 209–225.

Bucher K., Stober I. and Seelig U. (2012) Water deep inside the mountains: unique water samples from the Gotthard rail base tunnel, Switzerland. *Chem. Geol.* **334**, 240–253.

Caine J. S. and Tomusiak S. R. A. (2003) Brittle structures and their role in controlling porosity and permeability in a complex Precambrian crystalline-rock aquifer system in the Colorado Rocky Mountain front range. *Geol. Soc. Am. Bull.* **115**, 1410–1424.

Chan L.-H., Edmond J. M. and Thompson G. (1993) A lithium isotope study of hot springs and metabasalts from Mid-Ocean Ridge Hydrothermal Systems. *J. Geophys. Res.: Solid Earth* **98**, 9653–9659.

Chan L.-H., Gieskes J. M., Chen-Feng Y. and Edmond J. M. (1994) Lithium isotope geochemistry of sediments and hydrothermal fluids of the Guaymas Basin, Gulf of California. *Geochim. Cosmochim. Acta* **58**, 4443–4454.

Decarreau A., Vigier N., Pálková H., Petit S., Vieillard P. and Fontaine C. (2012) Partitioning of lithium between smectite and solution: an experimental approach. *Geochim. Cosmochim. Acta* **85**, 314–325.

Dellinger M., Gaillardet J., Bouchez J., Calmels D., Louvat P., Dosseto A., Gorge C., Alanoca L. and Maurice L. (2015) Riverine Li isotope fractionation in the Amazon River basin controlled by the weathering regimes. *Geochim. Cosmochim. Acta* **164**, 71–93.

DePaolo D. J. (2006) Isotopic effects in fracture-dominated reactive fluid–rock systems. *Geochim. Cosmochim. Acta* **70**, 1077–1096.

Devidal J.-L., Dandurand J.-L. and Gout R. (1996) Gibbs free energy of formation of kaolinite from solubility measurement in basic solution between 60 and 170 °C. *Geochim. Cosmochim. Acta* **60**, 553–564.

Francois L. M. and Goddéris Y. (1998) Isotopic constraints on the Cenozoic evolution of the carbon cycle. *Chem. Geol.* **145**, 177–212.

Gimeno M. J., Auqué L. F., Acero P. and Gómez J. B. (2014) Hydrogeochemical characterisation and modelling of groundwaters in a potential geological repository for spent nuclear fuel in crystalline rocks (Laxemar, Sweden). *Appl. Geochem.* **45**, 50–71.

Gislason S. R., Arnorsson S. and Armannsson H. (1996) Chemical weathering of basalt in Southwest Iceland; effects of runoff, age of rocks and vegetative/glacial cover. *Am. J. Sci.* **296**, 837–907.

Grimaud D., Beaucaire C. and Michard G. (1990) Modelling of the evolution of ground waters in a granite system at low temperature: the Stripa ground waters, Sweden. *Appl. Geochem.* **5**, 515–525.

Guillong M., Meier D. L., Allan M. M., Heinrich C. A. and Yardley B. W. D. (2008) SILLS: A MATLAB-based program for the reduction of laser ablation ICP-MS data of homogeneous materials and inclusions. In *Laser Ablation ICP-MS in the Earth Sciences: Current Practices and Outstanding Issues* (ed. P. Sylvester). pp. 328–333.

Henchiri S., Clergue C., Dellinger M., Gaillardet J., Louvat P. and Bouchez J. (2014) The influence of hydrothermal activity on the Li isotopic signature of rivers draining volcanic areas. *Proc. Earth Planet. Sci.* **10**, 223–230.

Huh Y., Chan L. H., Zhang L. and Edmond J. M. (1998) Lithium and its isotopes in major world rivers: implications for weathering and the oceanic budget. *Geochim. Cosmochim. Acta* **62**, 2039–2051.

Huh Y., Chan L. H. and Edmond J. M. (2001) Lithium isotopes as a probe of weathering processes: Orinoco River. *Earth Planet. Sci. Lett.* **194**, 189–199.

Huh Y., Chan L. H. and Chadwick O. A. (2004) Behavior of lithium and its isotopes during weathering of Hawaiian basalt. *Geochem. Geophys. Geosyst.* **5**.

Kisakürek B., James R. H. and Harris N. B. W. (2005) Li and δ^7Li in Himalayan rivers: proxies for silicate weathering? *Earth Planet. Sci. Lett.* **237**, 387–401.

Kittrick J. A. (1966) Free energy of formation of kaolinite from solubility measurements. *Am. Mineral.* **51**, 1457.

Labhart T. P. (1999) Aarmassiv, Gotthardmassiv und Tavetscher Zwischenmassiv: Aufbau und Entstehungsgeschichte. In *Symposium Geologie Alptransit, Zürich* (eds. S. Loew and R. Wyss). Balkema, Rotterdam, pp. 31–43.

Lasaga A. C. (1984) Chemical kinetics of water-rock interactions. *J. Geophys. Res.* **89**, 4009–4025.

Lemarchand E., Chabaux F., Vigier N., Millot R. and Pierret M.-C. (2010) Lithium isotope systematics in a forested granitic catchment (Strengbach, Vosges Mountains, France). *Geochim. Cosmochim. Acta* **74**, 4612–4628.

Li G. and West A. J. (2014) Evolution of Cenozoic seawater lithium isotopes: coupling of global denudation regime and shifting seawater sinks. *Earth Planet. Sci. Lett.* **401**, 284–293.

Liu X.-M., Wanner C., Rudnick R. L. and McDonough W. F. (2015) Processes controlling δ^7Li in rivers illuminated by study of streams and groundwaters draining basalts. *Earth Planet. Sci. Lett.* **409**, 212–224.

MacQuarrie K. T. B. and Mayer K. U. (2005) Reactive transport modeling in fractured rock: a state-of-the-science review. *Earth-Sci. Rev.* **72**, 189–227.

Marschall H. R., Pogge von Strandmann P. A. E., Seitz H.-M., Elliott T. and Niu Y. (2007) The lithium isotopic composition of orogenic eclogites and deep subducted slabs. *Earth Planet. Sci. Lett.* **262**, 563–580.

Masset O. and Loew S. (2013) Quantitative hydraulic analysis of pre-drillings and inflows to the Gotthard Base Tunnel (Sedrun Lot, Switzerland). *Eng. Geol.* **164**, 50–66.

May H. M., Klnniburgh D. G., Helmke P. A. and Jackson M. L. (1986) Aqueous dissolution, solubilities and thermodynamic stabilities of common aluminosilicate clay minerals: kaolinite and smectites. *Geochim. Cosmochim. Acta* **50**, 1667–1677.

Mazurek M., Jakob A. and Bossart P. (2003) Solute transport in crystalline rocks at Äspö—I: geological basis and model calibration. *J. Contam. Hydrol.* **61**, 157–174.

Michard G., Pearson, Jr., F. J. and Gautschi A. (1996) Chemical evolution of waters during long term interaction with granitic rocks in northern Switzerland. *Appl. Geochem.* **11**, 757–774.

Millot R. and Négrel P. (2007) Multi-isotopic tracing (δ^7Li, δ^{11}B, ^{87}Sr/^{86}Sr) and chemical geothermometry: evidence from hydrogeothermal systems in France. *Chem. Geol.* **244**, 664–678.

Millot R., Scaillet B. and Sanjuan B. (2010a) Lithium isotopes in island arc geothermal systems: Guadeloupe, Martinique (French West Indies) and experimental approach. *Geochim. Cosmochim. Acta* **74**, 1852–1871.

Millot R., Vigier N. and Gaillardet J. (2010b) Behaviour of lithium and its isotopes during weathering in the Mackenzie Basin, Canada. *Geochim. Cosmochim. Acta* **74**, 3897–3912.

Misra S. and Froelich P. N. (2012) Lithium isotope history of Cenozoic seawater: changes in silicate weathering and reverse weathering. *Science* **335**, 818–823.

Molinero J., Raposo J. R., Galíndez J. M., Arcos D. and Guimerá J. (2008) Coupled hydrogeological and reactive transport modelling of the Simpevarp area (Sweden). *Appl. Geochem.* **23**, 1957–1981.

Nagy K. L., Blum A. E. and Lasaga A. C. (1991) Dissolution and precipitation kinetics of kaolinite at 80 degrees C and pH 3; the dependence on solution saturation state. *Am. J. Sci.* **291**, 649–686.

Nordstrom D. K., Ball J. W., Donahoe R. J. and Whittemore D. (1989) Groundwater chemistry and water–rock interactions at Stripa. *Geochim. Cosmochim. Acta* **53**, 1727–1740.

Palandri J. L. and Kharaka Y. K. (2004) A compilation of rate parameters of water-mineral interaction kinetics for application to geochemical modeling. US Geological Survey.

Pettke T., Oberli F., Audétat A., Guillong M., Simon A. C., Hanley J. J. and Klemm L. M. (2012) Recent developments in element concentration and isotope ratio analysis of individual fluid inclusions by laser ablation single and multiple collector ICP-MS. *Ore Geol. Rev.* **44**, 10–38.

Pistiner J. S. and Henderson G. M. (2003) Lithium-isotope fractionation during continental weathering processes. *Earth Planet. Sci. Lett.* **214**, 327–339.

Pogge von Strandmann P. A. E., Burton K. W., James R. H., van Calsteren P., Gíslason S. R. and Mokadem F. (2006) Riverine behaviour of uranium and lithium isotopes in an actively glaciated basaltic terrain. *Earth Planet. Sci. Lett.* **251**, 134–147.

Pogge von Strandmann P. A. E., Burton K. W., James R. H., van Calsteren P. and Gislason S. R. (2010) Assessing the role of climate on uranium and lithium isotope behaviour in rivers draining a basaltic terrain. *Chem. Geol.* **270**, 227–239.

Pogge von Strandmann P. A. E., Elliott T., Marschall H. R., Coath C., Lai Y.-J., Jeffcoate A. B. and Ionov D. A. (2011) Variations of Li and Mg isotope ratios in bulk chondrites and mantle xenoliths. *Geochim. Cosmochim. Acta* **75**, 5247–5268.

Pogge von Strandmann P. A. E., Porcelli D., James R. H., van Calsteren P., Schaefer B., Cartwright I., Reynolds B. C. and Burton K. W. (2014) Chemical weathering processes in the Great Artesian Basin: evidence from lithium and silicon isotopes. *Earth Planet. Sci. Lett.* **406**, 24–36.

Pogge von Strandmann P. A. E. and Henderson G. M. (2015) The Li isotope response to mountain uplift. *Geology* **43**, 67–70.

Pogge von Strandmann P. A. E., Burton K. W., Opfergelt S., Eiríksdóttir E. S., Murphy M. J., Einarsson A. and Gislason S. R. (2016) The effect of hydrothermal spring weathering processes and primary productivity on lithium isotopes: Lake Myvatn, Iceland. *Chem. Geol.* **445**, 4–13.

Polzer W. L. and Hem J. D. (1965) The dissolution of kaolinite. *J. Geophys. Res.* **70**, 6233–6240.

Reed M. and Palandri J. L. (2006) *SOLTHERM.H06, a Database of Equilibrium Constants for Minerals and Aqueous Species.* Available from the authors, University of Oregon, Eugene, USA.

Reesman A. L. and Keller W. D. (1968) Aqueous solubility studies of high-alumina and clay minerals. *Am. Mineral.* **53**, 929.

Richter F. M., Mendybaev R. A., Christensen J. N., Hutcheon I. D., Williams R. W., Sturchio N. C. and Beloso, Jr, A. D. (2006) Kinetic isotopic fractionation during diffusion of ionic species in water. *Geochim. Cosmochim. Acta* **70**, 277–289.

Sanjuan B., Millot R., Ásmundsson R., Brach M. and Giroud N. (2014) Use of two new Na/Li geothermometric relationships for geothermal fluids in volcanic environments. *Chem. Geol.* **389**, 60–81.

Sanjuan B., Millot R., Innocent C., Dezayes C., Scheiber J. and Brach M. (2016) Major geochemical characteristics of geothermal brines from the Upper Rhine Graben granitic basement with constraints on temperature and circulation. *Chem. Geol.* **428**, 27–47.

Schaltegger U. (1994) Unravelling the pre-Mesozoic history of the Aar and Gotthard massifs (Central Alps) by isotopic dating—a review. *Schweiz. Mineral. Petrogr. Mitt.* **74**, 41–51.

Schwertmann U. (1988) Occurrence and formation of iron oxides in various pedoenvironments. In *Iron in Soils and Clay Minerals* (eds. J. W. Stucki, B. A. Goodman and U. Schwertmann). Springer, Netherlands, Dordrecht, pp. 267–308.

Seelig U. and Bucher K. (2010) Halogens in water from the crystalline basement of the Gotthard rail base tunnel (central Alps). *Geochim. Cosmochim. Acta* **74**, 2581–2595.

Singleton M. J., Sonnenthal E. L., Conrad M. E., DePaolo D. J. and Gee G. W. (2005) Multiphase reactive transport modeling of seasonal infiltration events and stable isotope fractionation in unsaturated zone pore water and vapor at the Hanford site. *Vadose Zone J.* **3**, 775–785.

Sonnenthal E. L., Spycher N., Apps J. A. and Simmons A. (1998) Thermo-hydro-chemical predictive analysis for the drift-scale heater test. Lawrence Berkeley National Laboratory Report SPY289M4.

Sonnenthal E. L., Ito A., Spycher N., Yui M., Apps J. A., Sugita Y., Conrad M. E. and Kawakami S. (2005) Approaches to modeling coupled thermal, hydrological and chemical processes in the Drift Scale Heater Test at Yucca Mountain. *Int. J. Rock Mech. Min. Sci.* **42**, 698–719.

Spandler C., Pettke T. and Rubatto D. (2011) Internal and external fluid sources for eclogite-facies veins in the Monviso meta-ophiolite, Western Alps: implications for fluid flow in subduction zones. *J. Petrol.* **52**, 1207–1236.

Steefel C. I., Appelo C. A. J., Arora B., Jacques D., Kalbacher T., Kolditz O., Lagneau V., Lichtner P. C., Mayer K. U., Meussen H., Molins S., Moulton D., Parkhurst D. L., Shao H., Simunek J., Spycher N., Yabusaki S. and Yeh G. T. (2015) Reactive transport codes for subsurface environmental simulation. *Comput. Geosci.* **19**, 445–478.

Stober I. and Bucher K. (2015) Hydraulic conductivity of fractured upper crust: insights from hydraulic tests in boreholes and fluid-rock interaction in crystalline basement rocks. *Geofluids* **15**, 161–178.

Tardy Y., Trauth N. and Krempp G. (1972) Lithium in clay-minerals of sediments and soils. *Geochim. Cosmochim. Acta* **36**, 397.

Teng F.-Z., Rudnick R. L., McDonough W. F. and Wu F.-Y. (2009) Lithium isotopic systematics of A-type granites and their mafic enclaves: further constraints on the Li isotopic composition of the continental crust. *Chem. Geol.* **262**, 370–379.

Trotignon L., Beaucaire C., Louvat D. and Jean-François A. (1999) Equilibrium geochemical modelling of Äspö groundwaters: a sensitivity study of thermodynamic equilibrium constants. *Appl. Geochem.* **14**, 907–916.

Verney-Carron A., Vigier N., Millot R. and Hardarson B. S. (2015) Lithium isotopes in hydrothermally altered basalts from Hengill (SW Iceland). *Earth Planet. Sci. Lett.* **411**, 62–71.

Vigier N., Decarreau A., Millot R., Carignan J., Petit S. and France-Lanord C. (2008) Quantifying Li isotope fractionation during smectite formation and implications for the Li cycle. *Geochim. Cosmochim. Acta* **72**, 780–792.

Vigier N., Gislason S. R., Burton K. W., Millot R. and Mokadem F. (2009) The relationship between riverine lithium isotope composition and silicate weathering rates in Iceland. *Earth Planet. Sci. Lett.* **287**, 434–441.

Vigier N. and Goddéris Y. (2015) A new approach for modeling Cenozoic oceanic lithium isotope paleo-variations: the key role of climate. *Clim. Past* **11**, 635–645.

Waber H. N., Gimmi T. and Smellie J. A. T. (2012) Reconstruction of palaeoinfiltration during the Holocene using porewater data (Laxemar, Sweden). *Geochim. Cosmochim. Acta* **94**, 109–127.

Wanner C. and Sonnenthal E. L. (2013) Assessing the control on the effective kinetic Cr isotope fractionation factor: a reactive transport modeling approach. *Chem. Geol.* **337**, 88–98.

Wanner C., Sonnenthal E. L. and Liu X.-M. (2014) Seawater d^7Li a direct proxy for global CO_2 consumption by continental silicate weathering? *Chem. Geol.* **381**, 154–167.

Wanner C., Druhan J., Amos R., Alt-Epping P. and Steefel C. (2015) Benchmarking the simulation of Cr isotope fractionation. *Comput. Geosci.* **19**, 497–521.

Wimpenny J., Gislason S. R., James R. H., Gannoun A., Pogge Von Strandmann P. A. E. and Burton K. W. (2010) The behaviour of Li and Mg isotopes during primary phase dissolution and secondary mineral formation in basalt. *Geochim. Cosmochim. Acta* **74**, 5259–5279.

Wolery T. J. (1992) *EQ3/6: Software Package for Geochemical Modeling of Aqueous Systems: Package Overview and Installation Guide (Version 7.0)*. Livermore, California.

Wunder B., Meixner A., Romer R. and Heinrich W. (2006) Temperature-dependent isotopic fractionation of lithium between clinopyroxene and high-pressure hydrous fluids. *Contrib. Mineral. Petrol.* **151**, 112–120.

Xu T., Sonnenthal E. L., Spycher N. and Zheng L. (2014) TOUGHREACT V3.0-OMP Reference Manual: A Parallel Simulation Program for Non-Isothermal Multiphase Geochemical Reactive Transport. *LBNL Manual* <http://esd.lbl.gov/FILES/research/projects/tough/documentation/TOUGHREACT_V3-OMP_RefManual.pdf>.

Yang L. and Steefel C. I. (2008) Kaolinite dissolution and precipitation kinetics at 22 °C and pH 4. *Geochim. Cosmochim. Acta* **72**, 99–116.

Zhang L., Chan L.-H. and Gieskes J. M. (1998) Lithium isotope geochemistry of pore waters from ocean drilling program Sites 918 and 919, Irminger Basin. *Geochim. Cosmochim. Acta* **62**, 2437–2450.

Associate editor: Horst R. Marschall

6. SUMMARY AND CONCLUSIONS

Geological and geochemical information collected within the Earth's crust and on its surface often represent a series of coupled thermal-, hydraulic-, and chemical processes occurring in porous media at variable spatio-temporal scales. Along with the large increase in computational power, over the past 30 years the field of reactive transport modeling (RTM) has mastered the mechanistic simulation of non-isothermal geochemical and biogeochemical processes as well as their coupling to flow and transport rates. As a consequence, RTM has become an essential research approach for the Earth Sciences.

Conducting RTM is especially useful for studying and solving environmental challenges such as those implied by the UN Sustainable Development Goals 6 (Clean Water and Sanitation), 7 (Affordable and Clean Energy), and 13 (Climate Action). These Goals are linked to the Earth Sciences because they address processes occurring in strongly coupled systems located within or at the surface of the Earth.

This *Habilitationsschrift* describes the contribution of the Author in advancing the field of reactive transport modeling by presenting nine of the Author's publications on various RTM applications related to the topics of groundwater contamination, geothermal energy and silicate weathering. The main implications for using RTM in environmental geochemistry and thereby contributing to meeting the above-mentioned Sustainable Development Goals are as follows:

- The inclusion of stable isotopes into RTM simulations may provide fundamental new insights into the governing processes controlling stable isotope ratios in environmental samples. Therefore, the use of isotope ratios as proxies to identify sources or quantify processes strongly benefits from the application of RTM. Examples addressed in this *Habilitationsschrift* include the integration of Cr and U isotopes in RTM simulations to track and quantify Cr(VI) and U(VI) reduction, and the inclusion of Li isotopes to assess their use as a proxy for silicate weathering.
- Conducting RTM simulations generates numerous synthetic data that can be used to evaluate other numerical tools. For instance, using the output from RTM simulations for applying various solute geothermometry methods allowed assessing and improving their performance in estimating deep reservoir temperatures.
- Reactive transport modeling serves as a powerful tool for the integrated interpretation of multiple datasets obtained from field and laboratory studies. Applied to orogenic geothermal systems, such an integrative approach permitted estimation of the subsurface thermal anomaly of a particular system in the Swiss Alps. Moreover, it allowed identification of favorable settings for the exploitation of such systems for geothermal power production, thereby demonstrating that RTM constitutes an important exploration tool for geothermal systems.
- Owing to the strong increase in computational speed and the availability of more than 10 state-of-the-art RTM codes, the applicability of RTM simulations is mainly limited by the available thermodynamic and kinetic data, and by the existence of an extended geochemical, biogeochemical, hydrological, and geophysical site-characterization required to constrain and calibrate such simulations. Another challenge relates to numerically coupling the large range of length and space scales relevant to environmental geochemistry (Fig. 1-4).
- These limitations represent a major challenge for RTM applications aiming to accurately predict the future behavior of engineered interventions such as groundwater remediation, CO_2 sequestration or nuclear waste repositories. Therefore, the main strengths of RTM lies in the identification of the governing processes controlling coupled systems and in its capacity to integrate multiple datasets as discussed above.

- Based on the usefulness of RTM in unraveling coupled processes, additional disciplines will likely apply RTM in the future. Potential candidates include rhizosphere dynamics, watershed hydrogeochemistry, as well as climate change and biogeochemical cycling (Fig. 1-4). Thus, there are numerous opportunities for both new code development and for innovative laboratory as well as field studies to constrain and calibrate future RTM applications. Eventually, such activities will address additional environmental challenges and further contribute to meeting the listed Sustainable Development Goals.

ACKNOWLEDGMENTS

The contributions presented in this *Habilitationsschrift* reflect the fruitful collaboration with many colleagues from different organizations all over the world. I would like to thank all the 24 Co-authors for contributing to the nine *Habilitation*. Moreover, I highly appreciate the support from great mentors I received over the past 15 years. In alphabetical order these are Larryn Diamond, Urs Eggenberger, Urs Mäder, Eric Sonnenthal, Nicolas Spycher, and Carl Steefel. Insightful comments by Larryn, Diamond, Philipp Wanner and Loic Peiffer on an early version of this *Habilitationsschrift* are highly appreciated. Last but not least, I am very grateful for the great support from my wife Luca and my two children Nora and Joel.